

Proceedings of the workshop  
on  
Technical Aspects of a  
Very Large Volume Neutrino  
Telescope in the Mediterranean  
Sea



Amsterdam, 5-8 October, 2003

NIKHEF

## PROCEEDINGS ON THE WEB

<http://www.vlvnt.nl/proceedings>

## PHOTOGRAPH

Back cover : Credit Photo, Jan Koopstra, NIKHEF, Amsterdam, The Netherlands

## PROCEEDINGS EDITOR

E. de Wolf, NIKHEF, Amsterdam, The Netherlands

### **Additional Copies**

Requests for additional copies should be addressed to:

E. de Wolf, NIKHEF, Kruislaan 409, 1098 SJ Amsterdam, The Netherlands, email:

[e.dewolf@nikhef.nl](mailto:e.dewolf@nikhef.nl)

## ABSTRACT

The purpose of the workshop was to investigate detection techniques, design aspects and electronic and readout solutions for a future Very Large Volume water Cherenkov Neutrino Telescope (VLVvT) in the Mediterranean Sea. The workshop concentrated on techniques that are expected to be available in due time and assessed their feasibility, their optimisation for the VLVvT, their cost effectiveness and their R&D needs for the VLVvT.



## Scientific Advisory Committee

J. Carr	CPPM, France
R. Cashmore	CERN
G.V. Domogatsky	RAS, Russia
J.J. Engelen	NIKHEF, The Netherlands
E. Fernandez	IFAE, Spain
R. Klanner	DESY, Germany
J. Learned	University of Hawaii, USA
E. Migneco	INFN, Italy
L. Resvanis	NESTOR Institute, Greece
A. Watson	University of Leeds, UK



# Table of contents

<b>Organisation</b> .....	iii
<b>Overview</b> .....	v
<b>Industrial Exhibition</b> .....	vii
<b>Sponsorship</b> .....	vii

## INVITED PLENARY TALKS

<b>J. Carr</b> , The deep-sea neutrino telescope ANTARES.....	1
<b>E. Migneco</b> , The NEMO project .....	5
<b>S. E. Tzamarias</b> , NESTOR First Results .....	11
<b>E. Bernardini</b> , Results from the AMANDA Neutrino Telescope .....	17
<b>C. Spiering</b> , The IceCube Project .....	21
<b>C. Spiering</b> , The Baikal Neutrino Telescope: Results, Plans, Lessons .....	26
<b>J. A. Templon</b> , Grids and VLVvT Data Processing .....	30
<b>L. Gualdesi</b> , Design and testing of equipment for deep-sea research .....	34
<b>I. G. Priede</b> , Bioluminescence in the deep-sea: potential for interaction with sub sea detector arrays .....	41

## SUMMARY TALKS

<b>P. Vernin</b> , Summary of the Electrical Power Session .....	45
<b>M. Taiuti</b> , Summary of the Photodetection Parallel Session.....	46
<b>C. Spiering</b> , Summary of Sessions on Design Parameters, Simulation and Reconstruction .....	53
<b>G. Hallewell</b> , Summary of Architecture Parallel Session .....	67
<b>M. Musumeci</b> , Mechanics Parallel Session, .....	73
<b>E.G. Anassontzis</b> , Sea Operations for a km <sup>3</sup> neutrino telescope.....	77
<b>M. Sedita</b> , VLVvT Installation and Maintenance of the submarine network.....	81
<b>J..J. Hernandez-Rey</b> , Summary of Calibration Group .....	83
<b>M. de Jong</b> , Summary Readout-Electronics .....	85
<b>U. Katz</b> , Concluding Remarks .....	87

## PARALLEL WORKING GROUPS

### Design Parameters

<b>G. Riccobene</b> , Overview over Mediterranean Optical Properties, .....	93
<b>Zh.-A. Dzhilkibaev</b> , Comparison of OM Responses at Different Sites.....	99
<b>D. Zaborov</b> , Comparison of different KM3 designs using Antares tools .....	104
<b>J. Brunner</b> , Antares simulation tools.....	109
<b>P. Sapienza</b> , Status of simulations in NEMO .....	114
<b>A. Leisos</b> , Nestor Simulation Tools and Methods.....	119
<b>A. Tsirigotis</b> , Reconstruction, Background Rejection, Tools and Methods (NESTOR) ....	124
<b>Ch. H. Wiebusch</b> , Muon Track Reconstruction and Data Selection Techniques in AMANDA.....	129

## **ARCHITECTURE, SEA OPERATIONS, ELECTRICAL POWER SYSTEMS, MECHANICS**

<b>S. S. Thumbeck</b> , Subsea Electric and Optic Connections Allowing for Flexible System Architecture .....	135
<b>M. Sedita</b> , Consideration on the Installation, Management and Maintenance of a the Submarine Network for the km3 Telescope.....	139
<b>R. Cocimano</b> , A Proposal for the NEMO Power System, the NEMO Phase 1 Power System and Power Control System .....	143
<b>E. Heine</b> , Power Distribution.....	148
<b>M. S. Musumeci</b> , Mechanical Structures for a Deep Sea Water Neutrino Detector.....	153
<b>R. Occhipinti</b> , Design of the junction boxes for Nemo-phase1 .....	157
<b>A. Kappes</b> , Plastic Encapsulation of Electronics .....	159
<b>F. Ameli</b> , NEMO Phase 1 data transmission: considerations toward KM3.....	160

## **PHOTO DETECTION**

<b>S. Reito</b> , Facility apparatus for O.M. characterization.....	165
<b>A. Tsirigotis</b> , The NESTOR Optical Module.....	168
<b>M. Giunta</b> , The HPD Detector .....	173
<b>A. Bersani</b> , Development of Large Effective Area and Direction Sensitive Photodetector	176
<b>G. Anton</b> , A new concept of an OM based on wave length shifting fibers and photomultipliers.....	181

## **CALIBRATION, READOUT and DATA TRANSMISSION, ELECTRONICS**

<b>M. Circella</b> , Timing calibration in NEMO .....	183
<b>J. J. Hernandez-Rey</b> , Review of the Time Calibration Systems of ANTARES.....	187
<b>J.J. Hogenbirk</b> , Wavelength Division Multiplexing (WDM).....	193
<b>F. Ameli</b> , Synchronous Data Transmission Protocol for NEMO experiment .....	196
<b>D. Lo Presti</b> , Optical Module VLSI Full Custom Front-End Electronics .....	201
<b>C. A. Nicolau</b> , A 200 MHz FPGA-based PMT acquisition electronics for NEMO experiment .....	205
<b>P.K.A. de Witt Huberts</b> , A Conceptual Design of a Km3 Neutrino Observatory .....	209

<b>List of Participants</b> .....	215
-----------------------------------	-----



# Organisation

The workshop on Technical Aspects of a Neutrino Telescope in the Mediterranean Sea was organised by NIKHEF, The Netherlands' National Institute for Nuclear Physics and Particle Physics in Amsterdam. The workshop was held on 5-8 October, 2003 at NIKHEF, Amsterdam.

## Local Organisation Committee

E. de Wolf (chair)	NIKHEF
A. van Rijn	NIKHEF
U. Katz	University of Erlangen

## Scientific Program Committee

F. Ameli	INFN-Roma
E. Anassontzis	University of Athens
J. Brunner	CPPM
B. Dinkespiler	CPPM
G. Hallewell	CPPM
J.J. Hernandez-Rey	IFIC-Valencia
M. de Jong	NIKHEF
M. Musumeci	INFN-LNS
R. Papaleo	INFN-LNS
P. Piatelli	INFN-LNS
M. Sedita	INFN-LNS
I. Siotis	NCSR Demokritos
C. Spiering	DESY-Zeuthen
M. Taiuti	INFN
L. Thompson	University of Sheffield
S. Tzamarias	Hellenic Open University
P. Vernin	CEA-Saclay

## Workshop Secretariat

C. Doest	NIKHEF
----------	--------



# Overview

The program of the workshop included both invited plenary talks and parallel working groups. The focus of the workshop was on technical aspects of a deep sea water Cherenkov neutrino telescope: Design Parameters, Architecture, Sea Operations, Electrical Power Systems and Mechanics, Photo Detection, Calibration, Readout and Data Transmission, Electronics

## PLENARY SESSIONS

### P1 Chaired by P. Kooijman:

- **Welcome** by K. Gaemers, NIKHEF, Amsterdam, The Netherlands
- **ANTARES**, by J. Carr, CPPM, Marseille, France
- **The NEMO Project**, by E. Migneco, LNS-INFN, Catania, Italy
- **NESTOR**, by S.E. Tzamarias, Hellenic Open University, Patras, Greece
- **AMANDA – Status and Results**, by E. Bernardini, DESY-Zeuthen, Germany
- **IceCube**, by C. Spiering, DESY-Zeuthen, Germany
- **ApPEC**, by J.J. Engelen, NIKHEF, Amsterdam, The Netherlands

### P2 Chaired by P. Kooijman:

- **GRIDs: Why and How (you may use them)**, by J. Templon, NIKHEF, Amsterdam, The Netherlands

### P3 Chaired by C. Racca:

- **Theme: Photodetection**, by Y. Yoshizawa, Hamamatsu Photonics, Shizuoka, Japan
- **Data Transmission**, by M. van der Hoek, BAAS R&D-Coenekoop, The Netherlands
- **Design and Testing of Equipment for Deep-Sea Research**, by L. Gualdesi, Saclant Undersea Research Centre, La Spezia, Italy

### P4 Chaired by C. Racca:

- **Vertical Profiles of Bioluminescence in the North East Atlantic Ocean**, by M. Solan, University of Aberdeen, United Kingdom

### P5 Chaired by G. Anton:

- **Summary of Architecture Parallel Session**, by G. Hallewell, CPPM, Marseille, France
- **Mechanics Parallel Session**, by M. Musumeci, LNS-INFN, Catania, Italy
- **Sea Operations for km<sup>3</sup> Telescope**, by E. Anassontzis, University of Athens, University of Athens, Greece
- **VLVnT Installation and Maintenance of the submarine network**, by M. Sedita, LNS-INFN, Catania, Italy
- **Electrical Power System**, by P. Vernin, CEA-Saclay, France
- **Wild idea on Photon Detection**, M. Taiuti, INFN, Genova, Italy
- **Design Parameters**, C. Spiering, DESY-Zeuthen, Germany
- **Calibration group**, by J.J. Hernandez-Rey, IFIC-Valencia, Spain
- **Summary Readout Electronics**, by M. de Jong, NIKHEF, Amsterdam, The Netherlands
- **Concluding Remarks**, by U. Katz, University of Erlangen, Germany

## PARALLEL WORKING GROUPS

### A1 – Design Parameters - Chaired C. Spiering:

- **Aim of the Session**, by C. Spiering, DESY-Zeuthen, Germany
- **Overview over Mediterranean Water Properties**, by G. Riccobene, INFN-LNS, Catania, Italy

- **Benchmark Parameters for Future km3 Detectors**, by C. Spiering, DESY-Zeuthen, Germany
- **Benchmark Detectors for Comparative Simulations**, by S.E. Tzamarias, Hellenic Open University, Patras, Greece
- **Comparisons of OM Responses at Different Sites**, by Zh.-A. Dzhilkibaev, Institute for Nuclear Research, Moscow, Russia
- **ANTARES Simulation Tools**, by J. Brunner, CPPM, Marseille, France
- **Simulation in the BAIKAL Experiment**, by I. Belolaptikov, JINR, Dubna, Russia
- **Status of Simulations in NEMO**, by P. Sapienza, INFN-LNS, Catania, Italy
- **NESTOR Simulation and Tools**, by A. Leisos, Hellenic Open University, Patras, Greece
- **AMANDA Simulation Tools**, by S. Hundertmark, Stockholm Universitet, Sweden
- **Method for Reconstruction of Muon Tracks**, by A. Heijboer, NIKHEF, Amsterdam, Netherlands
- **Event Reconstruction in the BAIKAL Experiment**, by I. Belolaptikov, JINR, Dubna, Russia
- **NESTOR Reconstruction, Background Rejection Tools and Methods**, by A. Tsigotis, Hellenic Open University, Patras, Greece
- **Muon Track Reconstruction and Data Selection Techniques in AMANDA**, by C. Wiebusch, University Wuppertal, Germany

**A2 – Architecture, Sea Operations, Electrical Power Systems and Mechanics - Chaired by G. Hallewell, M. Sedita, M. Musumeci and E. Anassontzis:**

- **SEACON**, by K. Hall, SEACON LTD, Norfolk, United Kingdom
- **Ocean Design**, by Ocean Design Inc, Ormond Beach, Florida, USA
- **Nexan Cables**, by J.E. Seip, Nexans Norway AS, Oslo, Norway
- **Antares experience with Electro-Optical cables**, by P. Lamare, CEA/Saclay, France
- **Considerations on Electrical Power Distribution for a km3 scale Detector**, by M. Sedita, INFN-LNS, Catania, Italy and P. Vernin, CEA/Saclay, France
- **AC and DC Power Systems for ANTARES**, by A. Calzas, CPPM, Marseille, France
- **NEMO 3 phase proposal**, by R. Cocimano, INFN-LNS, Catania, Italy
- **Distribution of Electrical Power**, by E. Heine, NIKHEF, Amsterdam, The Netherlands
- **Efficient high voltage supplies and dividers**, by T. Wright, Electron Tubes Ltd, Middlesex, United Kingdom

**A3 – Photo Detection - Chaired by M. Taiuti:**

- **Mission statement and Aim of the session**, by M. Taiuti, INFN, Genova, Italy
- **The ANTARES OM**, by P. Vernin, CEA/Saclay, France
- **The NEMO OM**, by S. Reito, INFN, Catania, Italy
- **The NESTOR OM**, by A. Tsigotis, Hellenic Open University, Patras, Greece
- **Hemispherical PMTs for Large Volume Neutrino detectors**, by T. Wright, Electron Tubes Ltd, Middlesex, United Kingdom
- **Developments for Large Format Detectors**, Y. Yoshizawa, Hamamatsu Photonics, Shizuoka, Japan
- **Smart Ideas for Large PMTs**, by S. Flyckt, Photonis, Brive, France
- **The HPD detector**, by M. Giunta, INFN, Pisa, Italy
- **On the Development of Direction Sensitive and Large Area Light Detectors for Huge Volume Water Cherenkov Radiators**, by A. Bersani, INFN, Genova, Italy
- **A new Concept of an OM based on Wavelength Shifting Fibers and Photo Multipliers**, by G. Anton, University of Erlangen, Germany
- **Wild Thoughts about Photo Detection**, by P. Kooijman, NIKHEF, Amsterdam, The Netherlands

**A4 – Calibration, Readout and Data Transmission, Electronics- Chaired by J.J. Hernandez-Rey and M. de Jong**

- **Mission statement**, by J.J. Hernandez-Rey, IFIC-Valencia, Spain
- **Timing calibration in NEMO**, by M. Circella, INFN, Bari, Italy

- **Review of the Time Calibration of the ANTARES neutrino telescope**, by J.J. Hernandez-Rey, IFIC-Valencia, Spain
- **Review of the positioning in ANTARES**, by L. Thompson, University of Sheffield, United Kingdom
- **Calibration and Photo detection: the hybrid concept**, by M. de Jong, NIKHEF, Amsterdam, The Netherlands
- **Calibration Issues**, by J.J. Hernandez-Rey, IFIC-Valencia, Spain
- **Multi Wavelength Multiplexing**, by J. Hogenbirk, NIKHEF, Amsterdam, The Netherlands
- **Synchronous Data Transmission Protocol for NEMO**, by F. Ameli, INFN-Roma1, Roma, Italy
- **CWDM data transmission for the VLVnT**, by T. Legou, B. Dinkespiler, CPPM, Marseille, France
- **NESTOR Readout Electronics, DAQ and Calibration**, by S. Tzamarias, Hellenic Open University, Patras, Greece
- **Front end for Optical Module**, by D. Lo Presti, INFN, Italy
- **Readout system on chip**, by H. Le Provost, CEA/Saclay, France
- **FPGA based PMT acquisition electronics for NEMO**, by C. Nicolau, INFN-Roma1, Roma, Italy
- **PM Pulse Processing for the VLVnT**, by T. Legou for the CPPM Electronic Group, Marseille, France
- **DAQ: Comparison with an LHC experiment**, by J. Panman, CERN, Geneva, Switzerland
- **Opto-electronics**, by M. van der Hoek, BAAS R&D-Coenekoop, The Netherlands

## INDUSTRIAL EXHIBITION

Companies exhibiting were Electron Tubes Ltd, Hamamatsu Photonics Deutschland GmbH, Nautilus Marine Service GmbH, Ocean Design Inc, Photonis Inc, Seacon Europe Ltd.

## SPONSORSHIP

The workshop was sponsored by:

- Electron Tubes Ltd
- Hamamatsu Photonics Deutschland GmbH
- Nautilus Marine Service GmbH
- Ocean Design Inc
- Photonis Inc
- Seacon Europe Ltd
- Stichting Conferenties en Zomerscholen in de Kernfysica
- Stichting HEF



# Plenary Talks





# The deep-sea neutrino telescope ANTARES

J. Carr

Centre de Physique de Particules de Marseille / IN2P3-CNRS  
163 Ave. de Luminy, 13288 Marseille, France  
carr@c ppm.in2p3.fr

## I. INTRODUCTION

The ANTARES Neutrino Telescope is under construction at a site off the south coast of France near the city of Toulon. The international collaboration building the detector was formed in 1996 and now comprises scientific institutes from France, Netherlands, Italy, Spain, Germany, United Kingdom and Russia which was formed in 1996. The project started with a phase of research and development between 1996-2000 involving explorations of possible sites and developments of technology. After the successful completion of the R&D phase and the choice of the site for the deployment of the detector, the collaboration started the construction of a first deep sea neutrino telescope in 2000. The construction of this telescope is now well advanced with a schedule for completion in 2006.

## II. SCIENTIFIC OBJECTIVES

ANTARES aims, with other similar projects world-wide, to open a new field of scientific exploration of the universe. Neutrino detection provides a novel tool to explore high-energy phenomena in astrophysical objects because the neutrinos will escape without interaction from the dense matter clouds surrounding some sources and travel to the earth undeviated by inter-galactic magnetic fields. Hence it is possible to obtain unique information on the nature of known objects and perhaps to observe hereto-unknown sources.

In addition to exploratory astrophysics, the scientific programme of ANTARES, includes aspects of particle physics. It is now widely accepted that the vast majority of the matter in the universe is not in the usual form of matter known on the earth and in the solar system : atoms, molecules and their sub-components but in as yet unknown form called "Dark Matter". The name dark matter was chosen because this matter does not form luminous objects visible with classical optical telescopes. And for this reason new techniques are necessary to discover its nature. It is expected that dark matter is distributed throughout and beyond our local galaxy; ANTARES will search for concentrations of dark matter which emit neutrinos from the very centres of the earth, sun and Milky Way galaxy.

## III. DETECTOR CONCEPTS

The telescope detects neutrinos by observing the Cherenkov light produced by muons in the sea water with the muons originating from interactions of the neutrino in the sea water around the detector or in the rock below it. A matrix of light detectors, in the form of photomultipliers in glass spheres: "optical modules", is deployed near the sea bed suspended on independent lines. This matrix of light detectors enables the direction of the muon track to be measured with a precision of a few tenths of a degree and at high energies the muon track direction is closely aligned with that of the neutrino such that the neutrino direction is measured with similar precision. To obtain this angular resolution the location in space of the optical modules must be known in real time with a precision of about 20 cms and the arrival time of the light must be measured with a precision of the order of 2 ns. Figure 1 illustrates the principle of neutrino detection with the undersea telescope.

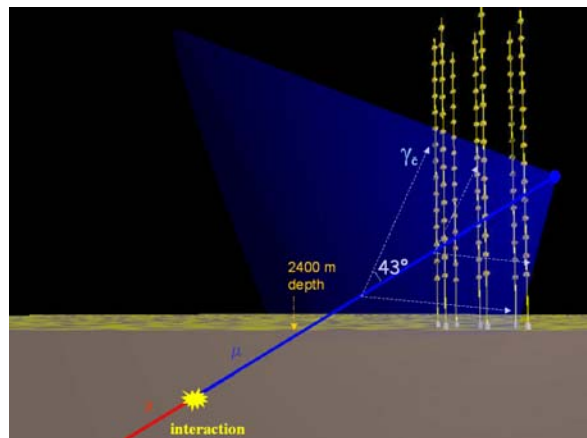


Figure 1: The principle of a Deep Sea Water Cherenkov Neutrino Telescope

## IV. DETECTOR ARCHITECTURE

The geometrical layout and readout architecture of detector have been optimised taking into account four criteria: total detection efficiency; neutrino direction precision; background rejection and cost. The maximum detection efficiency requires the maximum instrumented volume and is

optimal with a homogeneous distribution of light detectors; the best neutrino direction precision is also improved with similar considerations. The background reduction requires optical modules closely spaced enough to be able to recognise tracks by timing associations within the distribution of random hits due to the light backgrounds in the sea water from radioactive decays in 40K and from bioluminescence. Cost considerations lead to grouping of the light detectors.

The detector geometry chosen by ANTARES is a compromise between the homogenous spacing indicated by the efficiency and precision criteria and the clustering indicated by the background and cost criteria. The layout of the detector is shown in figure 2. The optical modules are arranged in groups of three on lines (strings) with a total height of 420 m which are weighted to the sea bed and stretched nearly vertical by floaters at the top. The sea bed at the site is at a depth of 2400m and the optical modules are positioned at depths between 2300m and 2000m. A line has a total of 75 optical modules arranged in 25 storeys with the groups of three light detectors. In total by 2006 the ANTARES detector will have 12 lines.

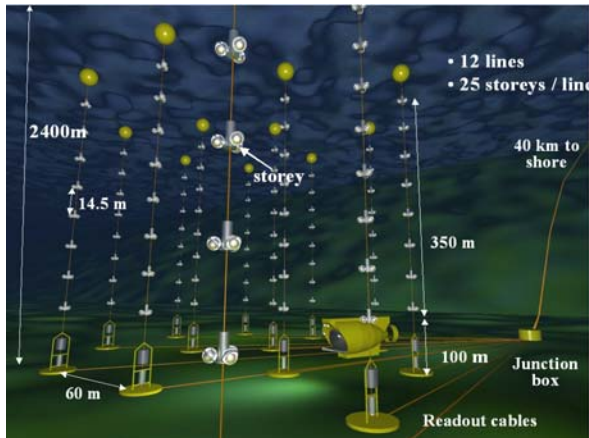


Figure 3: The layout of the ANTARES Neutrino Telescope on the sea floor.

The default readout mode of ANTARES is to readout the time and amplitude of any light signal above a threshold corresponding to 1/3 of a photo-electron for each optical module. These signals are then treated in a computer farm on shore to find hit patterns corresponding to physics events. The grouping of three optical modules in a storey allow local coincidences to be made for this pattern finding and also in certain circumstances to form local triggers in the sea to reduce the readout rate. The bioluminescence rate at the site varies with season and it is planned that when the singles rate is too high for the throughput of the data acquisition system then this local trigger will be used to reduce the data flow to acceptable levels. In addition the front end electronics allows a more detailed readout of the light signal than the standard time and amplitude mode. With this detailed readout it is possible to sample the full waveform of the signal with 128 samples separated by about 2ns. This mode enables special

calibration studies of the electronics and gives the possibility for extra information for complex signals.

The readout architecture of the detector has several levels of multiplexing of the photomultiplier signals. The first level is in the "Local Control Module (LCM)" in each storey of the detector where the analogue electrical output of the photomultipliers are digitised in a custom built ASIC chip, the "Analogue Ring Sampler (ARS)" and then treated by a data acquisition card, containing a FPGA and microprocessor, which outputs the multiplexed signals of the three local optical modules on an Ethernet optical link. These links from 5 storeys, forming a "Sector", are then mixed in an Ethernet switch in every fifth storey in the "Master Local Control Module (MLCM)" and the combined link output is sent with a particular wavelength to a "Dense Wavelength Division Multiplexing (DWDM)" system in an electronics container "String Control Module (SCM)" at the bottom of every line. In this module the outputs from the five MLCM in the line are multiplexed on one pair of optical fibres. These fibres are then connected to the "Junction Box" on the seabed via interlink cables. In the junction box the outputs from up to 16 lines are mixed together onto the submarine cable which goes to the experimental shore station on the coast at La Seyne-sur-Mer. The optical links between each MLCM and the shore station are connected only using passive components.

The electrical supply system has a similar architectural structure as the readout system. The submarine cable supplies up to 4000v, 10a AC to a transformer in the junction box. The outputs from the transformer are via independent secondary circuits at up to 500v, 4a and is transmitted to the lines via the interlink cables to a power supply "String Power Module (SPM)" in the same container as the SCM at the line bottom. This power supply sends up to 400v DC to the MLCM's and LCM's in each storey which contain "Local Power Boxes (LPB)" to provide the various low voltages required by each electronics card.

## V. PHASE OF R&D AND SITE EXPLORATION

Between 1996 and 2000 the ANTARES collaboration was engaged in various activities of research and development for the deep sea technology necessary for the experiment and in choosing an appropriate site.

The site exploration program for ANTARES quickly concentrated on the site off the French coast, at 42° 50'N 6° 10'E with a depth of 2400m, which was ultimately chosen. This site has been fully evaluated in terms of water quality, sedimentation rate and geological stability. The absorption length light at the site has been measured to be 45-60 m in the blue and 25-30 m in the ultra-violet, the scattering length for large angle scatters is greater than 100 m and the loss of light transmission through the glass housings of the optical modules has been evaluated in measurements lasting 8 months to be less than 2% / year. Extensive studies of the bioluminescence rate at the site have been carried out for short periods of time on various occasions, leading to the conclusion that this background will give a dead time of <5%

in the photo-multipliers given the electronics design of the detector. Many of the results of this program have been published [ref 1-3]. At the end of the site evaluate program the chosen location was surveyed in detail both visually and with sonar by the CYANA submersible of IFREMER in 2000.

A significant part of the early research and development program concerned the optical module which is the Cherenkov light detector and so the primary element of the telescope. The optical module is a glass sphere housing a large surface area photomultiplier with active high voltage distribution system and the components of these devices were carefully selected. Extensive evaluations of photomultipliers produced in three companies, Hammamatsu, Photonis, and ETL, were made. A mu-metal magnetic shield against the earth's magnetic field was designed. Production techniques were developed including the difficult task of ensuring the optical coupling between the photomultiplier and the glass sphere with a silicone gel. These developments [ref4] lead to the optical module which is currently in mass production for the ANTARES telescope. The associated readout ASIC chip, the ARS, was initially developed at this early stage of the project.

The ANTARES detector lines move freely under the influence of the sea current; the top of the lines having up to a 10 m horizontal displacement with a maximal current of 20cm/sec. In order to achieve the required angular resolution of the telescope, an acoustic positioning system was developed by the ANTARES team in collaboration with industry. This system consists of hydrophones on a numbers of positions on the lines and transponders on the sea bed which communicate with each others with sound impulses. Measurements of the transit times of the sound signals with measurements of the sound velocity in the sea water lead to position measurements of all the optical modules with a precision of better than 20cms

Another aspect of the R&D phase involved sea deployment techniques. In November 1999 a "Demonstrator Line" was deployed on a test site near Marseille at 42° 59'N 5° 17'E with a depth of 1200m This line had a height of 340m with 7 active optical modules and an acoustic positioning system. The operation of this line for several months until its recovery in June 2000 enabled the verification of the optical modules and acoustic positioning system in-situ in the sea as well as giving valuable experience in sea operations for the team. The data from this demonstrator line enabled the reconstruction of downward going cosmic rays and a measurement of precision of the acoustic position system of better than 5cms.

## VI. SEA FLOOR CONFIGURATION

In October 2001 the first permanent element of the ANTARES telescope, the submarine cable of length 45km, was laid between the site and the beach of Les Sablettes in La Seyne-sur-Mer. On land the electrical energy for the detector is supplied from a power supply in a cabin close to the beach and the optical fibre continue to the shore station in the Institut Michel Pasha at a distance of 45 km. In November

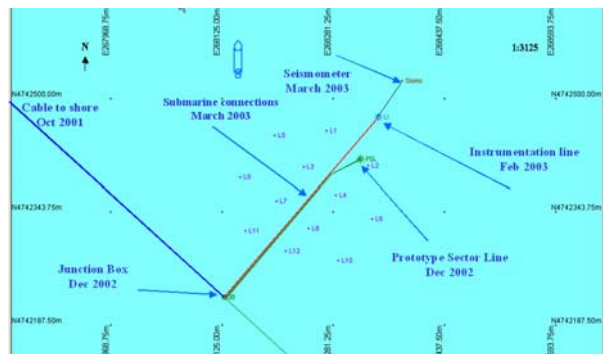
2002 the junction box was connected to the cable and deployed on the sea bed. Figure 3 shows the configuration of the detector on the seabed.

## VII. FINAL PROTOTYPE LINES

During 2002 a final short prototype optical line, "Prototype Sector Line (PSL)", and a prototype instrumental Line, "Mini Instrumentation Line (MIL)", were constructed and tested in a dark room in the laboratory. The two lines were deployed and connected on the ANTARES site in sea operations between December 2002 and March 2003. Figure 4 illustrates the items deployed on the ANTARES site up to March 2003.

Following the line connections, data taking started from the control room in La Seyne with both of the lines functioning successfully. Extensive data was taken with the PSL until July 2003 when it was recovered. The MIL developed a water leak and was recovered in May after one month of operation.

The prototype testing showed a number of problems during the sea operation and these have been diagnosed in the laboratory after the line recoveries. The water leak in the MIL was due to a type of commercial connector which we now believe has a design fault; for the future, the corrective action will be to avoid using this type of connector. In both lines there were faults in the distribution in the line of the time reference clock due to broken optical fibres. The cause of the broken fibre is understood as the use of a sub-standard plastic tube in the line cables; for the future steel tubes will be used to protect the optical fibres.



The background light levels in an undersea neutrino telescope are dominated from radioactive decay of <sup>40</sup>K in the sea water salt and from bioluminescence. During the operation of the PSL the rates of background light from bioluminescence were significantly higher than the values measured during the initial site explorations. In these early tests the measurements were made with autonomous mooring lines which recorded PMT counting rates in a memory which

yielded the rates over periods of a few weeks following recovery of the lines. In the PSL data there are certain periods of some weeks where the data loss would be greater than the 5% expected from the initial tests.

## VIII. FINAL STEPS IN THE TELESCOPE CONSTRUCTION

The next step in the construction of the ANTARES telescope will be the installation of a new instrumentation line towards the end of 2004. The installation of the full 12 lines of the detector will take place during 2005 and 2006. It is expected that the first exciting science results of the detector, opening up this new field of astroparticle physics in the northern hemisphere, will be available during 2006.

## IX. REFERENCES

1. 'Sedimentation and fouling of Optical Modules at the ANTARES site', P. Amram et al., (ANTARES Collaboration). *Astropart. Phys.* **19** (2003) 253.
2. 'Water Transparency at the ANTARES Site', P. Amram et al., (ANTARES Collaboration). Submitted to *Astropart. Phys.*
3. 'Background light in potential sites for the ANTARES undersea neutrino telescope', P. Amram et al. (ANTARES Collaboration), *Astropart. Phys.* **13** (2000) 127.
4. 'The ANTARES Optical Module', P. Amram et al., (ANTARES Collaboration), *Nucl. Instrum. Meth.* **A484** (2002) 369.

# The NEMO project

E. Migneco<sup>□</sup>, S. Aiello<sup>□</sup>, E. Amato<sup>□</sup>, M. Ambriola<sup>□</sup>, F. Ameli<sup>□</sup>, G. Andronico<sup>□</sup>, M. Anghinolfi<sup>□</sup>, M. Battaglieri<sup>□</sup>, R. Bellotti<sup>□</sup>, A. Bersani<sup>□</sup>, A. Boldrin<sup>□</sup>, M. Bonori<sup>□</sup>, A. Capone<sup>□</sup>, L. Caponnetto<sup>□</sup>, F. Cafagna<sup>□</sup>, M. Circella<sup>□</sup>, R. Cocimano<sup>□</sup>, R. Coniglione<sup>□</sup>, M. Cordelli<sup>□</sup>, M. Costa<sup>□</sup>, S. Cuneo<sup>□</sup>, A. D'Amico<sup>□</sup>, V. D'Amico<sup>□</sup>, C. DeMarzo<sup>□</sup>, R. DeVita<sup>□</sup>, C. Distefano<sup>□</sup>, A. Gabrielli<sup>□</sup>, E. Gandolfi<sup>□</sup>, A. Grimaldi<sup>□</sup>, R. Habel<sup>□</sup>, A. Maliano<sup>□</sup>, M. Leonardi<sup>□</sup>, L. LoNigro<sup>□</sup>, D. LoPresti<sup>□</sup>, A. Margiotta<sup>□</sup>, A. Martini<sup>□</sup>, M. Masetti<sup>□</sup>, R. Masullo<sup>□</sup>, R. Mosetti<sup>□</sup>, T. Montaruli<sup>□</sup>, M. Musumeci<sup>□</sup>, C. A. Nicolau<sup>□</sup>, R. Occhipinti<sup>□</sup>, R. Papaleo<sup>□</sup>, C. Petta<sup>□</sup>, P. Piattelli<sup>□</sup>, G. Raia<sup>□</sup>, N. Randazzo<sup>□</sup>, S. Reito<sup>□</sup>, G. Ricco<sup>□</sup>, G. Riccobene<sup>□</sup>, M. Ripani<sup>□</sup>, M. Romita<sup>□</sup>, A. Rovelli<sup>□</sup>, M. Ruppi<sup>□</sup>, G. V. Russo<sup>□</sup>, M. Russo<sup>□</sup>, P. Sapienza<sup>□</sup>, J. P. Schuller<sup>□\*</sup>, M. Sedita<sup>□</sup>, M. Spurio<sup>□</sup>, I. Sokalski<sup>□</sup>, M. Taiuti<sup>□</sup>, L. Trasatti<sup>□</sup>, L. Ursella<sup>□</sup>, V. Valente<sup>□</sup>, P. Vicini<sup>□</sup>, G. Zandarini<sup>□</sup>, S. Zavatarelli<sup>□</sup>

(The NEMO Collaboration)

- a) INFN, Laboratori Nazionali del Sud, Catania (Italy)
- b) INFN, Sezione di Bari & Dipartimento di Fisica e Politecnico dell'Università di Bari, Bari (Italy)
- c) INFN, Sezione di Bologna & Dipartimento di Fisica dell'Università di Bologna, Bologna, (Italy)
- d) INFN, Sezione di Cagliari & Dipartimento di Fisica dell'Università di Cagliari, Cagliari (Italy)
- e) INFN, Sezione di Catania & Dipartimento di Fisica dell'Università di Catania, Catania (Italy)
- f) INFN, Sezione di Genova & Dipartimento di Fisica dell'Università di Genova, Genova (Italy)
- g) INFN, Laboratori Nazionali di Frascati, Frascati (Italy)
- h) INFN, Gruppo Collegato di Messina & Dipartimento di Fisica dell'Università di Messina, Messina, (Italy)
- i) INFN, Sezione di Roma 1 & Dipartimento di Fisica dell'Università di Roma "La Sapienza", Roma, (Italy)
- j) Istituto Nazionale di Oceanografia e Geofisica Sperimentale, Sgonico (TS), (Italy)
- k) ISMAR-CNR, Sezione di Venezia (Italy)
- l) IAMC-CNR, Sezione di Messina, (Italy)

## Abstract

The activities towards the realization of a km<sup>3</sup> Cherenkov neutrino detector, carried out by the NEMO Collaboration in the past five years, are described. Long term exploration of a 3500 m deep site close to the Sicilian coast has shown that it is optimal for the installation of the detector. A complete feasibility study, that has considered all the components of the detector as well as its deployment, has been carried out demonstrating that technological solution exist for the realization of the km<sup>3</sup> detector. The realization of a technological demonstrator (the NEMO Phase 1 project) is under way.

## I. INTRODUCTION

The realisation of a km<sup>3</sup> scale detector for astrophysical neutrinos is considered today one of the most important aims of the next decade. Up to now only smaller scale detectors have been realized or are under way [1-4], demonstrating the feasibility of the technique of Cherenkov detection of the secondary muons in deep waters or ice. However, the realisation of a km<sup>3</sup> scale detector needs a further improvement of the technologies by means of appropriate R&D studies.

The Mediterranean Sea offers optimal conditions, on a worldwide scale, to locate the telescope and several sites have been proposed by the European collaborations active in the field. Moreover, it has full complementarity, in terms of sky coverage, with the ICECUBE detector [5] that is under construction at the South Pole.

The NEMO Collaboration was formed in 1998 with the aim to carry out the necessary R&D towards the km<sup>3</sup> neutrino detector. The activity has been mainly focused on the search and characterization of an optimal site for the installation and on the development of a feasibility study of the detector.

More recently the realization of a small scale technological demonstrator, the so called NEMO Phase 1 project, has been started.

## II. SITE SELECTION AND CHARACTERIZATION

The installation of the km<sup>3</sup> detector needs a complete knowledge of the site physical and oceanographical characteristics over a long time period. Therefore, the NEMO Collaboration has performed, since 1998, a long term research program to select and characterise an optimal deep-sea site. This activity has demonstrated that the abyssal plateau in the Ionian Sea (fig. 1) close to the southernmost cape of the coast

\* on leave from DAPNIA/SPP CEA Saclay, France

of Sicily (Capo Passero) shows excellent characteristics to host the km<sup>3</sup> underwater neutrino detector.

More than 20 sea campaigns have been performed to study water optical characteristics, oceanographical properties (like currents, sedimentation and seabed geology). A comprehensive discussion of the Capo Passero site properties is given in [6].

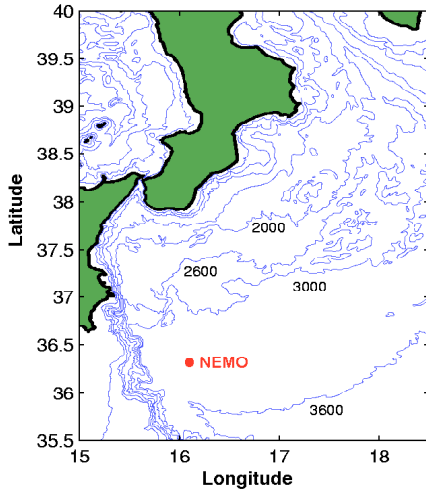


Figure 1: The south Ionian sea, showing the location of the site selected and characterized by the NEMO collaboration.

The site was selected after a series of measurements in the region at varying distance from the coast. Its location at about 50 km from the shelf break about 80 km from the coast (see figure 1) was chosen to ensure the best condition of stability in time of the water parameters and avoid any perturbation coming from the presence of the shelf break. A geological survey of the area verified the flatness and the absence of any evidence of recent turbidity events (which occur when sediments of the continental shelf slide down the continental slope and are therefore of potential great danger for the detector). The nature and structure of the seabed was studied in detail in order to design the mooring structures of the neutrino detector.

### A. Light transmission properties

Water transparency can be parametrised in terms of light absorption ( $a$ ), scattering ( $b$ ) and attenuation ( $c$ ), which is the combined effect of the first two [7]. These quantities have to be measured *in situ*. We used a set-up based on a CTD probe (that measures water salinity and temperature as a function of depth) and on the AC9 transmissometer (that allows the measure of light absorption and attenuation in nine different wavelengths, 412 to 715 nm) [8].

Since 1998 we have investigated several deep sea sites near the Italian coast and, after accurate analysis, we have selected Capo Passero as candidate site for the neutrino telescope installation. A series of campaigns, aimed at studying the seasonal and long term behaviour of oceanographic and optical properties of the site, has also been conducted. In figure 2 we show the absorption and attenuation

lengths in the blue region (440 nm) measured at the depths of interest for the telescope (more than 2500 m) in different campaigns. The measured values of the absorption length are about 70 m, close to the one of optically pure water. Seasonal variations are negligible and compatible with the instrument experimental error.

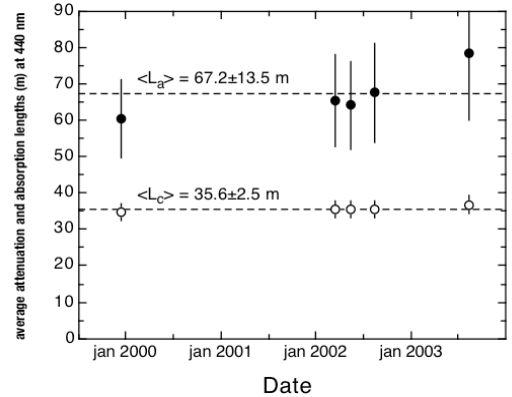


Figure 2: Values of the absorption and attenuation lengths in the blue region (440 nm) measured during five different campaigns. The reported values are the average in the depth region 2850-3250 m. Dashed lines represent average values over the five different campaigns.

### B. Optical background

Optical background in the seawater comes mainly from two natural causes: the decay of <sup>40</sup>K, which is present in seawater, and the so called *bioluminescence* that is the light produced by biological organisms. Of these two effects the first one shows up as a constant rate background noise on the optical modules (roughly 15±20 kHz on 10" PMT at 0.5 s.p.e. threshold), while the second one, when present, may induce large fluctuations (both in the baseline and as presence of high rate spikes) in the noise rate. We have measured the optical noise in Capo Passero and Toulon, by means of a set up consisting of two 8" photomultipliers and the associated electronics. In the Capo Passero site an average rate of about 25 kHz has been measured, with rare high rate spikes due to bioluminescence. This results is in agreement with the distribution of bioluminescent bacteria measured in Capo Passero [6], that shows a very low concentration of these bacteria at depths greater than 2500 m.

### C. Oceanographical parameters

Deep sea currents have been continuously monitored in Capo Passero since 1998. The analysis points out that the behaviour of the deep sea currents in the area is almost homogeneous on the part of the water column that has been monitored (bottom 500 m) with very low average values (around 3 cm/s) and peaks not exceeding 12 cm/s.

The downward flux of sediments has also been analysed. The annual average value of material sedimenting at large depth in Capo Passero is about 60 mg m<sup>-2</sup> day<sup>-1</sup>, a rather low value as expected for an oligotrophic environment such as the Ionian Plateau.

### III. R&D ACTIVITIES OF THE NEMO COLLABORATION

#### A. Microelectronics

The power dissipation of the electronics installed in deep sea represent a serious issue. It should be, therefore, reduced as much as possible. Therefore, we have undertaken the design and realization of full custom VLSI ASICS to be used for the front end electronics of the detector [9]. The trigger, photomultiplier signal classification, fast analog sampling and slow digital conversion, event time stamp, data packing and transfer functions are performed by the designed chip.

#### B. Development of new PMTs

The photomultipliers employed to detect the Cherenkov light produced by muons are a critical component of the detector. It is required that the energy and the timing resolutions are good enough to detect a rather small number of Cherenkov photons and, by using the related time information, to reconstruct the muon track orientation. Presently available photomultipliers generally match these requirements, however the possibility to recognize the Cherenkov light direction could drastically reduce the background primarily generated by the  $^{40}\text{K}$  decay, allowing to improve the detection performances at lower neutrino energies. The NEMO collaboration is presently developing a prototype based on an improved version of the BAIKAL hybrid PMT coupled to a matrix of Winston cones [10].

#### C. Computer simulations

Simulations in NEMO aim to support the feasibility study for an underwater  $\text{km}^3$  detector. In particular, the performances of a detector based on towers and the dependence of these performances on the site features, such as the depth and the optical water properties, are investigated. Recently, a common effort has been undertaken together with the ANTARES collaboration aiming at the design of the  $\text{km}^3$  telescope using the ANTARES software package [11]. A more extensive presentation of the simulation activities is given in [12].

### IV. FEASIBILITY STUDY FOR A $\text{KM}^3$ DETECTOR

A great deal of work has also been done to carry out a study of the technical feasibility of the  $\text{km}^3$  detector, taking into account all of its components and their deployment, that eventually yielded the preliminary project of the detector described in the following. The study was carried out in close contact with leading companies in the field of deep sea operations.

#### A. Definition of the detector architecture

It is clear that the architecture of the  $\text{km}^3$  detector should stem from a compromise between performances and technical feasibility of the detector. Of course cost is also an issue.

Computer simulations were undertaken in order to define a suitable architecture to be analysed afterwards in terms of technical feasibility. As a first approach one can consider filling up a volume of about one  $\text{km}^3$  with a lattice of equally spaced sensors. The spacing should be of the same order of the absorption length of light in water. In our simulation we have taken the horizontal and vertical distance between downlooking sensors equal to 60 m. This turns out in a total number of 5600 sensors arranged in 400 strings. The performances of such a detector in terms of effective area and angular resolution are shown in figure 3.

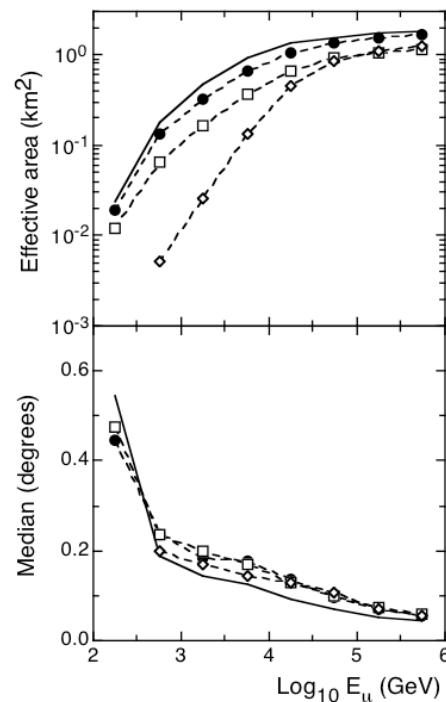


Figure 3: Effective areas and median angles between true and reconstructed muon tracks as a function of muon energy for different detector configurations. Regularly spaced (60 m) lattice of downlooking OM (5600 OM in total) with 20 kHz background (solid line); 9x9 array of “NEMO towers” (5832 OM in total) with different background rates: 20 kHz (full dots), 60 kHz (open squares) and 120 kHz (open diamonds). Quality cuts were applied in the NEMO array cases in order to achieve similar angular resolutions.

Although the solution of arranging the sensors along a string presents some advantages in terms of simplicity, this architecture can be difficult to realise due to the close distance between strings (60 m) compared with their total height (780 m). Moreover, the large number of structures to be moored and connected raises the cost of the detector.

Therefore, alternative solutions for the architecture, in which the number of structures is reduced by gathering a relatively large number of sensors on each one of them, should be studied. In particular, constraints on the distance between structures (larger than about 120 m) and on their height (smaller than 1 km) were suggested by a preliminary feasibility study in terms of construction, deployment and maintenance operations of the detector within reasonable costs. Following these suggestions, we have proposed a

structure (that is described in more detail in the following) composed by a square array of “NEMO towers” (see section IV.B) shown in figure 4. The proposed architecture is “modular”, in the sense that it is expandable with the addition of extra towers, and configurable with different sea floor layouts. At present it should be considered as a reference for a deeper feasibility study.

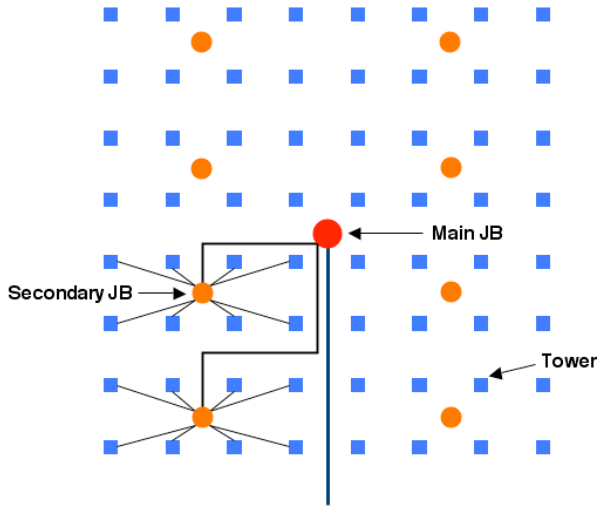


Figure 4: The reference layout of the detector considered in the feasibility study.

The performances of this architecture in terms of effective area and angular resolution were evaluated by means of computer simulations. In the top panel of fig. 3 effective areas after quality cuts are reported for different values of the optical background rate. At 20 kHz, which is close to the measured value in Capo Passero, the detector based on NEMO towers (full circles) exhibits an effective area only slightly smaller than the homogenous detector (solid line). With increasing background rate up to 120 kHz a stronger and stronger reduction in the effective area is observed when quality cuts are applied to obtain a good angular resolution (see bottom panel of fig. 3). The results are described in detail in [12].

### B. Mechanical Structures

Optical modules and instrumentation will be mounted on a structure that we have called *tower* [13]. It is a three dimensional structure composed by a sequence of storeys (that host the instrumentation) interlinked by a system of cables and anchored on the seabed. The structure is kept vertical by an appropriate buoyancy on the top.

The final features of the tower (number of storeys, number of optical modules per storey, distance between the storeys) can be optimized following the results of numerical simulations. However, the modular structure of the tower will permit to adjust these parameters to the experimental needs.

In the preliminary design we have considered a 18 storey tower, where each storey is made with a 20 m long pipe

hosting two optical modules at each end (4 OM per storey). The vertical separation between storey is fixed at 40 m, giving a total active height of 680 m. An additional spacing of 150 m is added at the base of the tower, between the anchor and the lowermost storey to allow for a sufficient water volume below the detector. In its working position each storey will be rotated by 90°, with respect to the up and down adjacent ones, around the vertical axis of the tower.

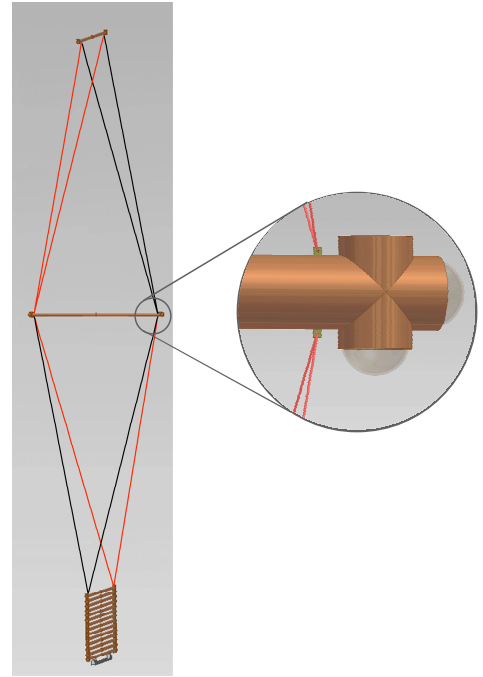


Figure 5: The NEMO tower (partly packed with two unfurled storeys) with a close up view of one end of the tube with the optical module assembly.

One of the advantages of this structure is represented by the fact that it can be compacted, by piling each storey upon the other, to simplify transport and deployment. The structure is unfurled, reaching its operating configuration, only after its deployment on the seabed.

### C. Data transmission

For a 5000-6000 OM neutrino telescope the expected data rate (essentially due to background and assuming a rate of about 30 kHz) is on the order of 20-30 Gbps, while the distance over which the data have to be transmitted can be of the order of 100 km. These considerations recommend the use of a fibre optics transmission system and a power consumption as low as possible.

Furthermore, a common timing must be known in the whole apparatus at the level of detection device to allow correlation in time of events. In this sense, a favourable choice is the use of synchronous protocols. For example, the Synchronous Digital Hierarchy (SDH) protocol, which embeds data, synchronism and clock timing in the same serial bit stream, allows an easy distribution of the clock signal to the whole apparatus.



Many devices are available off-the-shelf with present technology to implement a data transport suited to the  $\text{km}^3$  detector. Just few years ago data multiplex/demultiplex was realized with Time Division Multiplex (TDM) techniques acting on electric signals, with high power consumption and big processing complexity. Nowadays the same operations are carried out by Wavelength Division Multiplex (WDM) techniques using totally passive components.

Line termination devices, i.e. electro-optical transceivers, are the only active components needed for the connection. The great advantages in terms of power consumption, reliability, and simplicity recommend this technique as a perfect candidate for final  $\text{km}^3$  detector.

#### D. Power distribution

An evaluation of the total power budget needed for the  $\text{km}^3$  detector can be made considering an approximate load of 18 W at the level of each storey (four OMs plus some instrumentation with related electronics) plus some extra load at the level of the Tower Base (100 W) and of the Junction Boxes (200 W). This leads to a total amount of power required of about 27 kW.

Several solutions for the energy distribution system have been analysed: in direct current, in alternate current mono phase and alternate current three phase. These solutions have been compared in terms of voltage drops and Joule losses [14]. The three phase AC systems presents some advantages in terms of losses and reliability. This system can be used for the energy distribution up to the level of the local electronics module in each storey where a conversion to DC is made.

### V. THE NEMO PHASE 1 PROJECT

The technological solutions proposed for the  $\text{km}^3$  detector require an adequate process of validation. For this reason we have decided to realize a technological demonstrator, at the Underwater Test Site of the Laboratori Nazionali del Sud in Catania, consisting in a subset of the proposed  $\text{km}^3$  detector and including some critical elements like junction boxes, towers, data and power transmission system. This project is called NEMO Phase 1.

The NEMO Phase 1 system will be composed by a network of Junction Boxes (a main one and two secondary) and two Nemo Towers as described in section IV.A.

#### A. The LNS Test Site

The Test Site of the Laboratori Nazionali del Sud (LNS) consists of an electro-optical submarine cable, to connect the underwater installation to shore, and a shore station.

The cable system is composed by a 25 km main electro-optical cable, splitted in two branches, each one 5 km long. One branch will be dedicated to the NEMO Phase 1 experiment, while the other one will host the first underwater seismic monitoring station, called SN-1, realized by the Istituto Nazionale di Geofisica e Vulcanologia (INGV). The cable

carries 6 electrical wires, 4  $\text{mm}^2$  in diameter, and 10 monomode optical fibres G-652.

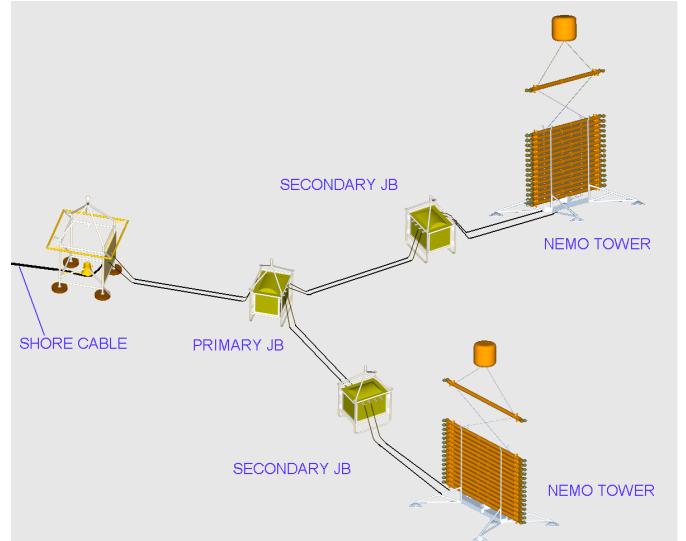


Figure 6: Schematic layout of the NEMO Phase 1 project.

A shore station, located inside the port of Catania, will host the energy power system of the laboratory, the instrumentation control system, the landing station of the data transmission system and the data acquisition, as well as a mechanics and electronics laboratory for the assembly of the components.

#### B. Junction Boxes

An alternative design to the standard Titanium pressure vessels used for junction boxes operating in seawater for a long lifetime has been developed. The approach is to decouple the pressure and the corrosion problems. Therefore, the proposed JB will be made by a pressure resistant steel vessel hosted in a fibreglass container to avoid direct contact between steel and sea water. The fibreglass container will be filled with oil to compensate the external pressure. This solution should improve the reliability and also reduce costs by avoiding the use of expensive alloys. A detailed description of the design is given in [15].

#### C. Data transmission system

Considering NEMO Phase 1 as a feasibility test toward the  $\text{km}^3$  detector, its data transport system has been designed based on technical choices that allow scalability to a much bigger apparatus [16].

The basic idea consists of making the smallest, though most significant, fraction of the  $\text{km}^3$  apparatus, i.e. a junction box plus a complete tower. Moreover, connection reliability has been taken into account as a key issue in the design.

At the centre of each floor of the tower an electronics circuit, called Floor Control Module (FCM), is placed. The FCM collects data from the floor photo-multipliers (PMTs) and the floor control and auxiliary signals, creates an STM-

1/SDH data stream at about 155 Mbps, and send data toward the land side laboratory. From the opposite direction, the FCM receives slow control data, commands and auxiliary information, and the clock and synchronizations signals needed for apparatus timing.

Bidirectional data transport is realized by means of a single optical fibre connecting the FCM with the Tower Junction Box (T-JB) located at the base of the tower. Inside the T-JB a WDM device is placed, which packs all the bidirectional bit streams coming from all the floors onto a single fibre directly linked to the on shore side. Actually, in order to provide redundancy, data streams are doubled and re-directed onto two fibres using a “power splitter”. The one fibre of the two used to carry the meaningful information is chosen on the on-shore station.

The underwater structure has a complementary on-shore counter part, where all optical signals are converted back to electrical signals. In the on-shore laboratory the Primary Reference Clock (PRC), which is used to give the same timing to all the towers of the apparatus, is also located. Assuming that the two fibres per tower maintain their integrity, the designed system provides other experiments with a further bidirectional channel.

#### D. Electrical power system

Since the Phase 1 project is intended as a test of the km<sup>3</sup> technologies, for the electrical power system the same design choices proposed for NEMO, with the appropriate changes due to the constraints imposed by the already existing electro-optical cable, were taken. A preliminary design of the power control system was made [14]. This should be able to acquire currents and voltages plus some environmental parameters, such as temperature, humidity, etc., inside the boxes, switch the power on and off to each feeding line, both under ordinary and fault conditions, detect failures and remotely control the breakers in order to continue feeding the JB interested by the fault.

## VI. CONCLUSIONS

The realization of a km<sup>3</sup> telescope for high energy astrophysical neutrinos is a challenging task at the frontiers of astroparticle science. Several collaboration in Europe are already working on the realization of first generation demonstrators. More efforts are needed to develop a project for the km<sup>3</sup> detector.

In its five years of activity the NEMO collaboration has contributed in this direction by performing an intense R&D activity.

An extensive study on a site close to the coast of Sicily has demonstrated that it has optimal characteristics for the telescope installation, in particular for what concerns the water optical properties and for its proximity to already existing infrastructures like the LNS in Catania.

A complete study has been performed to analyse all the detector components both in term of their technical feasibility and their installation. This study, which has produced as a result a preliminary design of the detector, has shown that a detector with effective area over 1 km<sup>2</sup> is realizable at an affordable cost.

The realization of a demonstrator of some of the key technological solutions proposed for the km<sup>3</sup> detector has been started at the underwater Test Site of the LNS in Catania. This project foresees the realization of a underwater laboratory that will be constituted by a network of three junction boxes and a couple of instrumented tower following the design proposed by the NEMO collaboration. The completion of this project is foreseen by the end of 2006.

## VII. REFERENCES

- 1) I.A. Belolaptikov et al., *Astrop. Phys.* 7 (1997) 263.
- 2) J. Carr, in these proceedings; see the ANTARES website at <http://antares.in2p3.fr>.
- 3) S.E. Tzamarias, in these proceedings; see also the website at <http://www.nestor.org.gr>.
- 4) E. Andres et al., *Astrop. Phys.* 13 (2001)1; see also the website at <http://amanda.uci.edu>.
- 5) C. Spiering, in these proceedings; see the ICECUBE website at <http://icecube.wisc.edu>.
- 6) G. Riccobene, in these proceedings.
- 7) C.D. Mobley, *Light and Water*, Academic Press, San Diego (1994).
- 8) A. Capone et al., *Nucl. Instr. and Meth.* A487 (2002) 423.
- 9) D. Lo Presti, in these proceedings.
- 10) A. Bersani, in these proceedings.
- 11) D. Bailey, *Monte Carlo tools and analysis methods for understanding the ANTARES experiment*, Ph.D. thesis, Univ. of Oxford (2002); J. Brunner, in these proceedings.
- 12) P. Sapienza, in these proceedings.
- 13) M. Musumeci, in these proceedings.
- 14) R. Cocimano, in these proceedings.
- 15) R. Occhipinti, in these proceedings.
- 16) F. Ameli, in these proceedings.

# NESTOR First Results

## Electronics - DAQ - Data Analysis

### VLVvT Workshop 2003

S. E. Tzamarias

Hellenic Open University for the NESTOR Collaboration

tzamaria@eap.gr

#### Abstract

The first floor of the NESTOR underwater neutrino telescope was successfully deployed, during March 2003, fully equipped with electronics. We briefly outline the NESTOR project, the analysis methods and techniques, and we present results using 30% of the accumulated triggers.

## I. INTRODUCTION

The NESTOR (Neutrino Extended Submarine Telescope with Oceanographic Research) neutrino telescope is detecting the Cerenkov radiation produced by  $\nu$  - induced muons and/or showers of charged particles in a large volume of sea water. The NESTOR site is located at the South West of Peloponnese (Greece), at the seabed of the Ionian Sea. In fact this is where one finds the deepest waters in Mediterranean sea, 5200m. The NESTOR collaboration has located a  $8km \times 9km$  horizontal plateau at a depth of 4000 m [1, 2]. The plateau is at a mere distance of 7.5 nautical miles from shore. Extensive studies of environmental properties have been made [3, 4]. These measurements show that the water transmission length is  $55 \pm 10$  m at a wavelength  $\lambda = 460nm$ . The underwater currents have been measured and they have been found minimal, i.e. a few centimeters per second [5].

Extensive core samples of the sea bottom sediments over the site have been analyzed. They indicate a slow accumulation rate of 7 to 18 cm over 10000 years giving a firm clay deposit for good anchoring. There is no evidence of any submarine rock falls [6].

In November 1994, a side-scan sonar and air pressure gun were used to survey the site area and the cable route to Methoni. Maps of the sea bottom were produced to a scale of 1:10000 using differential GPS for position location [7].

## II. NESTOR DETECTOR

The basic detector module of the NESTOR neutrino telescope is the tower shown in Figure 1. It consists from 12 rigid hexagonal units, floors, with a vertical distance between them of 30m. The tower is connected to the shore by a 30km long electrooptical cable, containing a conductor and 18 fibers. Each hexagonal floor is made out of titanium, with a diagonal of 32 m. At the tip of each arm of the hexagon there is a pair of

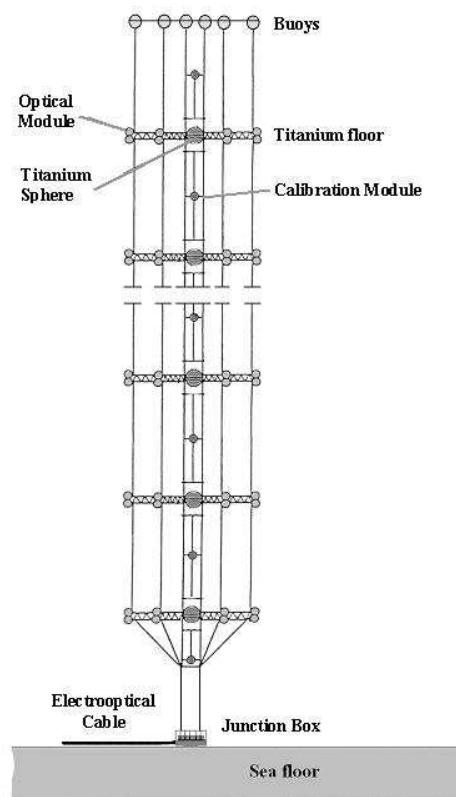


Figure 1: NESTOR Tower

two 15 inch photomultiplier tubes (PMTs) inside benthos glass housings [8, 9], one looking upwards and the other downwards, as it is shown in Figure 2. Above and below of each floor they are calibration modules used for timing and gain monitoring purposes. The electronics, which are responsible for signal sensing, triggering, digitization and data transmission to the shore, as well as to control and monitor the PMTs, are housed inside a large titanium sphere (1m in diameter) located at the center of the floor.

The effective area of a NESTOR Tower in reconstructing throughgoing muons of energy  $> 10TeV$  is greater than  $20000m^2$ , whilst the energy threshold of such a detector is as low as 4 GeV for contained tracks. It has to be emphasized

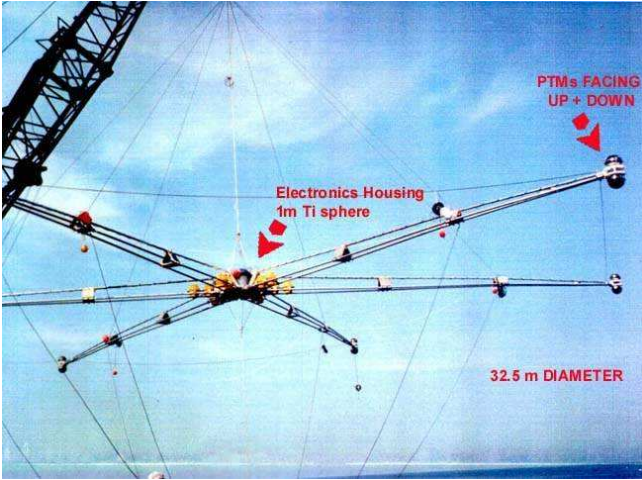


Figure 2: A photograph of the NESTOR Floor taken during deployment.

the ability of the NESTOR telescope in detecting extra high energy downcoming cosmic neutrinos which otherwise cannot be detected because of the opacity of the earth.

### III. READOUT AND DATA ACQUISITION SYSTEM

The NESTOR Readout and Data Acquisition System (RDAQ) follows a data-driven architecture with waveform capture and capabilities for forming local (per floor) coincidence to reduce processing requirements. Each floor unit has its own RDAQ subsystem consisting of four distinct hardware elements: a) A

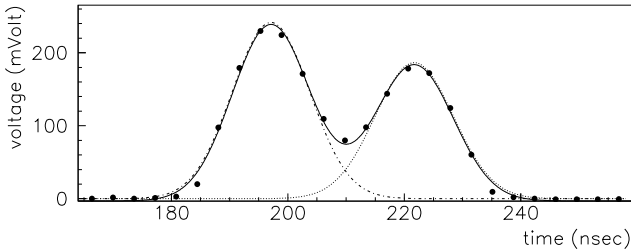


Figure 3: Double pulse separation. The waveform has been fitted by a double gaussian shape.

“floor board” within the titanium sphere in each floor, including: PMT pulse sensing, majority logic event triggering, waveform capture and digitization, data extraction, event formatting and transmission via optical fiber uplink and FPGA/PLD reprogramming via optical fiber downlink.

The heart of this element is a novel waveform digitizer ASIC, developed at LBNL, the “Analog Transient Waveform Digitizer” (ATWD). Each ATWD has four channels and it contains 128 common-ramp, 10-bit, Wilkinson ADCs which after activation, digitize simultaneously all 128 samples of a selected channel. The sampling is generated by an active delay line; no

clocks are involved in waveform capture. The sampling rate is determined by a single external current and may be varied from 200 MHz to 2 GHz. To capture the NESTOR PMT signals, as well as to recognize overlapping pulses, the sampling speed has been chosen to be 282 MHz (i.e. 3.54 ns sampling period). For this choice, the dynamical range of each ATWD channel (128 samples) corresponds to 453 ns.

The double pulse separation capabilities of the ATWD is demonstrated in Figure 3 where it is shown (a part of) the digitized waveform of a PMT. In parallel to the above basic functions, the floor board provides several calibration and monitoring options. As an example one channel in each ATWD has been retained for sample speed calibration (on an event by event basis) by digitizing the waveform of a 40MHz clock signal.

b) A “slow controls board”, inside the titanium sphere, connected to the floor board by a simple digital interface which controls and monitors the PMTs high voltage, controls the calibration LEDs and monitors the environmental conditions.

c) A two way single-fiber optic link between each floor and the shore station.

d) A “shore board”, at the shore counting room, which broadcasts a global 40 MHz clock signal via downlink to the floor board, receives the uplink data and transmits them to the second level triggering system. The downlink also has the capability of reprogramming the FPGA/PLDs within each floor.

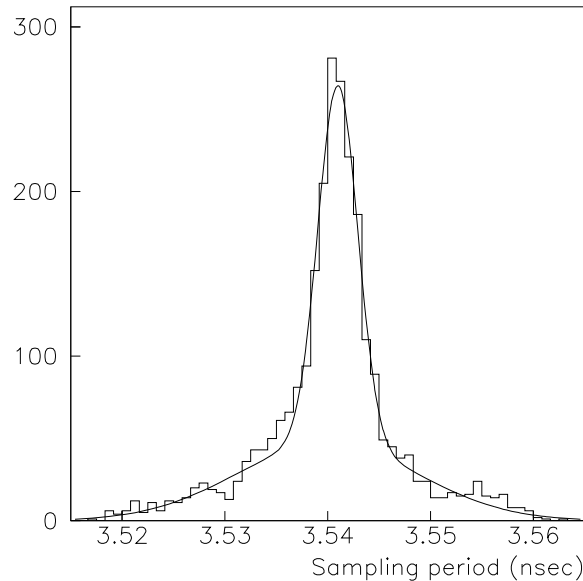


Figure 4: Variation of the sampling period of an ATWD during data taking.

A “floor-trigger” occurs when the local coincidence requirement is satisfied on the floor. The time of a floor-trigger is defined as the leading edge of the majority logic signal and the occurrence of such a trigger initiates waveform capture by

the ATWD. This time stamp is also used at the shore to build a global event combining experimental information from several floors.

All the functions of the RDAQ electronics and the online software has been extensively studied in the laboratory by using the calibration LED system. Furthermore the robustness of the system has been successfully tested under near-realistic conditions during deployments of fully equipped floors at the Bay Test Station. In Figure 4 it is demonstrated the stability of the ATWD sampling period during a data taking run. Each entry to this histogram corresponds to the estimated value of the sampling period, using the captured waveforms of the 40 MHz clock. The root mean square of this distribution is 6.4 ps which is negligible compared to the mean value of the sampling period of 3.54 ns.

#### IV. DEPLOYMENT AND DETECTOR PERFORMANCE

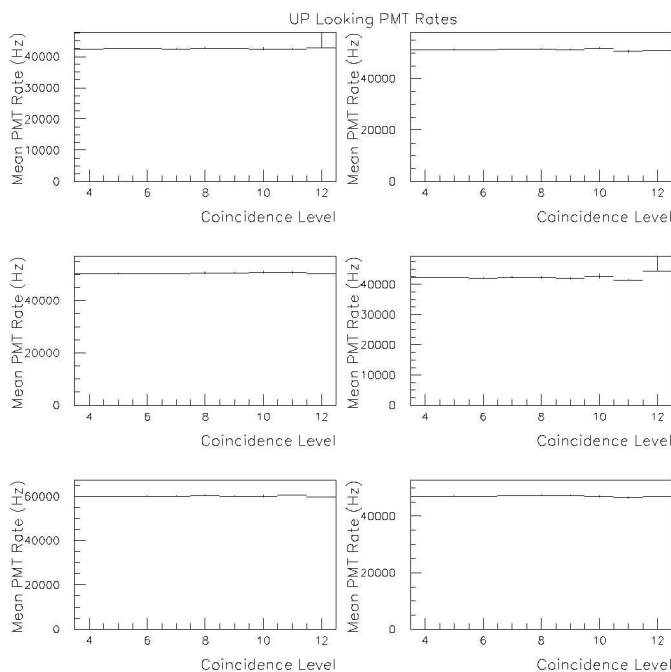


Figure 5: The PMT rates as functions of the selection trigger criteria (coincidence level).

After a successful operation by using the cable ship TENEO of TYCOM in January 2002, an electrooptical junction box, the sea-bottom station (pyramid) with a number of associated instruments such as underwater current meter, Ocean Bottom Seismometer, nephelometers, compass, pressure gauges etc., were deployed at 4000m and connected to the end of the electrooptical cable. For the first time ever data were transmitted routinely from the deep sea in real time. Unfortunately the onset of bad weather did not allow the deployment of any other part of the detector. The NESTOR deployment tech-

niques and methods were published in the cover article in the July issue of Sea Technology, a leading marine industry journal [10].

In March 2003, using the cable ship RAYMOND CROZE of France Telecom, a hexagonal floor was deployed fully equipped with electronics and associated environmental sensors to a depth of 4000m. In the control room, during the deployment and operation of the detector, the parameters of the detector were continuously monitored. These include the floor orientation (compass and tilt meters), temperatures, humidity and hygrometry within the Titanium sphere, PMT high voltages, as well as data from other environmental instruments mounted on the sea-bottom station (pyramid), such as pressure meters, current meters, etc.

The optical background due to  $K^{40}$  beta decay plus the thermionic noise from the PMTs contribute a baseline signal level of 50 kHz per PMT. The PMT rates are constant with respect to the time and they do not depend on the trigger criteria (coincidence level). Figure 5 demonstrates the unbiased of the selection trigger by presenting the average PMT rates as functions of coincidence level. The  $K^{40}$  optical background, mainly at the single photoelectron level, is routinely used to monitor the PMT gains [11].

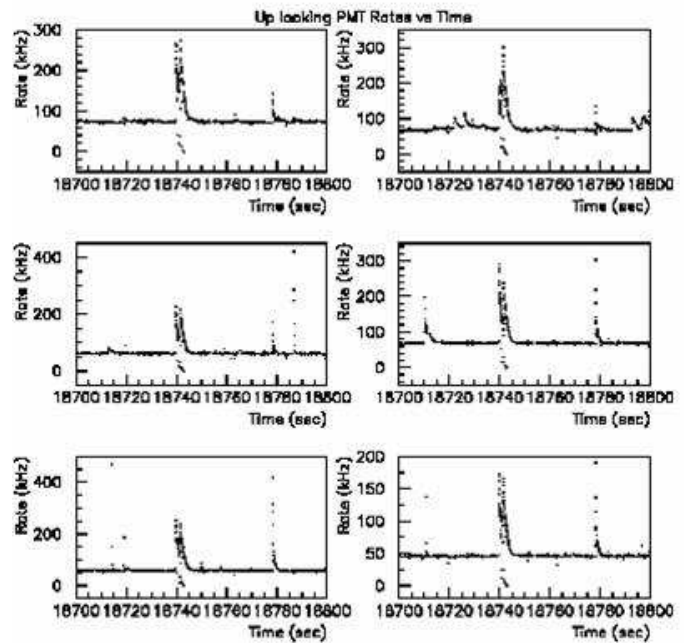


Figure 6: .  
The Rate of the six uplooking PMTs versus time during bioluminescence activity

However there are period of times where the PMT rates are significantly higher. This effect, shown in Figure 6 is a result of the bioluminescence activity of living organism populations. The signal bursts due to the bioluminescence activity have a variable duration 1 to 10 seconds and are easily identified and rejected. The contribution of bio-activity to the dead

time of the detector has been estimated from the accumulated data to be of the order of 1% of the active experimental time.

Calibration in the sea uses LED flasher modules mounted above and below the detector floor. Using light pulses from the calibration system several experimental parameters (e.g. PMT timing, gains etc.) can be monitored. Further analysis of the calibration data, results to in situ measurement of PMT characteristics, such as slewing and Transit Time Spread (TTS) [11].

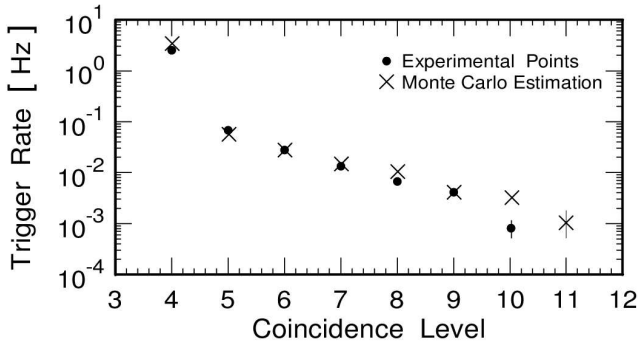


Figure 7: Measured and Monte Carlo estimated trigger rates of  $\geq 4$ -fold coincidences at the 0.25 p.e. threshold level.

In order to quantify the detector performance several experimental parameters have been measured and compared with the Monte Carlo simulation of the apparatus. For a detailed report see [12]. In Figure 7 the measured trigger rates for different coincidence trigger levels are compared with the corresponding Monte Carlo [12] estimations based on the Okada atmospheric muon flux parametrization [13], the natural  $K^{40}$  radioactivity in the sea water and PMT dark current. Also

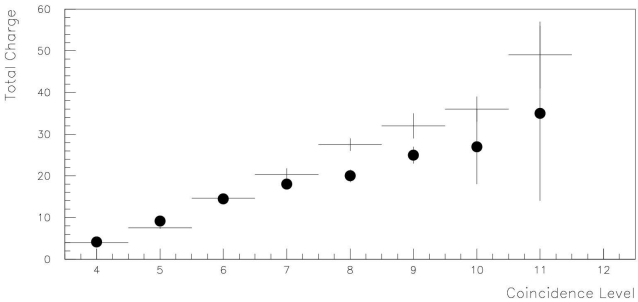


Figure 8: Measured and Monte Carlo estimated accumulated charge for  $\geq 4$ -fold coincidences at the 0.25 p.e. threshold level.

Figure 8 demonstrates the agreement between the data and the Monte Carlo estimation of the total accumulated charge (the total measured number of photoelectrons), inside the trigger window, for different selection criteria (coincidence level).

In the offline data analysis, the digitized waveform of each PMT has to go through a processing procedure in order to subtract baselines and to be corrected for attenuations, slewing, etc. This processing stage utilizes calibration parameters de-

termined in the laboratory before the deployment. As a result of the signal processing the fast rise time of the PMT pulses is recovered (8 nsec at the single photoelectron level), multiple pulses are easily disentangled and also the arrival time, the pulse height and the total charge are accurately determined [11].

In order to reconstruct tracks, events with more than five active PMTs within the trigger window are selected. The estimation of the track parameters is based on  $\chi^2$  minimization using the arrival times of the PMT pulses. In most cases the procedure converges to two or occasionally several minima, often due to an inherent geometrical degeneracy. To resolve this ambiguity, a second level algorithm is used that takes account of the measured number of photoelectrons at each PMT and the number expected from the candidate track, and performs a likelihood hypothesis comparison. Figure 9 shows the dig-

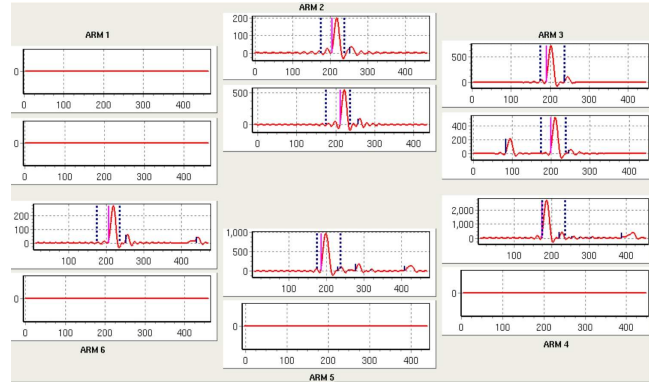


Figure 9: Digitized PMT waveforms, after signal processing, from a typical event selected with a four-fold majority trigger. The upper and lower traces for each of the six detector arms are from the up and down-looking PMTs. A single photoelectron gives a mean pulse height of 120mV. (NESTOR 2003 Event 2213-Run 78-BFile 70.)

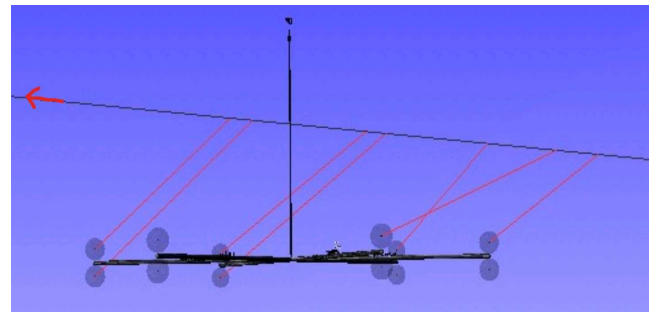


Figure 10: A pictorial representation of the reconstructed muon track, which corresponds to the PMT pulses shown in Figure 9. The lines originating from the muon track represent the Cerenkov light paths to the photomultipliers. The zenith angle of this track has been estimated to be  $93^\circ \pm 14^\circ$ . At a depth of 4000m, upcoming or horizontal reconstructed tracks are good neutrino candidates.

itized PMT waveforms, after signal processing of a selected event, whilst Figure 10 shows a pictorial representation of the reconstructed track that corresponds to this event.

Several tests of the track reconstruction procedures have been carried out using both data and Monte Carlo generated events. The results demonstrate that the estimation of the track parameters is unbiased. As an example, Figure 11 shows the

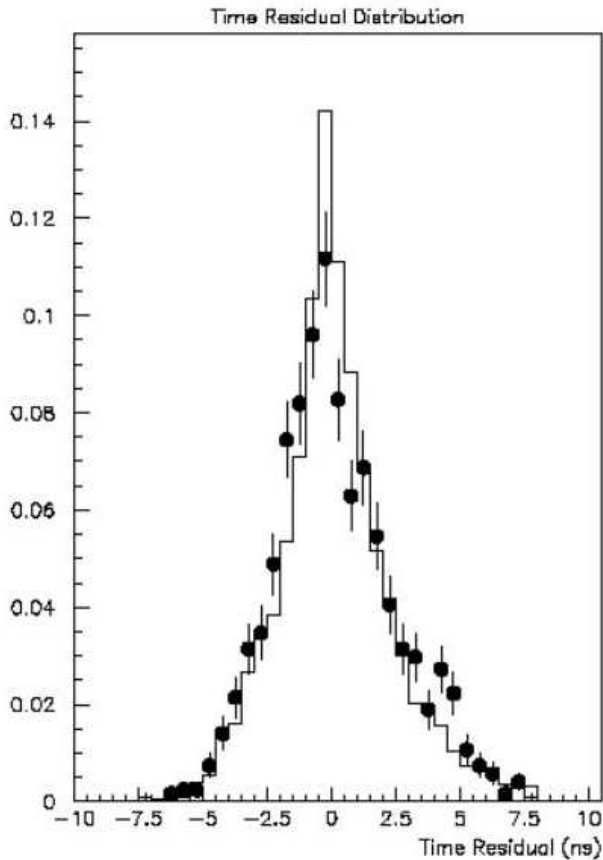


Figure 11: Time residuals of the PMT pulses to the fitted track for data (solid points) and Monte Carlo (solid line).

agreement between data and Monte Carlo events concerning the time residuals of the PMT pulses to the fitted track. Also in Figure 12 it is demonstrated the performance of the fitting procedure by comparing the normalized time residuals (pulls) to a gaussian of a mean zero and a sigma 1. Figure 13 shows the measured zenith angular distribution (solid points) of reconstructed events using a fraction ( $\sim 30\%$ ) of the collected data. The reconstructed tracks used in this measurement have been selected by means of the minimum  $\chi^2$  fit ( $\chi^2$  probability  $> 0.1$ ), the track quality based on the number of photoelectrons per PMT and on the total accumulated photoelectrons per hit per track ( $> 4.5$ ). The histogram shows the predicted angular distribution of atmospheric muon tracks (for the NESTOR floor geometry and reconstruction efficiency) derived from Monte Carlo calculations using Okada's phenomenological model.

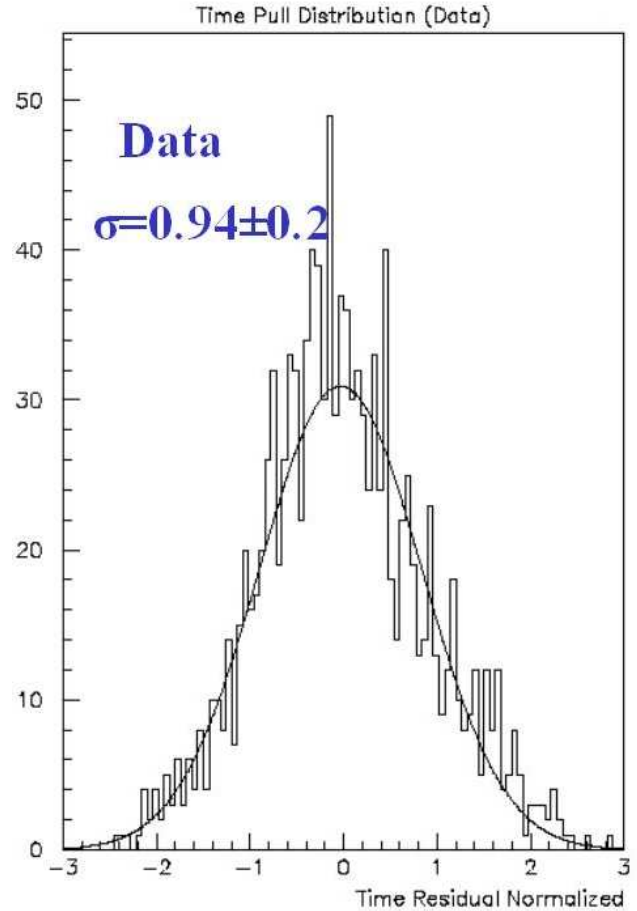


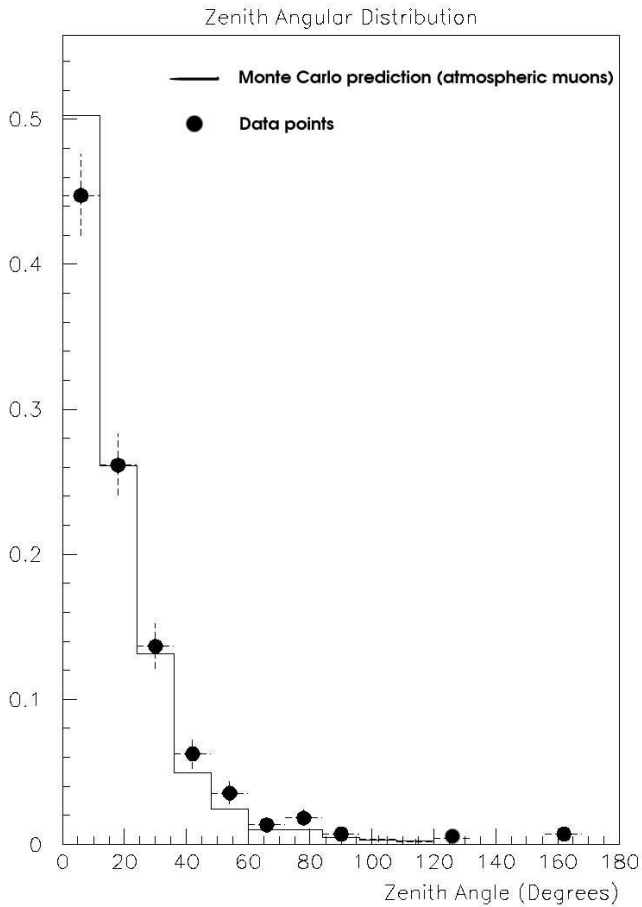
Figure 12: Normalized time residuals (pulls) of the PMT pulses to the fitted track for Data.

## V. CONCLUSION

The NESTOR underwater neutrino telescope construction is well under way. The detector deployed is well understood and the data quality is excellent. Efficient neutrino detection will require the deployment of at least four floors, which is planned for next year.

## REFERENCES

- [1] L. K. Resvanis (1992), 2nd NESTOR International Workshop, 1992, L. K. Resvanis editor.
- [2] L. K. Resvanis et al. High Energy Neutrino Astrophysics (1992), V. J. Stenger, J. G. Learned, S. Pakvasa and X. Tata editor.
- [3] Khanaev (1992), 2nd NESTOR International Workshop, 1992, L. K. Resvanis editor.
- [4] E. Anassontzis (1994), Nuclear Instruments and Methods **A349**, (1994), 242.



[13] A.Okada 1994 *Astroparticle Physics* **2** 393.

Figure 13: Monte Carlo expectation of the zenith angular distribution of atmospheric muons at 4000m (solid line), compared to the zenith angular distribution of reconstructed events (solid points)

- [5] Demidova, 2nd NESTOR International Workshop (1992), L. K. Resvanis, editor.
- [6] E.Trimonis, 2nd NESTOR International Workshop (1992), L. K. Resvanis, editor.
- [7] V. Lykousis et al. "Submarine Power Link and Data Highway NESTOR/LAERTIS Cable Route Surveying. Morphological and Sedimentological Study", Athens, 1995.
- [8] E.G.Anassontzis, et.al., "The Optical Module for the NESTOR Neutrino Telescope", *NIM A* **479** (2002) 439-455.
- [9] A.Tsirigotis, "The NESTOR Optical Module", these proceedings.
- [10] E.G.Anassontzis & P.Koske 2003, *Sea Technology* **44** 10.
- [11] A.Tsirigotis, "Reconstruction, Background Rejection, Tools and Methods (NESTOR)", these proceedings.
- [12] A.Leisos, "NESTOR Simulation Tools and Methods", these proceedings.



# Results from the AMANDA Neutrino Telescope

E. Bernardini for the AMANDA Collaboration

DESY-Zeuthen, D-15735, Zeuthen, Germany

Elisa.Bernardini@desy.de

## Abstract

The AMANDA Cherenkov telescope uses the South Pole ice cap to search for neutrinos from extraterrestrial sources. The detector is operated since the year 1996. It was deployed over several campaigns and the final configuration was reached in January 2000. Here we present a few results on the search for a diffuse flux of  $\nu_{e,\mu,\tau}$ , for  $\nu_{\mu}$  emitted by point sources or accompanying gamma-ray bursts, for magnetic monopoles and the results of the indirect searches for dark matter. No significant excess of events has been observed so far and upper limits are reported.

## I. INTRODUCTION

The main scope of the Antarctic Muon and Neutrino Detector Array (AMANDA) is to look for sources of high-energy neutrinos. The AMANDA detector (figure 1) is located at the Geographic South Pole and uses the ice cap (about 3 km thick) as both an interaction and detection medium. The instrument consists of an array of 677 optical modules (OMs) on 19 strings, most of them located at depths between 1.5 and 2 kilometers [1].

A first prototype (operated since 1997) comprised 302 OMs on 10 strings and is referred to as AMANDA-B10. The final configuration (AMANDA-II) was reached in the year 2000.

Each optical module consists of an 8-inch photomultiplier tube (PMT, Hamamatsu R5912-2) housed in a glass pressure sphere. Analog PMT signals are transmitted to the surface via electrical (strings 1-10) and optical cables (strings 11-19) and recorded with a time resolution of about 5 ns.

The polar ice is not homogeneous but shows a series of

horizontal layers with different optical properties, which reflect the climatological changes in the past. At a wavelength of 400 nm (corresponding to the maximum sensitivity of the OMs) the average absorption length is 110 m and the average effective scattering length is 20 m.

AMANDA-II is optimized to detect muon tracks of energy above 1 TeV. Tracks are reconstructed from the arrival times of the Cherenkov photons at the PMTs, with a resolution of  $2-2.5^\circ$ , depending on energy and direction. The muon energy can be estimated from the intensity of the Cherenkov light emission, mostly due to pair production and bremsstrahlung.

An independent detection channel is provided by cascades, which result from  $\nu_{e,\mu,\tau}$  neutral-current and from  $\nu_e$  and  $\nu_{\tau}$  charged-current interactions. The direction of the parent neutrino cannot be as accurately inferred as compared to the muon channel, but the neutrino energy, being fully deposited in the detector, can be reconstructed with 30% accuracy.

The performance of AMANDA-B10 had been extensively studied using atmospheric neutrinos [2]. A recent analysis of the AMANDA-II 2000 data extends the experimentally determined energy spectrum of atmospheric neutrinos up to 100 TeV [3].

Section II summarizes AMANDA results on the search for extraterrestrial neutrinos. They include the search for a diffuse  $\nu_{\mu}$  and  $\nu_{e,\mu,\tau}$  flux and the search for  $\nu_{\mu}$  point sources and GRBs. The results on a search for magnetic monopoles and the indirect search for dark matter particles are reported in section III.

## II. SEARCH FOR ASTROPHYSICAL NEUTRINOS

Most of the data recorded in AMANDA correspond to muons from cosmic rays. Event quality cuts allow the reduction of this contamination to the level of a few percent of the selected data samples. An unavoidable background to extraterrestrial neutrinos are neutrinos generated in the atmosphere. Various analyses are differently affected by the background and use dedicated strategies. A common feature is the optimization of the final selection cuts to achieve the best detector sensitivity<sup>1</sup>. In the following, reported upper limits are computed according to the Cousins-Highland [5] prescription, with unified Feldman-Cousins ordering [6, 7] and improved likelihood ratio test [8].

<sup>1</sup>The sensitivity is defined as the average upper limit from an ensemble of identical experiments, assuming no signal[4].

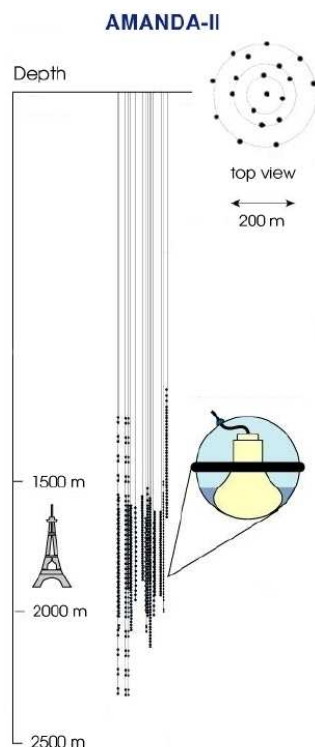


Figure 1: Schematics of the AMANDA detector

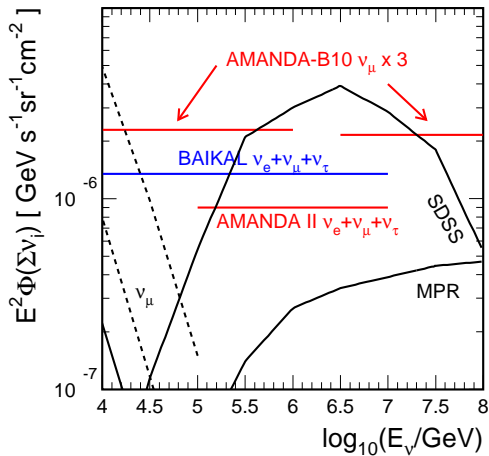


Figure 2: Limits on the diffuse flux of all types of neutrinos (cf. text).

### A. Search for a diffuse neutrino flux

A search for extraterrestrial neutrinos from unresolved directions (diffuse flux) can be performed using *upward going* muons. The major source of background is represented by atmospheric neutrinos and is separated from the signal on the basis of the different energy spectrum expected (softer for atmospheric neutrinos). The final event sample is hence selected via an energy dependent cut (the channel multiplicity), optimized on the detector sensitivity. The remaining events from the 1997 data sample (i.e. with the detector AMANDA-B10), are compatible with the expected background [9, 10]. The resulting 90% CL limit is  $dN/dE \cdot E^2 = 8.4 \cdot 10^{-7} \text{GeVcm}^{-2}\text{s}^{-1}\text{sr}^{-1}$ . The energy range which contains 90% of the expected signal (“sensitive energy range”) is 6-1000 TeV.

A similar analysis can be done using *downward going* muon events, at energy above a few PeV. At these energies the Earth is essentially opaque to neutrinos and a search for extraterrestrial sources must focus on almost horizontal events, where the expected signal accumulates. The background is represented by large bundles of downward going atmospheric muons, separated from the signal on the basis of the light output in the detector. The results obtained using the year 1997 data sample give no significant excess of events [11]. A 90% CL upper limit of  $dN/dE \cdot E^2 = 7.2 \cdot 10^{-7} \text{GeVcm}^{-2}\text{s}^{-1}\text{sr}^{-1}$  has been set, in the sensitive energy range from 2.5 to 6300 PeV.

An independent analysis can be performed using *cascades*. For typical astrophysical scenarios, the expected neutrino fluxes at the detector should show an equal contribution from all three flavors. The capability to detect all neutrino species considerably increases the sensitivity. The search for extraterrestrial neutrinos using cascade events is made feasible in AMANDA by the good energy resolution (about 0.2 in the logarithm of the energy [12]), which compensates for the reduced effective volume with respect to the muon detec-

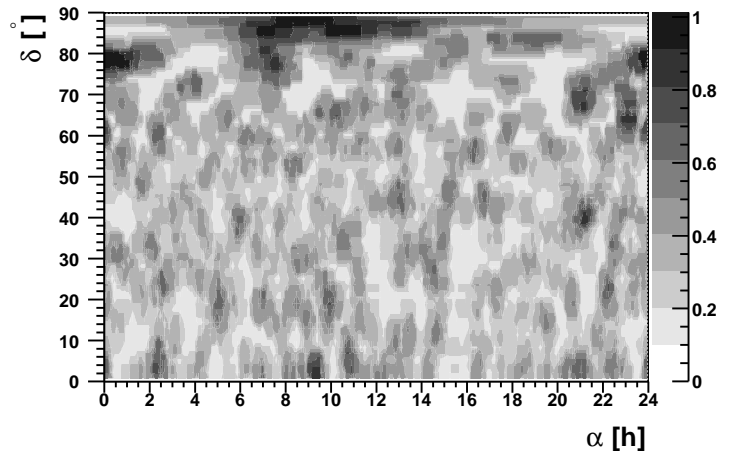


Figure 3: AMANDA-II neutrino upper limit sky-plot at 90% CL (year 2000 data). Limits are in units of  $10^{-7} \text{cm}^{-2}\text{s}^{-1}$ , for a generic  $E^{-2}$  energy spectrum integrated above  $E_\nu=10$  GeV.

tion channel<sup>2</sup>. The intrinsic background is mostly represented by downward going atmospheric muons which radiate a large fraction of their energy, initiating an electromagnetic cascade. This background is relatively low and effectively suppressed with energy dependent cuts. The preliminary results of an analysis performed on the year 2000 data have shown that a 90% CL upper limit  $dN/dE \cdot E^2 = 9 \cdot 10^{-7} \text{GeVcm}^{-2}\text{s}^{-1}\text{sr}^{-1}$  is achieved for the sum of all flavors [12], an order of magnitude lower than the previously published limit assessed with AMANDA-B10 [13]. The sensitive energy range of this analysis is 80-7000 TeV.

Figure 2 summarizes the results on the flux limits to all neutrino flavors. A multiplicative factor 3 has been applied to the limits obtained for  $\nu_\mu$ . The corresponding BAIKAL limit [14] and the SSDS prediction [15] and the MPR upper bound [16] are also shown. The falling lines represent the atmospheric neutrino fluxes.

### B. Search for $\nu_\mu$ point sources

The AMANDA-II detector shows an improved pointing resolution ( $2-2.5^\circ$ ) and on average a factor 5 better sensitivity, compared to AMANDA-B10 [17, 18]. A major improvement is observed towards the horizon, due to the larger radius.

A search for point sources has been performed on a selected sample of 699 upward going muon tracks from the 2000 data. This data sample is dominated by atmospheric neutrino induced events, with a remaining contamination from downward going muons of about 5% [18]. A binned search in the northern hemisphere indicated no significant excess above the background and upper limits are reported in figure 3.

A study of preselected directions also showed no significant excess. Upper limits are reported in table 1 for a few candidate sources. Note that the limit for the Microquasar SS433

<sup>2</sup>The signature of a cascade in AMANDA is essentially a point-like light source.

is very close to a recent prediction [19].

Table 1: Preliminary 90% CL upper limits, for a few selected candidate sources. Dec. is the source declination in degrees,  $n_{obs}$  is the number of events in the search bin and  $n_b$  the expected background. Neutrino limits ( $\Phi_V^{lim}$ , in units of  $10^{-8}\text{cm}^{-2}\text{s}^{-1}$ ), integrated above 10 GeV, are for a generic  $E^{-2}$  energy spectrum.

Candidate	Dec. [ $^\circ$ ]	$n_{obs}$	$n_b$	$\Phi_V^{lim}$
Markarian 421	38.2	3	1.50	3.5
Markarian 501	39.8	1	1.57	1.8
SS433	5.0	0	2.38	0.7
Cygnus X3	41.0	3	1.69	3.5
Crab Nebula	22.0	2	1.76	2.4
Cassiopeia A	58.8	0	1.01	1.2
M 87	12.4	0	0.95	1.0

### C. Neutrinos coincident with Gamma Ray Bursts

Data taken from 1997 to 2000 have been searched for high energy neutrinos spatially and temporally coincident with 317 GRBs detected by the BATSE satellite. No coincidences with triggered bursts have been observed. Assuming a Waxman-Bahcall spectrum ( $E_B=100$  TeV and  $\Gamma=300$ ), an upper limit on the flux of neutrinos at the earth of  $4 \times 10^{-8}\text{GeVcm}^{-2}\text{s}^{-1}\text{sr}^{-1}$  has been derived [20].

## III. OTHER PHYSICS TOPICS

Apart from sources of extraterrestrial neutrinos, AMANDA can search for neutrinos generated in annihilation processes of dark matter particles (such as WIMPs) in the center of the Earth or the Sun, or for relativistic magnetic monopoles, and monitors the Galaxy for supernova bursts. Here we give results from the first two topics.

### A. Indirect dark matter search

If cold dark matter consists of neutralinos, these would have gravitationally accumulated in the center of the Earth or in the Sun and annihilate. A possible signature would be an excess of neutrinos from those directions.

A search for neutrino-induced muon flux due to neutralino annihilation at the center of the Earth has been performed on the 1997 and 1999 data. The final event sample, represented by vertically upward going muons, is consistent with the expected background of atmospheric neutrinos [21, 22]. Figure 4 shows the derived upper limit, as a function of the neutralino mass. SUSY predictions for muon fluxes are given for comparison. The filled circles represent MSSM parameter combinations which are excluded by current direct searches, crosses mark combinations which could be excluded by direct searches at least ten times as sensitive as present ones.

The conditions are different for neutralino annihilation in the Sun: AMANDA-B10 did not achieve the resolution close to

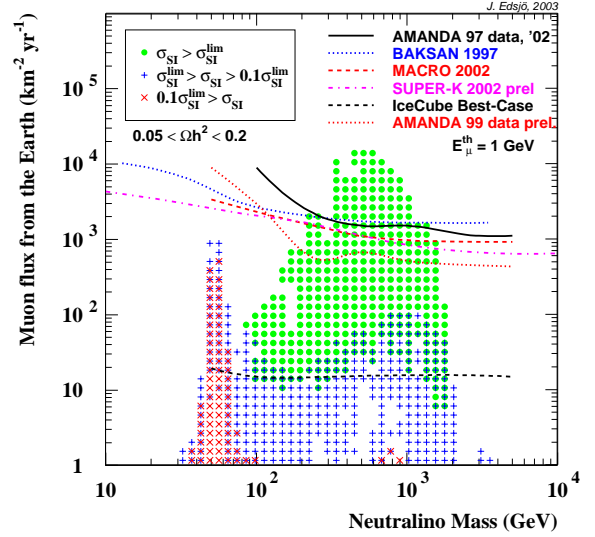


Figure 4: WIMP limits from indirect searches. Figure from [23]

the horizon necessary to identify neutrinos from the Sun. This analysis became feasible with AMANDA-II due to the wider volume. Preliminary results indicate that the sensitivity of the detector is competitive with results of direct searches.

### B. Relativistic magnetic monopoles

A search for relativistic magnetic monopoles in AMANDA is based on the higher expected light output for these particles, compared to muons (a factor of 8300 for a unit magnetic Dirac charge  $g = 137/2 \cdot e$ ). No event from the 1997 data has passed the search criteria based on this signature [24]. Figure 5 summarizes the limits obtained so far.

## IV. CONCLUSIONS

The analysis of data from AMANDA covers different fields and energy ranges, from a few hundreds of GeV up to EeV. All currently observed events are in agreement with background expectations and upper limits have been derived, which are in most cases the best available.

AMANDA has reached the sensitivity to observe astrophysical neutrinos required by most optimistic models. The analyses presented will be extended to a larger data sample and combined. In a few cases substantial improvement is expected incorporating the waveform information in the reconstruction and in the event selection, which is available after a hardware upgrade performed in 2003. The feasibility of underice neutrino telescopes has been proven by more than five years of operation of the AMANDA detector. This opens the way to the realization of cubic kilometer detectors (e.g. IceCube [25]).

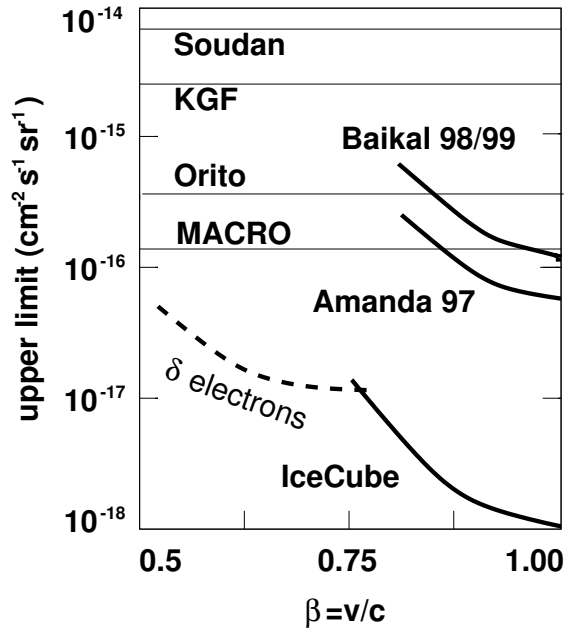


Figure 5: Present limits on the flux of relativistic monopoles. Also shown is the limit expected from a cubic kilometer detector. In the future this search could be extended to even lower velocities by detecting the  $\delta$  electrons generated along the monopole path.

## REFERENCES

- [1] R. Wischniewski, Proc. 27<sup>th</sup> ICRC, Hamburg (Germany), 1105 (2001).
- [2] J. Ahrens et al., Phys. Rev. D. 66, 012005 (2002).
- [3] H. Geenen, Proc. 28<sup>th</sup> ICRC, Tsukuba (Japan), 1313 (2003).
- [4] G.C. Hill and K. Rawlins, Astropart. Phys. 19, 393 (2003).
- [5] R.D. Cousins and V.L. Highland, Nucl. Instr. Meth. A 320, 331 (1992).
- [6] G.J. Feldman and R.D. Cousins, Phys. Rev. D. 57, 3873 (1998).
- [7] J. Conrad et al., Phys. Rev. D. 67, 012002 (2003).
- [8] G.C. Hill, Phys. Rev. D. 67, 118101 (2003).
- [9] J. Ahrens et al., Phys. Rev. Lett. 90, 251101 (2003).
- [10] G.C. Hill, M. Leuthold and J. Cooley, Proc. 28<sup>th</sup> ICRC, Tsukuba (Japan), 1317 (2003).
- [11] S. Hundertmark, Proc. 28<sup>th</sup> ICRC, Tsukuba (Japan), 1309 (2003).
- [12] M. Kowalski, Proc. 28<sup>th</sup> ICRC, Tsukuba (Japan), 1301 (2003).
- [13] J. Ahrens et al., Phys. Rev. D. 67, 012003 (2003).
- [14] G.V. Domogatskii et al., arXiv:astro-ph/0211571.
- [15] F.W. Stecker, Phys. Rev. Lett. 66, 2697 (1991), Errata, ibid 69, 2738 (1992).
- [16] K. Mannheim, R.J. Protheroe and J.P. Rachen, Phys. Rev. D. 63, 023003 (2001).
- [17] J. Ahrens et al., Astroph. J. 583, 1040 (2003).
- [18] T. Hauschildt and D. Steele, Proc. 28<sup>th</sup> ICRC, Tsukuba (Japan), 1305 (2003).
- [19] C. Distefano et al., Astroph. J. 575, 378 (2002).
- [20] R. Hardtke, K. Kuehn and M. Stamatikos, Proc. 28<sup>th</sup> ICRC, Tsukuba (Japan), 2717 (2003).
- [21] J. Ahrens et al., Phys.Rev. D. 66, 021005 (2002).
- [22] P. Olbrechts et al., Proc. 28<sup>th</sup> ICRC, Tsukuba (Japan), 1677 (2003).
- [23] J. Edsjo, arXiv:astro-ph/0211354.
- [24] P. Niessen and C. Spiering, Proc. 27<sup>th</sup> ICRC, HE 3.4, 1496 (Hamburg, 2003).
- [25] J. Ahrens et al., arXiv:astro-ph/0305196. Accepted for publication in Astropart. Phys.

# The IceCube Project

C. Spiering for the IceCube Collaboration \*

DESY Zeuthen, Platanenallee 6, D15739 Zeuthen, Germany  
christian.spiering@desy.de

## Abstract

This talk gives a brief description of goals, design, expected performance and status of the IceCube project.

## I. PHYSICS GOALS

The main goal of the IceCube project [1] is to extend the region of the Universe explored by neutrinos and thereby to test fundamental laws of physics, to obtain a different view of astronomical objects, and to learn about the origin of the highest-energy cosmic rays.

Science topics include the search for steady and variable sources of high energy neutrinos like Active Galactic Nuclei (AGN), Supernova Remnants (SNR) or microquasars, as well as the search for neutrinos from burst-like sources like Gamma Ray Bursts (GRB). The sensitivity of IceCube to astrophysical sources of high energy muon neutrinos is described in [2] and in Section V.

Similar to the Mediterranean projects discussed at this workshop, IceCube can also tackle a series of questions beside high energy neutrino astronomy. They include the search for neutrinos from the decay of dark matter particles (WIMPs) and the search for magnetic monopoles or other exotic particles like strange quark matter or the Q-balls predicted by SUSY models (see for reviews [3, 4]).

There are, however, two modes of operation which are not – or nearly not – possible for detectors in natural water. Firstly, due to the low light activity of the surrounding medium, the PMT counting rate is below 1 kHz. This enables the detection of feeble rate increases as caused, for instance, by interactions of Supernova burst neutrinos. IceCube can monitor the full Galaxy for MeV neutrinos from Supernova explosions. Secondly, IceCube can be operated in coincidence with a surface air shower array, IceTop. This allows to study questions like the chemical composition of cosmic rays up to  $10^{18}$  eV, to calibrate IceCube, and to use IceTop as a veto for background rejection.

## II. DETECTOR CONFIGURATION

The configuration of IceCube is shown in Fig. 1. IceCube is an array of 4800 optical modules (OMs) on 80 strings, regularly spaced by 125 m. It covers an area of approximately  $1 \text{ km}^2$ , with the OMs at depths of 1.4 to 2.4 km below surface. Each

string carries 60 OMs, vertically spaced by 17 m. The strings are arranged in a triangular pattern. At each hole, one station of the IceTop air shower array will be positioned. An IceTop station consists of two ice tanks of total area  $7 \text{ m}^2$ . Two of these tanks are being installed during the current (2003/04) season.

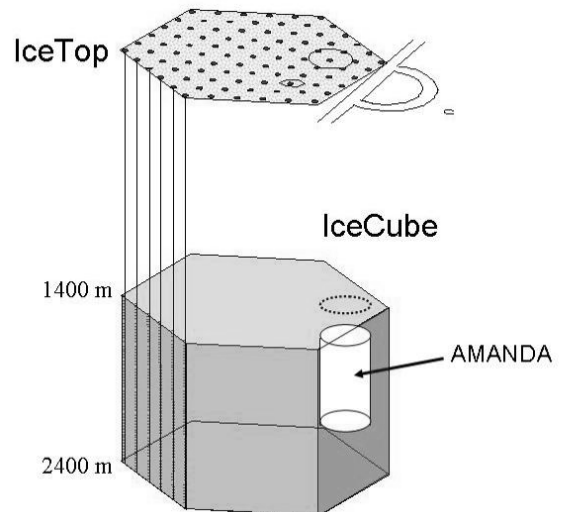


Figure 1: IceCube, IceTop and Amanda

The present Amanda-II detector [5] will be integrated into IceCube. The present runway as well as the old South Pole station, buried not far from Amanda under the snow, prevent an extension of IceCube into the corresponding area and therefore a central location of Amanda within IceCube. Still, IceCube will deliver efficient veto information for low energy cascade-like events or short horizontal tracks recorded in Amanda. Horizontal tracks could be related to neutrinos stemming from WIMP annihilations in the Sun.

Various configurations with the number of OMs ranging from 2400 (half the design number) to 9600 (twice the design number), with equally spaced strings and with nested subarrays of larger density, and also a variety of “exotic” configurations have been studied in detail [6]. The present configuration is tailored for best sensitivity to muon neutrinos in the energy range of TeV-100 TeV. Better sensitivity at low energy may be obtained by improved sensitivity of individual OMs (i.e. by application of wave length shifters [7], see below). Better sensitivity at higher energies as obtained by *additional* strings along sparsely equipped circle(s) around IceCube is discussed in [8].

\*a full author list is given at the end of this paper

### III. THE DIGITAL OPTICAL MODULE

The IceCube optical module is sketched in Figure 2. It contains a 10-inch diameter PMT HAMAMATSU R-7081. The main argument for this choice was, apart from excellent charge and time resolution, the low noise of only a few hundred Hz (at temperatures of -20 to -40 °C). Low dark noise of the PMTs is not a strong criterion for water detectors since in natural water the ambient noise dominates. In ice, PMTs can be operated without tight local coincidences if only their noise is smaller than a few kHz. A compromise with respect to noise would significantly deteriorate the performance, in particular for detection of low-energy Supernova neutrinos. The PMT is embedded in a transparent gel and shielded against the Earth's magnetic field by a mu-metal grid.

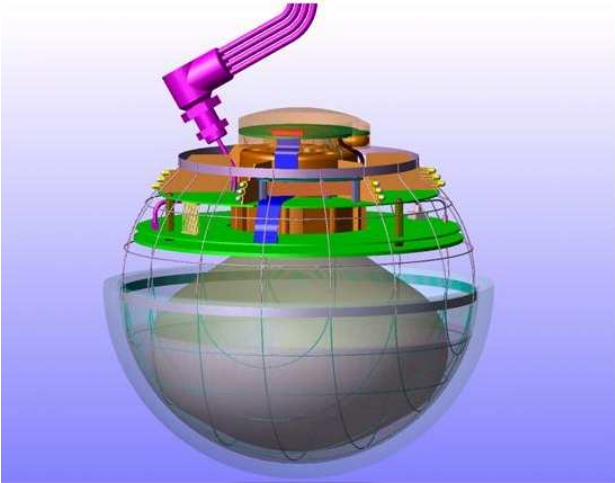


Figure 2: Schematic view of the IceCube DOM

The PMT anode signal (gain  $\sim 5 \cdot 10^7$ ) is digitized within the OM (or Digital Optical Module, DOM) and sent to surface via electrical twisted-pair cables, one twisted pair for two DOMs. The DOM contains several electronic components: the signal processing board, a LED flasher board for calibration purposes, and the PMT base with the high voltage power supply.

The requirements for time resolution and dynamic range are:

- waveform recorded with 250 MHz over the first 0.5  $\mu$ s and 40 MHz over 5  $\mu$ s.
- each pulse time stamped with 7 ns r.m.s.
- dynamic range 200 photoelectrons over first 15 ns and 2000 photoelectrons when integrated over 5  $\mu$ s.
- dead time < 1%
- noise rate < 500 Hz.

The fine sampling is done with the Analog Transient Waveform Recorder (ATWR), an ASIC with four channels, each capable to capture 128 samples with 200-800 Hz. The 40 MHz sampling is performed by a commercial FADC.

The effects of light scattering on the photon arrival time are dominant compared to effects of PMT jitter and time calibration. It has been shown that reconstruction quality only worsens if the jitter increases beyond 10-15 ns, resulting in a design value of 7 ns for overall timing accuracy. Time calibration over 2-3 km electrical cable with a few-nanosecond accuracy is a challenge. In IceCube it is solved by sending a bipolar signal from the DAQ to the DOM (see Fig. 3, left). The leading edge of this signal is synchronized to the surface clock common to all DOMs. The signal is considerably dispersed over 2 km cable and is subject to baseline variations and noise. Therefore the calibration signal arriving at the DOM is digitized by a FADC. The full waveform information allows for a correction with respect to the mentioned effects. Since the stability of the local oscillator in the DOM is better than  $10^{-10}$ , the calibration process has to be repeated only every 10 seconds.

The time offset is determined by a method known as Reciprocal Active Pulsing (RAP) [9]. In response to the calibration signal, after a well-defined delay  $\delta t$ , the same bipolar signal is sent back to surface and treated there in exactly the same way as the downward calibration signal had been treated in the DOM. This procedure yields an overall delay  $T_{roundtrip}$ . With the same signal treatment at surface and in the DOM, one gets  $T_{up} = T_{down} = 0.5(T_{roundtrip} - \delta t)$ . This information defines the time offset for each DOM and can be determined by multiple round trip measurements with better than 1 ns accuracy. Over all, the instantaneous accuracy of the time calibration is expected to be 5 ns r.m.s.

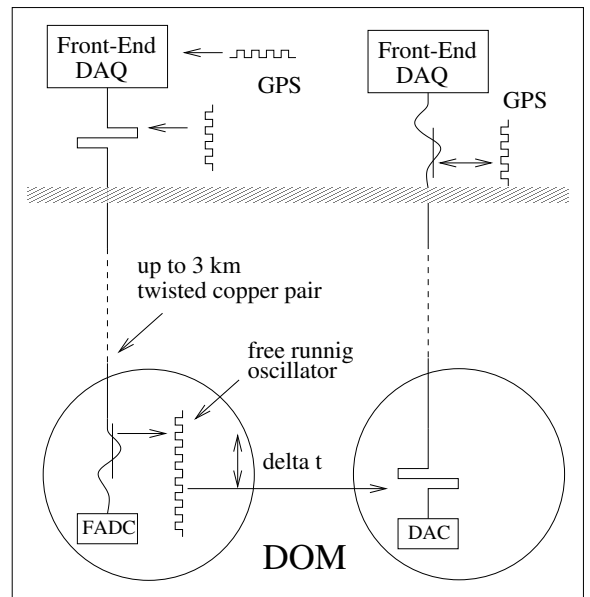


Figure 3: Principle of time calibration and offset determination

## IV. DRILLING AND DEPLOYMENT

The drill technology for IceCube is well understood from experience with several years of Amanda deployments. Holes of 60 cm diameter are drilled with 80 °C hot water. For IceCube, a new drilling system (Enhanced Hot Water Drill, EHWD) has been constructed. The power for heaters and pumps of the EHWD will be  $\sim 5$  MW, compared to 2 MW for Amanda. This, and larger diameter and length of the water transporting hoses, will result in only 40 hours needed to drill a 2400 m deep hole (three times faster than with the old Amanda drill). The fuel consumption is reduced by one third.

Mounting, testing and drop of a string with 60 DOMs is expected to take about 20 hours. Since the set-up of the drilling and deployment system at the beginning of the Antarctic summer season will be reduced from 5 to 3 weeks, deployment of 16 strings per season is feasible.

## V. PHYSICS PERFORMANCE

In this section, we summarize results on *track* detection at TeV to PeV energies published in [2]. IceCube performance at higher energies is considered in [11].

Figure 4 (top) shows the effective area after  $\sim 10^{-6}$  reduction of events from downward muons as a function of the muon zenith angle. Whereas at TeV energies IceCube is blind towards the upper hemisphere, at PeV and beyond the aperture extends above the horizon and allows observation of the Southern sky. Figure 4 (bottom) shows the effective area as function of the muon energy at the detector, averaged over the lower hemisphere. The upper curves refer to events passing trigger criteria (triangles) and fake event reduction (full circles). The other two curves show the effective area after tuning the cuts for best sensitivity to hypothetical steady point source fluxes which follow  $E^{-2}$  (stars) and  $E^{-2.5}$  (diamonds) power laws, respectively. The threshold is around 1 TeV for  $E^{-2}$  spectra. The energy-dependent optimum cut is applied to  $N_{ch}$ , the number of fired PMTs.

Fig. 5 shows the pointing resolution for neutrino-induced muon events after background rejection and assuming an  $E^{-2}$  spectrum. For not too steep angles the resolution is 0.6 to 0.8 degrees, improving with energy. We expect that evaluation of waveform information will improve these numbers significantly, at least at high energies. Paradoxically, the reason is the strong light scattering which is known to be a clear drawback with respect to the accuracy of first-photon arrival times. Part of this drawback can likely be turned into an advantage since scattering modifies the arrival time distribution as a function of distance between source and receiver. A wider distribution of a many-photoelectron signal recorded by a single PMT indicates a more distant source [12]. This additional information can be used to improve reconstruction, provided the amount of light is high enough to generate multi-photoelectron waveforms in many PMTs. However, a resolution as good as projected for water detectors seems hardly achievable.

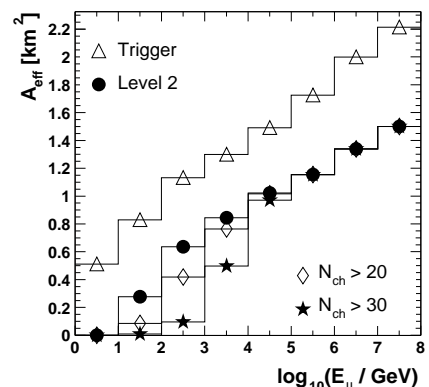
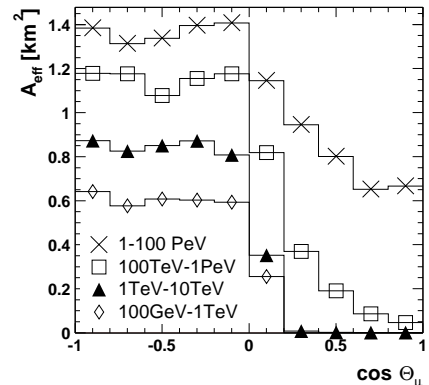


Figure 4: Effective area for muon as a function of zenith angle (top) and as a function of muon energy (bottom). The lower figures refers to muons from the lower hemisphere ( $\cos \theta < 0$ ). See text for further explanations.

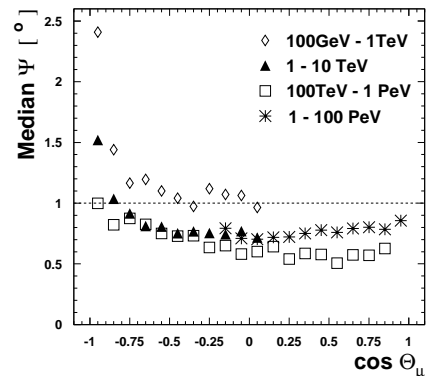


Figure 5: Pointing resolution (median space angle) for neutrino-induced muon events as a function of zenith angle

Fig. 6 shows the energy spectra of selected neutrinos for  $E^{-2}$  sources. (Note that Fig. 4 refers to muon energy, but Fig. 6 to neutrino energy). The top part shows the spectrum after fake event rejection and after cuts tailored to get best sensitivity to *point sources*. It confirms the TeV threshold demonstrated in Fig. 4. The bottom part shows the spectrum if the cuts are optimized for best sensitivity to a *diffuse*  $E^{-2}$  flux. Clearly the

large background from atmospheric neutrinos over  $2\pi$  or more requires harder energy cuts than in the case of point sources. The threshold is now about 100 times higher than for the point source analysis.

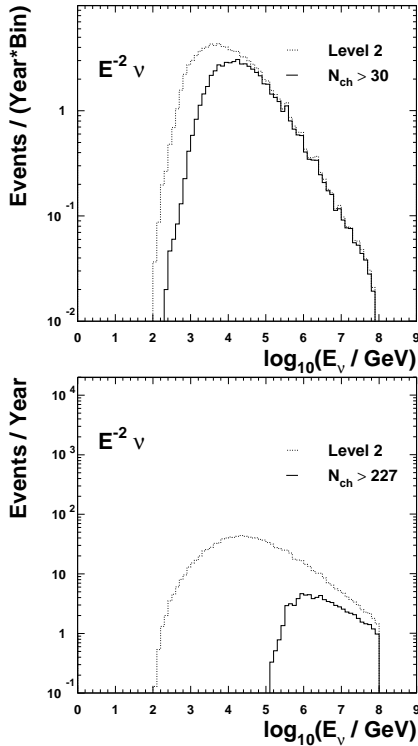


Figure 6: Energy spectra of selected neutrinos for a  $E^{-2}$  source. Cuts have been optimized to get the best sensitivity to point sources (top) and to a diffuse flux (bottom). The cutoff at  $10^8$  GeV is due to the limited energy range of the simulation.

Fig. 7 shows the expected sensitivity to diffuse fluxes as function of neutrino energy. Solid lines indicate the expected 90% c.l. limits for  $E^{-2}$  and  $E^{-1}$  spectra, respectively, calculated for a data taking period of three years. The lines extend over the energy range containing 90% of the expected signal. The dashed lines indicate the Stecker and Salamon model for photo-hadronic interactions in AGN cores [13]. The dotted line corresponds to the Mannheim, Protheroe and Rachen model on neutrino emission from photo-hadronic interactions in AGN jets [14]. In case of no signal, these models could be rejected with model rejection factor (mrf) [15] of  $10^{-3}$  and  $10^{-2}$  respectively. Also shown is the GRB estimate by Waxman and Bahcall [16] which would yield of the order of ten events coinciding with a GRB, for 1000 GRBs monitored.

Apart from tracks, IceCube can map *cascades*, with an energy resolution of about 30% at high energies. Compared to Amanda, IceCube has a much larger central volume shielded by outer "veto layers". This allows significantly better recognition of isolated cascades – an important issue for the detection of  $\nu_e$  or  $\nu_\tau$  interactions.

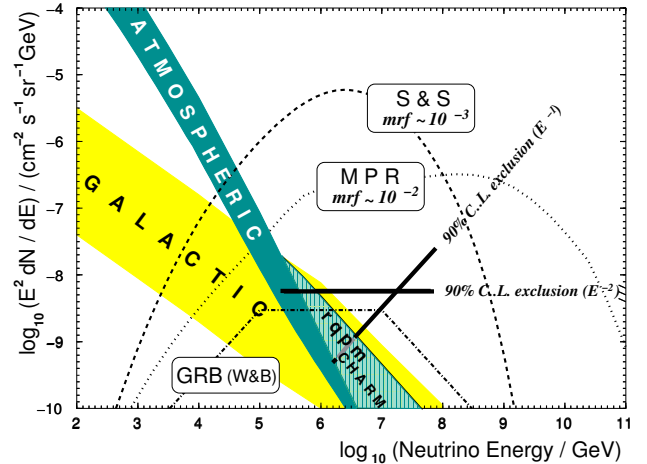


Figure 7: Expected sensitivities of the IceCube detector. See text for explanations.

## VI. POSSIBLE EXTENSIONS

Parallel to the implementation of the IceCube baseline design, methods are studied to extend the capabilities of the South Pole detector towards higher as well as towards lower energies. With a volume of a cubic kilometer, IceCube will surpass Amanda by a factor of 40 (and Super-K by a factor of 1000). These numbers refer to the sensitivity in the energy range of TeV-PeV.

For energies below a few hundred GeV the light emission is too low to fire many PMTs, and the effective volume decreases drastically. In order to increase the sensitivity at lower energies, more light has to be collected. First encouraging results have been obtained in production of transparent hats for the glass spheres housing the PMTs. These hats are doped with wavelength shifter which moves the light from wavelengths below 300 nm to wavelengths above 320 nm where the spheres are becoming transparent [7]. The resulting increase in light collection may be as high as 40%, following first measurements and estimates. This would result in a lower energy threshold and better reconstruction.

For energies above 100 PeV, on the other hand, expected neutrino fluxes are so small that even a cubic kilometer is not sufficient to catch a few events. Instead, volumes of ten or hundred cubic kilometers are required. With the given spacing of PMTs (17 m vertically, 125 m horizontally) this is not affordable, neither logistically nor financially. A larger volume could be reached by larger PMT spacing (see e.g. [8]). The increase of distance, however, is limited by the absorption length of light ( $\sim 100$  m) and the smaller amount of light reaching the PMTs. In order to allow a much larger spacing, an information carrier with smaller absorption in ice than light has to be used. Radio wave detection has been successfully applied to derive ultra-high energy flux limits with the RICE experiment, located above the Amanda experiment, at a depth of a few hundred meters [17]. Another method is the detection of acoustic



waves generated in high-energy particle cascades. The attenuation length of this signal in pure ice at  $-40^{\circ}\text{C}$  is about 2 km [18]. R&D work is underway to develop sensitive acoustic sensors with good signal-to-noise behaviour, to test them at accelerators, and to understand noise behaviour in open reservoirs of water and ice [19]. In-ice tests will show how well the method will work in natural ice.

## VII. STATUS AND OUTLOOK

The IceCube collaboration includes about 150 scientists from institutions in Belgium, Germany, Japan, Netherlands, New Zealand, Sweden, UK, USA and Venezuela. In the USA IceCube is handled as MRE (Major Research Equipment) project of the National Science Foundation, NSF. Funding of the start-up phase started in FY 2002. In the mean time, the project moved from the start-up phase to the implementation phase and is now fully installed as a MRE project. Apart from the US budget, significant funding has been approved in Belgium, Germany and Sweden.

The present plan foresees transportation of the EHW to the Pole at the end of 2004, and drilling of a few first holes in January 2005. Amanda will be integrated into the year-by-year increasing IceCube. The growing detector will take data during construction, with each string coming online within days after deployment. Construction of IceCube is to be completed in 2010, followed by  $\sim 10$  years of data taking.

## IceCube Author List

A. Achterberg<sup>25</sup>, M. Ackermann<sup>6</sup>, J. Ahrens<sup>15</sup>, J.N. Bahcall<sup>8</sup>, X. Bai<sup>1</sup>, R.C. Bay<sup>14</sup>, T. Becka<sup>15</sup>, K.-H. Becker<sup>2</sup>, J. Bergmans<sup>25</sup>, D. Berley<sup>16</sup>, E. Bernardini<sup>6</sup>, D. Bertrand<sup>3</sup>, D.Z. Besson<sup>9</sup>, E. Blaufuss<sup>16</sup>, D.J. Boersma<sup>6</sup>, S. Böser<sup>6</sup>, C. Boehm<sup>26</sup>, O. Botner<sup>24</sup>, A. Bouchta<sup>24</sup>, O. Bouhali<sup>3</sup>, T. Burgess<sup>26</sup>, W. Carithers<sup>10</sup>, T. Castermans<sup>18</sup>, J. Cavin<sup>22</sup>, W. Chinowsky<sup>10</sup>, D. Chirkin<sup>14</sup>, B. Collin<sup>12</sup>, J. Conrad<sup>24</sup>, J. Cooley<sup>21</sup>, D.F. Cowen<sup>12</sup>, A. Davour<sup>24</sup>, C. De Clercq<sup>27</sup>, T. DeYoung<sup>16</sup>, P. Desiati<sup>21</sup>, R. Ehrlich<sup>16</sup>, R.W. Ellsworth<sup>17</sup>, P.A. Evenson<sup>1</sup>, A.R. Fazely<sup>13</sup>, T. Feser<sup>15</sup>, T.K. Gaisser<sup>1</sup>, J. Gallagher<sup>20</sup>, R. Ganugapati<sup>21</sup>, H. Geenen<sup>2</sup>, A. Goldschmidt<sup>10</sup>, J.A. Goodman<sup>16</sup>, R.M. Gunasingha<sup>13</sup>, A. Hallgren<sup>24</sup>, F. Halzen<sup>21</sup>, K. Hanson<sup>21</sup>, R. Hardtke<sup>21</sup>, T. Hauschild<sup>6</sup>, D. Hays<sup>10</sup>, K. Helbing<sup>10</sup>, M. Hellwig<sup>15</sup>, P. Herquet<sup>18</sup>, G.C. Hill<sup>21</sup>, D. Hubert<sup>27</sup>, B. Hughey<sup>21</sup>, P.O. Hulth<sup>26</sup>, K. Hultqvist<sup>26</sup>, S. Hundertmark<sup>26</sup>, J. Jacobsen<sup>10</sup>, G.S. Japaridze<sup>4</sup>, A. Jones<sup>10</sup>, A. Karle<sup>21</sup>, H. Kawai<sup>5</sup>, M. Kestel<sup>12</sup>, N. Kitamura<sup>22</sup>, R. Koch<sup>22</sup>, L. Köpke<sup>15</sup>, M. Kowalski<sup>6</sup>, J.I. Lamoureux<sup>10</sup>, N. Langer<sup>25</sup>, H. Leich<sup>6</sup>, I. Liubarsky<sup>7</sup>, J. Madsen<sup>23</sup>, K. Mandli<sup>21</sup>, H.S. Matis<sup>10</sup>, C.P. McParland<sup>10</sup>, T. Messarius<sup>2</sup>, P. Mészáros<sup>11,12</sup>, Y. Minaeva<sup>26</sup>, R.H. Minor<sup>10</sup>, P. Miočinić<sup>14</sup>, H. Miyamoto<sup>5</sup>, R. Morse<sup>21</sup>, R. Nahnhaue<sup>6</sup>, T. Neunhoffer<sup>15</sup>, P. Niessen<sup>27</sup>, D.R. Nygren<sup>10</sup>, H. Ögelman<sup>21</sup>, Ph. Olbrechts<sup>27</sup>, S. Patton<sup>10</sup>, R. Paulos<sup>21</sup>, C. Pérez de los Heros<sup>24</sup>, A.C. Pohl<sup>26</sup>, J. Pretz<sup>16</sup>, P.B. Price<sup>14</sup>, G.T. Przybylski<sup>10</sup>, K. Rawlins<sup>21</sup>, S. Razzaque<sup>11</sup>, E. Resconi<sup>6</sup>, W. Rhode<sup>2</sup>, M. Ribordy<sup>18</sup>, S. Richter<sup>21</sup>, H.-G. Sander<sup>15</sup>, K. Schinarakis<sup>2</sup>, S. Schlenstedt<sup>6</sup>, D. Schneider<sup>21</sup>, R. Schwarz<sup>21</sup>, D. Seckel<sup>1</sup>, A.J. Smith<sup>16</sup>, M. Solarz<sup>14</sup>, G.M. Spiczak<sup>23</sup>, C. Spiering<sup>6</sup>, M. Stamatikos<sup>21</sup>, T. Stanev<sup>1</sup>, D. Steele<sup>21</sup>, P. Steffen<sup>6</sup>, T. Stezelberger<sup>10</sup>, R.G. Stokstad<sup>10</sup>, K.-H. Sulanke<sup>6</sup>, G.W. Sullivan<sup>16</sup>, T.J. Sumner<sup>7</sup>, I. Taboada<sup>19</sup>, S. Tilav<sup>1</sup>, N. van Eijndhoven<sup>25</sup>, W. Wagner<sup>2</sup>, C. Walck<sup>26</sup>, Y.-R. Wang<sup>21</sup>, C.H. Wiebusch<sup>2</sup>, C. Wiedemann<sup>26</sup>, R. Wischnewski<sup>6</sup>, H. Wissing<sup>6</sup>, K. Woschnagg<sup>14</sup>, S. Yoshida<sup>5</sup>

(1) Bartol Research Institute, University of Delaware, Newark, DE 19716,

USA

- (2) Fachbereich 8 Physik, BUGH Wuppertal, D-42097 Wuppertal, Germany  
 (3) Université Libre de Bruxelles, Science Faculty CP230, Boulevard du Triomphe, B-1050 Brussels, Belgium  
 (4) CTSPS, Clark-Atlanta University, Atlanta, GA 30314, USA  
 (5) Dept. of Physics, Chiba University, Chiba 263-8522 Japan  
 (6) DESY-Zeuthen, D-15738 Zeuthen, Germany  
 (7) Blackett Laboratory, Imperial College, London SW7 2BW, UK  
 (8) Institute for Advanced Study, Princeton, NJ 08540, USA  
 (9) Dept. of Physics and Astronomy, University of Kansas, Lawrence, KS 66045, USA  
 (10) Lawrence Berkeley National Laboratory, Berkeley, CA 94720, USA  
 (11) Dept. of Astronomy and Astrophysics, Pennsylvania State University, University Park, PA 16802, USA  
 (12) Dept. of Physics, Pennsylvania State University, University Park, PA 16802, USA  
 (13) Dept. of Physics, Southern University, Baton Rouge, LA 70813, USA  
 (14) Dept. of Physics, University of California, Berkeley, CA 94720, USA  
 (15) Institute of Physics, University of Mainz, Staudinger Weg 7, D-55099 Mainz, Germany  
 (16) Dept. of Physics, University of Maryland, College Park, MD 20742, USA  
 (17) Dept. of Physics, George Mason University, Fairfax, VA 22030, USA  
 (18) University of Mons-Hainaut, 7000 Mons, Belgium  
 (19) Departamento de Física, Universidad Simón Bolívar, Caracas, 1080, Venezuela  
 (20) Dept. of Astronomy, University of Wisconsin, Madison, WI 53706, USA  
 (21) Dept. of Physics, University of Wisconsin, Madison, WI 53706, USA  
 (22) SSEC, University of Wisconsin, Madison, WI 53706, USA  
 (23) Physics Dept., University of Wisconsin, River Falls, WI 54022, USA  
 (24) Division of High Energy Physics, Uppsala University, S-75121 Uppsala, Sweden  
 (25) Faculty of Physics and Astronomy, Utrecht University, NL-3584 CC Utrecht, The Netherlands  
 (26) Dept. of Physics, Stockholm University, SE-10691 Stockholm, Sweden  
 (27) Vrije Universiteit Brussel, Dienst ELEM, B-1050 Brussels, Belgium

## REFERENCES

- [1] <http://icecube.wisc.edu>  
 [2] J.Ahrens et al., accepted by Astroparticle Physics, astro-ph/0305196  
 [3] C.Spiering for the Amanda collaboration, Proc. 27th ICRC (2001) 1242.  
 [4] F.Halzen, astro-ph/0311004.  
 [5] see E.Bernardini, talk at this workshop.  
 [6] M.Leuthold, Proc. Workshop on Large Neutrino Telescopes, Zeuthen 1998, <http://www.ifh.de/nuastro/publications/conferences/proc.html>  
 [7] E. Resconi, paper to be presented at the Xth Vienna Conference on Instrumentation.  
 [8] F.Halzen and D.Hooper, astro-ph/0310152  
 [9] R.G.Stokstad et al., Preprint LBNL-43200, Berkeley 1998.  
 [10] C.Spiering, Journ.Phys.G: Nucl.Part.Phys.29 (2003), astro-ph/030368.  
 [11] S.Yoshida, R.Ishibashi, H.Miyamoto, astro-ph/0312078, to be subm. to Phys.Rev.D.  
 [12] see also C.Wiebusch, talk at this workshop.  
 [13] F.W.Stecker and M.H.Salamon, Space Sci.Rev.75 (1996) 341.  
 [14] K.Mannheim, R.Protheroe, J.Rachen, Phys.Rev.D63 (2001) 023003.  
 [15] G.G.Hill and K.Rawlins, Astropart.Phys.19 (2003) 393.  
 [16] E.Waxmann, J.Bahcall, Phys.Rev.D59 (1999)023002.  
 [17] I.Krvtchenko et al., Astroparticle Physics 20 (2003) 195 and astro-ph/0206371  
 [18] P.B.Price, Astropart.Phys.5 (1996) 43.  
 [19] R.Nahnhaue, <http://hep.stanford.edu/neutrino/SAUND/workshop/slides/>

# The Baikal Neutrino Telescope: Results, Plans, Lessons

C. Spiering for the BAIKAL Collaboration

DESY Zeuthen, Platanenallee 6, D-15738 Zeuthen, Germany

christian.spiering@desy.de

*The BAIKAL Collaboration:*

V. Aynutdinov<sup>1</sup>, V. Balkanov<sup>1</sup>, I. Belolaptikov<sup>4</sup>, L. Bezrukov<sup>1</sup>, N. Budnev<sup>2</sup>, A. Chensky<sup>2</sup>, D. Chernov<sup>3</sup>, I. Danilchenko<sup>1</sup>, Zh.-A. Dzhlkibaev<sup>1</sup>, G. Domogatsky<sup>1</sup>, A. Dyachok<sup>2</sup>, O. Gaponenko<sup>1</sup>, O. Gress<sup>2</sup>, T. Gress<sup>2</sup>, A. Klabukov<sup>1</sup>, A. Klimov<sup>8</sup>, S. Klimushin<sup>1</sup>, K. Konischev<sup>4</sup>, A. Koshechkin<sup>1</sup>, V. Kulepov<sup>6</sup>, L. Kuzmichev<sup>3</sup>, Vy. Kuznetsov<sup>1</sup>, B. Lubsandorzhev<sup>1</sup>, S. Mikheyev<sup>1</sup>, M. Milenin<sup>6</sup>, R. Mirgazov<sup>2</sup>, N. Moseiko<sup>3</sup>, E. Osipova<sup>3</sup>, A. Panfilov<sup>1</sup>, G. Pan'kov<sup>2</sup>, L. Pan'kov<sup>2</sup>, Yu. Parfenov<sup>2</sup>, A. Pavlov<sup>2</sup>, E. Pliskovsky<sup>4</sup>, P. Pokhil<sup>1</sup>, V. Polechshuk<sup>1</sup>, E. Popova<sup>3</sup>, V. Prosin<sup>3</sup>, M. Rosanov<sup>7</sup>, V. Rubtzov<sup>2</sup>, Yu. Semenyev<sup>2</sup>, B. Shaibonov<sup>1</sup>, C. Spiering<sup>5</sup>, B. Tarashansky<sup>2</sup>, R. Vasiliev<sup>4</sup>, E. Vyatchin<sup>1</sup>, R. Wischnewski<sup>5</sup>, I. Yashin<sup>3</sup>, V. Zhukov<sup>1</sup>  
(1) Institute for Nuclear Research, Moscow, Russia, (2) Irkutsk State University, Irkutsk, Russia, (3) Skobeltsyn Institute of Nuclear Physics MSU, Moscow, Russia, (4) Joint Institute for Nuclear Research, Dubna, Russia, (5) DESY-Zeuthen, Zeuthen, Germany, (6) Nizhni Novgorod State Technical University, (7) St. Petersburg State Marine University, St. Petersburg, Russia, (8) Kurchatov Institute, Moscow, Russia

## Abstract

We review recent results on the search for high energy extraterrestrial neutrinos, neutrinos induced by WIMP annihilation and neutrinos coincident with Gamma Ray Bursts as obtained with the Baikal neutrino telescope NT-200. We describe the moderate upgrade of NT-200 towards a  $\sim 10$  Mton scale detector NT-200+. We finally draw a few lessons from our experience which may be of use for other underwater experiments.

## I. INTRODUCTION

The Baikal Neutrino Telescope NT-200 is operated in Lake Baikal, Siberia, at a depth of 1.1 km. A description of the detector as well as physics results from data collected in 1996 and 1998 (70 and 234 live days, respectively) have been presented elsewhere [1, 2]. Here we present new limits including data taken in 1999 (268 live days).

We note that the year 2003 marks the tenth anniversary of the deployment of NT-36, the pioneering first stationary underwater array [3, 4]. Fig.1 shows a textbook neutrino event (an upward moving muon track) recorded with the early 4-string configuration of 1996 [5].

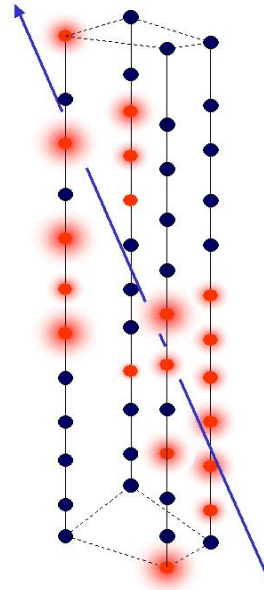


Figure 1: Upward going muon track with 19 fired channels, recorded in 1996. Hit channels are marked in color, with the size of the aura indicating the recorded amplitude.

## II. SEARCH FOR EXTRATERRESTRIAL HIGH ENERGY NEUTRINOS

The survey for high energy neutrinos is focused to bright cascades produced at the neutrino interaction vertex in a large volume around the neutrino telescope. Lack of significant light scattering allows to monitor a volume exceeding the geometrical volume by an order of magnitude. This results in sensitivities of NT-200 comparable to those of the much larger Amanda-B10 detector. The background to this search are bright bremsstrahlung flashes along muons passing far outside the array (see [6] for details).

Candidate events do not show a statistically significant excess of hit multiplicities compared to the simulated background from atmospheric muons. Assuming an  $E^{-2}$  shape of the neutrino spectrum and a flavor ratio  $\nu_e : \nu_\mu : \nu_\tau = 1 : 1 : 1$ , the new, preliminary 90% c.l. upper limit with respect to the flux of all three flavors is  $\Phi_{\nu_e+\nu_\mu+\nu_\tau} E^2 = 1.3 \cdot 10^{-6} \text{cm}^{-2} \text{s}^{-1} \text{sr}^{-1} \text{GeV}$ , about twice below previous results [6]. The preliminary limit on  $\tilde{\nu}_e$  at the W - resonance energy is:  $\Phi_{\tilde{\nu}_e} \leq 5.4 \times 10^{-20} \text{cm}^{-2} \text{s}^{-1} \text{sr}^{-1} \text{GeV}^{-1}$ . Fig. 2 shows the experimental upper limits obtained by BAIKAL (this work), and

AMANDA [7], as well as the projected sensitivity for NT-200+ (see below). Limits are compared to SSDS [8] and MPR [9] predictions. The slanted lines at the left side represent the atmospheric neutrino fluxes (dashed for  $\nu_\mu$ , solid for  $\nu_e$ ).

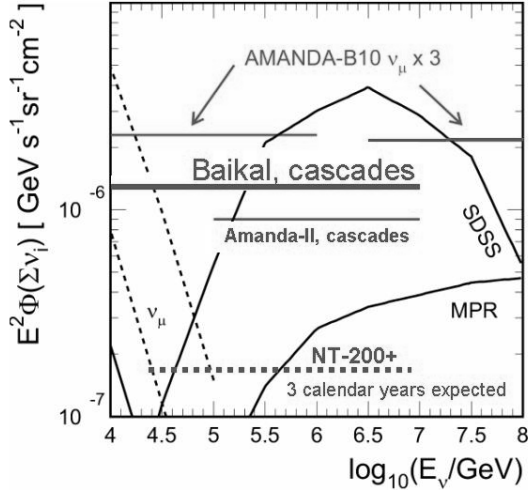


Figure 2: Experimental upper limits on neutrino fluxes (see text for explanation).

### III. SEARCH FOR NEUTRINOS COINCIDENT WITH GRBS

We have searched for high energy cascades coincident with 772 Gamma Ray Bursts (GRB) recorded between April 1998 and February 2000 by the BATSE detector and falling into on-line periods of NT-200 (386 triggered GRB, 336 non-triggered from Stern catalogue). After cuts for background reduction, we are left with one event within one of the  $\pm 100$ -second windows, where 0.47 events would have been expected from accidental coincidences. Precise limits on the fluence are being derived at present. With an effective volume in the Megaton range, NT-200 is the largest Northern detector for high energy neutrinos from GRBs.

### IV. SEARCH FOR NEUTRINOS FROM WIMP ANNIHILATION

The search for WIMPs with the Baikal neutrino telescope is based on a possible signal of nearly vertically upward going muons, exceeding the flux of atmospheric neutrinos (see [10]). Note that the threshold of  $\sim 10$  GeV for this analysis is lower than that of  $\sim 15$  GeV for atmospheric neutrinos spread across the full lower hemisphere. Fig. 3 (top) demonstrates that the angular distribution of events passing a special filter for events close to the vertical is well described by simulations including the effect of neutrino oscillations (assuming  $\delta m^2 = 2.5 \cdot 10^{-3} \text{ eV}^2$ ).

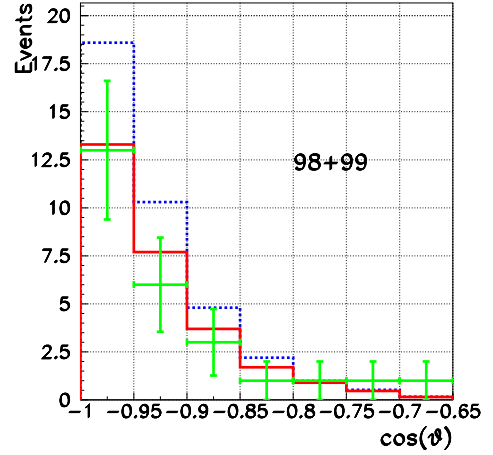


Figure 3: Angular distribution of selected neutrino candidates compared to expected distributions including (full line) and excluding (dotted line) the effect of oscillations.

With no significant excess observed, we derive improved upper limits on the flux of muons from the direction of the center of Earth related to WIMP annihilation. Fig. 3 (bottom) compares our new limits to those obtained by other experiments (see [10] for references).

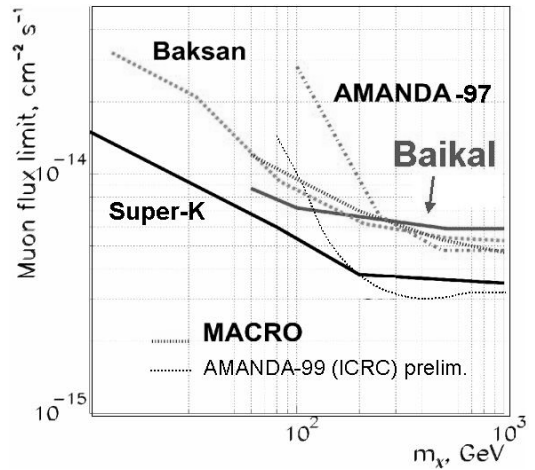


Figure 4: Flux limits from different experiments as a function of WIMP mass.

### V. UPGRADE TO NT200+

NT-200+ is an upgrade of NT-200 by three sparsely instrumented distant outer strings (see Fig. 5). The fenced volume is a few dozen Mtons. A prototype string of 140 m length with 12 optical modules was deployed in March 2003, and electronics, data acquisition and calibration systems for NT-200+ have been tested. The 3 strings allow for dramatically better vertex reconstruction of high energy cascades than with NT-200 alone (see Fig. 6). This, in turn, allows a much better determination

of the energy and makes NT-200+ a true discovery detector with respect to reactions within the mentioned fiducial volume. (This is in contrast to NT-200 which is an excellent exclusion experiment but would have certain difficulties to prove – for a single event outside its geometrical volume – that the signal is indeed due to a far high-energy event and not to a closer medium-energy event.) NT-200+ will be installed in 2004 and 2005.

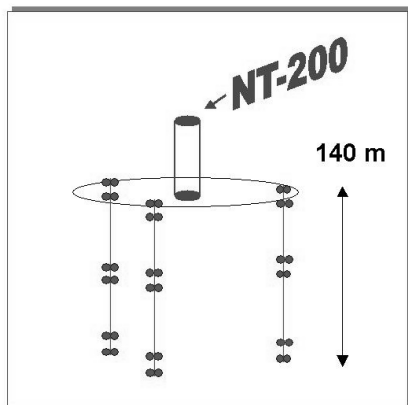


Figure 5: Configuration of NT-200+.

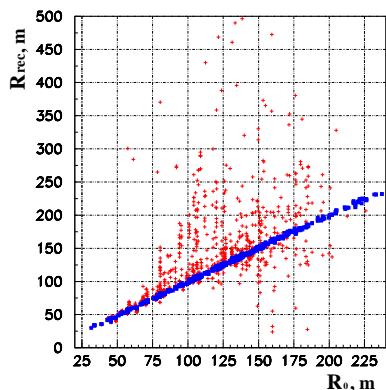


Figure 6: Reconstructed vs. simulated coordinates of cascades in NT-200+ (black rectangles) and NT-200 (crosses).

## VI. A GIGA-TON DETECTOR ?

First discussions have started on an even larger detector of the order of a cubic kilometer in Lake Baikal. The configuration of such a detector will be consequently tailored to certain classes of events and should complement Mediterranean arrays. A possible design was sketched in [2]. Given the drawbacks of stronger absorption and shallower depth compared to Mediterranean sites, this idea rests on the proven, stable deployment procedures, lower-cost considerations and possible national funding strategies. However, even in the case of strong

national funding, such a project would need international participation.

## VII. SOME LESSONS

We finally summarize some lessons which may be of use for all underwater arrays.

### A. Leakage

The early history of Baikal could have been written as a history of leaking feed-throughs, connectors and pressure housings. After having designed a special connector tailored to depths up to  $\sim 1.6$  km (the maximum depth in Lake Baikal), this phase was overcome. NT-36 did not suffer from leaks. In the mean time, more than 1000 connectors and feed-throughs are in operation at 1.1 km depth, and the failure rate is less than 1 per year. Clearly, detectors much deeper, like the Mediterranean ones, have to make use of different technologies. Still, it seems now obvious that instruments with hundreds of pressure spheres and more than thousand connectors can work in deep water over many years, with tolerable leakage rates – a statement which ten years ago would have been questioned by many oceanographers.

### B. Sedimentation

Sedimentation and bio-fouling are a concern in Lake Baikal. The performance of the up-down symmetric NT-36 detector, with the same number of optical modules facing upward and downward, was particularly affected by sedimentation [3]. The sensitivity of the upward looking modules with respect to atmospheric muons decreased to 35% after one year [11]. At present, only two of the 12 layers of NT-200 have upward facing modules. The glass spheres are dressed with a tapering hat of plastic foil. Much of the sediments glide along the foil and do not stick to the hat. The effect of sedimentation, i.e. a progressively decreasing sensitivity of the upward looking modules, is weakened, and an acceptable functionality may be kept by cleaning the hats once every two years. This is important since the outer strings of NT-200+ will be up-down symmetric. We conclude that symmetric configurations can be operated in Lake Baikal, but only if the optical modules can be easily hauled up, inspected and cleaned. The same limitation should hold for those Mediterranean sites with strong biological activity.

### C. Reliability and repair

The possibility to haul up the array and to repair connectors was a key for NT-200's operation. In the very beginning, about 40% of the optical modules turned non-operational after one year of operation due to failures in electronics. Clearly this was not tolerable, be it with or without the possibility to repair failed components. In the mean time the failure rate reduced to

less than 5% per year. This lower rate, combined with the possibility to repair failed components results in a tolerable regime of operation and maintenance. From our experience we would recommend designs which give a not too complicated access to deployed parts of the detector.

#### D. Electro-corrosion

With the reliability of the detector itself improving from year to year, we were faced by another, non-expected problem: we observed electro-corrosion along the cables to shore. Actually electro-corrosion was thought to be negligible since the fresh water of Lake Baikal is nearly free of minerals and salts and is a bad conductor of electricity. Much of the return current was thought to flow along the outer metal jacket of the shore cable (white arrows in figure 7) and not through the water.

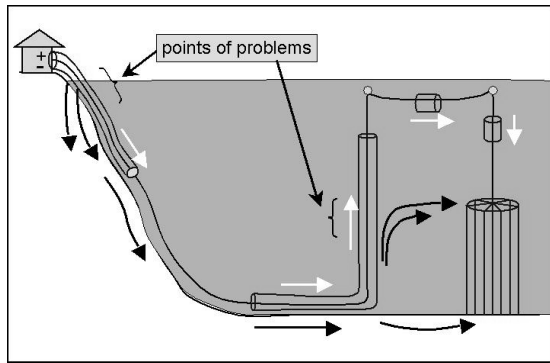


Figure 7: Electro-corrosion along shore cables. See text for explanations.

During the last year it became clear that the cable arming showed damages at the points indicated in the figure. The reason seems to be that close to the shore the current leaks into ground and propagates there with a low resistance compared to the cable, and that also current flows through the water at the depth of the big metallic, umbrella-like support frame of NT-200 (black arrows). At these points, strong electro-corrosion is observed. It led to the loss of two of the four shore cables in the last year. The cables will be replaced by new cables in 2004, and the distance between the vertical part of the shore cable and NT-200 will be increased.

Electro-corrosion should be an even stronger issue for salt water detectors, as shown by the DUMAND history. The Baikal experience can certainly not be translated to different designs of power distribution and return current. Still it may suggest that one should be prepared to unpleasant surprises and necessary design changes.

#### E. Staged approach

A staged approach seems mandatory when building a large instrument in a new and challenging environment like deep

water. The idea that one can already in the design phase account for all possible problems has been disqualified not only by the Baikal experience but also by DUMAND, NESTOR and ANTARES. The operation of prototype detectors and the readiness for technological modifications is of key importance.

#### F. Looking beyond the geometrical volume

Underwater detectors do not suffer from strong light scattering as does ice. Therefore the timing information from distant light sources is not strongly dispersed. This opens the possibility to monitor a huge volume around the detector. A few strings far outside, like those planned for NT-200+, can dramatically improve the sensitivity to PeV processes. Due to best background rejection, the most efficient region is that *below* the geometrical volume of the detector. Apart from stronger bottom water currents and slightly worse water quality close to ground, this may be another argument not to place the detector as deep as possible, but a few hundred meters above ground.

*This work was supported by the Russian Ministry of Research, the German Ministry of Education and Research and the Russian Fund of Basic Research (grants 03-02-31004, 02-02-17031, 02-07-90293 and 01-02-17227), Grant of President of Russia NSh-1828.2003.2 and by the Russian Federal Program "Integration" (project no. E0248).*

## REFERENCES

- [1] Zh.-A. Dzhilkibaev for the BAIKAL collaboration, Proc. Int. Workshop on Neutrino Telescopes (Venice 2001); and astro-ph/0105269.
- [2] G.V. Domogatsky for the Baikal collaboration, Proc. XXth Int. Conf. on Neutrino Physics and Astrophysics (Munich 2002) 353; and astro-ph/0211571.
- [3] I. Belolaptikov et al., *Astropart. Phys.* 7 (1997) 263.
- [4] Underwater: The tide turns, *CERN Courier* 33/9 (1993) 36.
- [5] I. Belolaptikov et al., *Astropart. Phys.* 12 (1999) 75.
- [6] V.A. Balkanov et al., *Astropart. Phys.* 14 (2000) 61.
- [7] see the talk of E. Bernardini in these proceedings.
- [8] F.W. Stecker et al., *Phys.Rev.Lett.* 66 (1991) 2697.
- [9] K. Mannheim, R. Protheroe, J. Rachen, *Phys.Rev. D* 63 (2001) 023003.
- [10] V. Balkanov et al., *Phys. Atom. Nucl.* 66 (2003) 503.
- [11] R.I. Bagdavev et al., *Nucl.Inst.Meth.* A420 (1999) 138.

# Grids and VLVvT Data Processing

J. A. Templon

NIKHEF, P/O Box 41882, 1009 DB Amsterdam, The Netherlands  
templon@nikhef.nl

## *Abstract*

This paper discusses computing with Grids. Particular attention is paid to the question, “when is it appropriate to use a Grid?” and examples are presented, primarily from high-energy physics. The paper closes with a discussion of how Grid technology might solve a particular problem within the VLVvT.

## I. INTRODUCTION

Grids are collections of computational resources that present software services enabling efficient distributed access and organization. Such grids are more complex to use than a “normal desktop computer”, perhaps in much the same way that a complete word-processing program is more complex to use than is a simple text editor. Grids have been conceived and built to solve certain computational problems, mostly involving distributed collaborations (your colleagues are not all located in the same building or even same continent as you) or involving a large dynamic range of computing needs (sometimes you could use ten thousand computers, but most times you only need about five).

High-Energy Physics (HEP) is making a strong investment in grids as of this writing. I will present some basic features about grids by exploring problem that HEP wants to solve using grids. I will conclude with a brief overview of the “state of the art” and a sketch of how grids might prove useful to the VLVvT community.

## II. THE HEP COMPUTATIONAL PROBLEM

High-energy physicists have at least two difficult computational problems to solve. The first involves the timely reconstruction of “what happened” during interesting collisions. The second deals with how to make sure that the entire *global* HEP community has easy access to the various data products from the detectors, and to the computational resources needed to analyze them.

### A. HEP Event Reconstruction

Event data – an event referring to an interesting collision between beam particles – collected in a HEP experiment is physically a large set (about 1 megabyte (MB) worth) of tuples of numbers. Typically about 100 of these one-MB events are recorded each second. Each tuple contains one number representing the identity of a particle detector that was “hit”, and one or more numbers providing information about the hit, such as time (when the hit occurred), or

amplitude (how much charge did the hit deposit in the detector). Physicists have built computer programs that take these sets of numbers, map them onto physical locations in the particle detector (using another large set of numbers known as a “geometry model” that says where each detector element can be found), and trace tracks – corresponding to particle trajectories – through these “hits”. The other information (such as amplitude or time) is used to infer properties (like particle type, momentum, and charge state) of the particles responsible for each trajectory identified. Each event may contain several thousand of these “tracks”, and once the tracks have all been processed, the program begins to search (based on user-specified criteria) for “interesting” tracks signifying an “interesting” collision.

These computations are straightforward. The real problem comes from a severe mismatch in scale. A modern computer will spend about 90 seconds to carry out the above set of tasks for a single event. The particle detectors at the LHC will each produce about 100 events per second. If we wish to analyze the incoming data as it comes in, we need either computers that are nine thousand times as fast, or we need nine thousand computers working in parallel on the problem.

This estimate is quite conservative; there will be four LHC experiments producing data at the same time, data will be reprocessed a few times as algorithms and calibration constants improve, many simulated events must be produced, and individual physicists will be conducting large-scale analysis activities on subsets of the data. The LHC effort will certainly require many more than nine thousand computers.

### B. Distributed Collaboration

The collaborations of the four LHC experiments contain on the order of six thousand physicists, distributed over more than one hundred different institutes or universities in more than thirty countries. These physicists would each like to have fast and convenient access to the data products from their experiments. This alone is a problem – by 2008, each LHC experiment will have generated tens of petabytes of information. It is inefficient, impractical, and almost impossible for each of the hundreds of institutes to possess a complete copy of these data. Security is also an issue – competing experiments will wish to allow remote collaborators access to the latest analysis results, but will wish to protect them from remote competitors (and even local competitors!)

Computational resources must also be shared. A quick calculation shows that the LHC will need at least six computers per physicist, but each physicist will usually need either one computer (for writing a PowerPoint presentation)

or hundreds (to perform a large-scale analysis and generate the content of the presentation). In the absence of an infinite computing budget, resource sharing is required.

### III. THE GRID SOLUTION

Grids are currently being constructed, deployed, tested, and refined in order to solve problems like the HEP one just described. Three main facilities are needed to make a grid useful to a user.

- 1) The grid must provide entry points to the user, so that a computational task can be instantiated on the grid and can make use of the data and CPUs it needs to produce the required result.
- 2) The grid must have some facility that can locate resources satisfying the user's request. It is hardly practical to expect the user to know the exact hostnames and configuration of hundreds of machines spread over several continents.
- 3) The grid must have some facility for determining whether a user is authorized to use each of the resources it identifies, and whether the identity claimed by the user is really correct. The identity may be granted because of who the user is, or perhaps only because the user can establish that (s)he is an authorized member of one of the LHC collaborations.

#### A. User Services

Grid users typically instantiate tasks on grids by submitting a task description to a *resource broker*. The task description typically includes the name of a command to run, and any arguments it requires. This is similar to typing e.g. `ls /home/templon/higgsDir` on a desktop computer. The user typically also specifies additional information such as how much time the job might take to complete, how much physical memory is needed, how many CPUs, and so on. The resource broker needs this information to identify suitable computers on which to run the task, as a typical grid contains a wide variety of machines.

The user submits this job, from a machine normally external to the desired grid, using client software that knows how to communicate with the resource broker, which is a service running on some other computer inside the grid. This client software sends the task description, and any data files needed that reside on the user's workstation (*i.e.* files not located in the grid) to the resource broker machine. The resource broker matches the user's request with suitable computing resources, chooses one of the matches, and passes the task to the selected resource for execution. The broker periodically checks the task status. When the task is completed, the broker retrieves any user-directed output and stores it for later retrieval by the user. The broker also logs the various actions taken such as "accepted task description", "selected execution site tbn09.nikhef.nl", "job completed", "output ready".

A second important entry point into the grid is that of data access. As just mentioned, a user can arrange to have input data sent along with the task description, and have output data deposited for later retrieval, but in general this facility is meant for small amounts of data like configuration files (input) or log files (output). The giga- and terabyte-sized input and output files will normally be located on grid *Storage Elements*, which are computers that have access to massive amounts of storage space, and present grid-enabled access facilities. The grid presents facilities for reading and writing to these mass storage areas. One way to do so is to request access to an entire file; the grid returns a local filename that can be opened by the user's program defined in the task description. This file may have been copied from a remote site on the user's behalf, or may have already been at the selected execution site. This is quite likely if the requested file was listed as part of the task description, as the resource broker will attempt to send the task to a site already possessing a copy of the file requested.

Work is underway to provide transparent grid access to files as well. If a user ran a program locally by typing `analyze_data /home/templon/bigfile`, the grid task will include a line like `analyze_data grid:templon_bigfile`. The grid software will then ensure that when the program opens this grid file, the bytes will be accessible. The grid software will hide the actual transfer mechanism from the user; the actual bytes may come from a normal `read()` of a local file, or may be sent over the network from a remote storage facility.

#### B. Resource Location

When a grid consists of hundreds of sites presenting a wide variety of computing resources, a facility is needed for keeping track of the (host) names of the site entry points for computing and storage, as well as the capabilities and characteristics of the resources behind these entry points. In general these facilities are called *information systems* in grid jargon. Information systems are crucial to grids, because the list of resources contained by some grid's information system essentially *defines* that grid. Hence an institute wishing to join "SuperGrid" installs the SuperGrid software and configures the services to publish their existence to the SuperGrid information system. When the publication is accepted, the institute's computer resources are now part of SuperGrid. If the institute configures the services to publish not only to SuperGrid but to UltraGrid as well, these services are now in two grids simultaneously. This property of grids opens many interesting possibilities for collaboration, as well as many potential security problems.

Another type of resource location service is often called the *replica location service* (RLS) and deals with data located in the grid. As previously mention, data files are located on grid *Storage Elements* (SEs). Normally these data files are transferred onto a single SE when they are first put "into the grid". Data access requests by executing tasks may result in *replication* of these data files to other sites, so that identical copies can be found at several locations. The RLS is a catalog that maps *logical names* – for example `templon_bigfile`

in an earlier example in this article – to the various physical locations of the file. For example, asking the RLS of the EU DataGrid for the replicas corresponding to the logical name `python_v2_1.tar.gz` for the D0 experiment generates the following list of SE hostnames:

```
marseille-se01.datagrid.cnrs.fr
farm020.hep.phy.cam.ac.uk
ccgridli02.in2p3.fr
gppse05.gridpp.rl.ac.uk
heplnx12.pp.rl.ac.uk
tbn16.nikhef.nl
gw35.hep.ph.ic.ac.uk
grid007g.cnaf.infn.it
```

Furthermore it reports that the copy on the Rutherford Lab ‘gridpp’ machine (the fourth in the list above) can be found at the following location:

```
/dzero/generated/2003/10/16/filec4e3ed01-ffa4-11d7-b2b1-ee26a6679032
```

The information system is crucial in that it defines the grid. This makes it possible for a program to use the grid, or a site to join the grid, by knowing one piece of information – the location of the information system. The alternative is to inform programs of the entire list of resources in the grid – a list that will be out of date as soon as it’s constructed, given the dynamic nature of grids and the inevitable absence of a few sites at any given time due to various problems. The following sequence of actions, invoked when a task asks to retrieve a copy of a grid data file, illustrates the central role of the information system (IS):

- 1) User’s task asks replica manager (RM) tool for a copy of logical file “fred”
- 2) RM tool asks IS for location of RLS
- 3) RM contacts the RLS at this location and asks for list of copies
- 4) RM contacts the IS and asks for the location of the nearest Replica Optimization Service (ROS)
- 5) RM contacts the ROS and presents the list of locations
- 6) ROS contacts the IS for information on network speeds between these locations and the task location, selects the storage location with the highest bandwidth to the task-execution site
- 7) RM contacts the IS and asks for details on how to contact the selected storage site
- 8) RM contacts the storage site and retrieves a copy of the data comprising the logical file “fred”.

This is similar to what happens when you click an icon on your desktop – that is a “logical file”. The click initiates actions to determine the path name (on disk) corresponding to the picture on your screen; furthermore the disk driver software resolves this path name into a list of disk sectors on some partition of a disk, perhaps even a disk physically mounted on a different machine. Windowing systems would be much harder to use if their users had to know all these details.

If the information system fails, the grid ceases to exist. Similarly if the RLS fails, the grid contains no data. Grid

researchers and designers are currently working very hard on solving this *single-point-of-failure* situation.

### C. User Authorization, Authentication, and Access

Normally a user is required to present a username and password before gaining access to a computer. In the grid world this would entail providing accounts for all users on all machines, and either having an agreement that the names and passwords would be the same on all machines, or that users would need to send along a list of usernames and passwords for each machine as part of the task description. These solutions are inconvenient, impractical, and insecure.

The Grid solution organizes users primarily in terms of *virtual organizations*. In HEP, one of the LHC experiments is a virtual organization (VO); in the business world, a company like Nokia might be VO. Resource providers – sites operating grid-enabled computing and data services – make agreements to support various VOs. Users possess public/private key pairs that establish their authority; their public keys are registered with the VOs to which they belong. When a user’s task arrives at a site, the user’s identity is checked on the basis of the key information, which is also used to check that the user belongs to the claimed VO. If all checks are passed, the user’s task is instantiated in an anonymous account assigned to the relevant VO.

Note that the structure here is similar to that of the previous section – individual parts of the system do not need to know the full details (*i.e.* the complete list of users in the “ATLAS” VO). They only need to know the location of the information system. The IS knows the location of the ATLAS VO registry, that can then be queried to determine whether the user really belongs to the VO.

VO membership can be used in other ways, such as to assign priority to computing tasks, and to grant or deny permission to data products. Someone in the Nokia VO can create a grid file and set its permissions so that anyone else in the Nokia VO can read it (the explicit list of users is again not needed), but other VOs cannot.

## IV. STATE OF THE ART

As of this writing, the first generation of the large grid development and deployment projects are nearing completion. In the HEP world the EU DataGrid project [1] has the largest grid, followed closely by the US projects like PPDG (Particle Physics Data Grid) [2] and ivDGL (international Virtual Data Grid Laboratory) [3]. The author of this paper is most familiar with the EU DataGrid system and hence will describe the current situation for that project.

### A. Task Description and Brokering

The capabilities described in section III.A have been implemented and are working. Current research focuses on inter-task communication (the equivalent of unix pipelines) and on automatic decomposition and management of large



jobs; currently the user is responsible for partitioning large jobs prior to submitting them to the resource broker.

### B. Data Access and Replica Management

A flexible system has been developed to deal with grid data files, allowing users or their programs to find locations of files, request copies, or replicate files to other locations. Prototypes for the transparent-access facility are being constructed by the LCG project [4].

### C. Information Systems

The EU DataGrid project developed R-GMA (Relational Grid Monitoring Architecture) [5] as a platform for carrying the information system. It presents the information as a grid-wide SQL database enabling the kind of powerful queries needed by grid services. The implementation is as of this writing still being “hardened” for production use; as we indicated earlier, the grid only exists as long as the information system is functioning.

### D. Authentication, Authorization, and Access

The basic public-key infrastructure used in the EU DataGrid project makes heavy use of the Globus [6] toolkit libraries. As the EU DataGrid suite approaches production quality, security is becoming more important. Secure versions of all important services will be functioning within the next six months.

## V. USE OF GRID TECHNOLOGY IN A VLVvT

The figure below shows an example of how the VLVnT data distribution and processing might be handled. When detector data arrive at the shore, they will need to be processed immediately. The data rate (order 10 gigabyte/sec) precludes storage of the raw data for later processing; a modern 10 TB disk cache would be filled within twenty minutes. For this reason, a dedicated – meaning not distributed across a Grid – trigger farm will be required at the shore station. This farm (labeled “L1 trigger” below) will generate tracks from the raw data and reduce the flow of data to on the order of 1 megabyte/sec.

This stream can be stored locally and/or distributed to remote sites for further processing. The Grid may be of use in aiding this redistribution – files could be registered in a Grid data-management system and retrieved by remote users using grid data-management tools. Such a scheme rescues users from having to know which files are stored in which location – files containing the desired data will be located by issuing SQL-like queries to the data-management system rather than specifying specific file names located in specific directories on specific computers. One might even deposit the data in a distributed database system.

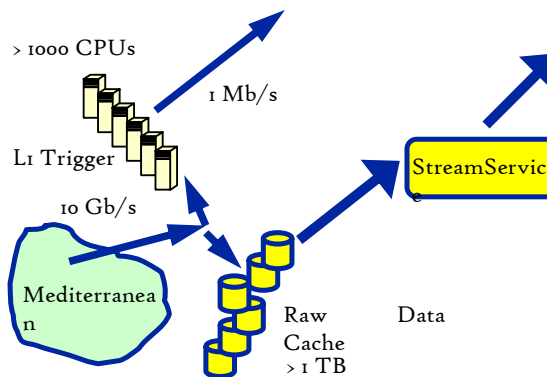


Figure 1: VLVvT data distribution

The right half of the figure addresses the rare, but important, occasion where remote access to the raw data is required. This will happen for instance when another observatory notifies the VLVnT team that a gamma ray burst has been detected in a particular direction. Given a timely notification (within a minute of the actual event), cached copies of the raw data can be redistributed to remote sites for processing. A one terabyte cache can save about two minutes of data. Network bandwidth of several gigabyte/sec is required in order to transfer the data. The current world record speed is five gigabyte/sec over a special link with special hardware. Given current trends in networking technology, it should be possible to build a Grid “stream service” providing this type of bandwidth on demand. Remote sites connected to the Grid can contact this service to connect to the data stream when necessary. This solution cannot replace the L1 trigger farm, since if the network link goes down or is congested, data are lost. However for the case of the raw data cache, one can freeze the cache until the data can be streamed to the remote farms, since these events are expected to be infrequent.

## VI. REFERENCES

- [1] <http://eu-datagrid.web.cern.ch/eu-datagrid/>
- [2] <http://www.ppdg.net/>
- [3] <http://www.ivdgl.org/>
- [4] <http://lcg.web.cern.ch/LCG/>
- [5] <http://www.r-gma.org/>
- [6] <http://www.globus.org/>

## VII. ACKNOWLEDGEMENTS

The author wishes to thank Mr. Antony Antony and Dr. David Groep for fruitful brainstorming sessions on how to use the grid to manage neutrino-telescope data distribution. Dr. David Groep also provided useful comments on a preliminary version of this manuscript, and Dr. Maarten de Jong helped by providing an outline of how the telescope data would be collected and processed.

# Design and testing of equipment for deep-sea research

Lavinio Gualdesi

Saclant Undersea Research Centre – 400, V.le S. Bartolomeo 19100 La Spezia, Italy  
gualdesi @saclantc.nato.int

## Abstract

This presentation draws on the synergy created by a regularly changing influx of scientists, engineers and naval officers from national laboratories, universities and other research institutions in almost every NATO nation. This unique research environment, a “centre of excellence” in underwater acoustics, oceanography, signal processing and ocean engineering at the Saclant Undersea Research Centre, La Spezia has been responsible under the terms of its charter for “applying science to NATO maritime operational requirements since 1959”.

A review of reliability criteria in the design and development of scientific equipment and the means by which it is deployed is followed by an overview of existing technology.

The complexity of a problem is mitigated by dividing it into component problems, which individually are more susceptible to a solution, which is subjected to rigorous testing.

Performance evaluation techniques and test facilities for deep-sea research equipment used at the Centre are described.

## I. SACLANTCEN OCEAN ENGINEERING

### A. A working team since 1959

It is not infrequent that, technical solutions for the most recurring problems of underwater scientific research are biased by too short-term experience or by theories not sufficiently validated during real and systematic endurance tests. The synergy created by changing influx of scientists, engineers and naval officers associated with a continuous sequence of sea experiments

provided consistency to a unique operational tool for the reliability of underwater research.

## B. Design and Feasibility Phase

The mission definition implies to define which instrumentation is vital for the mission success and what should be considered as a mission partial or total failure. (Fig. 1).

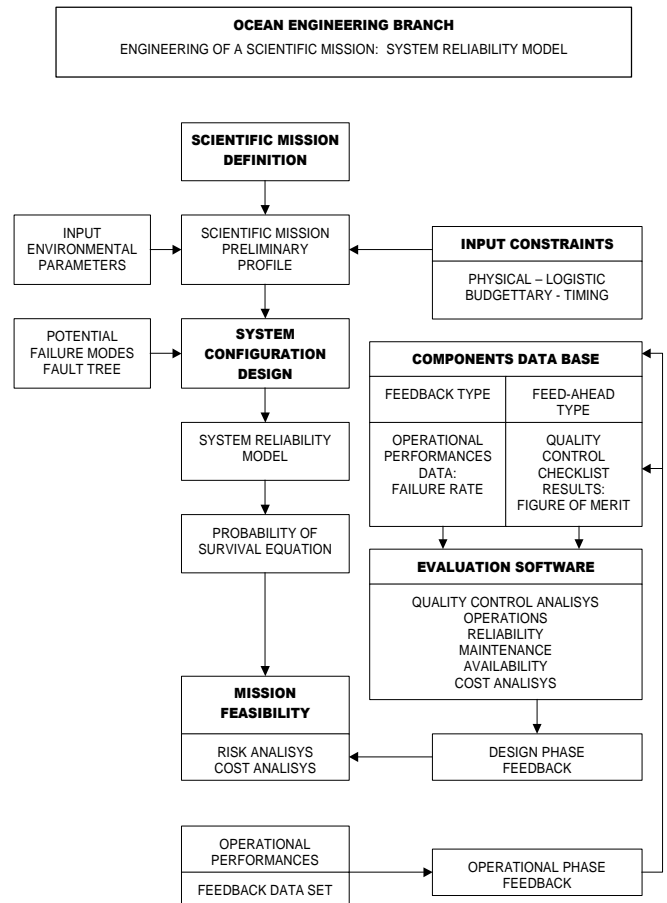


Figure 1 - System Reliability Model

The second step is to mitigate the complexity of a system by dividing it into component problems more susceptible to a ready in house solution

All the above components must be seen in the mission environment such as: vessel sea keeping, vessel's deployment and recovery facilities, working area characteristics and dominant weather problems.

This analysis leads to the system configuration design with the corresponding system reliability model. Simulations where extreme conditions are applied give the probability of survival equation that will be used in the project feasibility study. This quantitative analysis is based on risk analysis and cost analysis.

Therefore a typical design procedure is based on input constraints of various natures: logistics, budget, deadline, space, and weights.

The most valuable analysis tool is the component's database containing information on failure rate derived from actual operational performance. For components where waiting for a failure is not advisable, standard procedures are established and database provides a deviation rate from the quality control checklist, called figure of merit.

The evaluation software provides information on quality assurance, operations, reliability, maintenance, availability and cost analysis.

### C. Component Status

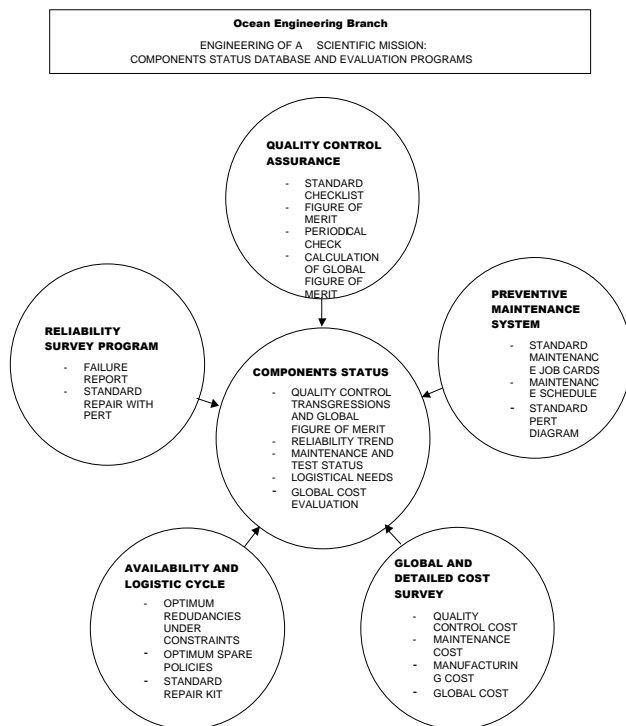


Figure 2 - Component Status

Since the above described data collection requires a resource investment, it has been adopted to monitor the research systems status under many aspects such as Quality Assurance Status, Reliability Trend, Maintenance Status, Logistic Needs, and Cost Evaluation.

Quality Assurance program provides: Standard checklist, Figure of Merit, Periodical Survey, System Reliability Program, through Failure Report analysis provides: Reliability Survey Calculations, Standard Repair with PERT.

Preventative Maintenance System supplies Standard Job Maintenance Cards, it updates Maintenance Schedules and it optimizes availability, by using PERT.

Availability and Logistic Cycle calculates; the optimum redundancies under various constraints and the optimum spare parts policy suggests when and where to store standard repair and maintenance kits, always to minimize down time.

System's Cost Survey is a simple accounting program that divides costs into Quality Control Cost, Failure Cost, Maintenance Cost and Manufacturing cost in order to monitor experiment's budget.

This last tool is particularly useful for the project manager to assess when production and maintenance costs are not anymore effective to reliability level.

This is possible because the simulation model provides a quantitative prediction of performances and the analysis of survival in extreme working conditions.

This is also very important when considering that the costs associated to a failure in deep mooring operations are much higher than the ones in shallow waters

### D. Laboratory facilities

Performance evaluation techniques to qualify components to be used in operational systems are based on test facilities.

Regardless they are used in shallow or deep-sea they are subject to standard test in the facilities hereunder described.

### *Pressure Tanks*

It is possible to simulate an equivalent ocean depth of 6000 m in a pressure tank with an inner diameter of 400 mm and a height of 1800 mm. Another test chamber accommodates instruments of 800mm diameter and 2000 mm in height up to 1000 meters. All test chambers are fitted with external connectors to allow dynamic tests like the underwater winch rotating for one month and a deep water switch operated 1000 times at its working depth

### *Cable Test Machine*

Cables reliability is obtained by a regular testing of rope and wire samples up to a maximum length of 20-m. sample @ 50 T. [5]. The computer driven test machine performs an automated ASTM Tensile test. In collaboration with Gottifredi e Maffioli Rope Manufacturers, Saclantcen is continuously exploring new fiber's properties, also simulating sea operational conditions in current and wave through elongation, fatigue, vibration and abrasion tests.

### *Climatic Chamber*

Instrumentation endurance and corrosion in salty environment are simulated in a climatic chamber for accelerated life test.

### *CTD Calibration Laboratory*

Oceanographic Calibration Facilities, WOCE Standard, for conductivity, temperature and depth (CTD) is a well established Service to Saclantcen and to most NATO Nation Navies and Research Communities with its three thermally controlled salt water baths, fully automated data acquisition, evaluation of secondary effects on sensors like pressure effects on temperature.

### *Transducers Calibration Tank*

A 4m by 4m transducers test tank is provided with a depth of 2 meters, together with a hydrophone's calibration tank for acoustic arrays. An experienced resin laboratory for cable and boards molding adds reliability and adaptability to various engineering needs.

### *Monesteroli Corrosion Test (Cinque Terre)*

The reason for installing an underwater site for direct endurance testing of alloys was to validate

components of various alloys through an in-situ compatibility test.

### *Elba Island. Marciana Marina*

A shore lab for engineering test of underwater scientific instrumentation and real time data collection is available where a scientific diving team may visually inspect equipment performance. [1].

## II. PRESENT SYSTEMS DEVELOPMENT

### A. *Barny Sentinel*

Barny Sentinel is a trawl-safe platform fitted with an Acoustic Doppler Current Profiler in service since 1996. [4].



**Figure 3 - Barny Sentinel Operations**

Lesson learned from Barny Sentinel:

Bottom layout monitoring system proved to be a vital tool for deployment.

A lifetime for individual components was assessed and new investments oriented.

Redundancy for overturned unit recovery was a successful design criterion.

Anti-collision design was a vital feature.

### B. *SWEEP*

Sweep is a spar buoy profiling CTD data through a winch, which makes it emerging on the surface to transmit real time data to a radio link. [2].

Lessons learned from SWEEP:

Winch on board the vehicle fitted with a spooling gear represents a viable technique.

The spar buoy shape of the vehicle is very stable in wave ensuring a reliable data link to satellite

SWEEP has a very high performance investment ratio.

### C. SEPTR

Based on positive Barny experience the platform was completed with a CTD profiler who is also transmitting ADCP data to a satellite radio link.

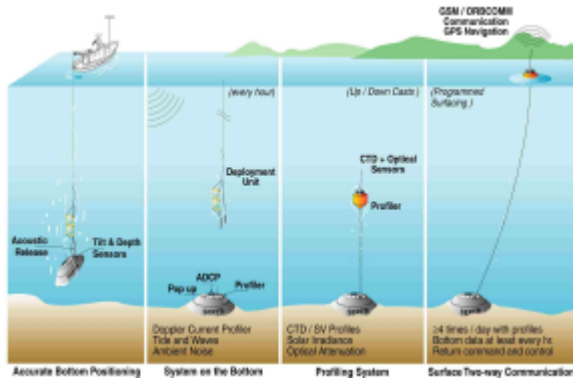


**Figure 4 - SEPTR Operations**

Lessons learned from SEPTR were: Also a bottom unit mounted winch demonstrated good performances. HDPE profiler's rope had no failures. Pop-Up recovery technique is reliable. ROV emergency recovery was successfully tested. Aluminum alloy must be abandoned when endurance is required.

### D. UNDERWATER RAIL FOR ACOUSTIC SOURCES CALIBRATION

Underwater lab for in-situ acoustic calibration. [3]. Using rail screwed to the bottom as opposed to traditional steel ballast offers the following advantages:

- Very precise positioning on the seafloor
- Keep mutual distances between close moorings very precise.
- It can be used to obtain an easier underwater connection.
- Although made with the help of divers in shallow waters, the rail-tower assembly is designed for an easy and quick procedure.

### E. The GIN sea period: 86-91

Development of buoy and mooring technology for long -term sea deployments in severe weather conditions in Greenland, Iceland and Norway area of operation brought to important achievements. [6]. More than 56 moorings were installed and successfully recovered for a total of

31buoys, 118 instruments over a 10 years program. [7] [8]. Maximum endurance deployment time was over one year. Less than 5% of loss, due to conflict with fishing activity, was the reliable result of this long campaign. [9].

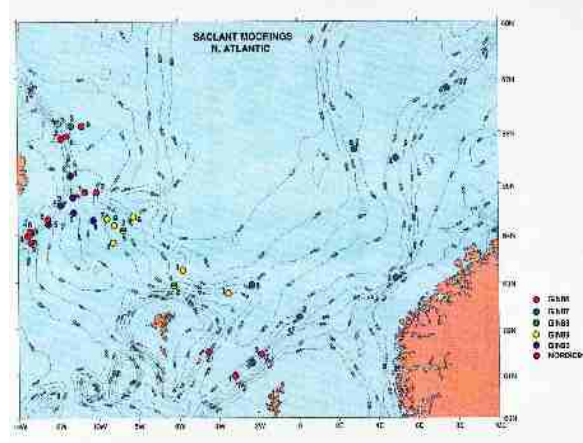


**Figure 5 - Greenland Iceland Norway Moorings**

### F. AUV Program at SACLANTCEN

The AUV program is carried out with an Ocean Explorer customized with a variety of sonar's for acoustic research.

### G. Research Vessel Alliance

The research vessel Alliance is the support vessel owned and operated by SACLANTCEN for the purpose of its scientific mission.



**Figure 6 - Research Vessel Alliance**

- Vessel's main characteristics are:
- Length 93 m
- Beam 15.2 m
- Draft 5.2 m
- Gross Tonnage 2450 t

Total shaft Power 2490 kW  
Max speed 16.3 knots  
Crew 24. Scientific Staff 23

### III. SPECIAL MATERIALS

#### A. Mission Definition

Develop a neutrino measuring range at 3500 meters depth. Maximize corrosion free endurance time (time between overhauls). Minimize maintenance time. Minimize failure risk. Respect budget constraints.

Between two extreme policies of using market available products and design to improve system reliability or invest in material performance research aimed to design and develop a system as a complete prototype a cost effective compromise is to be preferred such as to integrate market products into a customized system. This system must withstand depth pressure with an acceptable flexural deformation. It must preserve the relative motion between moving parts without an excess of friction also preserving it from corrosion for long time.

Non-magnetic or even non-conductive materials to avoid galvanic effects and influence compass related instrumentation must be preferred.

#### B. Titanium Alloy

Titanium alloy has an excellent response to corrosion and fouling. It is non-magnetic and it has a high mechanical strength and a medium availability.

Its higher cost is largely compensated by the use of less material weight to obtain the same strength and by savings in maintenance cost

Its low density and high strength candidates it for the best material to make effective pressure vessels, but coupling connectors and joints of different material may cause galvanic problems to them.

Welding Titanium alloys needs an expensive skilled procedure. It is important to establish a design policy: if the reference is Titanium alloy, any compulsory deviation from it must be considered as a case study. Only Composite Technology may be associated to it with careful design of the joints due to the different elastic properties.

#### C. Composite Materials

Composite Materials are corrosion free, non-magnetic and show damage propagation very low. A creative design is possible due to the fact that the designer makes its own production: it is virtually possible to change material density and composition at any section.

A good quality assurance system is needed to avoid transforming a creative design in arbitrary solutions during production phase.

Normally an expensive set of models and moulds are needed for each component. Therefore this solution becomes cost effective after a large number of components per mould (with the recent exception hereunder exposed).

Standard lamination process with woven roving creates a part with maximum flexural strength in 0-90 degree directions, with minimum strength along -45 +45 directions.

Reinforcement specialists to better isotropy have produced a special material woven along -45 +45 degrees.

Vinylester composites are the most chemical resistant and their utility in the field of corrosion free material has been proven by long-term performances.

Compressive strength of vinylester single-skin laminates shows values exceeding the pressures to which the structures is subjected in submarine service (400 bar) of a factor of 4.

With the fundamental requirement of performing as an underwater shelter for the protection of marine environment from petroleum spills, vinylester composite structure will be suitable for solving all design peculiar problems and giving an expected life cycle of 50 years.

Isopolyesters also have been successfully used in many corrosion resistant applications. However, vinylesters give the required answers to these specific problems by a number of documented case histories, which demonstrate better performance versus polyesters in the most severe applications.

Syntactic foam to encompass electronic boards with the associated wiring and underwater connector is also an available technology.



**Figure 7 - Syntactic Foam Enclosure**

Large plates may suffer from creep or even a buckling effect, which is particularly negative to moving joints. Potential solutions may be:

- A hybrid glass carbon reinforcement and unidirectional tapes along the strength lines
- A straight fiber sewed 0-90 degrees glass reinforcement

Solution for moving joints and rigid light parts:

- Hybrid sandwich composed by syntactic foam core and two titanium alloy skins
- Use a sandwich composed by a syntactic foam core and pre-impregnated FRP skins cured in oven

Finally this is a novel procedure to make inexpensive moulds:

Perform a CAD drawing of the model

Prepare the corresponding CAM file of the working sequence: a 7axis robot machines the CAD model followed by the lamination of the mould on the model.

Then the standard production of FRP parts out of the mould may start.



**Figure 8 - Model Machining with 7-axis robot**

## V. CONCLUSIONS

These notes may be concluded emphasizing that when handling with scientific experiments, it is very important to validate with laboratory and sea experience any design or feasibility studies. Appropriate laboratories and test sites are necessary to qualify research components. Only well proven components may be part of a system and an appropriate redundancy policy must be established. Material selection and validation may influence telescope endurance and maintenance.

Investing in a dedicated underwater vehicle for automated operation and maintenance may be cost effective. [10].

A bottom mounted automated robot may be supplied by the underwater Electro-optical cable because less power rate is needed.

Samples of existing technology and reliable procedures have been described.

In particular the long term mooring experience achieved in GIN Sea, the rail- tower assembly in a test site, laboratory and in-situ performance testing of critical components such as: connectors, cables and electronic boards molding. An effective selection of material combination obtained by direct sea performance and the experienced introduction of vinyl ester composites parts represents a suitable ground to make the ref. [10] proposal an attractive option.

A more automated maintenance procedure would decrease the sensor's strings down time and it will increase reliability and therefore detection's probability.

## VI. REFERENCES

- [1] P.A.Sletner, L.Gualdesi, R.Chiarabini, "Shore laboratory in support of GOATS", GOATS 2000, Conference Proceedings, SACLANTCEN, La Spezia, Italy, August 2001
- [2] R.Tyce, F.de Strobel, V.Grandi, and L. Gualdesi, "Shallow water expendable environmental profiler (SWEEP)", Oceans '99, Conference Proceedings, pp.1229-1233, March 1999
- [3] S.Fioravanti, A.Maguer, W.L.J.Fox, L.Gualdesi, and A.Tesei, "Underwater rail facility for highly controlled experiments at sea." Third European marine science and technology conference, Conference Proceedings, pp.55-68, Lisbon, Portugal, May 1998

[4] F.de Strobel, L.Gualdesi, "BARNY, a trawler safe, bottom mounted, ADCP platform for Mediterranean, long term, coastal water applications", J. Marine Env. Engg. Vol.4, pp.175-187, 1997 OPA (Overseas Publisher Association)

[5] L.Gualdesi, F.de Strobel, D.Di Massa, "An automated instrument for testing and monitoring oceanographic mooring cables and ropes", Oceans '96 MTS/IEEE, Conference Proceedings, pp.327-331, Ft Lauderdale, FLA.USA, September 1996

[6] L.Gualdesi, F. de Strobel, "Experimental Verification and Implementation of Mooring Line Trajectory Prediction Model Based on ADCP Data Input." MTS 94, Conference Proceedings, pg.827-832, Washington D.C., USA, 1994.

[7] T.S.Hopkins, P.Giannecchini, L.Gualdesi, A.M.Mouchet and P. Zanasca, "Atlantic Inflow Experiment, GIN Sea Cruise '87", SACLANTCEN Memorandum Ser. N. SM-250, December 1991

[8] T.S.Hopkins, P.Giannecchini, L.Gualdesi and P. Zanasca, "Atlantic Inflow Experiment, GIN Sea Cruise '86", SACLANTCEN Memorandum Ser. N. SM-231, March 1990

[9] F. de Strobel, T.S. Hopkins, L. Gualdesi "Deployment of an Acoustic Doppler Current Profiler using a Low-Drag Subsurface Multisensor Flotation Package: Design Criteria and Results", Presented at the Fourth IEEE Conference on Current Measurement, Silver Spring, MD. April 1990.

[10] M. Sedita - INFN LNS in these proceedings.



# Bioluminescence in the deep-sea: potential for interaction with sub sea detector arrays

E. J. V. Battle, I. G. Priede, P. M. Bagley & M. Solan

Oceanlab, University of Aberdeen, Newburgh, Aberdeenshire, AB41 6AA, UK  
e.battle@abdn.ac.uk

## Abstract

Bioluminescence, light emitted by living organisms is a well-known phenomenon in the surface layers of the world's oceans. Vivid light emission is often stimulated by the wake of ships and currents flowing around static structures. At depths where solar light becomes negligible (500-1000m below the surface), many animals have light emitting organs for signalling to members of the same species (e.g. for attracting mates) or to other species (e.g. to attract prey). Most studies on bioluminescence have been confined to depths less than 1000m, but it is known that the amount of bioluminescence decreases exponentially to the abyss at >4000m. Studies with a free fall instrument have allowed us to investigate bioluminescence from the surface to depths of 4800m in the north-east Atlantic ocean. There is never zero light emission and indeed most abyssal demersal fishes do have eyes indicating the presence of deep light sources. When an array (such as the ANTARES neutrino telescope) is deployed in the deep-sea it will detect three kinds of bioluminescence: spontaneous, stimulated and entrained. Spontaneous bioluminescence is the natural background activity of animals communicating with one another; stimulated bioluminescence is caused by impacts with or proximity to the array. Entrained emissions occur when animals (colonial salps, jellyfish) adhere to or entrain on the array. Even at 4000m we have detected seasonal changes in bioluminescence coupled to the annual cycle of bioproductivity in overlying waters. Neutrino telescopes should be located beneath the most oligotrophic waters that can be found in order to reduce interference from bioluminescence.

## I. BACKGROUND

Bioluminescence (most commonly blue-green light) is a ubiquitous phenomenon in the marine environment and has been the subject of numerous shallow water *in situ* studies [1, 2 and references therein, 3]. These studies have used ship tethered vehicles, manned submersibles and remotely operated vehicles (ROVs) to obtain *in situ* observations. These methods could affect the results obtained through indirect stimulation of bioluminescence as a result of shear stress (for example caused by ship-roll in the case of tethered vehicles) or could affect the behaviour of those animals studied as a result of bright lights and loud motors [4]. An autonomous system to measure bioluminescence *in situ* has several advantages in obtaining more realistic data from the marine environment.

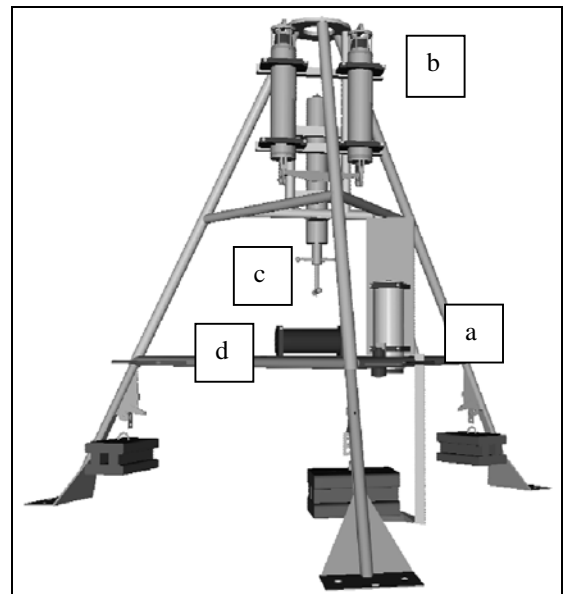


Figure 1: The ISIT Lander showing main components: a) ISIT camera, b) twin acoustic releases, c) current meter, d) controller housing

Oceanlab, at the University of Aberdeen, have developed a number of autonomous lander frames to carry out a variety of different *in situ* scientific experiments in the deep-sea. Of these the ISIT lander (Figure 1) is designed to measure bioluminescence using a low light monochrome ISIT (Intensified Silicon Intensifying Target) camera (Kongsberg Simrad, UK). The tripod lander is made of aluminium and supports the camera, current meter (recording depth, current speed and direction, temperature and salinity), twin acoustic releases as well as a housing containing the controlling electronics, battery and a DV tape recorder

The ISIT is operated in free fall mode descending towards the seafloor at  $34\text{m}\cdot\text{min}^{-1}$  with the camera pointing vertically downwards, viewing a mesh screen (mesh size  $1\text{cm} \times 1.8\text{cm}$ ) placed at a distance of 50cm. Organisms impinging on this screen are stimulated to luminesce by direct impact, shear forces (small organisms passing through the mesh) or destruction (delicate colonial types). Data were counted as number of events per unit time of descent which taking into account velocity and area was transformed into an estimate of number of potentially luminescent animals per cubic metre.



Figure 2: ISIT Lander deployment locations (white dots)

A total of 19 deployments have been carried out using the ISIT lander in the Porcupine Seabight and Abyssal Plains regions of the north-east Atlantic ocean during cruises aboard the RRS Discovery during April and August 2001 and March and September 2002 (Figure 2). The camera records directly to DV tape for subsequent frame by frame analysis of the number of bioluminescent events per minute. Deployments have taken place down to depths of 4800m.

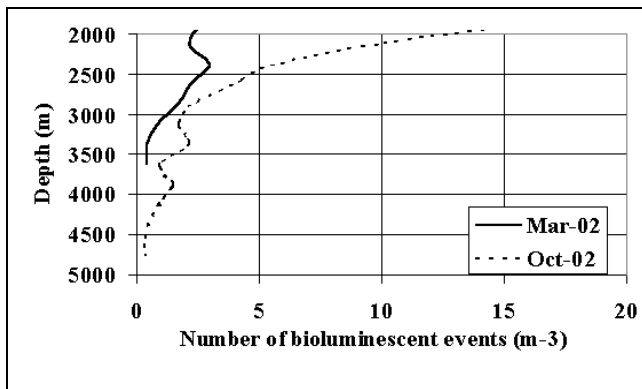


Figure 3: Vertical profile of number of bioluminescent animals per cubic metre below 2000m.

Figure 3 shows a summary plot of the number of bioluminescent events (animals) counted per cubic metre between 2000m and 4800m, typical of depths proposed for arrays. These data were grouped into 250m depth bins. Each season is an average of at least four deployments. A seasonal difference in the amount of bioluminescence observed occurs, with October deployments showing higher levels of bioluminescence all the way to the sea floor (Figure 4).

The ISIT camera lander allows identification of the types of bioluminescent emissions on the basis of dimensions, shape and duration. Thus Figure 5 shows the primary morphological types – small, large and gelatinous. Small events are most likely to be caused by small planktonic organisms such as copepods, large events by larger plankton or even fish. Colonial gelatinous events are those where the animal gets trapped on the mesh and glows intermittently until its supply of bioluminescent chemicals is exhausted.

Depth (m)	Average events per cubic metre	
	Spring	Autumn
2000	2.4	8.5
3000	0.7	1.4
4000	0.2	0.9

Figure 4: Table showing average number of bioluminescent events per cubic metre in spring and autumn.

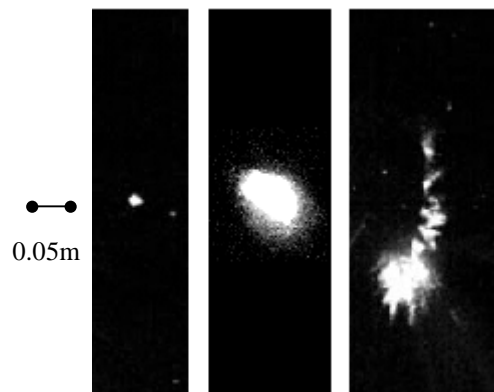


Figure 5: Grabbed images from ISIT video of (from left to right) small, large and gelatinous bioluminescent events

With regards to bioluminescent emissions in the vicinity of an array, these can be classified into three types (Figure 6). Spontaneous emissions occur without any external stimulation and can be both intraspecific or interspecific, these however are rare in the north-east Atlantic ocean [5]. Stimulated events occur as a result of shear stress or impact on the array structure. Entrained events are those of animals which adhere to the array, for example colonial animals such as salps or gelatinous planktonic species.

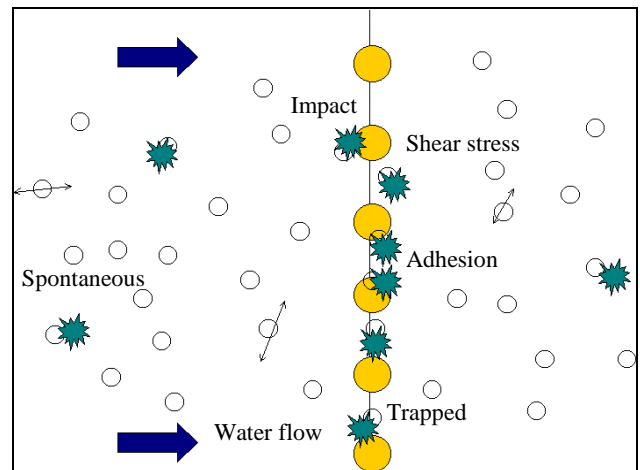


Figure 6: Illustration of three types of bioluminescent emission: stimulated, spontaneous and entrained

There are several biological factors that affect the possibility of bioluminescent emissions being detected by an array. Most important of these are the size and abundance of bioluminescent species. The locomotory ability of planktonic species will also influence their ability to avoid an array structure. Many organisms are thought to pass on the chemicals required for light emission from parent to offspring. Thus an organism's reproductive status will affect its ability to bioluminesce.

Most shallow water bioluminescence is produced by phytoplankton, namely dinoflagellates e.g. *Noctiluca sp.* The level of these planktonic species varies seasonally due to water column stratification and the reduction in the amount of nutrients available over the year. This impacts on the numbers of animals further up the food chain (including copepods and fish) many of which are an important component of the bioluminescent potential of the water column.

A measure of the amount of phytoplankton can be obtained by recording surface levels of chlorophyll, as available from, for example, the SEAWIFS project (<http://seawifs.gsfc.nasa.gov/SEAWIFS.html>). These maps provide a broad scale measure of the level of productivity in the world's oceans; but it should be noted that remote sensing algorithms are not yet well calibrated and do not replace the need for *in-situ* monitoring. Thus levels of high chlorophyll are associated with high levels of phytoplankton and thus it can be assumed relatively high levels of animals capable of emitting bioluminescence. Areas of low chlorophyll are termed oligotrophic.

The optimum site for an array would be in an area where the concentration of chlorophyll (and thus bioluminescence) in surface waters is low. Figure 7 shows SEAWIFS data for the north-east Atlantic and Mediterranean. Clearly the Mediterranean is an oligotrophic area. However, the proposed ANTARES site is located in the region of relatively high productivity in the Mediterranean, compared with more southerly / eastern locations.

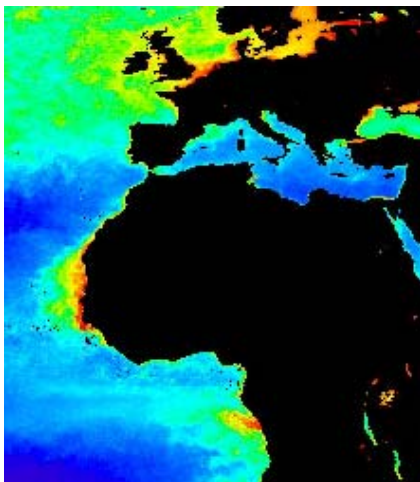


Figure 7: SEAWIFS map: areas of high surface chlorophyll red, areas of low surface chlorophyll blue.

In conclusion, bioluminescence profiles show a decrease in the amount of luminescence with increasing depth, and show a seasonal change in vertical distribution [6]. Our research has also shown the presence of bioluminescent organisms at all depths down to the seafloor at 4800m depth. An array will stimulate bioluminescent emissions, but generally levels of spontaneous bioluminescence will be low (data not shown). However entrapment and/or adhesion of luminous animals will at times be unavoidable.

## II. ACKNOWLEDGEMENTS

The authors wish to thank the captains and crew of RRS Discovery during cruises D252, D255, D260 and D266. Thanks to Professor Peter Herring for long term loan of his ISIT camera. This work was supported by NERC.

## III. REFERENCES

1. **Clarke, G. L. & Hubbard, C. J.** (1959) Quantitative records of the luminescent flashing of oceanic animals at great depths. *Limnol. Oceanogr.* **4**: 163-180.
2. **Widder, E. A. & Johnsen, S.** (2000) 3D spatial point patterns of bioluminescent plankton: a map of the minefield. *J. Plankton Res.* **22**: 409-420.
3. **Vereshchaka, A. L. & Vinogradov G. M.** (1999) Visual observations of the vertical distribution of plankton throughout the water column above Broken Spur vent field, Mid-Atlantic Ridge. *Deep-Sea Res. I*, **46**: 1615-1632.
4. **Herring P. J., Gaten E. & Shelton P. M. J.** (1999) Are vent shrimps blinded by science? *Nature.* **398**(6723): 116.
5. **Battle, E. J. V., Bagley, P. M, & Priede, I. G.** (in prep) In situ observations of benthic bioluminescence using an autonomous lander.
6. **Battle, E. J. V., Bagley, P. M. & Priede, I. G.** (in prep) Bioluminescence profiles in the north-east Atlantic ocean down to 4800m depth.



# Summary Talks



# Summary of the Electrical Power Session

P. Vernin, CEA Saclay, DSM/DAPNIA/SPhN, 91191 Gif sur Yvette CEDX, France.

pvernin@cea.fr

## Abstract

Antares and NEMO electrical power systems were presented and discussed. Most of the discussion focused on the long distance network for which we adopted the following case: a power of 50kW available at the level of the Junction Box (JB), a distance of 100km between the shore and the JB and a maximum voltage of 10kV between wires and sea allowed by the cable and the connectors.

### I. DC OR AC CURRENT?

DC currents have the advantage to reduce the active losses without any reactive loss at the price of a DC/DC converter of uncertain reliability.

AC currents have the advantage to allow easy and reliable offshore voltage transformation at the price of reactive losses and increased active losses. In addition, switching is easier in AC than in DC.

Both Antares and NEMO chose AC currents.

### II. SEA RETURN OR CABLE RETURN?

Sea return (in AC or DC) reduces the losses at a given conductor cross section and was adopted by Antares while NEMO rejected it for reliability, complexity and cost arguments.

### III. TYPE OF CABLE

Antares (42km, 16kW and 5kV) adopted a standard telecommunication cable having a relatively small Cu cross section ( $1 \times 17 \text{mm}^2$ ) for cost arguments.

NEMO (100km, 34kW and 10kV) plans to use a  $4 \times 25 \text{mm}^2$  cable to take advantage of the 3 phases power distribution.

### IV. TOPOLOGY

Several contributors insisted on the need of a redundant long distance network: two cable/JB systems in parallel between the shore and the site where each system is able to feed the whole detector.

Suggestions were made for the secondary network (between both JBs and the towers/lines): use of passive T-splitters to minimize the number of wet matable connectors and separate conductors and fibres to reduce the cost of these connectors.

### V. FUTURE

New technical developments on DC current networks and reliable DC/DC converters (Neptune project, Power Companies) could push us to reconsider in the coming years the DC option for the VLVnT. This option could be attractive for distances of the order of 100km or more.

### VI. CONCLUSIONS

A large variety of solutions is presently tested by Antares, NEMO and Nestor for the electrical power system. The result of these tests will be the starting point of an optimized design for the VLVnT. Innovative solutions need a R&D effort. Some of them were emphasized during the workshop:

- deep sea cable
- redundant network
- passive T-splitters
- wet matable connectors
- reliability comparison between AC and DC
- high reliability DC/DC converters

Many aspects of the detector are strongly correlated to the power system and must be discussed coherently: architecture, data transmission, power consumption of the electronics, deployment, maintenance,...

# Summary of the Photodetection Parallel Session

M.Taiuti

INFN, Via Dodecaneso, 33, I-16100 Genova, Italy  
mauro.taiuti@ge.infn.it

## *Abstract*

Here the contributions to the Photodetection parallel section are summarized and critized. It has been proved that the present technology is well under control, but new solutions to allow more collected light or the detection of the Cherenkov light direction could be critical in the design of a larger volume neutrino detector. A systematic investigation using Monte Carlo simulations is required to determine the effectiveness of the proposed improvements.

## I. INTRODUCTION

This session has been devoted to the review of the technical solutions adopted by the individual experiments to realize the optical modules and to the discussion of new developments and possible new solutions. Several contributions from the ANTARES, NEMO and NESTOR collaborations as well as from ELECTRON TUBES, HAMAMATSU and PHOTONIS have permitted to draw a rather clear picture of where we are and what we could achieve in a reasonable-near future.

## II. THE PRESENT STATUS

It is clear that the present solutions are limited by the size of the glass sphere that hosts the photomultiplier and the related electronics. Thus, being the diameter of the sphere equal to 17", the largest photomultiplier that fits in the sphere is the 13" manufactured by HAMAMATSU and adopted by the NESTOR collaboration. Alternatively, the ANTARES collaboration chose a slightly smaller 10" HAMAMATSU phototube. In all cases the glass sphere also contain the HV voltage divider, calibration sensors and a  $\mu$ -metal cage. Optical coupling to the glass is maintained with optical cement.

Several optical modules have been successfully deployed by the ANTARES and NESTOR collaborations while the NEMO collaboration is expecting to do the same shortly. The results of measured events and calibration procedures, presented in this workshop, prove that the present technology is well under control.

## III. POSSIBLE IMPROVEMENTS

Do exist possible new concepts of the optical module that could drastically improve the neutrino detector performances or reduce the costs? This is a rather important question because a) the optical modules cover approximately 20% of

the overall cost of a neutrino telescope, b) the presently adopted solutions could probably be too expensive to be used in a very large volume telescope.

Several improvements have been proposed and discussed in this session, aiming at increasing the single photoelectron resolution or alternatively, at increasing the amount of collected light by the single optical module or finally, at introducing new information such as the direction of the detected Cherenkov light.

A new HPD (Hybrid Photo-Detector) prototype capable to drastically improve the single photoelectron discrimination is under development by HAMAMATSU, while PHOTONIS could provide a large collecting surface using low-cost small hexagonal photomultipliers.

Groups and laboratories belonging to the ANTARES and NEMO collaborations have proposed even "wilder" ideas based on scintillating optic fibers, or cylindrical sensitive surfaces to improve the amount of collected light, or matrixes of Winston cones coupled to position sensitive devices to detect the direction of the Cherenkov light. Details can be found in the individual contributions to this session.

## IV. CRITICISMS

How effective would be the proposed solutions? We have first to learn from past experience, particularly from the first attempt by PHOTONIS to produce a smart photomultiplier several decades ago: it will be difficult to expect that the industries would presently spend much money in an R&D activity.

New solution would certainly arise from research laboratories and in this picture, what has been here presented looks very promising. However, the required effort in manpower, time and money required to develop and realize the presented projects must be well justified.

It is really necessary to locally increase the light collection efficiency or would be more effective the improvement of the detector homogeneity by increasing the number of optical modules? And, would the information on the direction of Cherenkov light reduce the impact of the  $^{40}\text{K}$  background in the muon trajectory reconstruction thus increasing the detection efficiency at lower neutrino energies?

These questions arose during the final discussion but at this stage of the project it has not been possible to give a clear answer and the systematic study of the effectiveness of the proposed solutions should be realized using detailed Monte Carlo simulations of the detector.



## Summary of the Photo Detection Parallel Session

Talk by M. Taiuti

## Summary of the Photo Detection Parallel session

Talk by M. Taiuti

## Wild Idea on Photon Detection

- ± 10 contributions
- ± Status of present Optical Modules
- ± News from industry
- ± Concepts and Criticism in view of the VLVnT

### Conditions:

- 3000 m under water at least
- $^{40}\text{K}$  background of single photons at  $300\text{Hz}/\text{cm}^2$
- Some bioluminescent background
- Signal depends on energy and distance
  - Low energy muon : R~50m photon flux =  $0.02/\text{cm}^2$
  - High energy muon : R~50m photon flux =  $0.2/\text{cm}^2$
  - Hadronic shower: R~50m photon flux =  $1.0/\text{cm}^2$
  - Electron shower E=1TeV close by flux >  $100/\text{cm}^2$
  - Electron shower E=1PeV close by flux >  $10^5/\text{cm}^2$

### Requirements:

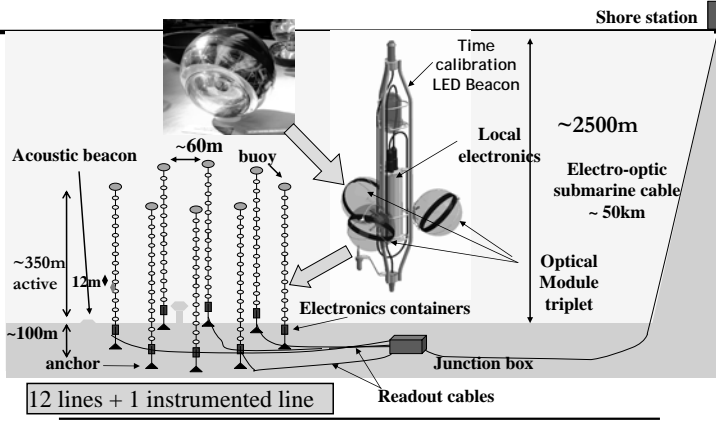
- Large area
- High quantum efficiency
- Good single photon resolution
- High dynamic range
- $4\pi$  solid angle

Has to fit in a transparent pressure vessel

## Monday, 7 Oct. Program

- ± ANTARES (P.Vernin), NEMO (S.Reito) and NESTOR (L.Resvanis) Optical Modules
- ± News from Electron Tubes (A.Wright), Hamamatsu (Y.Yoshizawa) and Photonis (S.Flyckt)

## The 0.1 km<sup>2</sup> Detector



## Optical modules – PMT's Specs

### To summarise:

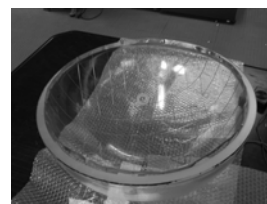
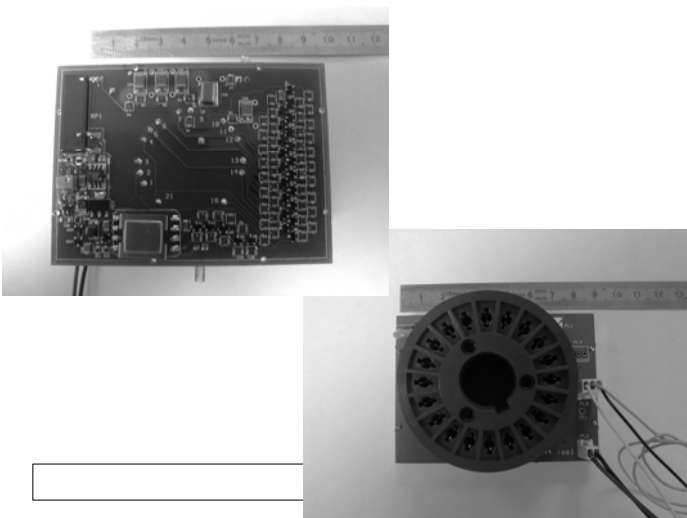
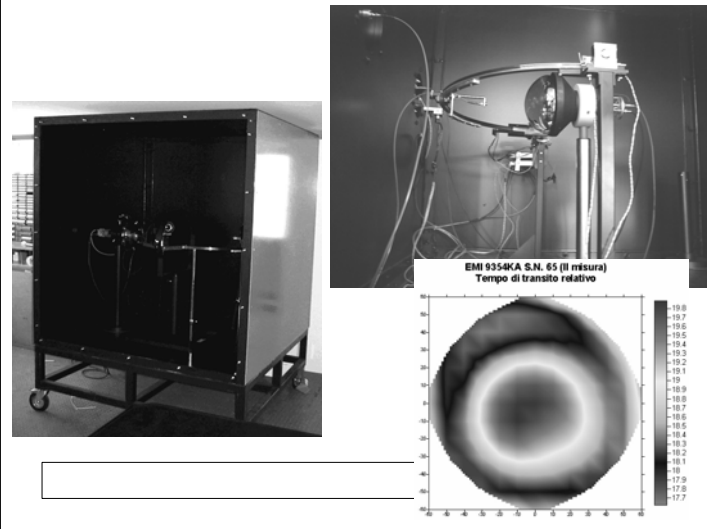
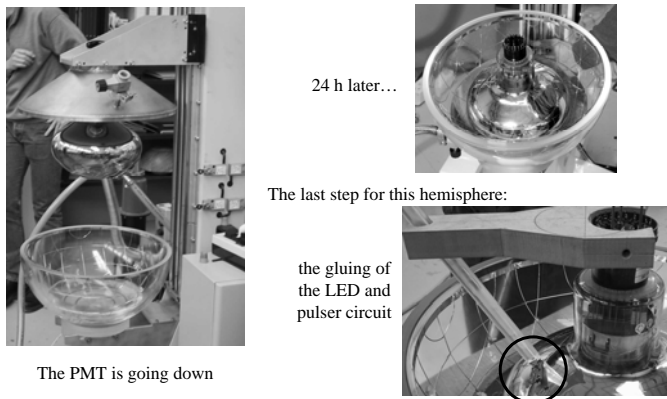
- ❖ Sensitive area  $\cong 500 \text{ mm}^2$
- ❖ (quantum  $\oplus$  collection) efficiencies  $> 16 \%$
- ❖ Amplification  $2 \cdot 10^8$  for HV  $< 2500 \text{ V}$

At working point ( $\cong$  amplification =  $5 \cdot 10^7$ )

- ❖ Transit time spread  $< 3.6 \text{ ns}$  (FWHM)
- ❖ Dark count (@ 0.3 spe)  $< 10 \text{ kHz}$
- ❖ Peak/valley  $> 2$
- ❖ Shape of signal  $t_r < 5 \text{ ns}$   $t_w < 12 \text{ ns}$  and  $t_f < 15 \text{ ns}$
- ❖ Pre, late and after pulses  $< 1 \%$ ,  $2\%$ ,  $10 \%$

in the window [.1, 16] ms after  
 in the window 10, 100] ns after  
 in the window [-100, -10] ns before the true pulse

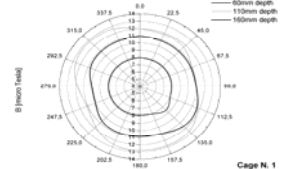
## Optical module - Assembly (2)



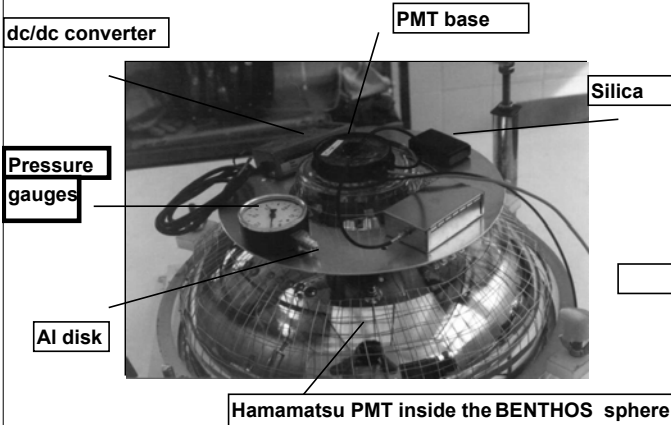
Mu-metal wire 1 mm

Strip 11x0.25 thk

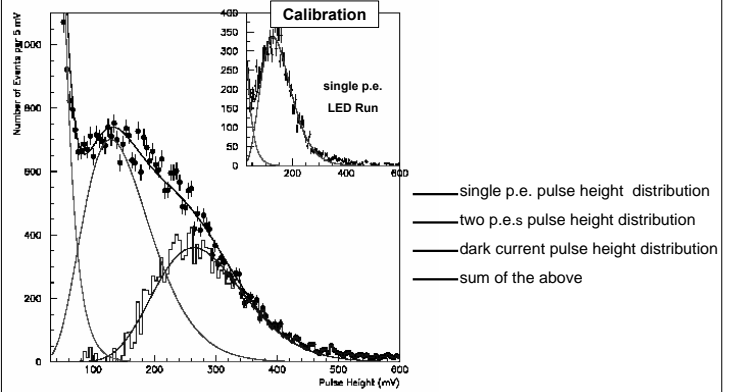
Total shadow 3-4 %



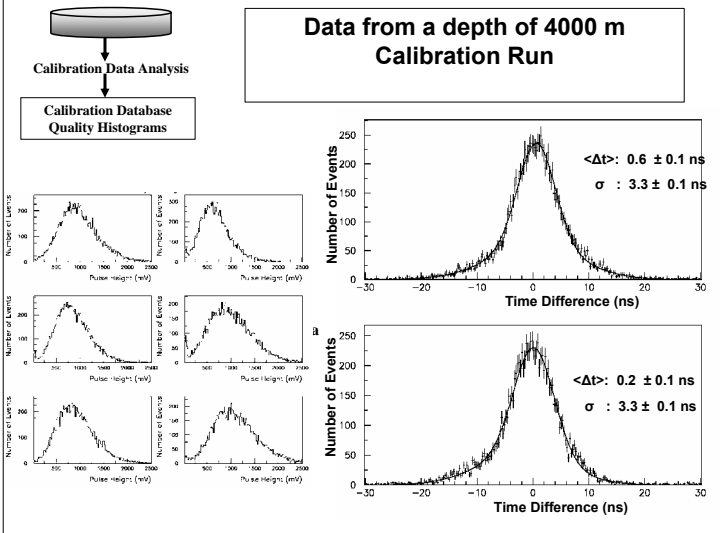
## The NESTOR Optical Module



## Data from a depth of 4000 m PMT Pulse Height Distribution



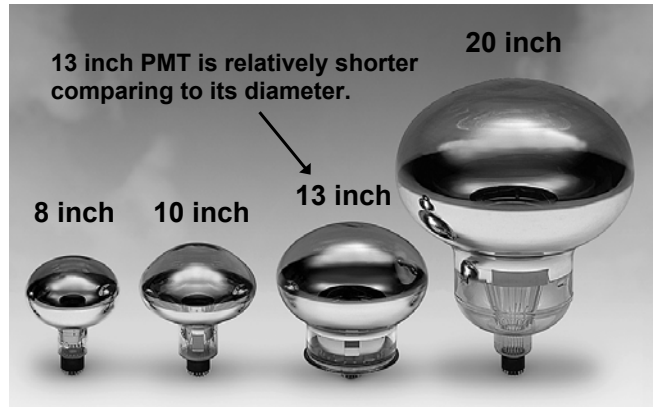
## Data from a depth of 4000 m Calibration Run



Hamamatsu Photonics K.K. Electron Tube Center

HAMAMATSU

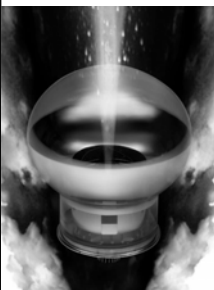
## Large Format PMT Lineup



Hamamatsu Photonics K.K. Electron Tube Center

HAMAMATSU

## General Specification of R8055



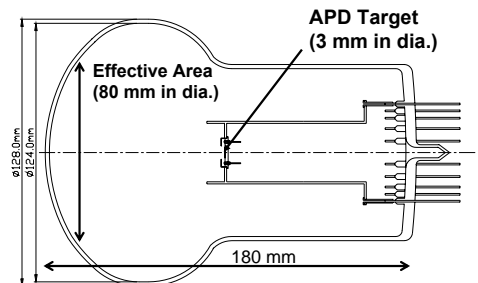
Window	: Borosilicate
Photocathode	: Bialkali
Tube Diameter	: 13 inch (332 mm)
Tube Length	: 332 mm
Dynode Type	: Box and Line / 10-stage
Nominal Gain	: $1E+07$ at 1500V
TTS (FWHM)	: 2.8 ns typ.
Rise Time	: 6.0 ns typ.
P/V ratio	: 2.7 typ.
Dark Counts	: 10 KHz typ.

Hamamatsu Photonics K.K. Electron Tube Center

HAMAMATSU

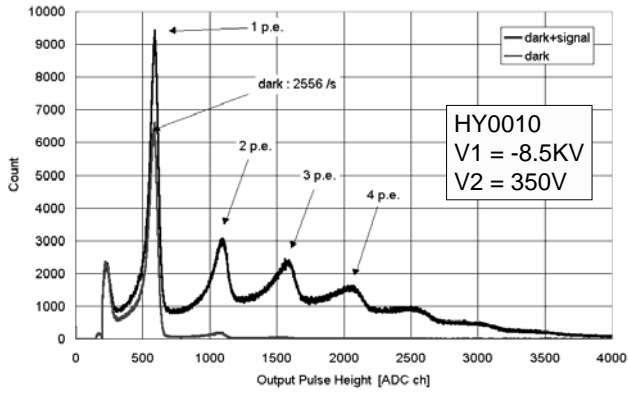
## Sketch of 5 inch HPD

This 5 inch HPD was made as feasibility study.  
 Glass bulb of 5 inch hemispherical PMT was used.



HPD : Hybrid Photo Detector

### PHD with Multi photoelectrons

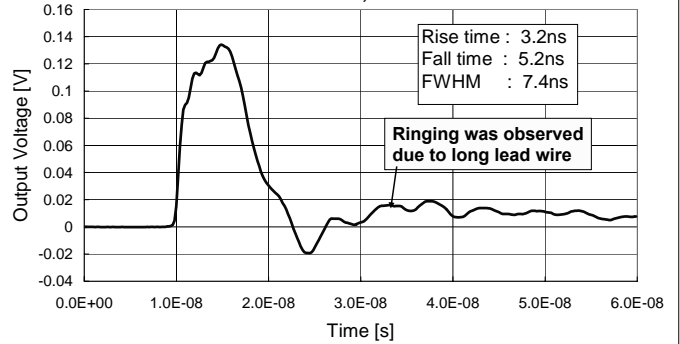


Electron Tube Division #1

### waveform

Output Waveform : HY0005 (8kV, 153V)

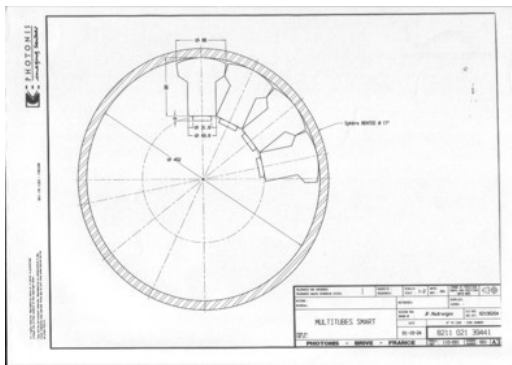
<Bombardment Gain : 900, Avalanche Gain : 30>



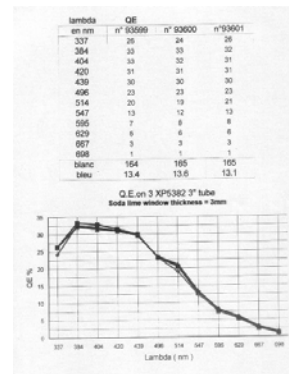
Electron Tube Division #1

(TO-8 type HPD : Rise time = 1.2 ns, Fall time = 13 ns)

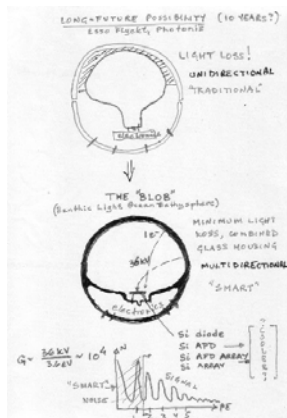
### Multiple PMTs/OM



### High QE



### The BLOB



### Status „smart“ PMTs

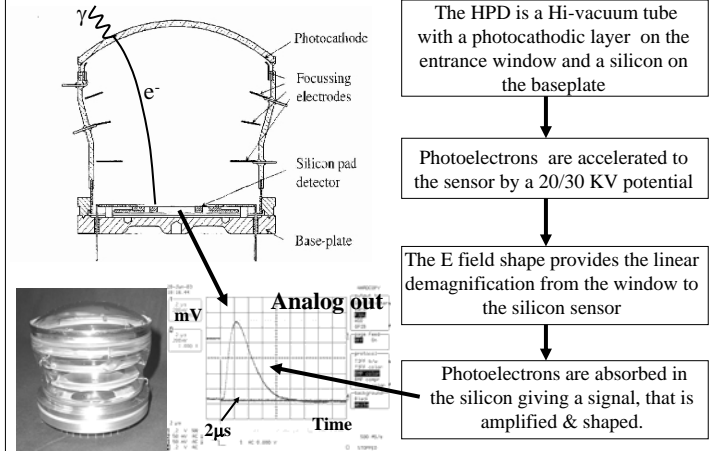
- Philips made ~ 30; invested 1 M\$!
- 200 Quasars in Lake Baikal!!!
- No ongoing production



## Tuesday, 8 Oct. Program

↓ M.Giunta (INFN-PI), A.Bersani (INFN-Ge), G.Anton (U.Erlangen), P.Kooijman (NIKHEF)

### HPD Working Principles: vacuum tube



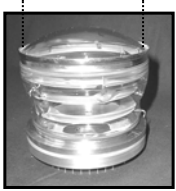
### The 5", 10" (and 20") HPDs



Michele Giunta

Currently the TOM HPDs are:

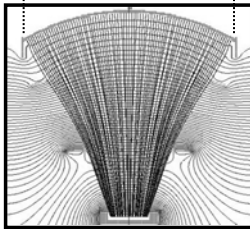
5" Bialkali & 5" Rb<sub>2</sub>Te borosilicate



10" Bialkali borosilicate window



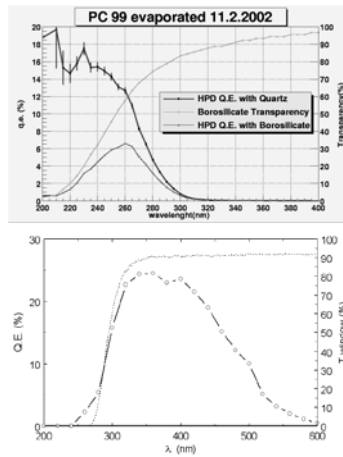
20" (!) only simulated in the e optics



### HPD: Quantum Efficiency



Michele Giunta



### UV Rb<sub>2</sub>Te 5" Q.E

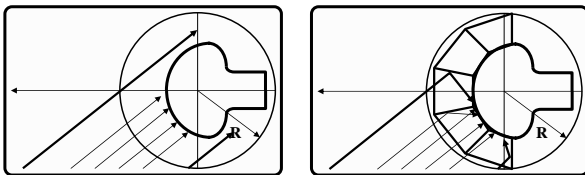
The low value measured is due to the borosilicate cut. The red line is the expected value if the HPD had a quartz window.

### Visible Bialkali 10" Q.E

Measured spectral response in the visible band. A 24% peak is reached.

### Direction Sensitive Light Collection

- \* A PMT cannot determine incoming photons direction
- \* This can be achieved with a proper light collection system
- \* This can be used with a multianodic PMT or with an array of PMTs



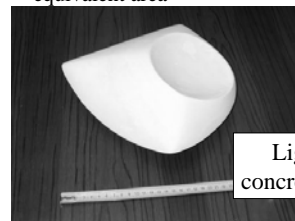
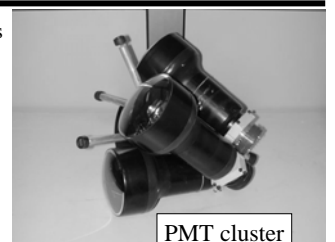
7 Oct. 2003



### Light Guide

Light guide for a system of four 5" PMTs

- \* Simple structure
- \* Plexiglas light guides
- \* High reflectivity coating
- \* Good directionality and 10" effective equivalent area



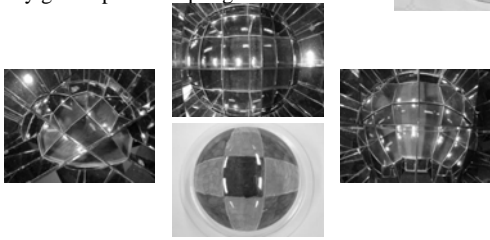
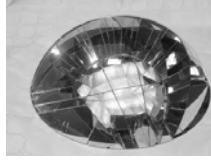
7 Oct. 2003



## Light Collector

Light collector for multianodic PMT (or HPD)

- \* Simple and cheap material (aluminised PETG)
- \* Preserves directionality
- \* Slightly improves light collection efficiency
- \* Allow very good optical coupling with BS

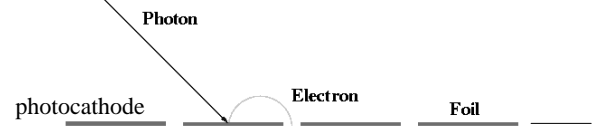


7 Oct. 2003

*Handwritten signature*

Use a "GEM" foil but not in gas??

Only use the foil to focus produced pe's



APD or multiplication dynodes  
 Reflective cathode and HPD type device combined  
 Hard to make in a sphere shape, but maybe foil is not necessary. Could be more solid.

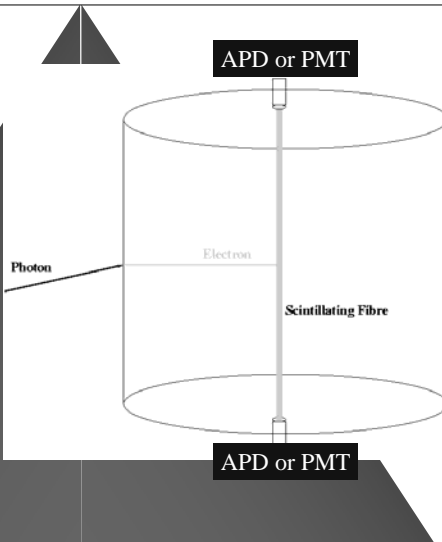
Even wilder....

A la BAIKAL PMT  
 Could be made quite long

Double readout  
 gives good timing

Obviously 30 kV is  
 not easy.

Fairly simple device



## Summary

⚡ New products or ideas from industries

⚡ New concepts (directionality, high collecting light efficiency)

⚡ but...

## Conclusive Remarks

⚡ Detector design specifications and simulations are required to **REALLY** prove the effectiveness of the proposed improvements (Energy range, Shape, ...)

⚡ A photodetector development program should be included in the financial request to EU

# Summary of Sessions on Design Parameters, Simulation and Reconstruction

C. Spiering

DESY Zeuthen, Platanenallee 6, D15739 Zeuthen, Germany  
christian.spiering@desy.de

## I. AIM OF THE SESSION

The aim of the session was to obtain an overview on the status of simulations for a km<sup>3</sup> detector in the Mediterranean, as well as the existing tools for simulation and reconstruction [1]. All large underwater/ice projects – Amanda, Antares, Baikal, Nemo, Nestor – reviewed their corresponding tool-sets and gave examples for simulation results. The session also aimed to determine appropriate benchmark parameters for the physics performance and possible benchmark detector configurations. Finally, necessary but still missing environmental parameters as input for simulations have been discussed.

## II. APPEC RECOMMENDATIONS

As a starting point, I would like to recall the recommendations which have been formulated by the Peer Review Committee of ApPEC (Astroparticle Physics European Coordination) at the session on Mediterranean projects for neutrino telescopes in July 2003. The committee strongly supports the efforts towards a km<sup>3</sup> scale detector in the Northern Hemisphere and recommends to form a single, coherent collaboration collecting all efforts underway. The ApPEC PRC asks for a report on optical properties of water at all considered sites, including seasonal variations, and using the same devices. The PRC also asks for more information on the optical background and on sedimentation. It finally requests comparative simulations about the impact of depth and water properties to some benchmark detectors (thereby focussing to the central goals of underwater neutrino telescopes). A new review is scheduled for summer 2004.

## III. STATUS

Actually, there are already clear steps in the direction of the recommendations mentioned above.

- Water properties (see the talk of G. Riccobene [2]):
  - Long-term measurements of sedimentation similar to ANTARES are being performed at the NEMO site.

- The measurement of of the volume scattering function is under preparation.
- all three collaborations (ANTARES, NEMO, NESTOR) envisage to cross-calibrate site information and measure water parameters at the NESTOR site with the AC-9 device.
- Comparative studies:
  - Comparative studies of km<sup>3</sup> detectors at different depths, with different noise rates and with three principal architectures have been done in a first approach of the ANTARES and NEMO collaborations (see the talks of D. Zaborov [6] and P. Sapienza [9])
  - Also for NESTOR, numerous km<sup>3</sup> simulations have been performed [10].
  - An exercise on the responses of optical modules at sites with the optical water parameters measured for Lake Baikal, AMANDA and ANTARES has been performed in [5].

## IV. PHYSICS BENCHMARK PARAMETERS

Parameters benchmarking the performance of the different detector configurations at different sites should reflect the dominant research goal of underwater telescopes, namely *neutrino astronomy at high energies*. Certainly any additional functionality of a detector is welcome, even if the same functionality can be reached with other detectors, like e.g. those underground. This extra possibility should however not be weighted as strongly as the performance with respect to the central goals.

The following table is an attempt to reflect the discussions at the meeting. Clearly the definition of preferences is not without bias.

I note that, by purely technical reasons, configurations may be preferable which show good performance with respect to atmospheric neutrino oscillations and other low energy processes. As it was mentioned in several talks, a homogeneous string detector will be inferior to a tower-like array due to maintenance and stability considerations. Nested arrays, by defini-

Table 1: Weighting of Physics Goals for Benchmarking

Goal	Weight	Remarks
point sources	++	muons, no cascades energy TeV-PeV steady sources
<i>WIMPs:</i> Earth WIMPs	-	indirect search not competitive with direct searches
Solar WIMPs	+	go as low as possible in energy range
<i>Oscillations</i> atm. neutrinos	-	not competitive with SK/K2K unless spacing is unreasonably small
accel. neutrinos	-	at present too exotic as benchmark goal
Diffuse Fluxes	++	muons up (TeV-PeV) muons down (PeV-EeV) cascades
Others downgoing muons magnetic monopoles slow particles	- - -	only for calibration

tion, have regions of higher density and lower energy threshold. Still, a low energy threshold should not be a primary *physics* goal compared to excellent sensitivity above a TeV.

To what *parameter* should the performance be reduced? There have been controverse discussions on whether the *best achievable sensitivity* or the *effective area after tuning cuts to get the best sensitivity*, should be chosen. Certainly the effective area after rejection of fake events alone, or the angular resolution alone, do not give the correct answer. Optimum cuts are a function of running time – as also the requested angular resolution is. For instance, a resolution which is sufficient for a point source search on a map populated by 5000 neutrino events may turn out to be too poor when analyzing a plot with 30 000 events. The figure illustrates the relation between various parameters [3].

The Amanda collaboration prefers presentation of *sensitivities* (90% c.l. exclusion or  $5\sigma$  detection). This can be done for a  $E^{-2}$  spectrum or in the form of “model rejection factors”. (see [18] and the talks on Amanda [16] and IceCube [17] on this conference). In another approach, differential limits are calculated [19].

## V. BENCHMARK DETECTORS

The possibility to simulate the response of a dense, grid-type array containing all realistic configuration as sub-sets and getting the response of the realistic configurations by “re-triggering” was investigated by S. Tzamarias [4]. It turned out

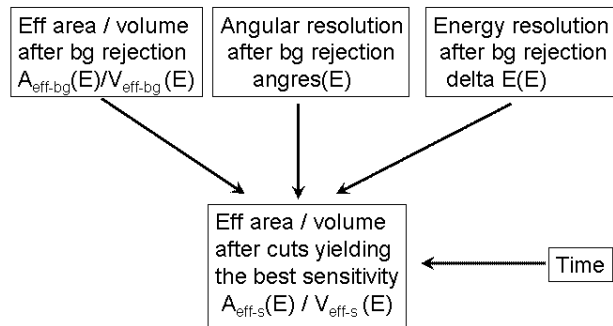


Figure 1: Parameters determining the detector performance

that, given the diversity of the various realistic designs, a very fine grid would have to be chosen and the CPU time would be inacceptably high. Instead, the reduction of competing designs to 3-5 concrete benchmark designs is proposed.

## VI. TOOL SET FOR SIMULATION AND RECONSTRUCTION

Overviews over the simulation tools have been given in [11] (AMANDA), [7] (ANTARES), [8] (Baikal), [9] (NEMO) and [10] (NESTOR).

The simulation chain covers

- air shower generation, mostly based on CORSIKA and HEMAS,
- muon propagation using e.g. MUSIC and MUM in ANTARES, Baikal and NEMO, MMC in AMANDA, GEANT or alternatively a simple parameterization in NESTOR,
- assumptions on neutrino flux, e.g. the Bartol flux for atmospheric neutrinos or an  $E^{-2}$  for astrophysical sources,
- neutrino event generators, like GENHEN in ANTARES or ANIS [20] in AMANDA and Baikal,
- generation of brems-, pair and hadronic showers and tracking of particles, using GEANT-3 in ANTARES, GEANT-4 in NESTOR, or alternatively fast parameterizations,
- photon propagation, including light absorption and scattering, sometimes using “scattering tables” which tabulate the light field as a function of distance, OM orientation and photon arrival time. (Note that the simulation of photon propagation in ice is much more complicated than in



water, since scattering as such is much stronger, and since ice layers with different absorption and scattering make Antarctic ice strongly non-homogeneous.)

- simulation of the detector response, sometimes using full waveform information.

The contribution of J. Brunner [7], exemplifies the full chain in detail, using the ANTARES Monte Carlo.

Tools and methods for reconstruction have been reviewed in [15] (AMANDA), [12] (ANTARES), [13] (Baikal), and [14] (NESTOR).

Early reconstruction algorithms are based on  $\chi^2$  fits. Optical background, photon delays due to scattering and delayed light from showers along energetic tracks require the replacement of the simple  $\chi^2$  functional by carefully parameterized likelihood functions (see e.g. the talks [12, 15]). Reconstruction is intimately connected to background rejection, be it the rejection of the depth-dependent background of atmospheric muons, or – with respect to extraterrestrial neutrinos – the omnipresent background of atmospheric neutrinos. The typical angular resolution for muon tracks after cuts on background is  $\sim 3$  degrees for NT-200,  $\sim 2$  degrees for AMANDA-II,  $\sim 0.7$  degrees for IceCube and  $\sim 0.2$  degrees for ANTARES. Appropriate use of the amplitude information or even full waveform information can improve the direction and energy resolution significantly [15, 17, 14]. Note that for resolutions below 1 degree the absolute angular calibration, not the resolution, may dominate the performance for point source searches.

## VII. NEXT STEPS IN SIMULATION

The participants agreed that a task force group on detector simulation should be formed. This group should discuss the *KM3NeT* simulation strategies, the task sharing, the exchange of tools and results. The group would define a working plan and help to generate input for the envisaged Design Study. The first new results on comparative studies are expected for the ApPEC review in summer 2004.

The participants agreed that a site decision should not be prioritized in the initial phase. Instead, *benchmark* detectors/sites characterized by a tuple of parameters should be simulated. Such parameters could be the depth (e.g. 2.5, 3.5. and 4.5 km), the noise (e.g. 25 kHz, 50 kHz, and high-state noise of 300 kHz) and 3-4 basic architectures.

Only in a later step the translation to the “real-site language” would be performed. Only then, physics arguments should be confronted with arguments of infrastructure, logistics etc. A site which is clearly weaker in physics performance would have to have strong arguments on the technology/infrastructure side to be selected for a km3 detector.

Input from the performance of the prototype detectors at the ANTARES and NESTOR site is required as early as possible – not for the simulation but for a final decision on architecture and site.

## REFERENCES

- [1] C.Spiering: Aim of the session, talk at session A1.1
- [2] G.Riccobene, Overview over Mediterranean Optical Properties, talk at session A1.1
- [3] C.Spiering, Benchmark parameters for a km3 detector, talk at session A1.1
- [4] S.Tzamarias, Benchmark detectors for comparative simulations, talk at session A1.1
- [5] D.Djilkibaev, comparison of OM responses at different sites, talk at session A1.1
- [6] D.Zaborov, Comparison of different km3 designs using Antares tools, talk at session A1.1
- [7] J.Brunner, Simulations tools for Antares, talk at session A1.2
- [8] I.Belolaptikov, Simulation tools in the Baikal experiment, talk at session A1.2
- [9] P.Sapienza, Status of the simulation in NEMO, talk at session A1.2
- [10] A.Leisos, NESTOR simulation tools and methods, talk at session A1.2
- [11] S.Hundertmark, Simulation tools in Amanda, talk at session A1.2
- [12] A.Heijboer, Methods for reconstruction of muon tracks, talk at session A1.2
- [13] I.Belolaptikov, Event reconstruction in the Baikal experiment, talk at session A1.2
- [14] A.Tsirigotis, NESTOR: Methods of reconstruction and background rejection, talk at session A1.2
- [15] C.Wiebusch, Muon track reconstruction and data selection techniques in Amanda, talk at session A1.2
- [16] E.Bernardini, talk on Amanda at this workshop
- [17] C.Spiering, talk on IceCube at this workshop
- [18] G.Hill and K.Rawlins, *Astropart. Phys.* 19 (2003) 393.
- [19] M.Ackermann et al. (Amanda coll.), Search for neutrino-induced cascades with Amanda-II, to be submitted to *Astropart.Phys.*
- [20] M.Kowalski and A.Gazizov, *Proc. 28th ICRC*, 1459.

Summary of Parallel Session on  
Design Parameters, Simulation and  
Reconstruction

Talk by C. Spiering

**Design Parameters**  
**Sessions A1.1 and A2.1**

Plenary Report

C. Spiering  
VLVNT Workshop Amsterdam  
October 2003

→ low bioluminescence

→ low bioluminescence  
→ far from big rivers

→ low bioluminescence  
→ far from big rivers  
→ far from inflow of other debris

→ low bioluminescence  
→ far from big rivers  
→ far from inflow of other debris  
→ possibility to install an air shower  
array for calibration

- low bioluminescence
- far from big rivers
- far from inflow of other debris
- possibility to install an air shower array for calibration
- total complementarity to IceCube

- low bioluminescence
- far from big rivers
- far from inflow of other debris
- possibility to install an air shower array for calibration
- total complementarity to IceCube
- no problems with Coriolis force

North Pole !

### **ApPEC Recommendations Neutrino Telescopes**

- With the aim of constructing a detector of km<sup>3</sup> scale in the Northern hemisphere, both in view of size and competition with IceCube: form a single coherent collaboration collecting *all* the efforts underway
- Prepare report to ApPEC PRC with following informations:
  - optical properties of water, incl. seasonal variations and using the same devices
  - optical background and sedimentation
  - comparative simulations about impact of depth and water properties to some benchmark km<sup>3</sup> detectors (focussing to the central goals of Nu Telescopes)
- Single design study in the European FP6 framework
- New review in one year (summer 2004)

#### Promising steps:

- Long term measurement of sedimentation a la Antares at NEMO site (just one example)
- next: measurement of volume scattering function
- Collaborations envisage to cross calibrate site informations by measuring water parameters at NESTOR site with AC-9 device
- Comparative studies of detectors at different depths, with different noise rates and with 3 principal architectures have been done in a first approach (Dmitry Zaborov, Piera Sapienza). Also Nestor has done a lot of km<sup>3</sup> simulations.

#### Next steps in simulation:

- Form a task force group on detector simulation:
- Agree on a working plan (October)
  - Input to application for a European Design Study (November)
  - First results on comparative studies to ApPEC (Next spring/summer)
  - don't prioritize site decision in initial phase but just simulate benchmark detectors characterized by a tuple of basic parameters (say depth 2.5, 3.5 and 4.5 km, noise 25,50 kHz and „high“, 3-4 basic architectures)

- Translate to the „real site language“ in a later step
- only then, pure physics arguments should be confronted with technology/infrastructure etc. arguments
- a site which is clearly weaker in „physics performance“ would have to have strong arguments on the technology/infrastructure site to be selected for a km3 detector
- Input from the performance of detectors at the Antares/Nestor site as early as possible (not for simulations but for a final decision on architecture and site).

	ANTARES	NEMO	NESTOR
Depth (km):	2.4	3.4	4-5
Factor downward muon intensity	← -5 →		← -3 →
Absorption length (m):	50 (60)	65	55-70
	Same device		
External steady noise: (kHz/8 inch tube)	40-60	20-30	20-30 (10 <sup>4</sup> )
Sedimentation:	strong	smaller	smaller
Distance to shore (km):	20 (10)	70 (70)	20 (15)

↗  
Shore station (closest shore)

- Background from misreconstructed downward muons
- Visibility of sky
- Influence of bioluminescence. dead-times and background rejection
- Limitations due to sedimentation/biofouling (up/down OMs)
- Distance to shore

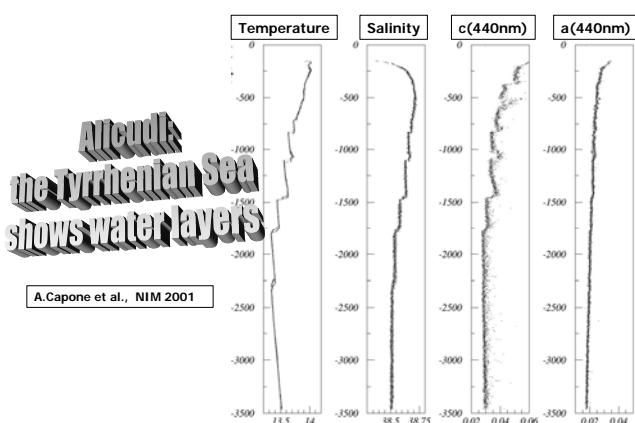
#### Direct effects

Light absorption coefficient ( $\lambda$ )	number of Cherenkov photons on PMT
Light scattering coefficient ( $\lambda$ )	timing of Cherenkov photons on PMT
Volume scattering function ( $\lambda$ )	
Light refraction index (T, S, P, $\lambda$ )	timing of Cherenkov photons
Optical noise	spurious hits, PMT and electronics dead time

#### Indirect effects

Sound velocity (T,S,P)	position of PMTS
Sedimentation rate	light scattering + PMT temporary obscuration
Biofouling	PMT permanent obscuration
Currents	positioning increase bioluminescence reduce sedimentation

**G. Riccobene**



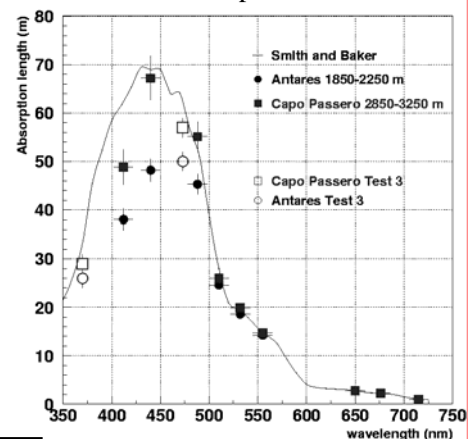
A.Capone et al., NIM 2001

The systematic error is due to the calibration of the instrument.

It has been evaluated to be:  $\Delta a(\lambda) \approx \Delta c(\lambda) \approx 0.002 \text{ m}^{-1}$

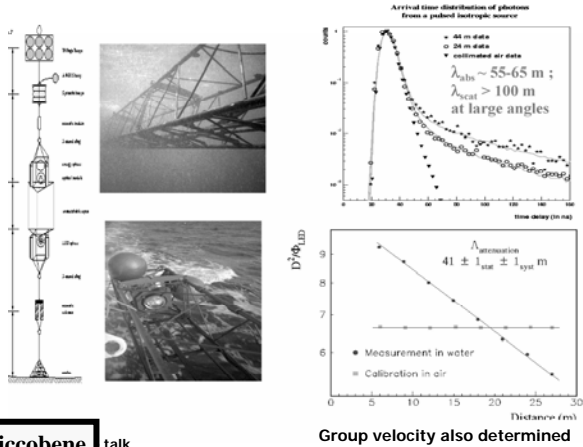
**G. Riccobene**

AC9+Test 3' data: Capo Passero and Toulon



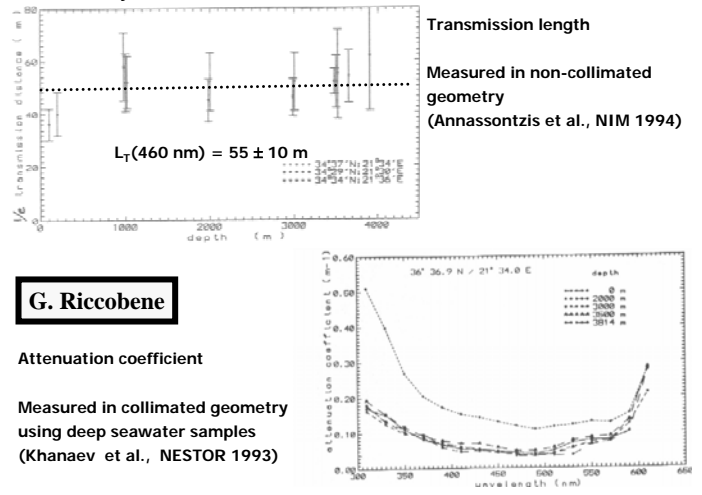
**G. Riccobene** esy of J-P Schuller

### Toulon data from ANTARES Collaboration Water Transparency



G. Riccobene talk

### Pylos data from NESTOR Collaboration



G. Riccobene

### Main physics goals proposed as basis for benchmarking procedure

- Point source search (excluding WIMPs)
  - steady sources ? +
  - transient sources -
  - muons +
  - cascades -
  - energy range ?
- WIMPs
  - Earth WIMPs not competitive with direct searches -
  - Solar WIMPs +
  - energy range go as low as possible

C.Spiering

### Main physics goals proposed as basis for benchmarking procedure (cont'd)

- Atm. neutrino oscillations -
  - not competitive with SK & K2K if not the spacing is made unreasonably small
  - nested array a la NESTOR 7-tower ?
  - proposal: → no optimization goal
  - no benchmark goal
- Oscillation studies with accelerators -
  - too exotic to be included now

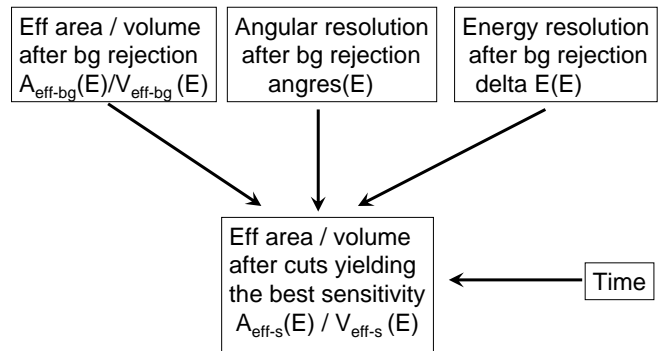
C.Spiering

### Main physics goals proposed as basis for benchmarking procedure (cont'd)

- Diffuse fluxes
  - muons up and down +
  - cascades +
- Others
  - downgoing muons
    - physics -
    - calibration ?
  - monopoles -
  - slowly moving particles -
  - ...

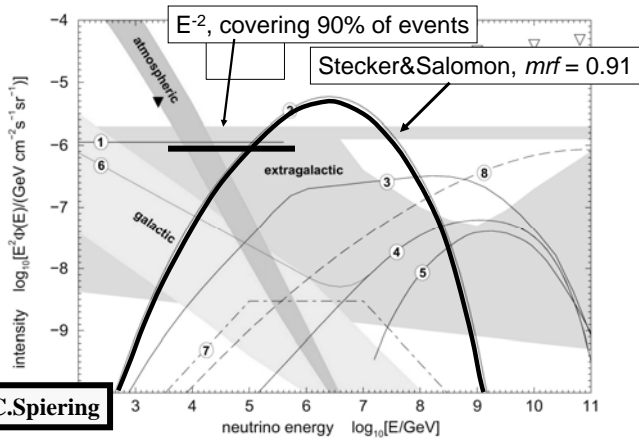
C.Spiering

### Benchmark Parameters



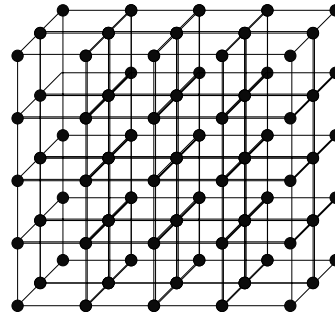
C.Spiering

### Integral Limits



C.Spiering

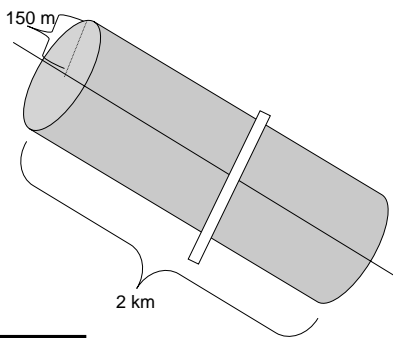
Can we use a generic, dense detector as the basic tool in our design studies?



A GRID type Detector

S.Tzamarias

### Mean Number of "Candidate" PMTs per "Track"



	MeanNumber of "Candidate" PMTs per Track
NEMO	550
NESTOR	1070
ANTARES	11000
GRID	140000

Shadowing  
NESTOR:  $0.4 \cdot 10^{-3}$   
GRID:  $12 \cdot 10^{-2}$

S.Tzamarias

### The "obvious" way to proceed

Define the values of the relevant environmental parameters, for the candidate sites, based on published data (water optical properties, K40 background, bioluminescence activity, bio-fouling, atmospheric background fluxes and absorption)

Simulate the response of an optimum detector (at a given site) to  $e$ ,  $\mu$  and  $\tau$  (vertices). Events are produced equal (or almost equal) probably in phase space.

Use standard tools to simulate the physics processes. Include in the simulation the K40 background.

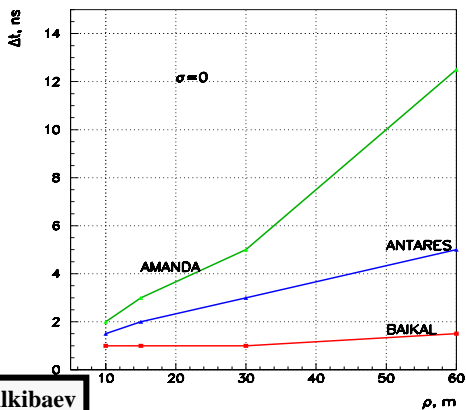
Simulate in detail the OM response and ignore effects of (in a first approximation will be the same to all the different designs) the readout electronics, triggering and DAQ.

Produce "event tapes" including the "generation" information and the detector response (e.g. deposited charge and arrival time of each PMT pulse). The "event tapes" and the relevant data basis should be available to the other groups.

Reconstruct the events and produce DST's including the "generation" and reconstructed information (e.g. direction, impact parameter, flavor, energy) for each event. The DSTs should be available to the other groups.

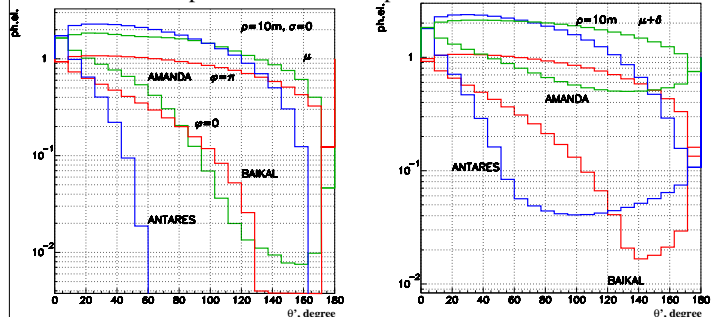
S.Tzamarias (Ntuples) to express the tracking efficiency and resolution as a function of the direction and energy (and impact parameter)

### FWHM of the time distribution (without scattering)



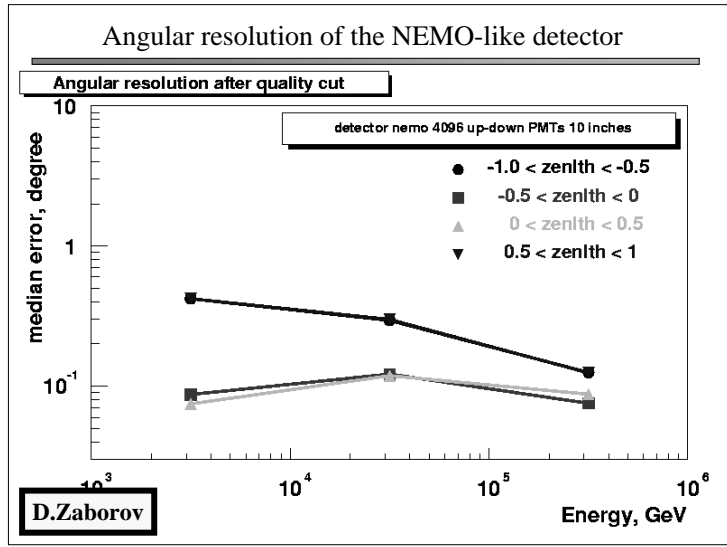
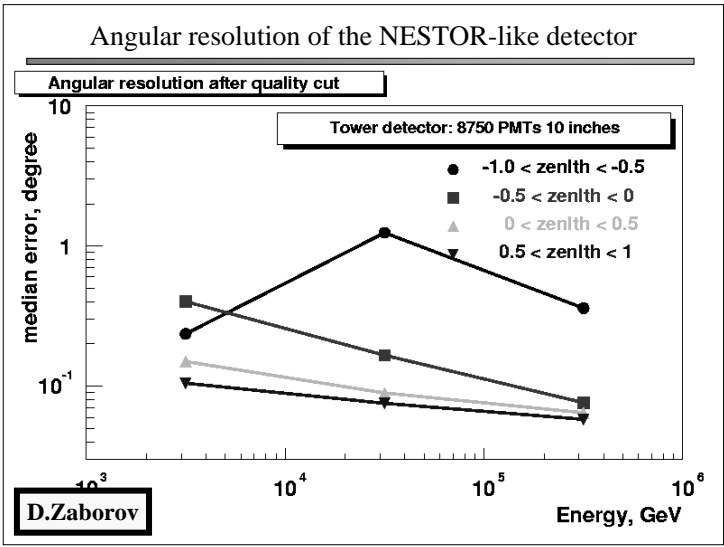
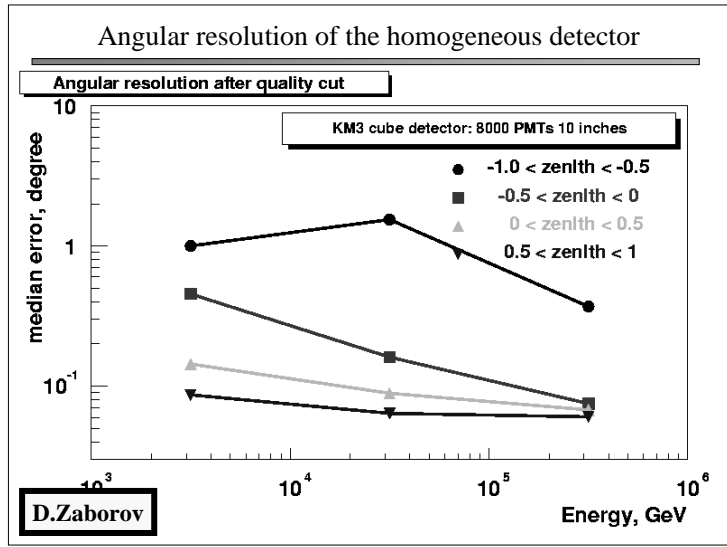
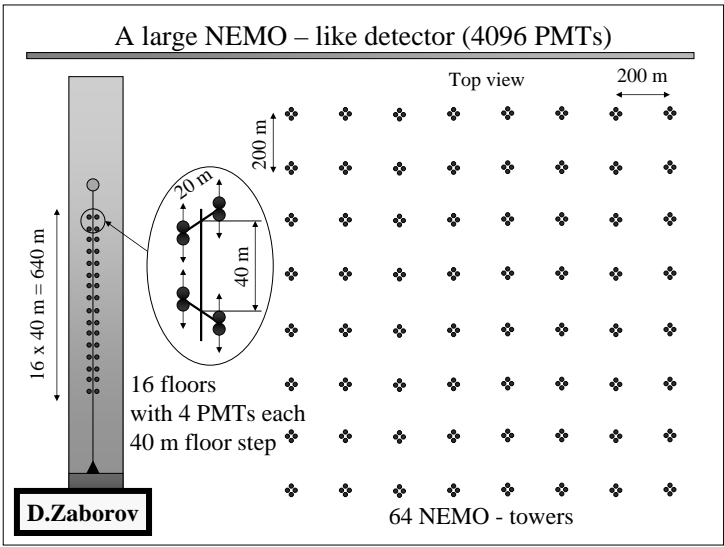
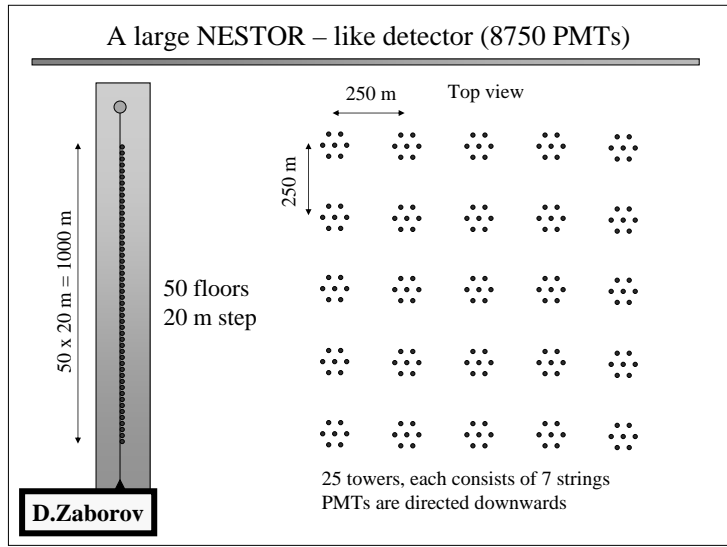
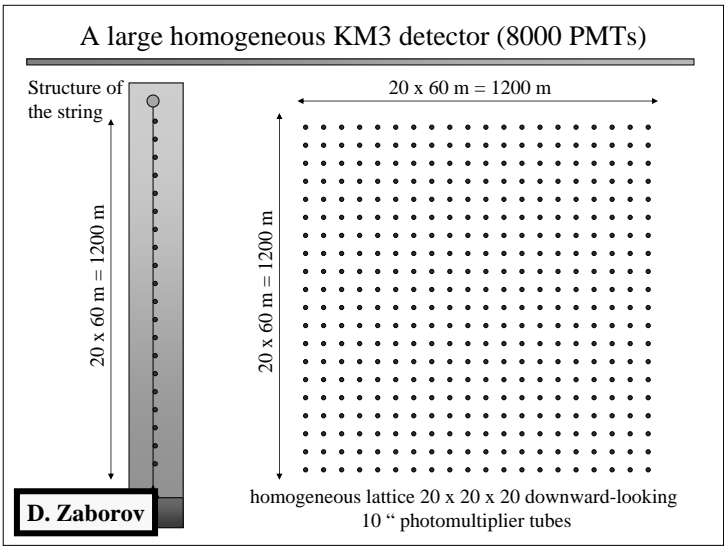
Dz.Dzhilkibaev

### Dependence of OM response on its orientation



Dz.Dzhilkibaev

	anisotropy	Blind zone
BAIKAL	~50	4 %
ANTARES	~50	25 %
AMANDA	~ 4	-



Istituto Nazionale di Fisica Nucleare  
Laboratori Nazionali del Sud

## Atmospheric muon simulations

A. Margiotta et al

The depth of the site is related to the shielding from atmospheric muons

HEMAS code (vrs7-02) has been used to simulate the atmospheric down-going muon flux at sea level for zenith angles up to about 85°

MUSIC code has been used to propagate muons from sea level to the detector can at 2400 m and 3400 m underwater

**Strong muon flux and multiplicity reduction at 3400 m, especially at large angle**  
Effect on detector performance is under investigation

P.Sapienza

Istituto Nazionale di Fisica Nucleare  
Laboratori Nazionali del Sud

## Simulation of NEMO detectors with OPNEMO

OPNEMO code (S. Bottai and T. Montaruli) is a fast first generation Monte-Carlo tool

OPNEMO has been used to define km<sup>3</sup> detector lay-out and triggers in the NEMO Collaboration

Main limitations:  
- scattering of light not taken into account  
- track reconstruction in presence of optical background not implemented  
- ...

It has provided indications for the detector

P.Sapienza

Istituto Nazionale di Fisica Nucleare  
Laboratori Nazionali del Sud

## Detector configurations – OM arrangement - OPNEMO without optical background (C. Distefano et al)

surf.  $\mu$  generation  
N<sub>string/tower</sub> = 64  
H<sub>string/tower</sub> = 600 m  
N<sub>PMT</sub> = 4096  
D<sub>PMT</sub> = 10"  $\sigma_{PMT}$  = 2.5 nsec  
d<sub>y</sub> = 180 m  
 $\lambda_d(450 \text{ nm}) = 40 \text{ m}$

P.Sapienza

Istituto Nazionale di Fisica Nucleare  
Laboratori Nazionali del Sud

## Simulations of NEMO detectors with the ANTARES software package (R. Coniglione, P.S. et al)

During the ANTARES meeting held in Catania on september 2002, the ANTARES and NEMO collaboration agreed to start a stronger cooperation towards the km<sup>3</sup>. In particular, activities concerning site characterization and software were mentioned. By the end of 2002, ANTARES software was installed in Catania by D. Zaborov.

P.Sapienza

Istituto Nazionale di Fisica Nucleare  
Laboratori Nazionali del Sud

## Optical background dependence

In order to make comparisons for the same angular resolution quality cuts must be applied

Regular lattice 400 strings 60m x 60m  
NEMO 140 dh 9x9 20 kHz with qual. cuts  
NEMO 140 dh 9x9 60 kHz with qual. cuts  
NEMO 140 dh 9x9 120 kHz th. 1.5 p.e. & q. c.

P.Sapienza

## Water properties Refractive index

Wave length window 300-600nm  
Refraction index function of pressure, temperature salinity (depth dependence in the detector neglected)

$$n_g = \frac{n_\phi}{1 + \frac{dn_\phi}{d\lambda} \frac{\lambda}{n_\phi}}$$

Group velocity correction (ignoring group velocity degrades Angular resolution by factor 3)

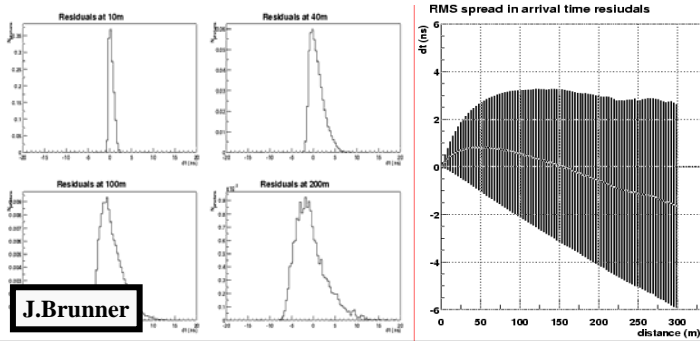
J.Brunner



## Water properties Dispersion

Cherenkov photon propagation done for ONE wavelength (CPU time)  
Dispersion correction added at PMT depending on distance  
At 50m comparable to PMT tts !

Examples: Effect of dispersion , no scattering



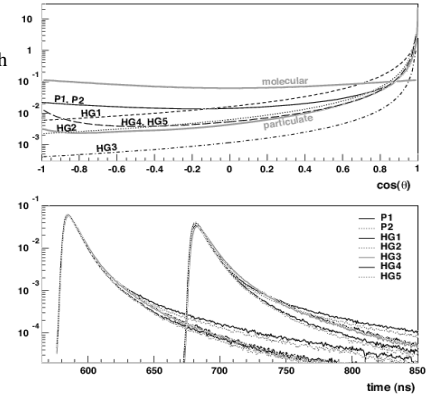
J.Brunner

## Water properties Scattering

Study of various water models  
Which are not incompatible with  
Antares measurements

Effect on time residuals:  
Mainly tail but also peaks

Result:  
Ignorance on details of  
Scattering introduces  
30% error on angular resolution  
10% error on eff. area



J.Brunner

- Full simulation chain operational in Antares
- External input easily modifiable
- Scalable to km3 detectors, different sites
- Could be used as basis for a km3 software tool box

J.Brunner

### Simulation tool

#### 1. Light propagation :

$L_{sc} \approx 30\text{-}50\text{m}$ ;  $L_{abs} \approx 20\text{m}$   $\Rightarrow$  for showers with energy up to  $\sim 10$  TeV and muons up to  $\sim 50$  TeV scattering of light in medium can be ignored.

For higher energies scattering is taken into account on the base of long term measurements of parameters of scattering.

#### 2. Accurate simulation of time response of a channel on fact of registration is provided.

#### 3. Atmospheric muons:

CORSIKA with QGSJET.

#### 4. Muons from atm. neutrino:

- cross-sections - CTEQ4M (PDFLIB)
- Bartol atm. neutrino flux

I.Belolaptikov

#### 5. Angular distribution for hadronic showers is the same as for el.-m. showers.

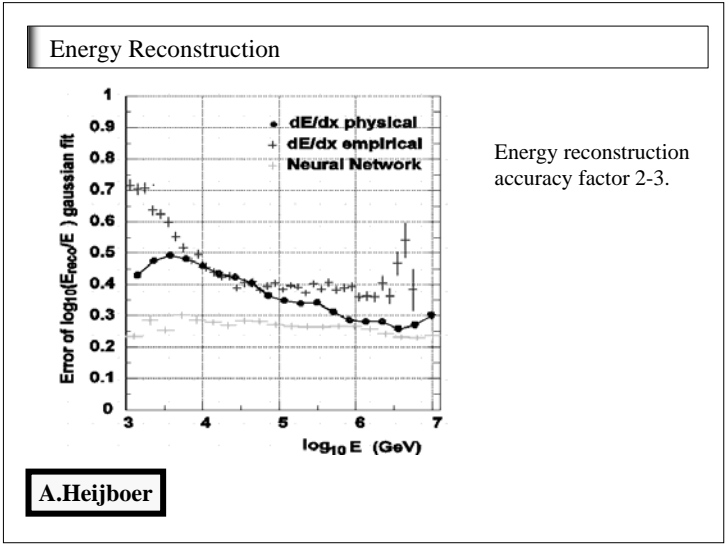
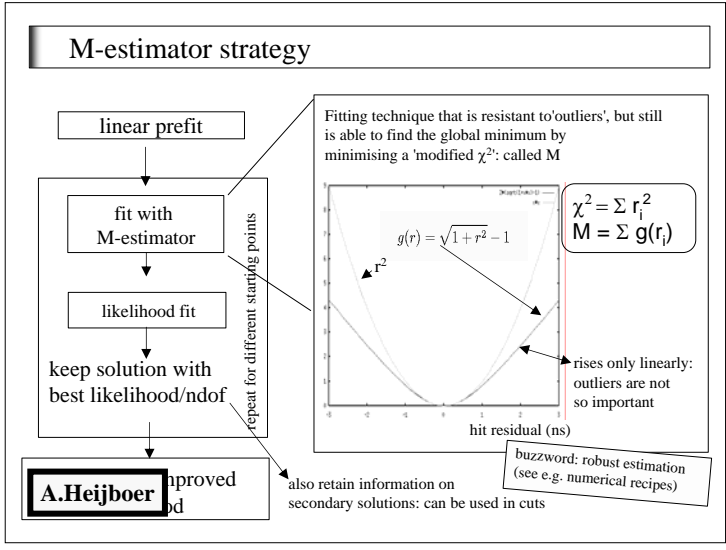
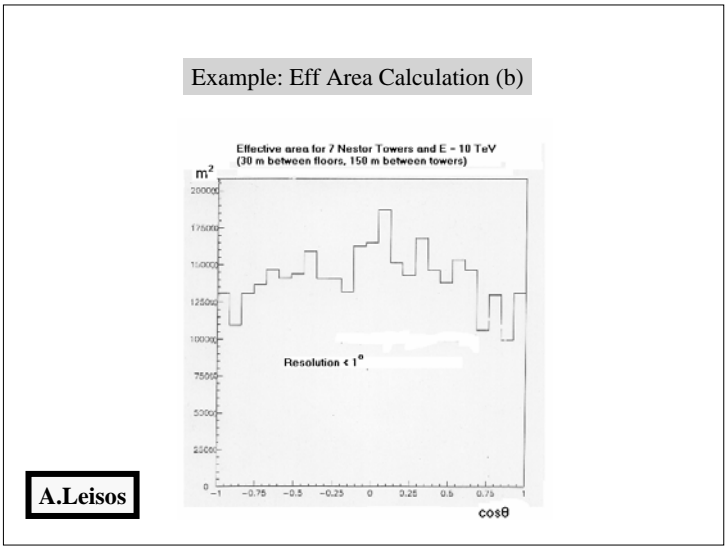
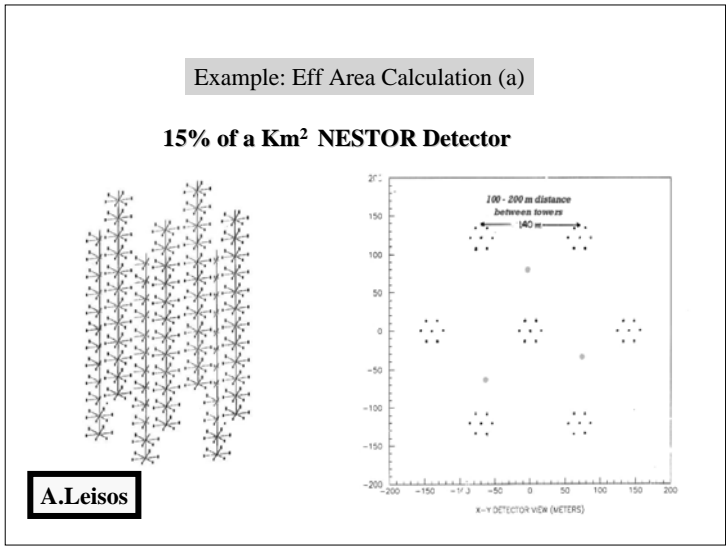
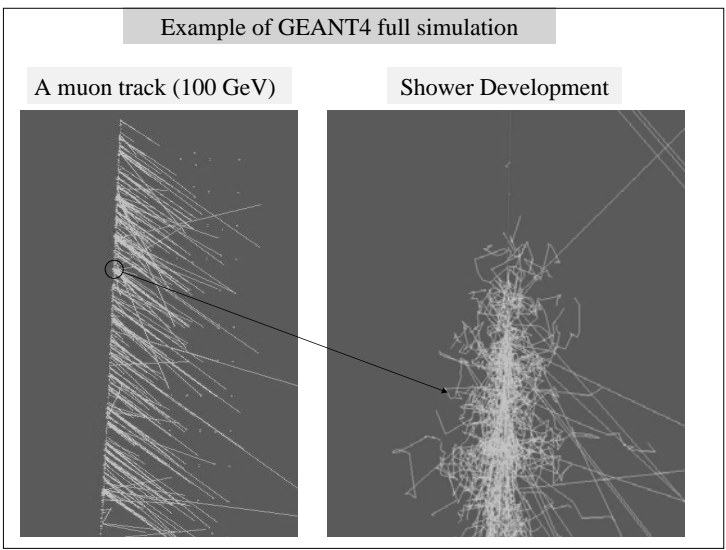
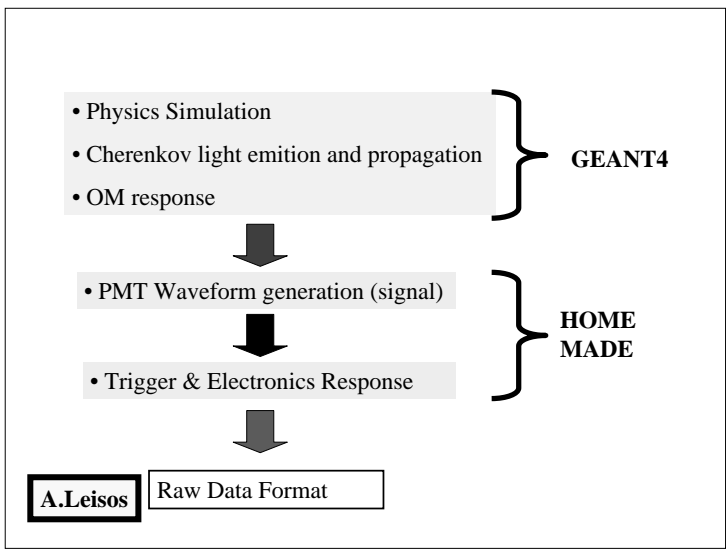
4. **Lepton transport** in media and in the array is done by MUM. Showers with energy  $> 20$  MeV are considered as catastrophic losses.
5. **Dead time and random** hits of measuring channels are included in code. Efficiencies of channels are measured experimentally in situ.
6. For simulation of **high energy neutrinos** we are going to use ANIS code.

I.Belolaptikov

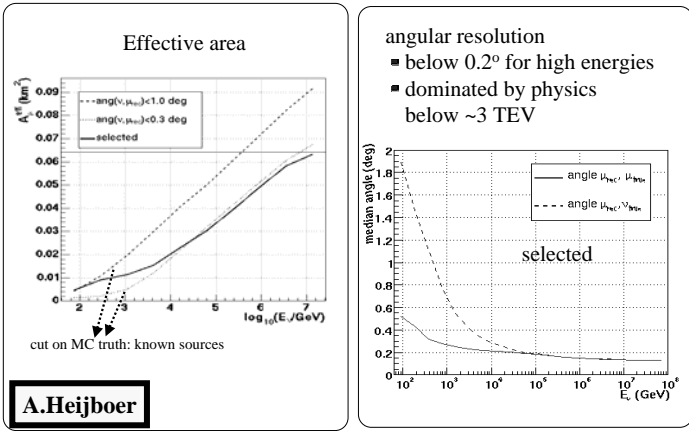
### S.Hundertmark: Simulation in Amanda

- AMASIM
- Versatile, mature system, open for alternative modules
- Peculiar for Amanda: strong scattering layered ice
- Ang.error upgoing tracks  $\sim 2^\circ$

S.Hundertmark



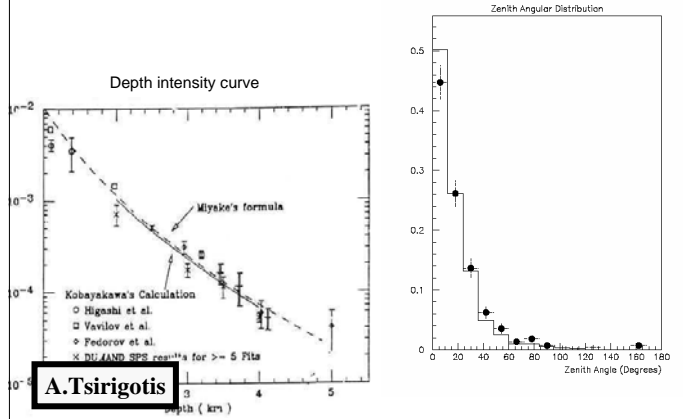
## Results: Effective area and pointing resolution



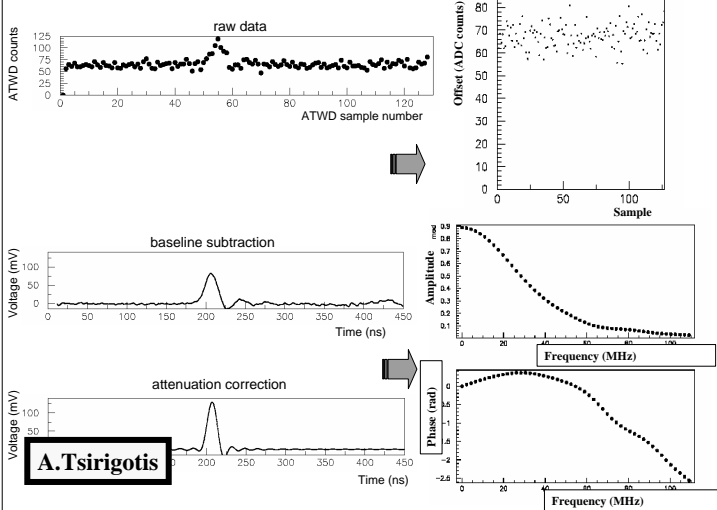
## Background Sources

Cosmic ray muon background

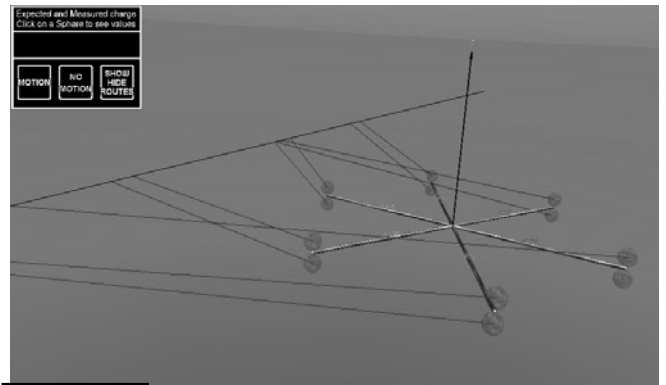
Atmospheric muon angular distribution  
Okada parameterization



## Signal processing

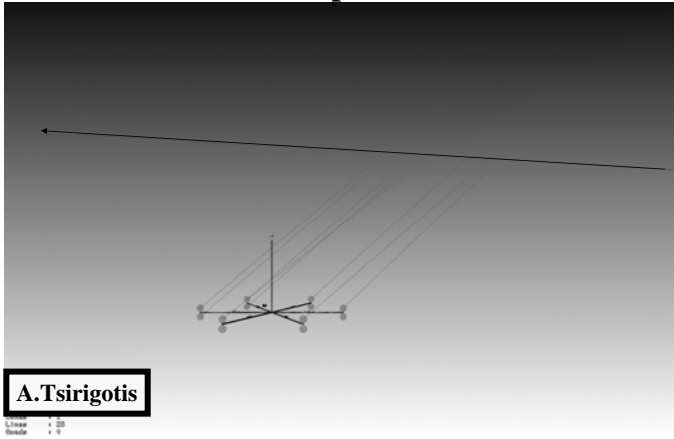


## Track Reconstruction...



Run: 81\_127 Event: 1789

## Pictorial Representation



## I.Belolaptikov: Reconstruction in Baikal

- Ang.error upgoing tracks  $\sim 3^\circ$
- „Allowed region“  $\rightarrow$  allowed theta, phi regions from time differences between pairs of OMs (no fit)

**I.Belolaptikov**

### C.Wiebusch: Reconstruction in Amanda

- Critical due to light scattering
- appropriate likelihood („Pandel“) + clever cuts → effective bg reduction, ang. error for upgoing tracks ~ 2°
- Improvements: likelihood parametrization, layered ice, include waveform

C.Wiebusch

### Summary

Much known about water properties – presumably enough for detector optimization and site comparison

Cross calibration measurements done/underway for Antares/Nemo sites, planned to include Nestor site.

Lot of comparative simulations done in all three collaborations.

Wide spectrum of tools for simulation and reconstruction. Many standard programs common to two or even all three collaborations (Corsika/Hemas, MUM/Music, Geant 3/4, ...)

May also use tools of Amanda/Baikal

Seems to be not too difficult to converge to a common simulation framework for optimization

### Next steps in simulation:

Form a task force group on detector simulation:

- Agree on a working plan (October)
- Input to application for a European Design Study (November)
- First results on comparative studies to ApPEC (Next spring/summer)
- don't prioritize site decision in initial phase but just simulate benchmark detectors characterized by a tuple of basic parameters (say depth 2.5, 3.5 and 4.5 km, noise 25,50 kHz and „high“, 3-4 basic architectures)

# Summary of the Architecture Parallel Session

Talk by G. Hallewell

# Summary of Architecture Parallel Session

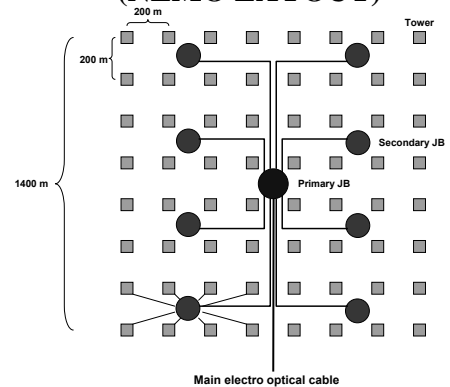
G. Hallewell/ CPP Marseille  
P. Piattelli/ LNS Catania

Parallel Session A1.2.  
Architecture: First session mainly devoted to undersea connectivity

Chair: G. HALLEWELL, P. PIATTELLI

- 14:00 - 14:20 Sea con, K. HALL
- 14:20 - 14:40 Ocean Design, S. THUMBECK
- 14:40 - 15:00 Nexans cables, J. SEIP
- 15:00 - 15:20 Antares Experience with Electro-Optical Cables, P. LAMARE
- 15:20 - 15:40 DISCUSSION

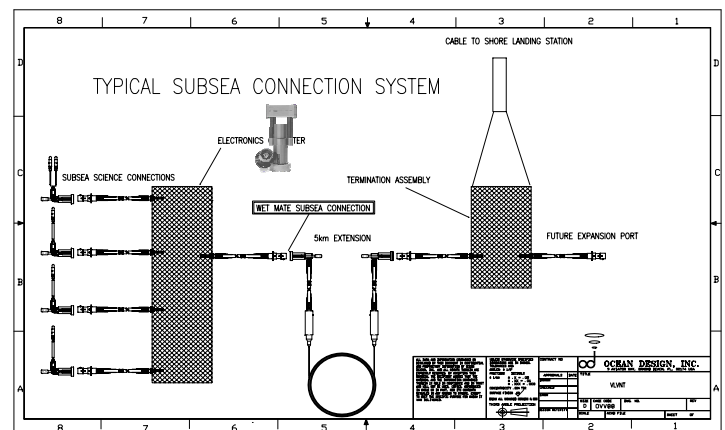
## EXAMPLE OF SEA FLOOR GEOMETRY OF A KM3-SCALE DETECTOR (NEMO LAYOUT)



### Some Architecture Concerns

- (A) Connectivity
  - (1) Wet mateable electro-optic connectors  
(determined by the need (or not) for a ROV for making underwater connections)  
(What is/will be available from Ocean Design/Sea Con?) (8 fibers/4 conductors?)
  - (2) Dry mateable E/O connectors  
(e.g. Sea Con 48/1 as used in Antares for shore cable termination)
- (B) Junction Boxes
  - Layout with Primary and Secondary JB's?
  - What to put in JB?
  - How to Reduce Cost by separating Pressure Blocking and Corrosion Blocking

### Subsea Connectors



**Example of Hybrid (electrical, fibre-optic) wet-mateable connector:**  
(Ocean Design Mk II used in ANTARES:  
2 electrical and 4 fiberoptic pathways)

Mating (Unmating) force ~ 80 lbs (40 lbs):  
well within range of ROV  
Max voltage 1000V, (!)  
Insertion loss < 0.5 dB  
Reflection < -30dB

Ocean Design manufacture Hybrid W-M connectors  
with up to 8 fibre-optic pathways



**ANTARES JB OUTPUTS:  
16 ELECTRO-OPTIC HYBRID WET-MATEABLE CONNECTORS  
(~50% COST OF JUNCTION BOX)**

## SeaCon Fibre Optics Wet-Mate



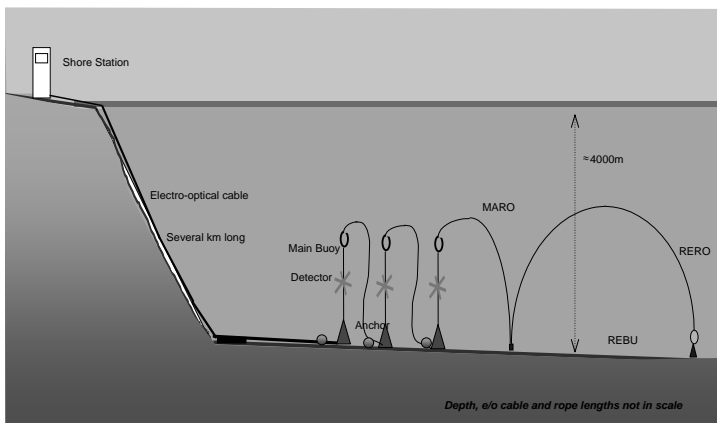
## HydraLight – Features

The ROV HydraLight version offers the following additional features over the successful HydraStar series:

- Significantly improved optical performance
- Superior highly compatible fluorosilicone elastomers
- Superior synthetic oil compensation fluid
- Protective cover over plug sliding sleeve
- Fully seawater compatible interior
- Additional qualification testing
- Stronger operating springs
- 8-channel optical only
- Modular ROV handle interface



*Deployment schematic of towers*



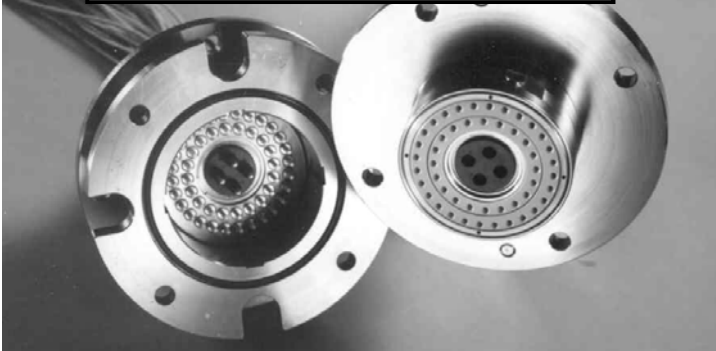
## STATUS OF WET-MATEABLE CONNECTORS

- ❖ Two Companies (Ocean Design, SeaCon) manufacture these connectors:
- ❖ Fully mateable down to lowest depths envisioned for an underwater neutrino telescope:
  - (1) Hybrid Wet-mateable connectors  
presently limited to 8 fibreoptic pathways with Max. Electrical Rating 1000V DC (Ocean Design, SeaCon 'Hydra star')  
(ANTARES does not exceed 500V AC at its junction box outputs)
  - (2) Fibre-optic Wet-Mateables:  
SeaCon HydraLight (8 f/o), Microstar (4 f/o: non-retentive: vertical insertion)
  - (3) Electric Wet-Mateable  
SeaCon CM series: up to 3.3kV AC

**PRELIMINARY CONCLUSION:  
SEPARATE ELECTRICAL AND FIBREOPTIC CONNECTORS  
UNLESS VOLTAGES < 1000V CAN BE ASSURED  
FROM PRIMARY JUNCTION BOX**

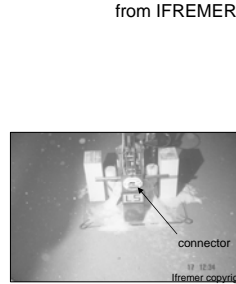
**Dry-Mate Hybrid Electro-optical Connectors  
are less of a problem for High Voltage:**

**Example from SeaCon:  
(48 fibres, 1 electrical conductor (4 parallel pins):  
used at 5000V AC in ANTARES)**

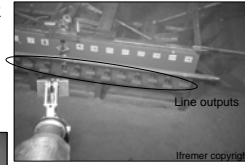


### Experience

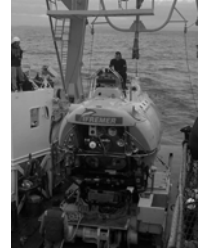
- Junction box installed at sea December 2002
- 1 sector line immersed in December 2002
- 1 instrumented line immersed in February 2003
- 2 lines connected in March 2003 by the manned submarine Nautille from IFREMER



Line socket



Junction box

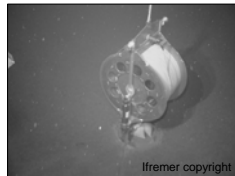


Nautille



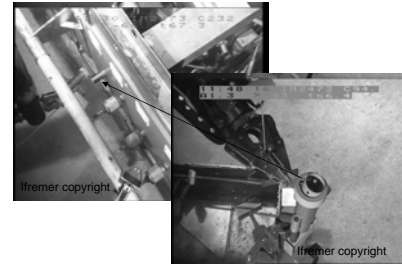
### Line connection sequence

- Link rolled on a drum
- Drum launched from the boat
- Submarine launched
- Drum recovery
- Drum placed near the JB
- JB connection (checked from the shore)
- Link unrolled
- Line connection (checked from the shore)
- Drum released to surface
- Submarine recovery



### Sector line connection

- Mechanical problem on a bulkhead during JB connection
  - ✓ Connector misalignment during connection



- Connection on new JB bulkhead : OK
- Connection on the line : OK

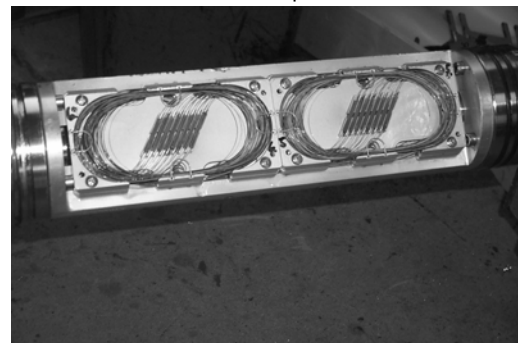
The 2 lines were operated from this date

## NEXANS URC-1, >8000 km



Nexans URC-1 Double Armored Cables with fibre counts up to 384 fibers

A reminder view is pictured below:



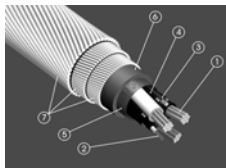
URC-1 Joint box for 384 fibres after qualification test disassembly

### Steel Armoured ROV Umbilical with 4000m depth rating

Investigation of the submarine topography and geology, installation on seabed and exploration of resources are moving towards deeper waters. Hence, control umbilicals used for ROV's must be designed for more challenging operational conditions.

By going deeper, attention has to be paid to the cable weight and dimensions as these are the main contributors to the mechanical forces acting on the cable. At the bottom section, the hydrostatic pressure has to be taken into account. It is of importance to keep the outer dimension at the lowest possible level, so as to reduce hydrodynamic drag forces and strumming acting on the cable.

A Technical Description of the 4000m cable design is available upon request; refer to RS035.



**1 Power Supply, ROV motor**

Three 16mm<sup>2</sup> Copper Conductors rated to 3.3kV. Capable of transferring up to 200kVA over 4500m of cable.

**2 Signal**

A selection of max 12 SMMM optical fibres protected by a laser welded steel tube.

**3 Power Supply, Instrumentation**

Two 1.5mm<sup>2</sup> Copper Conductors supplying power to the ROV instrumentation.

**4 Earth Conductors**

Copper Conductors with semiconductive insulation, used to detect fault currents and drain any charges building up in the cable.

**5 Shield**

Copper Laminate increases the effect of Earth Conductors.

**6 Sheath**

A layer of thermoplastic polyester is applied. Protects the cable core and enables easy termination.

**7 Armouring**

Three layers of high-strength steel wires provide tensile strength and torque balance.

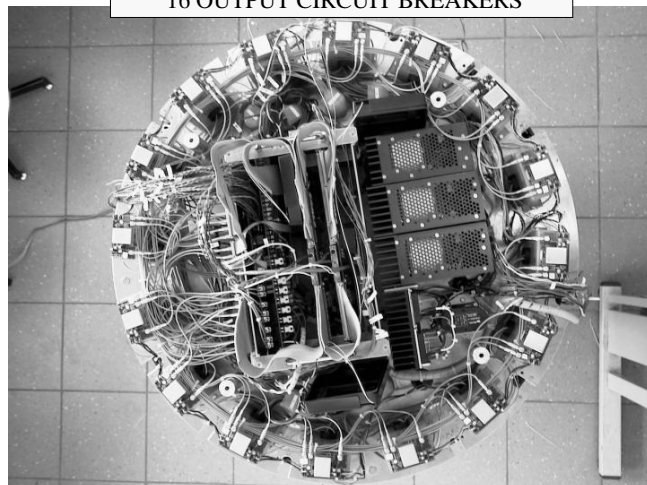
## ANTARES JB on Castor Deck



Underwater Hookups March 2003, see June 2003 CERN Courier



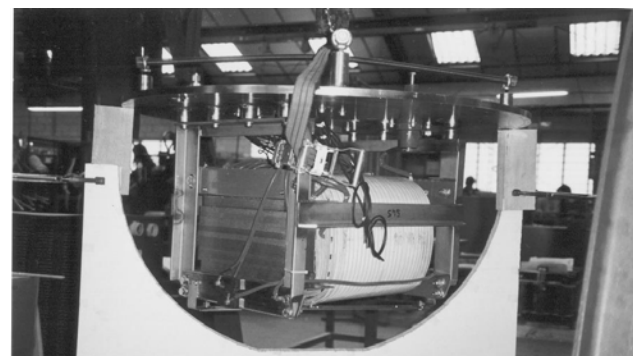
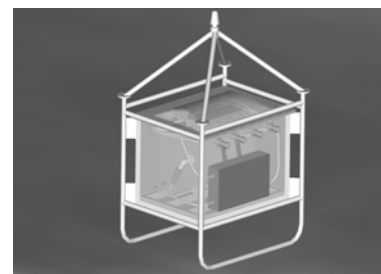
ANTARES JB: INTERNAL ELECTRONICS, 16 OUTPUT CIRCUIT BREAKERS



NEMO Junction Box Concept

**JB oil filled, pressure compensate:**

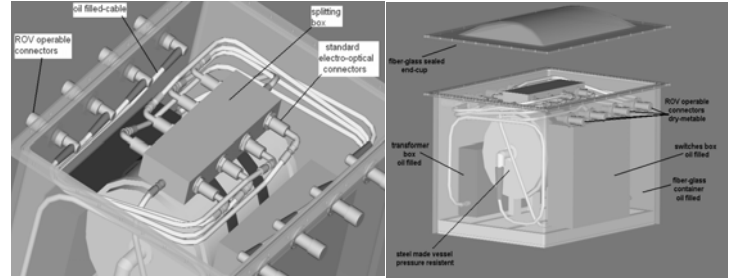
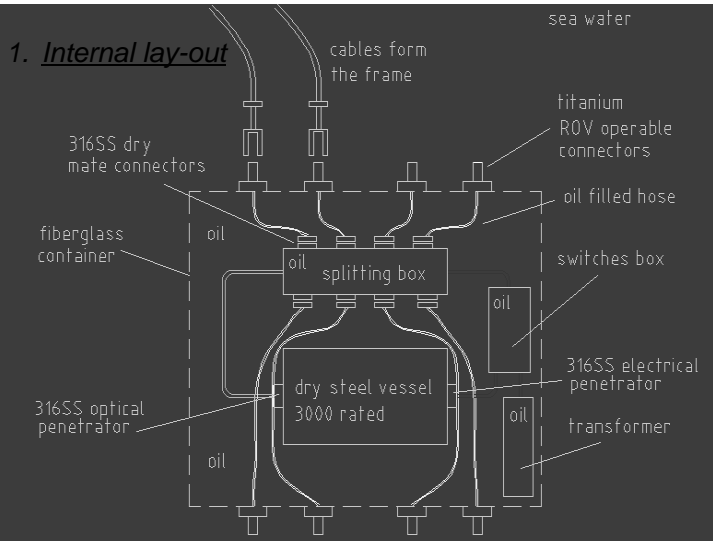
1. internal lay-out
2. steel pressure vessel
3. step-down transformer
4. fiberglass container, with internal



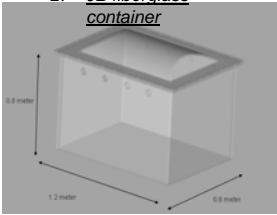
**ANTARES JB 4400V → 500V Transformer (lower hemisphere)**



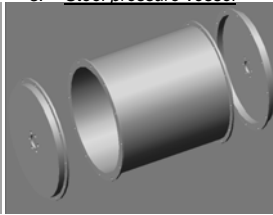
**1. Internal lay-out**



**2. JB fiberglass container**



**3. Steel pressure vessel**



**4. transforme**



**5. Internal frame**







# Summary of Mechanics Parallel Session

Talk by M. Musumeci

Mario MUSUMECI VLVvT workshop



## Mechanics parallel session

Critique Of ANTARES MECHANICS, S.CUNEO

Analysys of mechanics ideas or NEMO, M.MUSUMECI R. OCCHIPINTI

Composite material for deep sea water detectors, L.GUALDESI

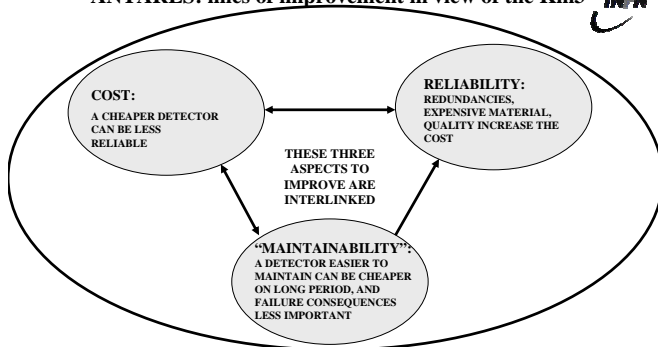
Presentation on NESTOR mechanics, E.ANAZONTZIS

Plastic encapsulation of electronics, A.KAPPES

Mario MUSUMECI VLVvT workshop



## ANTARES: lines of improvement in view of the Km3

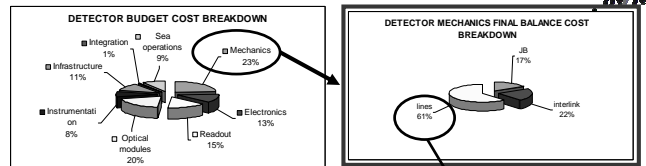


BUT, GIVEN THE QUANTITIES INVOLVED, A STRONG COMMERCIAL ATTITUDE AND AN EFFECTIVE MANAGEMENT CAN ALLOW SIGNIFICANT COST REDUCTIONS

Mario MUSUMECI VLVvT workshop

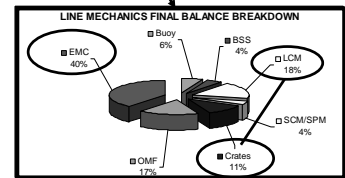


## ANTARES: costs of the mechanics



MECHANICS ENGAGE A SIGNIFICANT AMOUNT OF THE DETECTOR BUDGET  
THUS, EN AFFORT ON THAT FIELD IS WORTH TO REDUCE DETECTOR OVERALL COSTS

- SOME GENERAL SUGGESTIONS:
- USE OF STD COMPONENTS/SIZES
  - ALTERNATIVE MATERIALS (FIBREGLASS vs TITANIUM)
  - STRONG PROJECT MANAGEMENT / COMMERCIAL ATTITUDE
  - TAKE ADVANTAGE OF LARGE SERIES PRODUCTION COST SCALEFACTOR
  - SIMPLIFY THE DESIGN



Mario MUSUMECI VLVvT workshop



## ANTARES: mechanics reliability



AFTER THE EXPERIENCE, IT SEEMS THAT MECHANICS RELIABILITY COULD BE SIGNIFICANTLY INCREASED IF APPROPRIATE RESOURCES ARE DEVOTED TO QUALITY ASSURANCE

- MANUFACTURER CHANGED DESIGN WITHOUT NOTICE
- TIME PRESSURE ON THE PROJECT
- ACCEPTANCE TESTS INAPPROPRIATE

EMC FIBRE FAILURE

- ORIGINAL SUPPLIER WRONG SPECIFICATION, HOLES MACHINED TOO LARGE
- CORRECTIVE INFORMATION AVAILABLE, BUT NOT ENOUGH EMPHASIZED
- MISMATCH HOLE-CONNECTOR



- POOR EXPERIENCE ON THE CABLE
- ACCEPTANCE TESTS INAPPROPRIATE
- A CABLE/MOLDING FAILURE COULD NOT BE DETECTED

WATER LEAK

- POOR HANDLING OF MATERIAL
- POST-ASSEMBLING CONTROL HARD TO BE DONE
- CARBON STEEL NUTS WERE INTEGRATED WHERE TITANIUM WAS FORESEEN



- POOR DOCUMENTATION HANDLING
- MANUFACTURER WORKED ON PRELIMINARY DRAWINGS
- AISI304 PARTS WERE INTEGRATED WHERE TITANIUM WAS FORESEEN



CORROSION

Mario MUSUMECI VLVvT workshop



## NEMO

### The goals of the mechanical development for the KM<sup>3</sup>

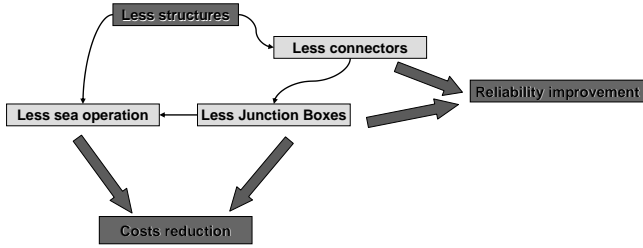
The main goals of the work made by the NEMO collaboration to optimize the design of an ultra deep water submarine neutrino detector were the followings:

- ✓ Reduce the cost to instrument a km<sup>3</sup> detector by means of:
  - Use of towers, that permit to enlarge the spacing between the vertical structures
  - Realization of a modular layout for the detector;
  - Utilization of composite material;
- ✓ Reduce the maintenance costs of the detector by means of:
  - Study of innovative connection methods;
- ✓ Simplify the deployment operations of a 3D structure;
- ✓ Avoid mechanical stresses on the electro-optical cables during the deployment and the lifetime of the detector;

Mario MUSUMECI VLVvT workshop

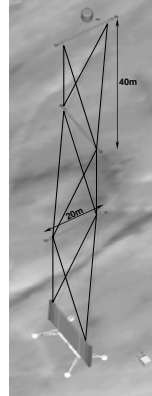


### STRUCTURE REDUCTION EFFECTS



### NEMO

#### Current configuration of the NEMO proposal for a tower



The supports for the PMT are made of pipes in Glass Reinforced Plastic (GRP) interconnected by means of synthetic fiber ropes.

The employ of a composite material allow a great costs reduction for the raw material supply

Using commercial measures, GRP pipes can be found at very low costs.

The diameter of the pipes is 0.45m and its thickness is of 5.9 mm. The length of a storey is 20m

Each level of the tower is distanced with respect to the previous and the next one of 40m.

Moreover it is rotated around the vertical axis of 90 degrees.

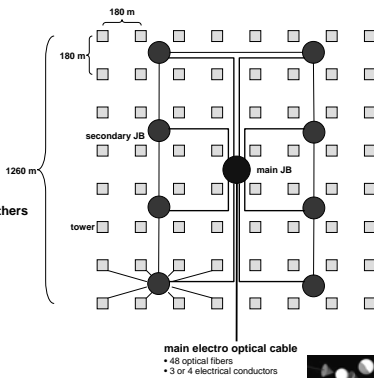
It is possible to modify, with some boundary conditions, the specific weight of the GRP in order to make the storey neutral in water.



### NEMO

#### current proposal of general layout for Km<sup>3</sup> detector

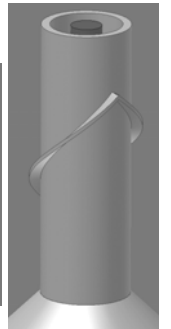
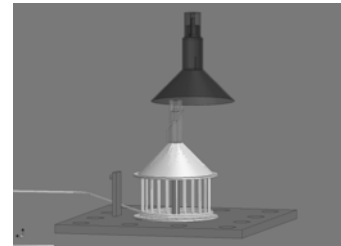
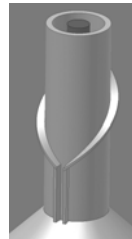
- n. 1 main Junction Box
- n. 8-10 secondary Junction Box
- n. 64 + 80 towers
- ~180 m between each row and the others
- ~180 m between each columns and the others
- 16 storeys for each tower
- 64 PMT for each tower
- > 4096 PMT



main electro optical cable  
+ 48 optical fibers  
+ 3 or 4 electrical conductors



#### A possible self connecting system



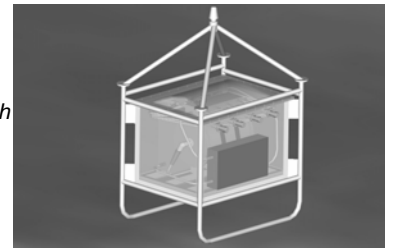
### MODUS

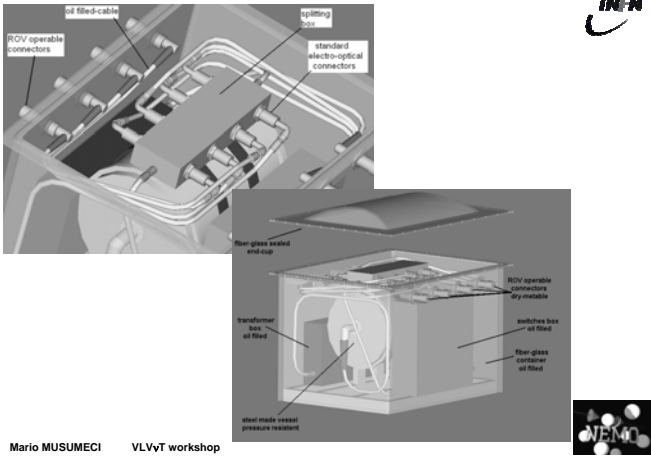
#### submarine vehicle for GEOSTAR deployment/recovery



#### JB oil filled, pressure compensate:

1. internal lay-out
2. steel pressure vessel
3. step-down transformer
4. fiberglass container, with internal steel frame





## Objectives

- Develop a measuring range at 3500 meters depth
- Maximize corrosion free endurance time (time between overhauls)
- Minimize maintenance time
- Minimize failure risk
- Respect budget constraints



## Two Main Options

- Use market available products and design to improve system reliability
- Invest in material performance research aimed to design and develop a system as a complete prototype
- A cost effective compromise of above is to integrate market products into a customized system



## Targets

- Withstand depth pressure with an acceptable flexural deformation
- Preserve the relative motion between moving parts without an excess of friction
- Preserve for long time the surface integrity avoiding corrosion
- Privilege non magnetic or even non conductive materials to avoid galvanic effects and influence compass related instrumentation



## Titanium Alloys

- Excellent response to corrosion and fouling
- Non magnetic
- High mechanical strength
- Medium availability
- Its higher cost is largely compensated by the use of less material weight to obtain the same strength and by savings in maintenance cost



## Design Policy

- It is important to establish a design policy:
  - if the reference is Titanium alloy, any compulsory deviation from it must be considered as a case study
  - only Composite Technology may be associated to it with careful design of the joints due to the different elastic properties.

## Composites Advantages

- Corrosion free
- Non magnetic
- Damage propagation very low
- Creative design due to the fact that the designer make its own production:
  - it is virtually possible to change material density and composition at any section



## Design consideration

- Modular system with built in redundancy
- "All" connections to be made in air
- Use ships of opportunity and non highly specialized surface vessels for deployment
- Use locally available transport vessels
- No use of bathyscaphs or ROVs
- Retrieval and expandable
- Inoxidable material



## Material considerations



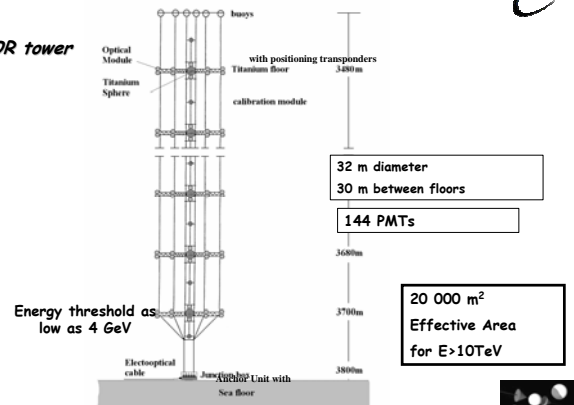
### >Inoxidable material

- **Stainless steel** > inoxidable > many alloys > sensitive in cavity corrosion > steel ropes and shackles
- **Aluminium** > special alloy > anodized
- **Titanium**
- **Plastics** > PVC, Polyethylene > ropes
- **Glass fibers** > light and strong > water ingress?
- **Glass** > PMT > housing > inoxidable

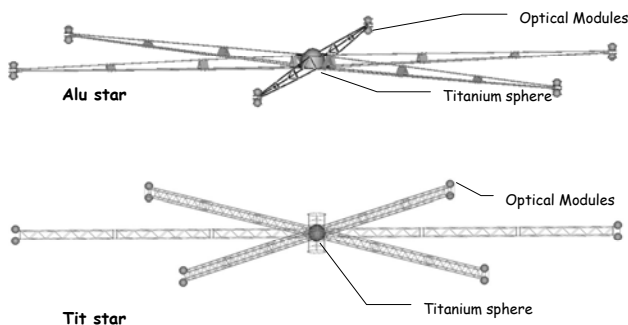
### > Isolation with plastic or rubber



## NESTOR tower



## NESTOR star



## Titanium sphere



## Summary of Sea Operation Parallel Session

Talk by E.G. Anassontzis

## Sea Operations for "km<sup>3</sup>" neutrino telescope

VLVvT  
E.G. Anassontzis  
University of Athens  
NESTOR COLLABORATION  
workshop

5-8 October 2003  
NIKHEF - Amsterdam

### Deployment considerations

- Modular system with built in redundancy
- Detector configuration
  - Towers (NEMO, NESTOR) Strings with many light sensor points per deployment per depth level
  - Strings (ANTARES) Strings with several light sensor points per deployment
- Connections to be made
  - in air (NESTOR)
  - in underwater (ANTARES, NEMO)
- Use ships of opportunity and non highly specialized surface vessels for deployment
- Use locally available transport vessels
- Retrievable and expandable

VLVvT Workshop - 5-8 October 2003 - NIKHEF, Amsterdam

NESTOR

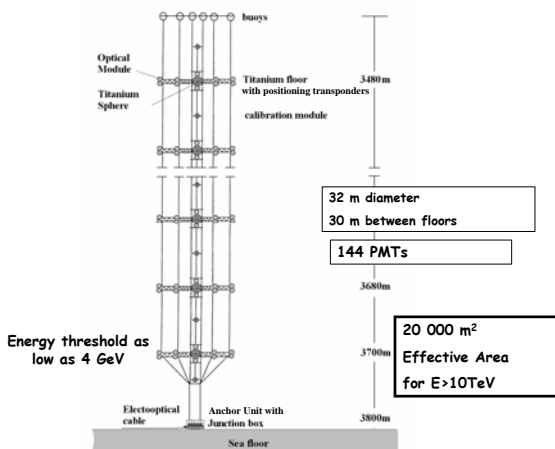
### .... Deployment considerations

- Use ships of opportunity and non highly specialized surface vessels for deployment
- Use locally available transport vessels
- Use of bathyscaphs or ROVs ?
  - NO (NESTOR)
  - YES (ANTARES, NEMO) Dynamic positioning
- Vessels with dynamic positioning
- Short base line detector positioning
- Sea state working conditions up to 4+ beaufort

VLVvT Workshop - 5-8 October 2003 - NIKHEF, Amsterdam

NESTOR

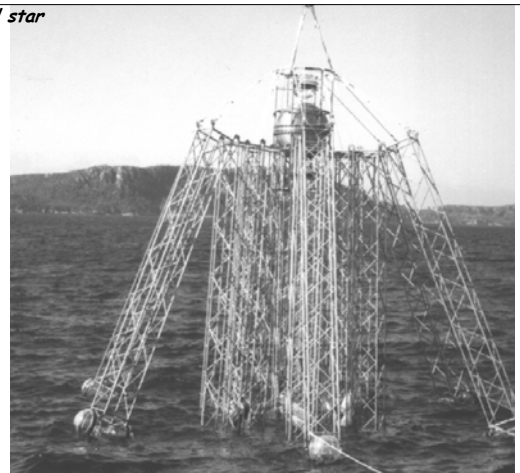
NESTOR tower



VLVvT Workshop - 5-8 October 2003 - NIKHEF, Amsterdam

NESTOR

Folded star



VLVvT Workshop - 5-8 October 2003 - NIKHEF, Amsterdam

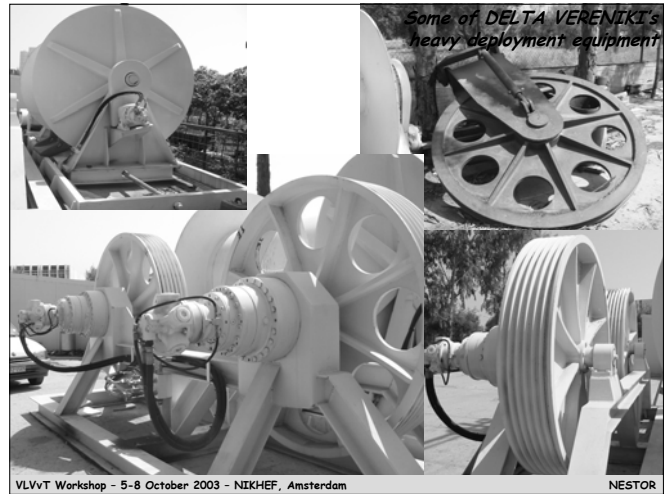
NESTOR



*Typical cable-laying ships*

VLVVT Workshop - 5-8 October 2003 - NIKHEF, Amsterdam

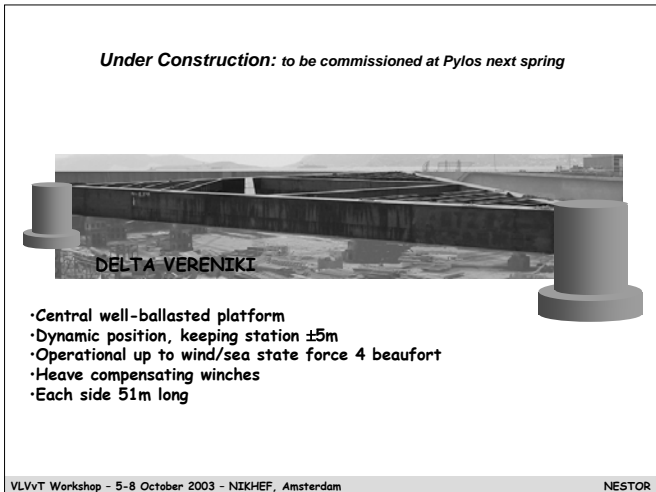
NESTOR



*Some of DELTA VERENIKI's heavy deployment equipment*

VLVVT Workshop - 5-8 October 2003 - NIKHEF, Amsterdam

NESTOR



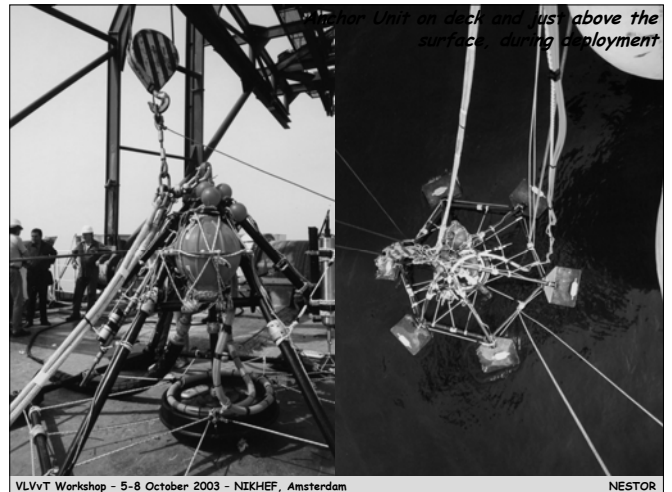
*Under Construction: to be commissioned at Pylos next spring*

DELTA VERENIKI

- Central well-ballasted platform
- Dynamic position, keeping station  $\pm 5m$
- Operational up to wind/sea state force 4 beaufort
- Heave compensating winches
- Each side 51m long

VLVVT Workshop - 5-8 October 2003 - NIKHEF, Amsterdam

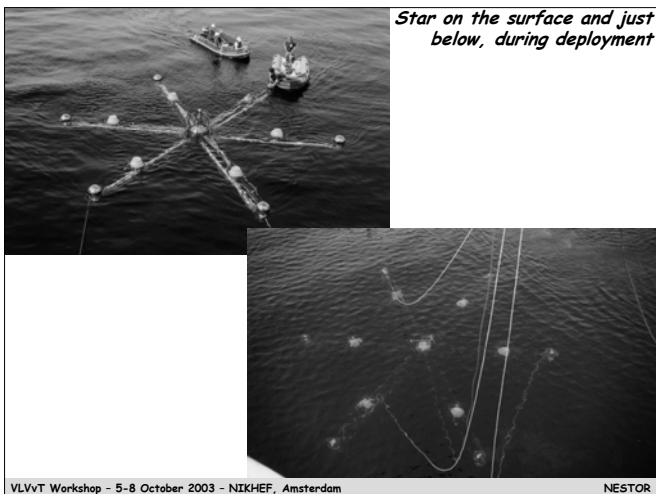
NESTOR



*Star Unit on deck and just above the surface, during deployment*

VLVVT Workshop - 5-8 October 2003 - NIKHEF, Amsterdam

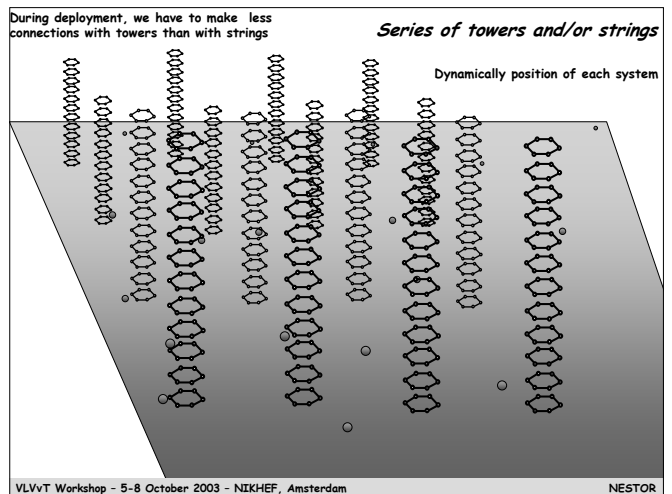
NESTOR



*Star on the surface and just below, during deployment*

VLVVT Workshop - 5-8 October 2003 - NIKHEF, Amsterdam

NESTOR



During deployment, we have to make less connections with towers than with strings

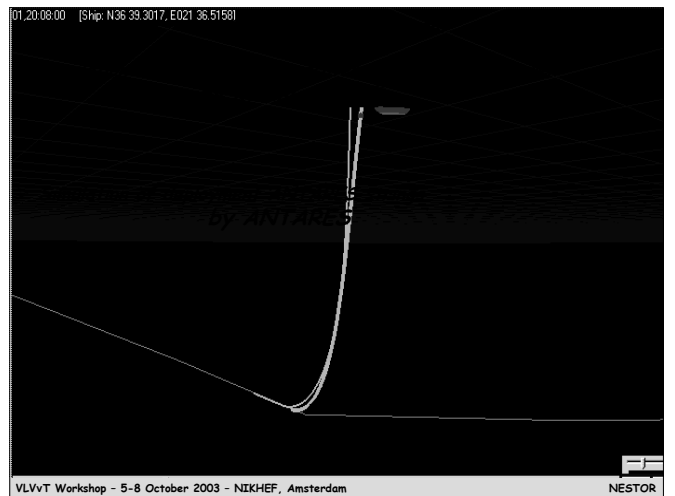
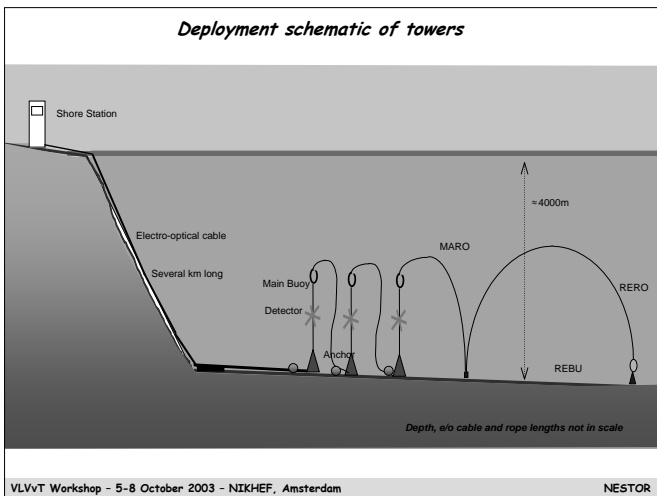
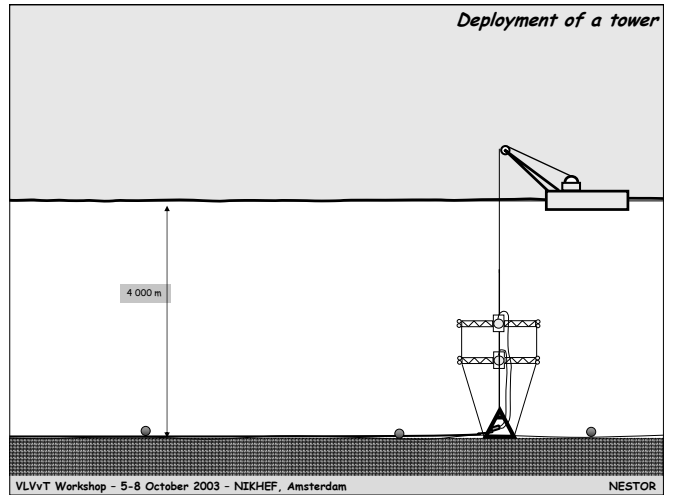
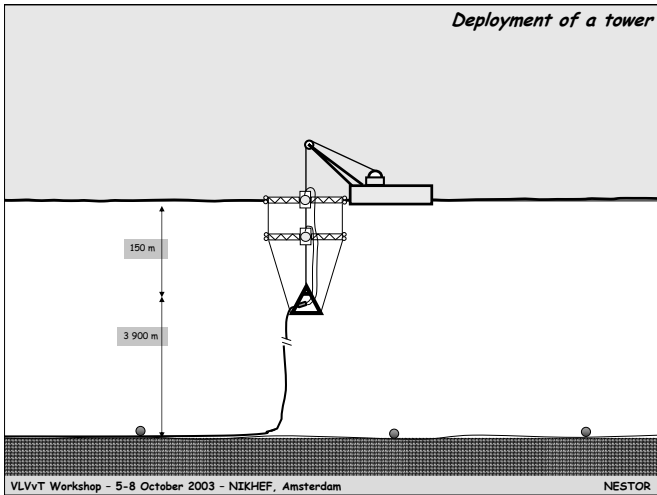
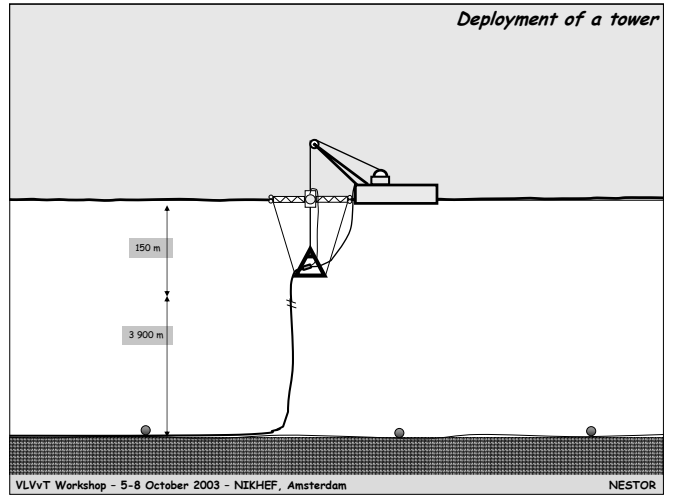
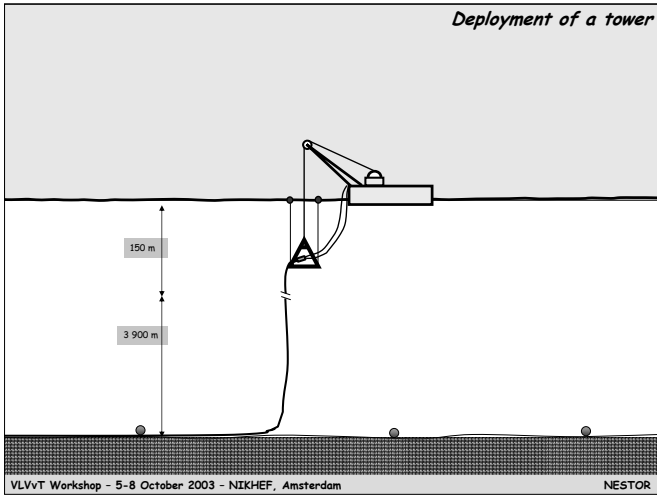
*Series of towers and/or strings*

Dynamically position of each system

VLVVT Workshop - 5-8 October 2003 - NIKHEF, Amsterdam

NESTOR





*Conclusions*

ANTARES (with IFREMER) have shown that they can deploy string like detector with success

NEMO believe that they can deploy tower like detector

NESTOR have shown that they can deploy tower like detector with success

We can deploy jointly the km<sup>3</sup> Very Large Volume  $\nu$  Telescope

VLVVT Workshop - 5-8 October 2003 - NIKHEF, Amsterdam

NESTOR



*end*

INFN M. Sedita VLVvT workshop Amsterdam 05-08 October 2003 NEMO

## VLVnT Installation and Maintenance of the submarine network

The Maintenance aspect present some difficult as their cost is very high. For this reason it's important:

- Redundancy where possible
- Reliability prevision
- Develop recovery and deployment techniques to avoid DP vessels
- Develop tools to increase automation

INFN M. Sedita VLVvT workshop Amsterdam 05-08 October 2003 NEMO

Criteria for selecting the Km3 Power System components is long term reliability

The reliability target for the Km3 Node Power System is a Mean Time Between Failures (MTBF) on the order of 500,000 hours which is equal to approximately 60 years. This high value is due to number of nodes (String/Tower). With 60 node we expect a failure every year. For the control system the reliability could be more high 1,000,000 hours MTBF.

Reliability Results from other subsea application

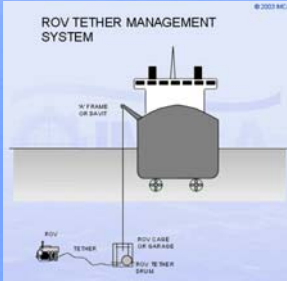
Node MTBF	No Failures*	<= 1 Failure*	<= 2 Failures*	<= 4 Failures*
30 Years	43%	71%	81%	89%
60 Years	61%	86%	92%	95%

\* Failure is defined as loss of node

- calculations show that with node MTBF of  $10^6$  hours, half the nodes will fail in the lifetime of the project
- improving this performance is essential
- a plan of test to destruction, rather than estimate MTBF, may be a useful alternative

INFN M. Sedita VLVvT workshop Amsterdam 05-08 October 2003 NEMO

1. Using a special vessel equipped with dynamic positioning system and a ROV with robotic manipulator driven by the umbilical.
2. Use a bottom mounted ROV supplied by the underwater electro-optical cable



ROV TETHER MANAGEMENT SYSTEM

INFN M. Sedita VLVvT workshop Amsterdam 05-08 October 2003 NEMO

### DP Vessel Limitation

- Building the electric network with the Junction Box Hubs for string connectors is to be considered as a standard job for a DP vessels and ROV when strings/towers are not yet installed.
- More complicate and dangerous is the same operation from the surface when delicate optical sensors have been installed in instrumentation field.
- The Maintenance Costs could be very High and implies:
  - a choice on the limit of fault string/towers that remain inactivated
  - Redundancy
  - Reliability of the entire system

INFN M. Sedita VLVvT workshop Amsterdam 05-08 October 2003 NEMO

### Special DP vessel and ROV techniques

Assumptions:

- To deploy main Junction Box and string/towers underwater connecting stations together with the cable network for the string field
- The secondary JB have been deployed by the special DP Vessel with ROV and they are in their final location on the seabed.

INFN M. Sedita VLVvT workshop Amsterdam 05-08 October 2003 NEMO

### Autonomous Underwater Robot on a bottom rail

- The concept is to relay in a bottom referenced fixed path for an Autonomous Underwater Vehicle also fitted with robot to operate the string connectors and with self-propulsion to move them in the field for installation and maintenance
- The fixed path is obtained with a rail network to reach the individual string location

### Rail Features and Construction

- Rail is made out light composite profile fixed to the bottom in sections
- Its deployment must be done by DP Vessel and ROV
- Underwater assembly can be assigned to a special version of the AUV which would align, connect and fix to the seafloor the modular rail sections.

### Rail Network Design

- Rack-rail will be only a passive path fitted with mechanical stoppers in the limits and the cross over. No points are provided.
- From a side line with two end stations (Terminuses) an array of 90 degrees rail sections is made for the corresponding number of the string line
- On the right and on the left of these sections reaches to individual string/tower stations are provided.

### Rail Design Criteria

- Propulsion on the rack rail is obtained by motors fitted on the vehicle.
- Changing of direction is obtained by elevating the whole vehicle by a piston with a plate located on its lower surface and by a 90 degree rotation. Lowering the vehicle in this new direction and retracting the piston will complete the changing in direction.

### Autonomous Underwater Robot Features

- Energy is obtained by set of battery.
- Battery are regularly recharged when the AUR is docked at the docking terminuses located at both ends of the side rail section.
- All AUR actions are pre-programmed.
- Tasks and coordinates are down-loaded, from shore by the communication system, at the Docking station.
- An Under Water winch is provided at the Docking Terminuses to link the strings with the surface in up-down modes

### Autonomous Underwater Robot Modules Main Characteristics

- Rack rail interface actuators for propulsion and direction changing piston
- Battery Package
- Engine Room
- Electronic Compartment
- Automatic Clutching System and its Sensors
- Strings Manipulating System

# Summary of the Calibration Parallel Session

Talk by J.J. Hernandez-Rey

## Calibration group

(convenors: Juan.J.Hernandez@ific.uv.es and L.Thompson@sheffield.ac.uk)

### “Mission statement”

- **Define** the **detector parameters** (“calibration constants”) that must be determined to operate an undersea km<sup>3</sup> telescope at the desired accuracy.
- **Establish** the **precision** at which this parameters must be/ can be estimated.
- **Propose** the **systems** that may be used to reach this goal.
- **Study concrete solutions**, adapted to the selected final design, to implement these systems.

Version 8/10 11:30

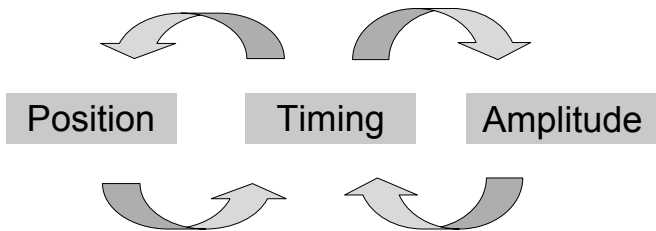
## Calibration goals

Determine the necessary constants to allow the reconstruction of events in

space

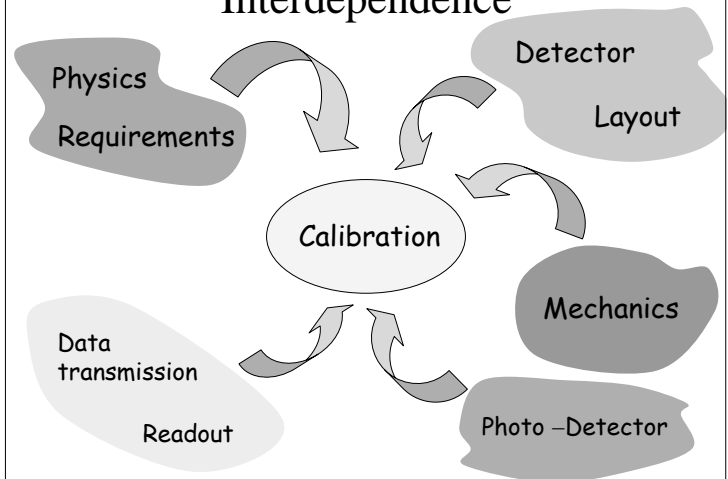
time

energy



All other constants (temperature, voltages) are used to determine these parameters

## Interdependence



## Positioning

### Position calibration

Absolute

Relative

w.r.t. external objects

depends on site

- GPS + acoustic transponders
- Moon?
- Local geological peculiarities?
- Other detectors?

New ideas are most welcome

among inner components

depends on detector design

- Semi-rigid/fixed parts: tiltmeters, compasses
- Moving parts: Non-luminous devices (sonic, other?)

## Time

### Timing calibration

Absolute

Relative

w.r.t. to UTC

Should not be a major problem (in the msec range)

But several junction points would mean new problems in relative calibration

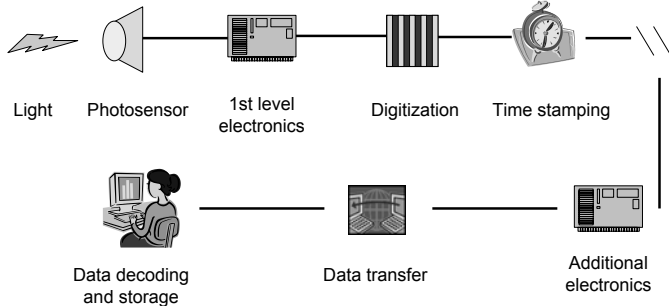
among inner components

extremely important

- Affects reconstruction efficiency and angular resolution
- Limited by intrinsic processes: photosensor time fluctuations, medium time dispersion, electronics.



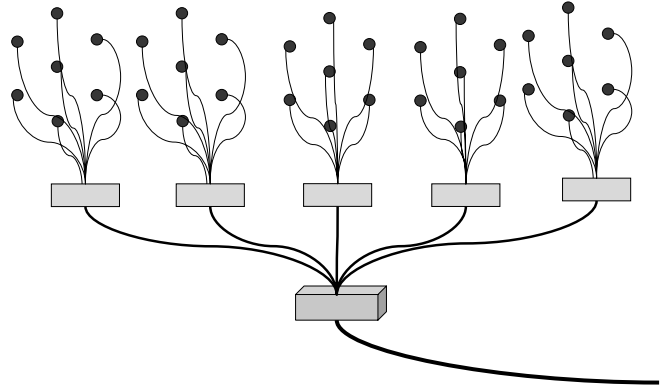
## Timing calibration



Each level can introduce **delays**, **jitters** and **shifts** with time

**At which levels** is convenient to have time calibration? **How?**

## Timing calibration




## Amplitude

- Photodetectors can be calibrated at the laboratory (the site is a “quiet” place).
- For conventional PMTs, gain can be monitored via  $^{40}\text{K}$  (site dependent).
- Transparency losses are more difficult to monitor.
- New devices may need different calibration.

## R&D road map

- Study the scalability to  $\text{km}^3$  of existing techniques and technologies.
  - Position:
    - Positioning within one detector “unit” (string, tower, etc) and “sub-unit” (storey, floor, star).
    - Relative positioning between “units” Acoustic devices? Systematics @ 1km? Horizontal tracks. How frequently?
    - Absolute positioning (GPS plus several reference points?)
  - Timing:
    - Clock based: echo system, synchronous data.
    - Optical calibration within detector units: through fibers? through the water (shadowing)?
    - Optical calibration among detector units: needed? (redundancy is not a luxury) Feasible? (distance between beacon-OM  $\sim \lambda_{\text{abs}}$  and  $\lambda_{\text{scat}}$ )
  - Amplitude :
    - Gain calibration via  $^{40}\text{K}$
    - Overall monitoring (transparency loss) more difficult (site dependent)

## R&D road map (continued)

- Explore new ideas in all domains:
  - Independent calibration array?
    - Far-fetched idea: needs to be studied in detail
  - Synchronous Digital Hierarchy 
  - $\nu$  beam from CERN??
  - ...
- Start studies with some likely designs

## Summary

- The review of existing/near future detectors showed common basic approaches to calibration.
- Are these concepts scalable to a  $\text{km}^3$  detector?
- New ideas are needed and already some appeared and were discussed.
- Calibration is closely related to other topics. Next step requires an interaction with convenors of other task groups.



Summary Readout-Electronics

F. Ameli, T. Legou and M. de Jong

- introduction
- front-end electronics
- data transmission
- data processing
- slow control/calibration

input parameters\*:

- $\sim 10^4$  photon detectors
- 50 – 100 kHz background rate
- $\sim 5 - 10$  Byte per "hit"

↓

total data rate  $\approx 2.5 - 10$  GB/s

\*cost  $\Rightarrow$  sparse detector  $\Rightarrow$  single photon detection

- digitalisation<sup>†</sup>:

off-shore  $\Leftrightarrow$  on-shore

↓

electronics  
clock system  
power  
mechanics

- data distribution:

address  $\Leftrightarrow$  time-domain

- data processing:

software  $\Leftrightarrow$  hardware

<sup>†</sup>original photon signal is digital!

front-end electronics:

- analogue signal processing
  - Time-Over-Threshold
  - rise-time and decay-time
  - total charge
  - sampling (frequency  $\sim 100 - 500$  MHz)
  - time accuracy?
  - dynamic range?
- front-end data processing
  - FPGA (= embedded processor)
  - VLSI

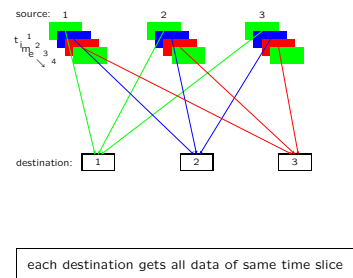
- optical modulation

- 1 colour-fibre for each PMT
- digital/analogue!
- direct addressing (slow control)

- data transmission

- CWDM ( $10 \text{ Gb/s} \times \lambda_{1-8} \times 100$  fibres)
- DWDM ( $1 \text{ Gb/s} \times \lambda_{1-128} \times 100$  fibres)

Data distribution concept:



data processing:

- comparison with CMS is encouraging
- cost/complexity ⇒ fast algorithm(s)
- output  $\leq 1$  MB/s ⇒ reduction  $10^3 - 10^4$
- new physics ⇒ flexible ⇒ software
- efficiency ⇒ complete data sample
- logic
  - democratic ⇔ speed
  - hierarchical ⇔ detector topology
  - $1 \leftrightarrow 2$  SPE ⇔ photon-detector

filter criteria:

- causality (Čerenkov light)
- slow motion (mono-poles)
- (a priori) directional information
- (a priori) time information

↓

software

- slow control
  - embedded processor with local bus
  - each instrument as Ethernet node
  - remote fibre-optic sensing
- calibration/instrumentation
  - what?
  - how often?
  - auto-calibration

calibration:

calibration	photon-detection
read/write	(mainly) read
slow IO	slow I/fast O
duty cycle $\leq 10\%$	duty cycle 100%
subset of nodes	all nodes

↓

separate physically the calibration and photon-detection systems

"Hybrid concept":

- calibration units:
  - number of nodes  $\sim 10\%$  of total
  - "known" technology
  - redundancy
  - maintainability
  - low duty cycle ⇒ low power
- photon-detection units:
  - number of nodes  $\sim 90\%$  of total
  - no maintenance ⇒ very reliable
  - low power
  - if R&D completed ⇒ "easy" to build

summary:

- workshop is a good start (to be continued)
- significant R&D work started on front-end electronics
- new ideas for data transmission
- data filtering:
  - software way ...
  - physics!
- calibration specifications?



## Concluding Remarks

Talk by U. Katz

## Concluding Remarks VLV $\nu$ T Workshop Amsterdam, 6-8.Oct.2003

Uli Katz, Univ. Erlangen

**This is NOT thought to be the  
summary of summaries!**

### 1) Where we are, where we want to go

- After almost 20 years: first  $\nu$ T's in sea water "ante portas"
- Everybody is enthusiastically anticipating the future
- But: until recently lack of coherence, no united effort
  - no backup by politics and funding agencies
  - no realistic roadmap to "the KM3 project"
  - support by astroparticle community subject to conditions
  - no chance to obtain world-wide consensus on

**NEED FOR A CUBIC KILOMETER  $\nu$ T  
IN THE MEDITERRANEAN**

- NOW: the FP6 program has triggered a "unification process"
  - common effort to obtain funding
  - will it develop to a common effort to design and construct KM3?
- Time scale: given by "community lifetime" and competition with ice detectors
  - interest fades away if KM3 comes much later than IceCube
  - remember: IceCube ready by 2010
  - we better start NOW (even without EU money?)! . . .

Imagine we fail at this point: What would it mean?  
A FUTURE WITHOUT A NORTHERN-HEMISPHERE  $\nu$ T?

**HOW DULL !!!**

### 2) Physics Objectives and Implications for KM3

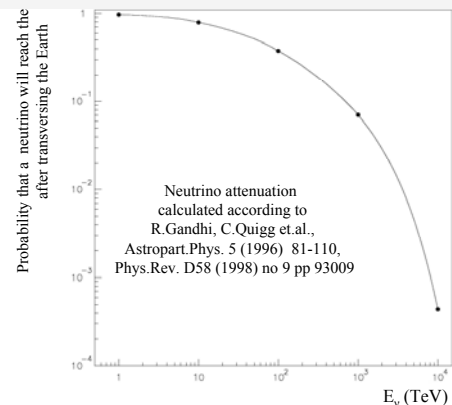
Physics objectives of current & future  $\nu$ Ts:

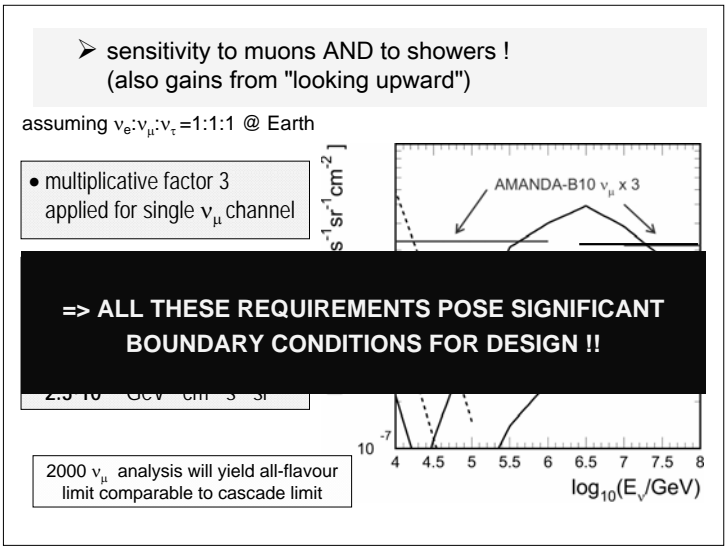
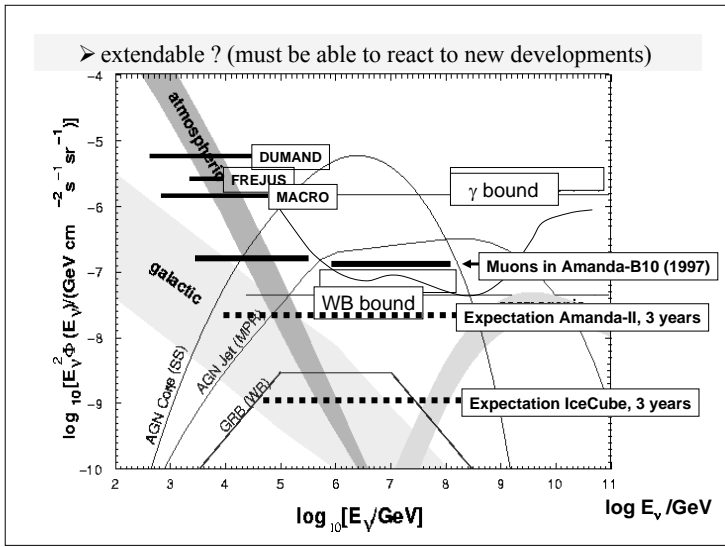
- |   | importance for KM3 |
|---|--------------------|
| <ul style="list-style-type: none"> <li>▪ astrophysics: diffuse fluxes, point sources                             <ul style="list-style-type: none"> <li>➢ point sources: need good angular resolution, medium energies</li> <li>➢ diffuse fluxes: large energies</li> </ul> </li> </ul> | ***                |
| <ul style="list-style-type: none"> <li>▪ dark matter ("low energies")                             <ul style="list-style-type: none"> <li>➢ What happens, if LHC discovers something?</li> </ul> </li> </ul>   | **                 |
| <ul style="list-style-type: none"> <li>▪ neutrino oscillations                             <ul style="list-style-type: none"> <li>➢ Probably covered by dedicated experiments</li> </ul> </li> </ul>  | (*)                |
| <ul style="list-style-type: none"> <li>▪ others:</li> </ul>   | t.b.worked out     |

**NEEDS DISCUSSION, ENERGY RANGE CRUCIAL FOR DESIGN !**

=> **Basic requirements:**

- affordable !
- 4 pi acceptance ?

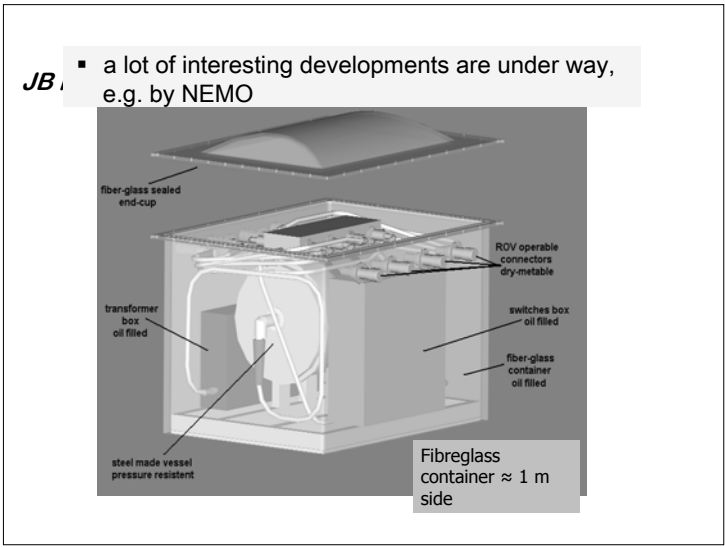
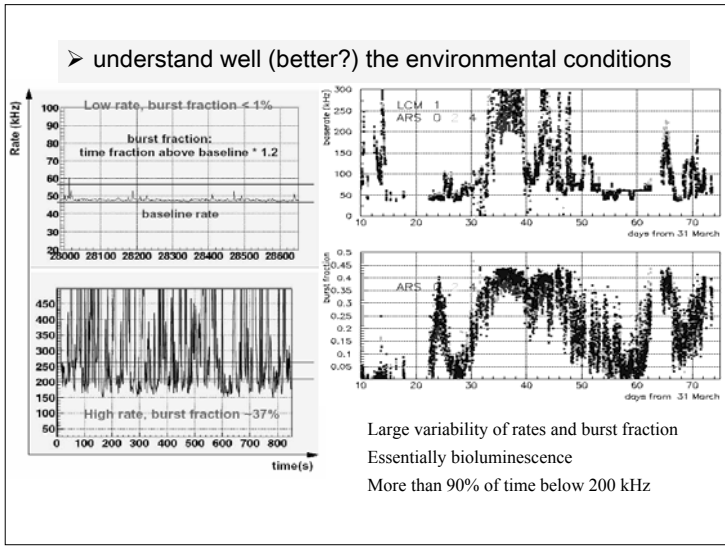




### 3) Lessons to be learned from current projects

- Lots of tested technological solutions
  - which of them can be used "as are"?
  - Needs critical review !**
  - offer basis for (some? many?) future developments
  - WARNING: existing solutions are well-tested, low-risk ... BUT may reduce acceptance for new, better approaches

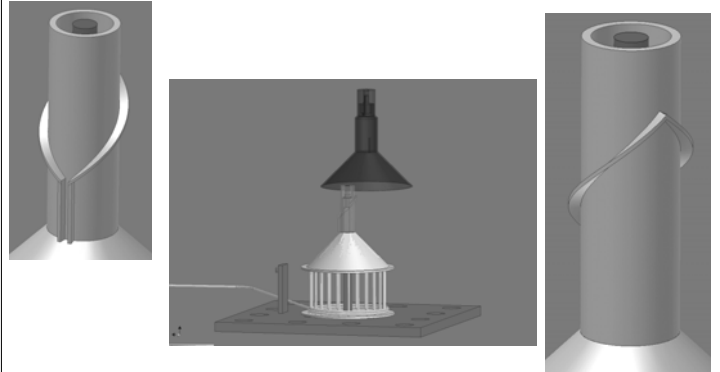
- Make best use of experience gained!
  - crucial failures may appear where they are the least expected
    - **complexity of detectors must be reduced**
    - **quality control and assurance will be a central topic**
  - time schedules are difficult to control but are crucial for the KM3 project
    - Imagine **construction and deployment take longer than the detector lifetime!** (IceCube: ~50%)
    - **DANGER: technical solutions outdated by ~10 years at construction time** (imagine building km3 with technology from 1990).



#### 4) Asking Questions and Collecting Options ...

- **... is the most important task right now**  
since it helps us to identify problems, find solutions and to initiate / continue / intensify the necessary R&D steps
- **a selection of such questions/options (strongly interrelated!):**
  - => How will the detector look like?
    - which structures are optimal?
    - dry or wet connections, or wet from top, or ...?
    - how to avoid single point failures?
    - star or linear or circular interconnection topologies or ... ?
    - how to optimize architecture? - **needs thorough simulation!**
  - => Sea operations are a major part of the project and must be considered from the very beginning

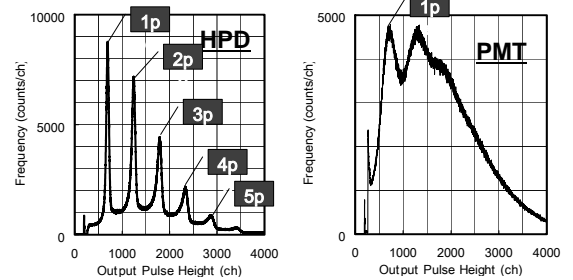
=> Dry or wet connections, or wet from top, or ... ?



Mario MUSUMECI for VLVvT workshop

- => What materials to use?
  - replacement(s) for titanium?
  - composite solutions
  - polyurethane encapsulation (as for hydrophones)?
- => Cables and connectors?
  - connectors are extremely expensive – how to reduce number, in particular wet-matable ones
  - reliability is crucial !

=> **Which photodetectors?**  
can we improve on:  
quantum efficiency \* sensitive area / cost ?  
time resolution?  
single photon electron resolution?



**Remember:** 10% larger PM distance @ same efficiency  
=> ~ 30% more detector volume !

=> **is directional sensitivity possible?**

I. SIMION simulations show that shape of existing BAIKAL PMT can be improved to provide one-one correspondence and timing improvement

III. Coupling to a light guide system also provides information on the detected light direction

II. Coupling to a position sensitive detector provides information on the photoelectron emission point

- => How to get data to shore (and from shore to detector)?
  - needs integrated concept for sensor – frontend electronics – data transport – technology on shore
  - Promising approach using commercial optical solutions
  - Can we send analogue signals to shore?

=> How do we calibrate the detector?

- are current calibration tools adequate/scalable/reasonable?
- is it feasible/helpful to separate detection and calibration units?
- do we need a surface array? How to decide and design it?

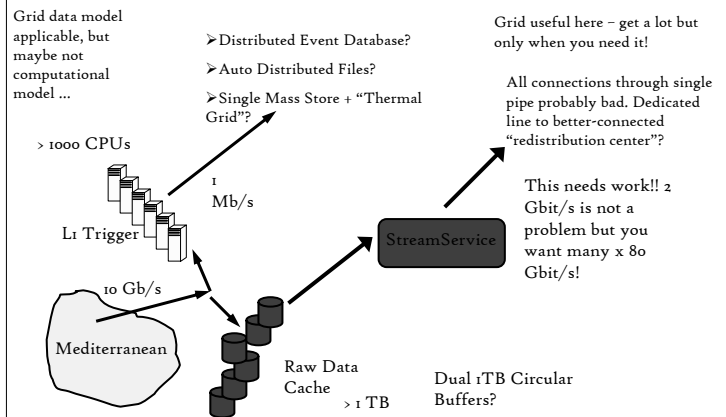
## Cooperation with Industry

- **ν telescopes do and will need industrial partners for various components**
  - cables and connectors
  - IT solutions for data transport
  - photo sensors
  - glass spheres
  - deep-sea technology, . . .
- **Many companies followed invitation to VLV<sub>v</sub>T workshop**
  - mutual interest !?
  - we must find / maintain suitable "interfaces" to describe needs and problems
  - we astroparticle physicists must not re-invent the wheel, even if we are capable of doing so !
- **Integration of SME's in Design Study is of strategic value and politically adequate**

## Cooperation with other Scientific Partners

- **ESONET (biology, oceanography, environment, . . . )**
  - there seems to be a lot of potential for synergetic cooperation
  - we'll have to understand how to combine our interests without compromising our scientific goals
- **GRID**
  - mutual interest in cooperation !?
  - may provide solutions for a data analysis and reconstruction

## VLV<sub>v</sub>T Reconstruction Model



## The Future

### Design Study:

Call expected by 11.11.2003

Brussels deadline for proposal: 4. March 2004

ApPEC will review astroparticle proposal for DS's and possibly issue recommendations / priority list (meeting in Munich, 25.11.2003)

Jos Engelen: "KM3 project fits very well into DS frame"

If successful: provides funding for R&D studies (3 – 4 years)

Result can / should / must be a **technical design report**

=> start construction of detector thereafter

## Site Decision

- decouple site decision from R&D work towards KM3
- for simulations, use "site" as "mathematical symbol" including
  - depth
  - distance to shore
  - water transparency
  - bioluminescence
  - sedimentation
  - . . .
- However, the final detector design needs the site decision => this sets the/a time scale !

**We NOW have the HISTORICAL chance to realize KM3**  
**No guarantee – but realistic possibility**  
**LET 'S GO FOR IT !**

- be open to all ideas and options
- solve open questions on scientific basis

**Thanks to all who contributed to the workshop**  
**and will carry on the efforts towards KM3 !**

- VLVvT Workshop was first in a series  
=> next location and date to be announced soon

**See you all there !**



# Design Parameters





# Overview over Mediterranean Optical Properties

G. Riccobene for the NEMO Collaboration

INFN-LNS, Via S. Sofia 44, I-95123 Catania, Italy  
riccobene@lns.infn.it

## Abstract

The detection of high energy astrophysical neutrinos is one of the major challenges of particle physics and astrophysics for the coming years. It is presently accepted that only a  $\text{km}^3$  scale detector could achieve such a goal and it is believed that an underwater Cherenkov detector located in deep seawater is an optimal solution. The installation of Cherenkov detectors in natural radiators, such as seawater, requires a deep knowledge of the properties of the medium in the deployment site. Due to possible changes of sea properties as a function of time, careful long-term measurements are needed in order to select and study the  $\text{km}^3$  installation site. These data are also mandatory to provide the right input parameters for Montecarlo and event reconstruction codes. For several years, the ANTARES, NEMO and NESTOR Collaborations have been measuring optical and oceanographic characteristics at their marine sites, natural candidates for the construction of the Mediterranean  $\text{km}^3$  neutrino telescope. Present data indicate that deep seawaters in the Ionian Plateau, have optical properties comparable to optically pure seawater and a low concentration of bioluminescent bacteria.

## I. STUDY OF MEDITERRANEAN DEEP SEA SITES

The Mediterranean Sea offers the most favourable conditions for the construction and maintenance of an underwater  $\text{km}^3$  Cherenkov neutrino detector in the Northern Hemisphere. The future Mediterranean neutrino telescope must be installed in a site, not too far from the coast, having the following characteristics: great depth (according to the present submarine technology limits) to minimise the atmospheric muon flux background; low presence of dissolved organic and inorganic particles, which worsen light transmission properties of seawater and increase the fouling on optical surfaces; low concentration of bioluminescent bacteria; low geoseismic activity and sea-current intensity.

Three Collaborations are presently working with the aim of building the Mediterranean  $\text{km}^3$  detector: ANTARES [1], NEMO [2] and NESTOR [3]. Each collaboration is working on a site that could be considered as candidate for the installation of the  $\text{km}^3$  detector.

The ANTARES site is located at 2400 m depth, 40 km SE offshore the city of Toulon (France). The collaboration has already deployed several underwater structures, equipped with instrumentation which permits an online monitoring of a number of site parameters.

The NESTOR site is located at 3800 m depth 20 km SW offshore the town of Methoni, close to the town of Pylos

(Greece). A bathymetric study of sea bottom in this site evidences, despite the presence of a quite steep escarpment with ravines and high raises access to the shore, the presence of a deployment region (at 3800 m depth) relatively uniform and smooth (aspect ratio 1%) over a size of 5 square nautical miles [4].

The site proposed by NEMO is located at 3400 m depth in the Ionian Plateau, 80 km SE of Capo Passero, the southernmost cape of Sicily (Italy). The seabed is flat for more than  $100 \text{ km}^2$  and the area is known to be oligotrophic, i.e. waters show a reduced biological activity [5].

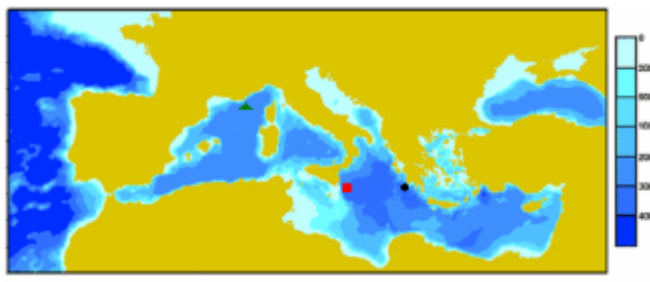


Figure 1: Locations of the sites of ANTARES (Toulon, green triangle), NEMO (Capo Passero, red square) and NESTOR (Pylos, black circle).

In the following we give a short review of the optical properties of water measured by the ANTARES, NEMO and NESTOR Collaborations in their three sites of operation.

## II. LIGHT TRANSMISSION PROPERTIES

In underwater Cherenkov neutrino telescopes seawater acts both as neutrino target and as radiator of Cherenkov photons produced by relativistic charged particles. The telescope detection volume, as well as the angular and energy resolutions, strongly depends on the water optical parameters.

In order to characterise the transparency of seawater, as a function of photon wavelength, it is necessary to measure the so called *inherent optical properties* (IOP): the absorption  $a(\lambda)$ , scattering  $b(\lambda)$  and attenuation  $c(\lambda)=a(\lambda)+b(\lambda)$  coefficients [6]. Roughly speaking, the absorption coefficient affects light signal amplitude and characterises the detector granularity and the detection volume, while scattering affects the direction of light propagation and the arrival time distribution of photons on optical modules, then the detector angular resolution.

IOP of water are strongly wavelength dependent. In particular absorption length reaches the maximum in the range  $350\div 550 \text{ nm}$ , overlapping the region in which PMTs have the highest quantum efficiency and Cherenkov emission is more

intense. Scattering, on the other hand, is higher at 300–450 nm wavelengths and may be parameterised by a sum of two contributions: Rayleigh (with a  $\lambda^{-4}$  spectral dependence and a forward-backward symmetry) on molecules and Mie (roughly with a  $\lambda^{-2}$  spectral dependence and a forward peaked angular distribution) on larger particles. Other parameters commonly used in literature are the effective scattering coefficient  $b^{eff}(\lambda) = b(\lambda) \cdot (1 - \langle \cos(\vartheta) \rangle)$ , where  $\langle \cos(\vartheta) \rangle$  is the average cosine of the scattering angle, and the effective attenuation coefficient  $c^{eff}(\lambda) = a(\lambda) + b^{eff}(\lambda)$ . The determination of these two parameters needs the knowledge of another IOP, the scattering angular distribution  $\beta(\lambda, \vartheta)$ , or volume scattering function.

Optical properties of natural seawater depend on water temperature, salinity and on the concentration, dimension and refraction index of particulate (dissolved and suspended, organic and inorganic). These parameters are different in different marine sites and are strongly function of depth and may change as a function of time. It is therefore extremely important to measure optical parameters *in situ* and to repeat measurements over a wide time window [7].

The NEMO Collaboration has measured light transmission properties in a number of Mediterranean deep sea sites using a set-up composed by a standard CTD probe and by a WETLabs AC9 transmissometer [8]. The main feature of the used apparatus is the possibility to measure, as a function of depth, profiles of several physical parameters of the water column: temperature, salinity, light attenuation and absorption coefficients over nine wavelengths (412, 440, 488, 510, 532, 555, 650, 676, 715 nm). The accuracy of the AC9 in the determination of  $a(\lambda)$  and  $c(\lambda)$  is about  $2 \times 10^{-3} \text{ m}^{-1}$  [9]. Hereafter we will quote, for each site, the values for absorption and attenuation coefficient, as the average values of  $a(\lambda)$  and  $c(\lambda)$  measured over an interval of 500 m,  $\sim 150$  m above the seabed. This is, indeed, the range of depths interesting for a  $\text{km}^3$  neutrino detector. Further details about the measurement procedure and data analysis can be found in reference [9].

NEMO has preliminarily investigated four deep sea sites ( $\sim 3500$  m) close to the Italian Coasts: two located in the Southern Tyrrhenian Sea, in proximity of the islands of Alicudi and Ustica [10], two in the Eastern Ionian Plateau, respectively  $\sim 50$  km and  $\sim 80$  km offshore Capo Passero. The values of  $a(\lambda)$  and  $c(\lambda)$  measured in the the region of Capo Passero are better than the ones measured in the other sites. In particular the values of  $a(\lambda)$  are close to the ones of optically pure seawater:  $67 \pm 13 \text{ m}$  at  $\lambda = 440 \text{ nm}$  [5]. The collaboration has then chosen the most offshore out of the two sites in the region of Capo Passero, in order to work in a stable and quiet environment, avoiding the known instabilities that may happen in marine regions close to shelf breaks or steep rises [5].

Following these results, NEMO started a long term study of the Capo Passero site looking for possible seasonal changes of oceanographic and optical properties. Figure 2 shows, as a function of depth, the values of water salinity and temperature together with the absorption and attenuation coefficient ( $\lambda = 440 \text{ nm}$ ) recorded with the AC9-CTD setup in five

campaigns conducted in December 1999 (2 deployments, red dots), March 2002 (4 deployments, green dots), May 2002 (2 deployments, yellow dots), August 2002 (2 deployments, orange dots) and July 2003 (2 deployments, light blue dots).

Seasonal variations are only appreciable in shallow waters, while, at depth  $> 2000 \text{ m}$ , the profiles of the water column properties are almost superimposed (within the instrumental error).

In order to compare the optical properties in Capo Passero site and Toulon, the ANTARES and NEMO Collaborations have conducted two joint campaigns in July (Toulon) and August (Capo Passero) 2002. The campaigns allowed to cross check data measured with the AC9 and with the Test-3' device, operated by the ANTARES Collaboration. Test-3' can determine light absorption and scattering lengths measuring and comparing, by means of a 1" PMT and a TDC, the amplitude and time distribution of photon bursts emitted by an isotropic light source ( $\lambda = 374.5 \text{ nm}$  and  $\lambda = 472.5 \text{ nm}$ ) at two distances of 24 m and 44 m [11].

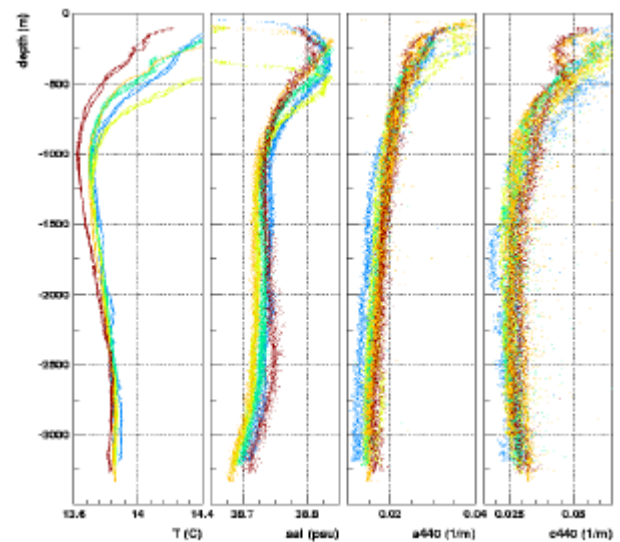


Figure 2: Profiles of temperature ( $T$ ), salinity ( $S$ ), absorption coefficient ( $a$ ) and attenuation coefficient ( $c$ ) and at 440 nm, measured in the Capo Passero site. The profiles refer to five different campaigns: December 1999 (red dots), March 2002 (green), May 2002 (yellow), August 2002 (orange) and August 2003 (light blue).

The result of these measurements is summarised in figure 3, where is shown, as a function of wavelength, the absorption length ( $L_a(\lambda) = a(\lambda)^{-1}$ ) measured in Toulon and in Capo Passero, using the AC9 and the Test-3'. In the same figure we also plot the values of  $L_a(\lambda)$  measured, in March 2002, near the NEMO Test Site (28 km East offshore the port of Catania, depth  $\sim 2050 \text{ m}$ ). The absorption length of optically pure seawater is indicated with a solid black line [12].

In figure 4 we report the attenuation lengths, measured with the AC9, during the same naval campaigns in Capo Passero, Toulon and Catania. These values, different from the ones expected for optically pure water, show the effect of dissolved scattering particles. It is worthwhile to mention that the measurement of the attenuation coefficient with the AC9

is made with a geometry having a finite angular acceptance in the forward direction (about 0.7 degrees). This may produce underestimation of the attenuation coefficient, especially in coastal waters where the contribution of the forward peaked Mie scattering is larger.

A lower value of the attenuation length,  $L_c(460\text{nm}) \sim 25$  m, is obtained by the NESTOR collaboration measuring, in laboratory, seawater samples collected at 3800 m depth at the Pylos site [13] (see figure 5). Differences with the Capo Passero and Toulon AC9 data may be probably attributed either to contamination of water samples, or to proximity to the shelf break, or to a narrower forward acceptance of the instrumentation used by NESTOR.

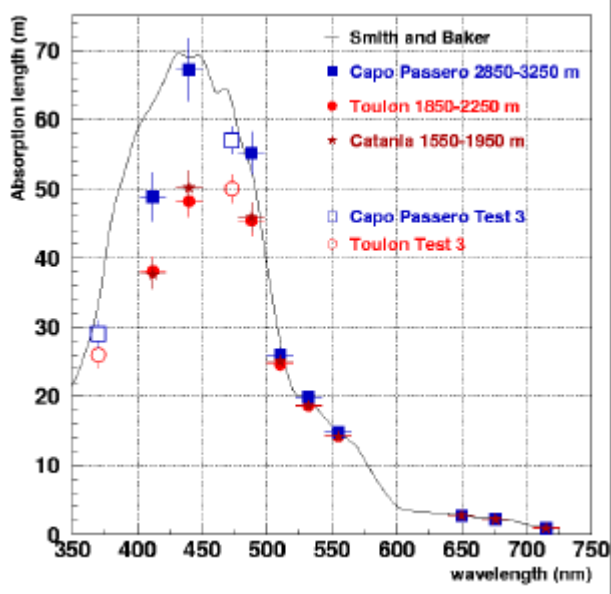


Figure 3: Light absorption lengths as a function of wavelength measured with the AC9 and with Test-3' during the joint NEMO-ANTARES campaigns in year 2002. Solid blue squares: Capo Passero (AC9 average, depth 2850÷3250 m). Solid red circles: Toulon (AC9 average, depth 1850÷2350 m). Open blue squares: Capo Passero (Test-3', ~ 3100 m depth). Open red circles: Toulon (Test-3', ~ 2200 m depth). Purple star: Catania Test Site (AC9 data, 1550÷1950 m). Black solid line: optically pure seawater absorption length [12].

The AC9 attenuation data cannot be directly compared to the measurements carried out in conditions of not collimated geometry published by NESTOR, which quote at Pylos site  $L_c^{eff}(460\text{nm}) = 55 \pm 10$  m [14], and ANTARES,  $L_c^{eff}(460\text{nm}) = 41 \pm 1 \pm 1$  m [11]. We already pointed out, indeed, that the estimation of  $c^{eff}$  requires the measurement of the average cosine of the volume scattering function distribution  $\beta(\lambda, \vartheta)$ . This function strongly depends on the amount, dimension and refraction index of the particulate in water and must be directly measured. In order to measure the volume scattering function the NEMO collaboration has designed and constructed a new device, DEWAS (Deep water Scattering-Meter), at present under test and calibration, able to measure  $\beta(\lambda, \vartheta)$  in the range  $0^\circ < \vartheta < 180^\circ$  and in the wavelength window  $430 < \lambda < 590$  nm [15].

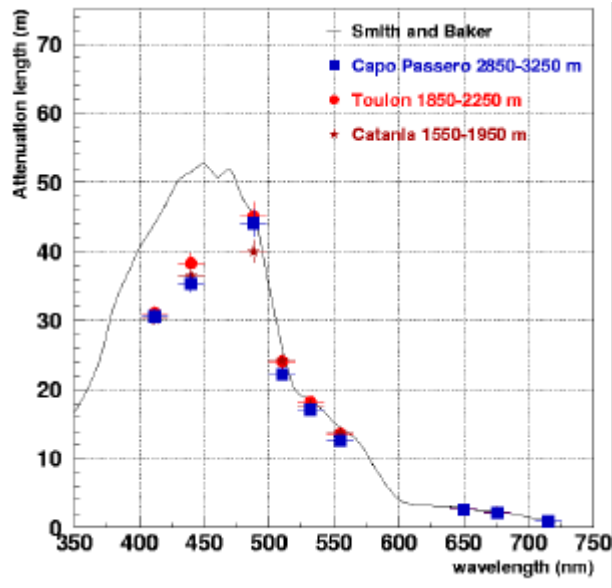


Figure 4: Light attenuation lengths as a function of wavelength measured with the AC9 during the joint NEMO-ANTARES campaigns in 2002. Solid blue squares: Capo Passero (AC9 average, depth 2850÷3250 m). Solid red circles: Toulon (AC9 average, depth 1850÷2350 m). Purple star: Catania Test Site (AC9 data, depth 1550÷1950 m). Black solid line: optically pure seawater attenuation length [12]

The ANTARES collaboration has also performed independently other measurements of absorption and scattering length in the Toulon site. Typical results for the absorption length in Toulon, measured at 470 nm, range between 45 and 65 meters, while the effective scattering length has been evaluated to be greater than 100 m [11].

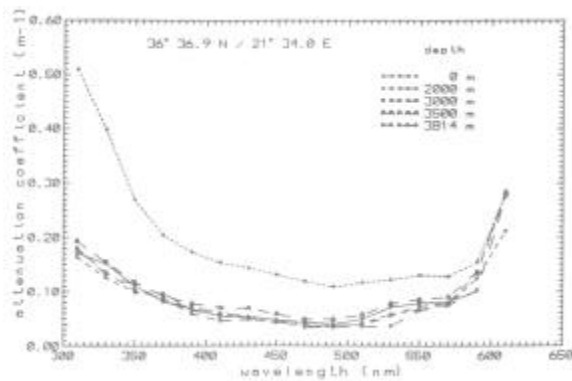


Figure 5: Attenuation coefficients as a function of wavelength measured by the NESTOR Collaboration at different depths in the Pylos site [13].

### III. OPTICAL BACKGROUND

Optical background in the sea comes mainly from two causes: the Cherenkov light produced by electrons originated by the  $^{40}\text{K}$  decay (the most abundant beta radioactive isotope dissolved in seawater) and the so called bioluminescence, i.e. light produced by biological organisms. The first effect shows up as a constant rate background noise on the optical modules, while the second one, when present, may increase the value of

the baseline rate and induce large fluctuations upon the baseline. The bioluminescence effect can therefore cause long DAQ dead time.

In the two joint campaigns of July and August 2002, NEMO and ANTARES have measured the optical noise in Capo Passero and Toulon. Two stand alone devices were used in both sites: the NEMO-<sup>40</sup>K apparatus, which consists of two 8" photomultipliers (EMI 9356KA) and their readout electronics, and the ANTARES Test-1, which is similar to the previous one, but uses two 10" PMTs (Hamamatsu R7081-20).

In the Capo Passero site at about 3000 m depth, the NEMO-<sup>40</sup>K device measured, for a deployment period of about 4 days, an average rate of  $28.5 \pm 2.5$  kHz at 0.35 s.p.e.threshold (figure 6, left). The optical background rate in Toulon is comparably higher: the NEMO-<sup>40</sup>K device has measured, in 4 days, an average rate of  $58 \pm 3$  kHz (figure 6, right) [5]. This result is compatible with the lowest values of optical background baseline rate measured with the ANTARES "prototypal sector line" discussed in the following (see figure 10).

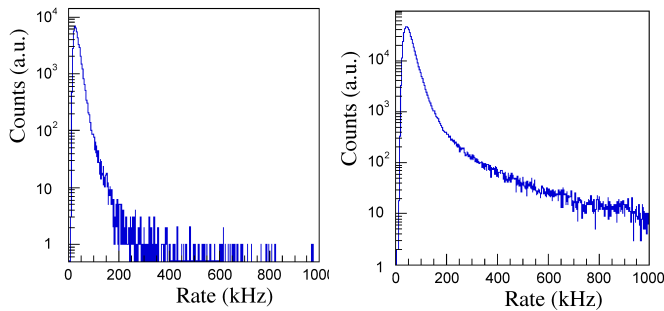


Figure 6: Distribution of the optical background rate measured with the NEMO-<sup>40</sup>K device in Capo Passero, August 2002 (left) and in Toulon, July 2002 (right).

The low level of bioluminescence measured in Capo Passero is also demonstrated by results of biological analyses: water samples recovered in this region are characterised by a low concentration of bioluminescent bacteria, whose amount is close to zero at depths greater than 2500 m [5], as shown in figure 7. Many other data in literature (see M. Solan, in these proceedings) confirm, indeed, that the Ionian Plateau waters are characterised by a much lower bioluminescent activity compared to other Mediterranean sites.

The Test-1 device was deployed for 2 days in Capo Passero (at ~ 3000m depth), where it measured a baseline rate of 15 kHz at 0.5 s.p.e. and a baseline rate of about 33 kHz at 0.35 s.p.e. thresholds. Few events of bioluminescence are measured per hour, as shown in figure 8. For comparison we show, in figure 9, a measurement of optical noise rate made with Test 3' in Toulon site (April 2001). The figure evidences the presence of several high rate spikes due to bioluminescence, over an average baseline rate much higher than the one measured in Capo Passero.

Test-1 was, then, deployed again in Capo Passero from March to July 2003. The present preliminary analysis confirms the data taken in August 2002: the optical

background rate baseline is low and constant and the burst fraction is negligible [16].

Optical background in Toulon site has been monitored for several months with an array of 15 optical modules equipped with 10" PMTs (the so called "prototypal sector line"). Reported data, representing a sample of 80 days, are shown in figure 10: the noise baseline strongly fluctuates, as a function of time, from a level of 50 kHz to a level of more than 250 kHz, with a strong contribution of bioluminescence bursts [19]. The correlation of these events with deep sea current intensity is under study.

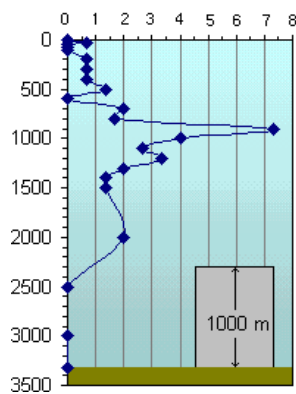


Figure 7: Profile of the concentration of bioluminescent bacteria (in  $\text{CFU ml}^{-1}$ ) as a function of depth, measured in Capo Passero.

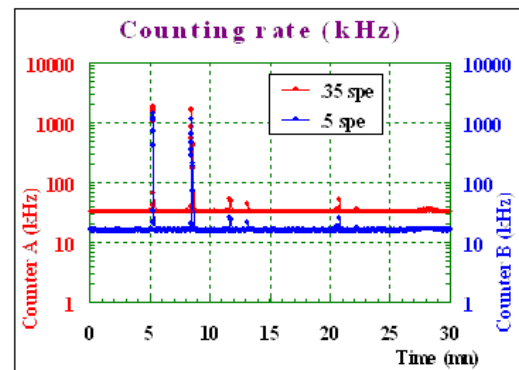


Figure 8: Optical noise rate as a function of time recorded in Capo Passero with Test-1 (August 2002). The upper set of data points (red) refers to PMT signal acquired at 0.35 s.p.e. threshold, the lower set refers to the same signal acquired at the threshold of 0.5 s.p.e. [16].

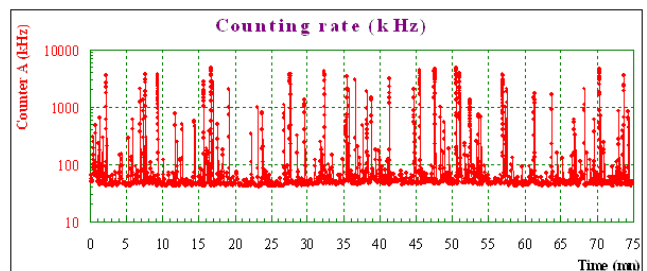


Figure 9: Optical noise rate as a function of time recorded in Toulon with Test-1 in April 2001 (threshold 0.5 s.p.e) [16].

The NESTOR Collaboration has recently estimated the optical noise at the Pylos site using the 12 PMTs deployed in March 2003. The contribution of bioluminescence to the triggered event sample has been evaluated to be about 1% of the experiment active time [3].

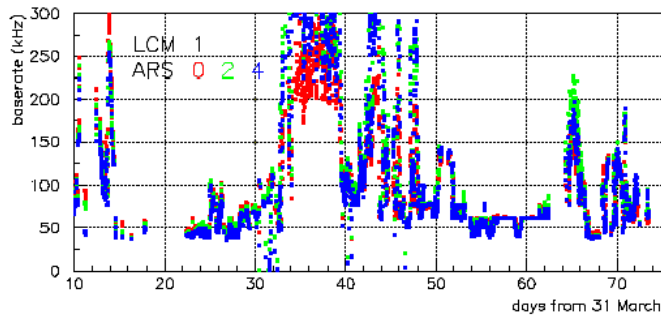


Figure 10: Optical noise rate baseline, as function of time, measured by one storey (three optical modules) of the ANTARES “prototypal sector line” deployed in Toulon [19].

#### IV. FOULING ON OPTICAL SURFACES

Another important parameter to characterise the site properties is the value of sedimentation and fouling on optical surfaces as a function of time. This phenomenon causes a degradation of the light transmission properties of the glass spheres that host the optical modules, setting a time limit to the performances of the optical modules underwater.

ANTARES has determined the long term effect of biofouling using an autonomous deep sea station that measures the transparency of the glass spheres as a function of time and of the zenith angle. In the Toulon site, despite a fairly large sediment accumulation rate, a slow growth of biofilm substrate has been measured, implying a loose adhesion of sediments to the glass surfaces. This deposit can be therefore “washed” by currents: data show an increase of transparency of the optical module after periods of more intense sea currents. Results demonstrate that fouling is only significant for surfaces facing upwards. At the optical module equator, the reduction of the transparency is less than 2% per year, as shown in figure 11. Therefore, for the downward oriented optical modules of the ANTARES detector, the reduction of transparency due to the fouling is expected to be small even after several years of operation [16,17,18].

This result is in agreement with the measured downward flux of sediments conducted by ANTARES collaboration in the Toulon site. The set of data covers the period July 1997-December 1997. The flux is typically less than  $100 \text{ mg m}^{-2} \text{ day}^{-1}$  in summer, increasing up to  $350 \text{ mg m}^{-2} \text{ day}^{-1}$  in autumn and winter, due to clays dragged by rivers [17,18].

In the framework of the joint NEMO-ANTARES site characterisation activity, the described biofouling underwater station is now moored in Capo Passero. The experiment is running since March 2003 and will be recovered during spring 2004. A short-term measurement (40 days) of biofouling effects has been carried out, using a similar device, by the NEMO Collaboration in January-February 2000. These few

data do not show transparency reduction even in the most upward direction (5 deg) [10]. The result is consistent with the recorded average value of the downward flux of sediments at 3000 m depth, which is about  $20 \text{ mg m}^{-2} \text{ day}^{-1}$  during winter. The peak value,  $160 \text{ mg m}^{-2} \text{ day}^{-1}$ , is usually recorded in spring, due to increase of surface biological activity. This low values are expected for the oligotrophic pelagic environment of the Ionian Plateau [10].

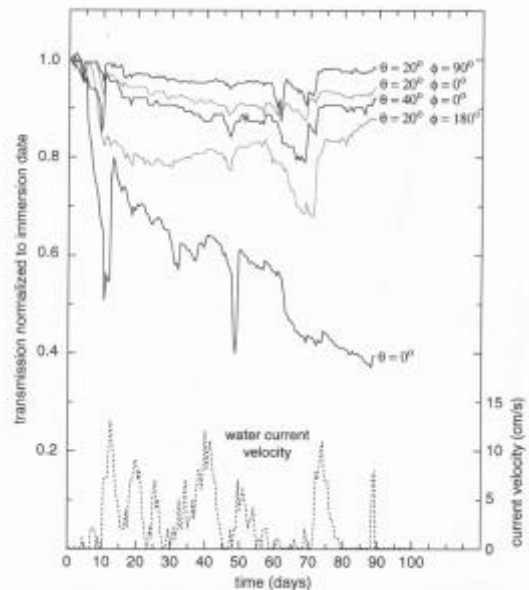


Figure 11: Light transmission as a function of deployment time, measured in Toulon site, with an autonomous station operated by the ANTARES Collaboration. Measurements are taken using 5 photodiodes glued in different position ( $\theta$  zenith angle,  $\phi$  azimuth angle) inside a benthic sphere. Measurement for each of the five photodiodes are normalised to unity at the device immersion date. The deep sea current velocity is indicated at the bottom of the figure [1].

#### V. CONCLUSIONS

A large number of measurements of water optical properties in the Mediterranean Sea have been carried out in the framework of the site selection activity for the construction of the future  $\text{km}^3$  neutrino telescope.

Data show that the light absorption length can reach, in some deep sea sites, values comparable to optically pure seawater. Since these characteristics are different from the ice ones (water shows much longer scattering length and a bit shorter absorption length compared to ice) a submarine  $\text{km}^3$  neutrino telescope should have complementary detection characteristics compared to the under-ice one: better angular resolution for the Mediterranean  $\text{km}^3$ , better energy resolution for the ICECUBE [19].

In particular optical, oceanographic and biological data indicate the Ionian Plateau as a stable and oligotrophic environment, optimal for the installation of the Mediterranean  $\text{km}^3$ .

It is important to mention that the properties of marine environments may change as a function of time, therefore they must be monitored for long time and cannot be extrapolated from short time series or single measurements. For this reason the NEMO and the ANTARES Collaboration have conducted a joint activity to monitor site properties for a long time and to cross check site parameter measurements in Toulon and Capo Passero. This activity, still going on, has provided the needed knowledge of site parameters over several years, allowing a direct comparison between the two sites.

The NEMO collaboration has also shown that, even if in principle, for sea operations, coastal sites may be preferable, the vicinity to shelf breaks and escarpment may induce seasonal or even unexpected variations in the site. This effect has been observed comparing the very good and stable properties measured in the Capo Passero site (3400 m depth, 40 km from the Maltese Escarpment) with the ones measured in a site, ~3000 m deep, closer to the Sicilian Coast and to the Maltese Escarpment (~10 km) [5].

## VI. REFERENCES

- [1] J. Carr, in these proceedings; see also ANTARES web page at <http://antares.in2p3.fr>.
- [2] E. Migneco, in these proceedings; see also NEMO web page at <http://nemoweb.lns.infn.it>.
- [3] S. Tsamarias, in these proceedings; see also NESTOR web page at <http://www.nestor.org.gr>
- [4] E.G. Anassontzis, Proceedings of the 3<sup>rd</sup> NESTOR Workshop, Pylos (1993), 614.
- [5] The NEMO Collaboration, *Study and characterization of a deep sea site for a km<sup>3</sup> underwater neutrino telescope*, report to ApPEC (2002), available at <http://nemoweb.lns.infn.it/sitereport>.
- [6] C.D. Mobley, *Light and Water*, Academic Press, San Diego (1994)
- [7] S.Q. Duntley, Journal of the Optical Society of America, 53 (1963) 214.
- [8] <http://www.wetlabs.com>
- [9] V. Balkanov et al., Nuclear Instruments and Methods, A-498 (2003) 231.
- [10] A. Capone et al., Nuclear Instruments and Methods, A-487 (2002), 423.
- [11] N. Palanque-Delabrouille, Proceedings of the XXVI ICRC, HE 6.3.20, 1999.
- [12] C. Smith and K. Baker, Applied Optics, 20 (1981), 1965
- [13] S.A. Kanaev and A.P. Kuleshov, Proceedings of the 2<sup>nd</sup> NESTOR Workshop, Pylos (1992), 253.
- [14] E.G. Anassontzis et al., Nuclear Instruments and Methods, A349 (1994), 242.
- [15] L. Pappalardo et al., Nuclear Physics B (Proc. Suppl.), 87 (2002), 525.
- [16] J.P. Schuller, internal communications to the ANTARES and NEMO Collaboration Meetings.
- [17] P. Amram et al., Astropart Physics, 19 (2003), 253.
- [18] P. Amram et al., Astropart Physics, 13 (2000), 127.
- [19] <http://icecube.wisc.edu>

# Comparison of OM Responses at Different Sites

Zh.-A. Dzhilkibaev<sup>1</sup>, A. Gazizov<sup>2</sup>, and Ch. Spiering<sup>2</sup>

<sup>1</sup>INR, 60th October Anniversary pr., 7a, 117319 Moscow, Russia

<sup>2</sup>DESY-Zeuthen, Platanenallee 6 - 15738 Zeuthen, Germany

## Abstract

We have simulated the response of optical modules in deep underwater and under-ice neutrino telescopes and study its dependence on the optical characteristics of the surrounding medium (coefficients of absorption and scattering, as well as light dispersion). Results are presented for the case of single muons passing an optical module at different distances.

## I. INTRODUCTION

In this paper, we will investigate the response of optical modules (OMs) of large neutrino telescopes to muon tracks. We will compare the response of OMs used in three experiments: the Lake Baikal neutrino telescope NT-200 [1] located at 1 km depth in the Siberian lake, the ANTARES telescope [2] being assembled at 2 km depth in the Mediterranean close to Toulon, and the AMANDA telescope which is deployed at a depth of 1.5 - 2 km in the Antarctic ice shield [3]. The response depends on the light propagation between muon track and OM, i.e. on absorption, scattering and light dispersion, from the parameters of the OM itself, its dimensions as well as its spectral and angular sensitivity, and from the orientation of the OM with respect to the muon track.

Results of our Monte Carlo simulations are given for single optical modules. In reality, OMs may be operated not as single OMs but in pairs (Lake Baikal) or even in triplets (ANTARES). Some of the conclusions which are obvious for an isolated OM have to be modified if OMs are operated in coincidence.

The results of this paper have been obtained by Monte Carlo simulations of the propagation of Čerenkov radiation in various media. The Monte Carlo code is the one exploited in the BAIKAL collaboration [4].

## II. CHARACTERISTICS OF MEDIA AND OPTICAL MODULES

### A. Čerenkov radiation, phase velocity and light dispersion

A muon moving in a refractive medium with a speed  $v$  higher than the speed of light in this medium emits Čerenkov radiation [5]. The vector of the photon velocity  $\mathbf{v}_c$  has an angle  $\theta_c$  with respect to the particle trajectory according to  $\cos(\theta_c) = 1/(\beta n)$  ( $n(\lambda)$  is the “phase” index of refraction of the medium,  $\beta = v/c$  is the velocity of a particle measured in units of the speed of light in vacuum), with  $|\mathbf{v}_c|$  being equal to the group velocity of light with wavelength  $\lambda$  propagating in the medium:

$$v_c = \frac{c}{n_g(\lambda)}, \quad n_g(\lambda) = n(\lambda) - \lambda \frac{dn}{d\lambda}. \quad (1)$$

The values of group and phase propagation velocities in transparent media differ by several percent ( $v_{ph} = c/n$ ). However,

as pointed out in [6], the use of the phase velocity in the analysis of underwater data causes an error in the light arrival time, which may be as high as 10 – 15 nsec at distances of 100 m between light source and OM.

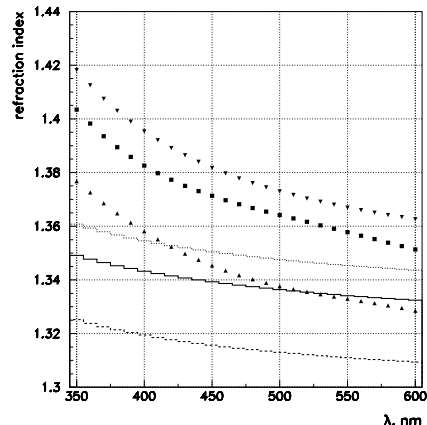


**Figure 1.**  $n(\lambda)$  (lines) and  $n_g(\lambda)$  (symbols) as a function of wavelength  $\lambda$ . From top to bottom: Mediterranean water, Baikal water, Antarctic ice.

The wavelength range of photons detected in underwater experiments typically lies between 350 nm and 600 nm. Fig. 1 shows the wavelength dependence of the coefficient of refraction for the sites of three neutrino telescopes, BAIKAL [6], AMANDA [7] and ANTARES [8]. The solid curve corresponds to Lake Baikal, the dashed curve to Antarctic ice and the dotted curve to the Mediterranean site. As mentioned above, the velocity of photon propagation is governed by the parameter  $n_g$ , formula (1). Fig. 1 also shows the parameter determining the light arrival times,  $n_g$ , as a function of wavelength (symbols).

### B. Optical properties of the medium

The main parameters determining the light propagation through transparent media are the coefficients of absorption,  $k(\lambda)$ , scattering,  $\sigma(\lambda)$ , and the scattering function  $\chi(\lambda, \cos \theta)$ .

Figs. 2-4 show the values of the optical parameters for BAIKAL [9], AMANDA [10] and ANTARES [11]. (Note that not the measured values itself but the tabulated values used in the simulations are given in the figures.)

### C. Characteristics of optical modules

Optical modules house photodetectors of the type QUASAR ( $d = 37$  cm) for BAIKAL [12], Hamamatsu R7081-20 ( $d = 20$  cm) for AMANDA [13] and Hamamatsu R5912-02 ( $d = 25$  cm) for ANTARES [14]. The spectral dependence of the OM sensitivities used in our calculations is given in Fig. 5. The angular dependence of the OM sensitivities normalized to their maximum value is presented in Fig. 6.

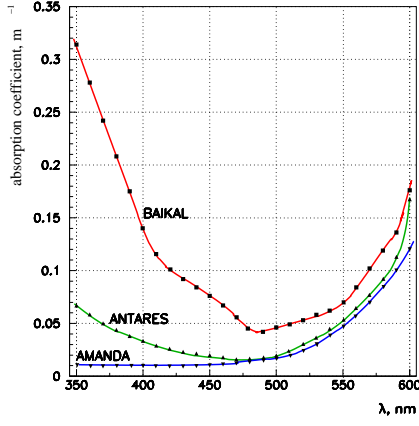


**Figure 2.** Spectral dependence of the absorption coefficient for Baikal water, Antarctic ice and Mediterranean water.

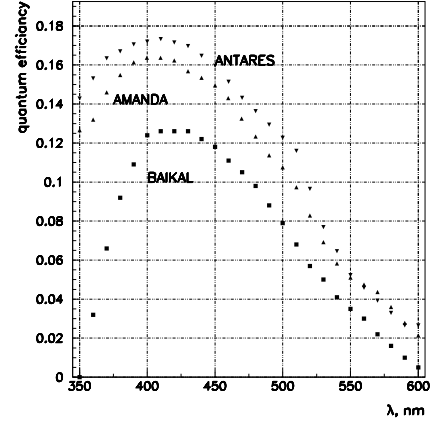


**Figure 5.** Spectral sensitivity of optical modules of experiments BAIKAL, AMANDA and ANTARES.

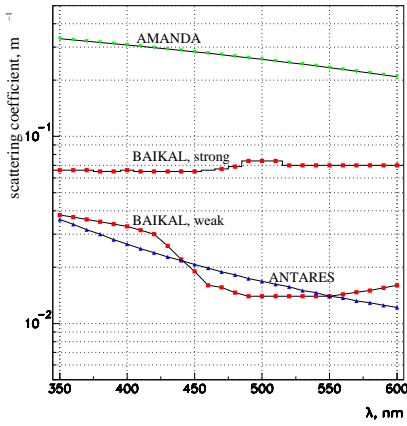


**Figure 3.** Spectral dependence of the scattering coefficient for Baikal water, Antarctic ice and Mediterranean water.

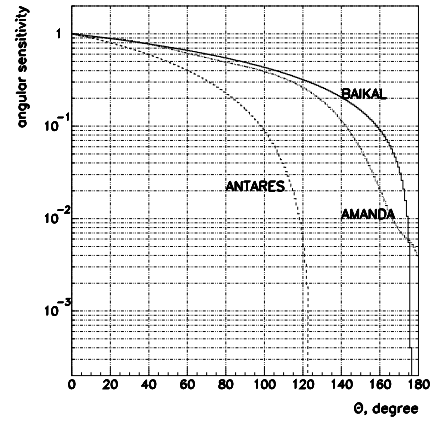


**Figure 6.** Angular sensitivity of optical modules of experiments BAIKAL, AMANDA and ANTARES.

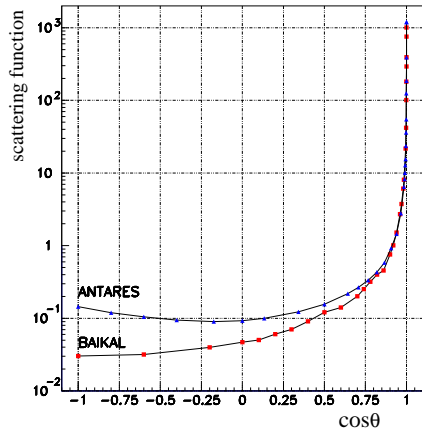


**Figure 4.** The scattering functions of Baikal and Mediterranean water.

#### D. Coordinate system

Fig. 7 defines the coordinate system used for the following simulations. A muon passes the optical module at a distance  $\rho$ . The vector  $\rho$  is normal to the muon track and points from the track to the OM. The OM points to direction  $\Omega_{om}(\theta', \varphi)$ . The polar angle  $\theta'$  is counted from axis  $z$  which is antiparallel to the muon direction, and angle  $\theta = \pi - \theta'$ . The azimuthal angle  $\varphi$

is the angle between vector  $\rho$  and the projection of vector  $\Omega_{om}$  to the normal to muon trajectory plane.

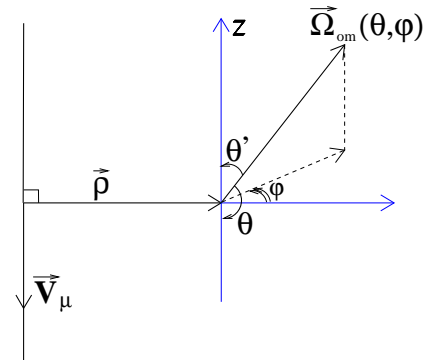


**Figure 7.** The coordinate system.

### III. COMPARISON OF DIFFERENT EXPERIMENTS

#### A. Average number of photoelectrons for the case of no scattering

The time distribution of the average number of photoelectrons in an OM in the case of no scattering is governed by



the spectral dependence of light velocity and absorption coefficient. In Fig. 2 it was shown that light absorption in Mediterranean water and in Antarctic ice is significantly weaker than in Baikal water. Moreover, the spectral dependence of the absorption coefficient of Baikal water has a pronounced minimum around 480 nm.

Fig. 8- 9 show the time distributions of photoelectrons due to Čerenkov radiation of the muon itself, for  $\rho = 10$  and 60 m. Solid, dashed and dotted curves correspond to Baikal water, Mediterranean water and Antarctic ice, respectively. The shapes of the time distribution depend on the width of the transmission window in the various media. Since only photons with wavelengths in the transmission window survive, and since this window is small in the case of Baikal water, the width of the time distribution for Baikal water is less influenced by dispersion and is narrower than in media with wider transmission windows.

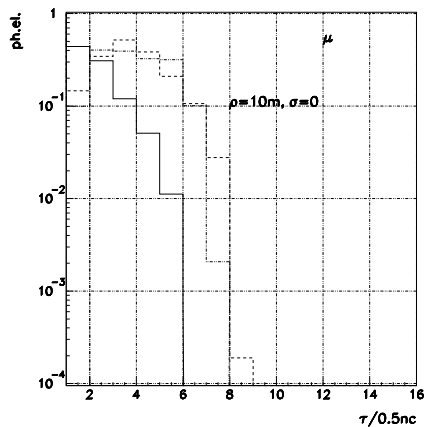


**Figure 8.** Time distributions of the OM response to muons in various media at  $\rho = 10$  m and without taking scattering into account. Solid, dashed and dotted curves correspond to Baikal water, Mediterranean water and Antarctic ice, respectively.

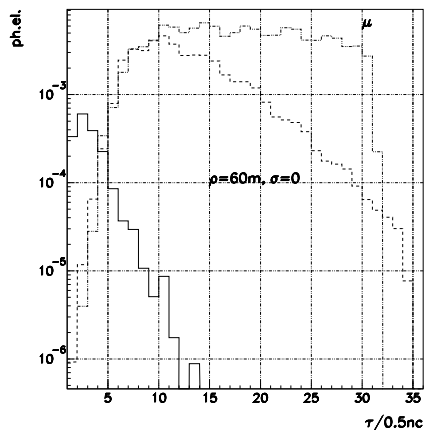


**Figure 9.** The same as Fig. 8, but for  $\rho = 60$  m.

In Fig. 10 the width (half maximum) of the time distribution is plotted as a function of  $\rho$  for the case of no scattering. Varying  $\rho$  from 10 m up to 60 m, the width for Baikal water increases from 1 nsec to 1.5 nsec, for Mediterranean water from 10

1.5 nsec to 5 nsec and for Antarctic ice from 2 nsec to 12.5 nsec.

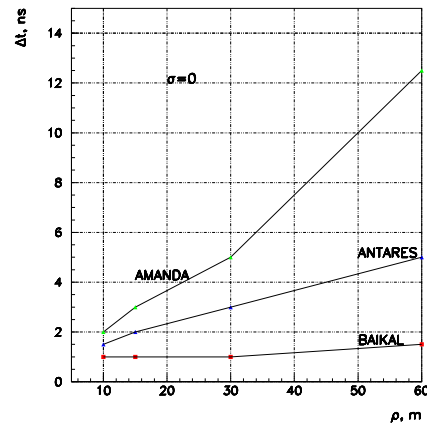


**Figure 10.** FWHM of the time distribution as a function of the distance  $\rho$  to the track for the case of no scattering.

Thus, due to the stronger absorption, the number of photons reaching the PMT is smaller in Lake Baikal when compared to Mediterranean water. On the other hand, the Baikal time distribution is narrower, due to the smaller transmission window and the resulting smaller dispersion. The stronger dispersion for Mediterranean water may influence the accuracy of track reconstruction and has to be taken into account in simulations. The dispersion is strongest for AMANDA, but the resulting delays are small compared to the delays due to scattering (see next section).

### B. Average number of photoelectrons including scattering

Fig. 11 shows the distributions of the average number of photoelectrons in an OM at  $\rho = 10$  m as a function of the OM polar angle  $\theta'$  for two fixed values  $\varphi = 0$  and  $\varphi = \pi$ .

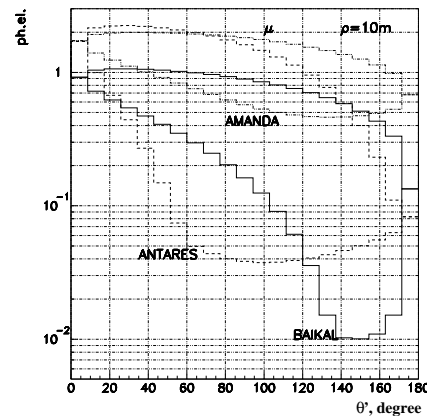


**Figure 11.** Number of photoelectrons as a function of the OM polar angle  $\theta'$ .

The figure demonstrates that for an OM turned away from the muon track and for the experiments AMANDA and ANTARES, the OM response is practically completely dominated by scattered photons. In case of ANTARES, due to the specific angular

sensitivity of the OM (see Fig. 6), scattered photons dominate about 25 % of the total solid angle  $4\pi$ .

The time distributions of the OM response in the 3 media are given in Figs. 12-14. Distances are  $\rho = 10$  m, 25 m and 60 m for Figs. 12, 13 and 14, respectively. Results are shown for the OM oriented opposite ( $\cos\theta = -1$ ) and parallel ( $\cos\theta = 1$ ) to the muon velocity vector. Scattering as well as spectral dependence of the light group velocity are taken into account. The time distributions of Baikal water correspond to the weak scattering case (curve “BAIKAL, weak” in Fig. 3).

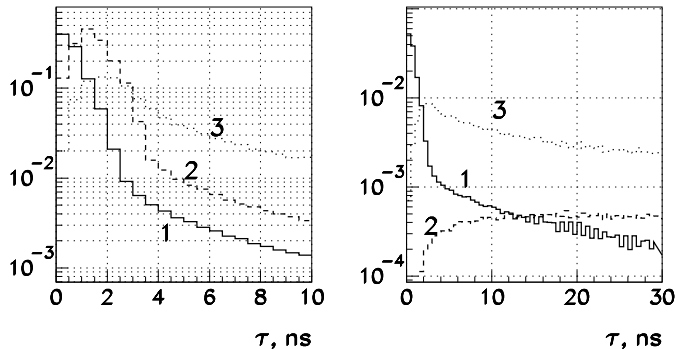


**Figure 12.** Time distribution of the OM response for  $\rho = 10$  m;  $\cos\theta = -1$  (left),  $\cos\theta = 1$  (right). Curves 1, 2 and 3 correspond to Baikal water, Mediterranean water and to Antarctic ice, respectively.

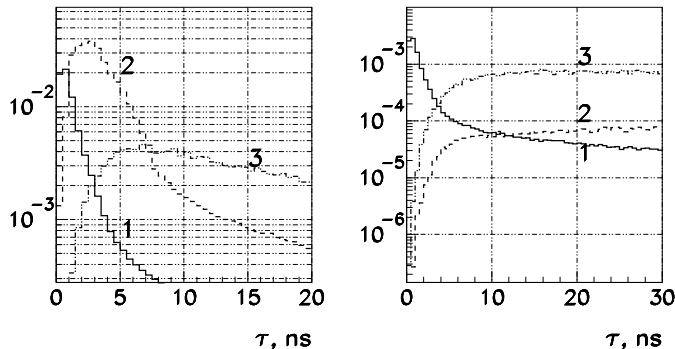


**Figure 13.** The same as in Fig. 12, but for  $\rho = 25$  m.

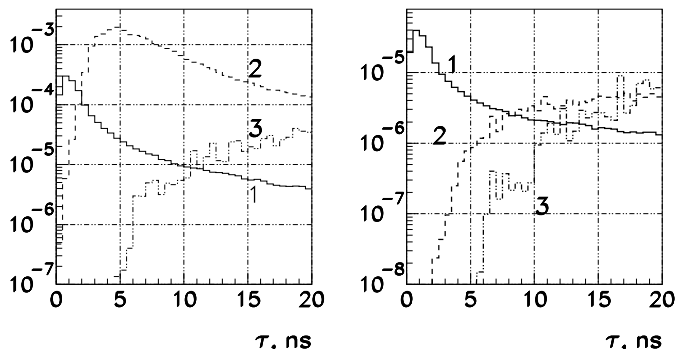


**Figure 14.** The same as in Fig. 12, but for  $\rho = 60$  m.

Scattering has a small effect on the width of the time distribution in Baikal water. At distances up to 60 m from the muon trajectory the time distributions have a pronounced peak, which is formed by direct photons.

In Antarctic ice, for small distances from the muon track ( $\rho = 10$  m), scattering causes a widening of the time distribution and shifts its maximum to higher time delays. With increasing distance to the track, the contribution of scattered photons starts to govern the time distribution. The time distribution becomes essentially wider, while the spectral dependence of the light velocity results in an additional shift towards larger delays.

In the case of Mediterranean water and OM orientation antiparallel to the muon trajectory, the width of the distribution is mainly defined by the spectral dependence both of the light velocity and of the absorption coefficient. Scattering causes an additional widening of the distribution at large distances from the muon trajectory. For orientation  $\cos\theta = 1$ , the OM does not detect the direct radiation from the muon, and the response is completely determined by scattered photons. The influence of the spectral dependence of the light velocity results in a systematic shift towards larger delays.

Figs. 15-16 give, as a function of distance, the average number of photoelectrons integrated over time. The dependence is shown for two OM orientations ( $\cos\theta = -1$  and  $\cos\theta = 1$ ). The solid curves correspond to the case when scattering is taken into account, dashed curves describe the case of no scattering. Curves 1, 2 and 3 correspond to Baikal water, Mediterranean water and Antarctic ice, respectively.

For  $\cos\theta = -1$ , as a consequence of weak light absorption, distributions in ice and Mediterranean water at  $\rho > 10$  m lie significantly higher than in Baikal water. The influence of scattering on the decrease of the light intensity with distance is negligible for Baikal water, small for Mediterranean water and large for Antarctic ice (about a factor 2 at 60 m).

For  $\cos\theta = 1$ , scattering in Baikal water is still negligible. In ice, on the contrary, scattering completely determines the value of the spatial distribution. In the case of Mediterranean water, the spatial distribution of photoelectrons is governed by scattered photons, but this occurs due to the angular dependence of the OM sensitivity in ANTARES.

#### IV. SUMMARY

We have analyzed the influence of the optical parameters of water or ice on the response of single optical modules in neutrino telescopes to muons. We have illustrated how the measured arrival times and amplitudes of a Cerenkov light signal behave for parameter values typical for three sites of such telescopes: Amanda, Antares and Lake Baikal. This study is not intended to compete with the simulation of groups of optical modules in a full detector, which often are switched in local coincidences of pairs (like Baikal) or triplets (like Antares). In such coincidences the first responding OM defines the time. This results in a higher probability of the channel to be triggered by direct photons as compared with the analogous probability for a single OM. The study should, however, complement the full simulation in the sense that it gives a qualitative under-

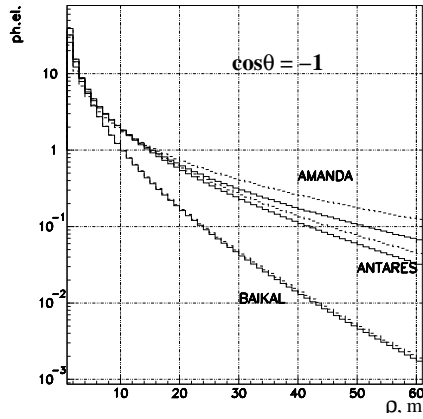


**Figure 15.** Number of photoelectrons as a function of distance to the muon for  $\cos\theta = -1$ . Dotted curves correspond to the case of no scattering.

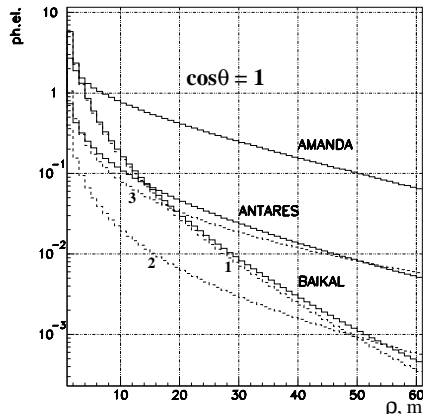


**Figure 16.** Number of photoelectrons as a function of distance to the muon for  $\cos\theta = 1$ . Dotted curves 1, 2 and 3 correspond to Baikal water, Mediterranean water and Antarctic ice, respectively. Curves are given for the case of no scattering.

standing of some basic dependencies behind the response of a full detector.

We have shown that there are orientations of OMs for which the recorded signal would be entirely due to secondary processes like  $\delta$  electrons (or showers due to pair production or bremsstrahlung) if not light scattering would give also photons from the muon itself a chance to reach the sensitive area of the OM. For an OM in Lake Baikal this region covers about 4% of the total solid angle, in the case of Antares even 25%. Also, the distribution of the arrival times for photons from the muon itself and from secondary processes differ considerably. Since light from showers along high energy muon tracks behaves similar in many respects to that from showers [14], the results shown can give a guidance when optimizing an array to either low or high energy events. In low energy events most light is produced by the muon itself, and OM orientation and light dispersion can modify the arrival time and amplitude response much stronger than in the case of high energy events.

The effect of light dispersion is negligible in the strongly scattering Antarctic ice but has to be taken into account in wa-

ter. The strength of the effect depends on the window of transmission. The larger this window, the more photons are collected, but also the stronger the arrival time distribution is widened by light dispersion. In Baikal water with a narrow transmission window, the widening of the time distribution due to dispersion does not exceed 1.5-2 nsec. In Mediterranean water, with its much wider transmission window, the time smearing may become as large as 3-5 nsec, the latter being larger than the PMT timing accuracy.

## V. REFERENCES

- I.A. Belolaptikov *et al.*, *Astropart. Phys.*, Vol. 7 (1997) 263-282.  
P. Amram *et al.*, *Astropart. Phys.*, Vol. 13 (2000) 127-136.  
E. Andres *et al.*, *Astropart. Phys.*, Vol. 13 (2000) 1-20.  
E.V. Bugaev, M.D. Galperin, Zh.-A.M. Dzhlkibaev, E.A. Osipova, Preprint INR AS USSR P-0508, Moscow 1987.  
I.E. Tamm, I.M. Frank, *J. Phys. USSR*, Vol. 1, No. 5-6 (1939) 439.  
L.A. Kuzmichev, *NIM*, Vol. A482 (2002) 304-306.  
P.B. Price, K. Woschnagg, *Astropart. Phys.*, Vol. 15 (2001) 97-100; hep-ex/008001, 2000.  
J. Brunner, Internal Antares report ANTARES-site/2000-01 (2000).  
B. Tarashansky. Ph.D. thesis. M: INR RAS (1999) (in Russian).  
V. Balkanov *et al.*, *NIM*, Vol. 498 (2003) 231-239.  
K. Woschnagg *et al.*, 26th Int. Cosmic Ray Conf., Salt Lake City, USA, Vol. 2 (1999) 200-203.  
D.J.L. Bailey, Antares Internal Report ANTARES-site/2000-05 (2001).  
R. Bagdjev *et al.*, *NIM*, Vol. A420 (1999) 138-154.  
Ch. Wiebusch, Internal Amanda Memo (1996).  
P. Amram *et al.*, *NIM*, Vol. A484 (2002) 369-383.  
A. Capone *et al.*, Proc. of the 26th Int. Cosmic Ray Conf., Salt Lake City, USA, HE 6.3.05 (1999).  
Zh. Dzhlkibaev and B. Shaibonov, "Influence of Optical Parameters on the High Energy Cascades Response of Optical Modules in Deep Underwater Experiments" Preprint INR-1073/2002, Moscow (2002).

# Comparison of different KM3 designs using Antares tools

D. Zaborov

Institute for Theoretical and Experimental Physics, Moscow, Russia  
zaborov@itep.ru

## Abstract

Various layouts of Cherenkov neutrino telescopes of cubic kilometer scale are considered. The preliminary results of full Monte-Carlo simulation of the detector geometries are presented. Detector efficiency and angular resolution have been calculated. The efficiency of presently available neutrino reconstruction methods is analyzed.

## I. INTRODUCTION

Great interest in the field of high energy neutrino experiments has already led to the foundation of three collaborations intending to build large-scale water Cherenkov detectors: ANTARES[1], NESTOR[2] and NEMO[3]. Flux estimates for various astrophysical sources (e.g. neutrinos from AGNs) require an instrumented volume of  $1 \text{ km}^3$  or larger (KM3). The development of such a unique experimental setup requires extensive Monte-Carlo studies.

The aim of the simulation presented here is to estimate the possible performance of a  $\text{km}^3$ -scale water Cherenkov detector and to test the reconstruction technique using simulated events. In principal the simulation allows a comparison of different detector designs. However, clearly a KM3 project will require development of special reconstruction software. Therefore the obtained results should be considered as a first iteration of the studies.

The described simulation starts from muon generation. Starting simulation from neutrinos would allow calculating an effective area for neutrinos directly. However, a consideration of the efficiency for muons is convenient to compare the effective area with the geometrical area and therefore to understand better a reconstruction efficiency.

## II. DETECTOR GEOMETRIES

Three different designs of a KM3 detector are characterized with various degrees of homogeneity.

1) A homogeneous cubic lattice of 8000 optical modules spaced with a step of 60 meters (see figure 1). Each optical module contains a 10-inch photomultiplier tube directed exactly downwards. Clearly this geometry is not quite optimal to be built. However, a simulation of this simplest geometry helps to understand the potential abilities of the technique.

2) A detector consisting of 25 towers located as a  $5 \times 5$  matrix with a step of 250 meters (see figure 2). Each tower can be

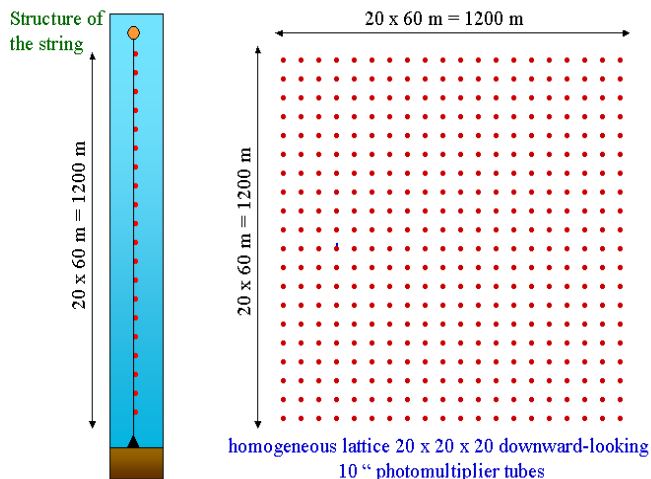


Figure 1: schematic view of the homogeneous detector (8000 PMTs)

considered as a set of 7 strings located at the center and at the corners of a hexagon with a side of 40 meters. Optical modules are located on 50 stories spaced with a step of 20 meters. The detector consists of 8750 downward-looking 10"-PMTs in total. Further on this geometry is called NESTOR-like.

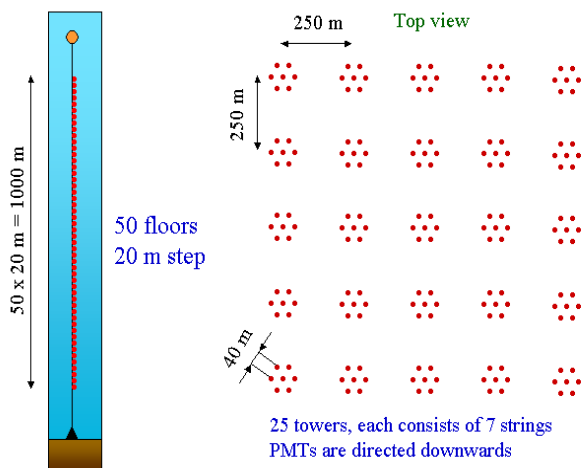


Figure 2: the layout of the NESTOR-like detector (8750 PMTs)

3) A geometry proposed by the NEMO collaboration (figure 3). The detector consists of 64 towers located as a matrix  $8 \times 8$  with a step of 200 meters. Each tower carries 64 optical modules located on 16 arms. We consider the so-called

NEMO up-down geometry, i.e. one half of the optical modules are downward-looking and the others are upward-looking. From one hand such a layout allows to observe all the sky at the same time. From the other hand a down-down geometry would have larger sensitivity to upward going "low energy" muons and thus should allow to expand the energy range. For general reasons the performance of both the up-down and the down-down geometries for horizontally-propagating muons should be the same. Upward-directed PMTs allow to reconstruct downward-going muons from direct Cherenkov light and, thus, to reduce the background of misreconstructed atmospheric muons. Since atmospheric muon background becomes less and less important with increasing energy, a reconstruction of downward-going high-energy neutrinos with high angular resolution becomes possible due to using of direct Cherenkov light. Note that this geometry has twice a smaller number of optical modules.

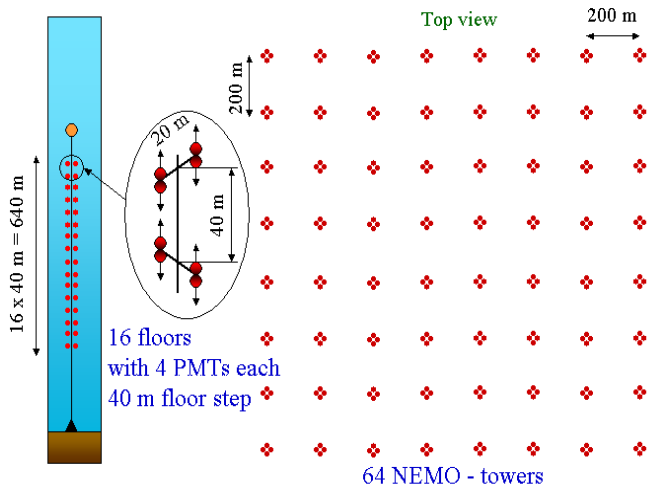


Figure 3: the layout of the NEMO-like detector (4096 PMTs)

### III. SIMULATION PROCEDURE

The major features of the simulation are the following:

- Track starting points are randomly distributed on the surface of the "can" volume defined as a cylinder surrounding the detector at several attenuation lengths distance.
- Muon track direction is isotropically distributed in  $4\pi$  sr.
- Muon energy is distributed within the energy range from 1 TeV to 1000 TeV with an  $E^{-1}$  flux. Note that at energies above 1 TeV most of the detectable neutrino interactions happens outside of the instrumented detector volume due to the long muon range. Thus most of the neutrino events look like muons coming from outside.

Cherenkov light emission and propagation are simulated assuming the characteristics of sea water at the ANTARES site [4]. The characteristics of the photomultiplier tubes correspond to Hamamatsu R7081\_20 [5]. Random K-40 noise is simulated and supposed to be 60 kHz which corresponds to the

ANTARES site [6]. Then electronics responses are simulated and the reconstruction procedure is applied.

The reconstruction procedure consists of the following steps:

- 1) Finding high amplitude hits (higher than 2.5 photoelectrons).
- 2) Causality filter based on time-distance relations between hits.
- 3) Track prefit using high amplitude hits or coincidences (3 independent hits are needed).
- 4) Background filter based on the prefitted track parameters.
- 5) Sequence of fit procedures (minimization of PDF using all available hits).

Finally quality cuts are applied and the effective area and the angular resolution are calculated. All the stages of simulation and reconstruction have been performed using currently available software developed for the ANTARES project.

### IV. DETECTOR PERFORMANCE

The dependence of the effective area for incoming muons on initial muon energy is shown on figure 4. Calculated values with statistical errors are shown. The solid curves are drawn to guide the eyes. As one can see the effective area of the homogeneous detector for upward-going muons is already comparable with its geometrical area at 5 TeV and increases with increasing energy. However, the efficiency decreases with decreasing muon zenith angle and the effective energy threshold moves to higher energies.

Figure 5 shows the angular resolution obtained within three energy subranges (1-10, 10-100, 100-1000 TeV). The calculations are performed separately for each of four subranges of zenith angle. Angular resolution has been calculated as the median value of the angular error distribution. The distribution in case of the homogeneous detector is shown on figure 6. Though statistical errors of the angular resolution are rather high below 10 TeV the plots give a general idea of the angular accuracy. In case of the homogeneous detector the best-obtained angular resolution is about 0.06 degree above 100 TeV.

As it can be seen the homogeneous detector is also able to detect downward-going muons. This fact should be explained as reconstruction using light which has been scattered on large angles. Degradation of the angular accuracy obtained with such events proves this assumption.

As seen from figure 4 at high energy the maximal efficiency for NESTOR-like detector is smaller than that for the homogeneous detector.

The NEMO-like detector is characterized by higher effective energy threshold due to its lower PMT density. In principle, a concentration of the optical modules within the towers should allow to increase the performance at low energy. Especially if the muon range becomes comparable with the characteristic size of the dense detector structures (towers). However, this also leads to a significant loss of detector efficiency

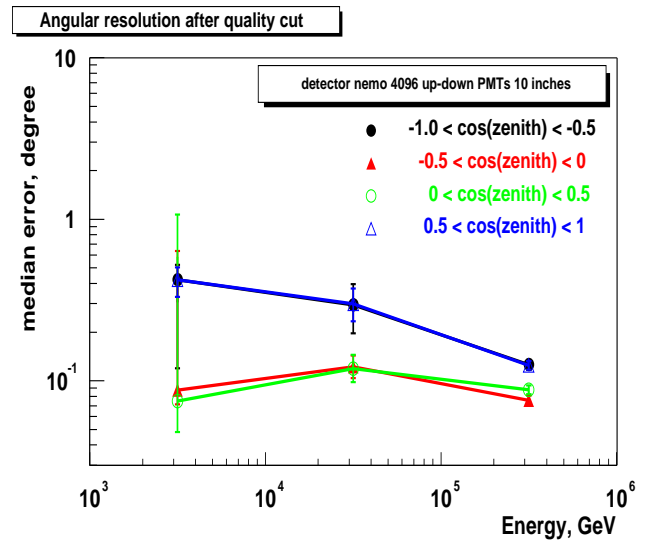
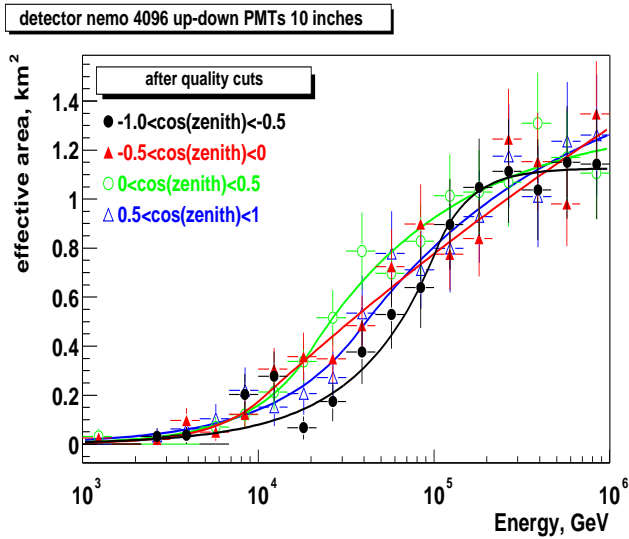
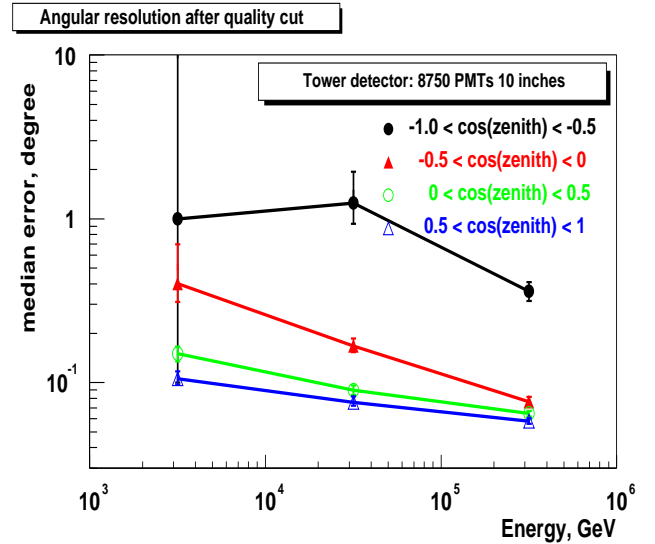
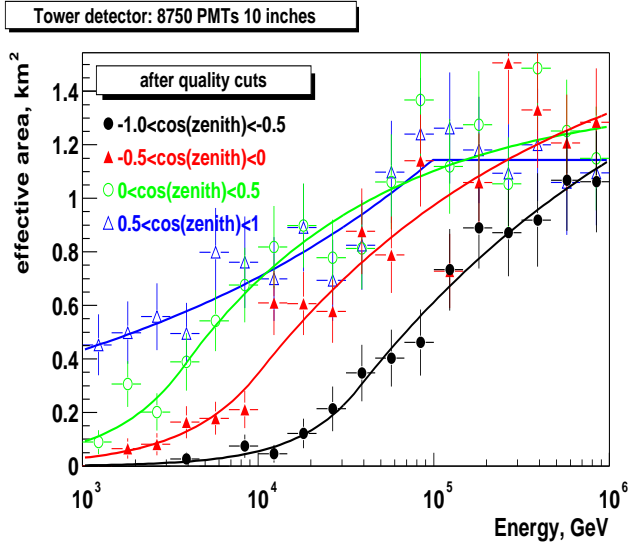
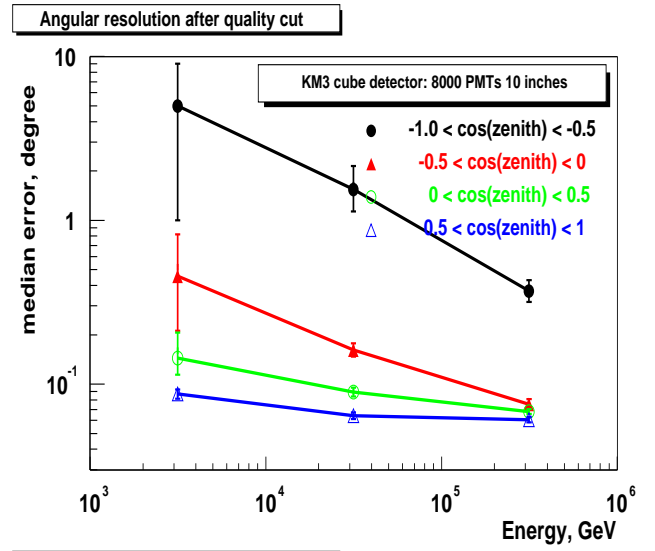
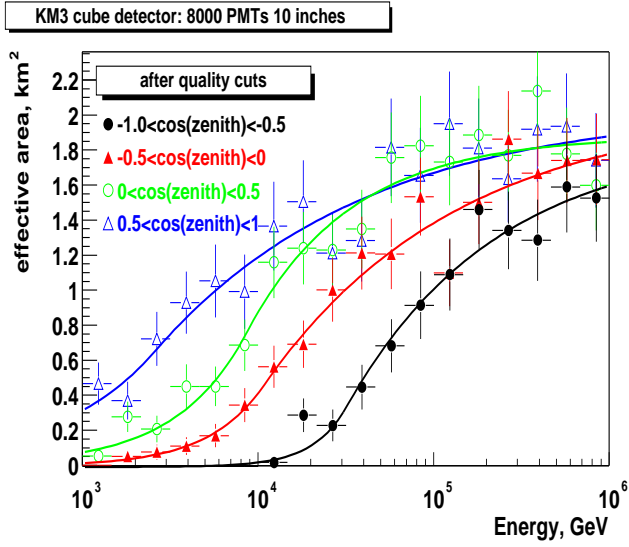


Figure 4: The dependence of effective area for muons on energy calculated separately in 4 subranges of zenith angle.  $\cos(\text{zenith})=1$  corresponds to upward-going muons. From top to bottom: the homogeneous detector, NESTOR-like detector, NEMO-like detector.

Figure 5: The dependence of angular resolution of muon track reconstruction on energy obtained in 4 subranges of zenith angle. From top to bottom: the homogeneous detector, NESTOR-like detector, NEMO-like detector.

in the "holes" of the detector layout if the step between the towers becomes too large with respect to the light absorption length ( $\approx 60$  m at ANTARES site). Lowering the reconstruction threshold (if possible) may allow to obtain better efficiency below 1 TeV and to make use of advantages of non-homogeneous geometry which are not visible in this study.

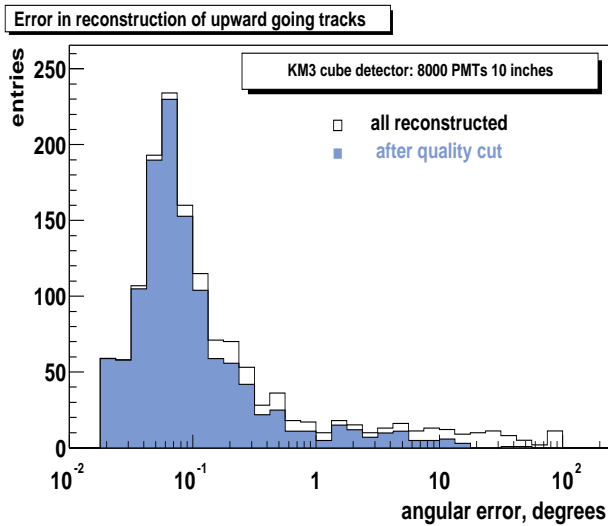


Figure 6: Angular error in muon track reconstruction. The distributions are integrated over the whole energy range (1..1000 TeV) and over the upper hemisphere of zenith angle ( $0.. \pi/2$ ).

## V. DISCUSSION

The muon track reconstruction requires sufficient amount of signal hits. The absolute minimal number of signal hits needed to reconstruct the main track parameters is 5 (x,y,z at fixed time, zenith and polar angles). The scatter plots of the number of "detected" hits versus muon energy is shown on figure 7. The observed location of the events on the plot can be explained in a following way: Muons penetrating the whole detector body under suitable zenith angle form the main group of events represented by a rather wide band. The points spread below the main band correspond to muons going through corners of the cube and to downward directed tracks. The events forming the band are scattered due to statistical fluctuations. In the case of a non-homogeneous detector the main group of events is expected to be stronger scattered due to non-homogeneous distribution of optical modules in the detector volume.

If the K-40 background is turned off then all the available hits can be used to perform the prefit (i.e. no amplitude cut needed). The effective area dependence obtained with the homogeneous detector in that case is shown on figure 8. However K-40 background light and Cherenkov light rescattering complicates the reconstruction and, as a consequence, increases the energy threshold. For example, the number of hits in the whole detector within a  $3 \mu s$  time window (time needed to traverse 1 km distance with speed of light) is about 1500. In fact, the re-

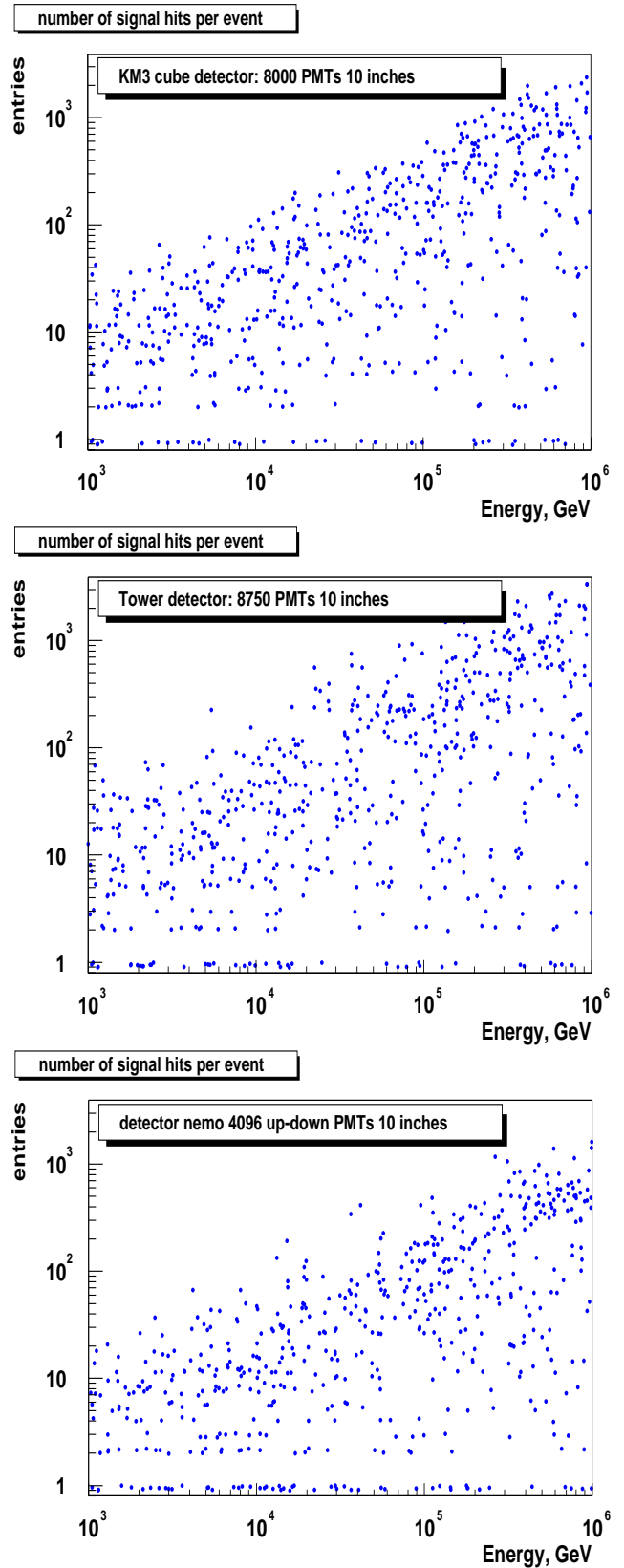


Figure 7: Scatter plot of number of signal hits versus incoming muon energy. The whole range of muon zenith angle is included. From top to bottom: the homogeneous detector, the NESTOR-like detector, the NEMO-like detector.

construction procedure should find and reconstruct the track using a mixture of signal hits among a considerably larger number of background hits. One can see on figure 4 that the effective area of the homogeneous detector reaches one half of its geometrical area ( $\approx 1.5 \text{ km}^2$ ) at approximately 3 TeV. Using figure 7 one can estimate a typical number of hits produced by 3 TeV muon in the homogeneous detector is ranging from 10 to 20. This number can be considered as the effective threshold of successful reconstruction. Such a threshold seems to be high comparing with the absolutely minimum hit number (5 hits). It is likely that the detector efficiency is limited by the prefit procedure. Further investigations of the software limitations are required.

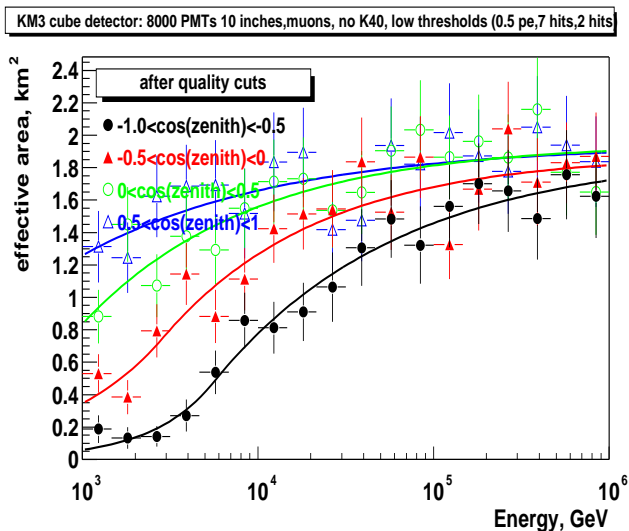


Figure 8: The effective area of the homogeneous detector obtained with low reconstruction thresholds and no K-40 background.

As an option a homogeneous detector identical to that shown on figure 1 except larger PMT size can be considered. As seen from figure 9 the detector consisting of 15-inch PMTs demonstrates approximately twice lower energy threshold comparing with its 10-inch version.

The following formula can be used to perform a cross-check of angular resolution.  $\Delta\psi = 2 \cdot c \cdot TTS/l$ . where  $c$  - speed of light; TTS - transit time spread of the PMT;  $l$  - characteristic baseline. In our case  $l \approx 1 \text{ km}$  because the detector size is smaller than range of 1 TeV muon. Thus,  $\Delta\psi = 0.05 \text{ degree}$ . This simple formula reflects an expected accuracy of localization of two visible track “endings” using hit times measured with a known error.

## VI. CONCLUSION

Monte-Carlo simulations of three different KM3 detectors have been performed using Antares tools. The homogeneous geometry demonstrates high detector efficiency starting from 1 TeV. The NESTOR-like geometry shows similar performance, however the maximally reached effective area is smaller than the

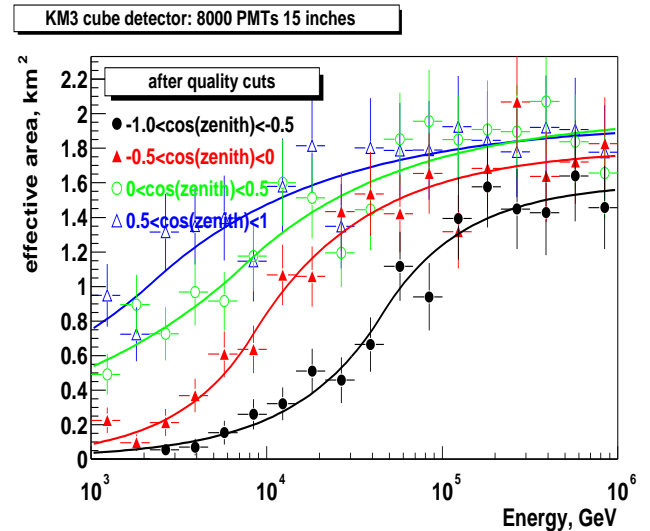


Figure 9: The effective area of the homogeneous detector consisting of 8000 downward-directed 15-inch PMTs.

one obtained with the homogeneous configuration.

The NEMO-like detector has a significantly smaller effective area than the homogeneous detector mainly due to its lower PMT density. A large distance between the towers and not completely understood limitations of the used reconstruction algorithms might be responsible for a relatively high energy threshold. All the geometries show an angular resolution of muon track reconstruction of about 0.1 degree or better.

The reconstruction software is a crucial part of a neutrino telescope project. Further investigations should be made to optimize muon and neutrino reconstruction algorithms.

## REFERENCES

- [1] ANTARES Collaboration, A deep sea telescope for high energy neutrinos, astro-ph/9907432 and <http://antares.in2p3.fr>.
- [2] Neutrino Extended Submarine Telescope with Oceanographic Research, Status Report, HENA Workshop, 2003 and <http://www.nestor.org.gr>.
- [3] C. De Marzo for the NEMO collaboration, Feasibility Studies for a Mediterranean Neutrino Observatory - The NEMO.RD project, Nucl. Phys Proc. Supp. 87, 433 (2000) and <http://nemoweb.lns.infn.it>.
- [4] Antares collaboration, Transmission of light in deep sea water at the site of the ANTARES neutrino telescope, in preparation.
- [5] P.Amram et al., The ANTARES optical module, Nucl. Instr. and Methods A484 (2002) 369 (astro-ph/0112172).
- [6] P.Amram et al., Background light in potential sites for the ANTARES undersea neutrino telescope, Astroparticle Physics 13 (2000) 127-136 (astro-ph/9910170).



# Antares simulation tools

J. Brunner

(on behalf of the Antares collaboration)

CPPM, 163, Avenue de Luminy, case 902, 13288 Marseille cedex 9, France  
jurgen.brunner@in2p3.fr

## *Abstract*

The simulation tools which are used by the Antares collaboration are presented. Their potentials and limitations are discussed.

## I. GENERAL SCHEME

The chain of programs which allow to simulate the detector response with respect to a neutrino or muon signal can be separated into three steps:

- Physics generator
- Cherenkov light emission and propagation
- Response of the photomultiplier tube (PMT) and its digitization

Apart from these steps there are secondary inputs from calibrations and external measurements. In the following each step will be discussed in detail.

## II. PHYSICS GENERATORS

Two basically different physics processes can produce detectable Cherenkov light: muons and muon bundles from cosmic ray interactions in the atmosphere and neutrino interactions in the vicinity of the detector.

### A. Atmospheric muons

Atmospheric muons are the remains of hadronic showers which are produced at 10-20 km height when cosmic ray particles (protons or light nuclei) interact with nuclei of the atmosphere. There are parameterizations of the atmospheric muon flux in terms of energy, zenith angle and depth. However these parameterizations do not describe the probabilities to observe two or more muons from the same cosmic ray interaction. Therefore a full simulation of atmospheric showers is performed, followed by the propagation of the remaining muons to the detector position. The high energetic cosmic ray interactions are simulated with the packages CORSIKA [1] and HEMAS [2]. Extensive comparisons between both packages have been performed. Though there are some differences both packages deliver compatible results when confronted with

data. An energy range from 1 TeV to 100 PeV is considered for the primary cosmic ray particles. At lower energies the produced muons cannot reach anymore the detector at a depth of more than 2000 m whereas at higher energies the primary flux becomes negligibly small. An angular range from  $0-85^\circ$  is considered including also close to horizontal atmospheric muon bundles which might be particularly dangerous in terms of background for neutrino signals. The simulation is done with a simple  $E^{-\gamma}$  spectrum for the primary flux for all nuclei. This allows a later reweighting with a chosen primary flux model. For the hadronic shower development in CORSIKA the package QGSJET [3] has been chosen, basically because it has the lowest CPU need among several packages with equivalent results. HEMAS uses instead DPMJET [4] to calculate the hadronic shower development.

As output of HEMAS and CORSIKA muon events at the sea surface are obtained. Each event contains a certain number of muon tracks with given energies, angles and relative position with respect to each other. A minimal energy of 500 GeV per muon is required. Lower energetic muons cannot reach a detector at 2000 m depth of water. Apart from this cut no assumptions concerning the Antares experiment have been used and the data sample can be reused for the simulation of the atmospheric muon yield in other underground/underwater experiments, e.g. for a future kilometer cube detector.

As a next step the muons are propagated to the detector position. The muon propagation programs MUSIC [5] and MUM [6] are used. They take into account all relevant energy loss processes for muons passing through matter up to the highest energies. MUSIC includes also multiple scattering (though negligible at the energy range of interest here).

The instrumented detector volume is surrounded by a cylindrical “can” which defines the limit of simple muon propagation versus propagation plus Cherenkov light generation. The “can” extends typically 3 attenuation lengths beyond the instrumented volume. The relevant numbers are illustrated in Figure 1.

The muons are stored at the can surface for further processing. Again an energy cut is applied, now 20 GeV to ensure that they can produce a detectable signal in the detector (the range of a 20 GeV muon is shorter than the distance from the can surface to the instrumented volume).

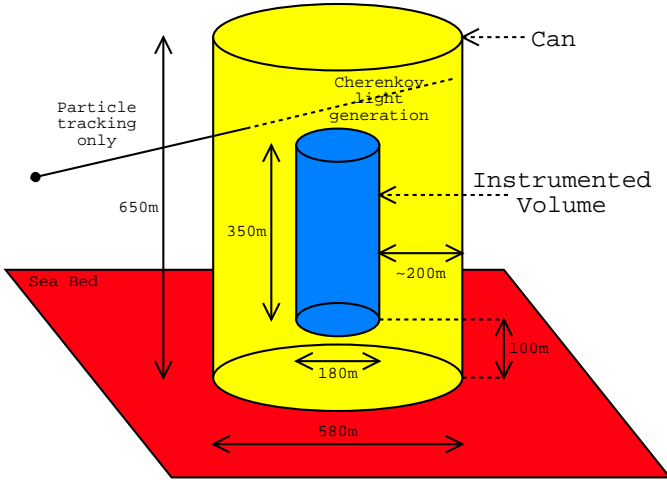


Figure 1: Relations between instrumented volume and “can” volume used for Cherenkov light simulation [7].

### B. Neutrinos

To simulate neutrino interactions in the surroundings of the detector the package GENHEN has been developed for Antares. All three neutrino flavors and both interaction channels (neutral current NC, charged current CC) are supported. First neutrino energy and zenith angle are chosen from a given input spectrum. Then the interaction vertex and the target nucleon are selected. The proton to neutron ratios in water and rock are taken into account. For  $\nu_e, \nu_\tau$  CC interactions and for NC interactions only vertices inside the “can” volume are considered. The fact that a  $\tau$  with PeV energies could reach macroscopic ranges ( $c\tau\gamma = 50$  m at 1 PeV) is ignored in the present implementation as well as the possibility of a muonic tau decay resulting in a high energetic long range muon after a  $\nu_\tau$  CC interaction. Instead for  $\nu_\mu$  CC interactions the muon range is taken into account. The vertex is positioned inside a volume which is defined by the maximal muon range for a given energy window [7]. The different densities of rock and water are taken into account for the calculation of the range. The resulting vertex distribution for an  $E^{-2}$  input spectrum between 100 GeV and 1 PeV is shown in figure 2. Zero on the vertical axis denotes the sea bed.

Once the vertex position and the target nucleon are chosen the neutrino interaction is simulated with LEPTO [8]. The CTEQ5 [9] structure function with NLO corrections are used. At very small Bjorken- $x$  there are no data to constrain the structure functions which leads to a 10% uncertainty on the total cross section at neutrino energies of 100 PeV.

The hadronisation is done with PYTHIA/JETSET [10]. The models and parameterizations which are included in these packages have been tuned to accelerator data at energies below 100 GeV. One should be aware that for the simulation of PeV neutrino interactions the results of the hadronisation from PYTHIA/JETSET might be wrong.

At energies below 100 GeV quasi-elastic and resonant reactions start to play a role. They are simulated with RSQ [11]

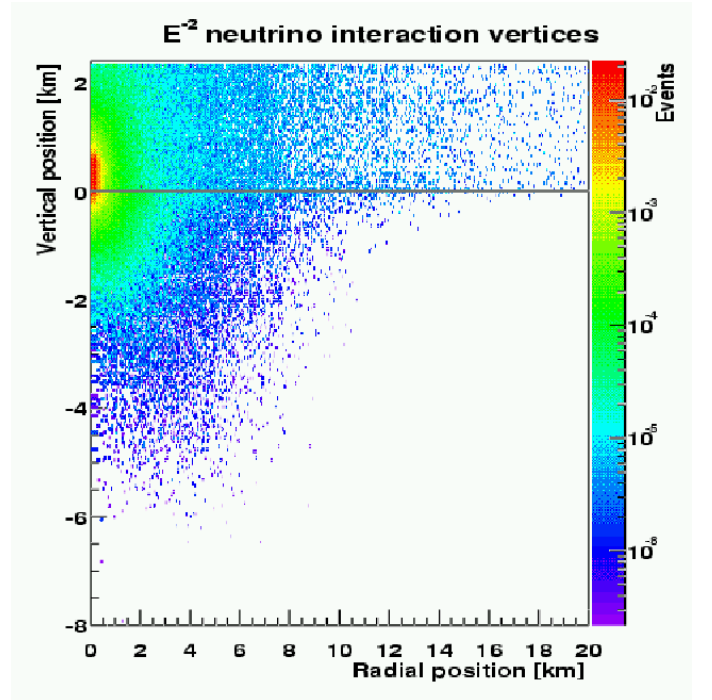


Figure 2: Distribution of neutrino vertices around the detector which produce a muon with  $E_\mu > 20$  GeV at the “can” surface. [7]

which has been integrated into GENHEN.

$\tau$  decays are handled with TAUOLA [12] which allows to take into account the polarization of the  $\tau$ s which are produced in neutrino interactions.

Neutrino energy sampling is done according to  $E^{-\gamma}$  which allows later reweighting with different flux models. The event weight contains also a factor which takes into account the opacity of the earth in function of neutrino energy and zenith angle with an earth density profile from [13]. For the opacity calculation the total cross section (NC+CC) is taken into account. Neutrino recreation in NC interactions or from  $\nu_\tau$  CC interactions followed by  $\tau$ -decay are ignored in the present implementation. This leads to a conservative (overestimated) value for the opacity.

If the neutrino vertex is inside the “can” volume all final state particles of the interaction (after hadronisation and decay of short-lived particles) are stored for further processing with the Cherenkov light simulation. If the neutrino interaction is outside the “can” only the muon is propagated to the can surface and stored there as it is done for atmospheric muons. For muon propagation MUSIC [5] or MUM [6] are used.

## III. TRACKING AND CHERENKOV LIGHT EMISSION

All long-lived particles which are stored as output of the physics generators are tracked through the water in the “can” volume. The composition and density of the water is adjusted

to the values at the experimental site.

For all particles but muons tracking is done with GEANT [14] with all relevant physics processes activated (energy loss, multiple scattering, radiative processes and hadronic interactions). At each tracking step the Cherenkov cone which is produced by charged particles is calculated. For all optical modules (OM) which are in the cone the hit probability is determined and converted into a photoelectron number using Poisson statistics. A wave length window of 300-600nm is considered and the wavelength dependent absorption length, quantum efficiency and transmission coefficients of the glass sphere and the gel are used to evaluate the hit probability. The relative orientation of the PMT with respect to the Cherenkov front and its angular acceptance is also taken into account. The arrival time is calculated based on the group velocity of the photon front and includes smearing factors from the TTS (transit time spread) of the PMT as well as from the wavelength dispersion, where the latter depends on the distance between track segment and OM. Light diffusion in the water is neglected because the present method is only applied to electrons and hadrons which are embedded in hadronic or electromagnetic showers. This makes the Cherenkov cone “fuzzy” - the same effect would be obtained by including light diffusion. Figure 3 illustrates the angular distribution of the Cherenkov light emitted by an electromagnetic shower. The Cherenkov peak is well visible but the tails extend over the whole angular range. It is noteworthy that this distribution is invariant with respect to the initial shower energy over a wide range of energies. This allows to parametrize the Cherenkov light production of electromagnetic showers which in turn economizes a significant amount of CPU time. Apart from the shown angular distribution only the initial energy (equivalent to the total light output) and the longitudinal shower profile are needed. The latter is described as usual by a gamma distribution [15]. The radial shower size is neglected as it does not exceed the Moliere radius of a few cm. No parametrization is used for hadronic showers because they exhibit much larger fluctuations and lead occasionally also to secondary muons. The simulation of hadronic interactions is done with the package GHEISHA which is integrated in GEANT [14]. However also this package has been tuned to data for energies below 100 GeV and might produce wrong results when applied to energies which are significantly higher.

Muons are treated differently to include also the effect of light diffusion. Before simulating physics events one has to create a set of “scattering tables”. This is done in the following way. 1m long muon track pieces are sent to GEANT within a large water volume. Energy loss, multiple scattering and radiative process below a given energy threshold (typically 0.1-1 GeV) are enabled. Unlike described in the paragraph above now individual Cherenkov photons are created and tracked in the water. A diffusion and absorption model has been implemented and allows to track each photon through various scattering processes until it gets absorbed or leaves the volume. Each time a photon penetrates one of several concentric spheres around the muon track origin, its position, direction and time is stored (Figure 4). This photon field is then convo-

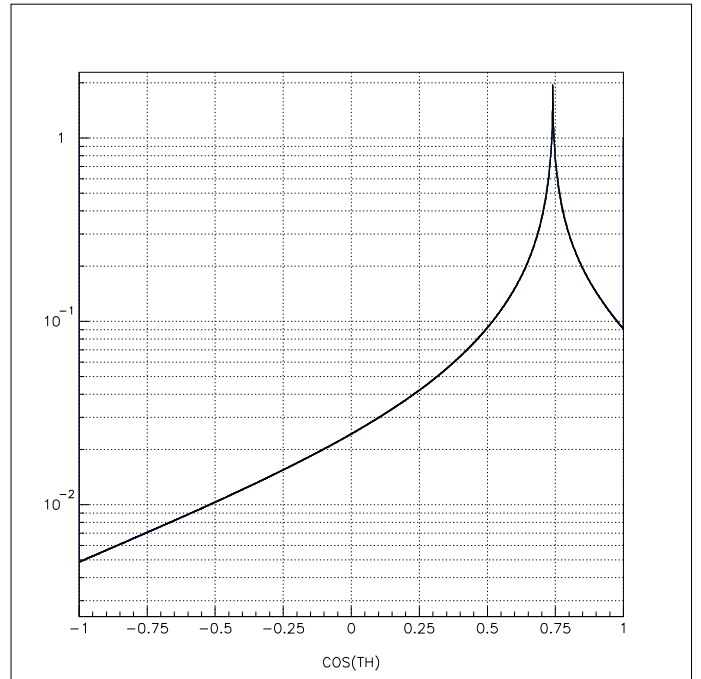


Figure 3: Angular distribution of Cherenkov light for electromagnetic showers with respect to the shower axis

luted with possible orientations of OMs in these spheres which leads to hit probability tables in a 5 dimensional parameter space: R - distance from muon origin,  $\theta$  - latitude on the sphere,  $\vartheta, \phi$  - orientation of OM with respect to muon direction, t - photon arrival time. These “scattering tables” are also created for electromagnetic showers and stored for the next processing step. Now muons from physics generator events are tracked in the usual “can” volume by MUSIC. After each tracking step the hit probabilities for all OMs are evaluated using the “scattering tables”. No Cherenkov photon tracking is necessary at this step. High energetic radiative processes like bremsstrahlung are also treated by MUSIC and their Cherenkov photon yield is given by the electromagnetic shower table. One set of scattering tables can be reused as long as the underlying scattering and absorption model has not to be changed.

## IV. DIGITIZATION

The simulation of the PMT response has been already described in the last section. We are left with a number of photoelectrons and an arrival time which includes a smearing due to the TTS of the phototube. In the Antares detector the hits are digitized by an ASIC with is called ARS [16]. Its behaviour can be approximated by setting few parameters like integration time, dead time and saturation. This allows already a rather realistic response. However there is also a more sophisticated simulation of its full functionality which includes as well the option of a fast signal sampling [16]. For real data the digitized signals are sent to the shore station where they are processed

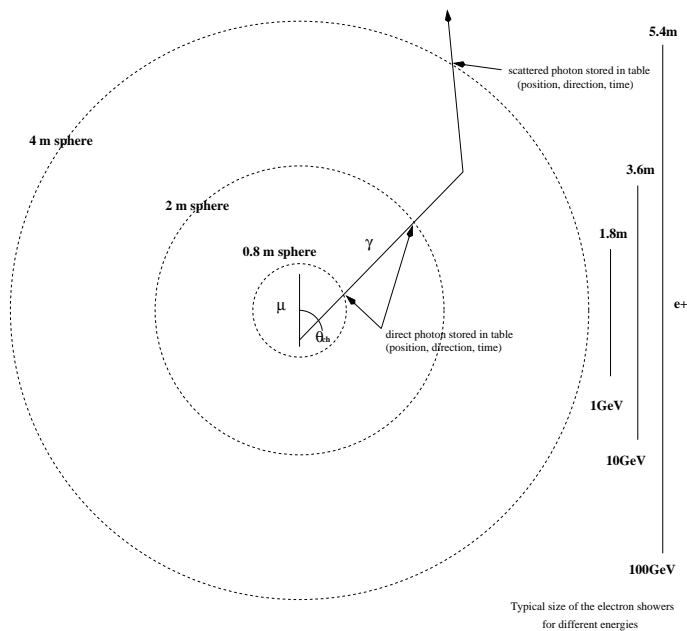


Figure 4: Scheme for creation of scattering tables

by a data filter farm which acts as a trigger. For the simulated data an offline version of the data filter is being developed.

## V. CALIBRATIONS

One of the most complex calibrations concerns the positioning of the detector elements. As the lines are freely floating in the sea currents their movement must be permanently monitored. Two systems are available. Each floor measures regularly its orientation with respect to the North and two tilts which allow to determine its orientation in space. An independent acoustic system allows a triangulation between several fix points at the sea floor and some measurements points which are distributed along each line.

A detailed simulation of these system has been set up. First a sea current is chosen. On its basis the deformation of the detector lines are calculated. Various mechanical constraints and parameters are taken into account. Then data from the acoustic system and the orientation measurements are simulated including a realistic smearing for each value. Finally a two step reconstruction establishes the position of all detector elements. It could be proven that this procedure allows to determine the position of each detector element to better than 10 cm.

Another calibration simulation is performed for the LED and laser beacons to perform an absolute time calibration for the PMTs. Laser and LED pulses are generated and the photons are propagated through the water. Specific scattering tables had to be created for this purpose. The correlation between the arrival times of the LED and laser photons at the different PMTs together with the precise knowledge of their positions (see above) allows to fix the relative time offsets between them

to better than 0.5 nsec.

For other calibrations no specific simulation programs exist. For the main simulation of physics events one assumes usually that the detector has been calibrated and only the precision of the calibration is used as additional factor which reduces the time or amplitude resolution of the measured hits.

The main detector element of Antares is the OM with the PMT. Its characteristics has been extensively studied and is described in [17]. Its most important features are the effective area, angular acceptance, TTS and the wavelength dependent quantum efficiency. All four are crucial for a correctly simulated detector response. The TTS is directly correlated with the angular resolution of the detector whereas the other parameters influence mainly its effective area. As the variations between different tested OMs are rather small the simulation code assumes identical parameters for all of them in the detector.

The environmental parameters at the Antares site have been measured over an extended period. The optical noise from radioactive decays and biological activity is described in [18]. For the simulation the noise is added before the digitization step. For most analyzes a constant noise level is assumed. Local variations due to bioluminescence bursts are ignored in the present implementation.

A publication which describes the water absorption and diffusion at the Antares site is under preparation. Its results are already used in the Antares simulation, in particular for the preparation of the scattering tables for the muons.

## VI. CONCLUSION

Antares has developed a complete set of simulation tools. Most of them are easily scalable to larger detectors and different environmental parameters. They could serve as a first step to simulate the performance of possible kilometer cube detectors.

## REFERENCES

- [1] D. Heck *et al.* CORSIKA, Forschungszentrum Karlsruhe Report **FZKA-6019** (1998).
- [2] E. Scapparone, HEMAS, arXiv:[physics/9902043](https://arxiv.org/abs/physics/9902043) (1999).
- [3] N.N.Kalmykov, S.S.Ostapchenko, A.I.Pavlov, *Nucl. Phys. B* (Proc. Suppl.) **52B** (1997) 17.
- [4] J.Ranft, *Phys. Rev.* **D51** (1995) 64; arXiv:[hep-ph/0002137](https://arxiv.org/abs/hep-ph/0002137) (2000).
- [5] P. Antonioli, C. Ghetti, E. V. Korolkova, V. A. Kudryavtsev and G. Sartorelli, *MUSIC*, *Astropart. Phys.* **7** (1997) 357, arXiv:[hep-ph/9705408](https://arxiv.org/abs/hep-ph/9705408).
- [6] I. A. Sokalski, E. V. Bugaev and S. I. Klimushin, *MUM*, *Phys. Rev. D* **64** (2001) 074015, arXiv:[hep-ph/0010322](https://arxiv.org/abs/hep-ph/0010322).

- [7] D. Bailey, “Monte Carlo tools and analysis methods for understanding the ANTARES experiment and predicting its sensitivity to Dark Matter”, PhD thesis, University of Oxford, United Kingdom, (2002).
- [8] G. Ingelman, A. Edin and J. Rathsman, LEPTO 6.5, Comput. Phys. Commun. **101** (1997) 108, arXiv:[hep-ph/9605286](#).
- [9] H. L. Lai *et al.*, CTEQ, Phys. Rev. D **51** (1995) 4763, arXiv:[hep-ph/9410404](#).
- [10] T. Sjostrand, PYTHIA 5.7 and JETSET 7.4, arXiv:[hep-ph/9508391](#).
- [11] G. D. Barr, “The separation of signals and background in a nucleon decay experiment”, PhD thesis, University of Oxford, United Kingdom (1987).
- [12] S. Jadach, Z. Was, R. Decker and J. H. Kuhn, TAUOLA 2.4, Comput. Phys. Commun. **76** (1993) 361.
- [13] R. Gandhi, C. Quigg, M. H. Reno and I. Sarcevic, Astropart. Phys. **5** (1996) 81, arXiv:[hep-ph/9512364](#).
- [14] GEANT program manual, CERN program library long writeup W5013, CERN (1993).
- [15] K. Hagiwara *et al.* (PDG Collab.), Phys. Rev. D **66** (2002) 010001, page 203.
- [16] J.S. Ricol, “Etude de la détection de monopôles magnétiques au sein du futur télescope à neutrinos Antares et caractérisation des performances du traitement des impulsions des photomultiplicateurs”, PhD thesis, Université de la Méditerranée- Aix Marseille II, France (2002).
- [17] P.Amram *et al.* (Antares collab.) Nucl. Instr. and Methods **A484** (2002) 369.
- [18] P.Amram *et al.* (Antares collab.) Astropart. Phys. **13** (2000) 127, arXiv:[astro-ph/9910170](#).

# Status of simulations in NEMO

P. Sapienza<sup>a</sup> for the NEMO collaboration

a) LNS-INFN, Via S. Sofia , 95129 Catania, Italy  
sapienza@lns.infn.it

## *Abstract*

Preliminary simulation results for a detector made of "NEMO-towers" are presented. Effective areas and medians of the angle between true and reconstructed muon track are shown. The influence of the optical background rate is also investigated.

## I. INTRODUCTION

In this paper we report on the present status of simulations in the NEMO collaboration. The NEMO project aims mainly at two specific issues:

- search and characterization of a deep underwater site for the installation of a km<sup>3</sup> Cherenkov detector;
- R&D activity for a km<sup>3</sup> underwater Cherenkov detector for high energy neutrino astronomy.

As a result of these activities a site 80 km far from Capo Passero has been indicated as a good candidate for the km<sup>3</sup> installation due to its excellent oceanographic and optical properties (see Riccobene paper in these proceedings). The engineering of most of the crucial component for a km<sup>3</sup> underwater detector is underway in NEMO FASE1 (see Migneco paper in these proceedings).

Simulations have the task of supporting these activities. The work reported in this paper is part of a work in progress and more complete simulations are needed, however since most of the results concern comparison between different environmental situations and different detector arrangements some indications can be gathered.

## II. SIMULATION RESULTS

The simulations reported in the following have been performed using different software packages. In section A the simulation of atmospheric muons and their propagation to the detector depth is described. In section B the results obtained with the OPNEMO software package for the optimization of the detector lay-out are reported, the optical background is not included. More recently, we have started a common effort together with the ANTARES collaboration towards the design of the km<sup>3</sup> in which the ANTARES software package is used. In section C the more recent results obtained using the ANTARES software package are shown.

### A. Atmospheric muons

The low neutrino fluxes expected for astrophysical sources require a huge shield for the down-going muons produced in the interaction of cosmic rays with the atmosphere. Indeed, although only up-going muons induced by astrophysical neutrinos are considered, down-going atmospheric muons mis-reconstructed as up-going represent a serious background for neutrino source signals.

The intensity of the atmospheric muon strongly decreases below the sea surface as a function of depth and zenith angle. Therefore, for a proper estimation of flux and muon event multiplicities a Monte-Carlo simulation is demanded. The complete simulation can be divided in three steps:

- cosmic ray interaction in the atmosphere (simulation of atmospheric showers);
- muon propagation in the seawater down to the detector;
- detector response simulation.

Since muon background rejection is a crucial issue for a neutrino telescope, we aim at comparing the response of km<sup>3</sup> detectors to down-going atmospheric muons at two different depths.

HEMAS (Hadronic, Electromagnetic and Muonic component in Air Shower) code (vrs7-02) [1] has been used to simulate atmospheric showers. HEMAS has been designed as a fast tool for the production of air showers initiated by hadron primaries. It allows the calculation of hadronic and muonic components of air showers above 500 GeV and electromagnetic showers above 500 keV. HEMAS takes into account the Earth curvature and therefore the simulation can be extended out to zenith angles of about 90°. The DPMJET hadronic interaction model has been used.

Muons were propagated from the sea level to the detector using the MUSIC code [2]. MUSIC (MUon Simulation Code) is a three dimensional Monte-Carlo code that takes into account multiple scattering, bremsstrahlung, pair production and inelastic scattering.

In this work primaries with energies ranging from 20 TeV to 200 PeV have been simulated with a flat angular distribution in  $\cos\theta$ . Primary composition was based on ref. [3]. Only the following five primaries have been taken into account: proton, helium, nitrogen, magnesium, and iron. With this primary composition the cosmic ray spectrum is well reproduced up to 10<sup>17</sup> eV. Muon angular distribution for

events corresponding to about 6 minutes of data taking for a  $\text{km}^3$  detector with an area of about  $16.4 \cdot 10^6 \text{ m}^2 \text{ sr}$  are reported in fig. 1 at the depths of 2400 m and 3400 m respectively, where 3400 m is the depth of Capo Passero site.

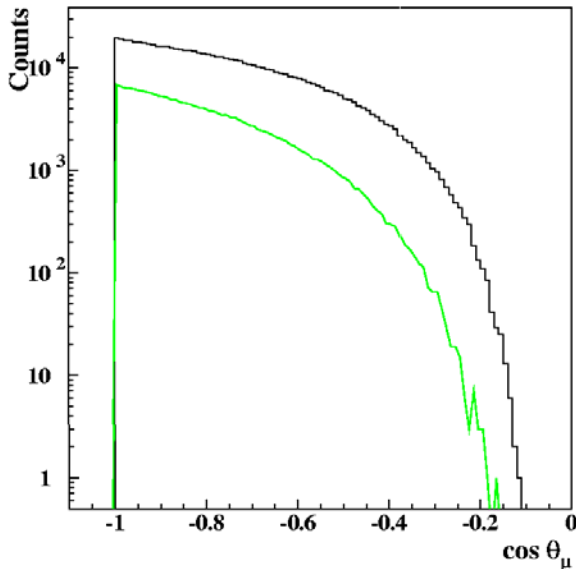


Fig. 1- Muon spectra at different depths (2400 m black and 3400 m grey) as a function of muon angles.

In fig. 1 a major flux reduction is evident for 3400 m depth. The ratio of the fluxes at 2400 and 3400m is about 3.7. However, the reduction factor is much more important at angles near the horizontal where about a factor 20 is observed at  $15^\circ$  over the horizontal. This strong difference is due to the large difference in water thickness seen at angles near the horizontal by the same detector placed at different depths.

The angles near the horizontal are particularly important for the high energy neutrino detection since neutrinos over 10 PeV are strongly absorbed by the Earth and consequently their best direction for detection is around the horizontal plane. Heavy energetic hadrons in cosmic rays produce very large showers in the atmosphere with high multiplicity of muons. The muon multiplicities at the two depths were also investigated. A much larger contribution of high multiplicity muons is also observed at 2400m [4]. Since a proper track reconstruction of multi-muon events represents a difficult task to achieve, the response of the detector has to be carefully evaluated, this analysis is in progress with more significant statistics.

### B. Detector lay-out

The design of the detector lay-out for a  $\text{km}^3$ -scale underwater Cherenkov neutrino telescope for high energy neutrino astronomy is a very ambitious task which will result as a compromise between many different requirements. The NEMO collaboration has decided to undertake a feasibility study for a  $\text{km}^3$  underwater detector based on towers. One of our main concerns in the definition of the detector lay-out has

been the feasibility in terms of present technology within a reasonable budget and time construction schedule. Indeed, the definition of the so called "NEMO tower" (see Migneco and Musumeci papers in these proceedings) originated from the merging of physics and technological requirements. In particular, constraints on the distance between towers (larger than about 120 m) and on their height (smaller than 1km) were suggested by a feasibility study in terms of construction, deployment, operation and maintenance of the detector within reasonable costs. Both the detector response and the construction, deployment and maintenance costs obviously depend on the total number of PMTs and towers (or strings). These figures for the configurations investigated are reported in table 1.

Detector configuration	NEMO64-180	NEMO-dh140
N° of PMTs	4096	5832
N° of bars	16	18
N° of towers	8x8=64	9x9=81
Tower distance	180 m	140m
Tower height	600 m	680 m
Bar length	20 m	20 m
Bar distance	40 m	40 m
Instrumented volume	0.93 $\text{km}^3$	0.88 $\text{km}^3$
PMT diameter	10"	10"
Bar configuration	see fig. 3	Down-horizontal

Table 1 - Main detector parameters of the configurations reported in this work.

In this section we report some results on detector response obtained with the Monte Carlo code OPNEMO [5]. This code generates muons on the surface of a box surrounding the detector, propagates the muons inside the box volume, simulates the light generated by muons, the detector response and performs a track reconstruction. Many simplifications are made in the code (i.e. the scattering of the light is not considered); the main limitation of the present version of the program is due to the fact that a reconstruction algorithm in presence of optical background has not been implemented. However, a systematic study of  $\text{km}^3$  detector performances with OPNEMO was carried out and several useful indications have been obtained on the dependence on several parameters such as the distance between towers, the absorption length, etc. [6]. These simulations lead to a detector configuration (NEMO64-180) with the characteristics reported in table 1.

As an example the median angles are reported in fig. 2 for different arrangements of the four PMTs on the bar (see fig.3).

In our opinion, an interesting option is represented by the dh configuration, which optimises the isotropy of the response avoiding the problem of having upward directed PMTs where the long terms response can be deteriorated by the biofouling.

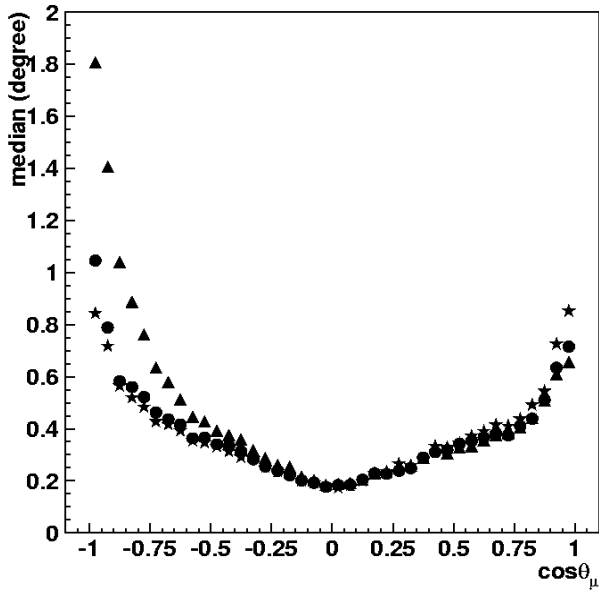


Fig. 2 – Median angles of  $\Delta\Omega$  between true and reconstructed muon tracks as a function of muon angles for different PMT arrangements in the bar (see fig. 3) (triangles d-d, circles d-h, stars u-d). Results obtained with the OPNEMO code (without optical background).

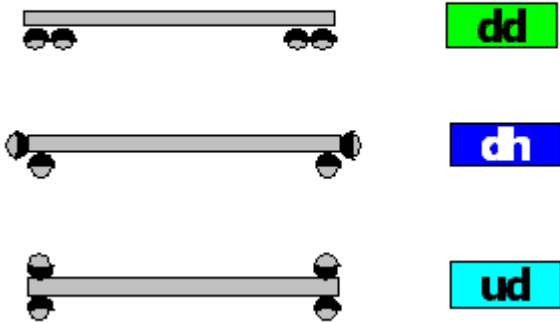


Fig. 3 –PMT arrangements in the bar.

### C. Detector performances

The sensitivity of a detector at different astrophysical neutrino sources is strongly dependent on the effective detector area and the pointing (angular) resolution as a function of energy. Therefore, the range of energies to be covered and especially the energy threshold has to be provided as input for the detector lay-out study. Indeed, while at energies larger than about 10 TeV the effective area is mainly dominated by the size of the instrumented volume, at energies around 1 TeV and below the PMT density dominates. Moreover, especially for a detector with structures (towers or

strings) at relative distance larger than 100 m, where the signals from low energy muons are blurred by the continuous flow of optical background signals due to the presence of the  $^{40}\text{K}$  and the bioluminescence, the background rejection represent a serious problem to cope with.

The response of the NEMO-dh140, which is a  $\text{km}^3$  detector configuration understudy in the NEMO Collaboration, at muons in the  $10^2$ - $10^6$  GeV energy range has been investigated. In particular, simulations with increasing optical background rate have been performed and the proposed detector lay-out has been compared with a homogeneous detector. The NEMO-dh140 configuration is made of 81 towers with a height of 680 m, arranged in a square pattern with 140 m distance between towers. Each NEMO-tower consists of 18 bars 20 m long and 40 m spaced. Consecutive storeys are orthogonal to each other. Each bar is equipped with 2 couples of PMTs at the two edges, each PMT couple consists of a down looking PMT and a horizontal one looking outside with respect to the tower axis. In this configuration each tower hosts 72 PMTs, namely 5832 PMTs for the whole detector. The main features of this detector are reported in table 1.

Simulations have been performed using the software developed by the ANTARES Collaboration [7]. These simulations are part of a work in progress and represent a first attempt to guide a more refined design of the detector. Indeed, further efforts are needed in order to fully exploit the features of our detector for the definition of triggers, event selection and reconstruction.

The simulation of the detector response to high energy neutrino fluxes consists of several different stages:

- interaction of neutrinos in the media surrounding the instrumented volume;
- propagation of the resulting particles until the detector horizon;
- detector response including optical background and electronic simulation;
- reconstruction track algorithms.

These tasks are undertaken by different codes in the ANTARES Monte Carlo. In the simulations shown in the following, we have generated up-going muons with a  $E^{-1}$  spectrum and a flat distribution in  $\cos\theta$  at the surface of a cylinder ("can") surrounding the detector which represents the detector horizon. A modified version of the code, which allows to simulate large detectors of  $\text{km}^3$  scale, was used [8]. The can radius offset was decreased from 200 m to 100 m and the optical background offset was increased from 500 ns to 1000 ns. Several reconstruction algorithms, based on different strategies can be implemented in the ANTARES simulation code, our simulations were performed using the so called "Aart strategy" [9] with a prefit based on high amplitude signals (greater than 2.5 p.e.).

We have made some modifications to the reconstruction code aiming at improving the detector performances especially in the lower energy range. In particular, space-time



correlated couples of PMTs at the bar edges were added to the above mentioned trigger. Simulations with varying the optical background rate were performed (20 kHz, 60 kHz and 120 kHz). The main performances of a NEMO tower based detector (NEMO-dh140) are shown in the general paper on NEMO by E. Migneco in these proceedings.

In this section, we focus on the dependence of the detector performances on the optical background rate. The angular resolution achievable for high energy neutrino astronomy with Cherenkov muon detectors is intrinsically limited by the spreading angle between the incoming neutrino and the produced muon. This angle is expected to decrease from about one degree at 100 GeV to a few hundredths of degree at about 1 PeV. The other contribution to the angular resolution is given by the relative angle  $\Delta\Omega$  between the incoming muon and the reconstructed muon track. Median angles of  $\Delta\Omega$  distribution as a function of muon energy are reported in fig. 3.a for the different background rates. Rather good values are obtained for the NEMO-dh140 detector at the lower simulated rate (20 kHz open circles).

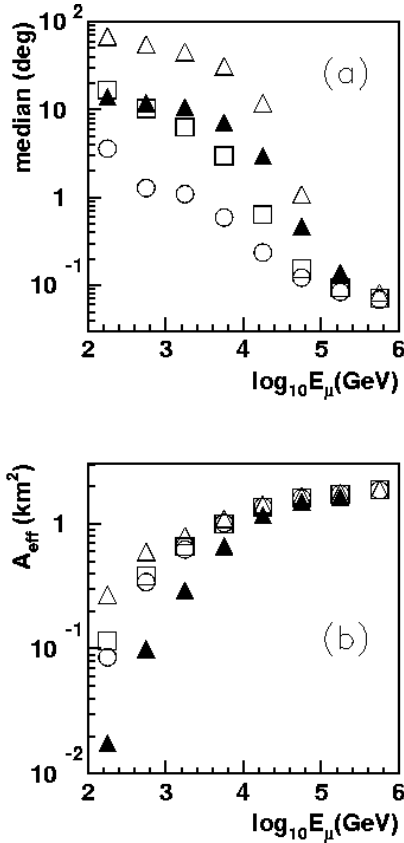


Fig 4 – Median angles (a) of  $\Delta\Omega$  between true and reconstructed muon tracks and effective areas (b) for NEMO-dh140 detector for 20kHz (open circles), 60 kHz (open squares) and 120 kHz (open triangles) background rate. Full triangles represent calculations at 120 kHz where 1.5 p.e. threshold have been applied (see text).

A value of 20 kHz for the optical background rate is consistent with several measurements made by the ANTARES

and NEMO collaborations in the Capo Passero site (see Riccobene paper in these proceedings). On the other hand, a strong deterioration of the angular resolution is observed with increasing rate (60 kHz open squares and 120 kHz open triangles of fig. 3.a). The full triangles of fig. 3.a represent a simulation at 120 kHz where a threshold of 1.5 p.e. (instead of the 0.5 default value) was set on all the PMTs. In figure 3.b the corresponding effective areas for reconstructed events are reported. The main features of fig. 3.b are the observation of similar results at 20 kHz and 60 kHz and a much steeper drop at energy below 10 TeV when a 1.5 p.e. threshold is applied to all the PMTs for the simulation at 120 kHz.

To improve the angular resolution, conditions on fit quality parameters of the reconstructed track can be applied (quality cuts) [10]. The quality cuts are also needed to eliminate the atmospheric muons badly reconstructed as upgoing muons. Since these muons represent the most serious source of background for the very low fluxes expected for high energy neutrino sources, very accurate simulations are needed as already pointed out in section A.

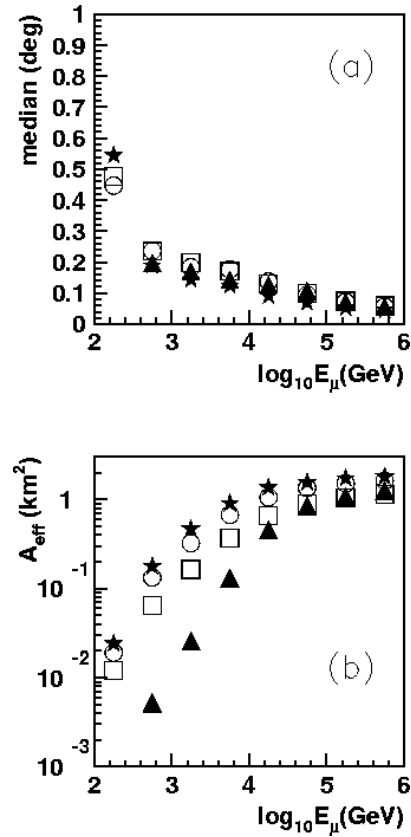


Fig 5 – Median angles (a) of  $\Delta\Omega$  between true and reconstructed muon tracks and effective areas (b) for NEMO-dh140 detector when quality cuts are applied. Same symbols as fig 3. Stars represent calculations for a 60m spaced homogenous detector.

To better evaluate the performance of our detector, we have also carried out a simulation for a 5600 PMTs homogenous detector. This detector is made up of 400 strings,

each strings equipped with 14 down-looking PMT 60 m spaced; the distance between strings is 60 m. An optical background of 20 kHz has been considered. This detector displays very good performances concerning both the angular resolution and the effective area (stars in fig. 4.a and 4.b). However, it is important to point out that this homogenous detector has to be considered only as an ideal detector to compare with. Indeed, due to the very large number of strings (400) and to the small distance between them (60 m), a detector of this kind doesn't seem convenient for technical reasons and costs.

For a fair comparison, effective areas should be compared conditions being equal with respect to angular resolutions. In fig. 4.a the angular resolutions after quality cuts are displayed. The quality cuts were set aiming at obtaining similar values to the lattice detector ones. Moreover, the obtained values are comparable with the mean angle between the incoming neutrino and the produced muon.

The effective area after quality cuts providing angular resolutions similar to the one obtained for the lattice detector are compared in fig. 4.b for the reconstructed events which survive to the quality cuts. The achieved angular resolution is paid in terms of effective area which is reduced especially in the lower energy range.

At 20 kHz the NEMO-dh140 effective area (open circles) is close to the regular lattice one (stars), while a stronger and stronger reduction of the effective area is observed with increasing background rate. This comparison indicates that a  $\text{km}^3$  detector based on NEMO-towers like NEMO-dh140 seems to fulfil the main requirements for high energy neutrino astronomy, especially for lower optical background rates.

One of the expected advantages of the towers with respect to the strings is the possibility of exploiting "local" coincidences in the bar or in nearby bars. The study of triggers and filtering procedures based on these "local" coincidences using the OPNEMO code and promising results have been already obtained [11]. A full simulation, starting from interacting neutrinos, is in progress. The optical water properties are expected to affect the detector efficiency and angular resolution. In particular, the number of detectable photons and the spreading on their arrival time depend on the absorption and scattering length respectively. For a proper evaluation of the candidate sites also the dependence on these properties should be evaluated.

### III. CONCLUSIONS

In summary, we have simulated the response of a  $\text{km}^3$  detector based on NEMO towers and we have reported some results.

In particular, a strong deterioration of the angular response is observed increasing the optical background rate from 20 to 120 kHz. On the other hand, when quality cuts are applied we are able to obtain a good angular resolution in all the cases with a consequent reduction in the effective areas especially at the lower energies. The comparison with an ideal detector, made of about the same number of PMTs arranged in a regular lattice pattern, confirms that a  $\text{km}^3$  underwater detector based on NEMO-towers represents a promising approach to the high energy neutrino astronomy.

The results presented in this report are part of a work in progress which aims at the design and the optimisation of the  $\text{km}^3$  detector.

### IV. REFERENCES

- [1] C. Forti et al., Phys. Rev. D42, 3668 (1990).
- [2] P. Antonioli et al., Astr. Phys. 7, 357 (1997).
- [3] J. R. Horandel, ICRC 2001 Proceedings.
- [4] *Monte-Carlo simulation of the atmospheric muon background in a  $\text{km}^3$  neutrino detector*, R. Coniglione, C. Distefano, A. Margiotta, A. Rizzo and P. Sapienza, for the NEMO-Collaboration, LNS Activity Report 2002, pag. 63
- [5] Montaruli, ICRC1999 Proceedings.
- [6] *Present status of simulations of NEMO performance*, LNS software group, internal notes and C. Distefano private communications
- [7] J. Brunner in these proceedings and references therein
- [8] D. Zaborov private communications and Zaborov and Brunner in these proceedings
- [9] A. Heijboer, ICRC 2003 Proceedings.
- [10] *Simulation of the performances of the  $\text{km}^3$  underwater NEMO telescope for high energy neutrinos*, R. Coniglione, E. Migneco and P. Sapienza for the NEMO-Collaboration, LNS Activity Report 2002, pag. 67
- [11] V. Valente and A. Capone private communications

# Nestor Simulation Tools and Methods

## VLVvT Workshop 2003

Antonis Leisos

Hellenic Open University  
for the NESTOR Collaboration  
leisos@eap.gr

### *Abstract*

We report on the simulation tools and methods used to describe the response of the NESTOR detector to signal and background sources.

A comparison between data distributions and Monte Carlo predictions was used to demonstrate the performance of the Nestor Simulation Package.

## I. INTRODUCTION

NESTOR (Neutrino Extended Submarine Telescope with Oceanographic Research) is a deep underwater neutrino detector, currently under construction, for deployment in the Mediterranean Sea near the city of Pylos (Greece) [1, 2]. The detector consists of 12 hexagonal floors (or stars) with a diameter of 32 m while the separation between floors is 30 m (Figure 1). In each arm of the star there are two almost hemispherical Cherenkov photon detectors, called Optical Modules (OM), arranged opposite to each other giving a  $4\pi$  detection capability.

In March 2003 a fully operational Nestor floor was deployed at a depth of 4000 m and more than five million events were recorded. The accumulated sample was large enough to make a comparison between the data distributions and the Monte Carlo predictions.

We have developed two simulation tools for our studies. The first one (Full Simulation Package) describes in detail the detector architecture and all the physical processes sensitive to an underwater neutrino telescope. It is the main tool for testing the overall performance of the detector's systems (i.e. calibration system, Data Acquisition system etc.) and it was extensively used in the data analysis of the 2003 Run. The second one (Fast Simulation Package) uses efficient parameterizations to increase the speed of the simulation and is mainly used for Monte Carlo studies of the design parameters of a very large volume neutrino telescope.

## II. THE FULL SIMULATION PACKAGE

There are two phases in the simulation process. The first one takes into account all the physical processes resulting in the production of cherenkov photons which travel in the water and finally hit the photo-cathode of the photomultiplier (PMT),

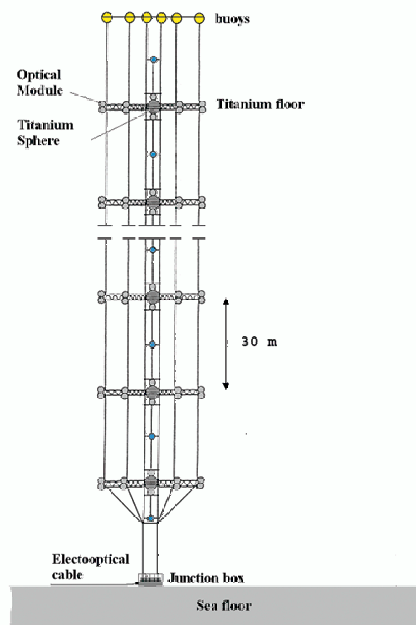


Figure 1: The Nestor Detector

while in the second one we simulate in detail the PMT response, the effects of the electronics and the Data Acquisition system.

### A. Phase I

The first phase of the simulation includes all the processes that can happen when a neutrino interacts or a charged lepton passes through the sensitive area of the detector. Since the signal is produced by the optical photons that hit the photocathode of the photomultipliers, special care is given to the Cherenkov radiation and the propagation of light in the water and inside the Optical Module. The tool used in this phase is the GEANT 4 Simulation package [3] and its interfaces with other packages like Pythia etc. All the energy losses of the particles are taken into account like multiple scattering, bremsstrahlung, ionization, muon-nucleus interaction etc. resulting in the formation of electromagnetic and hadronic showers. The tracking algorithm tracks every primary and secondary particle and in

each step Cherenkov photons are generated <sup>1</sup>. This is a very time and memory consuming process because each photon is tracked since it may interact either by absorption, or by scattering in the water (Rayleigh scattering) and in different media (Boundary processes).

As far as the detector is concerned, the Optical Module [4] consists of many components which are described analytically in the simulation. For that we utilized a detailed geometrical description of the benthos sphere (the glass housing of the PMT), the glycerin (the optical coupling between the glass envelope and the PMT) and the magnetic shield ( $\mu$ -metal) (Figure 2).

In addition we need to know the electrical properties of each component such as the absorption length and the refraction index with respect to the photon wavelength.

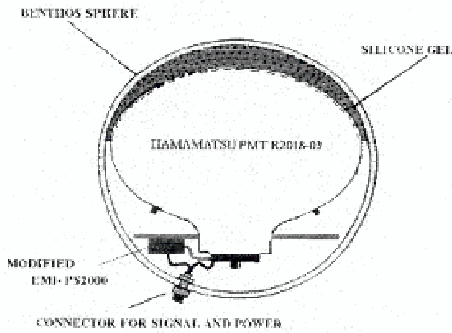


Figure 2: The Nestor Optical Module

In order to improve the speed of the simulation only the optical photons that can reach an Optical Module are generated. In Figure 3 you can see the pictorial view of a full GEANT 4 simulation. A muon track of energy 100 GeV passes parallel to the tower axis going downwards. Only a small percent of the Cherenkov radiation is actually produced <sup>2</sup> which comes not only from the muon track but also from secondary particles as the direction of the optical photons indicate <sup>3</sup>. The truth is that the event is much more complicated than it seems. The right side of Figure 3 shows a zoomed view of a track segment where there is a shower development.

### B. Phase II

The second stage of the simulation process includes the contribution of the background sources, the generation of the PMT waveforms and the effects of the electronics.

The simulation of the PMT waveform is based on the following assumptions:

1. The pulse height follows a distribution which is simply a Polya distribution (Figure 4a).

<sup>1</sup>For charged particles traveling faster than light in the water.

<sup>2</sup>Actually only photons that can reach the PMTs.

<sup>3</sup>For energetic muons the angle of the Cherenkov radiation in the water is about 43 degrees with respect to the muon direction.

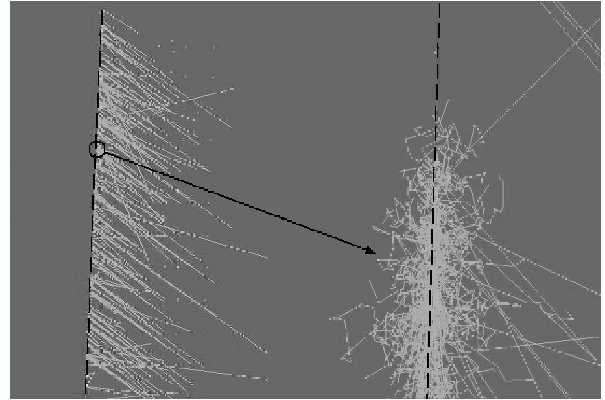


Figure 3: A pictorial view of a full simulated event.

(Left) A muon track (dashed line) going downwards, parallel to the Nestor tower axis. The solid lines indicate the tracks of the optical photons produced during the simulation. (Right) A zoomed view of a shower development at a certain segment of the muon track.

2. The pulse shape of a single photoelectron is the sum of two one-tailed Gaussians with rise time 8ns and falling time about 15 ns (Figure 4b).
3. The transition time spectrum of the pulses has been measured in the lab for each PMT separately (Figure 5).
4. The PMT response is a linear function of any phototelectron leaving the photocathode.

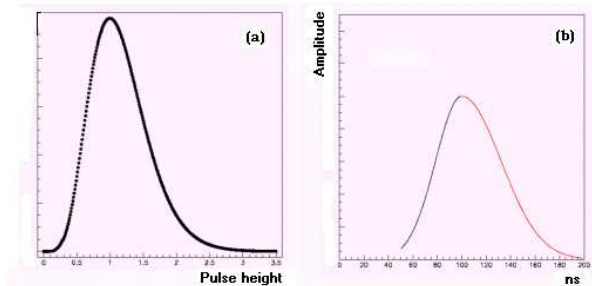


Figure 4: Waveform simulation.

(a) The pulse height distribution (Polya).

(b) The Simulated pulse as the sum of two Gaussians

Background pulses arise from the  $K^{40}$  radioactivity and the thermionic noise of the PMT. The characteristics of both contributions (e.g. pulse height distribution, increase in the counting rate etc.) have been measured and they are very well known [5, 6, 7]. As a consequence, the background contribution is treated in the simulation with the same method as the PMT pulses. The final waveform is the sum of all the signal

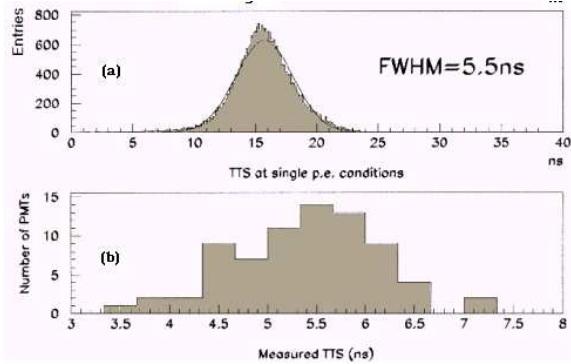


Figure 5: Transit Time measurements.  
 (a) The measured Transit Time spectrum at single photoelectron conditions.  
 (b) The distribution of the Transient Time Spectra.

and background pulses. To complete the simulation of the experimental signals we include the contribution of the electronics using detailed information concerning:

- The pulse attenuation and propagation inside the delay lines.
- The trigger formation.
- The digitization of the pulses.

The last step of the simulation procedure is the formation of the data, according to the raw data protocol of the Data Acquisition System. In this way, Monte Carlo events have identical form as the data and they can be analyzed with the same tools [8, 9].

### C. Performance of the Full Simulation Package

The performance of the detector simulation package is demonstrated by comparing the data collected in the 2003 Run [10] with the Monte Carlo predictions. We have used the distributions of several experimental parameters [10] to show that the data are in excellent agreement with the Monte Carlo predictions. As an example in Figure 6 and 7 we present the comparison between expected and recorded trigger rates as well as the expected and measured deposited charge per track.

For that purpose we produced a very large sample of Monte Carlo events (atmospheric muons plus  $K^{40}$  and thermionic noise) and we estimated the expected trigger rates of our detector and the expected collected charge per track, for various coincidence levels<sup>4</sup> and for two different cases.

In the first one, the trigger conditions were applied to pulses that were higher than one quarter of the single photoelectron level<sup>5</sup>, whilst in the second case only pulses higher than 120 mV (the single photoelectron level) were taken into account to the trigger logic. In both cases the simulation package agrees with the real data.

<sup>4</sup>The level of coincidence is defined as the number of different active PMTs within a time window.

<sup>5</sup>The single photoelectron level is about 120 mV.

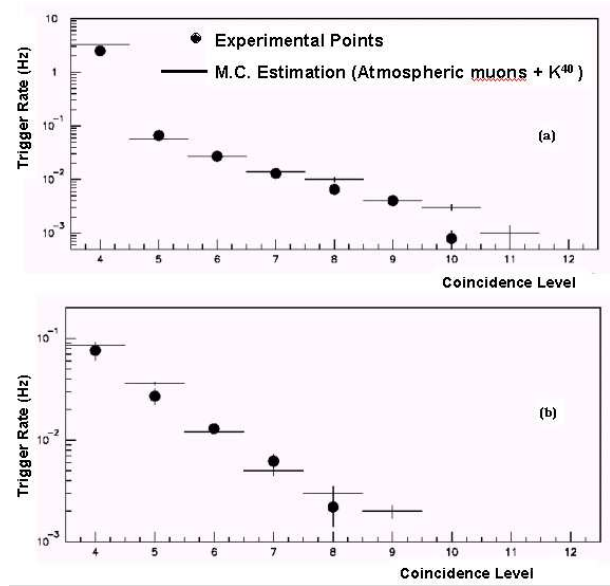


Figure 6: Comparison of the expected and measured trigger rates with respect to the coincidence level.  
 (a) Trigger Thresholds at 1/4 p.e.  
 (b) Trigger Thresholds at 1 p.e

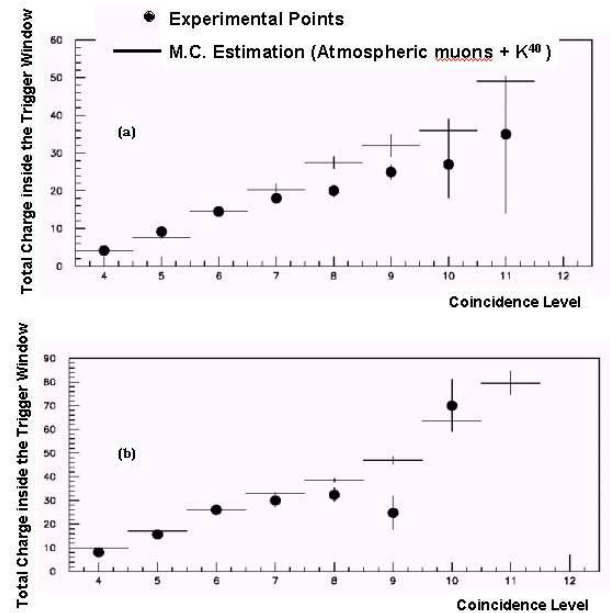


Figure 7: Comparison of the expected and measured deposited charge per track with respect to the coincidence level.  
 (a) Trigger Thresholds at 1/4 p.e.  
 (b) Trigger Thresholds at 1 p.e

## III. THE FAST SIMULATION PACKAGE

The Fast Simulation Package is a good approximation for the majority of the effects described in the previous section. The main differences with the Full Simulation concern:

- The use of photon flux instead of single photons.

- The parameterization of e/m showers.
- The parameterization of the PMT response.
- The treatment of the electronic effects.

Part of the fast simulation code is used by the fitting procedure for the estimation of the track parameters (i.e. azimuthal, polar angle and pseudo-vertex of the track). Although the relative timing of the pulses are usually used in the track reconstruction, it has been shown [10] that the total charge deposited in the PMT can dramatically improve the resolution of the track parameters. Practically it is impossible to compare the measured deposited charge at each PMT with the expected value, for each candidate track, using the Full Simulation code. In the Fast Simulation Package we parameterize the expected mean and the variance of the distribution of the number of photons that reach each PMT as a function of the track direction and the distance from the PMT.

In order to demonstrate the accuracy of this parameterization we compare the predicted deposited charge per PMT with the Full Simulation estimations, for a large sample of muon tracks following the OKADA parameterization [11] (atmospheric muons). Figure 8 shows the pull distribution de-

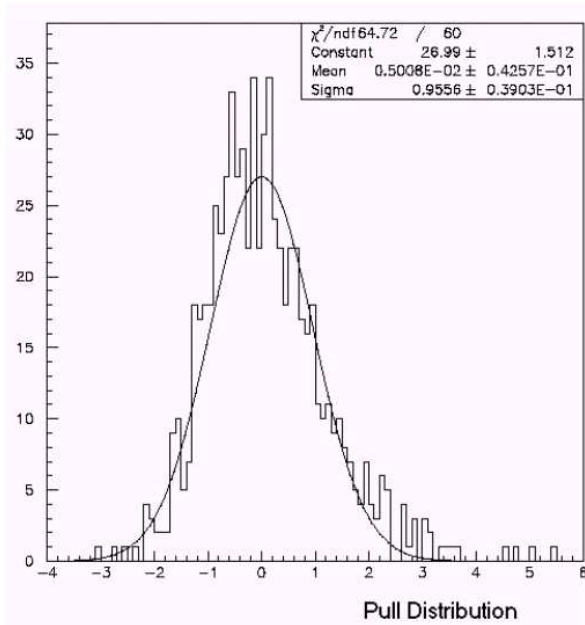


Figure 8: The Pull distribution ( $\frac{D_Q - E_Q}{\sigma_Q}$ )

defined as :

$$Pull = \frac{D_Q - E_Q}{\sigma_Q}$$

where,

$D_Q$  is the deposited charge in a PMT as the Full simulation code predicts,

$E_Q$  is the estimated charge calculated from the parametrization,  $\sigma_Q^2$  is the predicted variance by the parameterization.

The fact that the pull distribution is normal with mean zero and variance equal to unity, means that the parametrization is indeed unbiased and that the error estimation is correct.

A very common application of the Fast Simulation Package concerns the estimation of the effective areas of large neutrino telescopes like a fraction of the Nestor  $km^2$  detector.

For example in figure 9, it is shown the estimated effective area as a function of the muon energy for different configurations of a NESTOR tower.

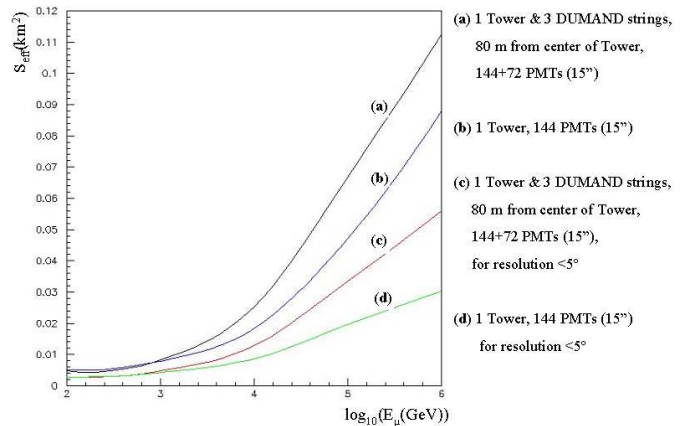


Figure 9: Effective area as a function of the muon energy for many different conditions.

## IV. CONCLUSIONS

The NESTOR collaboration has developed a very detailed detector simulation package (Full Simulation) based on the Geant4 framework. In order to simulate large neutrino telescopes (e.g.  $km^3$ ) a fast version of the version has been developed, by parameterizing, as functions of the physical parameters, complicated phenomena (e.g. e/m showers). Detailed comparisons proved that the fast simulation offers an adequate fast tool in simulating the performance of large neutrino telescopes.

## REFERENCES

- [1] L.K. Resvanis (1992), 2nd NESTOR International Workshop, 1992, L.K. Resvanis editor.
- [2] L.K. Resvanis et al. High Energy Neutrino Astrophysics (1992), V.J. Stenger, J.G. Learned, S. Pakvasa and X. Tata editor.
- [3] Geant 4 Simulation Package, [wwwasd.web.cern.ch/wwwasd/geant4/geant4.html](http://wwwasd.web.cern.ch/wwwasd/geant4/geant4.html)
- [4] E.G. Anassontzis et al., "The Optical Module for the NESTOR Neutrino Telescope", NIM A479(2002), 439-455

- [5] Khanaev (1992), 2nd NESTOR International Workshop, 1992, L.K. Resvanis editor.
- [6] E. Anassontzis (1994), Nuclear Instruments and methods A349, (1994),242.
- [7] A. Tsirigotis, phd in preparation.
- [8] A. Tsirigotis, “Reconstruction, Background Rejection, Tools and Methods”, these proceedings.
- [9] G. Bourlis, phd in preparation.
- [10] S.E. Tzamarias, “NESTOR first results. Electronics-DAQ-Data Analysis”, these proceedings.
- [11] A. Okada 1994 Astroparticle Physics 2 393.

# Reconstruction, Background Rejection, Tools and Methods (NESTOR) VLVvT Workshop 2003

A. Tsirigotis

Hellenic Open University for the NESTOR Collaboration  
tsirigotis@eap.gr

## Abstract

We report on the reconstruction and background rejection strategies used in NESTOR. The data collected during the 2003 Run will be used to demonstrate the tracking capabilities of the NESTOR detector and the performance of the reconstruction and background rejection algorithms.

## I. INTRODUCTION

The NESTOR (Neutrino Extended Submarine Telescope with Oceanographic Research) neutrino telescope is detecting the Cerenkov radiation produced by  $\nu$  – induced muons and/or showers of charged particles in a large volume of sea water. The NESTOR site is located at the South West of Peloponnese (Greece), at the seabed of the Ionian Sea. In fact this is where one finds the deepest waters in Mediterranean sea, 5200m. The NESTOR collaboration has located a  $8km \times 9km$  horizontal plateau at a depth of 4000 m [1, 2]. The plateau is at a mere distance of 7.5 nautical miles from shore. Extensive studies of environmental properties have been made [3, 4]. These measurements show that the water transmission length is 55m at a wavelength  $\lambda = 460nm$ . The underwater currents have been measured and they have been found minimal, i.e. a few centimeters per second [5]. Also the sedimentology analysis is completed [6].

## II. NESTOR DETECTOR

The basic detector unit is a rigid hexagon, shown in Figure 1, made out of titanium with a diagonal of 32 m. At the tip of each arm of the hexagonal floor there is a pair of two 15 inch photomultiplier tubes (PMTs) inside benthos glass housings [7, 8], one looking upwards and the other downwards. The electronics which are responsible for signal sensing, triggering, digitization and data transmission to the shore are housed inside a large titanium sphere (1m in diameter) located at the center of the hexagonal floor. The electrical pulses of the PMTs are digitized by the Analog Transient Waveform Digitizers (ATWDs) of the floor electronics board (developed at Lawrence Berkeley National Laboratory). The digitized waveforms are transmitted to shore, where the raw data are recorded.

By stacking 12 of these floors in the vertical, with a distance between them 30m, they create a tower shown in

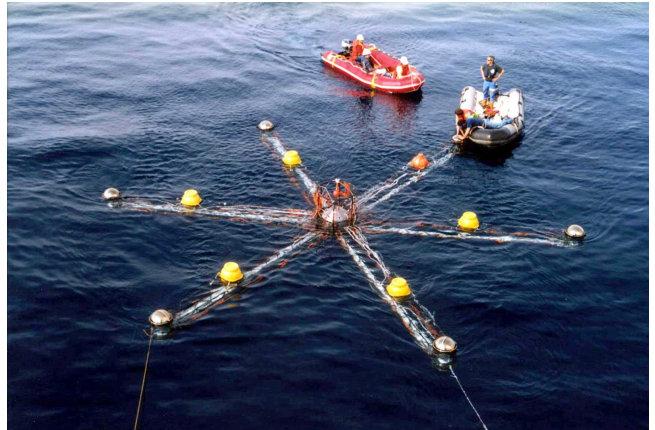


Figure 1: A photograph of the NESTOR Floor taken during last deployment, a few moments before it was lowered to 4000m

Figure 2, which is connected to the shore by an electrooptical cable (18 fibers plus 1 conductor). The effective area of a NESTOR Tower in reconstructing throughgoing muons of energy  $> 10TeV$  is greater than  $20000m^2$ , whilst the energy threshold of such a detector is as low as 4 GeV for contained tracks.

In March 2003, using the cable ship RAYMOND CROZE of France Telecom, the hexagonal floor shown in Figure 1 was deployed fully equipped with electronics and associated environmental sensors to a depth of 4000m. In the control room, during the deployment and operation of the detector, the parameters of the detector were continuously monitored. These include the floor orientation (compass and tilt meters), temperatures, humidity and hygrometry within the Titanium sphere, PMT high voltages, as well as data from other environmental instruments mounted on the sea-bottom station (pyramid), such as pressure meters, current meters, etc.

## III. BACKGROUNDS

As with any experiment, a good signal-to-noise ratio is the key to success. In a neutrino underwater experiment there are three sources of background.



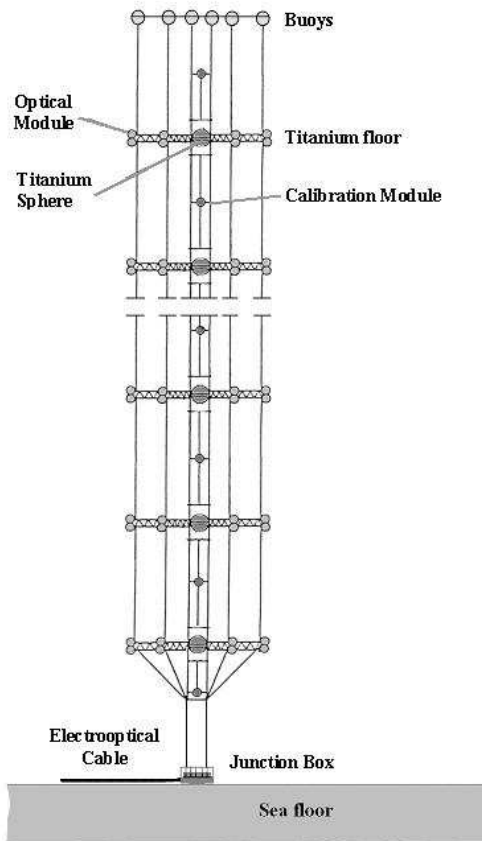


Figure 2: NESTOR Tower

### A. Radioactive Decay

The optical background due to  $K^{40}$  beta decay plus the thermionic noise from the PMTs contribute a baseline signal level of 50 kHz per PMT. This rate is constant as a function of the time and does not depend on the trigger criteria (coincidence level), demonstrating the unbiased of the selection triggers. The  $K^{40}$  optical background, mainly at the single photoelectron level, can be used for calibration purposes. In Figure 3 a typical pulse height distribution of a PMT during data taking is shown. This distribution is very well described as the overlap of the thermionic background shape and the Polya distributions for one and two photoelectrons, which have been established during the calibration runs in the laboratory.

$K^{40}$  optical background can be decreased by increasing the thresholds. The measured trigger rates using data collected with 4fold majority coincidence trigger as well as the Monte Carlo predicted trigger rates for atmospheric muons, are shown in Table 1. Increasing thresholds does not affect seriously the detection efficiency, while the  $K^{40}$  contribution to the trigger rate is significantly decreased.

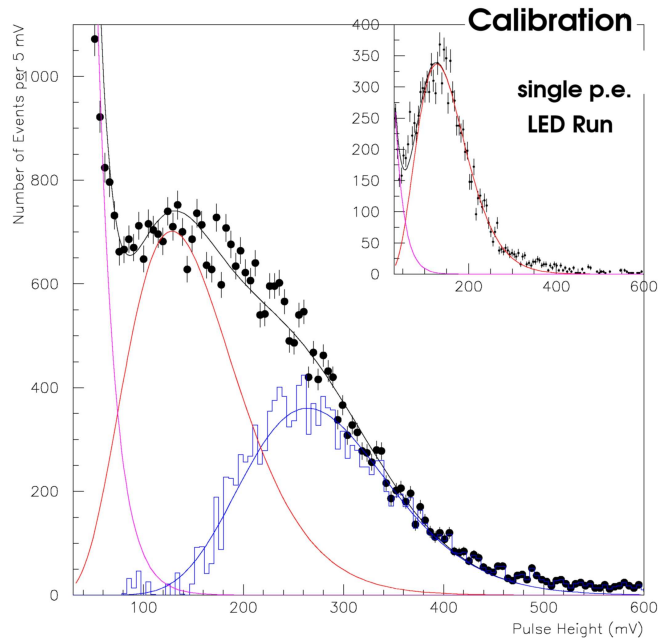


Figure 3: The Pulse Height distribution of one PMT using data from deep sea (main plot) and from calibration runs (insert plot). The three different components correspond to the PMT dark current, the single photoelectron, and the double photoelectron spectrum.

Table 1: Trigger Rates

	Thresholds at 30 mV	Thresholds at 120 mV
<b>Measured Total Trigger Rates (greater or equal to 4fold)</b>	$2.61 \pm 0.02 Hz$	$0.12 \pm 0.01 Hz$
<b>M.C. Prediction (atmospheric muons only)</b>	$0.141 \pm 0.005 Hz$	$0.12 \pm 0.01 Hz$

### B. Bioluminescence

There are period of times where the PMT rates are significantly higher than the 50 kHz baseline signal level, as shown in Figure 4. This effect is a result of the bioluminescence activity of living organism populations. The signal bursts due to the bioluminescence activity have a variable duration 1 to 10 seconds and are easily identified and rejected. Bioluminescence activity reduces exponentially with water depth, is correlated with water currents, and is site and season dependent [9]. At the NESTOR site the contribution of bio-activity to the dead time of the detector has been estimated from the accumulated data to be of the order of 1% of the active experimental time; values of up to 40% have been reported at other sites.

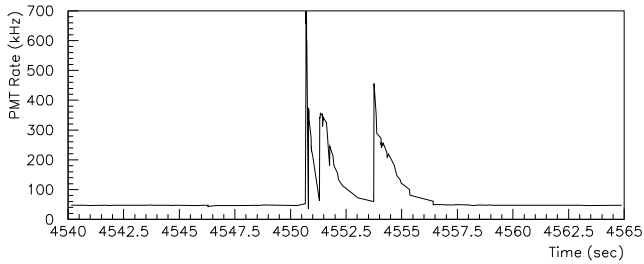


Figure 4: Typical photomultiplier rate as a function of time during bioluminescence activity.

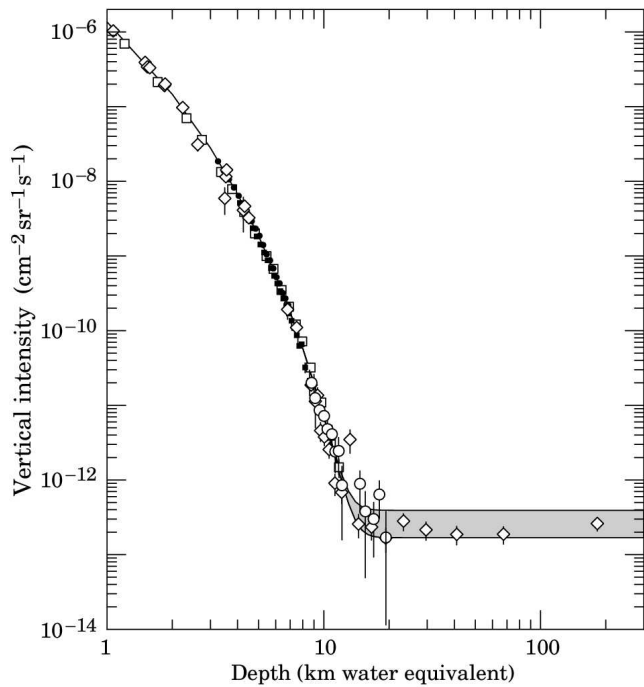


Figure 5: Cosmic-ray muons depth intensity curve [10]

### C. Cosmic Rays

Cosmic-ray muons represent the principal background for a neutrino telescope and this depends on the depth of the water “shielding”. In Figure 5 the depth intensity curve of cosmic-ray muons is shown. Notice that the attenuation between 1000 and 4000m is more than two orders of magnitude. Limiting the cosmic-ray background also removes many of the uncertainties in track reconstruction, such as wrongly assigning a downward-going muon as an upward-going track. Down coming atmospheric muons can be misreconstructed as upcoming neutrino induced muons (mirror tracks). Using the accumulated charge on each PMT we can reduce the mirror track background, as described in section V. The NESTOR collaboration’s decision to have upward, as well as downward-looking phototubes seems to be well justified. At 4000m an unambigu-

ous upward-coming or horizontal muon track must have been generated by a neutrino.

## IV. CALIBRATION AND SIGNAL PROCESSING

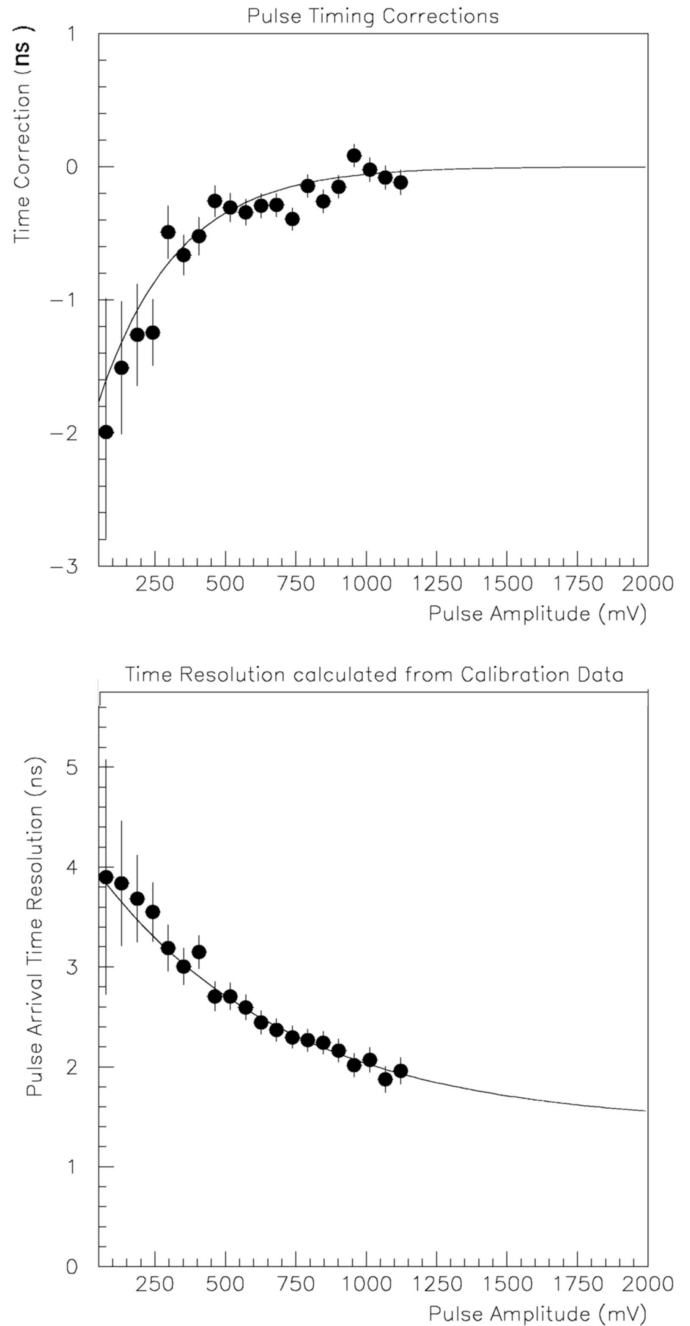


Figure 6: Slewing correction (top figure) and TTS (bottom figure) as a function of the pulse amplitude, estimated using calibration data taken during detector operation at 4000m. They are found to agree very well with the measured ones from calibration runs in the LAB.

Calibration in the sea uses LED flasher modules mounted above and below the detector floor. Using light pulses from the calibration system several experimental parameters (e.g. PMT timing, gains etc.) can be monitored. Further analysis of the calibration data, results to in situ measurement of PMT characteristics, such as slewing Transit Time Spread (TTS). Figure 6 shows the variation at the PMT pulse arrival time and the TTS as functions of the PMT pulse amplitude, as they have been estimated from the calibration runs.

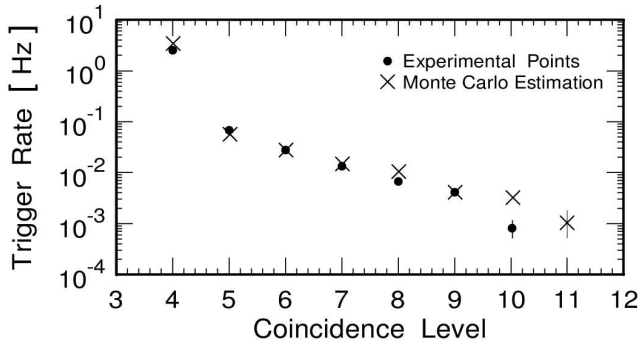


Figure 7: Measured and Monte Carlo estimated trigger rates of  $\geq 4$ -fold coincidences at the 0.25 p.e. threshold level.

In Figure 7 the measured trigger rates for different coincidence trigger levels are compared with the corresponding Monte Carlo estimations [11] based on the Okada atmospheric muon flux parametrization [12], the natural  $K^{40}$  radioactivity in the sea water and PMT dark current.

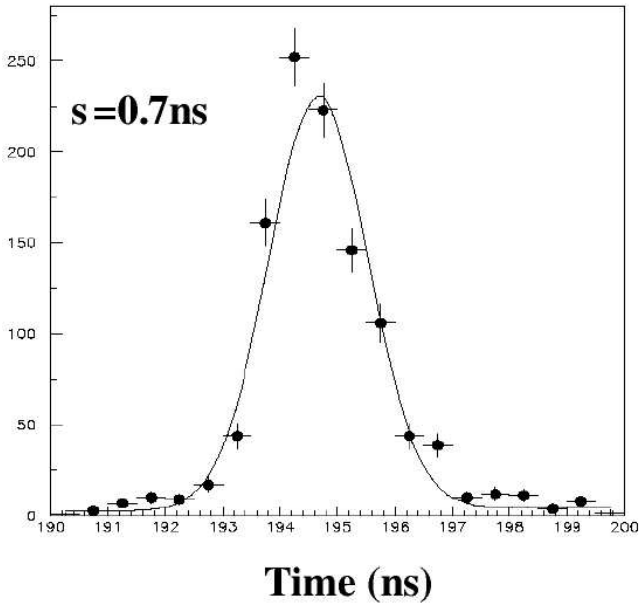


Figure 8: Software to hardware trigger time difference (arbitrary time offset)

In the offline analysis, the digitized waveform of each PMT has to go through a processing procedure in order to sub-

tract baselines and to be corrected for attenuations, slewing, etc. This processing stage utilizes calibration parameters determined in the laboratory before the deployment. As a result of the signal processing the fast rise time of the PMT pulses is recovered (8 nsec at the single photoelectron level), multiple pulses are easily disentangled and also the arrival time, the pulse height and the total charge are accurately determined. In the offline analysis the trigger is reformed and compared to the digitized hardware trigger transmitted to shore, on an event by event basis. In Figure 8 the software to hardware trigger time difference is shown, demonstrating the performance of the signal processing procedure.

## V. TRACK RECONSTRUCTION

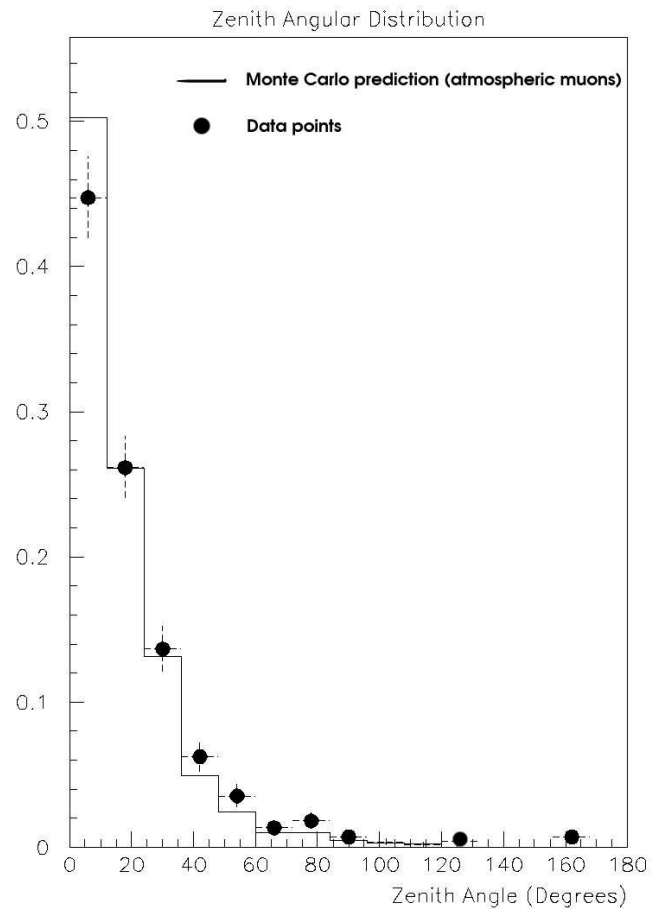


Figure 9: Monte Carlo expectation of the zenith angular distribution of atmospheric muons at 4000m (solid line), compared to the zenith angular distribution of reconstructed events (solid points)

In order to reconstruct tracks, events with more than five active PMTs within the trigger window are selected. The estimation of the track parameters is based on  $\chi^2$  minimization using the arrival times of the PMT pulses. In most cases the procedure converges to two or occasionally several minima, often due to an inherent geometrical degeneracy. To resolve this

ambiguity, a second level algorithm is used that takes account of the measured number of photoelectrons at each PMT and the number expected from the candidate track, and performs a likelihood hypothesis comparison.

Several tests of the track reconstruction procedures have been carried out using both data and Monte Carlo generated events [11]. The results demonstrate that the estimation of the track parameters is unbiased. Figure 9 shows the measured zenith angular distribution (solid points) of reconstructed events using a fraction ( $\sim 30\%$ ) of the collected data. The reconstructed tracks used in this measurement have been selected by means of the minimum  $\chi^2$  fit ( $\chi^2$  probability  $> 0.1$ ), the track quality based on the number of photoelectrons per PMT and on the total accumulated photoelectrons per hit per track ( $> 4.5$ ). The histogram shows the predicted angular distribution of atmospheric muon tracks (for the NESTOR floor geometry and reconstruction efficiency) derived from Monte Carlo calculations using Okada's phenomenological model.

## VI. Extension to many floors

Further improvements in the reconstruction efficiency are to be expected, but efficient neutrino detection will require the deployment of at least four floors, which is planned for next year. Each floor runs independently and the event is builded online from a collection of several sub-events when certain requirements (e.g. timing) are fulfilled.

In the case of many towers, using the hits on the PMT's of each tower, track segments are reconstructed. Then the matched track segments are combined to a global track fit, and a second iteration is performed in order to collect more points. Trivially the best strategy is to use all the PMTs independently of tower, but this is depended on the trigger, data transmission (e.g. optoelectronics) and DAQ architecture.

## REFERENCES

- [1] L. K. Resvanis (1992), 2nd NESTOR International Workshop, 1992, L. K. Resvanis editor.
- [2] L. K. Resvanis et al. High Energy Neutrino Astrophysics (1992), V. J. Stenger, J. G. Learned, S. Pakvasa and X. Tata editor.
- [3] Khanaev (1992), 2nd NESTOR International Workshop, 1992, L. K. Resvanis editor.
- [4] E. Anassontzis (1994), Nuclear Instruments and Methods **A349**, (1994), 242.
- [5] Demidova, 2nd NESTOR International Workshop (1992), L. K. Resvanis, editor.
- [6] E. Trimonis, 2nd NESTOR International Workshop (1992), L. K. Resvanis, editor.
- [7] E.G. Anassontzis, et.al., "The Optical Module for the NESTOR Neutrino Telescope", NIM A **479** (2002) 439-455.
- [8] A. Tsirigotis, "The NESTOR Optical Module", these proceedings.
- [9] M. Solan, "Bioluminescence in the Deep Sea", these proceedings.
- [10] K. Hagiwara et al, Phys. Rev. **D66**, 010001 (2002)
- [11] A. Leisos, "NESTOR Simulation Tools and Methods", these proceedings.
- [12] A. Okada 1994 Astroparticle Physics **2** 393.

# Muon Track Reconstruction and Data Selection Techniques in AMANDA

Christopher H. Wiebusch *for the AMANDA Collaboration*\*

University Wuppertal, Gausstraße 20, 42119 Wuppertal, Germany  
christopher.wiebusch@physik.uni-wuppertal.de

*Abstract*

We review track reconstruction methods and data selection techniques used in AMANDA. Special attention is given to future improvements which are in particular related to the capabilities of a new data acquisition installed in 2002/2003. It is based on the sampling of the full wave forms of photomultiplier signals by Transient Waveform Recorders (TWR).

## I. INTRODUCTION

Main aim of under-ice/water neutrino telescopes is the observation of high energy neutrinos. They are identified by detecting Cherenkov photons from secondary leptons and hadrons which are produced in charged and neutral current interactions of the neutrinos in or close to the detector.

Two main experimental signatures can be distinguished. The first are so-called *track-like* events. Here, a high-energy  $\nu_\mu$  creates in a charged current reaction a high-energy muon. The muon direction is nearly collinear with the neutrino direction and may travel distances of several kilometers through the ice. The emitted cone of Cherenkov photons is detected by a lattice of photomultiplier tubes (PMTs). The measured time and amplitude information is used to reconstruct the direction of the muon. Radiative energy loss processes generate secondary charged particles along the muon trajectory, which also produce Cherenkov photons. This additional light allows an estimate of the muon energy. At high energies ( $\gtrsim 1$  TeV) these secondary processes dominate the light yield and the pure Cherenkov cone of the muon can be distorted. In this paper we focus on this event type.

The other signature is called *cascade* and is related to  $\nu_e$  and  $\nu_\tau$  interactions and neutral current interactions from  $\nu_\mu$ . Hadronic and electro-magnetic cascades are confined to a volume of a few cubic meters. The optical signature is an expanding spherical shell of Cherenkov photons with a larger intensity in the forward direction. The reconstruction of these events is done using similar techniques and is described in [3].

## II. TRACK RECONSTRUCTION

### A. Likelihood Methods

The estimation of the muon track parameters  $\{\mathbf{a}\}$ , i.e. the direction, location, time and energy, is done by maximizing<sup>1</sup> the likelihood

$$\mathcal{L}(\text{Event} \equiv \mathbf{x} | \text{Track} \equiv \mathbf{a}) \quad (1)$$

with  $\{\mathbf{x}\}$  being the set of experimentally measured signal times and amplitudes in each PMT.

In an ideal environment photons would arrive at the positions of the PMTs at times purely determined by the track geometry. However, in AMANDA the dominant effect on photon propagation is scattering in the ice. On average this effect shifts arrival times to later times and it also modifies the probability of a hit. The time delay depends strongly on the distance,  $d$ , of the PMT from the track. Since the PMTs have a non-uniform angular response,  $p(t_{\text{res}})$ , it also depends on the orientation,  $\eta$ , of the PMT relative to the muon track. PMTs facing away from the track can only see light that scatters back towards the PMT photocathode. Unlike track reconstruction in water, it is mandatory to include a detailed model of the photon propagation in the ice in the fitting procedure.

The simplest likelihood function models the arrival times of single photo-electrons (SPE)  $i$  at the locations of the hit PMTs by a probability density function (p.d.f.)  $p_1$  for the time delay due to scattering

$$\mathcal{L}_{\text{time}} = \prod_{i=1}^{N_{\text{hits}}} p_1(t_i | \mathbf{a} = d_i, \eta_i) . \quad (2)$$

Note that one PMT may contribute to this product with several hits. The function  $p_1(t_{\text{res},i} | \mathbf{a})$  is obtained from the simulation of photon propagation through the ice.

Another important aspect of scattering in ice, different to water, is that the arrival time distribution of several photons is spread out in time. In particular for high energy events this spread in arrival time can last several  $\mu\text{s}$ . The first photon out of several is usually less delayed than the average single photon, which modifies the probability distribution of the detected hit time. Therefore the statistics in arrival times plays an important role when several photons are detected within one PMT.

Various more advanced likelihood descriptions allow to model the arrival time distributions of detected multi photo-electron signals (MPE), explained in [2]. Examples here are to

\*For a full authorlist see [1]

<sup>1</sup>Technically one usually minimizes  $-\log(\mathcal{L})$ .

describe the arrival time of the first out of  $N$  photons or the full distribution of arrival times detected e.g. by transient waveform recording (see section V. ) in a PMT. It is important to note that all these advanced likelihood descriptions can be constructed with the knowledge of the SPE p.d.f. and its cumulative only.

In a different approach, equation (1) is modified according to Bayes' theorem to maximize the total probability of observing an event

$$\mathcal{L}(\text{Track}|\text{Event}) = \mathcal{L}(\text{Event}|\text{Track}) \cdot \frac{\mathcal{L}(\text{Track})}{\mathcal{L}(\text{Event})} \quad (3)$$

Here,  $\mathcal{L}(\text{Track})$  can be identified as the prior probability of observing a certain track, while  $\mathcal{L}(\text{Event})$  is an overall normalization.

One important application [2, 4] is to model the well known zenith dependence of the flux of background atmospheric muons in a prior likelihood  $\mathcal{L}(\text{Track}) = P(\theta)$ . With this particular choice, some tracks, which would otherwise reconstruct as up-going, reconstruct as down-going tracks. This greatly reduces the rate at which penetrating atmospheric muons are mis-reconstructed as up-going neutrino events.

## B. Implementation

The most important aspect when implementing the likelihood function is the proper modeling of the optical properties of the ice. For this reason, dedicated Monte Carlo simulations of the photon propagation have been developed [6]. The result of these simulations are stored in large look-up tables and allow to retrieve the expected number of photons which hit an PMT and the p.d.f. of their arrival times as function of the geometrical track parameters.

Three different simulations methods of the photon propagation have been developed. In the simplest version vertical ice structures have been neglected and averaged ice parameters are used. Another simplification here is to use an effective wavelength dependency of scattering coefficients obtained from a convolution of the emitted Cherenkov spectrum with the cathode response and the distance dependency of the wavelength-dependent absorption. In the second, more advanced version, the same technique is used, but different vertical ice layers are introduced by simulating each PMT response according to its local optical environment. The most accurate, recent improvement is achieved by simulating the full photon propagation from its emission point to the receiving PMT, including the wavelength and depth dependency of scattering and absorption.

These tables which originally had been developed for the Monte Carlo description of the experiment can be used also to calculate the likelihood of arrival times (equation (1)). A reconstruction based on the simplest version of these tables has been implemented. However, most previous AMANDA analyses are based on a simplified parameterization of the probability density of arrival times, which we call *Pandel function*. It depends only on the distance of a track to the PMT and the

orientation of the PMT and is based on a Gamma distribution.

$$p(t_{\text{res}}) \equiv \frac{1}{N(d)} \frac{\tau^{-(d/\lambda)} \cdot t_{\text{res}}^{(d/\lambda)-1}}{\Gamma(d/\lambda)} \cdot e^{-\left(t_{\text{res}} \cdot \left(\frac{1}{\tau} + \frac{c_{\text{medium}}}{\lambda_a}\right) + \frac{d}{\lambda_a}\right)},$$

$$N(d) = e^{-d/\lambda_a} \cdot \left(1 + \frac{\tau \cdot c_{\text{medium}}}{\lambda_a}\right)^{-d/\lambda},$$

Here,  $c_{\text{medium}} = c_{\text{vac}}/n$  is the speed of light in ice,  $\lambda_a$  the absorption length,  $\Gamma(d/\lambda)$  the Gamma function and  $N(d)$  a normalization factor, which is given by equation 4. This formulation has free parameters  $\lambda$  and  $\tau$ , which depend on the distance  $d$  and other geometrical parameters. They are determined by a global fit to the above Monte Carlo models. A particular advantage of this function is that its cumulative can be calculated analytically, which simplifies the construction of multi-photon (MPE) likelihoods.

While AMANDA simulations are already based on the most advanced ice modeling, the reconstruction is still based on the simplest averaged ice-model which neglects vertical ice structures. Therefore the performance results presented here (section III. ) are not optimal. Improving the optical model of the likelihood will be a major subject of future improvements.

## C. Initial track

The likelihood reconstruction needs an initial track hypothesis to start the minimization. This track can be derived from fast, usually non-iterative algorithms which are also used for a fast initial event selection i.e. online filtering. The *Line-fit* algorithm [2], which was widely used since the DUMAND experiment, has been mostly replaced in AMANDA by a more efficient pattern recognition procedure: the *Direct Walk* algorithm [2]. It starts by selecting pairs of distant hits ( $d > 50\text{m}$ ) having a time difference corresponding to a relativistic connecting track. In the next step further associated hits are selected. Here, small time delays with respect to this track are consistent with scattered photons and are allowed. Initial track candidates are defined by a minimum number of 10 associated hits which are spread reasonably well along this track. In case of more than one track candidate a cluster search is performed on track candidates of small angular differences. The average direction of that cluster with most track candidates is finally selected as initial track. The other candidates can be interpreted as independent muon tracks and are used for reconstructing an alternative hypothesis.

## D. Likelihood Maximization

Not only the likelihood model itself but also the technical procedure of finding the maximum plays an important role during the reconstruction. We have found that a *Simplex* method is almost as accurate as gradient methods such as *Powell's* but much faster and can be used for maximizing the likelihood.

However, the likelihood is often characterized by several local maxima. Local maxima can arise e.g. due to symmetries of the detector. More complicated algorithms like *simulated annealing* have been used successfully in order to find the global maximum. The following simple iterative algorithm has been found efficient in finding the global maximum. The event is reconstructed  $N$  times with each a different random initial track and the largest found maximum is selected. In order to enhance the speed only the two direction angles are randomized and reasonable values are chosen for the time and spatial coordinates by shifting the track coordinates along the direction closest to the center of gravity of hits and by avoiding negative arrival times.

### E. Backgrounds and Data Selection Techniques

The quality of track reconstruction strongly depends on the data selection. Additional criteria are applied to reject background and select well reconstructed events. Usually these criteria (a) evaluate information which was not used in the reconstruction and (b) reject specific signatures of known background classes. An example for such backgrounds are high energy down-going muons, which emit a bright secondary cascades. These cascades can distort the Cherenkov cone and confuse the reconstruction. Important selection criteria are the total likelihood, the ratio of largest likelihoods found in the upper and lower hemisphere, the total number of unscattered photons, the *lever-arm* of the reconstruction and distribution of hits along the assumed track. An overview on the backgrounds and selection cuts is given in [2].

## III. TRACK RECONSTRUCTION PERFORMANCE

In the following we show the performance in angular resolution for the current implementation of the single photo-electron (SPE) reconstruction. The results are shown for simulated atmospheric neutrinos in AMANDA-II.

The angular resolution strongly depends on the applied data selection. For a selection typical for a physics analysis a median space angle error of about  $2^\circ$  is achieved. As shown in figure 1 the resolution is best for nadir angles of about  $45^\circ$ . For more vertical tracks fewer strings have a signal and the resolution degrades. For more horizontal tracks the resolution also becomes worse because of the geometry of AMANDA-II, which extends more into the vertical than into the horizontal direction. For IceCube [?], with a more symmetrical geometry, best results are achieved for the horizon and the resolution above 1 TeV is about  $0.6^\circ$  to  $0.8^\circ$ .

The dependence of the resolution on the muon energy is shown in figure 2. Best results are obtained for minimum ionizing muons of a few 100 GeV energy. For smaller energies the resolution becomes worse because the muon tracks are shorter. Also for larger energies the resolution slightly degrades because of the used SPE reconstruction model. At

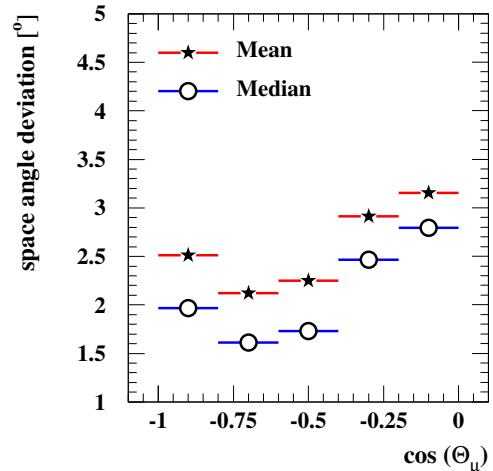


Figure 1: Space angle error as function of the zenith angle.

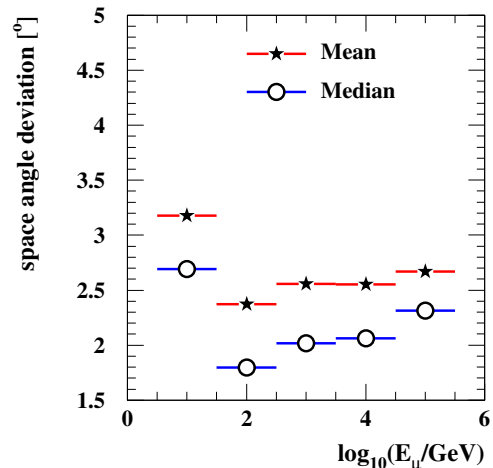


Figure 2: Space angle error as function of the muon energy.

higher energies the statistics of multi-photon arrival times is better modeled by the MPE reconstruction. Also the underlying reconstruction model of a single muon track is not sufficiently accurate here. Above  $\gtrsim 1$  TeV, light from secondary muon energy loss begins to dominate. It outshines and may distort the clean Cherenkov cone signature from the muon itself. Improving the performance at high energies is a major subject of current work.

Another important aspect is the dependency of the resolution and reconstruction efficiency from calibration and geometrical uncertainties. We have found that within the experimental uncertainties of a few ns, the performance is not affected. As example figure 3 shows, that for time calibration errors  $< 10$ ns the zenith resolution is not affected [2].

## IV. ENERGY RECONSTRUCTION

When searching for an excess of extraterrestrial high energy neutrinos over the steeply falling background of atmospheric

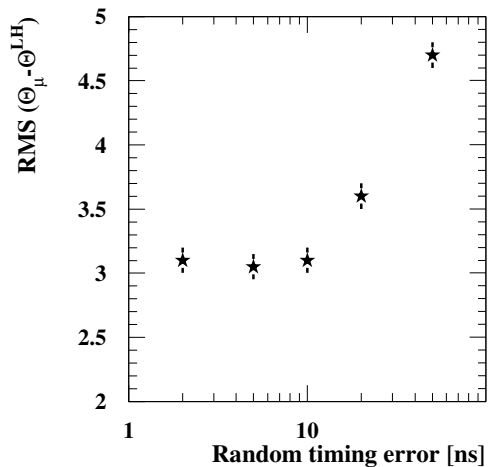


Figure 3: RMS error of the reconstructed zenith angle as function of a random time calibration error of PMTs

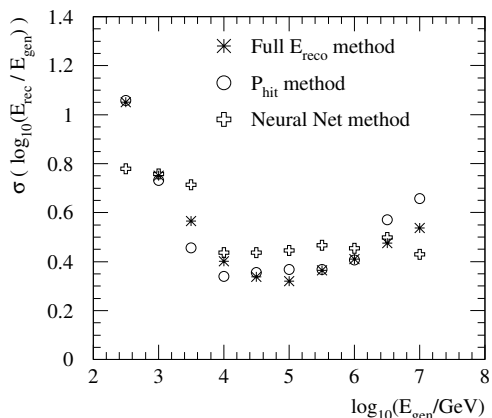


Figure 4: Energy resolution  $\sigma(\log_{10}(\Delta E_{rec}))$  as function of the simulated muon energy for 3 different reconstruction methods.

neutrinos it is of particular interest to reconstruct the muon energy. Several strategies have been developed to measure the muon energy and infer the initial neutrino energy. All methods have in common that they quantify the additional amount of light from muon energy loss which is registered in addition to the photons from the bare muon.

Figure 4 compares the resolution of different methods. The simplest method,  $P_{hit}$ , evaluates the probabilities of PMTs which have seen a signal and those which have not seen a signal with respect to their distance from the track. Interestingly, this method achieves a resolution comparable to the other more sophisticated algorithms. However at high energies  $E > 1\text{PeV}$  its resolution degrades due to the saturation of the relatively small AMANDA detector — essentially all PMT are hit. As improvement, the *Full  $E_{reco}$  method* evaluates the likelihood of the observed amplitudes in each PMT. Above 10 TeV its results are better than the  $P_{hit}$  method. A completely different approach to the previous methods, which model likelihoods of the observed photon signal, is the *Neural Net Method*. Here, the energy is inferred with an artificial neural network. Its in-

puts are simple observables which are correlated with the muon energy. Examples are e.g. the number of hit PMT or the mean duration of an event. Its resolution is on average slightly worse than the direct methods. Its advantages are that it has a relatively constant resolution and stable performance over the full energy range, which makes it particularly suitable for unfolding the energy spectra of muons [9]. Also, because of the simplicity of the used input observables, it is robust and independent of the quality of the geometrical fit. On the other hand we plan in the future to improve the resolution of the neural net by providing details on the track geometry as additional input observables.

## V. TRANSIENT WAVEFORM RECORDING

In the austral summer 2002/03 the AMANDA data acquisition has been substantially upgraded [8]. A total of 580 channels (well operating PMT installed at depths close to the core of AMANDA-II) are now read out with 100 MHz FADC Modules of 12bit amplitude resolution. This readout overcomes several deficits of the previous AMANDA DAQ [8] and improves the quality of recorded information. With this system the dead-time is reduced from typically 15% to nearly 0% which corresponds to an immediate gain in the sensitivity of the experiment. Previously only the edges of 8 hits above a fixed threshold were recorded with a multi-hit TDC and only the largest amplitude of all PMT hits was recorded with a peak sensing ADC. Especially for high energy signals the TWR DAQ is not limited by the number of hits. The yield in information is demonstrated in figure 5 which shows a recorded waveform of one PMT in a high energy event. The waveform shows several hits of small amplitude (1 p.e.). Two delayed larger bursts with multi photo-electron hits are clearly visible. The individual amplitudes and arrival times of photons can now be measured and the full time sequence of arriving photons deduced. Another prospect is the application of pattern recognition algorithms, i.e. in this example the appearance of a delayed double burst of multi photo-electrons amplitude is characteristic for a bright secondary muon energy loss. The individual recorded photons can thus be identified and classified. This allows to evaluate them separately with different dedicated reconstruction algorithms.

## VI. SUMMARY AND OUTLOOK

In the first years the reconstruction work in AMANDA was focused on establishing AMANDA as a working neutrino telescope. It was demonstrated that the huge background from down-going muons can be rejected [4] and a variety of physics results have been obtained [5]. The currently used methods are still subject to substantial improvements in three major fields in the future: First, the current reconstruction assumes a single minimum ionizing track, a model which is incorrect es-



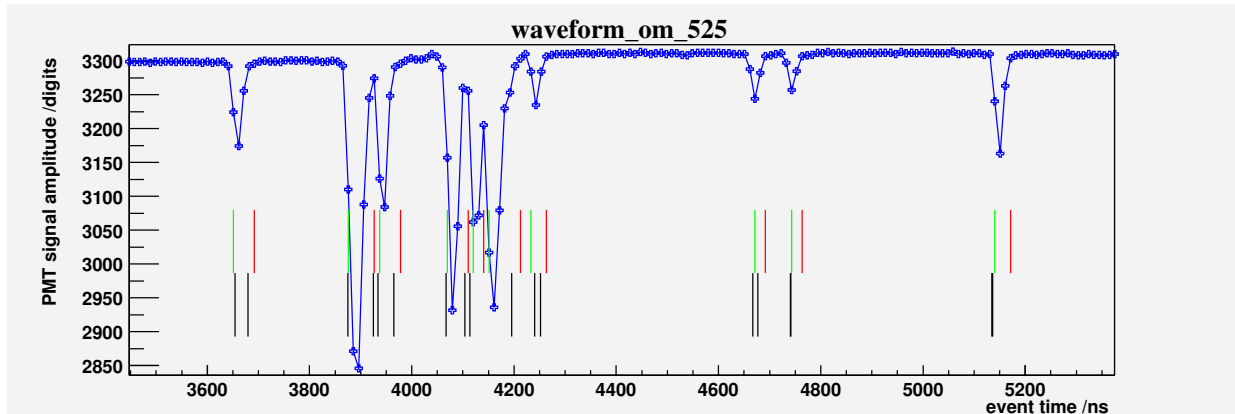


Figure 5: Example of a complex PMT waveform. The vertical lines show time-stamps as recorded by the the old DAQ and identified in new TWR DAQ, respectively.

pecially at high energies. Here, we hope to gain from pattern recognition algorithms, which will pre-classify the constituents of the event in muons and secondary cascades and assign the detected photon to these constituents for more specific reconstructions. Secondly the underlying likelihood function for the photon propagation is not based on the best knowledge of optical properties i.e. does not include their vertical dependence. A proper implementation of this has recently been done for the AMANDA Monte Carlo [6] and will be done also for the reconstruction. As third point the previously mostly used single photon likelihood model can be updated to properly model the multi-photon arrival times as more relevant for higher energies and use the full information available from the recorded waveforms.

## REFERENCES

- [1] J. Ahrens, et al. (The AMANDA Collaboration), *Search for extraterrestrial point sources of neutrinos with AMANDA-II*, accepted for publication by Phys. Rev. Lett., astro-ph/0309585.
- [2] J. Ahrens, et al. (The AMANDA Collaboration), *Muon Track Reconstruction and Data Selection Techniques in AMANDA*, submitted for publication to Nuclear Instruments and Methods A, August 2003.
- [3] J. Ahrens, et al., (The AMANDA Collaboration), Phys. Rev. D 67 (2003) 012003.
- [4] J. Ahrens, et al., (The AMANDA Collaboration), Phys. Rev. D 66 (1) (2002) 012005.
- [5] E. Bernardini, et al., (The AMANDA Collaboration), these proceedings.
- [6] S. Hundertmark, et al., (The AMANDA Collaboration), talk at session A1.2 (this conference) and *2nd Workshop on Methodical Aspects of Underwater/Ice Neutrino Telescopes*, DESY-PROC-2002-01, page 105.
- [7] Ch. Spiering, et al., (The IceCube Collaboration), these proceedings.
- [8] W. Wagner, et al., (The AMANDA Collaboration), Proc. 28<sup>th</sup> ICRC, Tsukuba (Japan), 1365 (2003).
- [9] H. Geenen, et al., (The AMANDA Collaboration), Proc. 28<sup>th</sup> ICRC, Tsukuba (Japan), 1313 (2003).



**Architecture**  
**Sea Operations**  
**Electrical Power Systems**  
**Mechanics**



# Subsea Electric and Optic Connections Allowing for Flexible System Architecture

Steven S. Thumbeck

Ocean Design, Inc., 9 Aviator Way Ormond Beach, Florida 32174 USA  
sthumbeck@oceandesigninc.com

## ABSTRACT

Scientists that deploy experiments in the deep sea have many challenges to overcome in, ensuring that their project will be successful. When an individual desires to build on land and create massive structures such as buildings or bridges, there are inherent obstacles. These activities on land alone are difficult to construct; designers and builders need to contend with schedules, labor, safety, weather and most times the physical scale of work that needs to be performed. Now consider taking large structures made of various materials and deploying them on the seafloor. The challenges become much greater and the result of failure may force a system to be abandoned. This paper evaluates the considerations for connection systems and their ability to create a flexible system while reducing overall system cost, maintaining reliability and increasing functionality.

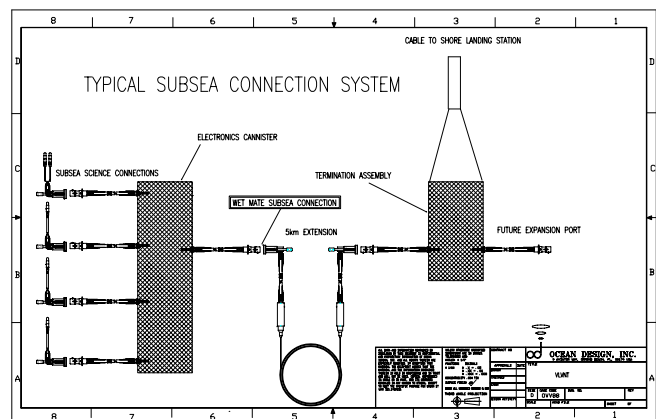
## 1. INTRODUCTION

As scientists place experiments on the seafloor, challenges arise. Each day obstacles surface and inventive solutions are proposed. Typically, a project has a proposal phase requesting funding, a design phase, and a prototyping phase, once the program is awarded. On larger scale systems, test beds or prototype systems demonstrate the feasibility of a project prior to the full system being funded. Even with the phased approach, the “real” test is when the scientist is out at sea on the installation vessel and the deployment is commenced. Many times the success of the program is determined during the initial phases of a program. When individuals are making choices they have many factors to consider, including and not limited to the ratio of total system cost in relationship to functionality and reliability. The ensuing discussions will evaluate subsea electric and fiber optic connections and their impact on the system, and how they should be rated against the factors of system cost, functionality and reliability.

## 2. WHO SHOULD USE SUBSEA CONNECTORS?

Not everyone should use subsea connectors. If a system does not need a component and it does not add value, then why add it. Only when the value of the component exceeds its cost should it be considered. What adds value? Value may be added to a system in a number of ways. Take the initial considerations from the introduction; total

system cost and functionality. With total system cost the obvious upfront impact is the connector price as a component. The total system cost would evaluate the expenditure associated with the servicing and or installation of the equipment. What type of vessel is required to perform the service? How many days will it take? Will weather affect the installation or service? Will adding a subsea connector help reduce these associated costs of ship time and maintenance? The answer in most cases is, yes. Secondly, what type of functionality will be achieved by utilizing subsea connectors versus the traditional hardwired approach? Most new subsea systems are quite large and complex structures. A typical installation would have a cable coming from shore to a remote location on the seafloor where various system components are located. At the cable end would be a termination assembly where the fiber communications and electrical power would be broken out. This structure is normally referred to as the termination or junction box. From the termination is the distribution point to various subsea components containing instruments and communication equipment, as shown in Drawing 1. The subsea connection would allow a deployment in stages. Each piece may be installed individually, including instruments as needed. This staged deployment method will minimize risks and safety concerns during operations in the event of severe weather conditions.



Drawing 1: Typical Subsea Connection System

### 3. COST / FUNCTIONALTY / RELIABILITY

Commercial companies have been working on the production and development of subsea connectors for many years. Some have been successful and some have not. During the consideration for development there are three components to determine if a connector would be suitable for use: *Price, functionality, reliability.*

#### 3-1. Price

Most of the cost savings can be realized in the operational, power savings, added bandwidth, EMI protection, elimination for the need of fiber to electric converters, and the subsequent data losses inherent in performing such a conversion. Initially, as in all emerging technologies, these connectors are viewed as quite expensive in comparison to their counterpart electrical connectors. However, as years pass and the volume of connectors increase, the prices will start to become more stable and the connectors will become affordable for more potential uses.

#### 3-2. Functionality

The functionality of the connector is the main technical and operational advantage that it provides. No conversions are needed and one may directly couple fiber or electric circuits subsea.

#### 3-3. Reliability

Newly introduced products, such as wet-mate connectors will always have reliability concerns. Wet-mate electrical connectors have over a decade of field history. More than 28,000 are estimated to be installed subsea. With this volume and field history fewer questions arise as to their reliability. By contrast, underwater mateable fiber connectors are relatively new to the market with roughly 3,000 units deployed world wide. The subsea electrical connectors utilize standard electrical sockets and electrical pins and are packaged for subsea use. Similarly, the optical circuits utilize standard epoxy polished optical ferrules and split sleeve technology. Mechanical materials such as Titanium, Stainless Steel and Natural rubber elastomeric compounds, have a longstanding history of performance for subsea applications. Reliability is usually equated to Mean Time Before Failure (MTBF). As follows:

$$MTBF = \frac{\text{Cumulative Service Hours}}{\text{Total Number of Failures}}$$

While the total number of failures are limited on electrical products, the reliability numbers calculated illustrate that the connectors are highly reliable. Optical connectors are still quite new and the data demonstrates that their performance is also highly reliable. Current MTBF data for wet-mateable optical and or electrical connectors would result in figures that are well in excess of 1,700 years for electrical WMC's and 386 years for optical WMC's.

$$\text{Electrical MTBF} = \frac{750,000,000 \text{ Hours}}{50} = 1712$$

$$\text{Optical MTBF} = \frac{16,300,000 \text{ Hours}}{5} = 386$$

### 4. SUBSEA CONNECTORS AND CONSIDERATIONS

There are a few basic styles of subsea connectors. Listed below are the three most common types and their attributes:

- Wet Pluggable (Interference type)  
Initial Cost: Low  
Repair Cost: Replacement  
Life expectancy: 7-10 Years  
Advantages: Low Cost  
Limitations: Life Expectancy  
Developed 1950's -1970's
- Dry Mateable Submersible  
Initial Cost: Medium  
Life expectancy: 25-30 Years  
Advantages: Durability Reliability  
Developed 1950's -1970's
- Wet-Mateable Pressure Balanced Oil Filled (PBOF)  
Initial Cost: High  
Life expectancy: 25-30 Years  
Advantages: Durability, Reliability  
Developed 1970's

When reviewing what types of connectors and accessories should be used for a system, there will be many concerns and considerations. Listed below are some of the basics that should be reviewed:

#### **Basic Information to be Assessed:**

- Operating Depth
- Component Materials (316LSS, Titanium)
- Number of Circuits
- Operating Voltage (AC/DC) / Amperage, Wattage

#### **Type Operation for Subsea Connectors:**

- Diver Make-up (Shallow Water)
- ROV Operable (Deep Water)
- Stab Plate (Multiple Connections)
- Dry Mate Submersible (Top Side Connected and Submerged)

#### **Types of Subsea Cables:**

- Multi-conductor Cable - (400M+ Lengths)
- Armoring (Synthetic / Galvanized Steel)
- Pressure Balanced Oil Filled (PBOF) Hose with Wire/Fiber Optic Components – (2-400M Lengths)

### Attaching the Cable to the Connector:

- Molding – Polyurethane / Polyethylene
- Field Installable Testable Assemblies (FITA)
- Hose Fittings – JIC / Barb / Integral

When selecting a connector the following questions should be answered to ensure the proper design and selection criteria are met:

### Related to Connectors:

Are there any special operating considerations (lubrication, maintenance)?

Mating/Demating Force?

Size and Weight?

Materials used, compatibility with system components?

Common system materials may include Structural Steel, Aluminum, Stainless Steel, Titanium, and PVC.

Mate/Demate Cycles?

Mate/Demate at depth?

Maximum Operating depth?

Life Expectancy?

What factory acceptance tests or qualification tests will be performed?

### Related to Terminations:

Has the particular cable been qualified for use with the termination?

Is sealing provided at all cable jacket layers, if so what type?

If the termination were to flood with water, would the unit still operate?

### Other Considerations:

- When using corrosive materials such as Stainless Steel or Steel are Cathodic Protection Systems utilized such as Zinc Anodes, Sea Water Ground Return or Epoxy Paints?

## 5. A TYPICAL SUBSEA WET-MATE OPTICAL CONNECTOR

When the first production wet-mate optic connectors appeared in the commercial market they were designed for general modem communications. The design of these connectors were based on the particular needs of the applications. Thus, the standard wet-mate connector has found its niche for high volume production. These optic wet-mate connectors operate up to 8 fibers or electric circuits that can handle up to 1Kv and a few amps. This style connector is ideal for use with standard modem equipment that would operate at approximately 120 VAC, 2 Amps. These connectors are well suited for standard communications equipment.

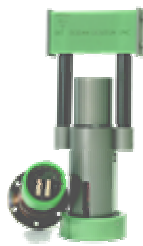


Photo 1: WMC

## 6. ALLOWING FOR SYSTEM RECONFIGURATION

Shown below in Figure 1 is a typical node for which a branch may be established allowing for multiple remote wet mate connections into a backbone communications cable. The trunk cable may be deployed through conventional methods utilizing a standard cable ship. Once the main cable is laid a smaller research style vessel may be used to deploy the node. Connection operations may be made into the backbone cable utilizing standard ROV's.

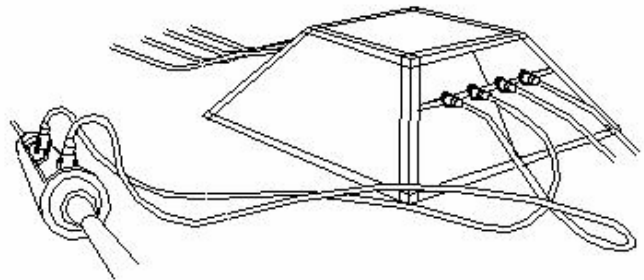


Figure 1: Typical Subsea Connection Node

## 7. EXISTING CABLED SYSTEM CONFIGURATION

Typical cabled systems as shown in Figure 2 have been hardwired and fixed point-to-point. A shore landing station houses all of the power and communications equipment. Based on distance, repeaters are used to extend the continuous length of the cable. Additionally, hardwired branching nodes are used to allow for splitting the cable to two locations. This architecture is extremely reliable; however, very difficult to reconfigure. Recovering the cable would require cutting it subsea and bringing it to the surface as described during the introduction. Such operations are time consuming, costly and weather dependant.

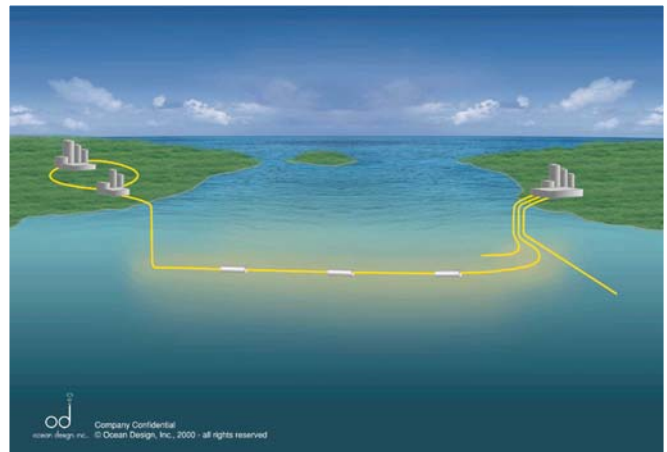


Figure 2: Typical Cabled System

## 8. FUTURE CABLED SYSTEM CONFIGURATION

With the recent advances in subsea optical connectors, more flexible system architecture may be achieved. Shown in Photo 2 (Courtesy Jamstec) is a typical subsea fiber optic connection being made at a depth of 2,100 meters.



Photo 2: Typical Subsea Optic Connection

It is proposed that a trunk cable can be installed with standard cable deployment vessels. Once deployed, research vessels may return and install; science nodes, seismic sensors, instruments, multi-leg branches to shore landings, and any other type of expansion to the cable system. Depicted below in Figure 3 is a system layout that illustrates a backbone cable with branching nodes and various distribution connections.

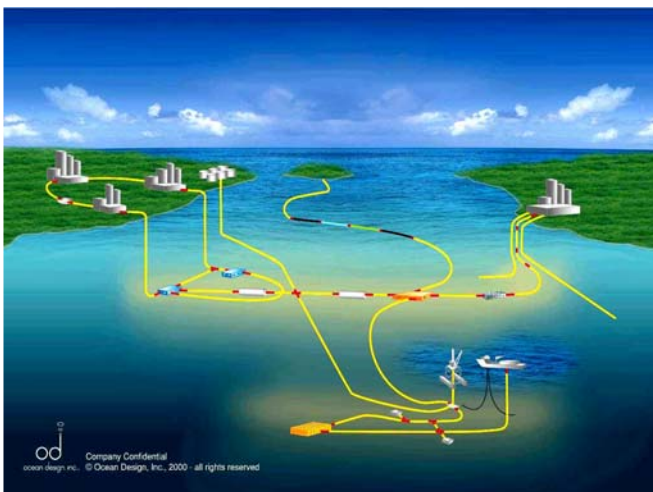


Figure 3: Typical System with Branching Nodes

## 9. CONCLUSION

Many decisions must be made during the development and design of large scale subsea systems. One of the many major considerations would be for the utilization of various subsea connections. It has been proposed that making these choices during the initial phase of a program will have a direct effect on the total system cost and functionality of the subsea system. The long term commitments and considerations should be made to further enhance the value of the subsea program.

## REFERENCES

- 1) Barlow, S.: Advances in undersea connector technology improve efficiency, *Lightwave*, pp.58-60, (October 1999).
- 2) Jenkins, D.: Underwater Mateable Connectors in the Military and Telecom Sectors, *UnderWater Magazine*, (September/October 2002).
- 3) Barlow, S.: The Ruggedization of Hybrid Wet-Mate Connectors, *Sea Technology*, (July 2000).
- 4) Cairns, J.: Hybrid Wet-Mate Connectors: "Writing the Next Chapter", *Sea Technology*, (July 1997).
- 5) Wright, P., Romanisko T.: Extending tieback distances to shore industry's next major objective, *Offshore*, (November 2001).
- 6) Wright, P.: Optical Fiber and Connectors: Critical for Future Subsea Systems, *Sea Technology*, (July 2001).
- 7) Thumbeck, S.: Pioneering Subsea Fiber Optic and Electric Solutions – Communication Interconnect advances and solutions for cabled observatory installation, operation and Maintenance (Focusing on wet-mate capabilities), Proceedings, Third International Workshop, Scientific Use of Submarine Cables and Related Technologies, (25-27 June 2003)



# Consideration on the Installation, Management and Maintenance a the Submarine Network for the km<sup>3</sup> Telescope

M. Sedita for the NEMO collaboration

LNS-INFN, Via S. Sofia 62, 95129 Catania, Italy  
sedita@lns.infn.it

## Abstract

The Management and Maintenance aspects, of an underwater facility, show a lot of difficulties, as their intervention cost is very high. For this reason it's important to develop: redundancy, reliability prevision, recovery and deployment techniques and tools to increase automation.

The NEMO collaboration [1] has investigated on the question about reliability cost vs. the maintenance balance. After considerations about actual technology, for underwater intervention, an R&D activity to increase automation is proposed.

## I INTRODUCTION

The present experiments that are in progress on underwater neutrino telescopes, show some critical aspects. The present approach, used in submarine activities, is strongly dependent on the available technology, which derives mostly from Telecommunication and Oil and Gas. The costs of underwater operations met by such companies are usually high but understandably well supported by companies' budget. The use of these technologies could present a serious problem for the scientific research, as it is strongly dependent on the lower economical resource available.

In this paper we describe how to establish a new basic approach for the management and maintenance of a large underwater apparatus like a km<sup>3</sup> telescope.

## II. RELIABILITY PREVISION

### A. *Deep Space Missions Similarity to Deep Sea Missions.*

In table 1 a comparison between deep space and deep sea mission is reported. [2]

### B. *Criteria for selecting km<sup>3</sup> components are long-term reliability.*

Reliability results from the Neptune project [2] indicate that if few, or none, failures are allowed, high node (Junction Box) reliability is required. Also calculations

show that with node MTBF of 10<sup>6</sup> hours, half of the nodes will fail in the lifetime of the project.

In addition the Neptune project [3] has to do with a cable network of about 3.000 km with 35 nodes. They assume the estimation fail to be about 3-4 nodes/year that represent 10%. The repair time could be as much as 6 months. Cost of node replacement with free ship time is estimated \$ 6-8M.

On Neutrino Telescope there are about 5.000 detectors and about 100 JB foreseen. Adopting the same criteria of Neptune it's reasonable that about 500 detectors and 10 JB/year will fail. This implies a partial loss of the system and high cost of maintenance. Therefore improving the reliability performance is essential.

A planning of test to destruction, rather than estimate MTBF, may be a useful alternative.

### A. *Thoughts on Mission Assurance (MA) Implementation.*

- Representatives from each MA discipline part of design team [2]
  - Close working relationship with design, fabrication, test engineers.
- Generate Mission Assurance & Safety Plan and Environmental Design & Test Plan early to avoid programmatic surprises later
- Perform system level fault tree analysis
  - Use failure rates and probabilities (I.e. where available data is relevant to application and environments)
  - Where data is unavailable perform accelerated tests on part of interest (e.g. connectors)

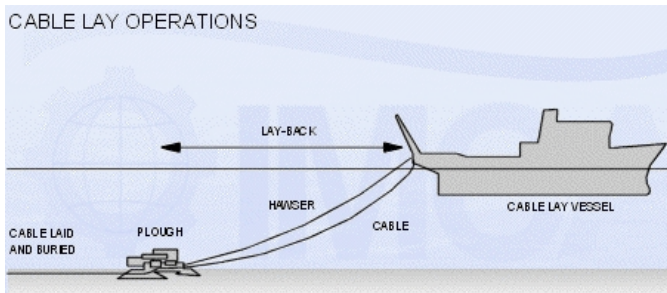
## III. UNDERWATER TECHNOLOGY STATE OF THE ART

### A. *Cable Lay and Repair Operations*

Modern fiber-optic cables are more fragile than traditional cables, so they have more limitations on loadings and bending radii. Thus it is now common to use full duplex DP (Dynamic Position) vessels for cable lay and repair.

DEEP SPACE	DEEP SEA
Long Life	Long Life
Environment driven signal (Temperature, Radiation, Micrometeoroids, Launch dynamics, EMI/EMC)	Environment driven signal (Temperature, Ocean chemistry, Pressure, Bio-Fouling, Deployment dynamics, EMI/EMC)
Pre-launch handling environment	Pre-deployment handling environment
Mix of new, inherited and modified inherited designs	Mix of new, inherited and modified inherited designs
System robustness traded with cost, science and operations impacts	System robustness traded with cost, science and operations impacts
Failures during operations are either costly and/or impossible to fix	Failures during operations are costly to fix often with significant delay

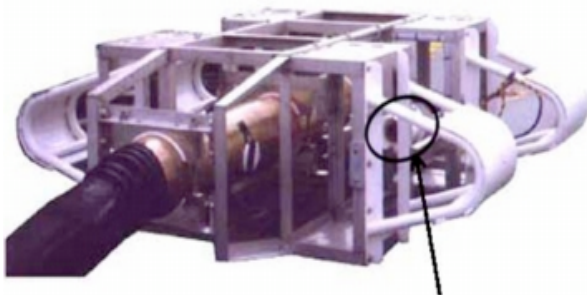
The cost of this operation normally is high.



### C. Main Cable connection to off shore distribution network

The market today offers different ways to realize Mateable Connection System using ROV technology [4] [5].

This solution is more useful especially for maintenance.



Under Water Mateable Connector

### C. Main Cable Maintenance

Telecommunications companies operating in the Mediterranean Sea established the MECMA TREATY (Mediterranean Cable Maintenance Agreement) *EU Case IV/37.669 (1999/C 311/04)*.

The purpose of this Agreement is to define the terms and conditions under which the Cables Ship Operators shall provide to the Maintenance Authorities services for repairing, maintaining and improving the submersible plant by means of Cables Ships and any other appropriate submersible tools at high quality standard for the Mediterranean telecommunications operators. The participation, of the cables owner, to this agreement gives

the possibility to have a strong cost reduction on cable maintenance in case of fault.

### MECMA CABLESHIPS AND BASE PORT

- The CS RAYMOND CROZE, which is owned by FRANCE CABLE & RADIO and operated by FRANCE TELECOM and which Base Port is LA SEYNE SUR MER, FRANCE.
- The CS TELIRI or CS CERTAMEN, which are owned and operated by ELETTRA and which Base Port is CATANIA, ITALY.
- The CS TENEO, which is owned and operated by TEMASA and which Base Port is VALENCIA, SPAIN.

### D. Off Shore distribution network

Cables technology and Deployment

- Cables

The market offers today a large variety of cables for underwater application the more viable are:

#### Armoured Umbilicals

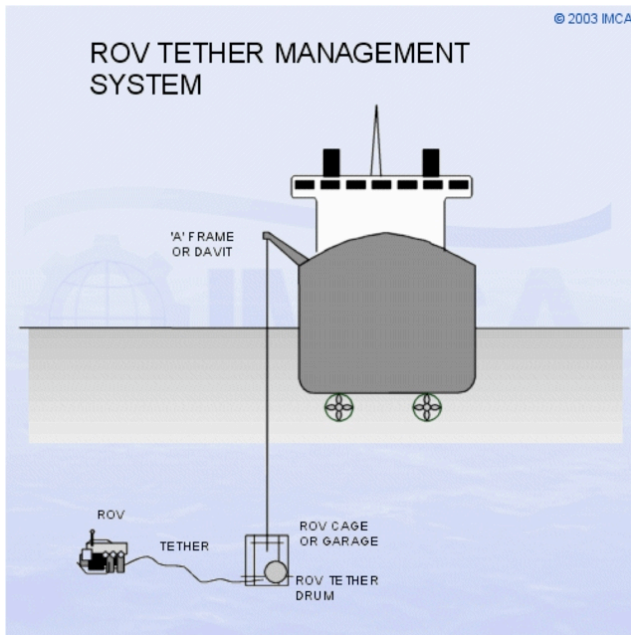
They are the most widely used cables; due to their limit on bending radius and to weight, their installation could be difficult with ROV use.

#### Oil filled pressure balanced.

This is a new generation, a self pressure compensating hose oil filled, their limit is on length no more than 250-300 m.

- Deployment

The most viable operation requires a DP vessel and a ROV with robotic manipulator driven by the umbilical.



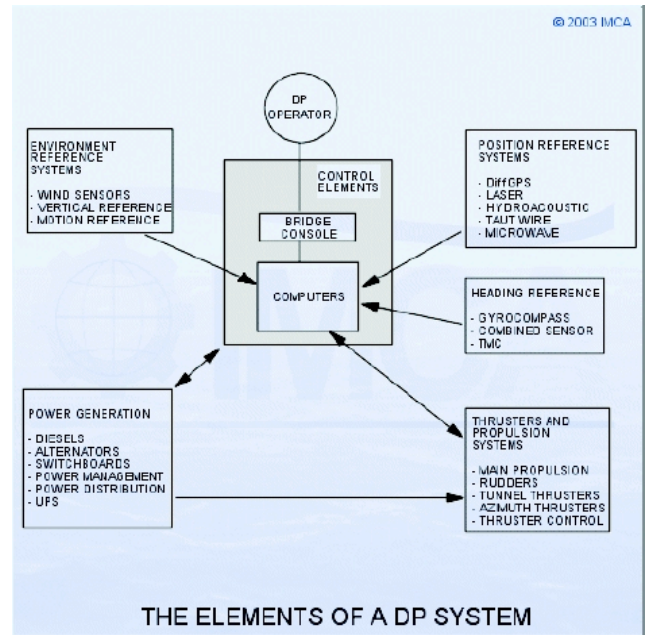
### E. Dynamic Position Vessel

Dynamic positioning (DP) is a very rapidly maturing technology, having been born of necessity as a result of the increasing demands of the rapidly expanding oil and gas exploration industry.

DP can be described as an integration of a number of shipboard systems to obtain the ability of accurate manoeuvrability. It can be defined as a system, which automatically controls a vessel's position and heading exclusively by means of active thrust.

DP vessels execute a lot of activities where precision is required like, subsea installation, survey, lifting (topside and subsea), exploration drilling, cable lay and repair, pipe lay (rigid and flexible pipe)...

DP systems have become more sophisticated, as well as more reliable. Computer technology, position reference systems and other peripherals are also improving and redundancy is provided on all vessels designed to conduct higher-risk operations.



### F. DP Vessel Limitation for km3 telescope

Building the electro-optical network with the Junction Box Hubs for strings/towers connectors is to be considered as a standard job for a DP vessel and ROV when strings/towers are not yet installed.

More complicated and dangerous is the same operation from the surface when delicate optical sensors have been installed in a relatively dense instrumentation field.

Also the maintenance cost could be very high and implies:

- a choice on the limit of fault strings/towers that remain inactivated;
- redundancy;
- reliability of the entire system.

Due to these limits on the management and maintenance aspects it's suggested to investigate other solutions.

## IV. BUILDING A SUBMARINE NETWORK FOR KM<sup>3</sup> TELESCOPE

### A. DP Vessel and ROV use

In a NEMO-like layout DP vessel and ROV are firstly used to deploy main Junction Box.

Then, the secondary JB's and string/towers underwater connecting stations, together with the cable network, will be deployed by DP vessel with ROV in their final location on the seabed.

### B. Autonomous Underwater Robot on a Bottom Rail

This technology is based on installing a bottom referenced fixed path for a special Autonomous Underwater Vehicle, equipped with a self-propulsion system. The fixed path is obtained with a rail network to reach the individual Strings/Towers location. Rail is made out light composite profile fixed to the bottom in sections. The rail deployment must be done by DP Vessel and ROV.

The underwater assembly can be assigned to a special version of AUV (Autonomous Underwater Vehicle), which would align, connect and fix to the seabed the modular rail. This AUV should be able to operate Strings/Towers connectors and to move itself in the path rail for installation, management and maintenance of the apparatus.

Rack-rail will be only a passive path fitted with mechanical stoppers in the limits and the cross over. No points are provided. From a sideline, with two end stations (Terminuses), an array of 90° rail sections is made for the corresponding number of the Strings/Towers line. On the right and on the left of these sections reaches to individual Strings/Towers stations are provided. Motors fitted on the vehicle obtain propulsion on the rack rail. Changing of direction is obtained by elevating the whole vehicle by a piston with a plate located on its lower surface and by a 90° rotation. Lowering the vehicle in this new direction and retracting the piston will complete the changing in direction.

### C. Autonomous Underwater Robot Features

Energy is obtained by a set of batteries.

Batteries are regularly recharged when the AUR is docked at the docking terminuses located at both ends of the side rail section.

All AUR actions are pre-programmed.

Tasks and coordinates are downloaded, from shore, by the communication system, at the Docking Station.

An Underwater winch is provided at the Docking Terminuses to link the strings/towers with the surface in up-down modes.

The main characteristics are:

- Rack rail interface actuators for propulsion and direction changing piston;
- Battery package;
- Engine Room;
- Electronic Compartment;
- Automatic Clutching System and its Sensors;
- Strings/Towers Manipulating System;

## V. CONCLUSIONS

It's strongly suggested to increase reliability prevision.

A detector installation technique based on a bottom mounted AUR, supplied by the underwater electro-optical cable, is feasible. This application is strongly related to the development of an automatic connection system [6] of the Strings/Towers on the seabed network. Also the technologies of all single parts that constitute the entire system already exist [7].

In summary, automation increasing will improve operating lifetime of the telescope, decrease the maintenance cost and fix fault tolerability.

## VI. REFERENCES

- [1] NEMO web page: <http://nemoweb.lns.infn.it/>.
- [2] R. Kemski - NASA-JPL Neptune Power CoDR Mission Assurance Concepts and Discussion June 2000, 2002 Internal Note
- [3] P. Lancaster - Alcatel for Neptune Project in these proceedings
- [4] S, Thumbeck- Ocean Design Inc. in these proceedings
- [5] K. Hall - SEA CON (Europe) Ltd in these proceedings
- [6] M. Musumeci - INFN LNS in these proceedings.
- [7] L. Gualdesi - SACLANTCen in these proceedings.

# A Proposal for the NEMO Power System, the NEMO Phase 1 Power System and Power Control System

R. Cocimano for the NEMO collaboration

INFN-LNS, Via S. Sofia n°62 Catania, Italy  
cocimano@lns.infn.it

## *Abstract*

The NEMO (Neutrino Mediterranean Observatory Project) collaboration is conducting an intense activity to develop technical solutions for a km<sup>3</sup> neutrino detector in the Mediterranean sea. In this framework, in order to evaluate which was the most suitable “Power Transmission System” (power delivery system) for the proposed NEMO laboratory, between alternating or direct current, a study was carried out. Several comparison have been done among all the possible systems and, at the end, the use of ac three phase seems to be more reliable and effective. It can be used not only for the power transmission system but also for the distribution one in order to obtain an improvement in reliability. A proposal for the NEMO power system was developed, 35 kW should be delivered 100 km from the shore. In this context, the NEMO collaboration is installing a *Test Site* at 2000m dept and 25 km offshore the port of Catania, (Sicily) to test a prototype of the detector. Consequently, for the NEMO PHASE 1 electrical power system were taken the same design choices proposed for NEMO with the appropriate changes. A preliminary design of the power control system was investigated, in order to feed the laboratory both in ordinary and fault conditions. The results presented in this paper are part of a work in progress.

## I. POSSIBLE ELECTRICAL POWER SYSTEM FOR NEMO

### A. NEMO layout

The proposed NEMO [1] observatory layout is the result of a compromise between physics request and the technical feasibility within a reasonable budget. The reference architecture that was considered in the feasibility study consist of 64 towers arranged in a square (8x8) array with a height of 750 m. Each tower consist of 16 tubes (storey) 20 m long and 40 m spaced. Each tube is equipped with 2 couples of Photomultipliers (PMTs) at the two ends. The principal elements that compose the observatory are the following:

- 16 storeys for each tower, where scientific instruments can be connected for communication and power,
- 64 towers,

- 8 *Secondary Junction Boxes* (JB), each one containing the electric and electronics devices for communication and power for a group of 8 towers,
- 1 *Primary Junction Box* that contains the electric and electronics device for communication and power of 8 *Secondary Junction Box*,
- the *main electro-optical cable*, 100 km long, that brings power and communication to the submarine laboratory from shore,
- a *Shore Station*, in which the on shore power control system, the data transmission and storage systems will be installed,

The distances that characterize the observatory are:

- Shore- Primary JB: 100 km,
- Primary JB - Secondary JB: 450÷600m,
- Secondary JB-Tower: 150÷300m,
- Base tower-1st storey:150m.

Once we know the detector layout and the approximate amount of power that should be delivered offshore (35kW), the next step is to decide if the power delivery system should be in alternated or in direct current.

### B. Power Transmission System

With “Power Transmission System” we define the portion of NEMO electrical power system that connects the shore station to the NEMO laboratory submarine site. In order to evaluate which was the most suitable “Energy Transmission System” for the proposed NEMO laboratory a study was carried out. Our study aims to answer to the following questions:

- Should this subsystem be designed to work in alternating or direct current ?
- Since all the loads to feed are in dc should we not use a dc power delivery system?

We have analysed all the possible solutions for the Electrical Power System, that are listed below:

- alternated current (ac) mono phase both monopolar (with sea return) and bipolar,
- direct current (dc) both monopolar (with sea return) and bipolar,

- alternated current three phase.

The monopolar systems, both ac and dc, have been rejected because:

- a single-line-to-ground fault causes the complete isolation of the system. This is a very good reason to reject such a delivery system because it means inadequate reliability,
- of corrosion and seawater pollution problems. In particular, the presence of electrodes raises the system complexity. They should be rightly dimensioned and designed and metal structures nearby the electrode should be rightly protected.
- periodic maintenance inspections should be done. This means very long delays and high cost due to undersea campaigns.

Several comparison have been carried out among the remaining systems: dc (bipolar), ac mono phase (bipolar) and three phase. These comparisons have been done with different values of line-to-line nominal voltage and kinds of cables. The most significant is the evaluation of voltage drops and power Joule losses with the following fixed values: power delivered (35 kW), end line-to-line nominal voltage (10 kV), cable conductors total section (75 mm<sup>2</sup>), cable length (100 km), power factor equal to 0.9 (expected value). As a result of this comparison it came out that dc voltage drop are 20% higher than three phase ones and dc power losses are 7% higher than three phase ones.

Other disadvantages of dc system are that:

- on shore conversion station presents major complexity and costs,
- higher conversion power losses, due to the presence of ac/dc and dc/dc, than electrical transformer ones,
- dc breakers are more expensive and, since it is difficult to interrupt dc, special design is required,
- lower reliability due the presence of electronic devices.

Concluding, for all the previous mentioned reasons the use of ac three phase seems to be more reliable and effective. It can be used not only for the power transmission system but also for the distribution one. In this way an improvement in reliability can be obtained by installing electrical transformers in critical points (such as the primary JB and secondary JB) and electronics devices (such as dc/dc or ac/dc converters) near each load (for example in each floor); as a results, a fault that occur to an electronic power supply will cause only a localized loss of power.

## II. NEMO ELECTRICAL POWER SYSTEM

Considering the option of a three phase delivery system as the best one we have developed a proposal for the entire NEMO power system.

The electrical loads considered in the preliminary design study are located in :

- Each Tower storey box. There are: 4 PMT, a data transmission module, some environmental parameters measuring systems, a position control system, an acoustic transponder. The power consumption is approximately 18 W.
- Each Tower box. There are: a data concentrator module, control electronics, some sensors to measure physic parameters. The power consumption is approximately 100 W.
- Each Secondary JB and Primary JB. There are: a data concentrator module, control electronics, some sensors to measure physic parameters. The power consumption is approximately 200 W.

The total amount of power required by the above mentioned loads is equal to about 27 kW.

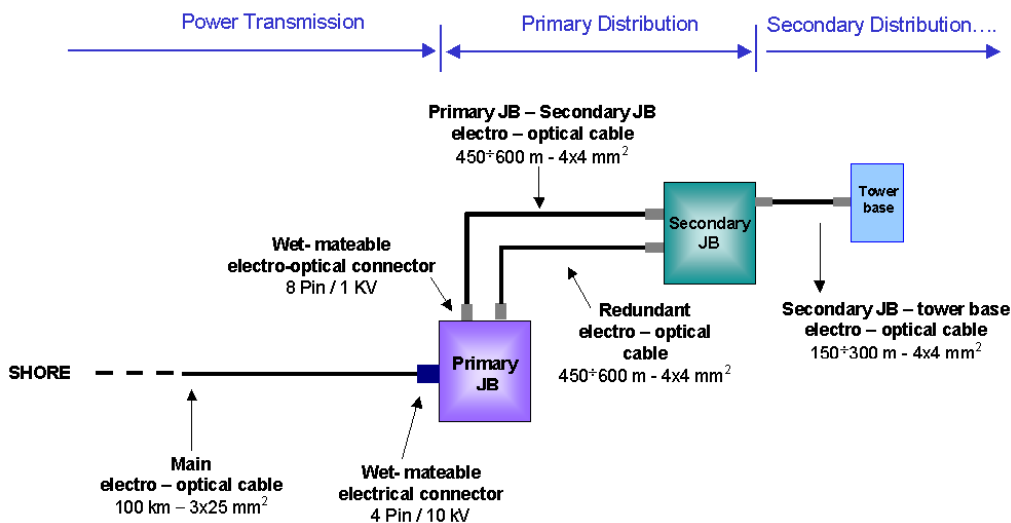


Figure 1: NEMO Electrical Power Subsystem: Power Transmission, Primary and Secondary Distribution systems.

The electrical power system has been divided in the following subsystems (see Figure 1):

- *Power Transmission System*, is the portion that goes from the shore to the submarine site, it can be realized in ac three phase.
- *Primary Distribution System*, goes from the Primary JB to the Secondary JB, with a redundancy in the electro-optical cable. This redundancy allows to feed one Secondary JB in case of a failure in its ordinary feeding cable. This system can be realized in ac three phase.
- *Secondary Distribution System*, goes from the Secondary JB to the storey box. It can be realized from the Secondary JB to top of the tower by ac three phase and from the tower backbone to each storey box by ac mono phase. All the storey loads should be distributed to the three phases to realize a balanced load. In each storey a linear power supply is present (see Figure 2).
- *Storey Distribution System* : goes from the storey box to the storey electrical loads. It can be realized in dc as all the loads are dc.

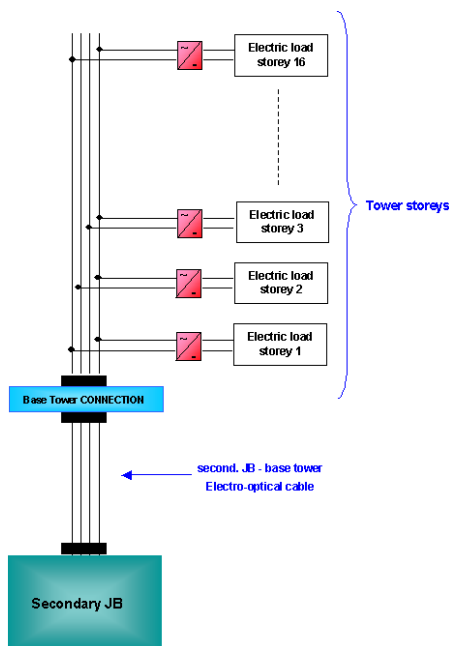


Figure 2: NEMO Secondary Distribution System.

The main electro-optical cable will be energized at 10 kV and will deliver 35 kW that is the total amount of power required by the submarine laboratory, Joule power losses included. The transformer present in the Primary JB steps down the voltage from 10 kV to 660 V, while the one present at each secondary JB steps down from 660V to 400V. The linear power supply present in each floor has to reduce the incoming supply from around 230V (phase-neutral voltage) to a more user-friendly lower voltage of 48V.

In this Figure 3 the main results of the study, such as the line-to-line voltage levels in each node, the power delivered

and the power losses are pointed out. The total amount of power required onshore is about 35 kW and the power losses (Joule losses in all the electro-optical cables and transformers and conversion losses) are less than 10 kW.

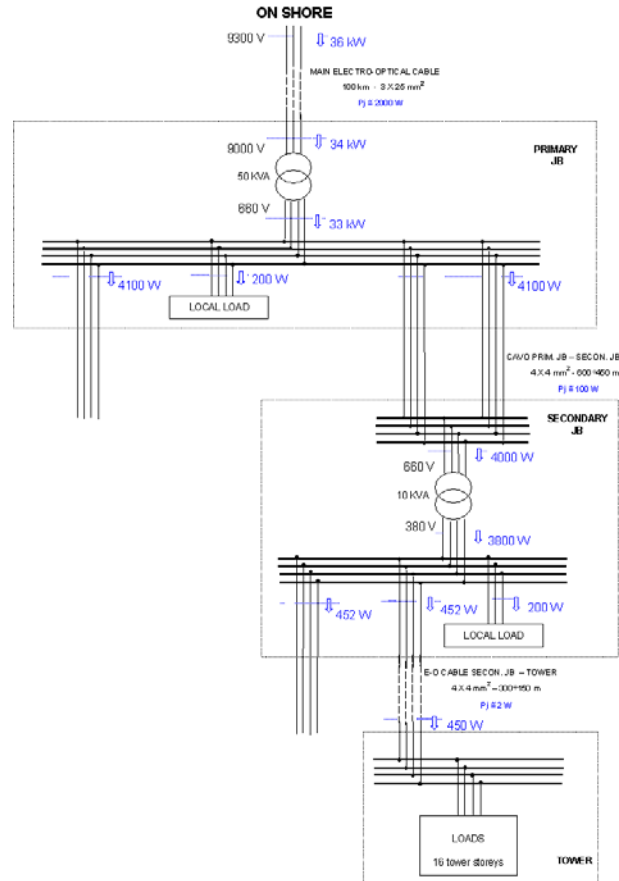


Figure 3: NEMO Power System.

### III. NEMO PHASE 1 ELECTRICAL POWER SYSTEM

The aim of NEMO PHASE 1 project [2] is to test all the elements that compose NEMO, such as: the electrical power system, the data transmission system, the control and diagnostics system. For this reason the NEMO collaboration has built a shore station and has installed a 25km long electro-optical cable that will permit power and data transmission to/from a test laboratory that will be located at 2000 m depth near the port of Catania. in Sicily.

The collaboration is hardly working for the design, realization and installation of a Primary JB, two Secondary JB and two Towers that will constitute a prototype of the detector. Consequently in NEMO PHASE 1 are taken the same design choices proposed for NEMO with the appropriate changes.

Both the main electro-optical cable, deployed in summer 2001, and the electro-optical wet-mateable connectors, commercially available, represent a constraint in the design of the power system. The former, presents 6 electrical conductors with a section of 4 mm<sup>2</sup>, 10 optical

fibres and a maximum allowable voltage of 1200V. The latter presents 8 optical fibers and/or electrical circuits, a maximum allowable current of 10 A and a maximum allowable voltage of 1000V. The power required off shore is equal to 1.4 kW.

In Figure 4 the main results of the study are shown: the line-to-line nominal voltage levels in each node, the power delivered and the power losses in the electro-optical cables. The total amount of power required on shore is 2 kW. It should be noted that a high Joule power loss and a high voltage drop is present in the main electro-optical cable. They are due to the constraints previously mentioned that do not allow to raise the voltage and the total conductors section.

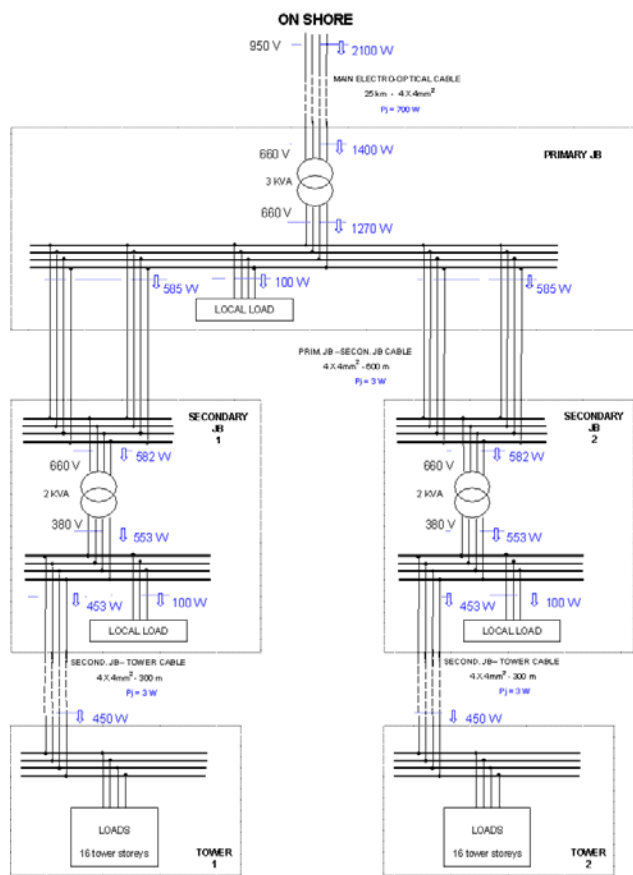


Figure 4: NEMO PHASE 1 Power System.

#### IV. NEMO PHASE 1 POWER CONTROL SYSTEM

The power control system should be able to:

- acquire physics parameters such as temperature, humidity, current, voltage, etc., inside the boxes,
- switch the power on and off to each feeding line, both under ordinary and fault conditions,
- reveal the electric fault and remotely control the breakers in order to continue feeding the JB interested by the fault.

A controller is present in each box and, as summarized in Figure 5, the communication between the field control

system and the shore can be realized by optical fibres while the communication among the field control levels can be realized with a conveyed waves system (the transmission means is represented by the electrical wires) since optical fibers are not available.

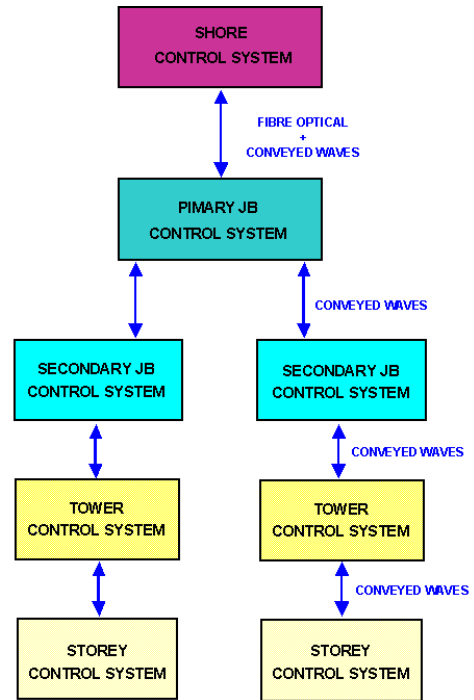


Figure 5: Control levels and means of communication present in the Power Control System for NEMO PHASE 1.

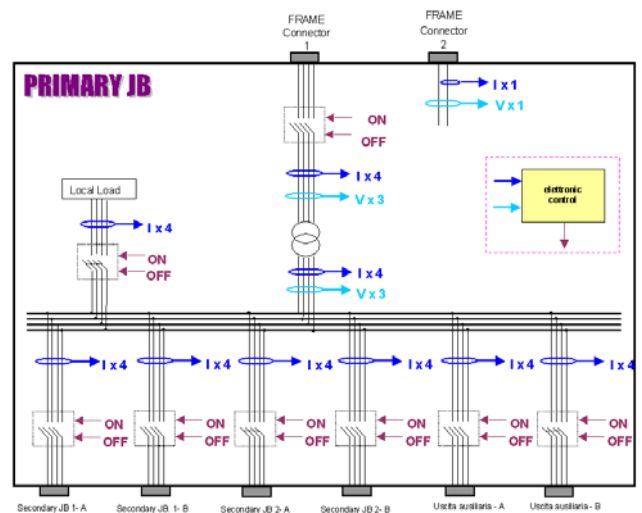


Figure 6: Devices inside the steel pressure vessel contained in the Primary JB for the NEMO PHASE 1 Power Control System.

During the design it will be important:

- to use, where it is possible, commercial devices already tested and used,
- to minimize the failure points to maximize reliability,
- to foresee the right redundancies.



- to foresee the storage of as much as possible devices in oil and high pressure environment. This is an important topic and is due to the JB design [3]. The JB is made of a pressure resistant steel vessel contained in a fibreglass box to avoid direct contact between steel and sea water.

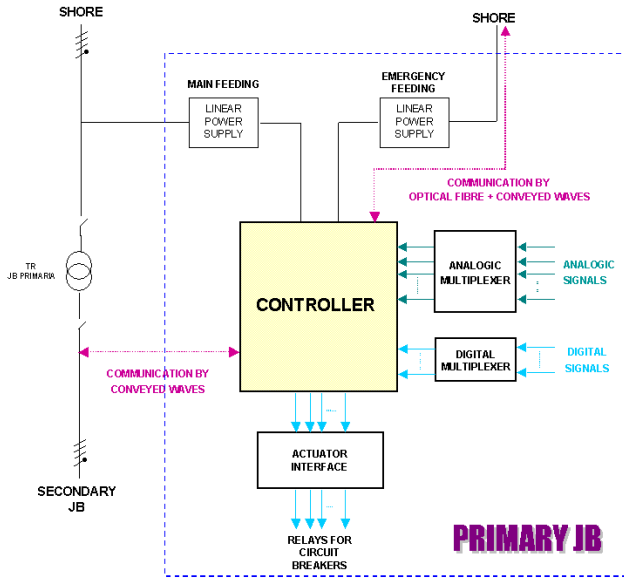


Figure 7: Devices inside the fibreglass box hosted in the Primary JB for the NEMO PHASE 1 Power control System.

The fibreglass box is filled with oil, in order to compensate the external pressure, and contains a transformer box, a breakers box, both filled with oil, and the steel pressure vessel that houses only the electronics devices that cannot stay in oil and under

pressure. This solution will improve on reliability, due to the reduced number of sealed connection that represent failure points and on costs reduction, due to the reduction of its dimensions and the use a low cost material, instead of expensive alloy such as standard titanium.

In Figures 6 and 7 the Primary JB is represented schematically. In particular, in Figure 6 is pointed out what is inside the fibreglass box filled with oil: the transformer, the breakers, the current and voltage sensors; in Figure 7 is shown, inside the dotted rectangle, what is inside the pressure vessel.

## V. CONCLUSIONS

This paper represent a summary of the work that has been in progress for a year. The use of an ac three phase power delivery system is justified principally by reliability. A proposal for the electrical power system for the NEMO project has been presented. In this framework we are carrying on a preliminary design of the electrical power system and a power control system for the prototype NEMO Phase 1. The results shown in this report are part of a work in progress.

## VI. REFERENCES

- [1] NEMO web page: <http://nemoweb.lns.infn.it/>.
- [2] E. Migneco in these proceedings.
- [3] R. Occhipinti in these proceedings.

# Power Distribution

E.Heine, H.Z.PEEK

NIKHEF, P.O. Box 41882, 1009 DB Amsterdam, The Netherlands  
erichn@nikhef.nl

## Abstract

When we talk about a facility, the infrastructure is independent from the detector-function, especially for power and communication networks. What are the possibilities for the power infrastructure with their pro's and contra's. How we have to look to redundancy and reliability and how to achieve a state of the art design.

## I. INTRODUCTION

From recent accidents in the United States and Italy, we have seen how important power is for each infrastructure. One of the conclusions in these cases is that the topology, redundancy and reliability are important issues at least. The same issues are important for a facility like a cubic kilometer detector.

In fact the power system is part of the infrastructure, as is the optical communication system, both work like a household power- or telephone outlet.

To design such an infrastructure we can follow the roadmap shown in figure 1.

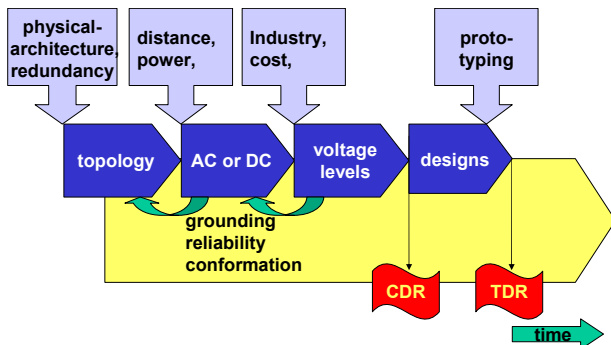


Figure 1: Road Map to design the power infrastructure

In general practice the power system design is routinely left until late in the design program. First nobody wants to touch it and prefers to design more exciting circuits and second rarely do engineers have a background in power systems, because bench supplies provide all the necessary power during the systems debugging stage. All too frequently, this leads to milestone effects in planning, penalties in budgets and a poor power system design.

From the start of the facility's design phase there is a need for a strong coordination of the power sector. Major topics to watch along the whole project are grounding, reliability, conformation and quality assurance.

The first figures we need to start the design are numbers for the expected power demand and the distance. Presently the estimates are 50-100kW and a distance of 100km.

## II. TOPOLOGY

To start with the power system design we need the physicists concept of the detector architecture. So far, where power is concerned, the ideas do not reach beyond a cubic with strings or towers anchored to the seabed. Figure 2 shows an example of a possible topology with some redundancy.

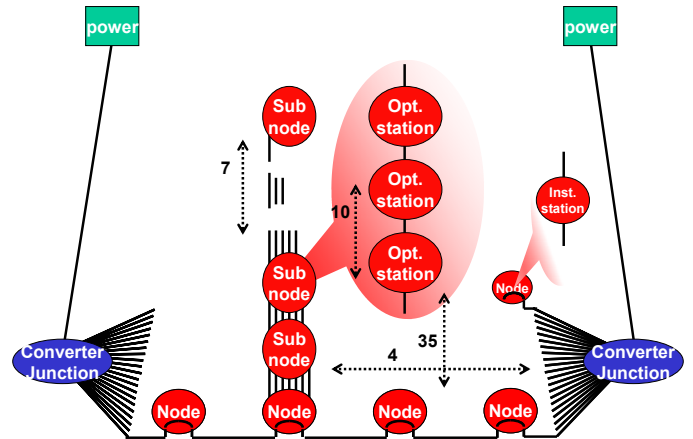


Figure 2 Example of a power grid

With respect to strings [1] and towers [2, 3], strings will need more nodes in the grid to achieve the same density in optical modules. On the other hand, if there is a power failure in a tower a bigger part of the detector will be out of operation.

Other topologies are tree structures, with one junction and sub-junctions connected to it, or a star configuration with several junctions or sub-junctions.

Using one or two cables from shore to facility doesn't have to be an issue. They can be installed as one loop of cable from shore to facility and back (ca. 1.5 M€ [4]). If the junctions are installed the cable is recovered on the facility. The cable is cut, the junctions are mounted on the cable and deployed with a maneuver space equal to the dept (ca. 3.5 km) which will be enough for a base of 1km.

More redundancy can be achieved with four converter junctions as shown in figure 3. If 2 junctions fail, 84% of the facility is still available. The real redundancy depends on the overload capability of the long distance stations. In this scheme each node is powered by two converter junctions. A scheme like this gives the opportunity to install the power in several phases along the growth of the facility. Another item is the compatibility with the optical communication network. In the scheme of figure 3 the optical network can be designed as several ring-structures along the node grid [5].

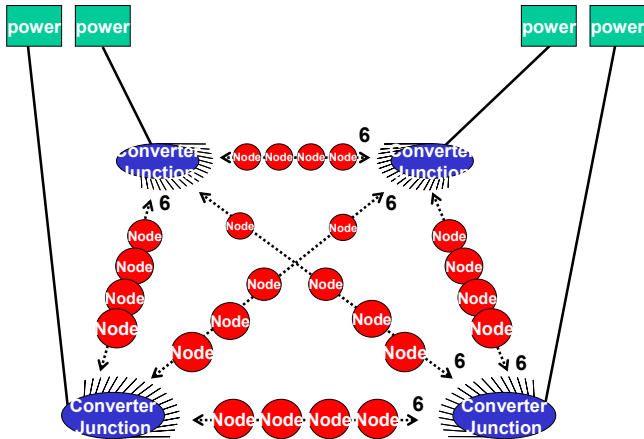


Figure 3 : Redundant power distribution

### III. AC OR DC

The options for AC or DC both have their own constraints but about the same complexity (money). We can divide the system in two major parts; long distance- and node-grid part. For both parts there are different constraints. Surveying industry, then there are several projects to link up to, like offshore windfarms [6], oil industry, power distribution [7, 8], telecom industry and railway power distribution. But in most of these projects the power numbers are a lot higher. Where losses occur in those projects the impact is much higher than in our facility.

#### A. Long distance power.

From shore to facility we have some choices within the constraints;

- AC or DC transmission and their cable behavior.
- Single wire connection with the sea as return or double wire system.

Both are important issues in relation to installation costs, losses (running costs) and redundancy (complexity and single point failures).

##### 1) AC or DC

AC/AC;

An AC system is a relatively simple system to the local nodes with only passive components like transformers. Electronic circuits can't compete with the reliability of transformers. In each node we have to convert the AC to a DC level, for each connected AC-line (figure 4). This conversion should be done in a way that there is a constant power load on the system with a power factor corrector (PFC). The regulations of the power supplier on shore set limits to the allowable load on one phase leg. This would mean more wires in the long distance cable and a 3 phase connection.

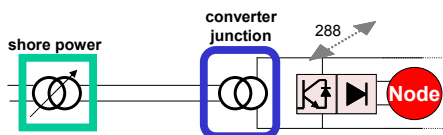


Figure 4: Long distance AC/AC system

AC/DC;

An AC system down to the converter junction and from there DC to the Nodes. It requires less electronic modules submarine (figure 5). Only in the converter junction a PFC is needed. If there is a 3 phase connection from the shore a full-wave rectifier circuit can do the job.

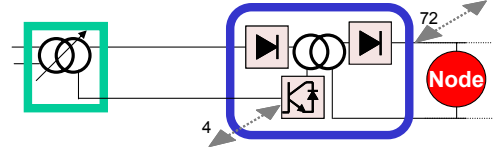


Figure 5: Long distance AC/DC system

DC/DC

More or less the same electronics as AC/DC is involved but the rectifier will be located on shore. The advantages will be clear; electronics on shore are less critical and the submarine cable losses are lower (figure 6).

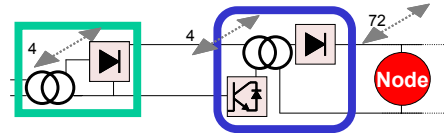


Figure 6: Long distance DC/DC system

##### 2) Cable behavior

Submarine cables are generally found with an electrical resistance of between 0.7 and 1.0Ω/km, a capacitance of 0.2μF/km and an inductance of 128μH/km.

The AC losses are conform  $(I_{load}^2 + (kU\omega C_{cable})^2)R_{cu}$ . Typical number for reactive losses are in the range of 100-150kVAR/km for a 33kV, 2 wire, cross-linked polyethylene cable [9]. These losses are independent of the transferred power. So, we can imagine that AC is an interesting option if the reactive losses are a fraction of the transferred power or if the losses are affordable in the running budget. The additional reactive current not only reduces the active current-carrying capability of the cable, but also requires a network to absorb the reactive current. For any length of about 10 km, some form of reactive power compensation will be required (figure 7).

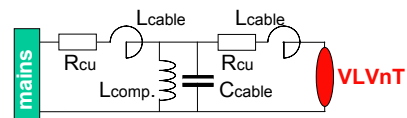


Figure 7: AC cable with reactive power compensation.

This compensation/km depends on the high voltage value; higher voltages means shorter distances between compensators. The factor k depends on the number of compensators. Capacitive current increases with increasing voltage.

A DC cable is less expensive, because for a given amount of isolation they can operate safely at higher current and voltage, so they allow up to two times more power transmission per cable. The losses are conform  $I_{load}^2 R_{cu}$ , reactive elements like capacitor and inductor are not playing a role. According to

figure 8, from a loss point of view, a DC-link would be the most favored solution.

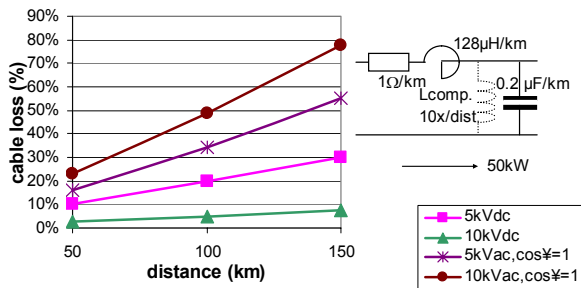


Figure 8: AC and DC losses for a given cable and power (50kW)

### 3) Number of wires

For long submarine cable transmissions, a return with ground/sea electrodes will be the most feasible solution. History learns that this is not a trivial matter. Like cooling systems with Freon or solder joints with lead in it, it is or becomes a subject of environmental directives.

In some cases, environmental constrains already prevents the use of electrodes. In those cases a metallic return path is used in spite of increased costs and losses.

If we use AC for the long distance it will likely be a 3 phase connection. This gives the advantage to use a simple three phase rectifying system to achieve DC for the power grid with an acceptable power factor. But in this case we also need inductive compensators along the cable what makes it expensive.

### B. Node grid

For redundancy reasons each node will be powered from two sources. The outputs of two converter junctions in parallel is perfectly possible with DC and more difficult with AC. Figure 9 shows a DC shared configuration. In this case the cable's copper resistance provides load sharing for free. Diodes in the junction prevent a reverse power flow. To do this with AC we need a double cable system with in each node two rectifier systems to parallel the currents at DC level or synchronizing circuits.

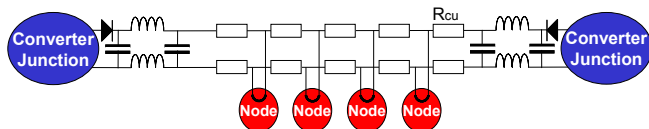


Figure 9: DC load sharing with two sources

It seems possible to make passive T-splitters in a cable for power and fibers as well. This means that there is only one wet mateable (expensive) connector necessary to each node.

## IV. VOLTAGE LEVELS

Voltage levels depend on the cable and connector types. For the long distance connection 1-10kV is usable. This value is used in telecom- and railway industries. Isolation of a high AC voltage cable needs a special treatment to prevent partial discharges [10] which affects the cable lifetime.

For the choice of the node-grid voltage we try to hook up to commercially used values. As shown above DC will be preferred. For DC, 380V will be a proper value to achieve low currents in the grid and to use of the shelf components for switching and conversion. This value is used frequently in large intermediate systems. The AC alternative would be 230V.

In the node only a switchyard is placed to control the sub-nodes. In this way only a sub-node is lost in case of a failure in an optical station or a instrumentation station. In each optical station there is a conversion to 42-48V. This voltage is a standard in telecom systems and the future standard in the automotive industry. Each function (or board) in the electronics will convert its required low voltages from the 48V. This avoids noise interaction between boards via the power lines.

A nice property of converters is that the input voltage can change by more then a factor of 2 without any effect on the output voltage. In this way a variable voltage drop caused by a variable number of working nodes as no influence on the voltage in the optical stations.

## V. DESIGN

To make realistic designs more specifications are necessary. Some design principles will be shown to refresh our knowledge;

### A. 3 phase rectifying

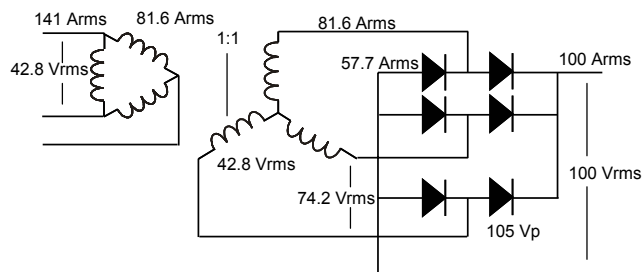


Figure 10: 3 Phase full wave rectifying.

A three phase full wave rectifier delivers a DC voltage with 4% ripple. This is more than sufficient for long distance or local grid.

### B. Power factor corrector

The PFC circuit provides an almost resistive load to the transformer. In the classic way, the rectifiers can only conduct current when the ac line voltage exceeds the voltage on the input filter capacitor (figure 11).

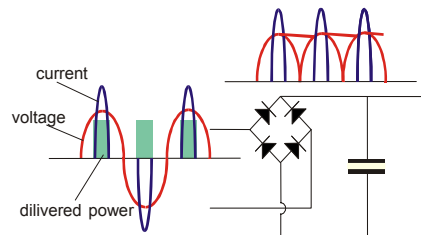


Figure 11: Classic rectifying

This typically occurs within 15 degrees of the crest of the ac waveform. The result is that the current pulses are 5 to 10 times higher than the average current. This leads to distortion of the voltage waveform, higher harmonics on the line and high losses ( $I^2R$ ). A PFC as shown in figure 12 increases the conduction angle of the rectifier and makes the input current waveform sinusoidal and in phase with the voltage waveform. This means that all the power drawn from the power line is real power, peak current and losses are much lower and there is no harmonic distortion. The result is a high efficiency rectifying.

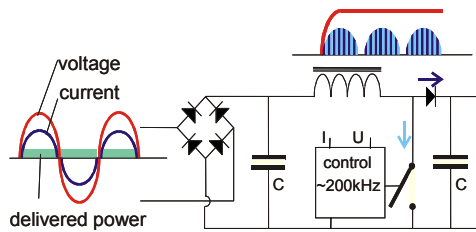


Figure 12: Power Factor Corrector

### C. DC/DC conversion

All DC conversions are based on the same switching principle as in the PFC circuit. The efficient operation of the switching power supply is achieved by ‘chopping’ the input voltage into pulses of which the width is controlled by a switching regulator controller (figure 13,14). Once the input voltage is converted to an ac rectangular waveform, the amplitude can be stepped down (or up) by a transformer (figure 15). For a given layout the efficiency can go up to 95%. This depends on the voltage ratio between in- and output and power variation.

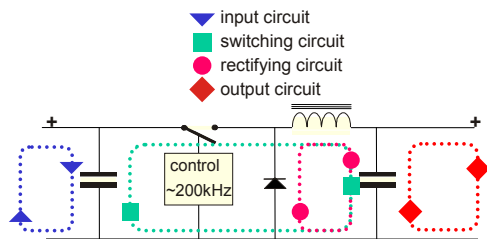


Figure 13: Buck converter

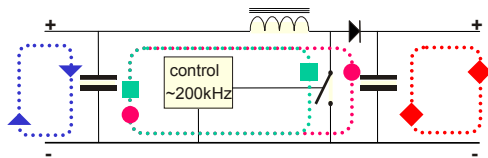


Figure 14: Boost converter

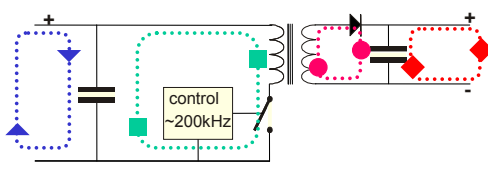


Figure 15: transformer isolated converter

## VI. GROUNDING

The basic elements of grounding are common knowledge to all technicians. But practice learns that a strong coordination in a project is necessary to achieve an electro magnetic compatible system.

- **Grounding is essential to relate all potentials to the environment.**
- **Prevent ground currents by use of one ground point in a circuit.**

A more or less complete configuration scheme is shown in figure 16.

- The mains in the shore station will be related to the neutral and therefore to the ground.
- The HV system will have two grounding points in some cases because the sea can be the return path.
- Node-system. There may be breakers in the junctions and if they are open, the output and source will stay grounded by using a high value resistor connected to ground. This connection takes no part in the circuit currents. Special voltage arrestors are needed to prevent voltage drift to the HV-side if transformers are used. The Node-system is connected by a two-wire system.
- Local systems are grounded (high resistive: ca. 1M $\Omega$ ) at one point in each optical station just to refer its potential to the environment.

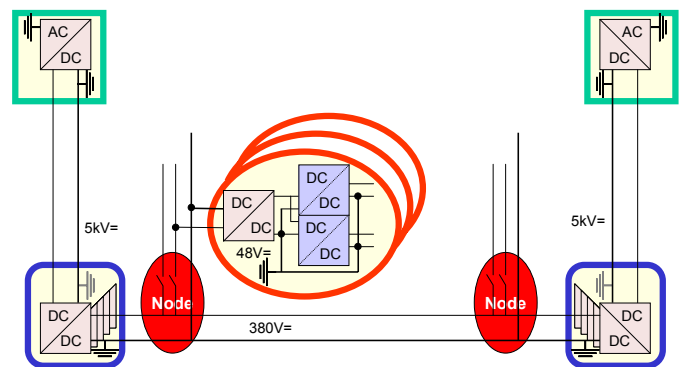


Figure 16: Grounding in a complete system

In normal operation there is no ground current unless the current is part of the power transmission like in the HV system where the seabed is the return. There are no corrosive currents in the seawater.

Metal parts (and housing) of a satellite are grounded to the sea through the mechanical construction of the string, tower or platform.

Of course all numbers are fiction and depend on the real layout of the facility. They are used to illustrate the power flow and the redundancy of the system. Moreover the numbers are selected looking at industry;

- 5kV is a value used in traction (railway) and telecom.
- 380Vdc is used as intermediate voltage in large systems especial if the source is 230Vac.
- The lowest voltage for the infrastructure will be 48V. This is the voltage to power most of the customers. 48V and is a frequently used intermediate value.

## VII. RELIABILITY

In many discussions there is no difference between reliability and redundancy. But these are two completely different issues. We can achieve redundancy with choices in the topology, but it tells nothing about the reliability of the used components. Reliability is not a question of over dimensioned components either.

### Reliability is something we create, not buy.

The pie chart of figure 12 will illustrate which issues are involved with reliability. This graphic is based on an 8 year experience of a firm specialized in reliability [11]. We can manage the reliability by quality control, by conceptual design reviews and test reports.

If we look at the graphic, we observe that component failure is not a major reason for system failure.

- Parts 22%; Part failing to perform its intended function.
- Design 9%; Inadequate design.
- Manufacturing 15%; Anomalies in the manufacturing process.
- System Management 4%; Failure to interpret system requirements.
- Wear-Out 9%; Wear-out-related failure mechanisms before system wear-out.
- No-Defect 20%; Perceived failures that can not be reproduced upon further testing.
- Induced 12%; An externally applied stress, like brake down of a cooling system, water, vibrations, etc.
- Software 9%; Failure to perform its intended function due to a software fault.

We see that besides component choice, workmanship in system management, design and manufacturing are very important.

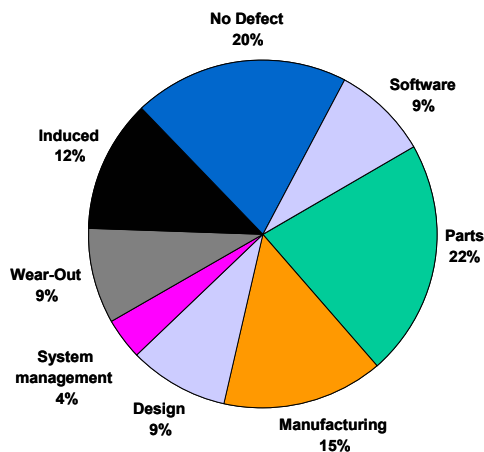


Figure 12: Reliability issues

## VIII. CONCLUSION

So far the comparison seems in favor of a DC/DC solution. But investigation has to prove this on the real numbers of losses, costs and complexity. Connection with industrial developments is important but the industry is

mostly focused on higher power levels like in offshore windfarms, oil-industry, railway grids.

Technical issues to investigate;

- DC for long distance is promising > breakeven study for redundancy and costs are necessary.
- Node grid gives redundancy.
- Node grid can be made using components of traction industries.
- Only 3 conversion steps from shore to board electronics.
- Each board / module makes its own low voltages.

Organization issues;

- Power committee recommended.
- Specify and guard the power budget.
- Coordination of the grounding system.
- Watching test reports, redundancy and reliability.
- Try to involve technical universities and industry.
- Coordination between power- and communication-infrastructures.

There is always certain risk to adapt new technology to soon, to get reliable products. On the other hand new technology gives the opportunity to make a system with an excellent performance for years without running in obsolete components.

## IX. REFERENCES

- [1] <http://antares.in2p3.fr>
- [2] <http://www.nestor.org.gr>
- [3] <http://nemoweb.lns.infn.it>
- [4] <http://www.neptune.washington.edu>
- [5] J. Hogenbirk, "Wavelength multiplexing introduction to km<sup>3</sup>", this workshop
- [6] S. D. Wright, "Transmission for offshore wind farms in the United States", University of Massachusetts
- [7] High voltage transmission, Siemens
- [8] HVDC light, ABB
- [9] W.Grainger, N.Jenkins, "Offshore windfarm electrical connection options".
- [10] S. Boggs, J. Densley, "Partial Discharges in 3-core Belted Power Cables", IEEE Electrical Insulation Magazine Vol. 16, No 5.
- [11] Denson, W, "A Tutorial: PRISM", Rac, 3Q 1999, pp. 1-2

# Mechanical Structures for a Deep Sea Water Neutrino Detector

Mario Salvatore Musumeci for the NEMO collaboration

INFN-LNS Via S.Sofia 62, 95123 Catania, Italy  
musumeci@lns.infn.it

## Abstract

The NEMO collaboration has undergone a great technological effort in the development of a proposal for a km<sup>3</sup> neutrino detector. A general layout was designed and the project of all the main components of the detector was realized. The aim of NEMO collaboration is to design a low cost and high reliability detector having the required physics performances. The design characteristics and deployment techniques of the mechanical structures proposed for the detector are presented.

## I. INTRODUCTION

The main goals of the work made by the NEMO collaboration [1] to optimise the design of a deep water submarine neutrino detector are the followings:

- reduce the cost of constructing a km<sup>3</sup> detector by:
  - grouping the optical modules in a limited number of structures to reduce the number of underwater connections;
  - realizing a modular layout for the detector;
  - using composite materials;
- reduce the maintenance costs of the detector by studying self automatic connection systems;
- simplify the deployment operations of 3D structures;
- avoid mechanical stresses on the electro-optical cables during the deployment and the underwater lifetime of the detector.

The first result of this work will be the construction of an underwater laboratory at ~ 25 km offshore the port of Catania at 2000 m depth. The laboratory will be equipped with all the basic components of the km<sup>3</sup> neutrino telescope proposed by NEMO collaboration. The laboratory aims at demonstrating the feasibility and the reliability of the technical solution studied by the NEMO collaboration. The project also aims at providing submarine connections for other research groups interested in carrying out multidisciplinary experiments in deep sea water.

## II. ADVANTAGES OF USING TOWER STRUCTURES

A detector realized by means of tower structures seems to have good capabilities in terms of local track reconstruction with respect to a string set. A reduced number of towers (81 for example) permits to obtain an effective area adequate for astrophysical neutrino detection. Numerical simulations show that this detector may approach the performances of a detector having an homogeneous distribution of PMTs displaced over

400÷500 strings having a spacing of 60 m [2]. The gain is therefore a great cost reduction and reliability improvement compared with the “homogeneous lattice” detector.

Assuming therefore comparable discovery capabilities for the two detectors, the use of tower will bring to a double advantage:

- improvement of reliability;
- costs reduction in sea operations.

In figure 1 we show a scheme, useful to explain the previous issue.

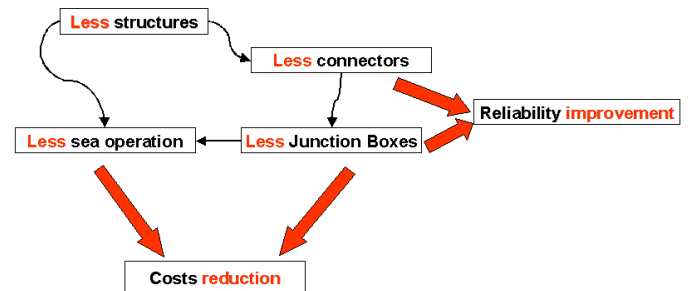


Figure 1 Use of tower reduces the number of underwater structures to be deployed and connected.

## III. THE NEMO DETECTOR

### A. General layout

The plan view of the detector proposed by the NEMO collaboration is shown in figure 2.

Squares represent the instrumented vertical structures (tower). Circles, represent Junction Boxes. Each tower is connected with secondary Junction Box as represented in the lower left corner only, to make the scheme clearer. Each secondary JB is connected with the main JB and with the two nearest secondary JBs. This will permit a great improvement in terms of reliability. The use of (a limited number of) secondary JB gives advantages from the point of view of the reduction of single point failure risk. In fact a single Junction Box having 64 or more holes to accommodate the connectors coming from the towers, will come out to have a reduced reliability.

The NEMO collaboration is at the moment developing an innovative vessel for the JB. This vessel is made of an inner part of steel and an outer part made of GRP; the volume between the two vessels is filled with dielectric oil. This solution permits to decouple the problem of the resistance to

corrosion in sea water, from the problem of the resistance to pressure [3].

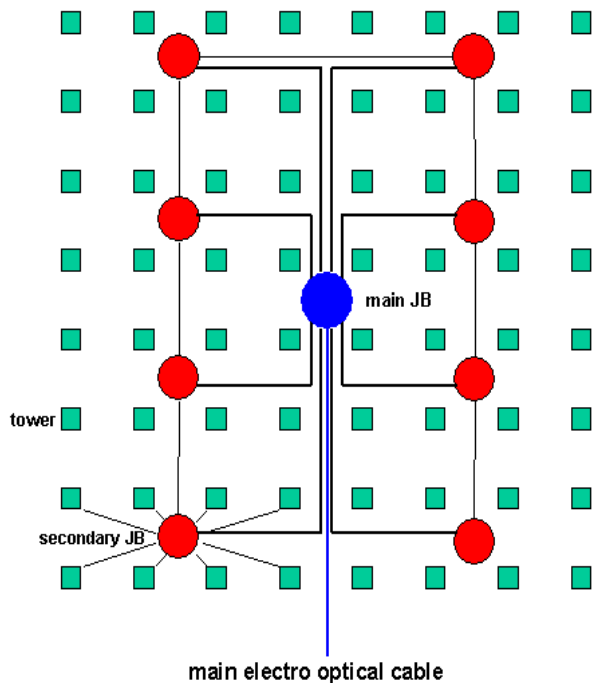


Figure 2 Top view of the proposed km<sup>3</sup> NEMO layout

### B. The instrumented towers

The vertical instrumented structures proposed by the NEMO collaboration for the construction of a km<sup>3</sup> neutrino detector, are made of a set of Glass Reinforced Plastic (GRP) tubes interconnected by means of ropes.

The tower is formed by a sequence of (16÷18) instrumented storeys (tubes). The tubes have a diameter of 0.45 m, a thickness of 5.9 mm and a length of 20 m. The distance between the neighbour storeys is 40 m. Moreover each storey is rotated around the vertical axis of 90 degrees with respect to the neighbours. The use of a composite material allows to easily tune the properties of the raw material.

The lower storey should be positioned at an height of 150 meters above the sea bed. Therefore, the tower will have a total height of 750÷850 m, depending on the number of storeys. In figure 3 an image of the tower is shown. Due to proportions ratio, we show just the first two storeys unfurled. The deployment and unfurling operations are described in the following.

### C. Materials

The ropes used to interconnect the storeys will be made of DYNEEMA™ fibers. The chosen rope diameter is 10 mm. The DYNEEMA™ is a fiber having a great resistance capability in sea water. No water absorption has been observed during many years of usage in underwater moorings.

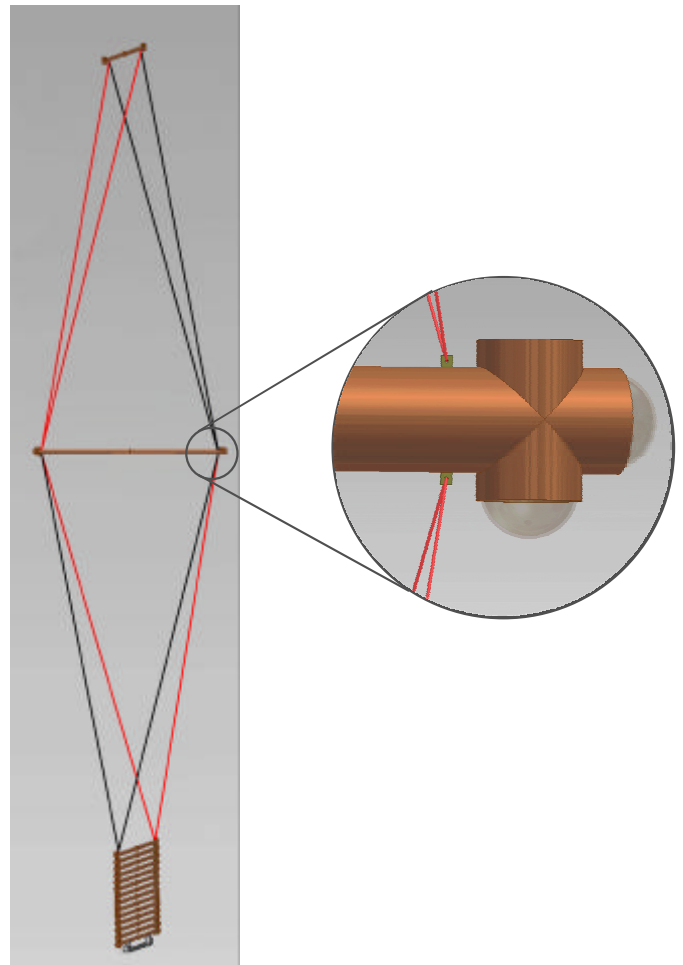


Figure 3 The tower during unfurling operation and the PMTs

The NEMO collaboration also carried out several test of water absorption in GRP. Three different kinds of GRP samples were immersed for six months at 3000 m depth in sea water. The samples were obtained by cutting the same commercial GPR pipe which have cylindrical surfaces coated with a protective liner. The samples differed for the external coating treatment that we applied:

- one was coated with an extra layer of protective liner on the whole external surface;
- one was coated with an extra protective liner only on the cutting surfaces;
- one was not coated with the extra protective liner.

After the recovery, the samples were weighted to estimate water absorption. Moreover they were subjected to load tests to estimate any changing in mechanical resistance.

No water absorption or changing in mechanical resistance was measured after the immersion period. An investigation on the use of the GRP for the realization of submarine structures was also conducted. In sea operations and applications several example were found, giving encouraging results on the capabilities of this material to resist to long immersion periods.



#### IV. SEA OPERATIONS

In a marine challenge like the realization of a very large neutrino detector in deep sea water, a large fraction of the budget is represented by the sea operations. In principle, in the field of deep sea water operations, the oil offshore industries have a very good expertise. For this reason an Italian oil company was consulted. The result was a study of mechanical feasibility regarding the detector proposed by the NEMO collaboration.

A detailed description of the deployment operations was done. In the following a summary of this work will be made with particular attention to the deployment of the tower. Since as the deployment of the Junction Boxes and the cables laying is an almost trivial operation, only the tower deployment will be described.

At the moment the collaboration is also carrying out some studies to investigate the possibility to simplify the submarine connections. The aim of this work is to avoid the use of expensive system (ROVs, dynamic positioning vessels) to anchor and to recovery the towers. This should result in a great cost reduction during the maintenances operations.

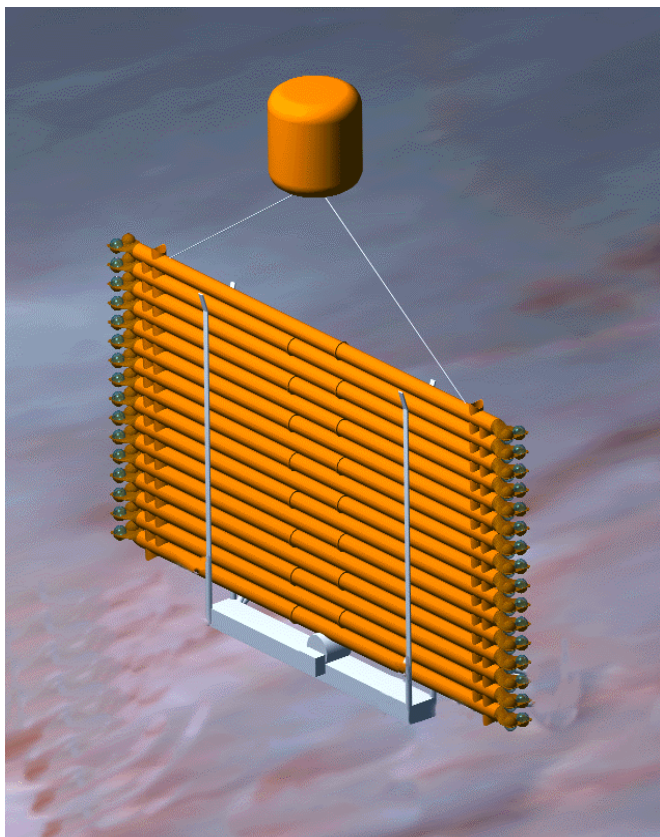


Figure 4 In this compact configuration the tower will have a total height of about 12 m. This will simplify the handling and deployment operations.

##### A. The tower deployment

During the transportation the tower should be compacted in a configuration like the one shown in figure 4.

Once deployed on the seabed, the tower can be unfurled by means of a system of ropes and winches, until it assumes the working configuration shown in figure 3.

#### V. PRESENT ACTIVITIES

At present the NEMO collaboration is carrying out the construction of a sub system of the NEMO apparatus. It will be installed in a test site located 25 km offshore the Catania harbour and will consist of:

- a submarine electro-optical cable;
- a main Junction Box;
- two secondary Junction Boxes;
- two tower.

It will be a complete sub system of the proposed NEMO  $\text{km}^3$  layout and it will have the goal to demonstrate the technical feasibility of the entire detector.

The cable, having four electrical wires and ten optical fibers, was deployed at the end of Summer 2001. During the Summer 2004 the submarine termination of the cable will be recovered in order to install wet mateable submarine connectors. This will allow to connect the shore laboratory at the port of Catania with the underwater test site facilities. The three Junction Boxes and the first tower are scheduled to be ready for deployment in Summer 2005. They will be, then, deployed and connected to the termination of the electro optical cable through ROV mateable connectors.

On the left lower corner of figure 5, the cable end and the frame supporting the electro-optical connectors is shown. The three circular vessel represent the Junction Boxes and the other two objects represent the bottom sockets of a couple of towers. Dimensions and the distances of the structures are not correctly scaled.

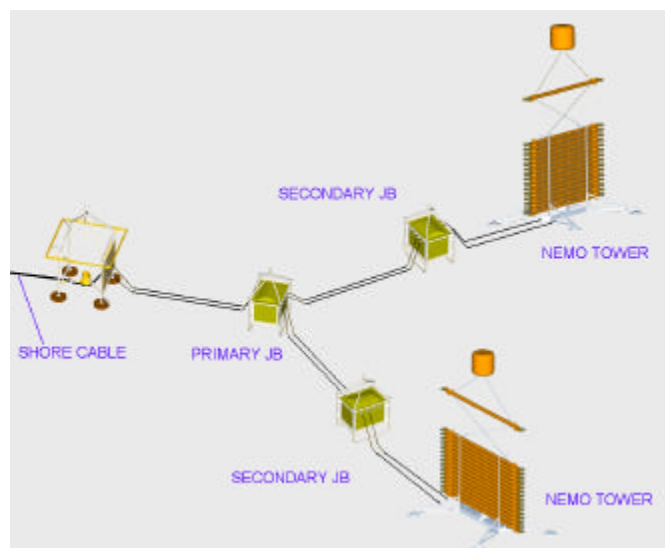


Figure 5 The test site layout

## VI. CONCLUSIONS

The NEMO collaboration has worked to define a general proposal for a km<sup>3</sup> neutrino detector. The result was:

- a general layout the detector, taking in account several issue (physical performance, reliability, deployment capabilities);
- the conceptual project of an unfurling tower to support the PMTs;
- the project of the Junction Boxes useful to interlink the towers

The collaboration is, at the moment, developing the executive design of the tower. The construction of the first tower prototype will start within 6÷8 months, in order to permit the contemporary deployment, during Summer 2005, of the tower prototype together with the Junction Boxes, presently under construction.

## VII. REFERENCES

- [1] E. Migneco in these proceedings see also NEMO web page: <http://nemoweb.lns.infn.it/>;
- [2] P. Sapiemza in these proceedings;
- [3] R. Occhipinti in these proceedings;

# Design of the junction boxes for Nemo-phase1

R. Occhipinti for the NEMO collaboration

INFN-LNS, via S. Sofia n° 62, 95125 Catania, Italy  
occhipinti@lns.infn.it

## Abstract

According with R&D philosophy of NEMO phase1 we have designed an alternative to the standard design of pressure vessels for junction boxes operating on seawater for a long lifetime, de-coupling the pressure problem from the corrosion problem. The JB is made by a pressure resistant steel vessel hosted in a fibreglass container to avoid direct contact between steel and sea water. The fibreglass container is filled with oil to compensate the external pressure. This solution improves the reliability due to the reduced number of sealed connections that can be a failure point. It also has economical benefits due to the use of a low cost material, instead of expensive alloys.

## I. NEMO PHASE-1: GENERAL DESCRIPTION

NEMO phase1 is an undersea cabled observatory, including the critical components of the km<sup>3</sup> detector proposed by the NEMO collaboration [1]. It will be installed at the LNS Test Site 25km offshore the port of Catania, at 2000m depth. The detector subsystem will host a number of science instruments for data acquisition in several research fields like astrophysics, marine engineering, geophysics, marine biology,..... Power and data will be transmitted using a cable equipped with 10 fibres and 6 electrical conductors, to the shore. The underwater termination of the electro-optical cable is connected to a frame which holds two stub-plates connectors "wet-mateable" and ROV (*Remotely Operated Vehicle*) operable.

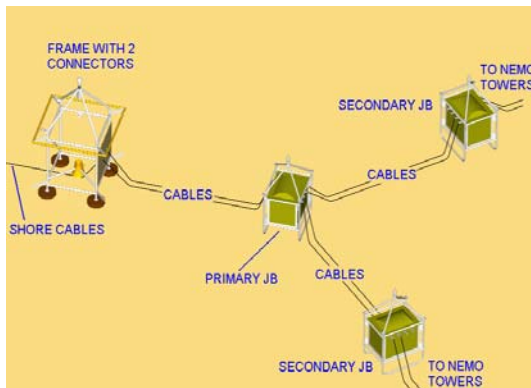


Figure 1: Interconnection between frame, primary and secondary jbs.

The two connectors will be used to make a redundant connection between the frame and the primary junction box. This is done in order to maximize the reliability of the system in case of cable damage or connectors failure. Two more double connections will also be made between the primary

junction box and the two secondary junction boxes. All these connections are made via standard, well tested, deep seawater cables terminated with wet-mateable connectors. The proposed network creates redundant paths to improve the system reliability.

## II. JUNCTION BOXES

In order to minimize the power losses along the line, the primary junction box is fed from the shore with 1kV three-phase AC [2]. The primary and the secondary JB's will be placed at a distance of about 200m. The primary JB will host a power transformer and several electronics devices for data acquisition and electrical switches used to switch off the line in case of cable failure. Therefore the JB is a critical component of an underwater detector since it could be a single point failure for the experiments. Furthermore, JB could be repaired only if we afford the expensive recovery operation in open deep sea. Nemo phase-1 JB's will be located at 2000 m depth for about ten years: therefore each JB has been designed to resist for the entire lifetime both to pressure and to corrosion. We have designed the JB de-coupling the pressure problem from the corrosion problem. The NEMO phase1 JB is made by a pressure resistant steel vessel subsea housing hosted into a fibreglass container to avoid direct contact between steel and seawater. Fibreglass container is filled with oil in order to compensate the external pressure.

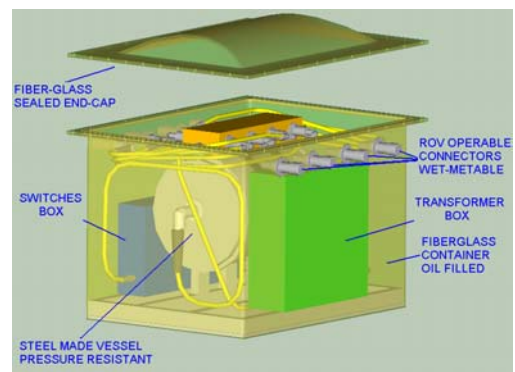


Figure 2: junction box, oil filled pressure compensate.

Electrical components, such as transformers, that can resist high pressures are positioned outside the subsea housing in order to reduce the dimension of the pressure vessel. Wet mateable (ROV operable) fixed mount bulkheads are fixed onto the wall of the fibreglass container (see fig.3). The connectors side within the fibreglass container has an oil filled cable that ends with a dry mateable electro-optical connector having 8 contacts: 4 optical and 4 electrical. All these cables

converge into a splitting box, equipped with the appropriate dry mateable hybrid connectors.



Figure 3: Internal lay-out of the JB components

Inside the splitting box optical fibres are separated from electrical conductors. All the optical fibres are grouped and inserted in an oil filled hose that connect the splitting box and the subsea housing. The hose is terminated with a stainless steel optical penetrator. The electrical wires are grouped together and inserted into another oil filled hose that is connected to the switches box, which is a vessel containing electrical components, like breakers and sensors. Some of the electrical conductors in the switches box reach a power transformer (oil-filled pressure compensated), through an oil-filled hose; the other conductors, that connects the switches box with the subsea housing, are inserted into another oil-filled hose, terminated with a stainless steel electrical penetrator. All the described components, housed inside the fiberglass vessel, are hold by an steel frame. The fiberglass container is fitted into a titanium frame that permits the deployment operation and hold the external connectors at an height adequate to ROV operations (see fig.4).

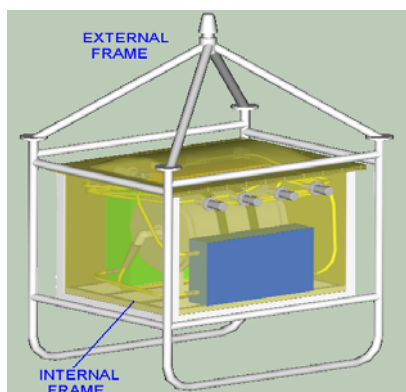


Figure 4: JB and its internal and external frame

### III. HEAT DISSIPATION

The power loss of the transformer must be dissipated through the walls, and in order to be sure that the safety temperature limit wouldn't ever been trespassed, we set up a FEA fluidynamic computational model. We considered a two dimensional model of the Junction Box. Heat dissipation of the electronics into the SH has been neglected due to its estimate low power /volume ratio. Instead, in order to

investigate the possibility to extend this Junction Box design to the final neutrino detector, we have implemented a simulation with the estimate power budget for the entire NEMO telescope (about 32kW), assuming a precautionary power loss ratio (8%). We simulated the convective motion of the dielectric oil taking into account the characteristic of the silicone oil that we will use to fill the JB. We have assumed as external temperature 284° K. We found the velocity and temperature distribution of the fluid inside the fiberglass container (see fig.5). Results of the simulation show that the temperature of the surface transformer box don't rise more than 10°C above the external temperature. This means that the heat is easily drained out through the walls of the JB. Transformer are usually expected to operate in the range 70-80°C, therefore the design seems to be satisfactory from the reliability point of view.

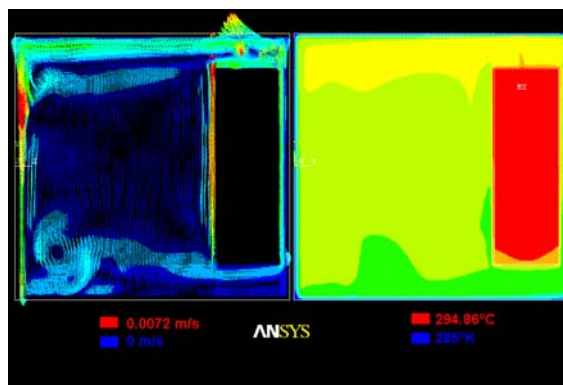


Figure 5: temperature distribution of the oil inside the FC

### IV. CONCLUSION

The mechanical design and its lay-out of the Nemo-phase I junction box has been completed, taking into account the operating conditions, the constrain, reliability and cost considerations. Some details are still under study, like the final design of the fiberglass container and its sealing, the internal and external frame, the deployment operation, but they aren't going to influence the feasibility of this system. The system, compared with standard titanium pressure vessel, like the Antares JB [3] improve the reliability due to reduced number of sealed connection and the double housing of the transformer; moreover, pressure vessel will be made in a less expensive alloy, this will introduce a significant decreasing in the detector budget.

### V. REFERENCES

- [1] E. Migneco in these proceedings.
- [2] R. Cocimano in these proceedings.
- [3] ANTARES JUNCTION BOX-MECHANICAL EXECUTIVE DESIGN AND MANUFACTURING, M. Ameri , M. Anghinolfi, S. Cuneo, R. Papaleo, F. Parodi, P. Prati, G. Raia, A. Rottura

# Plastic Encapsulation of Electronics

A. Kappes<sup>a</sup>, G. Anton<sup>a</sup>, U. F. Katz<sup>a</sup>

Physics Institute, University Erlangen, Erwin-Rommel-Str. 1, 91058 Erlangen, Germany  
alexander.kappes@physik.uni-erlangen.de, gisela.anton@physik.uni-erlangen.de, uli.katz@physik.uni-erlangen.de

## *Abstract*

We propose the use of polyurethane as encapsulation for electronic components in a future very large under-water neutrino telescope.

The protection of electronic modules against the hostile environment in the deep-sea poses a serious problem. For the current generation of under-water  $\nu$  telescopes the most common choice is the encapsulation of electronic components in a pressure-resistant stainless vessel made of titanium. The disadvantages of this solution are the high price for titanium which e.g. accounts for more than 50% of the costs for the electronic modules in the ANTARES detector, and the necessity to use penetrators resistant against a water pressure of 250 bar and more. A promising approach to circumvent the use of titanium are “composite solutions”, where the pressure resistant vessel made e.g. of steel is separated from the stainless cladding by an oil volume.

As an alternative we propose to cast the electronic components into polyurethane or similar kind of plastic material. A schematic drawing of a possible design can be seen in fig. 1. In case of cooling problems due to insufficient heat conduction through the polyurethane, titanium cooling pipes can be mounted in thermal contact to the heat-dissipating components. Open connections of these pipes to the sea water will allow for an automatic water circulation by convection. Pressure-sensitive electronic components can be encapsulated in a pressure-resistant vessel (need not be stainless) which is then casted into polyurethane. This design reduces the use of expensive titanium and water tightness is easier to obtain due to the elastic properties of the casting material.

The encapsulation method proposed here is a standard technique for deep-sea hydrophones. We think that this is an appealing alternative to the usage of titanium cylinders for the future very large  $\nu$  telescope in order to reduce costs and the risk of water leakages. We will study this option in more detail in the future.

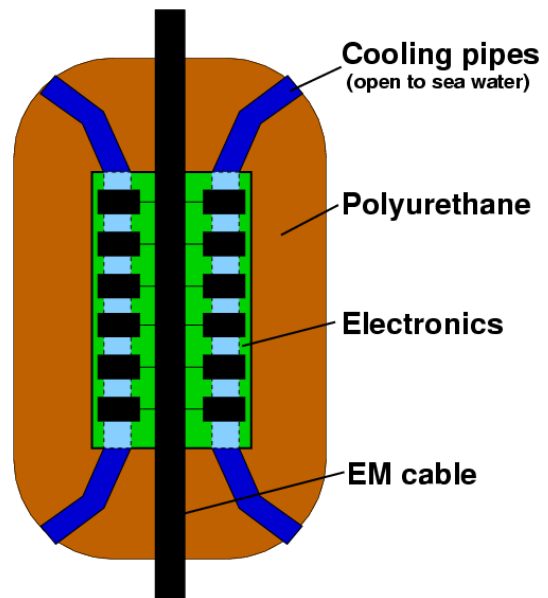


Figure 1: Schematic drawing of a possible design for the casting of electronic components in polyurethane.

---

<sup>a</sup> Supported by the German Federal Ministry for Education and Research, BMBF, grant no. 05CN2WE1/2

# NEMO Phase 1 data transmission: considerations toward KM3

F. Ameli, M. Bonori, C. Nicolau for the NEMO Collaboration

INFN - Sezione Roma1

fabrizio.ameli@roma1.infn.it, maurizio.bonori@roma1.infn.it, carlo.nicolau@roma1.infn.it

## Abstract

In very large underwater neutrino telescopes the number of photo-sensors is on the order of  $5 \cdot 10^3$  and the expected data rate of about 20 Gbps. The depth of the apparatus is about 4 km, and the distance from the shore is more than 100 km. These considerations recommend the use of a fiber optics transmission system to transport data bidirectionally to the underwater telescope. This paper presents a proposal for a data transmission system to be developed and tested in “NEMO Phase 1” experiment. Considerations about the scalability in a larger experiment are carried out on the basis of system performances.

## I. INTRODUCTION

Very large underwater neutrino telescopes will be based on detection of light produced by the Čerenkov effect. Photo-multipliers (PMTs) are expected to be on the order of  $5 \cdot 10^3$  and will yield a whole data rate which is roughly 20 Gbps. To obtain a suitable shielding using the sea, a depth of 4 km should be reached; this implies a distance from shore which is typically 100 km in the mediterranean sea. Furthermore, a common timing must be known in the whole apparatus at the level of detection device to allow correlation in time of events.<sup>1</sup>

These considerations recommend the use of fiber optics to realize the data transmission, the design of a system as much reliable as achievable, and a power consumption as low as possible.

In this sense, a favorable choice is the use of synchronous protocols. For example, the *Synchronous Digital Hierarchy* (SDH) protocol, which embeds data, synchronism and clock timing in the same serial bit stream, allows an easy distribution of the clock signal to the whole apparatus, and is defined for data transport over an optical medium. For a detailed explanation of SDH protocol see [1].

Many devices are available off-the-shelf with present technology to implement a data transport suited to KM3 experiment. Just few years ago data multiplex/demultiplex was realized with *Time Division Multiplex* (TDM) techniques acting on electric signals, with high power consumption and big processing complexity. Nowadays the same operations are carried out by *Wavelength Division Multiplex* (WDM) techniques using totally passive components.

In Fig. 1 is sketched the layout of “NEMO Phase 1”, which can be considered a feasibility test toward the cubic kilometer experiment called KM3. Reading the figure from right to

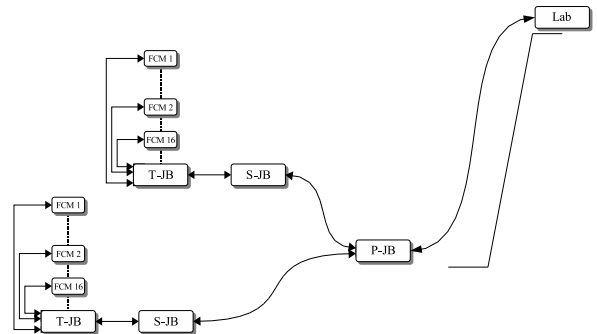


Figure 1: Block diagram of “NEMO Phase 1” apparatus.

left, i.e. from on-shore toward the apparatus, the main electro-optical cable is connected to the *Primary Junction-Box* (P-JB); then, fibers and power are split and connected to two *Secondary Junction-Boxes* (S-JBs), which, in turn, are connected to the *Tower Junction Boxes* (T-JBs) of the two towers which will be deployed.

This experiment is smaller than the KM3 whole apparatus though it is composed of all the main logical parts needed to test the KM3 experiment. Thus, its data transport system will be designed based on technical choices which allows scalability to a much bigger apparatus.

The most important unit of the apparatus is the *tower*, which is schematically shown in Fig. 2. The basic idea consists of making the tower a completely self-contained entity. Nonetheless, redundancy considerations will still hold in order to reach the reliability needed in such experiment.

The NEMO-tower consists of 16 floors, each containing a number of benthospheres which ranges from 4 to 8. The T-JB at the bottom of the tower is connected to all the floors and to the S-JB. At the center of each floor of the tower an electronics circuit, called *Floor Control Module* (FCM), is placed. The FCM collects data from the floor PMTs<sup>2</sup> and the floor control and auxiliary signals, creates an STM-1/SDH data stream at about 155 Mbps, and send data toward the land side laboratory. From the opposite direction, the FCM receives slow control data, commands and auxiliary information, and the clock and synchronization signals needed for apparatus timing [1].

In this paper we will focus on the optical data transport system. The FCM is provided with an electro-optical transceiver which converts the electric STM-1 bit stream at

<sup>1</sup>This consideration holds in case of data acquisition techniques currently implemented.

<sup>2</sup>See [2] for full details on PMT signal data acquisition, benthosphere control and connection set up.

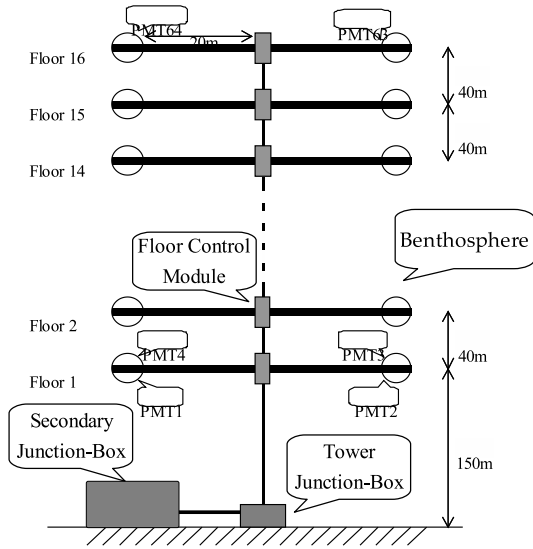


Figure 2: Schematic layout of NEMO tower.

155 Mbps into an optical stream. Therefore, the transmission system researched here will regard the connection from the FCM as far as the laboratory on shore.

## II. OPTICAL DATA TRANSPORT

Based on the scheme shown in Fig. 1, the whole optical transmission system connecting each FCM to the laboratory on the shore will be described. In Fig. 3 the parts involved in the optical data transport for the underwater apparatus are shown. The number of fibers and the aggregate data rates present at each sectioning point are also specified. For example, the FCM is connected to the T-JB using  $1 \times 155 \text{ Mbps}$ , i.e. one fiber supporting a 155 Mbps data rate.

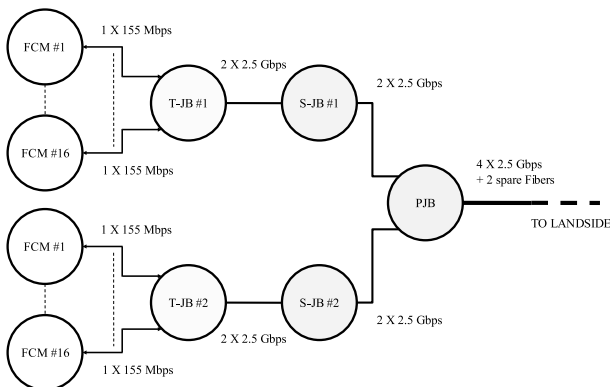


Figure 3: Block diagram of underwater data transmission system for NEMO Phase I. Number of fibers and data rate are given as well.

Bidirectional data transport at the floor level is realized by means of a single optical fiber connecting the FCM with the T-JB located at the base of the tower. The STM-1/SDH is the chosen protocol which encodes data with a bandwidth of

about 155 Mbps. Inside the T-JB a WDM device is placed, which packs the 16 bidirectional bit streams of the 16 floors and doubles the same whole stream over two fibers directly linked to the land side.

The underwater structure has a complementary on-shore counter part, shown in Fig. 4, where all optical signals are converted back to the electrical signals produced on the floors.<sup>3</sup>

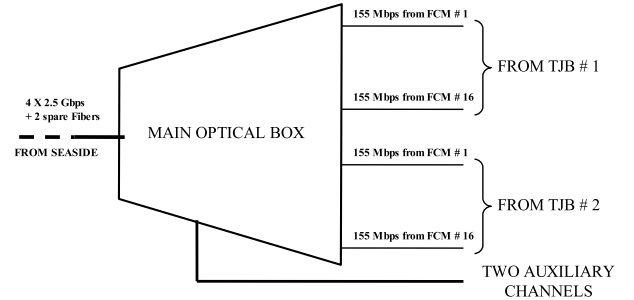


Figure 4: On-shore main optical box for floor data extraction.

The inner structure of each single component will now be explained in full detail.

### A. Under water optical system

As previously stated, the FCM board converts the STM-1/SDH electrical bit stream into an optical stream by means of a suited transceiver. The two optical streams, one per direction, are multiplexed onto a single fiber in order to reduce the number of fibers connecting the floor with the T-JB. The needed multiplexer (MUX) is a *Dense WDM* (DWDM) because signals transmitted/received by the FCM are compliant with ITU standard related to 200 GHz grid in C band. This choice is aimed at achieving greater reliability at the small price of an optical DWDM multiplex.

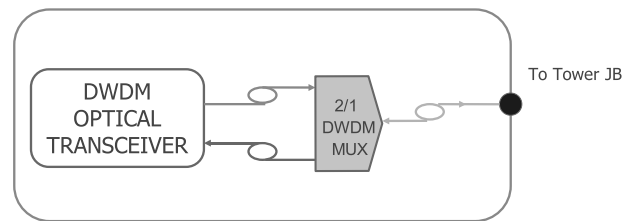


Figure 5: FCM electro-optical conversion and DWDM yielding a single fiber for both directions.

The 2 : 1 MUX in the FCM has a counter-part inside the T-JB, as shown in Fig. 6. Actually, in the T-JB there are as many 1 : 2 multiplexers as the number of floors per tower, i.e. 16. After restoring two fibers per direction per floor, we use

<sup>3</sup>The electro-optical conversion on-shore will be obtained using the FCM board, which is inherently bidirectional. For this reason we can neglect such conversion and taking into consideration only the extraction of optical STM-1 fluxes from the whole optical stream.

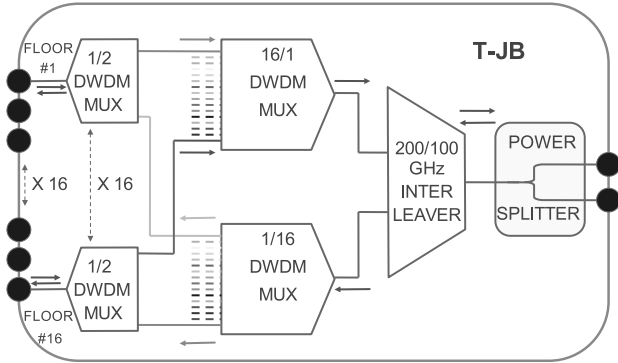


Figure 6: T-JB optical data transmission layout.

two 16 : 1 multiplexers to merge the fluxes of the 16 floors heading for the same direction: looking at the figure, the 16 : 1 DWDM MUX above conveys all the streams coming from the floors and going toward on-shore; the 16 : 1 DWDM MUX below is fed with a single fiber from on-shore, demultiplex the 16 streams and sends each of them to the 1 : 2 MUX. The two single fibers of the 16 : 1 MUXes are, then, combined together thanks to an *Interleaver* device. Reminding that the channels coming from each floors are spaced by 200 GHz, similarly the 16 channels arriving from on-shore will be spaced by the same amount. Moreover, the two set of frequencies will be staggered of 100 GHz so that there is no frequency overlap when merging them. On the right side of the 200/100 Interleaver we have a single fiber carrying all the streams related to the tower floors on both directions.

Actually, in order to increase reliability, this single fiber is doubled and data stream is re-directed onto two fibers, a main fiber and a protection fiber, using a “power splitter”. The two fibers drive two connectors, so that *cable redundancy* is guaranteed. How this splitting function is managed will be explained later during the discussion of the on-shore optical box.

The two fibers coming out of the T-JB pass through the S-JB unchanged. The manipulation inside the P-JB is due to the choice of providing an auxiliary unprotected channel for whatever use. In Fig. 7 is shown the content of the P-JB.

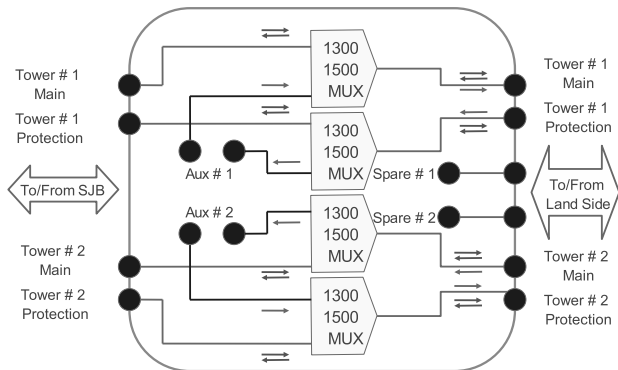


Figure 7: P-JB optical transmission components.

Using a 1500/1300 nm MUX, the two fibers per tower

can be used to insert two more fluxes, the first going to on-shore and the second coming from on-shore. This bidirectional channel provides an auxiliary channel which can be used for various purposes (a concurrent experiment, a monitor channel, etc.). Of course, the other two fibers connecting the P-JB with the second T-JB undergo the same treatment, i.e. they provide a second auxiliary channel. Each auxiliary channel is unprotected and will be effective only if both the main and the protection fibers are working properly.

On the right side of the P-JB there is the main electro-optical cable, connecting the experiment with the on-shore laboratory. Since it is provided with six fibers, four of them will be devoted to the two towers while the remaining twos either will be left free or will carry control signals for a separate power management system.

### B. Laboratory optical system

The laboratory optical system, which is called *Main Optical Box* (MOB), is the complementary counter-part of the underwater structure discussed previously. There are some simplifications obtained by less strict constraints due to the on-shore location of the apparatus. Instead some complexity is added to handle the underwater power splitter. In Fig. 8, a schematic diagram of the MOB is shown.

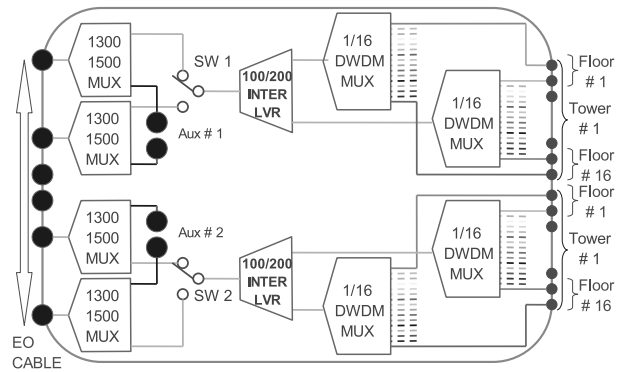


Figure 8: Laboratory main optical box layout.

The six fibers connected to the P-JB are connected to the left side of the box: the two auxiliary channels are extracted from the streams using the 1300/1500 nm MUXes. At this point, two “manual” switches are employed to decide whether the main or the protection fiber should be used. The decision is based on presence of optical signal or on data quality. In this way, the P-JB always sends data over the two fibers but only one stream at a time is selected in the MOB; similarly, data sent from on-shore are redirected only over one of the two fibers, to avoid complicate (and active) underwater selection inside the P-JB. The power splitter in the P-JB will continuously merge the two fibers but only one information flux will be physically present.

From now on, signals undergo exactly a complementary path with respect to underwater elaboration: a 100/200 inter-leaver restores two fibers per tower, each carrying a unidirec-



tional signal; then, two 1 : 16 DWDM MUX restore the two fibers per floor.

A simplification is due to the absence of the 2 : 1 MUX which connects the T-JB to the FCM. Two fibers can be directly connected to the on-shore FCM to extract floor data. Therefore, the streams at the right of the MOB represent optical data streams reproducing the in/out STM-1 fluxes at the floor level.

At this point of signal extraction, a big advantage of this system is the possibility of using standard telecommunication instruments to interface the STM-1/SDH data streams. It is possible not only checking for signal integrity and quality, but also extracting data itself.

### C. Optical Power Budget

A key issue for the feasibility of the proposed data transmission system is the calculation of the optical power budget. This calculation will be split in two parts: the first is the power loss, due to components and connections, strictly related to apparatus layout; the second is the transmitted power and receiver sensitivity, which are dependent on the specific transceiver employed.

In table 1 is shown the total power loss: the electro-optical cable taken into consideration is the one already deployed for NEMO Phase 1; thus the indicated loss is a measured value over the 30 km optical fiber. Concerning connectors, a total loss over the whole path has been reported, using worst values recommended by manufacturers of selected components. Same consideration holds for multiplexers and interleavers loss: manufacturer indication has been used adopting worst values for a conservative calculation.

Table 1: Total power loss due to optical system.

Location	Component	Loss (dB)
FCM	2:1 DWDM MUX	2
T-JB	1:2 DWDM MUX	2
T-JB	16:1 DWDM MUX	2
T-JB	200/100 GHz Interleaver	3
T-JB	1:2 Power Splitter	3
P-JB	1300/1500 nm CWDM MUX	2
Cable	Electro Optical Cable	6
MOB	1300/1500 nm CWDM MUX	2
MOB	200/100 GHz Interleaver	3
MOB	16:1 DWDM MUX	2
Path	Connectors	3
Total Power Loss		30

Regarding the transceiver, we cannot leave aside the specific device chosen. One of the possible candidates is the Agilent AFKC DWDM transceiver [3]: it provides the full range of C band wavelengths defined by ITU for the 100 GHz grid; it is compliant with SDH protocol up to STM-16, and has a minimum optical power budget of 33 dB which accounts for both the optical power transmitted and the receiver sensitivity.

Therefore, the optical margin achieved is about 3 dB,

which is enough to maintain the *Bit Error Rate* (BER) at a level as low as  $10^{-12}$  at 2.7 Gbps.<sup>4</sup>

Moreover, a *Forward Error Correction* (FEC) algorithm could be implemented to increment further the optical margin.

## III. CONCLUSION

A data transmission system has been proposed to transport data from NEMO Phase 1 apparatus to on-shore. Design choices has been taken considering a possible future use in KM3 experiment.

The widely applied WDM technique has shown many advantages: the optical path is totally passive, the only active component being the electro-optical transceiver; the lack of active components implies reliability, low power consumption, and small physical dimensions.

Concerning NEMO Phase 1 experiment, major benefits are: one single fiber is needed to connect the floor with the T-JB; in the P-JB, one auxiliary channel per tower is provided; two of the six fibers of the deployed electro-optical cable are left available to other purposes in the P-JB; a protection scheme of 1 + 1 is realized from the T-JB to the land laboratory and all the switches driving this redundancy are located on-shore. Last, but not least, all the selected components are available off-the shelf, i.e. industry supported and low cost.

## REFERENCES

- [1] F. Ameli, M. Bonori, and C. A. Nicolau. Synchronous data transmission protocol for NEMO experiment. In *VLVvT Workshop*. NIKHEF, Amsterdam, 2003. To be published.
- [2] F. Ameli, M. Bonori, and C. A. Nicolau. A 200 MHz FPGA-based PMT acquisition electronics for NEMO experiment. In *VLVvT Workshop*. NIKHEF, Amsterdam, 2003. To be published.
- [3] Agilent. Agilent AFKC-xxxx Hot-Pluggable DWDM Transceiver. Technical report, Agilent Technologies, 2003.

<sup>4</sup>In case of 155 Mbps bit stream this BER value causes 1 bit error every 1.8 hours.



# Photo Detection



# Facility apparatus for O.M. characterization

Santo Reito

On behalf of the Catania Microelectronic group  
INFN sez. Catania Via S. Sofia, 54 – 95120 Catania Italy  
Santo.reito@ct.infn.it

## Abstract

The detection characteristics of an underwater Cherenkov arrays of PMTs lead to well defined requirements for each optical module (O.M.).

Some of them require many tests in order to optimise the overall response of the O.M. .

To perform these tests we have designed a dark box equipped with a laser diode working at three wavelength (370, 420, 500 nm) connected with a optical fibre and a mechanical system allowing this scanning of the surfaces both of the PMTs and O.Ms..

The system let to preset a map of points where to perform the measures of TTS, gain and peak to valley ratio.

This system is completely automatized using a PC remote control.

With this apparatus we have performed measurements of Gain and variation of transit time (TT) and of his spread (TTS) for 8", 11" and 15" PMs delivered by EMI and Hamamatsu.

Some results are shown.

## I. THE DARK ROOM FOR O.M. CHARACTERIZATION

We have realized a 1,5 x 1,5 x 1,5 m dark box equipped with laser diodes that allows measures of energy and time resolutions.

The supports inside the dark box have been realized to be able to make measures both of the PMTs and O.Ms.



Figure 1: dark box

## A. Scanning System



Figure 2: scanning system

The scanning of the photocatode is performed by a system of movement of the optic fiber. It consists in a semicircular guide, on which the support of the optic fiber is moved. It is able to rotate of  $\pm 90^\circ$  in comparison to the horizontal position.

The support of the fibre and the guide are moved by two step motor controlled by the PC.

## B. Light source

We have used for the test as source 400nm a Laser to. The pulse the pulse width is about 60ps.

It can be driven by a external pulse generator.

We use single photoelectron method, so we need several N. D filter.

## C. Set up

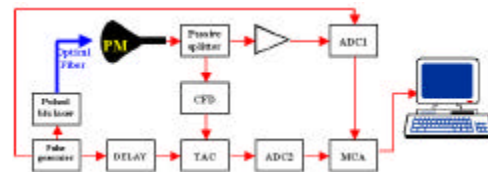


Figure 3: set up

## II. MEASUREMENTS

We have tested several Emi PM ETL 9354, 8", high gain ( $2 \cdot 10^7$  to  $-1500V$ ) and good timing (TTS<sub>fwhm</sub> 3ns, rise time 4ns, pulse FWHM 8ns).

Several measurements have been done.

### A. Gain

We calculate gain by

$$G = \frac{\langle Q \rangle}{A \cdot q_e} = \frac{(C_{\max} - C_p) q_c}{A \cdot q_e}$$

where  $\langle Q \rangle$  is the maximum of the gaussian that fit our signal (we need to subtract pedestal  $C_p$ )  $q_c$  is ADC resolution in pC/ch, A is the value of the amplifier.

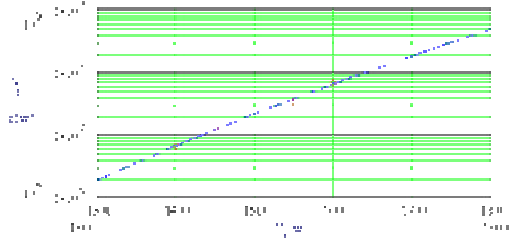


Figure 4: set up

We tested the linearity of the gain in relationship to the power supply

Table 1: Gain vs power supply

(V)	-1400	-1450	-1550	-1600
$G = \langle Q \rangle / A \cdot q_e \cdot 10^7$	0,649	1,33	3,26	6,50

### B. Peak to valley ratio

The Peak to valley ratio represents the signal to noise ratio so it's a good indicator of the resolution of the our device.

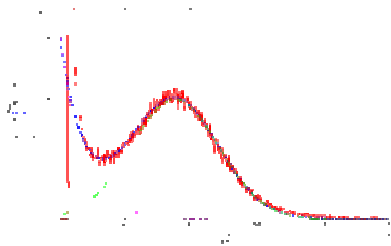


Figure 5: Peak to valley ratio

This value is about 2 in accord with manufacturers test.

### D. Uniformity measurements

To test the uniformity of the surface we have chosen 49 point of measure uniformly distributed.

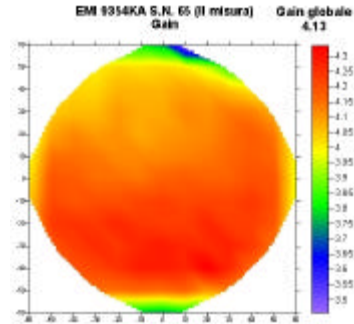


Figure 6: Gain

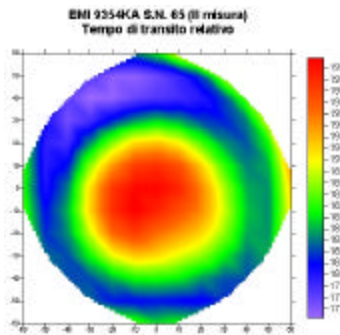


Figure 7: Time Transit

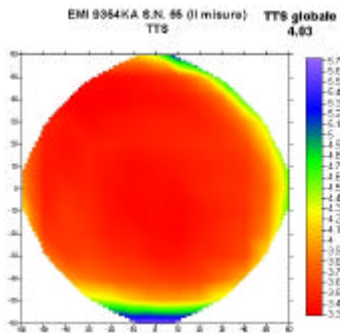


Figure 8: Time Transit Spread

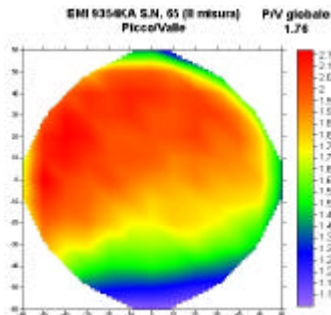


Figure 9: Peak to Valley ratio

Table 2: media value

$\lambda$ (nm)	Ser.N	HV (V)	TTS (ps)	Gain( $10^7$ )	P/V
400	65	1470	4030	4.13	1.76

### III. MU-METAL CAGE

To reduce the Earth's Magnetic Field we have realized a mu-metal cage. It fits the optical module shape.



Figure 10: mu-metal cage

It consist of wire about 1 mm and a strip of 11x0.25 thk.

The total shadow on the photocatode surface is about 4 %.

We have tested the value of the magnetic field inside the cage with a Hall detector, it reduced about 4 times the Earth magnetic field.

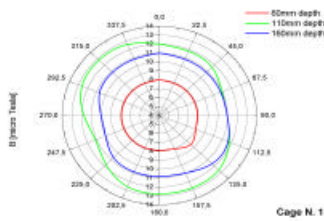


Figure 11: magnetic field vs. distance

We have repet same measures with cage

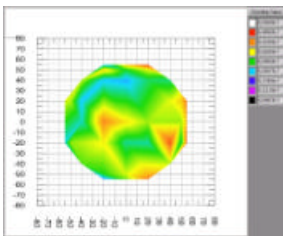


Figure 12 Gain with mu-metal cage

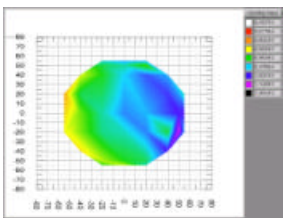


Figure 13 TTS with mu-metal cage

We have noticed a better uniformity in response.

### IV. CONCLUSION

We are working to optimise the measurement system.

To improve quantum efficiency measurements.

# The NESTOR Optical Module

## VLVvT Workshop 2003

A. Tsirigotis

Hellenic Open University for the NESTOR Collaboration  
tsirigotis@eap.gr

### Abstract

The key component of NESTOR underwater neutrino detector is an optical module employing a photomultiplier tube with a 15 inch hemispherical photocathode in a transparent glass pressure housing. Extensive tests have been made on the sensitivity, uniformity, time resolution, noise rates and mechanical properties of the module.

## I. INTRODUCTION

The NESTOR (Neutrino Extended Submarine Telescope with Oceanographic Research) neutrino telescope is detecting the Cerenkov radiation produced by  $\nu$  - induced muons and/or showers of charged particles in a large volume of sea water. The NESTOR site is located at the South West of Peloponnese (Greece), at the seabed of the Ionian Sea. In fact this is where one finds the deepest waters in Mediterranean sea, 5200m. The NESTOR collaboration has located a  $8km \times 9km$  horizontal plateau at a depth of 4000 m [1, 2]. The plateau is at a mere distance of 7.5 nautical miles from shore. Extensive studies of environmental properties have been made [3, 4]. These measurements show that the water transmission length is 55m at a wavelength  $\lambda = 460nm$ . The underwater currents have been measured and they have been found minimal, i.e. a few centimeters per second [5]. Also the sedimentology analysis is completed [6].

## II. NESTOR DETECTOR

The basic detector unit is a rigid hexagon, shown in Figure 1, made out of titanium with a diagonal of 32 m. At the tip of each arm of the hexagonal floor there is a pair of two 15 inch photomultiplier tubes (PMTs) inside benthos glass housings [7], one looking upwards and the other downwards. The electronics which are responsible for signal sensing, triggering, digitization and data transmission to the shore are housed inside a large titanium sphere (1m in diameter) located at the center of the hexagonal floor. The electrical pulses of the PMTs are digitized by the Analog Transient Waveform Digitizers (ATWDs) of the floor electronics board (developed at Lawrence Berkeley National Laboratory). The digitized waveforms are transmitted to shore, where the raw data are recorded. In the offline analysis, the digitized waveform of each PMT goes through a processing procedure and the arrival time, the pulse height and

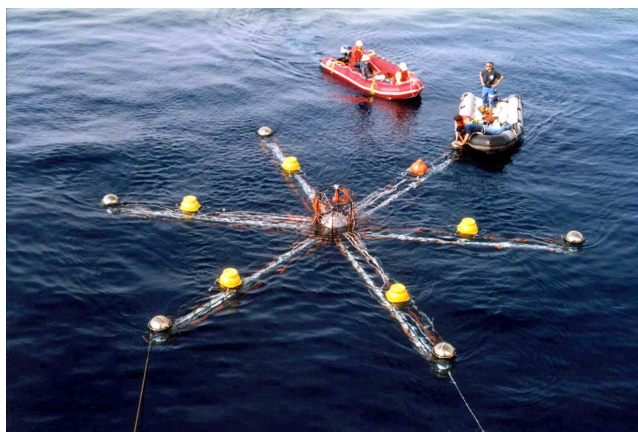


Figure 1: A photograph of the NESTOR Floor taken during last deployment, a few moments before it was lowered to 4000m

the total charge of each PMT pulse are accurately determined [8].

By stacking 12 of these floors in the vertical, with a distance between them 30m, they create a tower shown in Figure 2, which is connected to the shore by an electrooptical cable (18 fibers plus 1 conductor). The effective area of a NESTOR Tower in reconstructing throughgoing muons of energy  $> 10TeV$  is greater than  $20000m^2$ , whilst the energy threshold of such a detector is as low as 4 GeV for contained tracks.

In March 2003, using the cable ship RAYMOND CROZE of France Telecom, the hexagonal floor shown in Figure 1 was deployed fully equipped with electronics and associated environmental sensors to a depth of 4000m. In the control room, during the deployment and operation of the detector, the parameters of the detector were continuously monitored. These include the floor orientation (compass and tilt meters), temperatures, humidity and hygrometry within the Titanium sphere, PMT high voltages, as well as data from other environmental instruments mounted on the sea-bottom station (pyramid), such as pressure meters, current meters, etc.



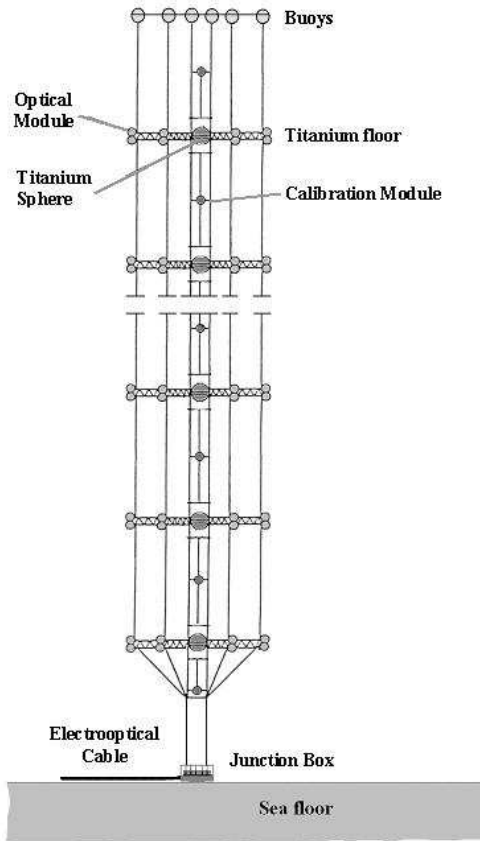


Figure 2: NESTOR Tower

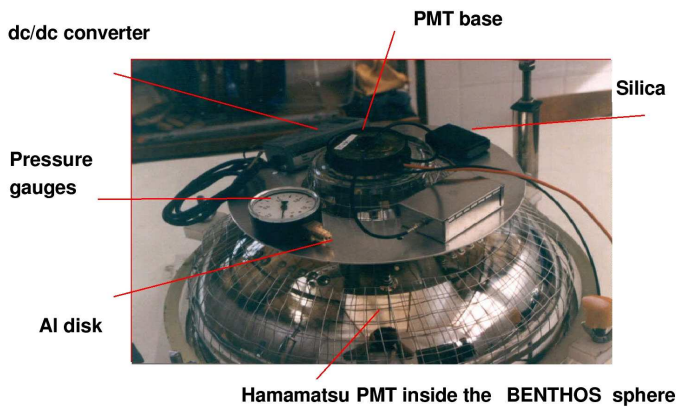


Figure 3: The NESTOR Optical Module.

### III. THE NESTOR OPTICAL MODULE (OM)

The OM, shown in Figure 3 during construction, consists of a photomultiplier tube (PMT) installed in a spherical glass pressure housing of 400mm inside diameter. This Benthos sphere, made out of two hemispheres with a ground glass interface,

can withstand the high external pressures, of about 400Atm, at operating depths. Optical coupling between the glass envelop of the PMT and the sphere is achieved by using a silicone gel or glycerin. The glass housing consists of two hemispheres of annealed, low expansion borosilicate glass; the equatorial surfaces are carefully ground to match each other. In Figure 4 the transparencies of the materials surrounding the photocathode are shown.

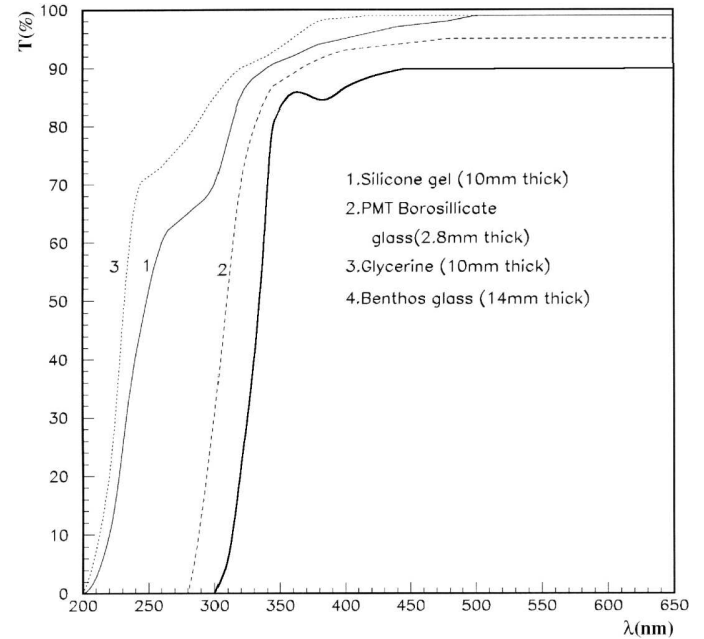


Figure 4: The transparencies of the silicon gel (1), of the PMT glass(2), of the glycerin(3) and of the glass housing (4).

Within the pressure sphere, each PMT is surrounded by a high permeability magnetic shield in the form of a  $\mu$ -metal cage, in order to reduce the effects of the Earth's geomagnetic field inside the PMT. The high voltage for the PMT is generated locally by a dc-dc converter, mounted on an aluminum disk.

Connection to the OM is through a single, high pressure, 7 pin electrical connector. The connector carries the PMT signal, as well as the low voltage supply, control and monitoring lines. Each OM is connected to the central titanium sphere housing the electronics, by a hybrid (twisted pairs and co-axial) cable.

#### A. The Photomultiplier

The lifetime and success of a deep underwater detector like NESTOR depends strongly on the quality and proper operation of its PMTs. For such a detector, the PMTs employed must meet certain requirements:

- High quantum efficiency of the photocathode is required, in order to have high detection efficiency which results in a large active volume, a high reconstruction efficiency and a lower energy threshold.

- Large angular coverage. The design of the NESTOR detector uses omni-directional combinations consisting of two back to back OMs. Each OM should cover efficiently the volume around it.
- Good timing response.
- Good pulse height resolution.
- Small dark count rate.
- Good linearity over a large dynamic range.
- Long time stability in gain.

These requirements are fulfilled by the Hamamatsu 15 inch PMT (type R2018-03). Also the newer Hamamatsu 13 inch PMT (type R8055-01) meets these requirements, providing a much better pulse high and time resolution [9]. In Figure 5 a cross section of the R8055-01 PMT is shown. The typical value

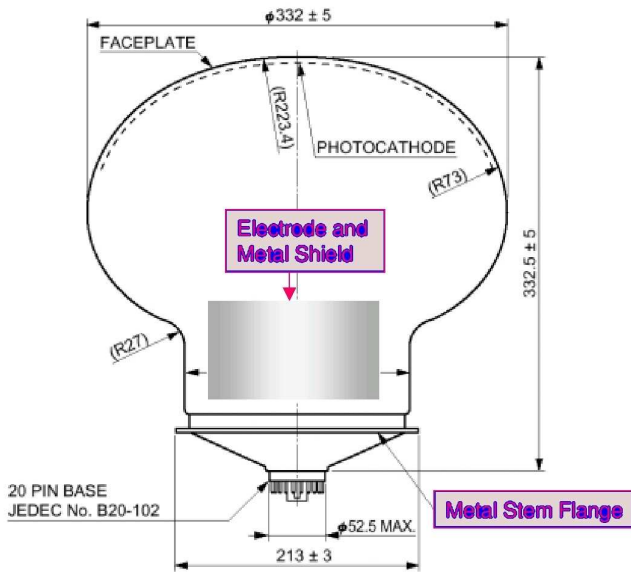


Figure 5: Dimensional Outline of the Hamamatsu R8055 PMT.

for the peak to valley ratio of the single photoelectron pulse-height distribution is 1.5 for the R2018-03 PMT and 2.7 for the R8055-01 PMT. The photocathode in both types of phototubes is coated with a bi-alkali compound which has high spectral sensitivity for blue light, spectral response extending from 300 to 650 nm, low thermal emission, and a typical maximum quantum efficiency of 20% (shown in Figure 6).

#### IV. TESTS PERFORMED ON THE NESTOR OMS

Extensive studies of the PMT performance have been performed both in the LAB and during operation in deep sea. The distribution of the Transit Time Spread (TTS) of R2018-03 PMTs has been established in the LAB, during calibration runs

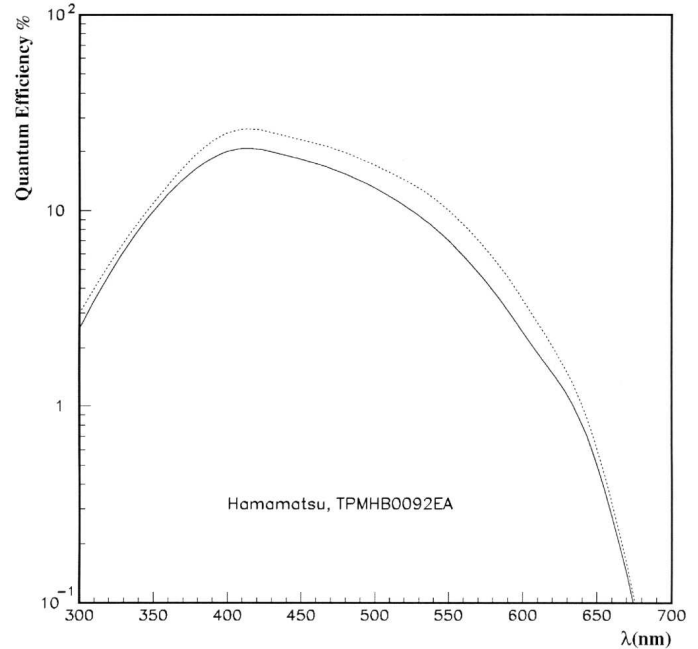


Figure 6: The quantum efficiency of the PMT R2018-03 versus the wavelength of incident photons (solid line).

and is shown in Figure 7. The mean value of the TTS for this type of PMT is 5.5nsec (FWHM). The 13 inch R8055-01 PMT has a better time resolution with a TTS at FWHM of 2.8 nsec [9].

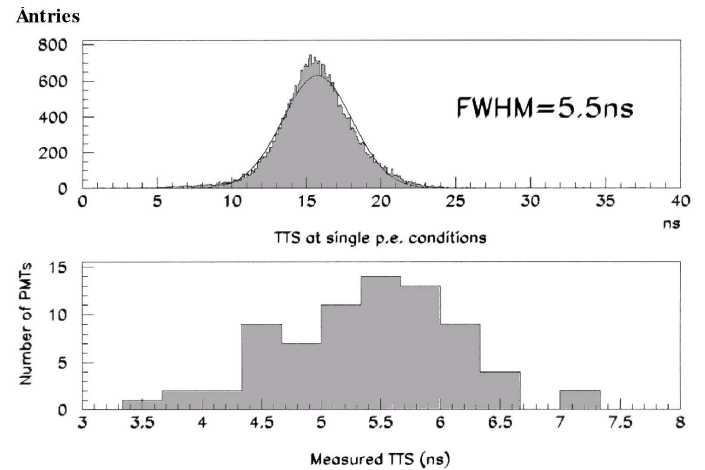


Figure 7: The typical TDC spectrum at the single photoelectron level of a type R2018-03 PMT. The lower plot shows the TTS (FWHM) distribution for many PMTs.

Calibration in the sea uses LED flasher modules mounted above and below the detector floor. Using light pulses from the calibration system several experimental parameters (e.g. PMT timing, gains etc.) can be monitored. Further analysis of the calibration data, results in situ measurement of PMT characteristics, such as slewing Transit Time Spread (TTS). Figure 8 shows the variation at the PMT pulse arrival time and

the TTS as functions of the PMT pulse amplitude, as they have been estimated from the calibration runs. In Figure 9 a typ-

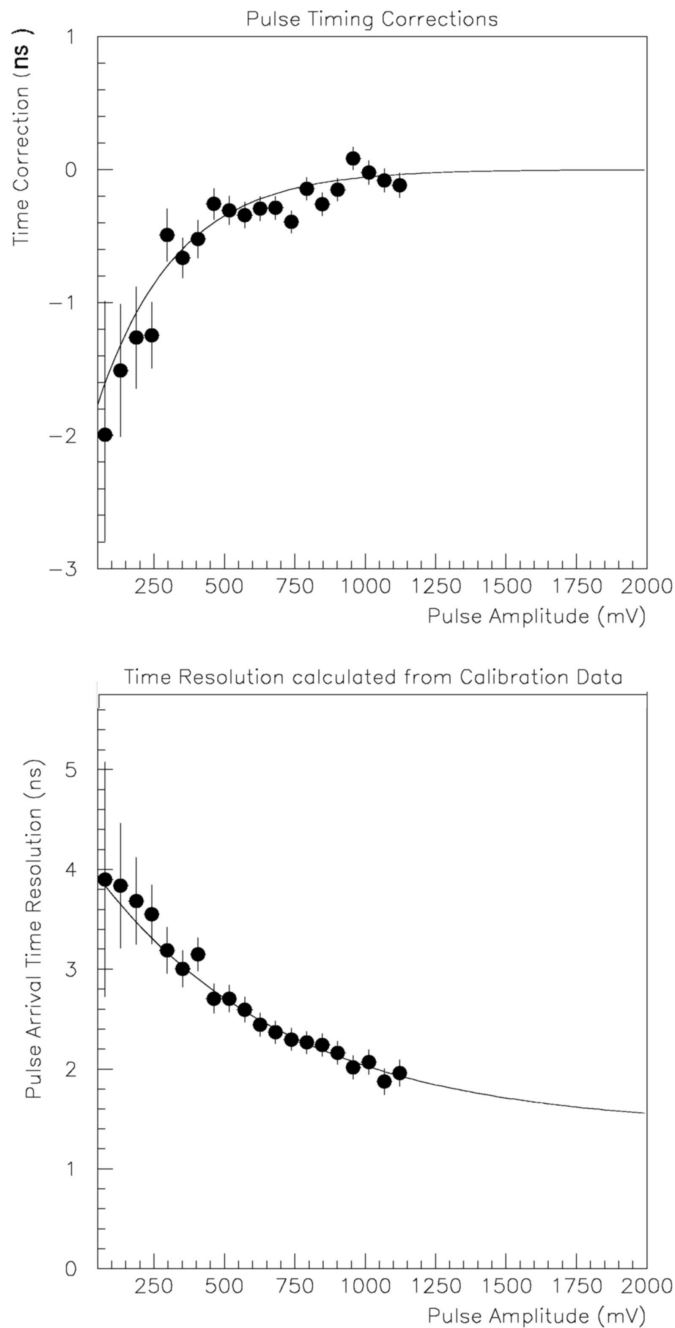


Figure 8: Slewing correction (top figure) and TTS (bottom figure) as a function of the pulse amplitude, estimated using calibration data taken during detector operation at 4000m. They are found to agree very well with the measured ones from calibration runs in the LAB.

ical pulse height distribution of a PMT during data taking is shown. This distribution is very well described as the overlap of the thermionic background shape and the Polya distributions for one and two photoelectrons, which have been established during the calibration runs in the laboratory. In Figure 10 the pulse arrival time difference for a pair of PMTs is shown, esti-

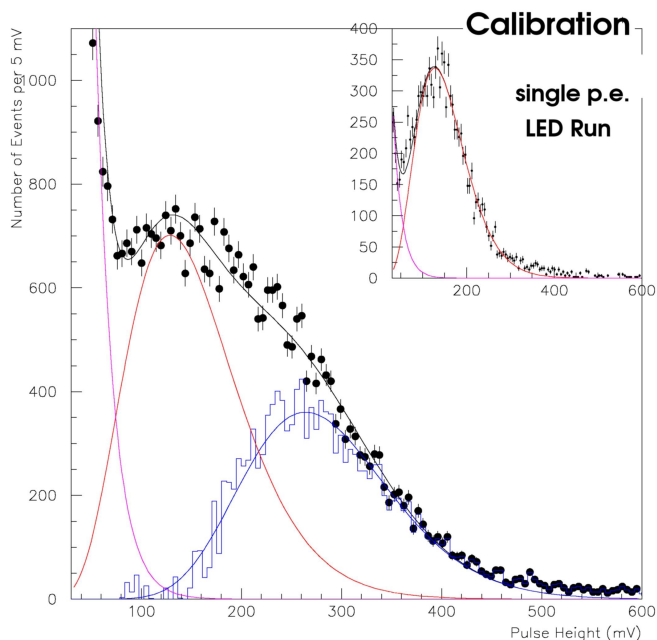


Figure 9: The Pulse Height distribution of one PMT using data from deep sea (main plot) and from calibration runs (insert plot). The three different components correspond to the PMT dark current, the single photoelectron, and the double photoelectron spectrum.

mated using calibration data taken during detector operation at 4000m.

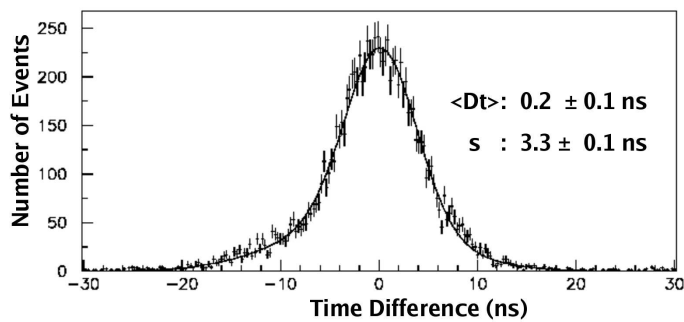


Figure 10: Pulse arrival time difference for a pair of PMTs.

## REFERENCES

- [1] L. K. Resvanis (1992), 2nd NESTOR International Workshop, 1992, L. K. Resvanis editor.
- [2] L. K. Resvanis et al. High Energy Neutrino Astrophysics (1992), V. J. Stenger, J. G. Learned, S. Pakvasa and X. Tata editor.
- [3] Khanaev (1992), 2nd NESTOR International Workshop, 1992, L. K. Resvanis editor.

- [4] E. Anassontzis (1994), Nuclear Instruments and Methods **A349**, (1994), 242.
- [5] Demidova, 2nd NESTOR International Workshop (1992), L. K. Resvanis, editor.
- [6] E. Trimonis, 2nd NESTOR International Workshop (1992), L. K. Resvanis, editor.
- [7] E.G. Anassontzis, et.al., “The Optical Module for the NESTOR Neutrino Telescope”, NIM A **479** (2002) 439-455.
- [8] A. Tsirigotis, “Reconstruction, Background Rejection, Tools and Methods”, these proceedings.
- [9] Aicher, Klaus Peter, “Latest Vacuum Photodetectors for High Energy Experiments”, RICH2002, NESTOR, Pylos, Greece, 5-10 June 2002. [www.nestor.org.gr/rich2002](http://www.nestor.org.gr/rich2002)

# The HPD Detector

M.Giunta<sup>a,1</sup> A. Piccioli<sup>b</sup> R. Pegna<sup>b</sup> I. Fedorko<sup>a</sup> N. Malakhov<sup>a</sup> A. Menzione<sup>a</sup> F. Raffaelli<sup>a</sup>  
A. Braem<sup>c</sup> E. Chesi<sup>c</sup> C. Joram<sup>c</sup> J. Séguinot<sup>c</sup> G. Sartori<sup>d</sup> P. Weilhammer<sup>c</sup>

<sup>a</sup> INFN, Sezione di Pisa

<sup>b</sup> Dipartimento di Fisica, Università di Siena and INFN, Sezione di Pisa

<sup>c</sup> CERN

<sup>d</sup> INFN, Sezione di Padova

<sup>1</sup> corresponding author: michele.giunta@pi.infn.it

## Abstract

The HPD detector is here described in the working principle and in the main characteristics, then some test results are shown. This detector is being developed to be applied to the CLUE IACT experiment, but shows attitudes for a large number of applications, from medical ones to neutrino detection.

## I. WORKING PRINCIPLE

The HPD [1, 2] (Hybrid Photon Diode/Detector) is a vacuum tube with an entrance window, quartz if UV sensitivity is required, and a semitransparent photocathode layer. Photoelectrons emerging from the photocathode are accelerated by a strong electrostatic field ( $-20/-30$  KV) and focused to the baseplate, equipped with a silicon sensor. The focusing effect is obtained with 3 or 4 ring electrodes placed at different potentials, growing from the negative  $HV$  to the ground (sensor). The final signal, some thousand electrons, is given by a single-step multiplication process: the energy gained by electrons from the electric field is dissipated in the silicon thickness, producing electron-hole pairs. Gain value and gain standard deviation are given by:

$$G = \frac{e\Delta V - K}{3.62 eV} \quad \sigma_G = \sqrt{FG}$$

where  $K$  is the energy lost in the metal layer on the sensor and  $F = 0.1$  is the Fano factor for silicon. This process, if compared to the PMT one (dynode cascade, multi-step multiplication), shows very small fluctuations: the HPD spectrum quality is clearly visible in the separation between photopeaks (figure 1).

In a HPD the sensor can be segmented, so this detector is a multipixel device without dead zones on the surface. This surface can be, at present, as large as  $500 \text{ cm}^2$  corresponding to  $10''$  diameter; a  $20''$  HPD had been successfully simulated in the electron optics and seems to be feasible.

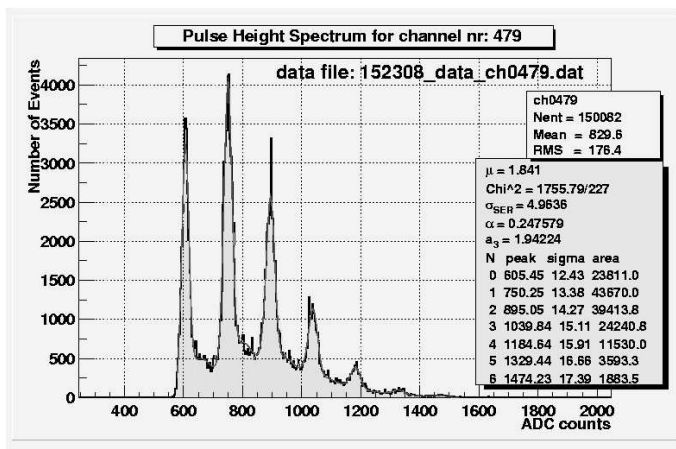


Figure 1: A typical HPD calibration spectrum. Separation between different photoelectron peaks is evident. Fit parameters, obtained using the FFT method proposed in [3], are represented together with the different peaks positions.

## II. CLUE EXPERIMENT, TOM PROJECT

CLUE [4, 5] is an ultraviolet IACT (Imaging Atmospheric Čerenkov Telescope) array (9 telescopes of  $1.8 \text{ m}$  diameter) located at La Palma, Canarian Islands (Spain)  $2.2 \text{ Km}$  asl.

The UV wavelength sensitivity was chosen to extend the experiment duty cycle allowing the telescope to work pointing directly to the moon and to take advantage of the background cut provided by the atmospheric ozone layer.

The CLUE focal planes are equipped with MWPCs, each having  $24 \times 24$  pixels and a  $190 - 230 \text{ nm}$  sensitivity window.

An important factor  $\simeq 20$  on the total amount of light can be obtained by replacing the existing MWPCs with a device having the spectral response of  $Rb_2Te$  ( $190 - 300 \text{ nm}$ ).

The TOM Project [6, 7] is now studying the possibility to upgrade the telescope performance replacing the MWPCs with  $10''$  HPDs, manufactured with  $Rb_2Te$  photocathodes on quartz windows.

### III. THE PRODUCED HPDS

The TOM collaboration is testing a 5'' UV HPD ( $Rb_2Te$  photocathode and borosilicate window) and a 10'' bialkali HPD, both of them having a 2048 pixel sensor [8, 9].

The applied potential between photocathode and sensor is 20 kV for the 5'' HPD and 30 kV for the 10'' one, corresponding respectively to 5000  $e^-$  and 8100  $e^-$  electrons pairs generated by photoelectrons in the silicon layer.

The silicon sensor is, for all our HPDs, 50 mm large and 300  $\mu m$  thick, segmented in 2048 pixels organized in 16 sectors each read by an IDEAS Viking VA3 chip (a charge integrating amplifier followed by a shaping amplifier) [10]. This chip has a 2  $\mu s$  shaping time and requires external trigger, but we're ready to mount a full-tested new chip, the VA-TA GP3 (IDEAS) with autotriggering circuit (150 ns shaping time) and sparse readout capability. The HPDs we're testing have the readout electronics located inside the vacuum tubes; due to the large number of channels the signals are serialised in order to contain the number of feed-throughs.

We produced 5'' HPDs both with visible photocathode (Bialkali,  $QE_{peak} \simeq 24\%$ ) and UV ( $Rb_2Te$ ,  $QE_{peak} \simeq 15\%$ ) with borosilicate window. A 10'' HPD in the visible range was recently produced and tested (figure 2). The ageing of this cathodes, produced at CERN, is proved to be good over 2 years, but we have until now no data for longer periods.



Figure 2: The 5'' (left) UV HPD and the 10'' bialkali HPD (right); the two tubes mount the same sensor and readout electronics.

### IV. LAB MEASUREMENTS

In order to study the pulse height spectrum properties, we used a hydrogen spark lamp to generate light pulses and trigger signals for the acquisition chain. Figure 1 shows the peak separation capability for the 5'' HPD: in this case the relative charge amplitude fluctuation is  $\frac{\sigma_1}{Q_1} = 0.1$ . In the case of the 10'' HPD,

which can be operated at higher cathode potential, a value 0.05 has been obtained [6].

These low values must be compared with those usually reached by PMTs: 0.4 in the best case. That performance allows for very precise photon counting, especially in low photon rate conditions where PMTs are less precise.

In order to calibrate each channel, we developed a FFT [7] method performing a fast and absolute calibration.

Imaging properties have also been measured during this test. Both the 5'' and the 10'' HPDs show a very linear transfer function, see figure 3.

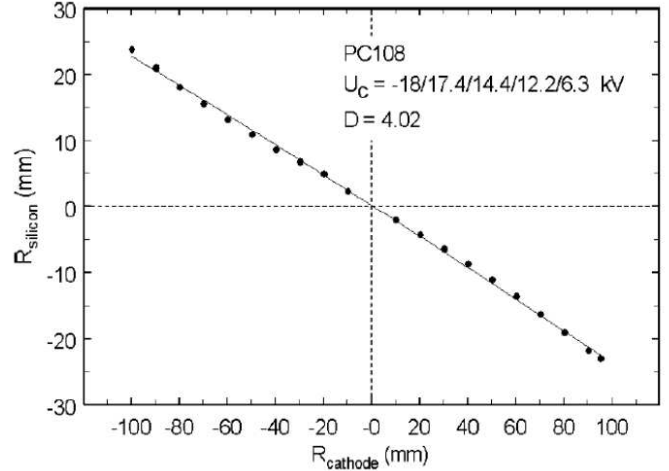


Figure 3: The photocathode projection on the sensor is very linear: here the silicon radial coordinate is plotted vs the window one for the 10'' HPD. The (inverse of the) slope of this line is called *demagnification*; we measured a demagnification of 4.02 for the 10'' HPD and 2.6 for the 5''.

The Point Spread Function obtained illuminating the HPD with a collimated light spot ( $\sigma = 0.7 mm$ ) from a  $H_2$  flash lamp, is 0.3 mm for the 5'' HPD ( $U_C = -20kV$ ) and 1.2 mm for the 10'' HPD ( $U_C = -30 kV$ ), see figure 4.

### V. MOUNTAIN MEASUREMENTS

In september 2003 we tested the HPD mounted in one of the CLUE telescopes. Taking advantage of the good separation between different photoelectron peaks we performed a very precise frequency measurement of a random light signal.

We used this feature to measure the frequency of the Night Sky Background (NSB). The analog output of a single pixel was sent to a discriminator producing a NIM signal 10 $\mu s$  long whenever the signal was over the  $V_{th}$  threshold set. The discriminator output was then sent to a counter that gives the number of events over threshold in a selected time periode (10s).

While  $V_{th}$  is between the pedestal value and the first photoelectron peak, the number of photoelectrons releasing this fraction of charge is small ( $\simeq 20\%$ ) so that the integral rate presents a plateau zone: see figure 5.

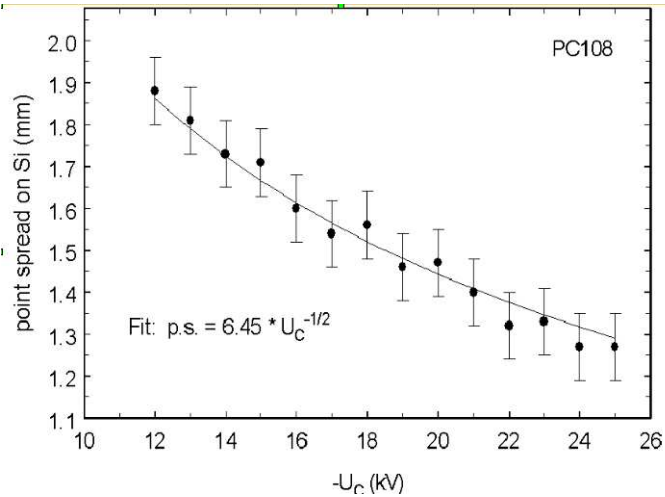


Figure 4: The PSF behaves like  $(HV)^{-1/2}$  as we expected. The sigma value of this function is here plotted as a function of the applied voltage.

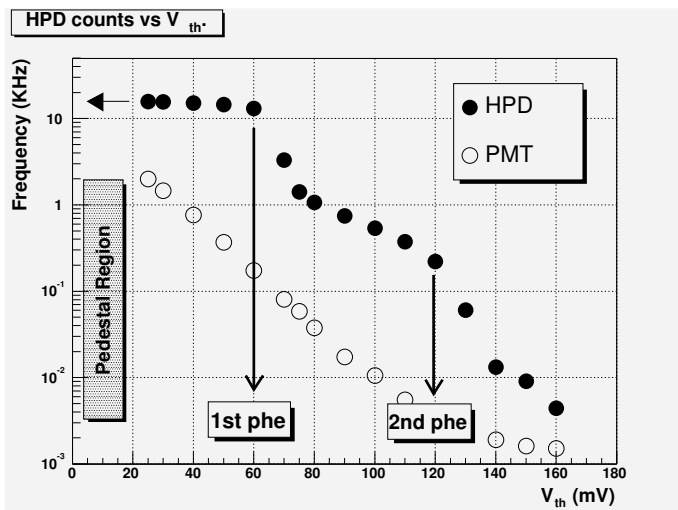


Figure 5: The NSB signal frequency measurement taken in La Palma (September 2003) with an HPD mounted in one of the CLUE telescopes (full circle). The rate dependence on discriminator threshold ( $V_{th}$ ) is plotted. The good separation between peaks produces the particular *stairs* shape (plateaux, falling zones) in the right side plot. The two vertical arrows correspond to the first and the second photoelectron peaks in the left-side spectrum. The horizontal arrow represents the *integrated* frequency. The same plot for a PMT (empty circle) is shown for comparison. HPD and PMT data have been taken simultaneously.

When  $V_{th}$  is over the first photoelectron peak position, the number of counts falls down. The same effect happens with next peaks. As a consequence, the integral rate versus  $V_{th}$  has a typical *stairs* shape: the first plateau level gives directly the integral rate of the random signal. The horizontal arrow in figure 5 indicates this value.

The figure also shows data simultaneously taken with a PMT having the same  $Rb_2Te$  photocathode; in this case there's no stair-shaped decrease because the PMT has not a clear photopeak separation as the HPD has.

## REFERENCES

- [1] C. Joram *Large Area Hybrid Photodiodes* **Nucl. Phys. B** 78(1999), 407-415
- [2] A. Braem et al. *Development, fabrication and test of a highly segmented hybrid photodiode* **NIMA** 478(2002), 400-403
- [3] T. Tabarelli de Fatis *Light spectra sum rule* **NIMA** 385(1997) 366-370
- [4] B. Bartoli et al. *Shower reconstruction in the CLUE experiment* **NIMA** 461(2001), 311-313
- [5] B. Bartoli et al. *Observation of  $\gamma$  sources using a new reconstruction technique in the CLUE experiment* **Nucl. Phys. B** 97 (2001) 211-214
- [6] C. Joram et al. *Design, Fabrication and Performance of the 10-inch TOM HPD* Presented to 9th Pisa Meeting on Advanced Detectors. Submitted for publication in **NIMA**
- [7] A. Piccioli et al. *Characterization of a potted 5-inch HPD with  $Rb_2Te$  photocathode* Presented to 9th Pisa Meeting on Advanced Detectors. Submitted for publication in **NIMA**
- [8] A. Braem et al. *Development of a 10" HPD with integrated readout electronics* **NIMA** 504(2003), 19-2
- [9] A. Piccioli et al. *HPD: new UV detector for Imaging Air Cherenkov Telescopes* **NIMA** 504(2003), 294-297
- [10] Integrated Detector & Electronics AS VA-family data sheets see [www.ideas.no](http://www.ideas.no)

# Development of Large Effective Area and Direction Sensitive Photodetectors

A. Bersani (for the NEMO collaboration)

Università di Genova and INFN sezione di Genova, via Dodecaneso 33, 16146 Genova, Italy  
Andrea.Bersani@ge.infn.it

## Abstract

In this note is described the status of the development of large effective area and direction sensitive photodetectors in Genova. We are developing a light guide system for multianodic devices or for PMTs array based on Winston's cone concept; we are also constructing a hybrid PMT with four-folded direction sensitive reading.

This work, held on in the framework of the NEMO collaboration, is intended to improve the light collection efficiency of the single OM and to maximize the information collectible, giving an additional information about the position of the track w.r.t. the OM itself.

## I. INTRODUCTION

In a large neutrino telescope the sensitive unit is the optical module, i.e. a glass sphere containing a photodetector and part or all the readout electronics. Up to now, every actual or proposed experiment (with the exception of Lake Bajkal, which will be extensively described later) is supposed to use as a photodetector a simple commercial PMT, 10 to 15" of diameter. We suggest the use of direction sensitive devices, in order to increase the efficiency of the detector decreasing the number of optical modules (OMs), in particular for tracks characterized by low hit multiplicity.

We are developing 2 different systems of light collection, one to be used with 4 commercial 5" PMTs, the other to be used or with an array of small PMTs or with a multianodic device, PMT or HPD, for example. In the meantime we are constructing a prototype of hybrid PMT based on reconversion of primary photoelectrons in a scintillator or in a proportional counter.

## II. LIGHT GUIDES FOR 5" PMTs

The first and simplest possibility we are investigating is the implementation of a system of 4 commercial 5" PMTs, coupled to the pressure resistant sphere with Plexiglas light guides.

We basically want to construct a specific Winston's cone to collect light to the PMTs, occupying the largest possible fraction of the volume of the sphere (fig. 1): for this reason the PMTs are not symmetric w.r.t. the sphere axis. This feature makes the light guide harder to be designed, so we

started constructing a plaster model of a single sector, and we are now producing a CAD model for factory production.

To ensure the reflection of the light we will use 3M™ Radiant Mirror [1] material, a multilayer reflective film which gives more than 95% (typically 97÷98%) reflectivity in the whole visible range. The reflective behaviour of this material is due to total reflection of light at the various interfaces between the different layers: this means that there is no metallic deposition that can cause electrical discharges involving the photocathode of the PMT.



Figure 1: 5" PMTs cluster



Figure 2: Plaster model of light guide



### III. LIGHT COLLECTORS FOR MULTIANODIC PHOTODETECTORS

As we saw in the previous section, a proper light collection system can convert the information on the direction of incoming light into an information on the position of the hit on the photocathode. Such a collector can be very effective if used in combination with a multianodic photodetector: in fact, actually available multianodic photodevices are usually characterized by a small and almost flat photocathode, features which make them not suitable as active elements in an OM of a neutrino telescope.

The very good segmentation and imaging capability of, for example, a HPD [2] make this device extremely interesting to reconstruct the position of the track w.r.t. the OM, provided that a proper system can direct the light coming from different directions to different regions of the photocathode. We are developing a “wasps’ nest” light collector which is expressly designed to achieve this goal: the idea is basically an implementation of an array of Winston’s cones which couples the inner surface of the pressure resistant sphere with the front window of the photodetector (see fig. 3).

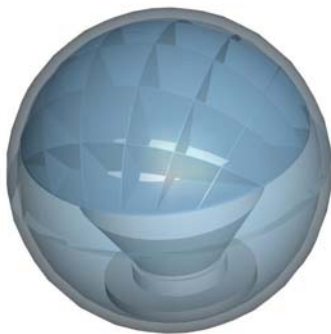


Figure 3: A 10” HPD coupled to a light collector

This collector slightly increases the light collection efficiency for directions near to the perpendicular to the axis (mainly due to the presence of the mirror at the bottom of the system, which is not oriented along a diameter of the same sphere as all the others mirrors), whereas there is a very good correspondence between incoming light direction and illuminated photocathode region. This can be argued looking at fig. 4, but it was also demonstrated with a simple simulation based on ray tracing used LITRANI (Light TRansmission in ANIsotropic media) code [3].

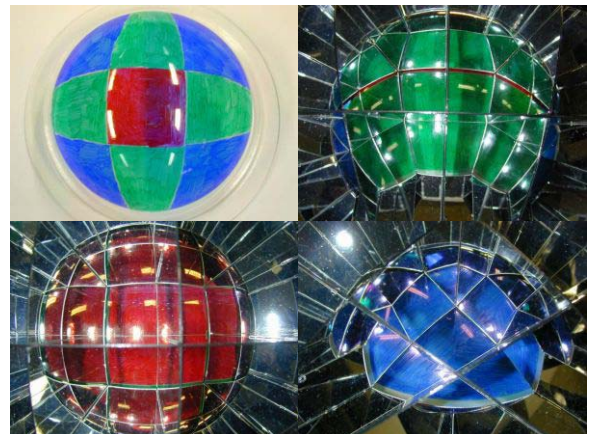


Figure 4: Different views of a coloured dome through the light collector

This system can be also used with an array of small commercial PMTs, but the geometrical coverage is of course better if one can have a single multianodic device in its focus.

At the moment of this writing, we have in our institute a prototype realized with aluminized PETG, which has a reflectivity in the visible region greater than 92% and that can be coupled to a 10” PMT. We are constructing a second prototype in which the reflective material is not metallic (to avoid eventual discharges of the photodetector), but is the 3M™ material which was already described in the previous section.

### IV. HYBRID PHOTOMULTIPLIERS

The most challenging project we are pursuing is a prototype of a hybrid photomultiplier based on the Lake Bajkal Quasar370 and the Philips SMART. This two objects have the same main features, i.e. a large, almost hemispherical photocathode from which the photoelectrons are accelerated to an inorganic scintillator by a high voltage (20 kV or so). The light produced in the scintillator is then read by a commercial small-diameter PMT. A schematic of the Quasar370 is in fig. 5.

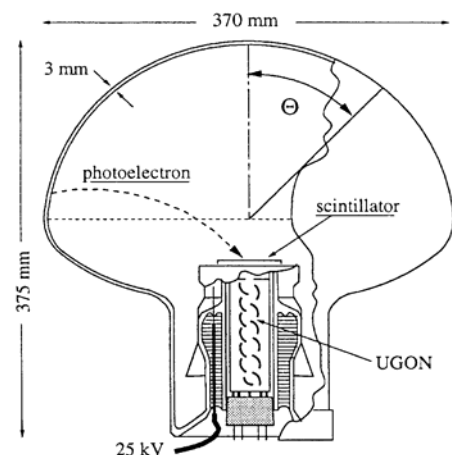


Figure 5: Schematic of a Quasar370

This kind of photodetector has two main positive features: better energy resolution and transit time spread (TTS) than an equivalent diameter PMT. The improvement of energy resolution is due to the high gain of the first step (the reconversion of the primary photoelectron in the scintillator): a typical spectrum of a Quasar370 tube is reported in fig.6. The decrease of TTS is possible if the trajectories of primary photoelectrons are optimized: in fact, TTS in large-diameter PMTs is mainly due to the difference in path-length of photoelectrons between the photocathode and the first dynode.

The aim of an optimisation of TTS was one of the guidelines of our development: for our 13” project, thanks to a careful design of the back half of the tube, the simulations said that TTS can be reduced (in the path between photocathode and scintillator) to approx. 1ns. This TTS has to be combined with the TTS of the PMT used to collect the light from the scintillator (which is less than 1ns for PMTs smaller than 2” of diameter) to obtain a total TTS smaller than 1.5ns, to be compared with the values for commercial PMTs of that diameter, i.e. 3÷5ns.

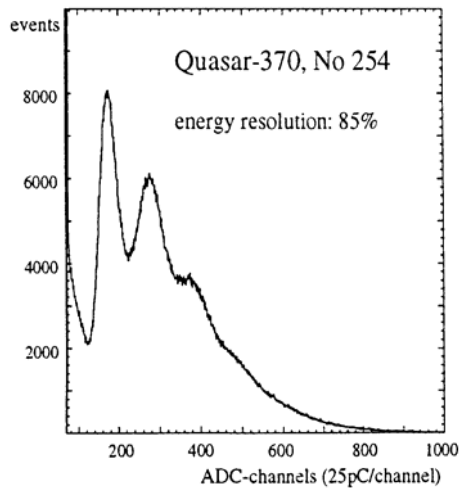


Figure 6: Spectrum of a Quasar370: it has to be noted the good separation on the single-photoelectron peak from background

The other guidelines of our project were a simple design, which is expressed in a perfectly hemispherical front half and a segmentation of the active area which is expressed by an optimisation of primary photoelectrons trajectories, to preserve a rough imaging in the focus of the accelerating potential. According to the simulations, at 25kV a pointlike source on the photocathode becomes a 5mm diameter spot on the scintillator (figs. 7 and 8).

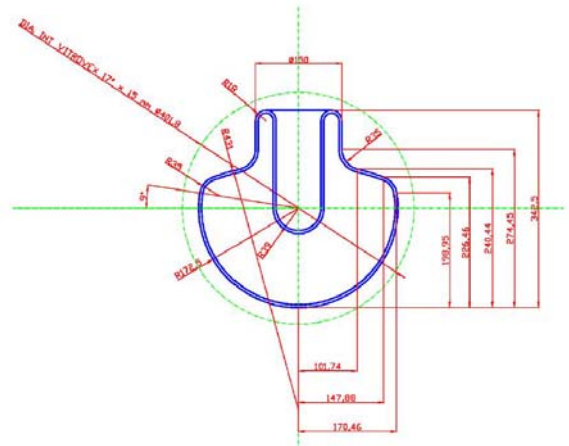


Figure 7: Improved design for our prototype

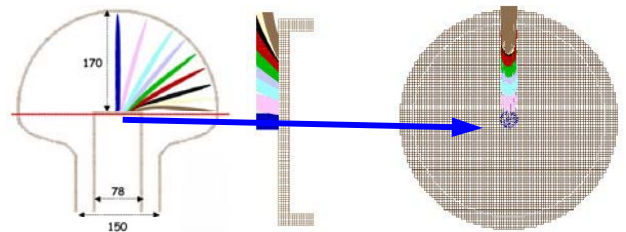


Figure 8: Imaging capability of our prototype at 25kV

To detect the photoelectrons, three ways were taken into account: silicon based detectors (such as in HPDs, this way was stopped trying to achieve a collaboration with expert people), “proportional chambers” and a scintillator, like in the original projects.

### A. Silicon based HPMT

As it is shown in [4] a silicon detector, s.a. a APD, can be used to detect primary photoelectrons. The performances of this device are very good in energy resolution but have to be improved in timing, if one decides to use them in a neutrino telescope. In principle, our prototype can be equipped with a system of silicon detectors, with almost no modifications w.r.t. the actual design.

We have contacts with people working on HPD at CERN and with industries involved in this kind of development, but, at this time, we are not directly following this path. For this reason, I won’t say more about this possibility.

### B. Gas based HPMT

A second possibility we are investigating is the use of a proportional chamber as photoelectron detector. We tested a “leak microstructure” (constructed by Mariano Lombardi, INFN-LNL), which consists of a copper plate at high negative voltage and an array of steel needles at 0V, in isobutane gas. An aluminized Mylar window, at the same potential of the copper plate, guarantees the right shaping of the electric potential. In this way, the electrons that enter the gas volume are attracted to the needles: at short distances to them, the gradient of the electric field is large, so there is a

multiplication due to ionisation, contained in a very small volume. A schematic of this detector is shown in fig. 9.

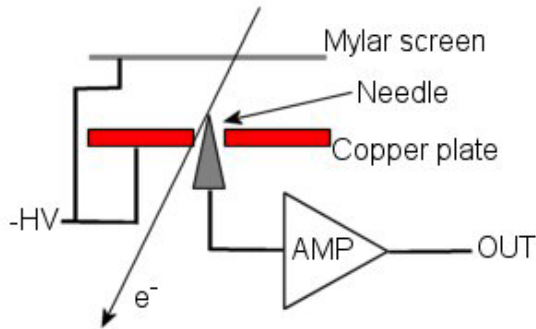


Figure 9: Schematic of a leak microstructure

In our set-up the distance between the copper plate and the Mylar window is 1mm and the needles are placed on a square grid of 1mm step. With HV set to  $-1500\text{V}$  and a fast, homemade amplifier we get signals of 100mV height,  $\sim 1\text{ns}$  rise time and  $\sim 40\text{ns}$  fall time. We also got a good time resolution for this device: mainly thanks to the Mylar screen, as a matter of fact, we got a time distribution of hits (measured in coincidence with a thin scintillator coupled to a  $\frac{1}{2}$ " PMT) whose spread was  $\sim 10\text{ns}$  FWHM.

The timing of this kind of detector, in principle, can be lowered to values  $\sim 4\text{ns}$ , choosing a proper gas mixture of isobutane and argon: this value is expected to be the physical limit because of the finite drift speed of the electrons in gas.

At present time, this solution is subleading with respect to the "scintillator based" one: in fact, it turned out that the implementation of the proportional counter into a HPMT is a challenging task, mainly because of the thinness of the window separating the gas from the vacuum where the photocathode is evaporated.

### C. Scintillator based HPMT

The main project we are developing is a "direct" improvement of the Quasar370 tube, i.e. a HPMT with a raw imaging capability. In our project, the YAP scintillator layer is "observed" by 4 1" PMTs: thanks to the focusing capability shown in fig. 8, we expect a good correspondence between the quadrant of the photocathode from which the photoelectron is emitted and the PMT that fires.



Figure 10: Implementation of the 4 PMTs in the centre of the HPMT

## V. STATUS AND PERSPECTIVES

### A. Light guides

At the moment of this writing, we have a prototype of the light guide for the 10" PMT and we are constructing another one with improved light collection efficiency at the edge. We plan to implement it in a glass sphere in the next months.

In the meantime, we are constructing a CAD model of the light guides for the 5" PMTs, which should be constructed before the end of 2003.

### B. Hybrid photomultipliers

We are getting know-how about photocathode evaporation on a smallest version of the glass bulb of the HPMT; in the meantime we are doing a series of mechanical tests on the largest version.

The vacuum line and control system for evaporation is complete and we expect to perform the first attempt in the first half of November.

### C. Simulations and far plans

Everything we are doing has to both by simulations and tests: we expect to perform a simulation of the performance of our devices implemented in a  $\text{km}^3$  detector in the first half of 2004.

We have also started the development of a facility to test complete OM in water: this will be done in collaboration with Pisa section of INFN and it will be used to test all our prototypes. Some test in collaboration with Saclay lab of IN2P3 is also foreseen to have a comparison with previous results

## VI. CONCLUSION

In Genova we are developing a series of solutions to achieve in a single OM more signals, bringing information about the direction of incoming photons.

We believe such kind of devices can ameliorate the performances of the detector without proliferation of the number of OMs and can also give more information for reconstruction of short tracks.

We are following two main projects: a system of light guides for multianodic devices or for arrays of PMTs and a particular type of hybrid PMT.

According to our plans, we expect to have fully functional and characterized prototypes before the second half of 2004.

## VII. REFERENCES

- [1] [http://www.3m.com/product/f\\_index/Film\\_3M\(TM\)\\_Radiant\\_Mirror\\_\(Z1\)\\_00.jhtml](http://www.3m.com/product/f_index/Film_3M(TM)_Radiant_Mirror_(Z1)_00.jhtml)
- [2] [http://ssd-rd.web.cern.ch/ssd-rd/Pad\\_HPDP/default.html](http://ssd-rd.web.cern.ch/ssd-rd/Pad_HPDP/default.html)
- [3] <http://gentit.home.cern.ch/gentit>
- [4] M.Giunta, *The HPD Detector*, in these Proceedings – Y. Yoshizawa, *Developments for Large Formats Detectors*, in these Proceeding

# A new concept of an OM based on wave length shifting fibers and photomultipliers

G. Anton

University of Erlangen, Erwin-Rommel-Str.1, D-91058 Erlangen, Germany  
Gisela.Anton@physik.uni-erlangen.de

## Abstract

The combination of a bundle of wave length shifting fibers directed to a photomultiplier is proposed as an optical module with increased acceptance.

## I. LIMITATIONS OF PHOTON DETECTORS

Large volume neutrino telescopes detect the Cerenkov light radiated by a muon which has been produced by a neutrino interaction. Photomultipliers (PM) are used to measure this Cerenkov light. In order to obtain a high detection probability the PM should have a large cathode area.

One approach to increase the detection probability could be the usage a funnel. Such a funnel increases the opening area of the system by reflecting photons by the mirror surface of the funnel and directing them onto the PM cathode. Such an approach can help if the direction of incoming photons is concentrated to a limited angular region. But in a neutrino telescope the Cerenkov photons may come from all directions almost isotropically to the PM. Due to this fact one has to regard the phase space of photons which can be detected by the PM. The Liouville theorem tells us that the phase space of an undisturbed system remains constant:

$$\Delta p \cdot \Delta x = const.$$

The phase space of the photons accepted by the PM is related to the angular acceptance  $\Delta\Omega$  and the opening area  $A$ :

$$\Delta\Omega \cdot A = const.$$

A passive system like a funnel can thus not increase the detection probability because it enlarges the opening area  $A$  on the one hand but it decreases the acceptance angle  $\Delta\Omega$  on the other hand.

## II. OPTICAL MODULE WITH WAVELENGTH SHIFTING FIBERS

The Liouville theorem can be overcome by transforming the incoming photons to another set of photons. This is for instance realized by a wavelength shifter, see fig. 1. Cerenkov

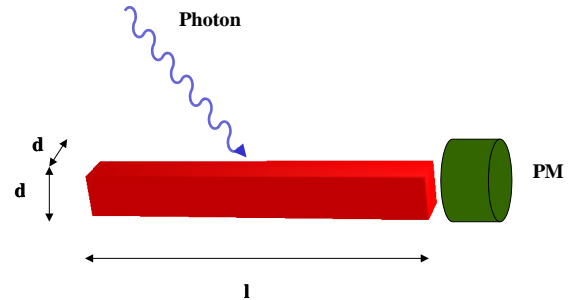


Figure 1: A photo sensor composed of a wavelength shifting bar and a photomultiplier

photons are absorbed in a wavelength shifting bar with a sensitive area  $A = d\dot{l}$ . An absorbed photon may be transformed to a wavelength shifted photon which may be emitted in the angular cone of total reflection such that it is guided to the end of the bar where it is detected by the PM. The advantage of such a system is the gain in photosensitive area  $A = d\dot{l}$  compared to the needed PM area  $A_{PM} = d^2$ . This gain factor  $f_G = l/d$  has to be compared to a loss factor  $f_{loss}$  which is composed of the Cerenkov photon absorption probability  $f_{abs} = \exp(-\mu d)$ , the transformation probability of creating a wavelength shifted photon  $f_{WLS}$  and the probability that such a photon is emitted within the cone of total reflection  $f_{cone}$ . Taking achievable numbers the losses altogether may result in

$$f_{loss} = f_{abs} f_{WLS} f_{cone} \simeq 0.9 \cdot 0.5 \cdot 0.2 = 0.1$$

It may be expected that these losses can be minimized further.

## III. POSSIBLE REALIZATION

The realization of a photo sensor for a neutrino telescope could look like in fig. 2. A bundle of wavelength shifting fibers is arranged such that a given disk as detection area is covered and the wavelength shifted photons are read out at one end by a fast PM.

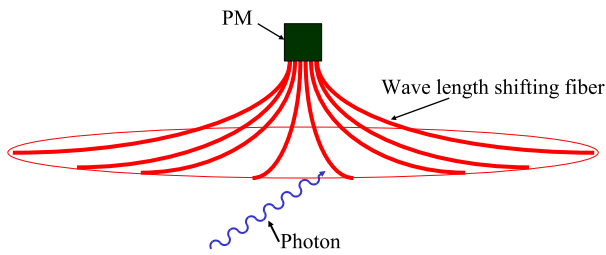


Figure 2: An optical module

The following numbers are given as an example for a possible realization. Taking a disk radius of 96 cm and a fibre of 2mm x 2mm diameter a total of 3000 fibers is needed to cover the disk resulting in a bundel area of 11cm x 11cm. The time dispersion due to the travelling of light inside the fiber is 3ns for a photon absorbed at the end of the fiber compared to a photon absorbed in the center of the disk. An additional time dispersion occurs due to the decay time of the wavelenght shifting material ( $\tau \simeq 2ns$ ). For the given area an overall gain factor ( $f_G/f_{loss}$ ) of 5.2 is achieved. This gain may be even larger for longer fibers but then also the time dispersion increases. The time resolution of the system will be investigated with simulation calculations.

The advantage of the proposed optical module is the possibility to optimize the components separately. A relatively small PM with low transit time spread and low noise, low pre-pulse rate and afterpulse rate may be choosen. The wavelenght shifting fibers may be embedded in a plastic structure which is pressure resistant in itsself and need not to be mounted in a pressure resistant housing. Also, other geometrical arrangements of the fibers could be evaluated which could be better adopted to the deep sea environment (water current etc.).

**Calibration  
Readout and Data Transmission  
Electronics**





# Timing calibration in NEMO

M. Circella for the NEMO Collaboration

Istituto Nazionale di Fisica Nucleare, Bari and Dipartimento di Fisica della Università di Bari  
Via Amendola 173, 70126 Bari, Italy

e-mail: marco.circella@ba.infn.it

## Abstract

This paper illustrates the project of the timing calibration system for the NEMO underwater neutrino telescope. We foresee a two-step procedure for measuring the offsets in the time measurements of the NEMO optical sensors, consisting of measuring separately the time delay for the synchronization signals to reach the offshore electronics from the onshore station, and the detection times of calibration signals delivered from suitable optical sources to the photomultipliers through an optical fibre distribution system. The NEMO prototyping activities foreseen at a test site off the coast of Sicily will allow the system described in this work to be operated and tested *in situ* in the near future.

## I. INTRODUCTION

Very large volume underwater or underice Cherenkov detectors represent nowadays the most common approach to neutrino astrophysics. The capabilities of these experiments are strictly dependent on how well time measurements are performed in the detectors. In fact, the reconstruction of the physical events, extracted from the large environmental background typical of the marine abysses, is based on the possibility to properly align in time the measurements performed by a large number of sensors located at considerable distances (several tens of meters, typically) from one another.

In all cases in which the signals are digitized and time-stamped offshore, two different tasks are required for aligning in time the measurements: synchronization of the electronics, i.e. the delivery of common clock signals to the whole apparatus, and timing calibration of the sensors, i.e. the measurement of how the local time measurements performed by the sensors compare to the time measured onshore. A further need is to relate the latter to UTC.

In this paper we illustrate the project of the timing calibration system of the NEMO neutrino telescope. In the framework of the preparatory studies for the development of an underwater detector at the km<sup>3</sup> scale on a joint European effort, the focus is on the approach to the solution of this calibration problem, and on the interconnection between it and the overall design of the apparatus, rather than on the technical choices available for the system implementation.

It turns out that, although this project is essentially tailored to the NEMO needs, our approach is essentially valid for all cases in which digitization is performed offshore. On the

contrary, the case in which analogue signals are sent from the apparatus to shore is considerably different. However, this is not a very convenient solution for very large volume detectors, and therefore will not be discussed here.

The NEMO project is introduced in the next section. Section III illustrates the NEMO apparatus. Then, Section IV illustrates the NEMO front-end electronics, with emphasis on how the data are digitized and the time measurements made. Section V illustrates the data transport system, with focus on the synchronization scheme of the offshore electronics. Finally, the project of the timing calibration system is introduced in Section VI.

## II. THE NEMO PROJECT

The opportunity to deploy a very large underwater neutrino telescope in the Mediterranean Sea is gaining substantial credit in recent times. Operating this detector at the same time as the ICECUBE apparatus at Antarctica will represent a tremendous achievement for neutrino astrophysics observations: the two detectors will ensure together a global coverage of the sky. Also, events coming from the common observation region in the sky will allow cross-calibrations between the measurements from the two experiments, which may be affected by different systematics. Moreover, operating from the northern hemisphere, a Mediterranean observatory will be able to detect neutrinos coming from the galactic center.

The NEMO (NEutrino Mediterranean Observatory) collaboration has been long active in Italy in the necessary R&D activities for the deployment of a km<sup>3</sup> neutrino telescope [1]. In 2000 a large subgroup of the collaboration decided to join and support the ANTARES experiment [2], aimed at the operation of a demonstrator apparatus at 2400 m depth 40 km off the coast of Toulon, France.

The NEMO Collaboration has identified a suitable site for installation of the km<sup>3</sup> underwater neutrino telescope at a depth of 3500 m about 80 km off the coast of Capo Passero, at the southernmost tip of Sicily, Italy. A preliminary design of the telescope has been completed in the past years, based on extensive R&D activities in low-power electronics, data transmission and mechanics for high-depth underwater structures.

The collaboration is now working on the development of a reduced-scale prototype of the apparatus, to be installed at an

underwater test site at 2000 m depth located 25 km off Catania, Italy (NEMO Phase 1).

### III. THE NEMO APPARATUS

The NEMO apparatus is described in detail in [1] and references therein. Here and in the next sections we introduce the main characteristics of the layout and functionality of the detector, in order to provide a better explanation of how the time measurements are made in NEMO and how the timing calibration system is integrated in the offshore electronics.

The telescope will consist of 64 towers arranged as in figure 1: the towers are located on a grid with 200 m pitch in both directions. The instrumented surface will therefore be a square of 1400 m side.

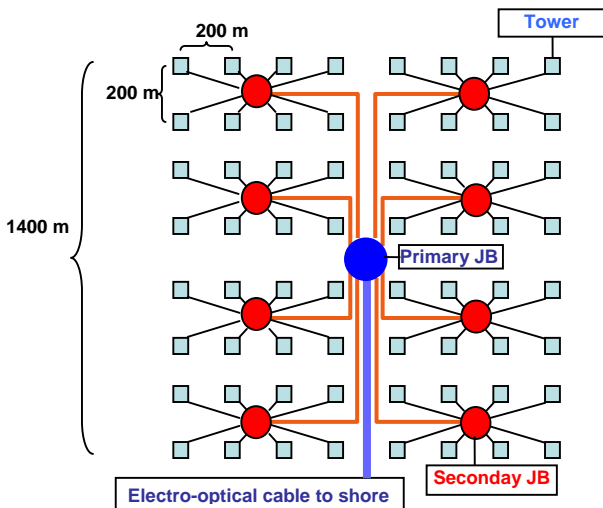


Figure 1: Layout of the NEMO apparatus.

An underwater network of electro-optical cables will ensure power distribution and all communications between the onshore station and the submarine structures. Two levels of junction boxes are foreseen: a Primary Junction Box (PJB) will terminate the main electro-optical cable from the shore. Eight independent cables will connect the PJB to eight Secondary Junction Boxes (SJB), each of which will be in turn connected to eight towers in a star connection.

The tower layout is shown in figure 2. As this figure shows, the tower is composed of 16 floors, spaced by 40 m. The bottom floor is at 150 m above the sea bed. At the bottom of this structure the Tower Junction Box (TJB) constitutes the interface of the tower to the rest of the apparatus. In particular, it will contain a passive optical multiplexer/demultiplexer block to implement the DWDM communication system described in Section V. There are plans to increase the height of the towers up to 18 floors, with essentially no practical consequences on this study.

The floors consist of 20 m bars of composite material, each equipped with four optical modules, each containing a photomultiplier tube and its associated electronics. The current design foresees that the optical modules are located at the two edges of each bar: the most promising configuration is to have two of them oriented downward, the other two

horizontally. There will be 64 optical modules on each tower and 4096 optical modules in the whole apparatus.

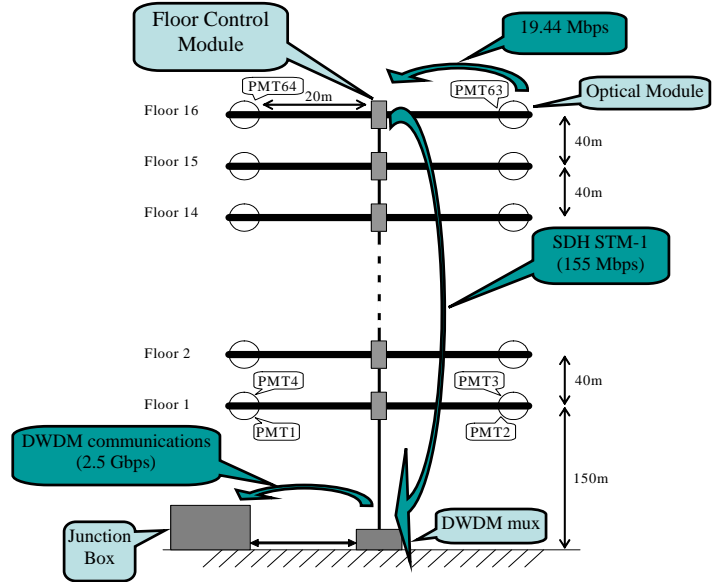


Figure 2: Layout of a NEMO Tower. Also shown are the data rates expected and some basic features of the data communication system.

The data acquisition of the optical modules of each floor is controlled by the Floor Control Module (FCM), which is in charge also for control of the local instrumentation and for all communications with the shore station.

### IV. FRONT-END ELECTRONICS – TIME MEASUREMENTS IN NEMO

The front-end electronics will be located inside the optical modules. The main features of the front-end electronics can be summarized as follows:

- the signals are compressed before sampling with a quasi-logarithmic law;
- the analogue signals are then sampled and digitized at the frequency of 200 MHz.

The latter operation will be performed with two staggered fast-ADCs operated at 100 MHz. For further details, see [3].

The communications between each optical module and the FCM will require three channels: a high-bandwidth (19.44 Mbps) channel to transfer the data from the optical module to the FCM; a lower bandwidth (~1 Mbps) channel for control communications from the FCM to the optical module; and a low-noise, low-frequency (1.215 MHz) clock distributed from the FCM to the optical modules of its floor. This clock signal is derived from the clock signal embedded in the data frames received from onshore and recovered in the FCM. In this way the whole offshore electronics will be synchronous to the reference clock distributed from the shore.

Commercial devices are used inside the optical module for increasing the frequency of the clock signal up to 100 MHz, which is then used to strobe all operations inside the optical module. An FPGA is in charge for ADC control, data

processing and all communications of the optical module with the FCM.

The data are recorded when a threshold value, remotely set from onshore, is reached. When this condition occurs, the readout of a 16-bit counter, which is incremented at 100 MHz, is also recorded to provide information on the pulse detection time. Periodic counter-reset commands are broadcasted from shore to the whole apparatus, and counted upon execution in each optical module. In this way, it is possible to determine the time of the individual samples with a resolution of 5 ns. The time of occurrence of the threshold condition is determined on the basis of a waveform analysis of the sampled data. The resolution achievable in this way is of the order of 300 ps [4].

## V. DATA COMMUNICATIONS AND SYNCHRONIZATION IN NEMO

A synchronous communication protocol will be used in NEMO. An appealing solution is the Synchronous Digital Hierarchy (SDH) protocol [5]: a standard Synchronous Transport Module – 1 (STM – 1) data flow will be established between each floor of the towers and the shore. At a data rate of 155.52 Mbps, this choice guarantees enough bandwidth to transport to shore all the data collected, without any offshore filtering. In fact, the data rate expected from each optical module, based on the background rate measured in the Capo Passero site, is of about 5 Mbps.

Each FCM collects the data from the four optical modules of one floor and arranges them in the STM-1 data frames. The overall data flow from one tower is thus of 2.5 Gbps.

A Dense Wavelength Division Multiplexing (DWDM) technique will be used to reach this high data rate with a simple architecture [6]: standard wavelengths at 100 GHz spacing will be used to communicate to and to receive data from each floor. Optical transmission multiplexing and demultiplexing will be performed with passive components in the TJB. No active components will be needed either in the PJB or in the SJBs for the data communications. By keeping the electro-optical conversions to the minimum, system reliability increases.

Symmetric systems will be implemented offshore and onshore. In this way, the data streams coming from the individual floors of each tower may be separated by means of simple passive devices. This gives the possibility to implement simple elaboration schemes onshore for detection of local signal coincidences. At the same time, it will be possible to address individual communications to the different floors of the towers from the shore station.

STM-1 data frames consist of 2430 bytes, serially transmitted in periods of 125  $\mu$ s. Each frame is composed of an *overhead*, consisting of control bytes in fixed position inside the frame for purposes of flow control (including frame alignment and transmission error control) and a *payload* (which amounts to about 150 Mbps out of the total bandwidth of 155.52 Mbps), intended for data transport.

The SDH standard implements a powerful mechanism of data encapsulation which allows the user to freely insert their data blocks inside the SDH data frame. For this purpose,

pointers are provided in the overhead section in which the position information of the data blocks is recorded. This information allows to reconstruct the correct data sequence on reception.

In case of NEMO, however, it is not foreseen to take advantage of this feature. A Positional Data Device Addressing (PDDA) mechanism will be used instead: specific position ranges in the data frame are intended for different devices. This a very efficient way to allow to send individual instructions from the shore to any offshore device. It is also possible to define position ranges which refer to more devices, so that instructions are delivered synchronously to them: this is particularly important for distributing the reset commands to the time counters inside the optical modules.

The STM – 1 interface inside the FCM will consist of an SDH mapper and an electro-optical transceiver featuring DWDM transmission. In particular, the mapper will be in charge of decoding the data frames received from the shore and to recover the embedded clock, as well as to encode the data frames to deliver to shore. The recovered 19.44 MHz clock will then be used to synchronize all devices inside the FCM and the data acquisition boards inside the optical modules of each floor.

The mapper delivers the payload data over a standard Telecom Bus Terminal Interface (TBTI) to an FPGA, which is in charge for all data acquisition operations inside the FCM. The FPGA implements the PDDA and is interfaced to the optical calibration system illustrated in the next section.

Overhead data will be sent from the mapper to a Digital Signal Processor (DSP), which will perform control functions inside the FCM and in particular will be in charge for data transmission control. Dedicated positional data will be sent from the FPGA to the DSP. Thus the DSP will be also able to receive control instructions from the shore and to configure remotely-controllable parameters inside the FPGA on request.

## VI. TIMING CALIBRATION IN NEMO

As anticipated in Section I, there are two separate needs to properly interpret the time measurements in NEMO as in any other neutrino telescope. Firstly, we need to compare the time measured in the shore station to UTC; secondly, we need to know how to compare the time measurements performed by the different sensors to the onshore time (or, equivalently, to one reference sensor).

We therefore speak of two significantly different operations:

- an ‘absolute’ timing calibration;
- a ‘relative’ timing calibration.

The level of accuracy required for these two operations is being extensively investigated through simulations. The target assumed in our project is of 1 ms for the ‘absolute’ calibration and 1 ns for the ‘relative’ calibration.

For the ‘absolute’ calibration we are developing a solution based on a GPS time synchronization system to be operated inside the shore station. This is not a very demanding application, so we will not discuss it further here.

The ‘relative’ timing calibration is a more difficult task, which requires an embedded system in order to track the

possible drifts of the time offsets during the operations of the apparatus underwater. The task of this embedded system would be essentially to measure the offsets with which the local time counters inside the optical modules are reset on reception of the reset commands broadcasted from the shore, i.e. the time delays for such commands to reach the individual optical modules. All time measurements are in fact referred to the readout of such counters, as explained in Section IV.

We propose to perform such measurements in two separate steps:

- an 'echo' timing calibration;
- an optical timing calibration.

The former will allow us to measure the time delay for the signal propagation from the shore to the FCM of each floor; the latter will allow us to determine the time offsets between the FCM and each optical module connected to it.

The 'echo' timing calibration will be based on the measurement of the propagation time of SDH data frames in a closed loop shore-FCM-shore. The capability of phasing the data frames transmitted by the FCM toward the shore station to the data frames received is essential for the success of this operation [5].

The 'echo' mechanism will be triggered by a specific command sent from shore. This same command, to be executed after a defined delay from the periodic time counter reset command, will also activate the optical timing calibration system.

There are no intermediate electro-optical conversions, which would otherwise contribute to the propagation time delays, between the shore and any FCM, as explained before. However, the propagation times even along the same optical fibres will be different for the two directions of propagation, due to the different wavelengths used in the two cases. Corrections will thus be needed to determine the propagation time for signals going from the shore to the offshore electronics from the round-trip delay measurement. A high-stability TDC will be needed for such measurement, provided with an interface to the shore SDH control station.

The optical timing calibration system will allow to measure the time delays between each FCM and the optical modules connected to it. A scheme of the proposed system, to be implemented on each floor of the NEMO tower, is shown in figure 3.

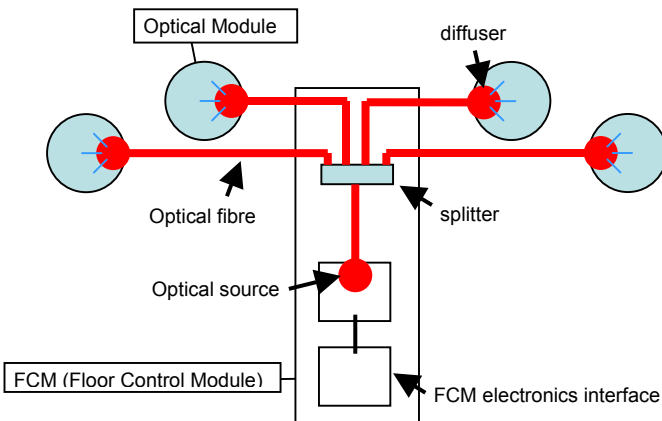


Figure 3: Scheme of the NEMO optical calibration system.

Inside the FCM a blue light pulse is generated from a calibrated optical source upon reception of the calibration command from the shore. This pulse is then injected into four optical fibres in order to simultaneously illuminate the optical modules of the plane. There are several choices available for implementing this system (e.g., for what concerns the optical source and the optical fibre to use), which are currently under evaluation.

This simple system represents an efficient way to distribute common calibration signals to groups of optical modules. This same approach could be extended to put up more complicated schemes, for instance by using the same calibration source to distribute signals to more than floor, possibly to the optical modules of a whole tower. The opportunity of such configurations should be however evaluated with respect to the increased system complexity.

It is anyway important to point out that the use of beacons to emit light flashes into the water, rather than using a fibre distribution system as proposed here, is not a convenient solution due to the peculiar arrangements of the optical modules on the NEMO tower and the large distances between them. More generally, there seems to be very marginal possibilities of using optical beacons in very large volume detectors, as a consequence of the large distances to cover.

## VII. CONCLUSIONS

The timing calibration is among the most delicate operations to perform for assuring the full functionality of large underwater neutrino telescopes. In this paper we have illustrated the major features of our project for a timing calibration system tailored to the need of the NEMO apparatus. This system will be validated during the ongoing prototyping activities of NEMO Phase 1.

## VIII. REFERENCES

- [1] E. Migneco (for the NEMO Collaboration), *The NEMO Project*, these proceedings.
- [2] J. Carr (for the ANTARES Collaboration), *ANTARES*, these proceedings.
- [3] C. Nicolau (for the NEMO Collaboration), *A 200 MHz FPGA-based PMT acquisition electronics for NEMO experiment*, these proceedings.
- [4] F. Ameli (for the NEMO Collaboration), *Data acquisition electronics for NESTOR deep-sea neutrino telescope: Project and tests*, Nucl. Instr. Meth. A423:146, 1999.
- [5] F. Ameli (for the NEMO Collaboration), *Synchronous data transmission protocol for NEMO experiment*, these proceedings.
- [6] F. Ameli (for the NEMO Collaboration), *NEMO Phase 1 data transmission: considerations toward km<sup>3</sup>*, these proceedings.

# Review of the Time Calibration Systems of ANTARES

Juan José Hernández-Rey  
(for the ANTARES Collaboration)

IFIC – Instituto de Física Corpuscular, C.S.I.C.– UVEG, apdo. 22085, E–46071 Valencia, Spain

Juan.J.Hernandez@ific.uv.es

## *Abstract*

We review the different systems devised by the ANTARES collaboration [1] to calibrate in time the ANTARES neutrino telescope. Since the reconstruction of the neutrino-induced muons relies mainly on the time of arrival of the Cherenkov photons that they emit when crossing the sea water, a precise time calibration of the detector is of utmost importance. The final angular resolution of the detector and its reconstruction efficiency will depend on the timing resolution that can be reached. Intrinsic time fluctuations in the detector components indicate that an accuracy of  $\sigma \sim 0.5$  ns in the relative time calibration among photomultipliers (PMTs) is an ambitious, but adequate goal. On the other hand, physics considerations indicate that an absolute time calibration of  $\sigma \sim 1$  ms is enough for all practical purposes. In this presentation we review the different sources of time uncertainties in the detector. We then describe the different systems that will be used to reach the aforementioned goals

## I. INTRODUCTION

The ANTARES detector [2] will consist of 12 strings anchored to the sea bed at 2400 m below sea level. Each string has 25 storeys and every storey consists of 3 optical modules (OMs) looking downward at  $45^\circ$  and separated from each other  $120^\circ$  in the horizontal angle. An optical module [3] consists of a 10” Hamamatsu R7081–20 PMT, its base and a pulsed LED housed in a pressure-resistant sphere.

The electronics of the storey is located in a pressure resistant titanium container forming the so-called Local Control Module (LCM). The LCM contains in particular the electronic chips that digitise the signal from the PMT anodes, the so-called Analogue Ring Samplers (ARS). An ARS first discriminates the signal by a threshold, typically equivalent to 0.3 SPEs (single photo-electrons). The charge of the pulse is then integrated during a programmable time interval (25–80 ns), an internal clock register is stamped and a Time to Voltage Converter (TVC) latched in order to determine precisely the time from the last clock cycle to the moment the threshold was crossed. The ARS has a pulse shape discriminator that allows to distinguish a waveform (WF) hit from an SPE hit. In the WF case, in addition to the normal SPE information (integrated charge, time stamp and TVC value) 128 samples of the analogue signal are stored. There are three ARS in each storey connected to the three PMTs bases in a token ring configura-

tion, so that two ARS serve every PMT in order to minimise downtime.

The clock system provides a common clock signal to all the ARS. The clock consists essentially of a high accuracy 20 MHz signal generated at the shore station and sent to the detector off-shore in optical form by means of a wave division multiplexing system (WDMS). The signal is sent at a wavelength of 1534 nm and returns at 1549 nm. Synchronised data commands can be superimposed on the clock signal, in particular *start* and *stop* commands, which together with a high precision Time to Digital Converter (TDC) are an essential component of one the clock calibration system that is described below.

The clock signal travels through more than 40 km of electro-optical cable and reaches the submarine junction box where it is distributed by means of a passive splitter to the different strings via the corresponding electro-optical link cable. At the bottom of each string, in the so-called String Control Module (SCM), the optical signal is regenerated, i.e. converted to electrical and back to optical and distributed to the different storeys of the string at wavelengths 1550 nm (outwards) and 1310 nm (inwards).

A dedicated board in the LCM of the storeys receives the clock signal and distributes it to the different components of the storey, in particular the ARS. All the boards in the SCM and LCMs are bi-directional, a feature that is essential to provide an in-built clock calibration system.

At regular intervals –at least every 800 ms– a common reset time stamp signal (RTS) is sent from the shore station to all the ARS. A counter at the LCM records how many of these RTS have been issued since the start of the run and this number is added to the data. The values of the RTS counters and the GPS times of the RTS signals are used off-line to assign the GPS time to the events.

The clock signal is in fact generated by a GPS device at 10 MHz and then doubled to obtain the final 20 MHz distributed signal. Therefore, the internal detector’s time can be synchronized to the time of the outside world, the Coordinated Universal Time by using the UTC information provided by this GPS generator.

## II. OFFSETS, DELAYS AND JITTERS

The delay between the moment in which the photon hits the PMT photocathode and the moment when the signal reaches

the TVC of the ARS (PMT–ARS delay) is of the order of 100 ns. This delay is dominated by the transit time (TT) in the PMT, with additional contributions from the cables that link the PMT base to the LCM and from the input time on the ARS.

The PMT transit time depends on the applied voltage, so there are channel-to-channel differences. Nevertheless, the shape of the dependence of this transit time on the photocathode to first dynode voltage ( $V_{kd}$ ) and on the first dynode to anode voltage ( $V_{da}$ ) is very stable and well-known. The amount of light does not influence the shape of  $TT(V_{kd})$  at any rate nor of  $TT(V_{da})$  if the the number of photoelectrons is smaller than  $\sim 20$ .

The difference in this PMT–ARS delay from one channel to another is expected to be  $< 10$  ns. The change in this delay from the calibrated values on-shore to the actual values once the detector is in place is expected to be small, at most 5 ns. Once in the sea, this delay is expected to be very stable and drift with time less than a couple of nanoseconds in the worst scenario. In any case, the *in-situ* calibration systems should be able to determine and monitor these delays and their possible shift.

The jitter on this delay, i.e. the event to event fluctuation is essentially due to the so-called transit time spread (TTS) of the PMT signal. This TTS has been determined to be  $\sigma \sim 1.2$  ns and is one of the main inherent sources of uncertainty in the time determination. The first raw of table 1 summarises these numbers.

Table 1: Summary of ANTARES time offsets and uncertainties.

Path	Delay	Stability	Jitter
PMT cathode ↓ ARS	$\sim 100$ ns	$\sim 2$ ns	1.2 ns
↓ LCM clock	$\sim 10$ ns	$< 0.2$ ns	$< 0.5$ ns
↓ Junction Box	2–4 $\mu$ s	$< 0.5$ ns	$< 0.1$ ns
↓ Master Clock	200 $\mu$ s	$\sim 1$ ns	$< 0.1$ ns

For a given PMT the dependence of the TTS on the photocathode to first dynode voltage is small ( $\sim 0.2$  ps/V) and the variation of the TTS from one PMT to another operating at the same voltage is negligible ( $\sigma \sim 0.06$  ns as determined for a sample of 912 PMTs). Other uncertainties in the PMT–ARS time delays are due to the time stamp and digitisation processes, but they are even smaller. The clock stability is  $\sigma < 0.05$  ns and the TVC of the ARS can determine the time with  $\sigma < 0.5$  ns.

The digitisation of the signal includes the stamping of the time as provided by the clock board on the LCM of each storey. The delays here are due to the tracks on the boards and the backplane of the LCM and the input and output delays. In this case, however, the delay –which is of the order of  $\sim 10$  ns– is similar in all the channels and extremely stable, so that varia-

tions will be  $< 0.2$  ns (see table 1).

The signal then goes from the clock board in each LCM to the Junction Box. Here the time delay, which is between 2 to 4  $\mu$ s, depends on the position of the corresponding storey with respect to the Bottom String Socket of the string and on the length of the cable that links the string to the Junction Box. No active component is involved in this path and the environmental conditions –mainly temperature– are very stable. Therefore, the difference of this delay from lab to sea is expected to be below 1 ns for all the channels and its variation of with time, once the string and the link cables are in the sea, should be smaller than 0.5 ns.

Finally, the signal will travel through more than 40 km of fibre optics from the Junction Box to the shore station. The delay is of the order of several hundred microseconds and its variation is mainly due to the section of the cable which is on the land and therefore undergoes higher temperature variations. However, also in this case the variation is smaller than 1 ns and since it is common to all the Optical Modules it only contributes to the absolute timing and therefore is well below specifications. In table 1 these numbers are summarised.

The transmission of the Cherenkov light through the sea water is also a source of intrinsic uncertainty in the determination of the time of flight of the Cherenkov photons. This is not of course an effect that can be corrected for by calibration and adds to the unavoidable uncertainty in the time determination, limiting the angular resolution and effective area of the detector (the other major source of irreducible time uncertainty is, as has been mentioned, the TTS of the PMTs). The transmission of light influences the detector’s performance through absorption, scattering and chromatic dispersion. At the ANTARES site, the absorption length is typically  $\sim 50$  m for blue light ( $\lambda \sim 475$  nm) and  $\sim 25$  m for UV light ( $\lambda \sim 375$  nm) [4]. The effect of scattering can be expressed in terms of an effective scattering length  $\lambda_{scat}^{eff} = \lambda_{scat} / (1 - \langle \cos\theta \rangle)$ . Using the standard approach of oceanographers and the measurements made by the ANTARES collaboration [4] this effective scattering length turns out to be  $\sim 300$  m in blue and  $\sim 110$  m in UV in the ANTARES site. In addition, due to the fact that PMTs are colour-blind, an additional uncertainty comes from the dependence of the group velocity of light on wavelength, i.e. the chromatic dispersion. Scattering and chromatic dispersion do not have additive effects, since the former tends to reduce the available range of wavelengths and therefore reduce the influence of the latter. The impact of these effects on time resolution cannot be described by a single number that could be compared with the precision reached by the calibration procedure. However, as a guideline we can mention that, at a distance of 40 meters between the track and the PMT, the time uncertainty due to these effects is of the order of 1.5 ns.

The time offsets and fluctuations produced in the path between the Junction Box and the shore–station affect equally to all the signals, so that any uncertainty there reverts in the absolute time determination. The stability is expected to be of the order of 1 ns and the precision with which the detector’s clock can be synchronised with the GPS provided UTC is  $\sim 2$  ns. No

physical source is expected to have such a flux that a precision in time smaller than 1 ms for the detector should be reached, so that the present accuracy is well within specifications.

### III. TIME CALIBRATIONS SYSTEMS

The relative calibration of the detector will be performed in the different complementary ways listed below:

- A A laser-fibre system in the laboratory
- B A clock calibration system
- C LEDs in the Optical Modules
- D Optical Beacons in the detector
- E Muon tracks

The first option consists in the on-shore calibration in a dedicated dark room in the laboratory of each string. The calibrations by the clock system and the LEDs in the OMs (options B and C) are designed to be performed once the detector is in place, but are also carried out during the calibration in the dark room. The optical beacons (option D) allow to calibrate the telescope via well-controlled pulsed light sources in-situ, taking all the possible effects into account, including the transmission of the Cherenkov light in the water. Option E will allow an overall cross-check of the timing calibration with real down-going muon tracks.

#### A. Laser-fibre calibration in the laboratory

The strings are first calibrated in a dark room by means of a laser-fibre system. A Nd-YAG laser emits high energy short pulses ( $E \sim 1 \mu\text{J}$  ;  $\sigma_t < 0.5 \text{ ns}$ ) of green light ( $\lambda = 532 \text{ nm}$ ) that are distributed to the optical modules by means of a splitter and optical fibres (see scheme in figure 1). The small PMTs in the LED beacons (see subsection D below) also receive the laser light so that a cross calibration between the optical modules and the optical beacons is possible. The dark room allows the calibration of one sector each time, i.e. one fifth of a string amounting to five storeys with 15 OMs in total. The fibres are cut so that their optical path is equal to an accuracy better than  $\pm 50 \text{ ps}$

In figure 2 we can see the results for the 5 storeys (15 OMs) of one sector of string without any correction whatsoever. The plots show the number of hits in each OM as a function of the arrival time of the signal. The difference in time between the peaks of OMs in different storeys ( $\sim 100 \text{ ns}$ ) is due to the time delay of the clock signal.

Several corrections are applied to the data. First, the offsets of the slope of each TVC with respect to the start of the clock cycle are measured and accounted for. The range of each TVC is also measured and corrected. Then the clock distribution time between storeys (see next subsection for details) is also estimated and subtracted. The results are given in the plot

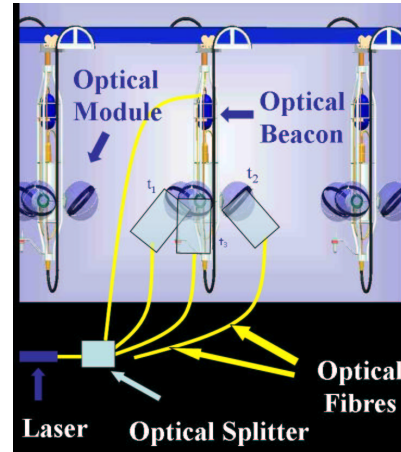


Figure 1: Scheme of the calibration system on-shore. A Nd-YAG laser emits high energy short light pulses which are distributed by means of a splitter-optical fibre system to the Optical Modules and the Optical Beacons allowing their relative calibration in time.

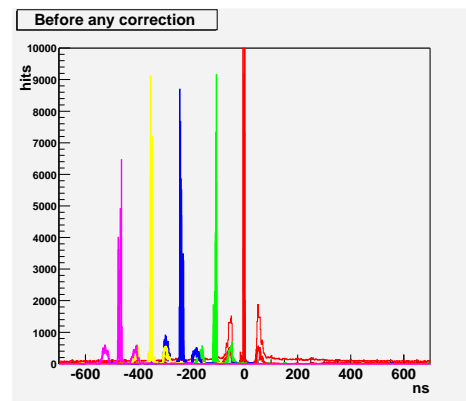


Figure 2: Number of hits as a function of the arrival time of the signal for the 5 storeys of one sector of string. Raw results before any correction.

of figure 3, where the corrected hit time is represented with respect to one of the digitising boards (ARS) taken as reference. The standard deviation of the signals is smaller than 1 ns and the offset between peaks is small, with a dispersion around a few nanoseconds. The measurement of these offsets and their use as starting values of the in-situ calibration is precisely the goal of this calibration. The source of these offsets is usually the difference in transit time between different PMTs.

#### B. Clock calibration

As already mentioned, a high precision 20 MHz signal is distributed to the different components of the detector. The time given by the TVC of an ARS is referred to the start of the corresponding clock cycle. The active components of the clock system, namely the clock boards in each storey LCM and in

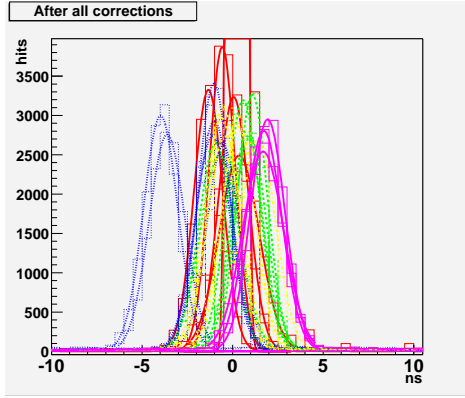


Figure 3: Number of hits as a function of the arrival time of the signal for the 5 storeys of one sector of string. Corrected results (see text for explanations)

the SCM at the bottom of the strings, are bi-directional. This feature used in conjunction with the capability of the system to send start and stop commands synchronized with the clock signal allows a precise determination of the round-trip delay of the signal.

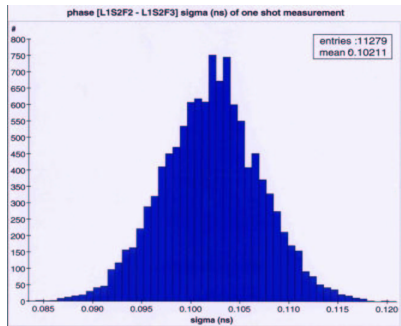


Figure 4: Distribution of the difference (“phase”) of the round-trip time of the common start and stop signals sent to two different LCM clock boards. A mean of 100 ps is obtained.

Measurements at the laboratory indicate that a precision of 0.1 ns can be obtained in the determination of the single-shot round-trip delay, as shown in figure 4. A sector of a string (PSL or *Prototype Sector Line*) and an instrumentation string (MIL or *Mini-Instrumentation Line*) were deployed in the sea and connected to a Junction Box at the beginning of 2003. The round-trip delay of the clock signal from the shore station to the SCMs at the bottom of each string and back can be seen in figure 5 (problems with the distribution via the fibres in the strings prevented the acquisition of similar data for the storey LCMs). In this figure the round-trip delay as a function of the data-taking time is shown. The distance between tick-marks on the y and x axes is 0.1 ns and  $10^5$  s ( $\sim 28$  hours), respectively. The blue (dark) points correspond to the MIL round-trip delays, the red (grey) points to the PSL delays plus an ad-

ditional offset of 572.72 ns added for the sake of comparison. The drift of the round-trip delays in the total range of  $\sim 16$  days of data-taking shown is  $\sim 0.6$  ns. This round-trip delay is constantly monitored and recalibrated with a precision of 100 ps.

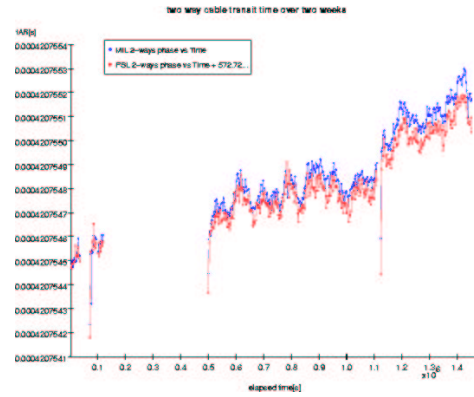


Figure 5: Round-trip delay of the clock signal from the shore to the bottom of the Mini Instrumentation Line (blue/black points) or to the bottom of the Prototype Sector Line (red/grey points) as a function of the data-taking time. The spacing between tick-marks is 0.1 ns and  $10^5$  s for the y and x axes, respectively. An offset of 572.72 ns has been added to the PSL round-trip delay for the sake of comparison

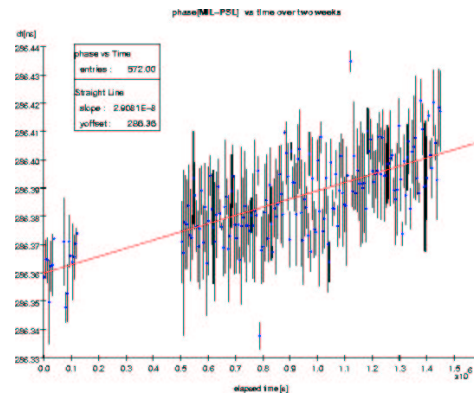


Figure 6: Distribution of the difference of the round-trip times for the PSL and MIL. The distance between tick-marks is 10 ps for the y-axis and  $10^5$  s for the x-axis.

The two curves follow each other rather precisely. In figure 6, the point-by-point difference in time between the two curves is shown. The spacing between tick-marks on the y-axis is now 10 ps. The drift in the difference during the  $\sim 16$  days is therefore  $\sim 50$  ps.

### C. LEDs in the Optical Modules

Inside each optical module there is a pulsed LED used to monitor the transit time of the PMTs. The blue LED is an HLMP-CB15 from Agilent whose intensity peak is at around 470 nm with a FWHM of 15 nm. It is pulsed by means of



a circuit based on an idea of Kapustinsky et al.[5] (see figure 7).

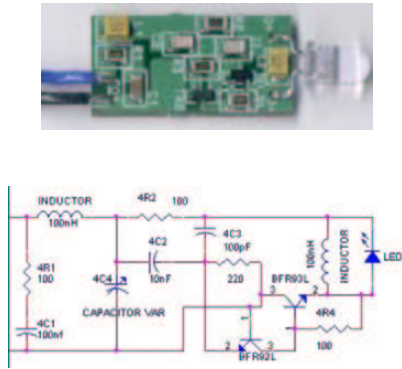


Figure 7: Picture and scheme of the LED pulser based on the design of reference [5]

The pulse rise time is  $\sim 2$  ns independently of the intensity of the pulse. The latter can be varied between 0 and  $\sim 40$  pJ, which corresponds to  $10^8$  photons approximately. The LED is encapsulated in a black cap with a small hole and installed in the rear part of the PMT, so that the photocathode is illuminated through the thin aluminised layer at the back of the tube. With this simple mechanical implementation, shadowing effects on the photocathode are avoided and a low illumination level is obtained. The overall pulse width of the LED varies between 4.5 and 6.5 ns, depending on the intensity of the pulse. The jitter in the trigger to pulse delay time is of the order of 100 ps and it can be triggered from single shot up to 10 kHz.

#### D. Optical Beacons

The Optical Beacons (OBs) will allow relative time calibration by means of independent pulsed light sources. Two kinds of beacons will be placed throughout the detector and will send light through the water: the LED beacons and the Laser beacons. The former will be placed every 5 storeys to a total of 5 per string and located in the upper part of the frame that supports the OMs. The latter will be placed at the bottom of some strings.

The LED beacon consists of six faces fixed to an hexagonal cylinder mounted inside a cylindrical glass container. Each face has six LEDs, five looking horizontally outward and the sixth facing upward. The pulser circuits are the same as those used in the OMs. Each LED beacon can produce between  $3 \times 10^7$  and  $3 \times 10^9$  photons per pulse depending on the configuration of LEDs selected and the amplitude of the driving voltage. A small and fast Hamamatsu H6780-03 photomultiplier within each beacon allows a precise determination of the exact time of the light flash. In figure 8, an LED beacon is shown in the mechanical frame of a storey.

The Laser Beacon (fig 9) is a much more powerful device that uses a diode pumped Q-switched Nd-YAG laser to produce pulses of  $\sim 1\mu\text{J}$  with a FWHM of  $\sim 0.8$  ns at a wavelength of



Figure 8: A 6-faced LED beacon is housed on a pressure-resistant glass cylinder fixed to the mechanical frame of an ANTARES storey.

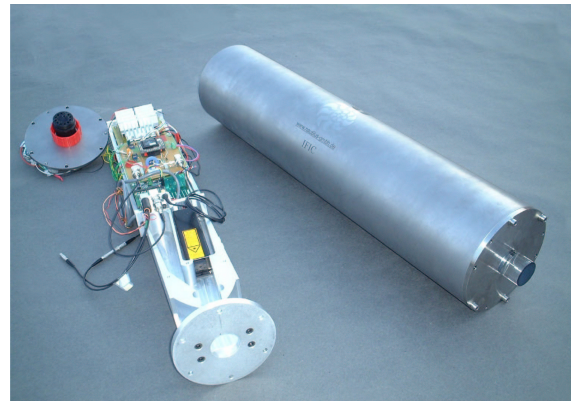


Figure 9: Laser Beacon components. The laser and its associated electronic components are fastened to an aluminium mechanical mounting. The cylindrical titanium container holds on its upper cap the quartz rod to avoid sedimentation.

532 nm. The laser is housed in a cylindrical titanium container and points upward. The beam is widened by a diffuser which spreads the light out to a cosine distribution. A quartz cylinder is bonded to the upper surface of the diffuser, so that the light exits through the vertical walls of the cylinder, where sedimentation is negligible. A built-in fast photodiode gives the actual time of emission of the flash.

Detailed Monte Carlo studies indicate that the system of optical beacons will be able to calibrate with an accuracy better than 0.5 ns the relative time offsets between all the PMTs of the detector.

Chromatic dispersion has in this case a negligible effect due to the narrow range of wavelengths involved. Scattering of light tends to change the shape and delay the pulses with the travelled distance. However, the use of the rising edge of the pulse minimises this effect. If the arrival time of the pulse

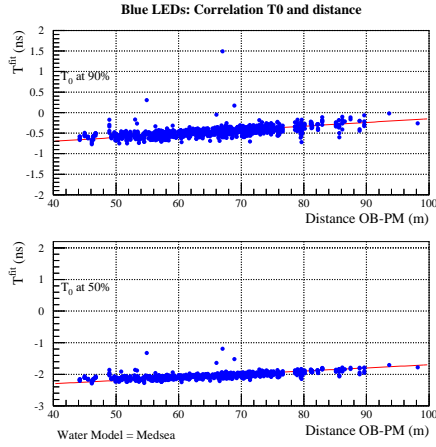


Figure 10: Dependence of the arrival time of the OB pulses as a function of the OB–OM distance when it is computed using the 90%–point of the rising edge of the pulse (upper plot) or 50%–point (lower plot)

is determined using the time when the signal reaches 50% of its maximum ( $T_{50}$ ) instead of the peak position ( $T_{100}$ ), its dependence on the Optical Beacon–Optical Module distance is small, as can be seen in figure 10. After correction by the analytical offset of its position (for a gaussian the  $T_{\alpha \times 100\%}$  point is at a distance  $\pm \sigma \sqrt{-2 \cdot \ln \alpha}$  from the peak position) and by the small distance dependence, the relative time of the OMs can be calibrated to a precision better than 0.5 ns (see figure 11). According to the simulation results, the expected uncertainties in the knowledge of the water model have a negligible influence on this result.

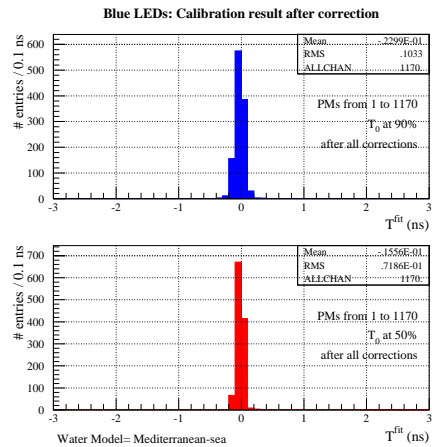


Figure 11: Relative time of the Optical Modules after calibration by the OBs once the distance dependence has been corrected.

### E. Muons

Around 10 000 downward going muons coming from cosmic rays interactions on the atmosphere will be reconstructed per

day in ANTARES. The time residuals of the reconstructed tracks can be used to cross-check the time offsets estimated by the calibration methods described above. A very preliminary estimate indicates that an statistical accuracy on the individual time offsets of  $\sim 0.1$  ns per day is possible. However, these downgoing muons have a somewhat different behaviour from the point of view of the detector’s response to the upward going muons coming from neutrino interactions. Studies are being carried out to estimate the systematic error that this difference may introduce.

## IV. SUMMARY

The correct time calibration of the neutrino telescope ANTARES is essential to optimise its performances. The low expected fluxes and physical variability of the neutrino sources indicate that an accuracy of 1 ms in the absolute time calibration is enough for all practical purposes. The goal of the relative time calibration between the OMs of the detector is set by the inherent event to event fluctuations introduced mainly by the PMTs, the electronics and the phenomena of transmission of light in water, namely 1.2 ns, 0.5 ns and a typical 1.5 ns, respectively. Therefore, calibrations in the time offsets below the nanosecond level are an adequate goal. In this contribution we have described the different systems that will be used in the ANTARES telescope to reach this precision and we conclude that the combined use of these complementary systems will attain the desired accuracy.

## V. ACKNOWLEDGEMENTS

The ANTARES project is funded in Spain by MCYT via grant FPA2003–531, which is partially supported by FEDER Funds. In the rest of Europe, the ANTARES project is funded by CEA, CNRS, Var Dept., PACA Reg., the City of La Seyne s/m and FEDER Funds (France), INFN (Italy), RFBR (Russia), FOM and NWO (The Netherlands) and PPARC (United Kingdom).

## REFERENCES

- [1] ANTARES Web site: <http://antares.in2p3.fr>; ANTARES proposal: E. Aslanides et al., astro-ph/99074232
- [2] ANTARES Technical Design Report, <http://antares.in2p3.fr>, July 2001.
- [3] Amram P. et al., Nucl. Instr. and Meth. Phys. Res. **A484** (2002), 369
- [4] Aguilar J.A. et al., ANTARES collab. “Transmission of light in deep sea water at the site of the ANTARES neutrino telescope”, to be published.
- [5] Kapustinsky J.S. et al., Nucl. Instr. and Meth. Phys. Res. **A214** (1985) 612

# Wavelength Division Multiplexing (WDM)

J.J. Hogenbirk, A.H. Kruijer

NIKHEF, P.O. Box 41882, 1009 DB Amsterdam, The Netherlands  
[jelle@nikhef.nl](mailto:jelle@nikhef.nl), [lexk@nikhef.nl](mailto:lexk@nikhef.nl)

## I. INTRODUCTION

In order to minimize data processing below sea level and therefore also minimize electrical power-needs and avoid difficult maintainable hardware, a simple but very powerful data network is required. What we will achieve as well is high data rates, high reliability, long-term stability, low volume mechanics, and openness for the users. The use of WDM (Wavelength Division Multiplexing) with related optical based components make such an approach feasible.

After developments in data networking and according to the OSI model (Open System Interconnection) of ISO (International Standard Association) much is changing and will be changed according to the three layers, physical layer, data link layer and network layer. All changes from the existing systems are related to the use of active and passive optical components in fiber networks.

Inserting the Ethernet TCP/IP protocol makes example to this model (tab. 1)

7	application	Application programs, e.g., electronic mail, etc.,
6	presentation	telnet, SMP, FTP
5	session	telnet, SMP, FTP
4	transport	TCP, UDP
3	network	IP
2	data link	connection, network interface cards <b>optical switches a.o.</b>
1	physical	twisted pair, wireless, <b>optical fiber</b>

Table 1: OSI model with Ethernet fitting

Did we connect to local area networks mainly with copper based wiring along with many EMC (Electro Magnetic Compatibly) constraints, now the optical glass fiber is gaining more and more on copper due to low cost for very high data rates, very long haul distances without signal amplification, flexibility, volume and no heed to EMC.

With the success of point-to-point connections with a large bandwidth over one fiber (10Gb/s is today's standard), DWDM (Dense Wavelength Division Multiplexing) makes this data link and especially the physical link factors faster and therefore the almost ultimate broadband data way.

## II. WDM, WHAT IT IS

Data to be transported across the glass fiber is modulated on laser light with a fixed wavelength. A second data stream is modulated on a different wavelength. The two wavelengths are multiplexed and sent across one fiber. At the destination point the wavelengths are de-multiplexed and the two data streams are demodulated to obtain the original signals. Many more wavelengths can be used to sent data over one single fiber (fig. 1).

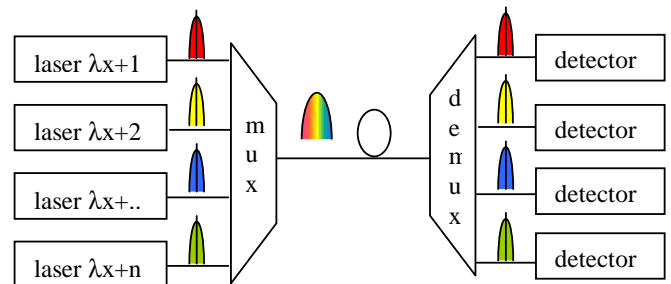


Figure 1: Simple WDM diagram

The ITU-T (International Telephone Union – Telecommunication) has defined standards for DWDM (Dense Wavelength Division Multiplexing) to 150 central wavelengths with 100GHz spacing and to 300 central wavelengths with 50 GHz spacing in the spectrum domain defined from 1491.88 nm to 1611.79 nm (fig.2).

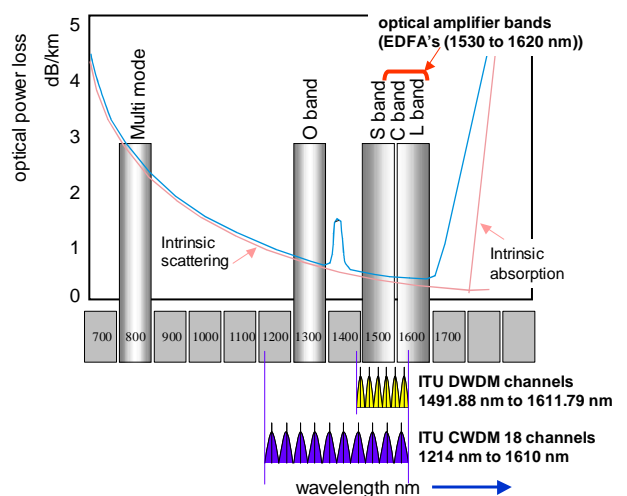


Figure 2: Spectral overview

In this spectrum single mode glass fiber has the lowest power loss and ranges of ca. 100 km without optical signal amplification are possible. Within the spectrum from 1530 to 1620 nm all optical amplifiers EDFA (Erbium Doped Fiber Amplifier) are available and manage to amplify (gain 25 dB)

the multiplexed signal at once.

Another system CWDM (Coarse Wavelength Division Multiplexing) coexists where 18 channels are defined. The main purpose for CWDM is to upgrade (older) existing networks with less well-specified optical networks.

### III. DWDM APPLICATIONS

The market for all optical components is growing. For the optical input to the fiber network many types of tuned narrow-wavelength DWDM lasers, like direct-modulated lasers, CW (Continuous Wave) -lasers and multiple-wave CW-lasers are presently available.

E.g. (fig. 3) The use of the newly appearing multiple-wavelength CW Laser: The output of such lasers is launched into one fiber. By an OADM (optical Add/Drop multiplexer) one constant wavelength can be filtered out of the DWDM signals residing on the fiber, directed to an optical modulator and the modulated optical signal is added back on the original fiber or if desired on a different fiber.

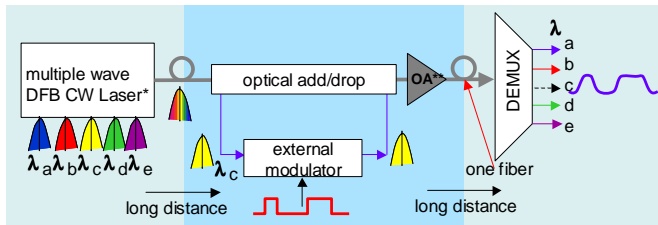


Figure 3: Single add/drop multiplexer with external modulator

On the market now many other optical modules are present star couplers, optical wavelength converters, wavelength switches, all-optical switches, splitters, circulators and optical amplifiers and various receiver modules. Many optical components are bi-directional and need no power what assuring to a long life time.

### IV. DATA TRANSPORT TECHNOLOGIES AND DWDM

After the OSI model the entire physical layer in fiber optics and the data link can operate independently according to the higher order layers -(fig.4).

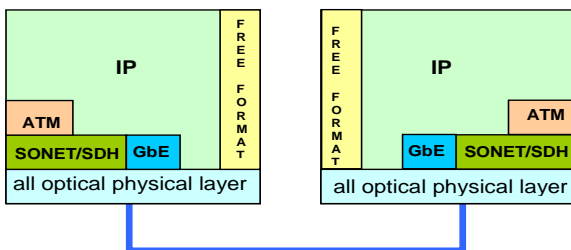


Figure 4: Transport to physical layer example

Peer to-peer connections can be routed on one unique wavelength. If fiber specifications and optical units are carefully observed, analogue signals can be transported transparently from point-to-point. We must notice that some commercially available optical components have an integrated signal restore system designed for digital signals.

### V. PROTECTION SYSTEM

The question is not whether we will have a DWDM network in the future VLVnT detector, but how failsafe can we make this network.

Basically a single DWDM fiber link carries all the data and maybe the control signalling too, anyhow a huge amount of very important and costly data. A single point failure, a bad connection or a broken fiber, in the connection is catastrophic.

Redundant fiber routing is fundamental to avoid disasters (e.g. fig. 5).

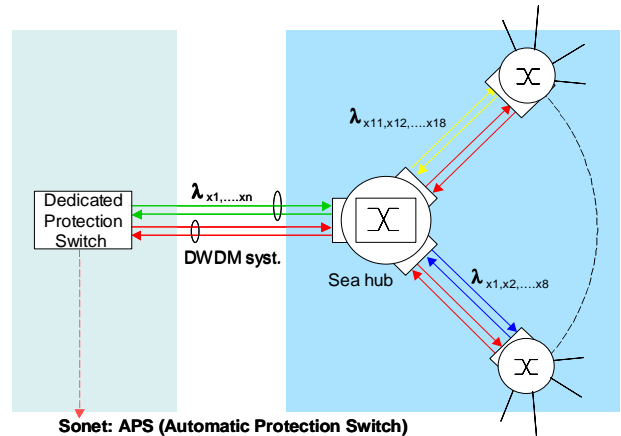


Figure 5: Redundant routing parallel connections

A backup fiber can be established by a different routing from the original fiber. Light is launched across one of the two fibers and at the destination point the fibers are combined. The signal to noise ratio for the receiving part must be taken into account. Adding fiber to the shortest fiber, compensates a difference in length. Tuneable optical delay lines can compensate fractions in nanometre range. When detecting “dark” fiber, a dedicated switch can, automatically, switch to a different fiber or maybe fiber system.

Presently developed redundant ring systems, are also described in SONET (Serial Optical Network) systems, (fig. 6).

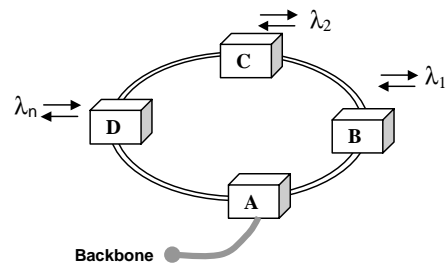


Figure 6: Unidirectional Path Switched Ring (USPR)

The data is transported on only one fiber and the second fiber is the backup fiber.

In “A” the complete DWDM multiplexer and de-multiplexer connect the data backbone to the ring data highway. Node B, C, and D contain optical ADD/Drop multiplexers and path-switches. When a fiber becomes “dark” switching to the backup fiber can automatically be done starting at “A”, where on try and error basis light must be detected in “A” after a

whole flow through the ring this rehearses up to the next nodes.

Two USPR rings construct the ultimate redundant network ring, where the second ring transports data in reverse direction. The second fiber is now used for ring control. (fig. 7)

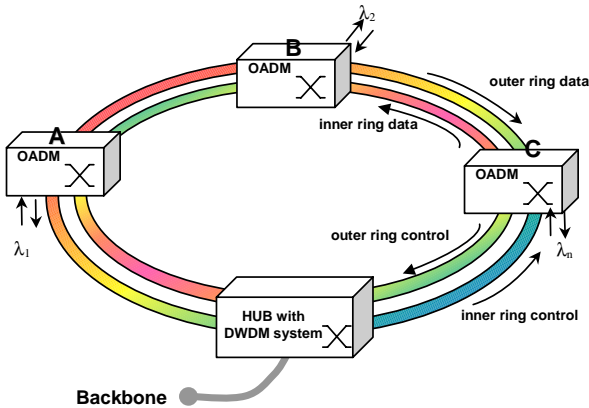


Figure 7: Bidirectional Line Switched Ring (BLSR)

In both rings the protection fiber is also used for the optical system control. E.g., if some calamity happens to one of the fibers then the data stream or control signals can be ported to the inner ring (fig.8).

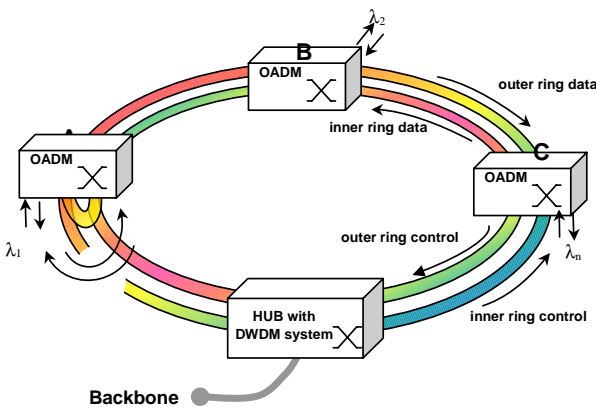


Figure 8: Bidirectional Line Switched Ring (BLSR).

With optical switch nodes a complex network configuration is possible (fig.9).

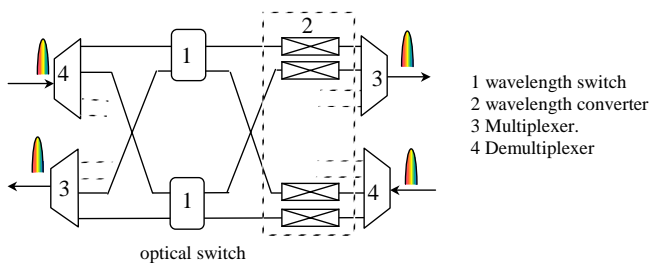


Figure 9: Optical switch node.

The wavelength-switches connect a chosen wavelength to a desired output. In order to do the right wavelength bookkeeping in the up-and down stream of the data flow, a wavelength converter can be implemented.

## VI. CONCLUSIONS

Designing an all-optical network for a VLVηT has the advantage of a highly reliable data transport system with very high bit rates.

Many optical components are bidirectional. Using different wavelengths as data carrier create a reasonably simple hardware setup. Modern fibers and fiber connection techniques like fusion splicing cause high network reliability and a long lifetime.

Cost reducing factor, compared to the more expensive optical components, is the absence of optical-electrical-optical repeaters per optical carrier. All optical amplifiers like the EDFA (Erbium Doped Fiber Amplifier) amplify all the wavelengths on a single fiber to a desired level. Electrical power needs is very much decreased. Many optical components don't use electrical power at all.

## VII. REFERENCES

- [1] <http://antares.in2p3.fr>
- [2] E.Heine, "Power Distribution", this workshop
- [3] Stichting voor postacademisch onderwijs in de technische wetenschappen. Course chair man prof. dr.ir.van Etten "Optische communicatie techniek"
- [4] Cisco systems, Inc. Text part number OL-0884\_01. "Introduction to DWDM for Metropolitan Networks"
- [5] Shaowen Song IEEE Canadian Review –Spring 2000. "DWDM And The Future Integrated Services Networks"

# Synchronous Data Transmission Protocol for NEMO experiment

F. Ameli, M. Bonori, C. Nicolau for the NEMO Collaboration

INFN - Sezione Roma1

fabrizio.ameli@roma1.infn.it, maurizio.bonori@roma1.infn.it, carlo.nicolau@roma1.infn.it

## Abstract

The generic constraints imposed by large submarine neutrino telescopes are discussed in order to choose the most efficient protocol for data transmission. Then a brief outline of NEMO architecture is given to identify the particular critical points needing the specification of a protocol.

After constraints evaluation, the STM-1 SONET/SDH protocol has been chosen for “NEMO Phase 1” experiment: a description of its characteristics is reported to evaluate how much the experiment requirements are fulfilled by this choice. A description of all the benefits brought by SDH protocols is given in full detail and, whenever possible, a comparison with different protocols is made.

Finally, some simple considerations are developed to show how this kind of protocol is suitable for being used in a submarine experiment with a complexity of the order of the  $\text{km}^3$ .

## I. INTRODUCTION

Present underwater neutrino telescopes rely on detection of Čerenkov light by means of photomultipliers (PMT). Even though some new approaches have been recently proposed and tested (e.g. acoustical detection), the use of PMTs is still planned for future very large neutrino telescopes.

Photons hitting PMTs generate “events”: the telescope goal consists of measuring both the arrival time of photon(s) and the shape of the electric signal. Two main considerations, which impact on data transmission choice, are the presence of a constant mean data rate and the necessity of distributing a common timing. The first is mainly due to PMT dark current and, for an apparatus deployed in the sea, to  $^{40}\text{K}$  radioactive decays. For example, an underwater 10” PMT produces events at a rate of about 50 kHz; in general, data rates between 20 and 100 kHz are considered reasonable. Most of the events can be thought of as produced by single photo-electrons (*spe*), i.e. signals with a small amplitude and a time length of about 50 ns. Assuming a commonly used value of 100 bits to code the *spe*, a typical total data rate is 5 Mbps (see, for example, [1, 2, 3]). This holds in case of no underwater trigger.

Regarding the timing issue, each event must be labeled by a time stamp, i.e. the arrival time of photon(s), in order to reconstruct tracks correlating hits on multiple PMTs. Setting a time stamp implies that the acquisition system, whatever its implementation, has a common timing for all the PMTs. Moreover, an absolute time or, at least, a relative phase between time stamps originating from different PMTs must be known.

This is the task of the time calibration procedure. At this stage of the project, an incremental technique will be adopted to reach the final desired precision: constraints will be posed on each item affecting calibration in order to guarantee the minimum precision which allows the final physical calibration to take place. The chosen data transmission system has to comply with this requirement to allow a correct reconstruction of events.

All the electronics and optical systems deployed at great depths have to be as reliable as possible because any kind of maintenance is impracticable; for electronics systems, the reliability requirement means reducing components, using industrial devices, applying aging procedures, and so on. Power consumption has to be minimized as well. Therefore, as a general remark, off-the-shelf devices, based on the most recent technologies and with the best performances, should be used.

Furthermore, the chosen data transmission affects the mechanical layout of the detector, with consequences on cables number, connectors, number of sectioning boxes; these are very expensive and vulnerable items which should be minimized as far as possible. Applying the same optimization philosophy, the selection of assessed standards for data transport allows reliable techniques using commercial components and widespread know-how.

In Fig. 1 is shown the schematic layout of the tower designed for NEMO experiment. Even though preliminarily, considerations have been carried out to extend this structure to a detector capable of an effective area of one  $\text{km}^2$ : 64 such towers can be arranged on a  $8 \times 8$  square grid with a spacing between towers of 200 m. Each floor is equipped with a number

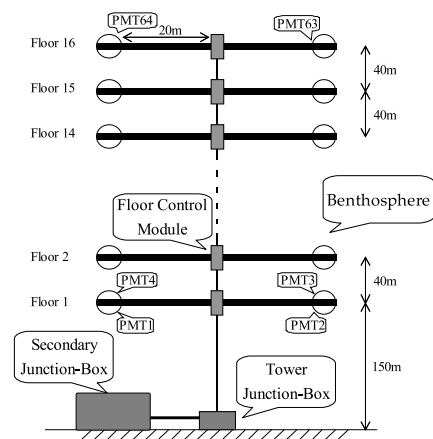


Figure 1: Schematic layout of NEMO tower.

of benthospheres, containing a PMT and the acquisition electronics [4], which ranges from 4 to 8. At floor center, electronics circuits are placed to handle the PMT data streams, to manage local control instruments, and to control the whole system. Data are transferred from the floor to the box at the base of the tower, which is called Tower Junction Box (T-JB); a counter-flowing data stream comes from the T-JB and transports data to each floor. The data transmission protocol discussed in this paper is defined at this level, i.e. for the connection of the floor with the T-JB. However, this link affects heavily subsequent data transmission choices, as will be explained later.

## II. SYNCHRONOUS PROTOCOL FOR NEMO DATA TRANSPORT

The constant mean data rate and the common timing needed at the whole apparatus scale, discussed in the previous section, led us to choose a synchronous protocol for data transport. The protocols taken into consideration embed the clock signal in the transmitted data stream; in this way, the receiver side can recover both clock and data and can provide a timing reference synchronous with the transmission clock. Therefore all the receivers fed by data streams originated by the same source clock are synchronous. This choice reduces the number of physical links needed to transfer data per each data flow direction. Immediate consequences are higher reliability (because of the smaller number of fibers or electrical links, i.e. connectors), ease of redundancy implementation, lower costs and a simpler deployment.

There is a vast number of devices which implement synchronous protocols, manufactured by many different companies; for example, a rapidly growing application is the serial backplane connection implemented with Serializer/Deserializer (SerDes) devices. Such devices allow data rate up to 10 Gbps and are conceived as bus extenders or backbone communication links for high speed buses. Usually, SerDes implement proprietary communication protocols defined at the physical layer.

To reach a higher level of data handling, a telecommunication standard has been chosen: the SONET/SDH protocol.<sup>1</sup> This standard is perfectly defined and represents the *de facto* protocol adopted by modern telecommunication apparatus. Many data rates are defined, as shown in Table 1, starting from 52 Mbps (STM-0) up to 10 Gbps (STM-64). As a telecommunication standard, features like durability, robustness, wide support and ease of integration with third parties components can be take for granted.

Beyond the definition of a physical layer, needed for data transport, a protocol layer is defined as well: user data are merged with an overhead data stream which manages, controls and implements the communication. SDH relies on the definition of Synchronous Transport Modules (STMs) and Virtual

<sup>1</sup>SONET stands for Synchronous Over NETWORK. SDH stands for Synchronous Digital Hierarchy.

Table 1: SDH/SONET data rates.

Designation	Data Rate	Payload Rate
STM-0 (OC-1)	51.48 Mbps	50.112 Mbps
STM-1 (OC-3)	155.52 Mbps	150.336 Mbps
STM-4 (OC-3)	622.08 Mbps	601.344 Mbps
STM-16 (OC-48)	2.49 Gbps	2.405 Gbps
STM-64 (OC-192)	9.95 Gbps	9.621 Gbps

Containers(VCs).

Specifically, the chosen SDH protocol is the *STM-1*, which supports a data rate up to 155.52 Mbps. Actually, after subtracting the overhead, about 150 Mbps are available to the user: these useful data are called *payload*. The selection of the STM-1 data rate is related to the amount of data produced at floor level in NEMO experiment. In fact, considering 8 PMTs per floor, the total amount of data is 40 Mbps. Reserving at least a factor two for redundancy and the possibility of integrating other local devices (such as hydrophones, environmental sensors, video cams, etc.), the payload is still big enough to accommodate the produced data<sup>2</sup>.

The great advantage of SDH protocol is the capability of transporting data formatted with most of present telecommunication protocols (ATM, T1, E1, ...). Even asynchronous data can be embedded in SDH payload using VCs: whatever the format is, the SDH overhead can keep track of VC position by means of *pointers* which address the VC itself inside the payload. In case of asynchronous protocols, the VC can slip with respect to SDH timing: it is up to pointers and offset mechanism to track VCs movements and to allow data recovery at terminal side.

SYNCHRONOUS TRANSPORT MODULE - 1

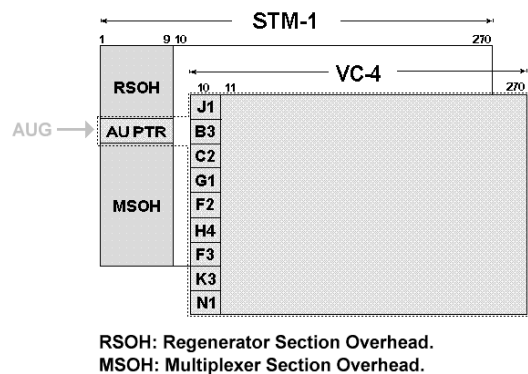


Figure 2: STM-1 protocol Virtual Container concept.

In Fig. 2 the STM-1 *frame* is shown: each frame lasts 125  $\mu$ s and is composed by 270  $\times$  9 bytes which yield a total

<sup>2</sup>Reminding that data transmitted from on-shore to the apparatus are a small percent of data generated off-shore, considering only the direction from off-shore to the land side is reasonable.

data rate of 155.52 Mbps. The available payload is  $260 \times 9$  bytes per frame, i.e. about 150 Mbps.

The concept of synchronization can be briefly summarized looking at the picture in Fig. 3: data are transported by a stream whose speed is fixed; frames last  $125 \mu\text{s}$ . Data are formatted as a VC-4 virtual container, which takes up all the available payload, i.e. about 150 Mbps. It is possible to transport data with smaller VC formats using an hierarchical add/drop structure specified by SDH protocol. A *zero padding* proce-

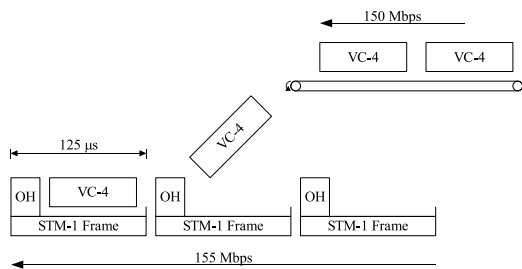


Figure 3: Ideal synchronization between STM-1 data frame and transported Virtual Container.

cedure can be applied if data to be transmitted are not enough to fill up the selected VC.

The STM-1 SDH protocol fulfills the two requirements made in the introduction: a synchronous channel is available for continuous data transport and a common timing is easily distributed by means of the serial bit stream. In our case the SDH multi-protocol capability is underused: data stream have to be strictly synchronous to the SDH timing, i.e. no slipping is possible between STM-1 frame and the transported VC. Therefore pointer mechanism is not needed.

### III. FLOOR CONTROL MODULE

The Floor Control Module (FCM) is an electronic circuit placed at the center of each floor in the tower (see Fig. 1). The FCM has the task of conveying to the T-JB all the data coming from the benthospheres (see section I. ) and from the local slow control interface (SCI) modules; of course, the FCM handles also the counter-flowing data stream, which comes from on-shore and goes to benthospheres and SCI modules.

In some sense, the FCM can be viewed as a *mapper* device, i.e. a component which collects information from different sources, packs all the data onto a single transmission protocol and sends the data stream to the T-JB; conversely, the data stream coming from the T-JB is de-mapped and sent to each destination device. The FCM is completely symmetrical, although data rates are much different for the two directions even for the same device.

The high bandwidth data format connecting the FCM with the T-JB, capable to accommodate all the floor information, is the SDH STM-1 data format, which provides a 155 Mbps serial bidirectional bit stream.

Figure 4 shows the block diagram of the FCM based on real electrical components. Reading this figure from right to left, i.e. from on-shore toward the benthospheres, the optical signal arriving to the floor from the T-JB is converted in a 155 Mbps electrical bitstream by the electro-optical *transceiver* (indicated in the block diagram as Finisar FTR-1631), which, in turn, feeds the *SDH mapper* device.

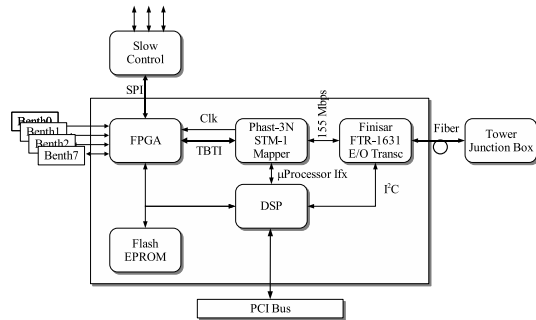


Figure 4: FCM block diagram.

The *SDH mapper* chosen is the *Phast-3N* from Trans-Switch Corp.; it is a STM-1/STS-3/STS-3c SDH/SONET Overhead Line Terminator and is capable of managing STM-1 data fluxes, separating the protocol overhead contained in the STM-1 frame, extracting error information and signaling bytes from the overhead, and allowing access to the payload, which is the set of bytes available to the user. The STM-1 data frame has already been schematically shown in Fig. 2.

The *Phast-3N* locks on the input data frequency extracting a clock signal from the serial bit stream; it then recovers byte alignment and data frame. Each frame lasts  $125 \mu\text{s}$  and consists of a matrix of  $270 \times 9$  bytes containing the protocol overhead (SOH), the VC overhead (POH), and the payload. Bytes are received from left to right row by row. The SOH is made up of the first nine columns of the frame (81 bytes), while the POH consists of one column (9 bytes). Specific data bytes embedded in the overhead are extracted on dedicated interfaces with separate clock and synchronism signals; the payload is available on a 8-bit 19.44 MHz parallel interface, which is called Telecom Bus Terminal Interface (TBTI).

The FPGA is timed using the recovered clock, which is synchronous with the on-shore source clock except for its jitter, which is an instantaneous period deviation on the order of few tens of picoseconds. All the devices connected to the FCM (benthospheres, slow control, etc.) are driven by clocks derived from the locally re-synthesized clock, in order to maintain all the apparatus synchronous: in this way, different events happening on different FCM boards are separated by fixed delays.

The STM-1 payload is received by the FPGA on the TBTI; data are extracted and redirected to each destination device using a *positional* decoding mechanism: bytes in the payload are numbered from 1 to 2340 and each device is assigned a certain number of bytes in a specific range. Therefore, the FPGA re-maps the assigned bytes to the destination device us-



ing a specific data interface. This mechanism is termed Positional Data Device Addressing (PDDA).

Reading Figure 4 from left to right, i.e. from the benthospheres to the T-JB, the opposite mechanism is implemented: the FPGA collects all the floor information to be conveyed by the STM-1 format implementing separate data interfaces with each device (benthospheres, slow control, and DSP). Each of these channels has its own electrical interface, communication protocol, and a dedicated FIFO memory inside the FPGA in order to buffer data exchange.

The DSP has a control role over the other components: it is devoted to programming, monitoring and managing both the electro-optical transceiver, the STM-1 mapper/de-mapper, and the FPGA. A local non-volatile memory (indicated in the block diagram of Fig. 4 as Flash EPROM) can be used to store start-up information, calibration tables, board parameters, and so on.

Moreover, the DSP will provide the board with a PCI bus; even though this bus will be useless in the under water tower, it is essential for debugging, easy and fast device reprogramming, for the possibility of distributing the board with a test software giving the opportunity to other groups to use and check performances. The choice of PCI bus is forced by STM-1 real-time data extraction: in fact the data rate supported by PCI bus can be pushed up to 120 MBps. Of course in the final release of the FCM board, the PCI bus will be abandoned and two versions of the board will be produced: the first for under water application, the second to be used on-shore in the receiving laboratory.

### A. Calibration

In order to synchronize the whole apparatus in a physical sense, measures of time differences from FCM to FCM or an opportune setup of devices must be realized. Referring to electronics device, the most suited word to define this *calibration* procedure would be *phasing* the devices. In fact it is necessary either knowing the relative time differences or putting in phase all the FCMs in order to take into account delays introduced by circuits and not only by different path lengths.

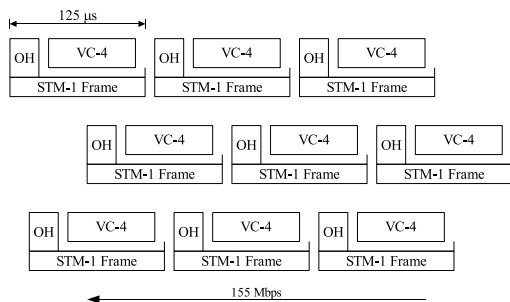


Figure 5: STM-1 streams driven by the same clock can be viewed as serial streams running at the same speed.

By definition, different STM-1 frames generated by different FCMs will be synchronous if driven by the same clock:

in Fig. 5 is shown a series of STM-1 synchronous data streams symbolically represented by sequences of frames running at the same speed. Relative time differences between streams will stay fixed after start-up transient time.

However, much more can be done exploiting a feature of the Phast-3N: streams can be put in phase triggering the device. The Phast-3N provides the possibility of a trigger signal to force the start of STM-1 frame transmission. Distributing such a trigger signal to all the FCMs, all the data stream will be in phase, as shown in Fig. 6.

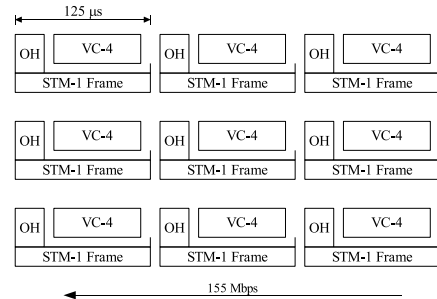


Figure 6: STM-1 data streams can be put in phase by means of a common trigger signal.

In figure 7 is reported the complete transmission chain which allows bidirectional data transport between on-shore and off-shore electronics. Input/output signals connecting the FCM with the T-JB are optical signals.<sup>3</sup> At first we assume that paths are of equal length, i.e. no time difference is introduced by different paths.

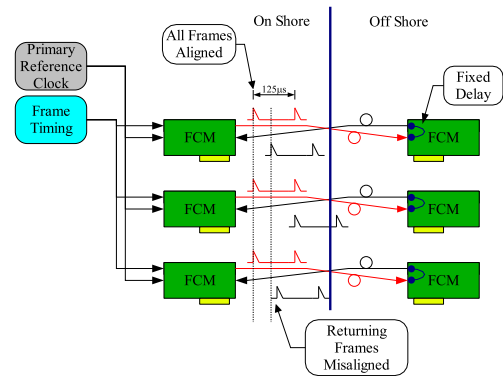


Figure 7: STM-1 SDH protocol used to implement the auto-calibration of electronics devices at the FCM level.

Each on-shore FCM is driven by the same clock signal, which is called, using the SDH terminology, Primary Reference Clock (PRC). In addition, a frame signal is fan out to the FCMs in order to trigger and time-align all the transmitted data streams. Therefore all the off-shore FCMs will receive

<sup>3</sup> It is planned to use “colored” transceivers complying with ITU standards to complete the data transmission system as explained in [5]

at the same time the synchronous and phased data streams. After the Phast-3N locks onto the received bit stream, the digital clock and frame signals will be the same for all the FCMs. Using these signals to re-time the transmitting side of off-shore Phast-3N allows the same mechanism described on-shore to be implemented: all the transmitted frames will be in phase.

Based on this procedure, the electronics system realizes a sort of auto-calibration up to the FCM level: all the FCMs in the under water apparatus are correctly aligned. This alignment can be used to issue commands able to calibrate the data acquisition system.

Introducing now the time difference due to different path lengths, it is clear that frames coming back to on-shore will be misaligned by an amount only dependent on the optical paths. The round trip delay is a measure of the time difference only due to path lengths.

## IV. CONCLUSIONS

Synchronous protocols in general seem to provide a feasible solution to data transport for underwater neutrino experiment. For NEMO experiment the SDH telecommunication standard has been adopted. Immediate benefits are great support and reliability, smaller number of links, i.e. less cables and connectors, low power electronics, cheap components and the definition of a standard for transmission on fiber optics. The latter characteristic allows easy integration with DWDM technology, which is already supported by SDH off-the-shelf devices.

A prototype electronics board has been designed for NEMO experiment in order to integrate the SDH protocol with proprietary protocols present on the floor. The purpose of the board is allowing data exchange between underwater electronics and land-side electronics by means of optical links. An useful feature is the definition of an auto-calibration mechanism which makes all the electronics delays of each FCM identical, apart from path lengths.

As soon as enough know-how is acquired with this protocol, a second release of the prototype will be realized to optimize power consumption, circuit space, and to take advantage of any technological progress made. For example, programmable logic intellectual properties which implement SDH STM-1 protocol are already available on the market and could be integrated in the FPGA.

## REFERENCES

- [1] F. Ameli and Al. A single photon detector for the measurement of optical activity in the deep sea. *Review of Scientific Instruments*, 73(12):4164–4168, 12 2002. Online Publication DOI: 10.1063/1.1515359.
- [2] F. Ameli, M. Bonori, and F. Massa. Measurement of optical background in the site for the NEMO KM<sup>3</sup> undersea neutrino telescope. *The European Physical Journal C*,

25(1):67–75, 2002. Online publication: 26 July 2002. DOI 10.1007/s10052-002-1015-x.

- [3] F. Massa. Optical radiation background from <sup>40</sup>K decays in undersea neutrino telescopes. *Eur. Phys. J. C*, 22(4):749–756, February 2002.
- [4] F. Ameli, M. Bonori, and C. A. Nicolau. A 200 MHz FPGA-based PMT acquisition electronics for NEMO experiment. In *VLVVT Workshop*. NIKHEF, Amsterdam, 2003. To be published.
- [5] F. Ameli, M. Bonori, and C. A. Nicolau. Data transport system for nemo experiment. In *VLVVT Workshop*. NIKHEF, Amsterdam, 2003. To be published.

# Optical Module VLSI Full Custom Front-End Electronics

D. Lo Presti

Physics Department, Catania University

Via S. Sofia, 54 –95120 – Catania - Italy

domenico.lopresti@ct.infn.it

## *Abstract*

A full custom VLSI ASIC, designed in AMS 0.35 $\mu$ m CMOS technology, as the front-end electronics for a km<sup>3</sup> cherenkov neutrino telescope optical module (OM), is presented. The trigger, photomultiplier (PMT) signal classification, fast analog sampling and slow digital conversion, event time stamp, data packing and transfer functions are performed by the chip. The main features of this solution are: low power dissipation, high resolution, high input dynamic, high time resolution and the possibility to remotely change all the acquisition parameters by slow control.

## I. SYSTEM DESCRIPTION

In this section we will describe the optical module (OM) front-end electronics proposed for the NEMO [1] underwater neutrino detector. The main objectives that must be achieved are: very low power because of the distance from the shore; only one submarine interconnecting cable to have the best reliability and to simplify the deployment; flexibility to give the possibility of changing parameters; very small dead-time to get good detector efficiency; high dynamic range to fit with different kinds of experiments; very good accuracy of experimental data; low costs, if possible!

In the following subsections we will translate these objectives into design specifications for the electronics and we will show how we foresee obtaining this result.

### *A. Power Consumption*

Power will be transferred to the detector at about 100 km from the shore. Since in these conditions the power transferable is limited, the electronics power consumption must be limited to not more than a few kW in the whole detector, which is less than 200-300 mW in the OM. This means that the solution proposed by the NESTOR collaboration is unreliable. We foresee contributing to obtaining this limited power consumption using, as much as possible, VLSI full-custom Action Specific Integrated Circuits (ASICs) in the OM.

### *B. Submarine Interconnections*

Apart from Nestor, all the other submarine Cherenkov detectors use interconnections between the optical modules, which lead to various solution that are heavy, expensive and not very reliable. We want to use only one penetrator, through which, apart from the DC power supply, information between OMs and local control units will flow, in a bi-directional way. The system will be certainly more reliable and will simplify the deployment.

### *C. Flexibility*

The choice of building coincidences between two or more OMs to limit rate and to obtain acceptable dead time in AMANDA [2] and in ANTARES [3] lacks flexibility. It is not possible, in practice, to change the detector. Even if one forecast proves to be wrong the whole system fails. If one wants a reasonable solution for the interconnections, coincidences must be limited to OMs in the same tower, but the latter does not seem an acceptable solution from the physics point of view. On the other hand to extend coincidences to adjacent modules in different towers makes the hardware more complex with incredible connections or requires a high-speed data transmission system among different modules, which seems unreasonable. It must be taken into consideration that to limit the dead time the coincidence window must be very small. BAIKAL [4], through a local coincidence between two opposite PMs uses a simple system, with a relatively small coincidence window. This solution dramatically raises the costs and worsens the dead times. For these reason we consider unfeasible the idea of hardware coincidences. NESTOR [5] employs software coincidences. The same solution is anticipated for NEMO. We calculate to be able to get about 0.075% dead time, while the expectation for the other experiments, apart from NESTOR, is of the order of 1%.

### *D. Collected and Transmitted Data*

BAIKAL roughly elaborates the information in the OM and transmits only a part of it. ANTARES and AMANDA

propose to perform 320 ns of auto triggered signal samplings at 400 MHz. In NEMO we foresee the transmission of few samplings (we say 10 samples equal to 50 ns) in the case of a Single Photo Electron (SPE) signal or a greater number in the case of a large, or long, signal or of a complex structure (i.e. 100 or 200 samples, equal to 500-1000 ns). In both cases the number of samples is held to be enough to draw form, energy and occurrence time with good precision. In every case the two parameters are not fixed. They can be changed remotely. We have not deemed it necessary to proceed to oversampling.

### E. Dynamic

The system proposed, can allow the attainment of a 20 bit dynamics. If, for power limitations and dead time ANTARES and AMANDA decide to use 8 bit ADC their limit is 16 bit. The dynamics of BAIKAL is limited to 100 PE (7 bit).

### F. Universal Time

We foresee accuracy analogous to that of AMANDA: around 1 ns.

### G. Costs

The choice of a single PM per module, under the same conditions of efficiency greatly reduces the costs. Also, the simplicity of interconnection reduces the costs both of installation and of maintenance.

## II. THE READOUT SYSTEM

In the following we describe, the architecture of the proposed readout system, represented in figure

From the PM two signals are extracted. The anode signal and the one extracted from one of the lower dynodes. When the PM anode signal, sent to the T&SPC (Trigger and Single Photon Classifier) module, makes a trigger event (enough to overcome the SPE/4 threshold) this module outputs a Start signal to the Control Unit. This starts the sampling mechanism performed by one of the two identical memories (Lira), whose size is  $3 \times 256$  cells. Actually the T&SPC furnishes, after about 60 ns, also the classification of the signal. If it is classified as NSPE (Non Single Photo Electron) the system performs 100 samplings. Otherwise, only 10 samplings.

Lira memory (Analogue Delay Line Italian acronym) is endowed with three identical channels one of which samples, simultaneously to the two PM signals, also the Master Clock (MC) at 20 MHz coming from the outside. This is done with the purpose of realizing a time recording system with about 1.4 ns rms resolution, increasable, if necessary, up to 0.7ns.

A 16-bit counter counts the clock cycles (16 bit correspond to about 3.3 ms). Every millisecond the slow control sends a reset signal to synchronize all the modules. At the trigger, the counter content is transferred to a FIFO to be subsequently used as a time stamp at 50 ns resolution.

Lira samples at the frequency of a Slave Clock (SK), 200 MHz. It is originated, through a frequency multiplier (PLL), starting from the same MC. From the moment that this last

MC is sampled at the SC frequency, the system acts as a temporal nonius.

One of the memories is always predisposed to perform the sampling. Nevertheless, it samples only for the preset number of times when the Trigger arrives. To be certain of capturing the signal coming from the PM, the latter is purposely delayed by the time necessary for the T&SPC to take the decisions of the case. When a signal has been entirely sampled, the memory, in which the sampling has happened switches to read phase and the other is ready to sample.

The reading phase happens at high speed (10 MHz). Only the cells that have been written in the channel are read. Actually only one of the two signals sampled by the PM (under the control of the Dyn signal) is read and transferred to the ADC. The signal sampled in the channel of the fine time does not go to an ADC but, since it is a signal made of levels, is introduced into an oportune logic for giving precise information on the arrival instant of the signal related to the MC. Once the content of a memory has been transferred and the ADC has ended the conversion this latter is put in a Power Down (PwD) state. In this way one can have a remarkable power saving, about 1/20. Few hits of Clock, furnished before taking back the reading, put the ADC into the condition of correctly taking back its job.

## III. ITEM OF THE OM

Anything which is commercially available and satisfies the technical and power consumption requirements will be adopted in the OM. Not included in this forecast are: the Switched Capacitor array Analogue Memory to capture the signal (Lira); the module which Triggers and Classifies the signals, T&SPC; the synchronous frequency multiplier (PLL); the Control system; the DC/DC conversion system to furnish power supply starting from the single one that enters from the penetrator; the low-power supply for PMT anodes and dynodes.

## IV. THE CAPTURE CHIP

Lira has been realized as a full custom Mixed ASIC. It is a switched capacitor array with a Voltage Sampling-Voltage Transfer topology[HALL1] [HALL2]. The memory samples three channels per second simultaneously at 200 Msamples.

In reading phase LIRA exhibits two simultaneous outputs: Os and Ot. The reading is made at 10 MHz frequency. According to NSPE signal, from Os the anodic or dynodic channel samples are extracted (Signal Output) and from Ot (Time Output) the MC samples. No commercial device having the same characteristics of LIRA is available.

We have already realized similar devices. For example one of 16 channels per 64 cells each, that samples at 40 MHz and reads at 3 MHz.

## V. CONTROL UNIT(CU)-SLOW CONTROL

The CU is dedicated to the supervision of the whole operation of the OM electronics. It also receives and opportunely rebroadcasts the signals for the slow control.

Actually the CU has been realized by the Bologna collaborators in a Field Programmable Gate Array (FPGA) XILINX XC4085-1PG559. Successively the same electronics will be implemented as a digital ASIC in Alcatel-Mietec 0.7 micron technology.

The Control Unit checks, among others, the state of the two buffer memories. One of them is always predisposed for sampling and the other for reading. In any case, the operations will be performed only when the CU enables them. Every time one of the two chips stops performing the data transfer towards the ADC, it is made to commute from the CU and becomes the sampling chip while the other one becomes the transfer chip. The CU, which knows if valid data exist and how much are in this memory, allows this transfer to be undertaken in the right conditions. From the T&SPC the CU receives the three signals: Start, Dyn and NSPE. On the basis of these signals it decides the cadence of the sampling, its duration and which of the channels, between anode and dynode, will be transferred toward the ADC. Besides it furnishes, with the trigger, the signal that makes the counter store the time information. The CkO signal is at 10 MHz for the reading. The PwD signal puts the ADC in standby to save power. It must be noticed that the ADC average duty cycle is 500 ksamples on the 10 Msamples possible.

The function of the memory depends on the R/W signal. Every time that this is commuted from the reading to the writing a narrow CR impulse is also furnished to reset the internal register.

Other signals furnished by the CU are R1 and R2 that serve to reset the cells of the SCA; SE1 and SE2 open the gates through which the SCA samples. S selects what between anode and dynode, to send to the ADC. Finally Time Stamp (TS) memorizes the MC counter.

The CU also checks the orderly flow of data from the ADC, from the two counters of coarse and fine time. To do this it has the  $R_{Tr}$  (Read Time fine),  $R_{Tc}$  (Read Time Coarse) signals and ACK (Adc Clock). To every signal it attaches, as a header, a custom sequence that identifies the Optical Module, and then the time, the number of effected samplings and the samplings themselves. Everything is packaged in a FIFO and transmitted to an external Local Control Unit, one for every row of Optical Modules.

The slow control is carried out in the Control unit. When remotely requested, it performs the following regulations: PM power supply; regulation of the threshold that switches on the trigger; regulation of the comparator threshold in the T&SPC that checks if the signal is very high; regulation of the number of samplings in the case of the SPE; regulation of the time interval within which the signal cannot have more than two intersections with the low threshold and is, therefore, a NSPE; regulation of the input/Output offset of the memory and the zero level of the ADC.

A test board has been developed and designed by the Bologna collaborators. It will allow the FPGA, or the successive ASIC implementation, to be tested separately or interfaced with the capture ASIC. The test board will, also, allow the bi-directional communication on a standard coaxial

50  $\Omega$  cable. The electronic board is intended both for testing purposes and for actual operating mode. In fact, the board allows one to test the FPGA and, eventually, the ASIC.

## VI. COMMERCIAL DEVICES

The ADC, the counter, the time stamp register, its FIFO and the Multiplexer are foreseen as low power consumption standard devices.

The ADC that can be used is the ADS901:  $C_i = 5$  pF; 10 bit, 3V, 20 MHz, Pd 15 mW (Stand by) - 45 mW full regime; in Power down mode it should go down to 18-20 mW because of the 10% duty cycle.

## VII. THE DEAD TIME

We have put under conservative conditions and we have estimated, pessimistically, that the trigger and classification system for the Single photoelectron signals recognize, at least 99% the signals from SPE. Then, for every 99 SPE signals there could be one NSPE. In the first case the system does 10 samplings, in the other it does 100.

We have, reproduced by a Montecarlo simulation, the pulse occurrence times with a 50 kHz rate (correspondent to the  $^{40}\text{K}$  decay detected by a 15" PM) and with a 22 kHz rate (related to a 10" PM detection). These times were needed to determine the memory occupation. Besides the simulator produces the NSPE signals with the anticipated pessimistic rate. The memory, once the transfer of its content has ended, is immediately predisposed to sample other signals. It is possible that, during the data transfer phase towards the ADC, the other memory is not empty and is found busy for the sampling of following signals. So it can happen that it fills up. If its reading frequency is not too small in comparison to its sampling frequency and the memory is deep enough, it is quite unlikely that this will happen.

According to our calculations, the dead time practically depends on the commutation time of the memories from reading to writing phase. In two or three clock cycles the memory can commute its function that is in 10-15 ns. Around 50.000/sec commutations are required, at the most  $T_m' = 15 \times 50 \times 10^3 \text{ ns} = 750 \mu\text{s}$ . But, the memory could not be able to commute because it is full and the other has not emptied yet. We have simulated this scenario. We calculated what happens for a 15" PM and a 200 position memory that operates in reading phase at 10 MHz. Every 50.000 pulses/sec, occurring every 2  $\mu\text{s}$  of average interval, the system loses 0.002% per second that is only one pulse per second. This one occupies around  $T_m'' = 50 \times 10^3 \text{ ns} = 50 \text{ ns} \ll T_m'$ .

If the memory has only 150 positions, the 50.000 pulses/sec lose 0.018% that is 9 pulses. They occupy around  $9 \times 50 \times 10^3 \text{ ns} = 450 \text{ ns} \ll T_m'$ .

Only if the memory has less than 100 locations, is something noticed. At 100 locations, the 50.000 pulses/sec lose 0.42%, that is 210 pulses that increase the dead time to  $10^5 \mu\text{s}$ . Once more this time is not meaningful in comparison to the term that derives from commutation. Despite all of this we believe that it is opportune to choose a depth of 200

positions because we could decide to make samplings longer than 100 and, that is, also than 200 (1  $\mu$ s). The dead time is inferior to  $750 \times 10^{-6}$ . That is less than 1%. To succeed in reducing the commutation time from 3 to 2 clock intervals means to halve it.

We did not start making calculations for smaller PMs because it is not of interest for us.

### VIII. THE ABSOLUTE TIME

The Master Clock serves for giving coarse time. It is counted by a 16 bit counter, which is reset periodically from the outside and simultaneously on all the modules every ms. The second, slave, Clock establishes the sampling cadence (every 5 ns). Every time a Trigger arrives, at least 10 samplings are performed, that is every channel is sampled for at least 50 ns. Then the Master Clock channel is also sampled. So, in this channel, for every Trigger one has a Low-high transition and another High-Low. In the case of a NSPE one has 10 transitions. The transition position gives the fine time with a resolution that, if one looks only at one transition can reach 1.4 ns, but with both, if the Master Clock has a 45% duty-cycle, can go up to 0.7 ns resolution.

### IX. ACTIVITIES STATUS

The Microelectronics group started the R&D work in order to build the Optical Module front end electronics for the NEMO telescope.

The aim is to design a full custom VLSI ASIC containing as many as possible circuitual blocks in order to reduce the total cost of the electronics, utilizing commercial devices for the other blocks.

During these last three years, many ASIC have been designed in order to realize the final OM front-end chip.

The technology used is the AMS CMOS 0.35 $\mu$ m, available for prototyping with costs accessible to the University research thanks to Europractice, a European silicon foundry society.

Through the testing and the performance measurement of the previous chips, it has been possible to improve each block topology or, in certain case, to repair some design errors.

In order of testing and measuring the chip performances, a dedicated PCB has been designed, using all the experience acquired during these years on this delicate topic.

The (PCB) test board will allow a semi automatic test of this chip to be possible. A digital DAQ board will be able to acquire data coming from the 10 bit flash ADCs, ADS 901, mounted on the board, which will codify LIRA01 AM output signals. The DAQ board is mounted into a notebook docking station. A dedicated software interface has been, just, developed to drive the data acquisition operations (LabVIEW).

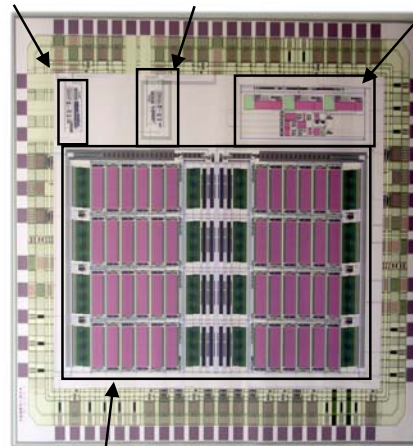
Several MATLAB-based procedures extract the static performance parameters from the data files. A scanning procedure has been implemented in order to correlate each

acquired memory cell read-out transient with its own cell and channel number.

After that procedure part of the time samples constituting a read-out cell transient is labelled with its correct cell number, for every cell in an acquired data file.

In figure 1 a plot of the new LIRA02 chip with the block descriptions is shown.

PLL Stand Alone 200 MHz Slave Clock      LIRA's PLL Shielded      T&SPC



LIRAX2 200 MHz Write freq. 10 MHz Read freq.

Figure 1: A plot of the LIRA02 chip

### X. CONCLUSIONS

The new LIRA02 chip will be tested as soon as possible.

First qualitative measurements affirm the correct functionality of the PLL stand alone.

Measurements on the previous versions of the chip demonstrated the full functionality of the T&SPC and its slow control interface.

Concerning the analog memory further tests are required in order to measure all the chip performances.

### I REFERENCES

- 1 NEMO web site: [nemoweb.lns.infn.it](http://nemoweb.lns.infn.it)
- 2 ANTARES web site: [antares.in2p3.fr](http://antares.in2p3.fr)
- 3 BAIKAL web site: [www.ifh.de/baikal/baikalhome.html](http://www.ifh.de/baikal/baikalhome.html)
- 4 DUMAND web site: [www.phys.washington.edu/~dumand](http://www.phys.washington.edu/~dumand)
- 5 ICECUBE web site: [icecube.wisc.edu](http://icecube.wisc.edu)
- 6 NESTOR web site: [www.nestor.org.gr](http://www.nestor.org.gr)
- 7 Halzen F, et al (AMANDA Collaboration).  
Prepared for *Int. Cosmic Ray Conf., 26th, Salt Lake City, UT, Aug 17-25, 1999.*  
<http://alizarin.physics.wisc.edu/karle/icecube/>
- 8 S. Panebianco D. Lo Presti G.V. Russo L. Caponetto C. Petta N. Randazzo S. Reito. Switched capacitor arrays analog memory for sparse data sampling. *Nuclear Instruments and Methods in Physics Research A*, 434:424-434, 1999.
- 9 D. Lo Presti -Optical Module Front-End VLSI Full-Custom ASIC for a Submarine Neutrino Detector - Phd Thesis 2003

# A 200 MHz FPGA-based PMT acquisition electronics for NEMO experiment

C. A. Nicolau for the NEMO Collaboration

INFN sezione "Roma1"

carlo.nicolau@roma1.infn.it

## Abstract

As a member of the NEutrino Mediterranean Observatory (NEMO) collaboration, the Rome electronics group is involved in the development of the photo-multiplier data acquisition front end.

First, physical and electronic requirements for the data acquisition system are identified. A block diagram is then shown and explained, giving full details of input/output channels, compression circuit, zero-skipping trigger settings, and self-calibration capabilities.

Finally, results obtained with a prototype board are shown and future developments are discussed.

## I. INTRODUCTION TO THE NEMO KM3 APPARATUS

The goal of the NEMO collaboration is the realization of one cubic kilometer underwater Čerenkov neutrino telescope, called NEMO KM3.

The proposed apparatus consists of 64 towers, placed on a square grid, 200 m apart. In Fig. 1 is shown a schematic layout of one tower. Each tower is composed of 16 floors.

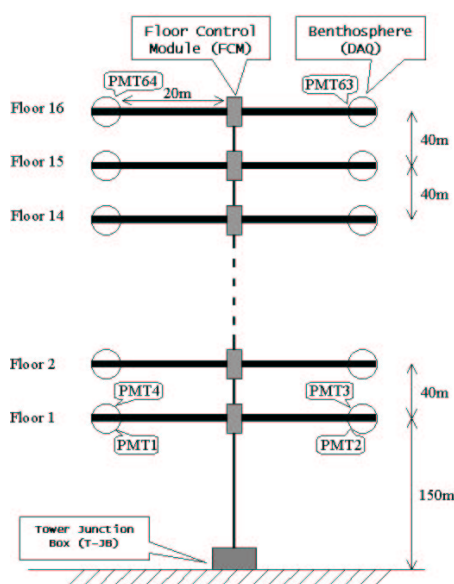


Figure 1: NEMO Tower block diagram.

At the ends of each floor there are four benthospheres, each containing one single photomultiplier (PMT). In addition,

each benthosphere contains the data acquisition front end and the high voltage power supply.

At the center of each floor a box is positioned, containing the so-called Floor Control Module (FCM) which connects the electronics inside the four benthosphere to the rest of the apparatus and performs some floor management.

## II. THE DATA ACQUISITION FRONT END

The main task of the data acquisition front end (DAQ) is to acquire the electric signal produced by the PMT and to transmit it in a suitable way to the FCM. In addition, the DAQ board supplies, controls and checks the DC power for the high voltage power supply unit which, in turn, supplies the PMT. Moreover, benthosphere's local controls, such as temperature, humidity, etc., can be managed by the DAQ board by means of some auxiliary analog input/output channels. In addition, some freely configurable digital input/output channels are provided as well as a LVTTTL RS-232 compatible serial port.

The basic choice in PMT data acquisition is digitizing the electric signal with a sampling frequency of about 200 MHz and a resolution of 8 bit. Signals produced by the selected PMTs are filtered to obtain a band-width lower than about 100 MHz and thus according to the Nyquist's theorem, the chosen sampling frequency is sufficient to keep all the PMT signal information intact. Taking into account sampling clock jitter and quantization noise, from previous experience on similar acquisition boards developed by the same group, the expected timing error is on the order of 300 ps [1]. With these choices the sampling data rate is 1.6 Gbps.

Referring to the site of Capo Passero located off the Sicily coast, the expected single photo electron (*spe*) rate with a 10" PMT is about 50 kHz [2, 3, 4]. This rate is mainly due to  $^{40}\text{K}$  decay and to PMT dark current. Considering a *spe* event length of about 50 ns and taking into account the amount of data needed to store time information of each event, the expected data rate produced by physical events is about 5 Mbps.

To reduce the sampling data rate to this value, a zero-skipping programmable digital threshold and a first-in first-out (FIFO) queue are implemented.

In order to detect the small signals produced by single photo electrons without affecting the input voltage range, a quasi-logarithmic passive analog compressor is implemented. The quasi logarithmic compression maintains the relative error constant over the whole signal range.

In Fig. 2 the DAQ functional block diagram is shown.

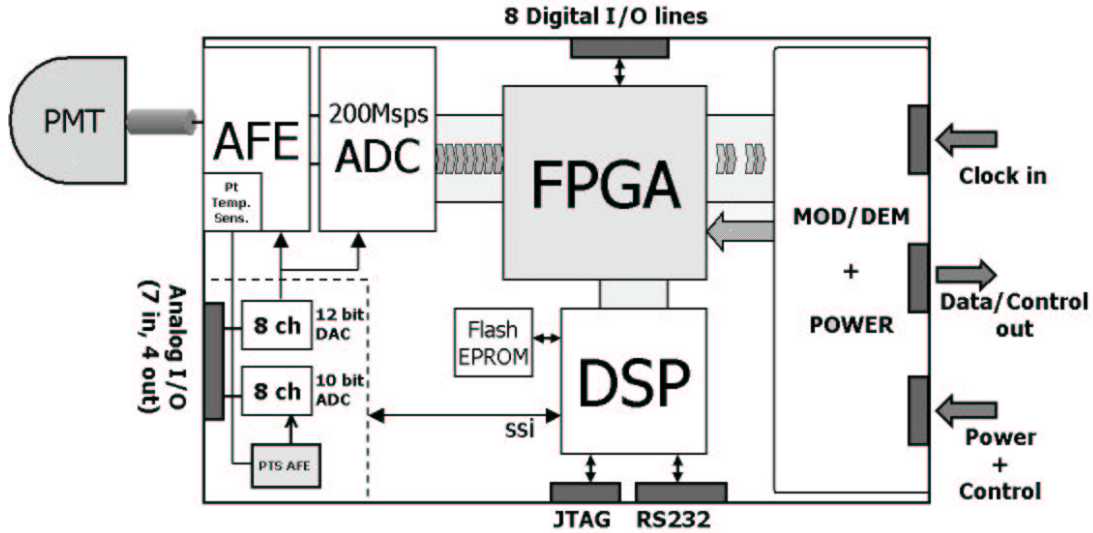


Figure 2: DAQ Board functional block diagram.

In the following section, we will give a description of the connections and of the input/output signals characteristics, reading it in a clockwise order. Then the main functional blocks will be detailed.

### A. Connections

Beginning from the left top side we find the connection to the PMT, whose signal is carried over a  $50 \Omega$  matched coaxial cable and conditioned by the Analog Front End (AFE).

On the upper side of the diagram there is the connection to the 8 general purpose digital I/O lines. These pins are directly controlled by the FPGA and are set for LVTTTL voltage levels, i.e. 0 V or 3.3 V respectively for '0' and '1' logical levels. Each pin can drive a current value as high as 24 mA.

On the right side, we find the connections to the FCM. This link consists of three shielded twisted pairs over which a 1.215 MHz clock signal, the slow control input data coming from the FCM (432 kbps), and the data output bitstream towards the FCM (19.44 Mbps) are carried. The power supply voltage (5 VDC) is transmitted in common mode by the FCM over the two data channels. The 1.215 MHz clock is generated by the FCM, which derives it from the 19.44 MHz signal of the SDH transmission protocol [5]. Since all the timings on the board depend on this signal, it is carried on a separate twisted pair in order to reduce the sampling clock jitter and, thus, to allow a better signal reconstruction. Data are received and transmitted with a synchronous serial protocol, and are encoded with a *no return to zero (NRZ) pulse position modulated (PPM)* code [6].

On the bottom side of the diagram, the LVTTTL RS-232 and JTAG interfaces are shown. These interfaces are provided by the DSP and can be used as a general purpose asynchronous serial interface the former, and as a debug port the latter.

Finally, on the left bottom side of the diagram, there are

the auxiliary analog input/output channels. There are 4 output channels and 7 input channels. The 4 output channels are provided by a 12 bit DAC and can produce signals in the range from 0 V to 2.5 V. One of these channels will be used to control the high voltage power supply. The 7 input channels are provided by a 10 bit ADC that can handle signal in the range from 0 V to 2.5 V. One of these channels will be used to monitor the voltage produced by the high voltage power supply. The 12 bit DAC and the 10 bit ADC are controlled by a Synchronous Serial Interface (SSI) integrated in the DSP.

### B. The analog front end

The analog front end consists of a completely passive analog circuit which performs a quasi-logarithmic signal compression. Since the compression is obtained by means of a diode, and since the characteristic curve of the diode varies with temperature, a platinum temperature sensor (PTS) is used to measure it. After some signal conditioning on the signal produced by the PTS, the temperature measure can be obtained reading one dedicated channel of the 10 bit ADC. Moreover, since the analytical calculation of the mentioned curve, with the required precision, is difficult, the system measures its compression curve during the so-called *self-calibration* procedure.

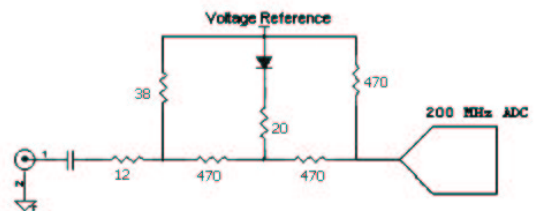


Figure 3: The compression circuit.



The schematic diagram of the compression circuit is reported in Fig. 3 while Fig. 4 shows the result obtained by the *self-calibration* procedure. In the first region (the first ADC channels) the compression curve is quasi-linear and the corresponding voltage quantization step is about 12 mV. Since *spes* events, which mainly constitute the background noise, produce a signal with an amplitude of about 120 mV, only 4 bits are needed to represent them. This fact permits to reduce the data rate produced by the DAQ board by using non lossy digital data compression algorithms.

From Fig. 4 we see that the resulting input voltage range is about 50 V and thus the equivalent dynamic of the data acquisition system is about 13 bit.

Moreover, considering the relative simplicity of the compression circuit, it is possible, by changing only the resistor values, to obtain different compression curves, in order to adapt the system to different kind of input signals.

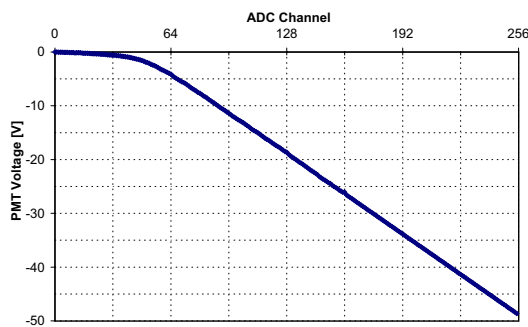


Figure 4: An example of compression curve, obtained by interpolating data produced by the *self-calibration* procedure. On the abscissae the numeric value read by the ADC is reported, while on the ordinates there is the corresponding voltage produced by the PMT

### C. The analog to digital conversion

In order to reduce the power consumption, instead of using a single 200 MHz analog to digital converter, two 100 MHz ADCs are used.

In fact, the sampling frequency is not exactly 200 MHz. The effective sampling rate is obtained by a 97.2 MHz square wave clock used to trigger the two ADCs: one being triggered on the rising edge of the signal, while the other one being triggered on the falling edge. This yields to an actual sampling rate of 194.4 MHz.

The 97.2 MHz clock is generated by the Phase Locked Loop (PLL) inside the DSP, which multiplies by a factor of 80 the 1.215 MHz clock received from the FCM.

The two ADCs are differential and could present different offset values. To overcome this obstacle, their positive inputs are fed by two 12 bit DACs. This way the two ADC offsets

are tuned to obtain the same zero value when the input signal is zero.

### D. The DSP

The DSP is mainly used as a board controller.

When the system is powered up, the DSP reads its program from the Flash EPROM and uploads the FPGA bitstream. It also controls the 12 bit DACs and the 10 bit ADCs - i.e. the auxiliary analog I/O channels, temperature sensing channel, and the offset and self-calibration channels - by means of its integrated SSI peripheral.

The integrated LVTTTL RS-232 compatible asynchronous serial interface can be used to control serial-compatible instrumentation as well as, during the firmware development phase, for programming and debugging purposes. Moreover, the DSP integrated JTAG interface can be used for hardware level DSP firmware debugging.

Finally, as already mentioned, its internal PLL is used to generate the 97.2 MHz square wave clock.

### E. The modulator/demodulator

The modulator/demodulator (MOD/DEM) connects the DAQ board to the floor control module. As already said, the connection consists of three shielded twisted pairs. The MOD/DEM contains the line drivers. All the channels, except the power line, are galvanically decoupled by means of three transformers.

In addition to the already mentioned 1.215 MHz clock line, there are the *control input channel* and the *data/control output channel*.

Over the *control input channel*, the DAQ board receives the *slow control commands*, i.e. offset settings, threshold settings, temperature sensing commands, auxiliary channels read and write commands, etc., and the *time critical commands* (see later for details).

Over the *data/control output channel*, the DAQ board sends the acquired data stream, and the slow control data, i.e. the results of the received slow control and time critical commands.

The power supply voltage (5 VDC) is carried in common mode over the twisted pairs of these two channels.

### F. The FPGA

The FPGA is the heart of the DAQ board. It is directly connected to the two 100 MHz ADCs, to the DSP and to the MOD/DEM.

Data produced by the ADCs are acquired by the FPGA which compares them with a programmable digital threshold. If the acquired data exceed the threshold level, "an event is opened", the time stamp is stored and sampled data start feeding the internal FIFO. The event will be closed when a certain number of samples is under the threshold level. The stored

time stamp is obtained by reading the time register, which is incremented on the rising edge of the 97.2 MHz clock.

Data present in the FIFO queue are then internally mixed with the slow control data produced by the DSP, encoded with a pulse position modulation (PPM) and then sent to the FCM with a data rate of 19.44 Mbps. Since the expected data rate produced by physical events is about 5 Mbps, the allocated data rate is over-dimensioned by a factor of about 4. Considering that the physical events follow a Poisson statistic, the depth of the FIFO and the rate at which the data are extracted from the FIFO are correlated with the probability of having dead time (corresponding to the filling up of the FIFO). The 128-stage FIFO queue implemented inside the FPGA guarantees that, except for bioluminescence events, this eventuality can be neglected.

The data that the FPGA receives from the FCM through the MOD/DEM contain both slow control commands, which are directly sent to the DSP to be processed, and time critical commands, which are executed directly by the FPGA at an hardware level.

In fact, all the commands that have to do with the board timing have to be executed with a fixed known delay and can not be executed by the DSP because of the unpredictable software execution delay. The time register reset is an example of such commands. This possibility guarantees that the local time counter of the DAQ board can be synchronized and phased with the local time of the FCM and thus with the time of the whole apparatus.

Moreover, being the 8 digital I/O lines directly controlled by the FPGA, it is also possible to produce hardware signals with known delay. For instance, a fast LED can be triggered by one of these pin in order to measure the PMT Transition Time Spread (TTS).

### III. CONCLUSION

A prototype of the described system has been realized. The prototype is composed of two square boards which occupies a 10x10 cm<sup>2</sup> area each, including a 7x10 cm<sup>2</sup> area allocated for the high voltage power supply unit (HVPSU). The power consumption of the prototype without HVPSU is about 950 mW.

A new release is under development, where a newer FPGA will reduce power consumption and will permit to increase the FIFO queue depth.

In future development, it will be possible to implement DSP functions in the FPGA to obtain a smaller board and lower power consumption.

Moreover, taking into account the final constraints for KM3 detector, it will be possible to optimize the number of the auxiliary channels, reducing the number of connectors, space and costs.

- [1] F. Ameli and Al. Data acquisition electronics for NESTOR deep sea neutrino telescope: Project and tests. *NIMPR*, A423:146–156, 1999.
- [2] F. Ameli and Al. A single photon detector for the measurement of optical activity in the deep sea. *Review of Scientific Instruments*, 73(12):4164–4168, 12 2002. Online Publication DOI: 10.1063/1.1515359.
- [3] F. Ameli, M. Bonori, and F. Massa. Measurement of optical background in the site for the NEMO KM<sup>3</sup> undersea neutrino telescope. *The European Physical Journal C*, 25(1):67–75, 2002. Online publication: 26 July 2002. DOI 10.1007/s10052-002-1015-x.
- [4] F. Massa. Optical radiation background from <sup>40</sup>K decays in undersea neutrino telescopes. *Eur. Phys. J. C*, 22(4):749–756, February 2002.
- [5] F. Ameli, M. Bonori, and C. A. Nicolau. Synchronous data transmission protocol for NEMO experiment. In *VLVVT Workshop*. NIKHEF, Amsterdam, 2003. To be published.
- [6] K. M. True. Long transmission lines and data signal quality. Technical Report AN-808, National Semiconductor, 1997.

### REFERENCES

# A Conceptual Design of a Km<sup>3</sup> Neutrino Observatory

Peter K.A. de Witt Huberts

NIKHEF P/O Box 41882, 1009 DB Amsterdam, The Netherlands  
[pdwh@nikhef.nl](mailto:pdwh@nikhef.nl)

## Abstract

In the implementation of a large neutrino observatory in the sea, extreme requirements must be imposed on operational reliability of the off-shore electronics in order to optimise operational availability and constrain maintenance cost.

I discuss an application of multi-colour Dense Wavelength Division Multiplexing (DWDM) to the conceptual design of a KM<sup>3</sup> neutrino detector, characterized by a minimal amount of off-shore electronics. Operational reliability and a cost estimate are discussed. Key issues concern the choice of the event format at the front-end signal processing level, the organisation of the control/calibration functions. Provided the reliability of the mechanical structures can be matched to that of the electronics, the design may ultimately possess the 'no-maintenance' feature (like AMANDA does).

## I. INTRODUCTION

With a view to constructing a KM<sup>3</sup> neutrino observatory, issues concerning optimisation and scalability of the current ANTARES design must be tackled. The future large detector will comprise 5000-10000 Photo Sensors. Up-scaling the current design would impose extreme requirements on operational reliability to achieve affordable maintenance cost and would lead to excessive off-shore power consumption and a large number of MEOCs and Junction Boxes. Optical data-transmission technology with dense wavelength division multiplexing (DWDM) is currently providing typically a hundred colour channels per optical fibre at 10Gb/s or more. For our purposes, such transmission speed largely exceeds the required bandwidth per Photo-Sensor, that will be typically (1-2) GHz in order to ensure sub-nanosecond time resolution. In the design of a future large detector, the following major objectives should be implemented

- Optimal reliability (leads to reduced cost of construction and operations)
- Reduced electric power consumption off-shore (results in a small number of MEOCs and JBs)

Using multicolour opto-electronic techniques, both the amount of complex electronics and the electric power consumption **off-shore** can be largely reduced by implementing three design features :

- A farm of lasers **on-shore** (therefore, readily serviceable) to provide the multicolour DWDM function
- Merge colour channels via passive Multiplexing/Interleavers into optical fibres and assign a specific colour to a specific OM (One PM-One Colour)
- Encode the analog output of the PM in its specific colour channel. Decoding and signal processing **on-shore**
- Event arrival-time calibration using Optical Time Domain Reflectometry (OTDR)
- Slow control implemented in e.g. a hybrid system, combining Synchronous Optical Network (SDH/SONET) and Asynchronous Transfer Mode (ATM).

Note: It is being assumed, there is no off-shore trigger, i.e. 'All Data to Shore'.

## II. LASER FARM ON-SHORE

The basic layout of the laser farm to produce 128 colors, route these to off-shore, split (1\*40) into 40 fibres (say) and amplify with Erbium Doped Fibre Amplifiers (EDFAs), is illustrated in Figure 1. Wavelength merging is performed via eight Multiplexers (1:16), four Interleavers (100/50 GHz) and one Coupler (4\*1).

For additional information on the optical components used and on optical- network architectures, please consult <http://www.agere.com/> and <http://www.alcatel.com/>.

Note: EDFAs, being indispensable devices in long-haul optical backbone networks, come in highly reliable implementations with twin drive lasers.

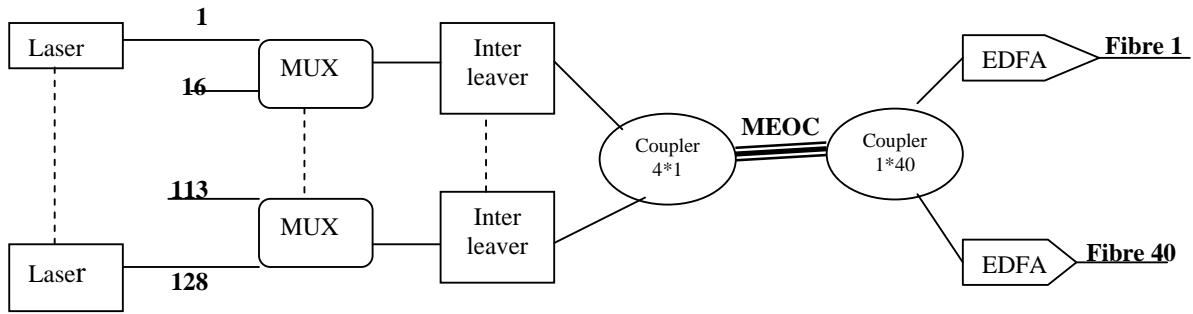


Figure 1: Layout of a laser farm on-shore and a multiplexer-interleaver network to merge 128 colours, route to the off-shore site via a Main Electro Optical Cable (MEOC) and feed 40 fibres, equipped with one EDFA each, to target ~5000 Photo Multipliers.

Optical Power budget

Laser (6dBm), Multiplexer-Interleaver-Coupler (-6dB), 40 km MEOC (-10dB), coupler (1\*40) (-16dB), EDFA (24dBm total output, 3dBm per colour).

### III. ONE PM- ONE COLOUR READOUT

De-multiplexing is performed with Optical Add Drop Multiplexers (OADM), as is illustrated in Figure 2.

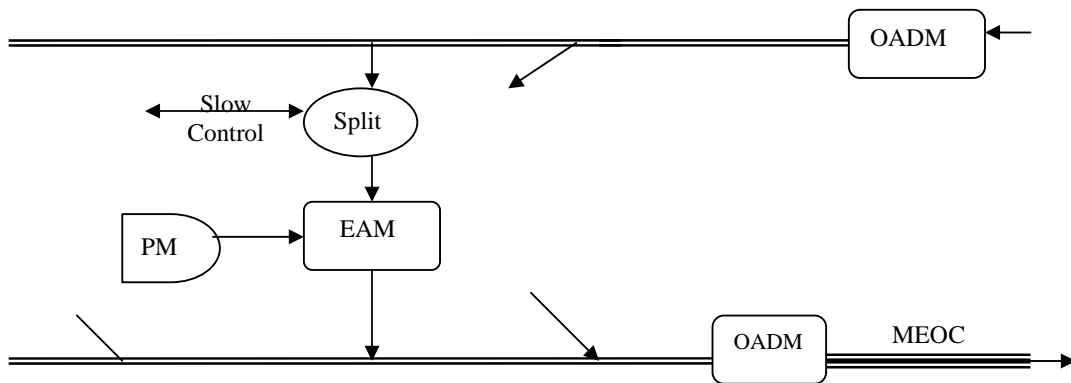


Figure 2: De-multiplexing and Multiplexing (OADM) and the Electro Absorption modulator (EAM) of a targeted Photo Multiplier (PM). Slow Control may be implemented with a synchronous link.

Optimising the distribution of wavelenghts for a given PM configuration requires R&D, in which specifications of Optical Components, (EM)Cable and Penetrator must be taken into account - reliability and cost are relevant parameters in the optimisation process.

#### IV. FRONT-END SIGNAL PROCESSING

In the current ANTARES design, extensive information on pulse heights and waveform is digitised by the Analog Ring Samplers (ARSs). However, neither in the event filter nor in track reconstruction waveform information is currently used. It is, therefore, likely that the information content of the analog output of the photo sensor can be reduced without losing a chief asset. There are several ways: 1. Process the PM output with a logarithmic amplifier to provide the required amplitude dynamic range and modulate the optical signal with the log(amplitude) signal. 2. Process the PM signal with a Time Over Threshold Discriminator (TOTD). I will here elaborate a bit on TOTD processing. For relatively large excursions over threshold, TOTD output appears to be proportional to Log(Amplitude) for PM-type signals. Thus, with a single PM-output, a large dynamic range can be achieved. Double-pulse resolution will be appropriate. An Electro Absorber (EA) (Voltage drive ~ 3V and a 30dB extinction ratio), driven by the TOT output, will cause the light output to return to zero (RTZ) during the interval of time that the pulse is over threshold. This signal is routed to shore via a return fibre. After de-multiplexing at the on-shore

end of the MEOC, pulse-width digitisation on shore then allows us to reconstruct PM amplitude and the arrival time of the event is digitised. Note: The effects of pulse pileup and the possible use of a multiple threshold TOTD, applied to obtain enhanced information of input pulse shapes (e.g. those, induced by huge amounts of light generated by e.g. ultra high energy tracks), should be investigated to fully evaluate the TOTD scheme.

#### V. EVENT TIMING

Superior angular resolution of track reconstruction being the chief asset of water Cherenkov detectors, a rather tough objective of a spread of smaller than 1 ns of inter-channel event arrival time must be accomplished. Differences of event-arrival time due to different fibre length can be calibrated by Optical Time Domain Reflectometry (OTDR), in the manner illustrated in Figure 3. Briefly, a specific PM is targeted by routing the output of the appropriate laser to the return fibre allocated to that PM, send a pulse towards the PM (the PM can be correctly targeted due to the bi-directional characteristic of an OADM) and measure the arrival time of the return signal. Optical power budget : Input pulse 6dBm, MEOC (-10dB), 2\*OADM (-12dB), MEOC (-10dB), return pulse power -26 dBm, a level sufficient to trigger an Avalanche Photo Diode (APD) (sensitivity : ~ -34dBm) and hence measure the propagation time delay , specific for the targeted PM , by a TDC.

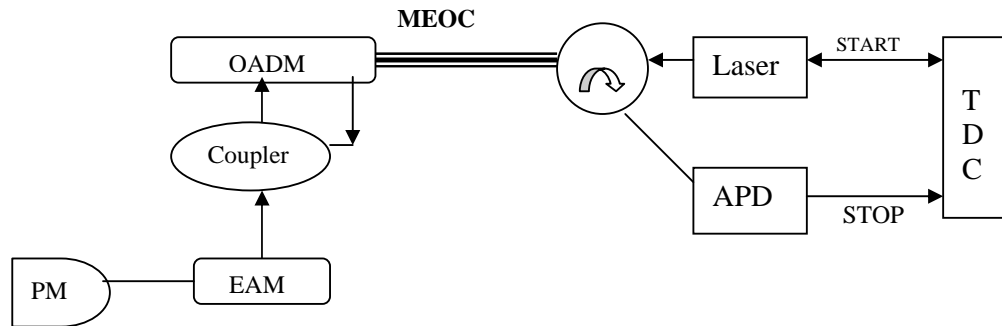


Figure 3 : System for calibration of propagation time of the return fibre, that carries an encoded PM signal to shore.

#### VI. CALIBRATION AND SLOW CONTROL

In the current ANTARES design, calibration is organised in a rather redundant system comprising localisation of OM/PM by sonar (one in each sector), compass / tilt meter (one per storey), light beacons at known positions and measurements of water environmental parameters to determine sound velocity. A calibration system with less redundancy may

be organised on the following principle (M. de Jong - public communication at the October 2003 VLVnD workshop (NIKHEF) – Acoustic positioning at the string base and determination of OM positions by a system of light beacons (LEDs, Lasers) positioned in dedicated calibration/instrumentation strings that are interspersed (one on ten, say)

with the event-tracking strings. A marked characteristic of a calibration operation is that its duty factor is low, which implies that the average electrical power consumption of the calibration electronics off-shore can be minimal.

## VII. OFF-SHORE POWER CONSUMPTION

Current power consumption per storey ranges between 25 and 32 W and amounts to ~800W per string comprising 5 sectors. By eliminating all off-shore electronics, except PM/Base/LED and tiltmeter-compass, electric power consumption per storey would be down by an order of magnitude. This implies that one String Power Module of the current design would be able to provide the electric power for about ten strings in the new, low power consumption configuration.

## VIII. COSTING (1 PM-1 COLOUR) READOUT

The reference cost figure is that of the current-ANTARES readout electronics in storeys – ARS, DAQ, Ethernet, DWDM - and in the String Control Module: cost per OM amounts to ~ 4 kEuro. Baseline cost figures for the One PM- One Wavelength Readout are as follows : Laser - 1000 E, Multiplexer - 1000E/channel, Interleaver - 10.000 E, EDFA - 25.000 E, OADM - 500-1000 E, EAM - 500-1000 E, APD 500 E, On-shore event decoder - ~100 E per PM. Cost related to propagation time calibration, is negligible because calibration of PMs will likely be performed sequentially and the cost of the on-shore high resolution time digitiser will be, therefore, shared by 5000 PMs.

With reference to Figure 1, the cost of the laser farm, multiplexers/interleavers and EDFAs per PM amounts to 250 Euro. This, added to the cost of OADM, EAM and APD results in a total estimated cost of 1800-2500 Euro per PM, i.e. about 50 % of the current cost of readout per PM. There will be additional cost savings because the LCMs of the current design can be disposed of, while the minimal-outfit electronics can be located in the Optical Module.

## IX. OPERATIONAL RELIABILITY

Given the lack of significant operational experience with the current ANTARES design, in particular where the long-term stability of the mechanical structures is concerned, an absolute value of System Mean Time Between Failure (SMBTF) is difficult, perhaps impossible, to assess at present. An evaluation of relative operational reliability, comparing the architecture of current- and future detectors, can be reasonably be performed., though. Let the structure be partitioned into the following sub-systems: 1. Photo Multiplier with base, glass sphere and links, 2. ARS\_MB, 3. Clock system, 4. Ethernet, 5. DAQ\_MB, 6. DWDM system, 7. Mechanical functions (water tightness of MLCM, penetrator, connector, robustness of EMC), 8. String Power Module, 8. Local Power Box. Criticality of a failure is sub systems 3, 4, 6, 7, 8, is heavy : loose a sector or worse (the entire string), in case e.g. that a waterleak in XLCM or EMC causes a short circuit of all of the outputs of the SPM. Criticality of a failure in subsystems 1, 2, 8 is relatively low: loose a storey.

Clearly, by eliminating the off-shore functions 2, 3, 4, 5, 6 and making the electrical power system more robust by adding redundancy and noting that the majority of components of the One PM- One Colour system are passive (EDFAs are very reliable due to the twin drive laser implementation), system reliability will be dramatically better than in the case of the current design. That is, provided water tightness in general and the (long-term) robustness of Electro Mechanical Cables can be adequately ensured. In addition, the simplified electronics off-shore will alleviate substantially the efforts in system engineering and quality assurance and quality control, required to meet a given system reliability objective. Ultimately, if sufficient reliability of the off-shore mechanical structures would be implemented, recovery of strings for repair could be completely abandoned in the 10-years lifetime of such a large neutrino observatory. Incidentally, this would put a sea-water neutrino observatory on the same footing as AMANDA, where repair of the structures, embedded in ice, are impossible by design.

## X. A KM<sup>3</sup> NEUTRINO OBSERVATORY

Here, I discuss a possible structure of a large neutrino observatory, shown in Figure 4. A hundred strings that each comprise 25 storeys, equipped with 2 Photo Sensors, are arranged in a network where rows of strings are fed by two Junction Boxes/ Communication Nodes. There is a total of 2\*48 optical fibres and the necessary copper wires available that can service a maximum of 2\*48\*128 PMs. Electrical power and optical-fibre routing is arranged in a ring network that can be configured (e.g. with optical cross connects) in such a way that system reliability of the optical/electrical network will be optimal. Clearly, extensive cost/reliability engineering will be needed to optimise detector availability.

A cost estimate can be made for the large neutrino observatory under consideration here, based on the costing of the current ANTARES detector and taking into account the costing of the One PM-One Colour readout as explained above. Let the detector be partitioned in the following sub systems – 1. String ( Float, BSS, SCM/SPM, Interconnecting Link, Beacons, Acoustics), 2. Storey ( Support Structure, OMs, MLCM, Instrumentation, EMC), Junction Box, MEOC, Router and Computer Farm. Base line cost figures for these sub systems in case of the large detector are: String – 145 kEuro, Storey – 14.5 kEuro, JB - 800 kEuro, MEOC – 2200 kEuro, Router/Computer Farm 1500 kEuro. Total cost of a 100-string detector comprising 5000 PMs – 100\*145+2599\*14.5+1600+4400+1500= 58.25 Meuro. Cost of the 10 calibration/instrumentation strings, sea operations, shore station and infrastructures are to be added to this amount.

Note that the cost of sea operations, associated with launching and connecting strings, depends very much on the ROV arrangements available. If a ROV would be purchased, the cost of launching and connecting one string would be ~ 50 kEuro.

## XI. SUMMARY AND CONCLUSIONS

I have described an approach to the design of a large neutrino observatory that has the objective to minimise the complexity of the off-shore electronics by applying (standard) multi-colour DWDM techniques. The benefits of such an approach are rather substantial - simplified system engineering, the effort required in Quality Assurance and Quality Control strongly reduced and a smaller cost per Photo Sensor channel, compared with that of the current ANTARES design. The costing of DWDM components may well turn out to be conservative because of a reduction of cost of components due to the foreseen growth of Metropolitan Area Networks. If sufficient reliability of the off-shore mechanical structures would be implemented, ultimately, recovery of strings for repair could be completely abandoned in the 10-years lifetime of a large neutrino observatory.

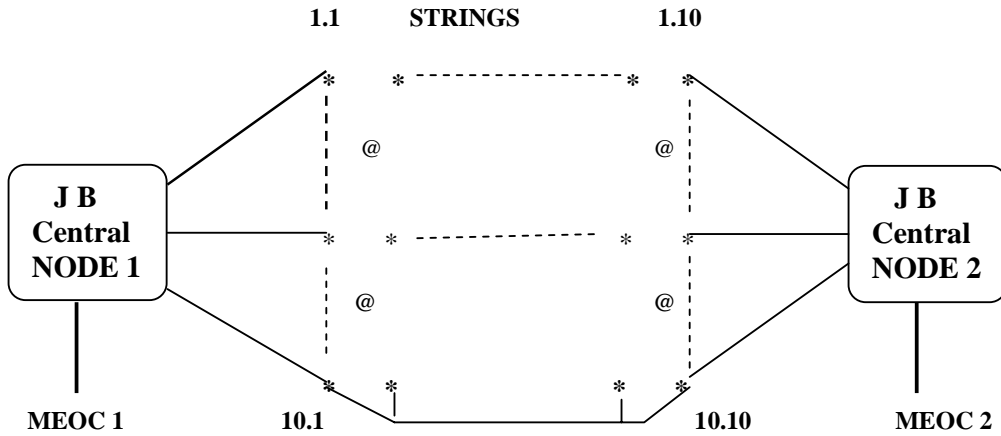


Fig 4 : Layout of a conceptual design of a km neutrino observatory comprising 100 strings with 50 Photo Sensors each, arranged in a ring network topology where the bases of detector strings in a row are linked together by a daisy chain. Instrumentation/calibration strings labelled '@' are interspersed with event-tracking strings.





# List of Participants



## LIST OF PARTICIPANTS

<p><b>Abich, Gerald</b> Nautilus Marine Service GmbH Blumethalstrasse 15 Bremen D-28209 Germany <a href="mailto:g.abich@nautilus-gmbh.de">g.abich@nautilus-gmbh.de</a></p>	<p><b>Belolapstikov, Igor</b> JINR Jolio Curie 6 Dubna 141980 Russia <a href="mailto:belolap@nu.jinr.ru">belolap@nu.jinr.ru</a></p>
<p><b>Aicher, Peter</b> Hamamatsu Photonics 314-5, Shimokanzo, Toyooka mura, Iwata gun Shizuoka 438-0193 Japan</p>	<p><b>Bernardini, Elisa</b> DESY Platanen Allee 6 Zeuthen 15738 Germany <a href="mailto:bernardi@ifh.de">bernardi@ifh.de</a></p>
<p><b>Ameli, Fabrizio</b> INFN - Sezione di Roma1 Ple. Aldo Moro 5 Rome 185 Italy <a href="mailto:fabrizio.ameli@roma1.infn.it">fabrizio.ameli@roma1.infn.it</a></p>	<p><b>Bersani, Andrea</b> INFN Genova via Dodecaneso 33 Genova 16162 Italy <a href="mailto:Andrea.Bersani@ge.infn.it">Andrea.Bersani@ge.infn.it</a></p>
<p><b>Anassontzis, Efstratios (Stratos)</b> University of Athens Physics Department Nuclear and Particle Physics Section Ilissia GR – 15771 Greece <a href="mailto:eanason@cc.uoa.gr">eanason@cc.uoa.gr</a></p>	<p><b>Brandi, Roberto</b> Sonsub S.p.A. Via Galileo Ferraris, 14 Marghera 30175 Italy <a href="mailto:roberto.brandi@sonsub.saipem.eni.it">roberto.brandi@sonsub.saipem.eni.it</a></p>
<p><b>Anghinolfi, Marco</b> INFN, Dipartimento di Fisica, Via dodecaneso 33, Genova I-16146 Italy <a href="mailto:anghi@ge.infn.it">anghi@ge.infn.it</a></p>	<p><b>Brunner, Jurgen</b> CPPM 163, avenue de Luminy Case 907 Marseille 13288 France <a href="mailto:brunner@cppm.in2p3.fr">brunner@cppm.in2p3.fr</a></p>
<p><b>Anton, Gisela</b> University of Erlangen Physikalisches Institut Erwin-Rommel-Str. 1 Erlangen D-91058 Germany <a href="mailto:Anton@Physik.Uni-Erlangen.de">Anton@Physik.Uni-Erlangen.de</a></p>	<p><b>Calcara, Massimo</b> In. Naz. Geofisica e Vulc Italy</p>
<p><b>Ball, Alan E.</b> CERN, EP Division mailbox F01200 Geneva CH – 1200 Switzerland <a href="mailto:alan.ball@cern.ch">alan.ball@cern.ch</a></p>	<p><b>Calzas, Alain</b> CPPM 163 Av de Luminy F13288 Marseille France <a href="mailto:calzas@in2p3.fr">calzas@in2p3.fr</a></p>
<p><b>Becherini, Yvonne</b> Univ. of Bologna and INFN Bologna viale Bertini Pichat 6/2 Bologna 40127 Italy <a href="mailto:Yvonne.Becherini@bo.infn.it">Yvonne.Becherini@bo.infn.it</a></p>	<p><b>Carr, John</b> CPPM 163 Ave de Luminy Marseille 13288 France <a href="mailto:carr@cppm.in2p3.fr">carr@cppm.in2p3.fr</a></p>

<p><b>Circella, Marco</b>  INFN Bari  via Amendola 173  Bari  70126 Italy  <a href="mailto:marco.circella@ba.infn.it">marco.circella@ba.infn.it</a></p>	<p><b>De Vita, Raffaella</b>  INFN Genova  via Dodecaneso 33  Genova  16162 Italy</p>
<p><b>Cocimano, Rosanna</b>  INFN - LNS  Via Santa Sofia n°62  Catania  95100 Italy  <a href="mailto:cocimano@lns.infn.it">cocimano@lns.infn.it</a></p>	<p><b>de Wolf, Els</b>  NIKHEF  PO box 41882  Amsterdam  1009 DB Netherlands  <a href="mailto:e.dewolf@nikhef.nl">e.dewolf@nikhef.nl</a></p>
<p><b>Confalonieri, Laura</b>  Hamamatsu Photonics  314-5, Shimokanzo,  Toyooka mura,  Iwata gun  Shizuoka  438-0193 Japan</p>	<p><b>de Witt Huberts, Peter</b>  NIKHEF  PO Box 41882  Amsterdam  1009 DB Netherlands  <a href="mailto:pdwh@nikhef.nl">pdwh@nikhef.nl</a></p>
<p><b>Coyle, Paschal</b>  CPPM  163 Avenue de Luminy  Marseille  cedex 09  France  <a href="mailto:coyle@cppm.in2p3.fr">coyle@cppm.in2p3.fr</a></p>	<p><b>Dzhilkibaev, Zhan-Arys</b>  Institute for Nuclear Research  60th October Anniversary pr. 7a  Moscow  117319 Russia  <a href="mailto:djilkib@ifh.de">djilkib@ifh.de</a></p>
<p><b>Cuneo, Stefano</b>  INFN-Genova  Via Dodecaneso 33  Genova  16146 Italy  <a href="mailto:cuneo@ge.infn.it">cuneo@ge.infn.it</a></p>	<p><b>Flaminio, Vincenzo</b>  Pisa University and INFN-Pisa  Via F. Buonarroti 2  Pisa  56100 Italy  <a href="mailto:vincenzo.flaminio@cern.ch">vincenzo.flaminio@cern.ch</a></p>
<p><b>D'Amico, Antonio</b>  Laboratori Nazionali del Sud - INFN  Via Libertà,30  Ramacca  95040 Italy  <a href="mailto:antonio.damico@ieee.org">antonio.damico@ieee.org</a></p>	<p><b>Flyckt, Ezzo</b>  Photonis  BP520 Avenue Roger Roncier  Brive  FR-19106 France  <a href="mailto:so.flyckt@photonis.com">so.flyckt@photonis.com</a></p>
<p><b>de Jong, Maarten</b>  NIKHEF  PO Box 41882  Amsterdam  1009 DB Netherlands  <a href="mailto:mjg@nikhef.nl">mjg@nikhef.nl</a></p>	<p><b>Giunta, Michele</b>  INFN-Pisa  Via F. Buonarroti, 2  Pisa  56100 Italy  <a href="mailto:michele.giunta@pi.infn.it">michele.giunta@pi.infn.it</a></p>
<p><b>De Marzo, Carlo N.</b>  University and INFN - Bari  Dipartimento Fisica - via Amendola 173  Bari  70126 Italy  <a href="mailto:demarzo@ba.infn.it">demarzo@ba.infn.it</a></p>	<p><b>Gualdesi, Lavinio</b>  Saclantcen  V.le S. Bartolomeo 400  La Spezia  19121 Italy  <a href="mailto:gualdesi@libero.it">gualdesi@libero.it</a></p>

<p><b>Hall, Kevin</b>  SEACON (Europe) LTD  Seacon House, Hewett road,  Gapton Hall Industrial, Estate  Great Yarmouth  NR31 0RB NORFOLK  United Kingdom  <a href="mailto:kevin@seaconeurope.com">kevin@seaconeurope.com</a></p>	<p><b>Kappes, Alexander</b>  Univ. Erlangen, Phys. Inst.  Erwin-Rommel-Str. 1  Erlangen  91058 Germany  <a href="mailto:kappes@physik.uni-erlangen.de">kappes@physik.uni-erlangen.de</a></p>
<p><b>Hallewell, Greg</b>  CPPM, Faculte des Sciences de Luminy  163 Avenue de Luminy, Case 907  Marseille  13288 France  <a href="mailto:greggh@cppm.in2p3.fr">greggh@cppm.in2p3.fr</a></p>	<p><b>Karg, Timo</b>  University of Erlangen  Erwin-Rommel-Strasse 1  Erlangen  91058 Germany  <a href="mailto:timo.karg@physik.uni-erlangen.de">timo.karg@physik.uni-erlangen.de</a></p>
<p><b>Heine, Eric</b>  NIKHEF  POB 41882  Amsterdam  1009 DB Netherlands  <a href="mailto:erichn@nikhef.nl">erichn@nikhef.nl</a></p>	<p><b>Katz, Ulrich</b>  Univ. Erlangen, Phys. Inst.  Erwin-Rommel-Str. 1  Erlangen  91058 Germany  <a href="mailto:katz@physik.uni-erlangen.de">katz@physik.uni-erlangen.de</a></p>
<p><b>Hernandez-Rey, Juan-Jose</b>  IFIC - Valencia  Universidad de Valencia  Investigacion de Paterna, apdo. 22085  Valencia  E-46071 Spain  <a href="mailto:Juan.J.Hernandez@ific.uv.es">Juan.J.Hernandez@ific.uv.es</a></p>	<p><b>Kooijman, Paul</b>  NIKHEF  Kruislaan 409  Amsterdam  1097 SJ Netherlands  <a href="mailto:h84@nikhef.nl">h84@nikhef.nl</a></p>
<p><b>Hoessl, Juergen</b>  Physikalisches Institut  Erwin-Rommel-Strasse 1  Erlangen  D – 91058 Germany  <a href="mailto:Hoessl@physik.uni-erlangen.de">Hoessl@physik.uni-erlangen.de</a></p>	<p><b>Kouchner, Alain</b>  Dapnia, Bat 141-piece 50  Orme des Merisiers  91191 Gif sur Yvette Cedex  France  <a href="mailto:kouchner@cea.fr">kouchner@cea.fr</a></p>
<p><b>Hogenbirk, Jelle</b>  NIKHEF  Postbus 41882  Amsterdam  1009 DB Netherlands  <a href="mailto:jelle@nikhef.nl">jelle@nikhef.nl</a></p>	<p><b>Kostarakis, Panagiotis</b>  University of Ioannina  Ioannina  Greece  <a href="mailto:pkost@cc.uoi.gr">pkost@cc.uoi.gr</a></p>
<p><b>Hundertmark, Stephan</b>  Stockholm Universtitet  Roslagstullsbacken 21  Stockholm  10691 Sweden  <a href="mailto:Stephan.Hundertmark@physto.se">Stephan.Hundertmark@physto.se</a></p>	<p><b>Kruijer, Lex</b>  NIKHEF  Kruislaan 409  Amsterdam  1098 SJ Netherlands  <a href="mailto:lexk@nikhef.nl">lexk@nikhef.nl</a></p>
<p><b>Jenkins, David</b>  Ocean Design, Inc.  9 Aviator Way  Ormond Beach  32174 Florida  USA  <a href="mailto:djenkins@oceandesigninc.com">djenkins@oceandesigninc.com</a></p>	<p><b>Lamare, Patrick</b>  CEA Saclay, DAPNIA/SEDI bat 534  Gif sur Yvette  91191 France  <a href="mailto:plamare@cea.fr">plamare@cea.fr</a></p>

<p><b>Lancaster</b>, Phil Alcatel / Neptune Christchurch way Greenwich London SE10 0AG United Kingdom <a href="mailto:phil.lancaster@asn.alcatel.co.uk">phil.lancaster@asn.alcatel.co.uk</a></p>	<p><b>Margiotta</b>, Annarita Univ. of Bologna and INFN Bologna Dipartimento di Fisica - viale C. Berti Pichat, 6/2 Bologna 40127 Italy <a href="mailto:margiotta@bo.infn.it">margiotta@bo.infn.it</a></p>
<p><b>Le Provost</b>, Herve C.E.A Centre d'Etudes de Saclay GiF-sur-Yvette 91 191 France <a href="mailto:h.leprovost@cea.fr">h.leprovost@cea.fr</a></p>	<p><b>Migneco</b>, Emilio LNS-INFN Via S.Sofia 64 Catania 95123 Italy</p>
<p><b>Le Van Suu</b>, Auguste CPPM 163, Avenue de LUMINY Marseille 13288 France <a href="mailto:levansuu@cppm.in2p3.fr">levansuu@cppm.in2p3.fr</a></p>	<p><b>Montaruli</b>, Teresa Universita' di Bari and INFN Via Amendola 173 Bari 70126 Italy <a href="mailto:montaruli@ba.infn.it">montaruli@ba.infn.it</a></p>
<p><b>Legou</b>, Thierry CNRS/IN2P3/CPPM case 907 163 Avenue de Luminy Marseille 13288 France <a href="mailto:legou@cppm.in2p3.fr">legou@cppm.in2p3.fr</a></p>	<p><b>Moussant</b>, Cyril Photonis Avenue Roger Roncier Brive FR-19106 France</p>
<p><b>Leisos</b>, Antonis Hellenic Open University Patras Greece <a href="mailto:leisos@nestor.org.gr">leisos@nestor.org.gr</a></p>	<p><b>Musumeci</b>, Mario INFN-LNS Via S.Sofia, 62 Catania 95123 Italy <a href="mailto:musumeci@Ins.infn.it">musumeci@Ins.infn.it</a></p>
<p><b>Lo Presti</b>, Domenico Catania University Via S. Sofia, 54 95120 Catania Italy <a href="mailto:Domenico.lopresti@ct.infn.it">Domenico.lopresti@ct.infn.it</a></p>	<p><b>Nicolau</b>, Carlo Alessandro INFN LabG18, Edificio E. Fermi (Nuovo Edificio dipartimento di Fisica), P.le Aldo Moro, 2 Rome 185 Italy <a href="mailto:carlo.nicolau@tin.it">carlo.nicolau@tin.it</a></p>
<p><b>Louis</b>, Frederic CEA DAPNIA / SEDI BAT 123 / Room 17 Gif su Yvette 91191 France <a href="mailto:flouis@cea.fr">flouis@cea.fr</a></p>	<p><b>Occhipinti Amato</b>, Rosario INFN - LNS Via S. Sofia N°62 Catania 95125 Italy <a href="mailto:occhipinti@Ins.infn.it">occhipinti@Ins.infn.it</a></p>
<p><b>Lubsandorzhev</b>, Bayarto Institut for Nuclear Research of RAS pr-t 60-letiya Oktyabrya 7A Moscow 117312 Russia <a href="mailto:lubsand@pcbai10.inr.ruhep.ru">lubsand@pcbai10.inr.ruhep.ru</a></p>	<p><b>Panman</b>, Jaap CERN Geneva Switzerland <a href="mailto:jaap.panman@cern.ch">jaap.panman@cern.ch</a></p>

<p><b>Peek, Henk</b>          NIKHEF          PB 41882          Amsterdam          1009 DB Netherlands  <a href="mailto:henkp@nikhef.nl">henkp@nikhef.nl</a></p>	<p><b>Rose, Joachim</b>          University of Leeds          Department of Physics and Astronomy          Leeds          LS2 9JT United Kingdom  <a href="mailto:h.j.rose@leeds.ac.uk">h.j.rose@leeds.ac.uk</a></p>
<p><b>Piattelli, Paolo</b>          Laboratori Nazionali del Sud, INFN          Via S. Sofia 44          Catania          95123 Italy  <a href="mailto:Piattelli@lns.infn.it">Piattelli@lns.infn.it</a></p>	<p><b>Ruppi, Martino</b>          INFN Bari          via Amendola 173          Bari          70126 Italy</p>
<p><b>Racca, Chantal</b>          IReS Strasbourg          23 rue du Loess          Strasbourg          F 67037 Strasbourg cedex 02          France  <a href="mailto:racca@in2p3.fr">racca@in2p3.fr</a></p>	<p><b>Sapienza, Piera</b>          LNS-INFN          Via S.Sofia 64          Catania          95123 Italy</p>
<p><b>Raia, Guido</b>          INFN-LNS          Catania          95123 Italy  <a href="mailto:raia@lns.infn.it">raia@lns.infn.it</a></p>	<p><b>Schlenstedt, Stefan</b>          DESY Zeuthen          Platanenallee 6          Zeuthen          15735 Germany  <a href="mailto:stefan.schlenstedt@desy.de">stefan.schlenstedt@desy.de</a></p>
<p><b>Reito, Santo</b>          INFN Catania          Via S. Sofia, 54          95120 Catania          Italy  <a href="mailto:Santo.reito@ct.infn.it">Santo.reito@ct.infn.it</a></p>	<p><b>Sedita, Mario</b>          INFN-LNS          Via S. Sofia 44          Catania          95100 Italy  <a href="mailto:sedita@lns.infn.it">sedita@lns.infn.it</a></p>
<p><b>Resvanis, Leonidas</b>          Nestor Institute          Pylos          Greece  <a href="mailto:Leonidas.Resvanis@cern.ch">Leonidas.Resvanis@cern.ch</a></p>	<p><b>Seip, Jon Enok</b>          Nexans Norway AS          PO box 130 Økern          Østre Aker vei 33          Oslo          509 Norway  <a href="mailto:jon.seip@nexans.com">jon.seip@nexans.com</a></p>
<p><b>Riccobene, Giorgio</b>          Laboratori Nazionali del Sud INFN          Via S. Sofia 44          Catania          95123 Italy  <a href="mailto:riccobene@lns.infn.it">riccobene@lns.infn.it</a></p>	<p><b>Siotis, Ion</b>          NCSR Demokritos          Athens          Greece  <a href="mailto:siotis@inp.demokritos.gr">siotis@inp.demokritos.gr</a></p>
<p><b>Romita, Michele</b>          INFN          Via Amendola 175          Bari          70026 Italy  <a href="mailto:michele.romita@ba.infn.it">michele.romita@ba.infn.it</a></p>	<p><b>Solan, Martin</b>          University of Aberdeen          United Kingdom</p>

<p><b>Spiering, Christian</b>  DESYS Zeuthen  Platanenallee 6  Zeuthen  D 15738 Germany  <a href="mailto:csspier@ifh.de">csspier@ifh.de</a></p>	<p><b>Tzamaris, Spyros</b>  Hellenic Open University  Patras  Greece  <a href="mailto:tzamaria@eap.gr">tzamaria@eap.gr</a></p>
<p><b>Steffen, Peter</b>  DESYS  Zeuthen  Germany  <a href="mailto:steffep@mail.ifh.de">steffep@mail.ifh.de</a></p>	<p><b>Van der Hoek, Mark</b>  BAAS R&amp;D-Coenecoop  The Netherlands</p>
<p><b>Stubberfield, Ron</b>  Electron Tubes Ltd  Middlesex  United Kingdom</p>	<p><b>Valdy, Pierre</b>  IFREMER  Zone portuaire de Bregailon  La Seyne sur Mer  83500 France  <a href="mailto:Pierre.Valdy@ifremer.fr">Pierre.Valdy@ifremer.fr</a></p>
<p><b>Sulak, Lawrence</b>  CPPM Marseille  163 Ave. de Luminy, Case 907  Marseille  F-13288 France  <a href="mailto:sulak@cppm.in2p3.fr">sulak@cppm.in2p3.fr</a></p>	<p><b>Vernin, Pascal</b>  CEA-Saclay  SPHN-CE Saclay  Gif sur Yvette  91191 France  <a href="mailto:pvernin@cea.fr">pvernin@cea.fr</a></p>
<p><b>Taiuti, Mauro</b>  Istituto Nazionale Fisica Nucleare  Via Dodecaneso, 33  Genova  I-16142 Italy  <a href="mailto:taiuti@ge.infn.it">taiuti@ge.infn.it</a></p>	<p><b>White, Richard</b>  University of Leeds  Physics and Astronomy Department  University of Leeds  Leeds  LS2 9JT United Kingdom  <a href="mailto:phy1rjw@leeds.ac.uk">phy1rjw@leeds.ac.uk</a></p>
<p><b>Thompson, Lee</b>  University of Sheffield  Hounsfield Road  Sheffield  S37RH United Kingdom  <a href="mailto:l.thompson@sheffield.ac.uk">l.thompson@sheffield.ac.uk</a></p>	<p><b>Wiebusch, Christopher</b>  University of Wuppertal  Gausstrasse 20  Wuppertal  42119 Germany  <a href="mailto:wiebusch@physik.uni-wuppertal.de">wiebusch@physik.uni-wuppertal.de</a></p>
<p><b>Thumbek, Steven</b>  Ocean Design, Inc  9 Aviator Way  Ormond Beach  32118 Florida  USA  <a href="mailto:stthumbek@oceandesigninc.com">stthumbek@oceandesigninc.com</a></p>	<p><b>Wright, Tony</b>  Electron Tubes Ltd  Middlesex  United Kingdom</p>
<p><b>Tsirigotis, Apostolos</b>  Hellenic Open University  Patras  Greece  <a href="mailto:tsirigotis@nestor.org.gr">tsirigotis@nestor.org.gr</a></p>	<p><b>Yoshizawa, Yuji</b>  Hamamatsu Photonics  314-5, Shimokanzo,  Toyooka mura,  Iwata gun  Shizuoka  438-0193 Japan  <a href="mailto:yosizawa@etd.hpk.co.jp">yosizawa@etd.hpk.co.jp</a></p>



<p><b>Zaborov, Dmitry</b> Institute for Theor. And Exp. Physics B. Cheremushkinskaja, 25, 117259 Moscow, Russia <a href="mailto:zaborov@itep.ru">zaborov@itep.ru</a></p>	
--	--